Universidad Autónoma de Madrid
Facultad de Ciencias Físicas
Departamento de Física Teórica

LEGACIES OF THE DUST

A multiwavelength study of protoplanetary disks and young exoplanetary systems

Ignacio Bustamante Bengoechea
Madrid, 2017

Universidad Autónoma de Madrid
Facultad de Ciencias Físicas

(Departamento de Física Teórica)

LEGACIES OF THE DUST

A multiwavelength study of protoplanetary disks and young exoplanetary systems

Dirigido por el **Dr. Bruno Merín** y el **Dr. Hervé Bouy**

Memoria presentada por
Ignacio Bustamante Bengoechea
para aspirar al grado de
Doctor en Ciencias Físicas

Madrid, Abril 2017

As for me, I am tormented with an everlasting itch for things remote. I love to sail forbidden seas, and land on barbarous coasts.

- Herman Melville, *Moby Dick*

I am driven by two main philosophies: know more today about the world than I knew yesterday and lessen the suffering of others. You'd be surprised how far that gets you.

- Neil deGrasse Tyson

I see the ghosts of navigators, but they are lost
As they sail into the sunset, they'll count the cost
As their skeletons accusing, emerge from the sea
The sirens of the rocks, they beckon me
Take my heart and set it free, carried forward by the waves
Nowhere left to run, navigator's son,
Chasing rainbows all my days
Where I go I do not know, I only know the place I've been
Dreams they come and go, ever shall be so,
Nothing's real until you feel

- Iron Maiden, *Ghost of the navigator*

(*El camarero limpia un vaso con el trapo. Es tarde. El único cliente, un joven sentado en la barra, con un café a su lado. Escribe. El camarero, aburrido, se acerca.*)

CAMARERO: ¿Escritor?

(*El joven, distraído, levanta la mirada del papel. Unas pocas líneas es lo único escrito.*)

JOVEN: ¿Cómo?

C: ¿Que si es usted escritor?

J: Ehm, no. Escritor no. Científico.

C: Ah. (*Pausa*) ¿Científico de qué?

J: Astrofísico.

C: Oh. (*Pausa*) ¿Estrellas y galaxias y planetas y demás?

J: Exacto.

C: Ah. (*Pausa*) ¿Y qué escribe?

J: Mi tesis doctoral.

C: Oh. (*Pausa*) Eso es muy difícil, ¿no?

J: Como todo. Si te gusta, no es difícil. Aunque esta parte es la más complicada de todas.

C: ¿Qué parte? ¿La introducción?

J: No.

C: ¿Resultados?

J: Tampoco.

C: ¿Las conclusiones, tal vez?

J: (*Niega con la cabeza*) Mhm. No.

C: Entonces, ¿cuál?

J: ¡Los agradecimientos!

C: Oh. Pensaba que eso sería fácil.

J: Pues no. Todo lo contrario.

C: Bueno, todo es empezar. Y veo que ya ha empezado.

J: Sí, pero no sé cómo continuar.

C: (*Señala con la mano.*) ¿Puedo?

J: (*Da la vuelta al papel y se lo acerca*) Claro.

C: (*Se aclara la garganta. Lee en voz alta*) "Cómo suele decirse,'si he visto más lejos es porque estoy sentado sobre los hombros de gigantes.'. En mi caso, me senté sobre los hombros de cinco gigantes, sin los cuáles este trabajo no habría sido posible, y a los que aprovecho estas líneas para agradecer su apoyo a lo largo de esta tesis."

(*Levanta la mirada*) Suena bien.
J: Gracias.
C: (*Continúa*) "En primer lugar, a mis co-directores de tesis, Bruno y Hervé. Lo más fácil sería agradeceros la oportunidad que me disteis para realizar la tesis con vosotros, aunque me quedaría corto. Muy corto. 'Si tienes buen director, tienes la mitad de la tesis hecha', alguien me dijo al empezar. Esa proporción no os hace justicia. Con vuestra ayuda, apoyo, dirección y paciencia no sólo me habéis formado como investigador, sino también habéis hecho de esta tesis una aventura gratificadora y emocionante, además de estimular (¡aún más!) mi curiosidad y mis ganas de aprender cada día. Gracias." (*Mira de nuevo al joven, con una sonrisa torcida*) ¿Agradeciendo al jefe?
J: Ya. Pero no son únicamente *jefes*.
C: Ah, ya veo. (*Continua*) "En segundo lugar, a Álvaro. Por guiarme en mis primeros pasos titubeantes, por responder a todas mis preguntas estúpidas (¡que hubo muchas!), por enseñarme el valor de la *ciencia lenta*, del rigor y del trabajo duro. Aunque esto no sea, de ninguna manera, lo más importante. Gracias por los viajes de trabajo que no fueron de trabajo, las carreras, las cervezas, las conversaciones envenenadas, los cafés, el ron, los selfies robados y los regalados. Y por las cenas románticas en Budapest." (*Levanta de nuevo la mirada*) ...
J: (*Mantiene la mirada*) ...
C: .... Ehem. (*Continúa*) "En tercer lugar, a Miguel. Por tu ayuda constante e incondicional resolviendo cualquier problema o conflicto, siendo el mejor *jefe* que uno podría desear. Sin tí aún estaría ahogándome en papeles, en asuntos burocráticos, en contratos y firmas. Gracias por ser el escudo que me protegía de todo ello, que me guiaba por los laberintos empresariales, para que me preocupara únicamente de hacer ciencia. Y, también, por los mojitos Californianos." (*A continuación, lee en silencio. Mira al joven, extrañado*) Lo siguiente no está en castellano.
J: Ya. Es para una persona en California.
C: Aah. Bueno. A ver cómo se me da de bien. (*Carraspea. Lee, con una pronunciación impecable*) "And last, but not least, to Julian. Not only for giving me the opportunity to accomplish the greatest achievement of my life (so far), but also for the constant support, help, patience and guidance throughout the experience. For all the explanations and answers, always with a smile, to all my stupid questions (again, several!). For allowing me my first observing nights (even with rattlesnakes and mountain lions). But, mostly, for showing me how to do science in the most humbling, exciting and rewarding of ways."

J: Vaya, buena pronunciación.
C: (*Levanta la mirada, sonriente*) ¡Gracias! Bueno, sólo veo unas líneas más. (*Continúa leyendo*) "A todos vosotros, mis gigantes, gracias. Tanto por ser el ejemplo del científico que quiero ser, como mis mentores (y, dentro de poco, mis colegas), y, como tambíen, mis amigos." (*Devuelve el papel*) No está mal.
J: Bueno, eso es todo lo que he conseguido de momento. (*Pone el papel frente a él*)
C: Ya veo. Pero lo siguiente es bastante fácil.
J: (*Mira extrañado*) ¿Lo es?
C: ¡Claro! Pero no con esto (*Señala el café. Retira la taza y saca una botella, sin etiqueta, y dos vasos de cristal*) Lo que queda hay que escribirlo desde dentro (*Se señala el pecho con el dedo*). Con esto será más fácil (*Sirve. Ambos beben. El joven no puede evitar una mueca. El camarero sonríe*). Bien, lo primero es lo primero. La gente del trabajo, del día a día. Es muy importante acordarse de ellas y ellos.
J: (*Pensativo*) Ummm. Tiene razón. De acuerdo. (*Escribe*) "No sólo estos gigantes me han acompañado durante el doctorado. Esta tesis se ha forjado también con la ayuda y apoyo de otros compañeros en el mismo barco, sin los cuales este viaje habría sido, como poco, mucho más aburrido. Gracias a Irene, a Mario, a Alba, a Jorge, a Paco, a Bea, a Isa, a Jesús, a Julia, a Pablo y a Rúa. Por los viajes en coche, con sus conversaciones de amores y desamores, de política, de querer prohibir Telecinco. Por hacer de las comidas la mejor parte del día, por las cervezas con final incierto en bares de rock, por las conspiraciones amorosas y los viajes pendientes. Encontrar gente con el mismo desorden mental que el tuyo es encontrar un tesoro. Gracias por ser como sois. Y por el melón."
C: Bueno, no va mal la cosa.
J: Jummm, puede. Pero aún no he terminado con esta parte.
C: Ah, de acuerdo, de acuerdo.
J: (*Escribe*) "También quiero agradecer al resto de compañeros del Centro de Astrobiología que ya pasaron por el trago de la tesis hace tiempo, pero que recuerdan el esfuerzo y la exigencia que requiere, y que me apoyaron una y otra vez con sus consejos y palabras de ánimo en algún momento, a mí y al resto de doctorandos. A Miguel, a Carmen, a Albert, a Jorge, a Nuria, a Margie, a Jesús, a Sergio y Antonio, y a todos los que me dejo. Gracias por hacer del CAB el mejor lugar de trabajo que uno pudiera desear. Y en especial quiero darte las gracias, Benja, por enseñarnos a mí y a todos con tu humildad, tu sonrisa perenne y tu forma de ser, no sólo la forma con la que se debe hacer ciencia, sino cómo ser mejores personas."
C: ¿Ya está?

J: Sí. Ya está.
C: Bueno, pues ahora, el siguiente grupo. (*Sirve de nuevo. Bebe*) ¡Las amistades!
J: Cierto, cierto. (*Mira el papel, pensativo*)
C: ¿Qué ocurre?
J: Nada. Que no sé por quién empezar.
C: Bueno, no importa demasiado. Todas y todos son importantes. Y seguro que lo saben.
J: Tiene usted razón. ¿Tal vez pudiera hacerlo por lugares?
C: ¿Agradecimientos geolocalizados? ¡Me gusta! (*Se sirve de nuevo. Bebe*)
J: Bien. (*Bebe lo que queda en el vaso. Escribe*) "Mucha más gente me ha acompañado en esta aventura, unos antes, otros después, y desde diferentes lugares." (*Deja de escribir*) Aquí tengo que volver al inglés.
C: No veo ningún problema.
J: De acuerdo. (*Escribe*) "Thanks to all the people at IPAC, CalTech, JPL and, overall, NASAdena. Thanks to Sara, Emily, Calen, Rahul, Eduardo, Ricky, Li-Yen, Giusseppe, and everybody else I am missing here. For the board games, the exercise, the beers after work, the trips to discover the US together, the hikes during day and night, the concerts, the parties, the music nights. And most of all, thank you for making me feel at home when I was more than 9,000 km away from it. And for trying to convince me to come back."
C: Eso cubre un lugar, imagino.
J: Sí. Ahora, el siguiente. (*Escribe*) "Esta aventura surgió hace doce años, en Madrid. Un cruce de caminos donde me asenté, y en donde conocí gente que ahora forma parte de mi vida, ahora y para siempre. Gracias, Laura y Alberto, por hacerme sentir en familia desde el primer momento que nos conocimos. Y por seguir haciéndolo. Gracias, Raquel, Dani, Miriam (y compañía), por dejarme entrar en *vuestra* familia, a pesar del tiempo que pasamos sin vernos. Gracias, Zama, Olga, Diana y Antonio, por las noches en bares de mala muerte, el rock and roll, y los viajes insesperados. Y gracias, Jorge, Nico, Vero y Elena, por recorrer el principio de este viaje conmigo. Gracias a tod@s, por hacer un hogar de este cruce de caminos."
C: Bueno, ¿ya ha terminado?
J: No, no. Para nada. Aún queda un lugar más. El más importante, aunque sea el más lejano en el tiempo
C: Oh, de acuerdo. (*Apura el vaso. Sirve de nuevo en ambos.*)
J: (*Bebe. Escribe*) "Todo tiene un comienzo, y este viaje no es una excepción. El germen, el origen, el principio de esta aventura se gestó al Norte, en mi casa, rodeado

de otra gente que se quedó conmigo, de una forma u otra, a lo largo del viaje, y sin los cuales esto no habría sido posible. Gracias, Ane y Marta, por hacerme ver el valor de la amistad. Gracias, David, Sergio y Adrián, por ser una de las razones por las que vuelvo una y otra vez a casa. Gracias por estar ahí siempre, a pesar del tiempo y de la distancia. Y gracias, Jon, por nuestra relación cuántico-espacio-romántica-temporal, y por hacer que nuestras noches juntos sean siempre, sin excepción, memorables."

C: (*Con las mejillas sonrosadas*) Bueno, bueno, parece que ya ha acabado con las amistades.

J: Mmm, no totalmente.

C: Oh, vaya.... ¿Aún queda alguien?

J: Si... alguien...

C: Bueno, bueno, veo que no sabe qué decir, o cómo decirlo. Igual le dejo solo para que lo piense. (*Se aleja, la botella vacía en la mano.*)

J: (*Apura el vaso. Mira el papel fijamente durante unos segundos. Piensa. Escribe*) "Llegas al final de un camino, largo, difícil, casi imposible, echas la vista atrás. Ves tus huellas en la nieve. Pero no son las únicas. Junto a ellas puedes ver las de tus compañeros de viaje. Levantas la mirada, y ahí están ellas y ellos, ojos cansados, sonrientes. En ese momento sabes que no podrías haber llegado al final solo. Y, con una sola mirada, lo agradeces. Así que te miro, Ínigo, por los días de fútbol, de discusiones de cualquier tipo, por los viajes de ida y vuelta a casa, por las ideas para cambiar el mundo (que algún día conseguiremos), y por ser la constante con mis orígenes. Y te miro, Jose, por los juegos, las conversaciones sobre la vida, la familia y el amor, por ver lo mejor que había en mí (cuando ya lo había olvidado) y ayudarme a recuperarlo, y por ser la constante conmigo mismo. Y, sobre todo, te miro a tí, Patricia, por acompañarme en este viaje desde el primer momento, por estar conmigo cada día a pesar de la distancia, por compartir todos los momentos (malos, buenos y mejores), por la confianza que a veces escaseaba, por los viajes que hicimos y por los que haremos, por ser la constante con mi destino. Esta tesis es tan vuestra como mía. Gracias."

C: (*Vuelve con otra botella en la mano. La abre. Sirve a ambos*). Bueno, entonces...

J: Ya está.

C: ¿Ya está todo el mundo?

J: (*Mira la hoja, dudando*) Mmm. Creo que sí. Espero no olvidarme de nadie.

C: Bueno, si lo hace, como le digo, sabrán que es un... ¿cómo se dice? Ah, sí. Un *honest mistake*.

J: Hmmm. Eso espero. (*Mira el papel, dubitativo*)
C: ¿Qué ocurre?
J: Que falta alguien
C: Aaah, ya veo. (*Guiña un ojo*) ¿Alguien especial?
J: Exacto.
C: Bueno, entonces, ¿cuál es el problema?
J: Pues... verá.... que en castellano, no puede ser.
C: Oh. ¿Y por qué no?
J: Porque no sabe castellano.
C: ¿Inglés?
J: Meeeh.
C: ¿Entonces?
J: Polaco.
C: ¿Polaco?
J: Polaco.
C: ¡Ja! ¡Bueno, eso si que es una casualidad! (*Extiende la mano*) Déme, déme el papel.
J: Eeeeh... ¿por qué?
C: Usted démelo, confíe en mí (*Bebe hasta apurar el vaso*)
J: Em.... bueno... (*Da la vuelta al papel, dudoso*)
C: (*Coge el papel enérgicamente*) ¿Chica especial, entonces? ¿Polaca?
J: (*Aún titubeante*) Eh, sí, eso es.
C: ¿Nombre?
J: Natalia.
C: Muy bien. (*Piensa unos segundo. Escribe enérgicamente*) "Natalia, dziękuję za przyłączenie się do końca tej podróży i początku następnej. Dzięki za bycie częścią mojego wszechświata." (*Lee lo recién escrito. Asiente conforme. Lo entrega de vuelta*)
J: ¿Pero qué ha escrito?
C: Algo bonito. Confíe en mí.
J: (*Lee, confundifo*) Eeeh. Bueno.
C: Es algo romántico.
J: Si usted lo dice. (*Relee el papel*) Bueno, pues ya está.
C: (*Sorprendido*) ¿Pero está seguro de que no falta nadie?
J: (*Dubitativo*) Ehm... no... no falta nadie.
C: ¿Seguro? (*Mirando insistentemente*).

J: Eso... creo... (*Repasa el papel con la mirada*)
C: ¿No se olvida de nadie?
J: Eeeh... (*Relee el texto. Mira al camarero*)
C: (*Mira al joven intensamente, cejas levantadas*) ....
J: (*Pensativo*) ...
C: .....
J: .....¡Ostras!
C: ¡Eeee–
J: ¡La familia!
C: –quilicuá!
J: ¡Ja! Eso dice mi madre.
C: Bueno, pues ya tiene donde empezar.
J: No. No me hace falta. No tengo que pensar qué poner aquí. Está muy claro, desde el principio.
C: ¡Pero si casi se le olvida!
J: A la familia nunca se le olvida.
C: Tiene usted razón.
J: (*Apura el vaso. Escribe.*) "Y, para finalizar, lo más dulce. El postre. Los agradecimientos que mejor saben. Los más merecidos y justificados. A la gente que me ha acompañado y apoyado mucho antes de que decidiera hacer cualquier cosa que he acabado haciendo en mi vida. Y los más sencillos. A mis hermanos, por ser el ejemplo de personas que aspiro a ser en esta vida. Y a mis padres, por absolutamante todo. Sin excepción. Gracias a los cuatro, por ser los guías de mi vida."
(*El joven deja el papel en la barra. Ha terminado.*)
C: ¿Ya está?
J: Ya está.
C: Bueno, pues ahora sólo queda una cosa por hacer.
J: ¿Cuál?
C: (*Agita la botella. Apenas hay líquido dentro. Sirve el restante en los vasos vacíos. Sonríe*) ¡Brindar!
J: ¡Ja! Está bien. (*Levanta el vaso*) ¡Por los objetivos cumplidos!
C: ¡Por las aventuras venideras!
J: ¡Por las amistades!
C: ¡Por la familia!
J: ¡Por el amor!
(*Brindan*).

Izarren hautsa egun batean bilakatu zen bizigai,
hauts hartatikan uste gabean noizpait giûaden gu ernai.
Eta horrela bizitzen gera sortuz ta sortuz gure aukera
atsedenik hartu gabe, lana egiûaz goaz aurrera
kate horretan denok batera gogorki loturik gaude.

Gizonak ba du inguru latz bat menperatzeko premia,
burruka hortan bizi da eta hori du bere egia.
Ekin ta ekin bilatzen ditu, saiatze hortan ezin gelditu,
jakintza eta argia; bide ilunak nekez aurkitu
lege berriak noizpait erditu, hortan jokatuz bizia.

Gizonen lana jakintza dugu: ezagutuz aldatzea,
naturarekin bat izan eta harremanentan sartzea.
Eta indarrak ongi errotuz, gure sustraiak lurrari lotuz,
bertatikan irautea: ezaren gudaz baietza sortuz,
ukazioa legetzat hartuz beti aurrera joatea.

Ez dadukanak ongi ahi daki euketzea zein den ona,
bere premiak bete nahirik beti bizi da gizona.
Gu ere zerbait ba gera eta gauden tokitik hemendik bertan
saia gaitezen ikusten: amets eroak baztertuRikan,
sasi zikiûak behingoz erreta bide on bat aukeratzen.

Gu sortu ginen enbor beretik sortuko dira besteak,
burruka hortan iraungo duten zuhaitz-ardaska gazteak.
Beren aukeren jabe eraikiz ta erortzean berriro jaikiz
ibiltzen joanen direnak : gertakizunen indar ta argiz
gure ametsa arrazoi garbiz egiztatuko dutenak.

Eta ametsa bilakaturik egiaren antziduri
herri zahar batek bide berritik ekingo dio urduri;
guztian lana guztien esku jasoko dute sendo ta prestu,
beren bizitzen edargai; diru zakarrak bihotzik eztu,
lotuko dute gogor ta hestu haz ez dadin gizonen gain.
- Mikel Laboa, *Izarren hautsa*

A mi familia.

List of contents

List of Figures

List of Tables

Abstract

The process of planet formation is intimately related with the birth of the host star. The new born star is surrounded by a disk of dust and gas, inevitable result of the conservation of angular momentum in these initial steps of mass collapse. This disk, in turn, will evolve with its host star, feeding it matter over time by accretion streams, and dissipating as the star matures. During this dissipation, dust grains will coalesce into larger bodies, and in some cases gain enough mass as to congregate into proto-planets, which eventually will establish a new planetary system.

This process of star and planet formation, though, is still not completely understood. More data and observations are needed to set constraints to the models and theories. There is where this thesis comes into play. This work is an observational enterprise, which main goal is the identification of certain objects thought to be indications of key moments on the process of star and planet formation.

One such kind of objects are transitional disks. These objects are considered to be one of the evolutionary steps in the process of disk evolution. They present infrared excesses at long wavelengths but little to none in the near-infrared. This is interpreted as a lack of dust in the inner regions of the disk, assuming that wavelength traces dust temperature, which is roughly proportional to the distance from the host star. This could have been caused by photoevaporation or dust clearance by a companion, possibly of planetary origin. In this work several transitional disks candidates were identified in the Lupus and Ophiucus star forming regions, using data from the Herschel Space Observatory. The identification of the transitional disks in these regions opens the door to future analysis. The objects identified in this work are perfect candidates for further follow-up.

The interactions between the star and the disk are also crucial to understand the process of the formation of planets. The young star accretes gas from its protoplanetary disk, a process that contributes to the emission of highly energetic photons, in the form of X-rays or UV. These emissions, in turn, interact with the disk, modifying its evolution. This creates a circular relation, between disk-star-X-ray-disk, which effects are crucial for the evolution of an early exoplanetary system: these X-ray photons play an essential role in the evolution of early planetary atmospheres. Analyzing these interactions and the processes that rule them, then, is of the utmost importance on the study of early exoplanet atmospheres. This work analyzes the relation between the accretion rates and the X-ray emission from a sample of sources in the Orion Nebula Cluster. An anti-correlation is found between both features, similar to that present in the Taurus Molecular Clouds. This could play

a crucial role in the evolution of the potential planetary atmospheres: an orbiting exoplanet in a system that is showing ongoing accretion processes could be shielded, by the accreted stream, of the high energetic photons from the early processes of star formation. Thus, its atmosphere would evolve 'protected' from these X- ray emissions. Thus, it is key to find young exoplanet candidates in PMSs with observable accretion processes.

The last step on the analysis of young planet formation is to actually identify such young objects. Planetary systems evolve drastically over time, in such a way that to study the formation of exoplanets, one has to look at the earliest stages of this process. Thus, looking for these objects in young star forming-regions is critical. In this work, and under the frame of the Palomar Transient Factory in Orion project, 15 transiting exoplanet host candidates were identified in the region around the young 25-Ori association. Their planetary nature should be confirmed, but if they are assumed to be exoplanets, and not brown dwarf binary systems, or spots in the photosphere, their close-in orbits would suggest a Type II migration scenario. They would be Hot Jupiters, with large radii and close to their host stars, in some cases even in the process of evaporating. Given the age of the association, and the lack of infrared excess pointing towards the presence of a cirumstellar disk around the host stars, the most plausible scenario could be a disk-planet interaction during the age of the association, which ended up pushing the candidates closer to their stellar hosts.

Several objects, key in the process of stellar and planetary formation, have been identified in this thesis, more data to be taken into account to study the overall picture. The next step would be to confirm their nature, so the constraints they pose to the theories, given their nature, age and distribution, were to be settled. Thus, the need of these kind of observational enterprises, which objective is the acquisition of more data, is demonstrated.

Resumen

El proceso de formación de planetas está íntimamente relacionado con el nacimiento de la estrella anfitriona. La estrella recién nacida está rodeada por un disco de polvo y gas, resultado inevitable de la conservación del momento angular en estos primeros pasos de colapso de materia. Este disco, a su vez, evolucionará con su estrella anfitriona, alimentándola con el tiempo a través de la acreción, y disipándose a medida que la estrella madure. Durante esta disipación, los granos de polvo se unirán en cuerpos más grandes y, en algunos casos, ganarán masa suficiente como para congregarse en proto-planetas, estableciendo finalmente un nuevo sistema planetario.

Sin embargo, este proceso de formación estelar y planetaria todavía no se entiende completamente. Se necesitan más datos y observaciones para establecer restricciones a los modelos y teorías. Aquí es donde esta tesis entra en juego. Este trabajo es una iniciativa observacional, cuyo objetivo principal es la identificación de ciertos objetos que se consideran como los indicios clave en el proceso de formación de estrellas y planetas.

Uno de estos tipos de objetos son los discos de transición. Estos objetos son considerados como uno de los pasos evolutivos en el proceso de evolución del disco. Presentan excesos infrarrojos a largas longitudes de onda pero poco a ninguno en el infrarrojo cercano. Esto se interpreta como una falta de polvo en las regiones internas del disco, suponiendo que la longitud de onda traza la temperatura del polvo, que es aproximadamente proporcional a la distancia desde la estrella anfitriona. Esto puede ser causado por la fotoevaporación o la eliminación de polvo por una compañera, posiblemente de origen planetario. En este trabajo se identificaron varios candidatos de discos de transición en las regiones de formación estelar de Lupus y Ophiucus, utilizando datos del Observatorio Espacial Herschel. La identificación de los discos de transición en estas regiones abre la puerta a futuros análisis. Los objetos identificados en este trabajo son candidatos perfectos para futuras observaciones.

Las interacciones entre la estrella y el disco son también cruciales para entender el proceso de la formación de los planetas. La joven estrella acumula gas a partir de su disco protoplanetario, un proceso que contribuye a la emisión de fotones altamente energéticos, en forma de rayos X ó UV. Estas emisiones, a su vez, interactúan con el disco, modificando su evolución. Esto crea una relación circular entre disco-estrella-rayos X-disco, cuyos efectos son cruciales en la evolución del joven sistema exoplanetario: estos fotones de rayos X desempeñan un papel esencial en la evolución de las primeras atmósferas planetarias. Analizar estas interacciones y los

procesos que las gobiernan, por tanto, es de suma importancia en el estudio de las primeras atmósferas exoplanetas. Este trabajo analiza la relación entre las tasas de acreción y la emisión de rayos X de una muestra de objetos en Asociación Molecular de Orión. Se encuentró una anti-correlación entre ambas características, similar a la presente en las Nubes Moleculares de Tauro. Esto podría jugar un papel crucial en la evolución de potenciales atmósferas planetarias: un exoplaneta en órbita en un sistema que está mostrando procesos de acreción podría estar siendo protegido, gracias al material acretado, de los fotones de alta energía. Por lo tanto, su atmósfera evolucionaría "protegida" de estas emisiones de rayos X. Por ello, encontrar jóvenes candidatos de exoplanetas alrededor de PMSs con procesos de acreción observables es clave.

El último paso en el análisis de la formación de planetas jóvenes es, de hecho, identificar observacionalmente estos objetos. Los sistemas planetarios evolucionan drásticamente con el tiempo, de tal manera que para estudiar la formación de exoplanetas, uno tiene que mirar hacia las primeras etapas de este proceso. Por lo tanto, la búsqueda de estos objetos en regiones de formación estelar es fundamental. En este trabajo, y bajo el marco del proyecto "Palomar Transient Factory in Orion", se identificaron 15 candidatos a exoplanetas en la región alrededor de la joven asociación 25-Ori. Su naturaleza planetaria debe aún ser confirmada, pero si se asume que son exoplanetas, y no enanas marrones en sistemas binarios, o manchas en la fotosfera, sus órbitas cercanas sugerirían un escenario de migración de Tipo II. Serían Júpiter Calientes, con radios elevados y órbitas cercanas a sus estrellas anfitrionas, en algunos casos incluso en proceso de evaporación. Dada la edad de la asociación y la ausencia de emisión infrarroja que indicara la presencia de un disco circumestelar alrededor de las estrellas anfitrionas, el escenario más plausible para su posición orbital podría ser una interacción disco-planeta, que terminó empujando a los candidatos más cerca de sus anfitriones estelares.

Varios objetos, clave en el proceso de formación estelar y planetaria, han sido identificados en esta tesis, lo que supone más datos a tener en cuenta para estudiar la imagen global. El siguiente paso sería confirmar su naturaleza, de forma que los límites que suponen para las teorías, dada su naturaleza, edad y distribución, fueran validadas. Así, la necesidad de este tipo de iniciativas observacionales, cuyo objetivo es la adquisición de más datos, es demostrada.

Chapter 1

Introduction

The curtain opens. A cold and dark molecular cloud enters the stage, opaque, invisible to the eye. Suddenly, the light changes, and under an infrared filter, the audience can finally see. The cloud now shines, bright, its filaments, clumps, global structure, all bare. Cosmic rays and far ultra violet irradiation can not penetrate it, its inner molecules protected. It gets colder inside, a fragile equilibrium set between pressure, temperature and gravity. Then, the inevitable. Maybe an external shock wave. Maybe the internal gradients in temperature. The cloud shakes, stumbles, and implodes. The equilibrium now lost, it collapses on itself in a myriad different parts. Molecular clumps and cores start to coalesce, their temperatures rising as the gas and dust concentrate in single spots. After a short time, these spots start to shine, bright, sparks of gas that light their surroundings. A new generation of stars has appeared.

Some larger, much larger than others, they coalesce, implode, shine, bright blue, hottest, biggest of them all... and fastest. Their little brothers take their time, much fainter than them. Much, much more numerous. The view zooms in one. The molecular core surrounds the baby star, its substance flowing down onto it. Not quite directly. The dust shifts. The gas twists. It turns, and rotates, surrounds the pup, caresses it, as it takes the shape of a disk. And all the while it feeds the toddler. It does not matter. The baby star cries, the highest, the strongest it's ever gonna cry in its life. X-ray tears strike the disk that is feeding it, ultraviolet howls evaporates it. And the disk, finally, starts to undo itself.

But not in vane. It does so in its own terms. It transitions, the closest to the host breaks up, disappears, a hole emerging amid disk and star. Not entirely void, though. As it recedes further, the disk leaves part of itself behind. Small pieces of dust coalesce, unite, far from the star which is trying to destroy them. They collide with one another, get larger, evolve... and migrate. The very parental disk which saw them appear, now pushes them closer to their new holder. The disk finally submits, and gives way. The star now quiet, its new family around it, with big giant gas brothers, and little terrestrial sisters. A new planetary system has been born.

The legacies of the dust.

This work is a compendium of beginnings. As a scientist, when trying to unravel the thread in which the universe is contained, and explain the physical properties that rule it, one has to commence from the very starting point. And, in the case of stellar astrophysics, that starting point would be the birth, formation and early evolution of stars. The first moments of stellar objects, although very brief in comparison to their total life-span, are key for understanding their future evolution. These stages are guided by the most active and violent processes in the life of the star, comparable in magnitude only to its final moments and eventual death. Their development will condition the presence of a potential planetary system, with potential exoplanets in the habitable zone, with potential water in liquid form and, thus, potential emergence of life as we know it. This is why studying and understanding this particular beginning and the processes that dominate it is of the utmost importance, as it would help answer the three main questions humanity has faced since the beginning of time. Where do we come from? Where are we headed? And, maybe the most important: are we alone in this journey?

As the watchful reader has already noticed, the *beginning* of a star is comprised of many *beginnings*. In the process of being born, the star hosts a proto-planetary disk which, in turn, can evolve into an exoplanetary system which, in turn, can be comprised by diverse kinds of exoplanets which, in turn, can potentially have the right conditions for the emergence of life. Shedding some light on understanding the links that unite all these processes is the main objective of this work. Several different objects play a crucial role in this process, all of them related with each other. The identification and analysis of these objects are the cornerstones of this work.

If the signatures of the early years of formation of a star can be detected in mature systems, by studying the initial conditions in which stars are born, the final state of the potential planetary system can be directly predicted. But there are strong orbital perturbations in the development of young planetary systems (planet migration or the Late Heavy Bombardment in the early solar system, for example) that potentially would erase all signatures of the earlier status of the system. However, the early features that are measured in young star forming regions can be extrapolated, and compared with the observable status in mature stars in the same fields.

There are two approximations one can follow in the field of astrophysics, both of them intertwined. The first one follows what has been done since the beginning of time: to observe the night sky, measure the motions of the spheres, their light,

acquire the data, discover new stars, new worlds, catalog and classify them, and add more information to the wall of space knowledge for further studies. The second approximation is to go to that wall, sit in front of it and... think. To try to explain what we are seeing, finding patterns, search for theories, develop hypothesis, make models which would describe the universe. In summary, to try and find the final equation that would define all that is and all that will be. These two approaches, the observational and the theoretical, are united and one cannot follow one path without the other. Nevertheless, projects are usually defined into one of these two frames. And this work falls into the first category: it is an observational enterprise, and its main objective is to find very special types of objects that could add more information and shed some light on the developing paradigm of star and planet formation.

Thus, as an observer, one tries to make use of the best telescopes, observatories and instruments available to acquire the best data possible. In the field of star formation, where longer wavelengths of observation are needed, the past decades have opened a vast range of possibilities in that regard. With the launch of *IRAS* (Neugebauer et al. 1984), *WISE* (Liu et al. 2008), *Spitzer* (Werner et al. 2004), and *Herschel* (Pilbratt et al. 2010), the horizon of infrared studies expanded exponentially. From their start up, thousands of new objects were detected and studied, answering many of the original questions in the field of star-birth, but bringing forth many more. Like the Hydra, when a question was answered, more sprouted from its remains. The same can be applied to the field of exoplanet detection. Not so long ago, the exoplanet paradigm stated the low occurrence rate of extrasolar planets. Then, after the installation of *HARPS* and the launch of *CoRoT*, many planetary systems were observed. And finally, with the discoveries from *Kepler*, this paradigm changed irrevocably: statistically, every star in the sky has at least one planet orbiting around (Petigura et al. 2013).

The formation of planets, one of the most intriguing questions of our days, is intimately related to the formation of stars, and one cannot study the former without the latter. These processes follow an entwined time-line, a story of birth, of surgence from the void. Several main characters play an essential part towards that goal. Their tale is yarned here, the actors presented and the plot developed.

Let us begin.

1.1 Prologue - The birth of the stars

Stars are born inside molecular clouds of gas and dust which, when triggered by an external or internal event, collapse on themselves, and start to coalesce onto a nucleus that will become a proto-star, and, eventually, a fully formed star. In this process, the proto-star is surrounded by a disk of dust and gas, inevitable result of the conservation of angular momentum in these initial steps of mass collapse. This disk, in turn, evolves with its host star, feeding it matter over time by accretion streams, and dissipating as the star matures. This dissipation and eventual disappearance of the disk can be the result of several processes, such as photo evaporation by its host, or by neighboring stars, although one possibility opens the door towards the next step on our understanding of our place in the universe: the formation of exoplanets.

The molecular clouds where stars are formed are usually defined as regions bound by gravity, dispersed by internal thermal pressure, and affected by magnetic fields, turbulence and rotational effects. They present a large range of masses (10^2-10^7 $M_\odot$), and surface densities of $\sim 100 M_\odot / pc^2$ (Roman-Duval et al. 2010). To determine the timescales of star formation, one has to get an idea of the lifetimes of these molecular clouds. The range of ages taken into account spans from ∼1-5 Myr to tens of Myr (Koda et al. 2009). These times depend on the density of the molecular cloud; for larger, denser clouds, a longer lifetime would be obtained than for smaller, clearer ones. Furthermore, not all the mass of the cloud turns into stars. Also, external events, such as supernovae explotions, massive star winds, galactic potential,... etc, play a key role in the evolution of molecular clouds. Their efficiency to produce stars is about ∼0.01 (Krumholz 2011). This means that only a small fraction of the mass of the cloud turns into stars, and the rest gets dispersed into the interstellar medium. More so, the star formation process in itself also affects the life span of molecular clouds, and the efficiency of further star appearance. The early formation of massive bright type O stars may produce an inner irradiation onto the cloud, dissociating molecules by photionization and photoevaporation, and dispersing it faster (Lada 1987).

During the first stages of the formation of a star, the molecular core surrounds the soon-to-be-formed stellar object, blocking the irradiation within and without the system, and thus making it only observable in the infrared regime (Lada and Wilking 1984; Wilking et al. 1989; Kenyon et al. 1990). The rotating molecular core continues to collapse, and ∼99% of its mass ends up concentrating in the central proto-star. The rest, following the conservation of angular momentum, forms a

disk of dust and gas around the stellar core, which gets heated by the irradiation of the central object. Eventually, this irradiation starts to dissipate the disk via photoevaporation. Accreting processes of gas from the disk onto the proto-star, outflows of mass dispersed outside the system, and congregation of larger dust grains into larger bodies, or even planetesimals, end up dispersing the disk. In the end, the proto-star is surrounded by the remains of the original molecular core, denominated debris disk. During this last stage, the disk is almost depleted of mass, no gas is being accreted onto the star, and the potential planetesimals have finished forming - a new planetary system has been born, and the star begins its main-sequence phase (Williams and Cieza 2011). Fig. 1.1 summarized this process.

Throughout the steps described above the new born star suffers crucial changes in its structure and morphology. These changes are recognized by different tracers and observable features, which identification is used to classify young stellar objects (YSOs). In particular, there are two main features used in this classification method: photometric infrared excesses and spectroscopic $H\alpha$ line or UV excesses. Each one of them is used to describe a certain feature of the YSO. The infrared excess traces the presence or absence of thermally irradiated matter around the proto-star. The $H\alpha$ or UV excesses traces the accretion of gas onto the star.

The IR-based categorization defines YSOs in Class 0, I, II and III, based on the spectral index, α_{IR}, of the spectral energy distribution (SED), between 1 and 100 μm (Lada and Wilking 1984; Lada 1987). Class 0 objects show only far-IR excess in the SED: the optical and near-IR irradiation of the proto-star is blocked by the surrounding envelope of gas and dust. Only one unique contribution, that of the heated bubble of gas and dust, is present in the SED (Andre et al. 1993). In the case of Class I YSOs, the envelope surrounding the proto-star is not opaque enough to block the inner optical irradiation, and the contribution of the new photosphere is observable in the SED. The longer wavelength flux presents increasing spectral index $\alpha_{IR} > 0$. This is a tracer of the surrounding envelope around the proto-star, starting its collapse onto the core and beginning the formation of the disk. Class II objects, on the other hand, present negative spectral index. This means that the infrared excess decreases with respect to the photosphere, pointing out the presence of a disk around the proto-star. Finally, Class III objects present faint or inexistent infrared excesses in the SED; the disk has been dissipated over time, any potential exoplanet has formed already and the star will soon start its main-sequence phase (Greene et al. 1994)

This categorization methodology presents some difficulties and exceptions. As

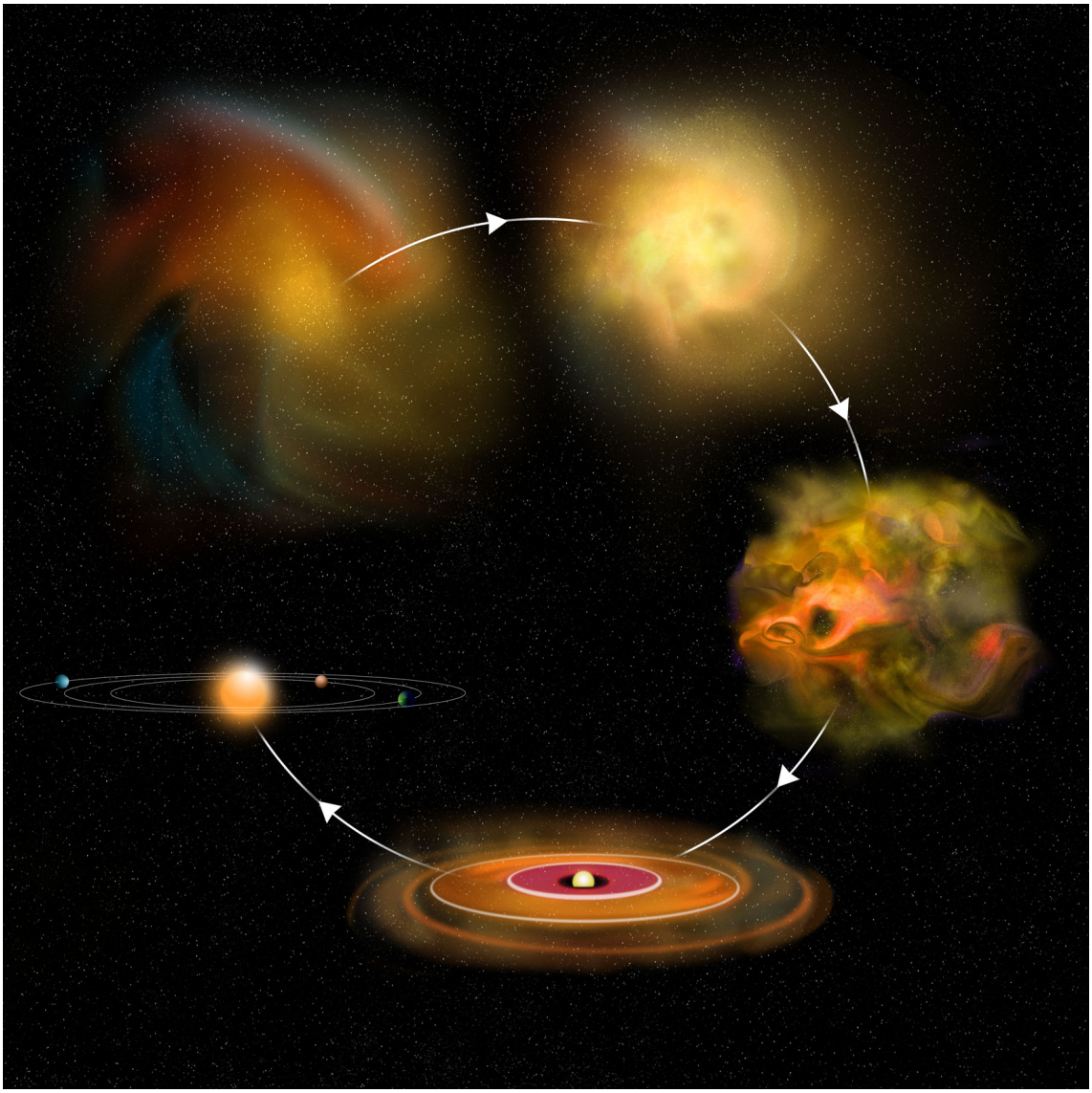

Figure 1.1: Star formation process. The molecular cloud stars to collapse, then the protostar get surrounded by a bubble of gas and dust, followed by the appearance of a disk, and finally a planetary system (CREDIT: Bill Saxton, NRAO/AUI/NSF).

can be inferred, the line of sight towards the source can affect the identification of some objects. An edge-on YSO with a disk would appear more extincted than it really is, and thus would be classified as less evolved. So Class I objects would be categorized as Class 0, and Class II as Class I (Robitaille et al. 2006). This is why other imprints are needed to ascertain the nature of these objects. Also, multi-wavelength variability and multiplicity of the sources has to be taken into account.

The $H\alpha$/UV emission-based categorization traces the presence or absence of accretion processes in the YSO, defining each one as classical T Tauri (CTTS) or weak-lined T Tauri (WTTS) stars, respectively. This classification is only viable in the case of optically observable objects; these features would not be measurable with the presence of an opaque dust and gas envelope surrounding the proto-star. Thus, they are usually identified with Class II (CTTS) and Class III (WTTS) objects from the SED classification. Historically, an equivalent width value of 10 Åwas the threshold applied to classify a YSO as CTTS or WTTS, but a mass and spectral type dependence was included, to take into account the lower continuum level of low-mass stars (Barrado y Navascués and Martín 2003; White and Hillenbrand 2003).

Fig. 1.2 shows an scheme of these classifications, and the interrelations between them.

Finally, YSOs are also differentiated because of their mass. If the star has a mass $\leq 2M_{\odot}$ it is denominated a T Tauri star. These are young pre-main sequence (PMS) stars of typical spectral types of M to F, with effective surface temperature ranging between 3000 and 7000 K. On the other hand, earlier stars are denominated Herbig Ae/Be stars, with masses $\geq 2M_{\odot}$. Different timescales and evolutionary process govern each one, and thus they should be treated separately (Joy 1945; Herbig 1962; Gray and Corbally 2009). Typical disk lifetimes are in the order of 5-10 Myr (Strom et al. 1989a; Hillenbrand 2008). These timescales refer to T Tauri stars (Haisch et al. 2001; Hernández et al. 2008). In the case of larger-mass Herbig Ae/Be, the disks dissipate faster and these timescale is reduced to $\sim$3Myr (Hernández et al. 2005). After this dissipation time, the disk has already dispersed, and only low signs of dust are detected. Accretion has halted and just warm contribution in the far-infrared and sub-mm is found. Most importantly, any potential planet has already formed.

The main characters of this story are part of the T Tauri family. Their origins are the scenery, and their evolution, the plot.

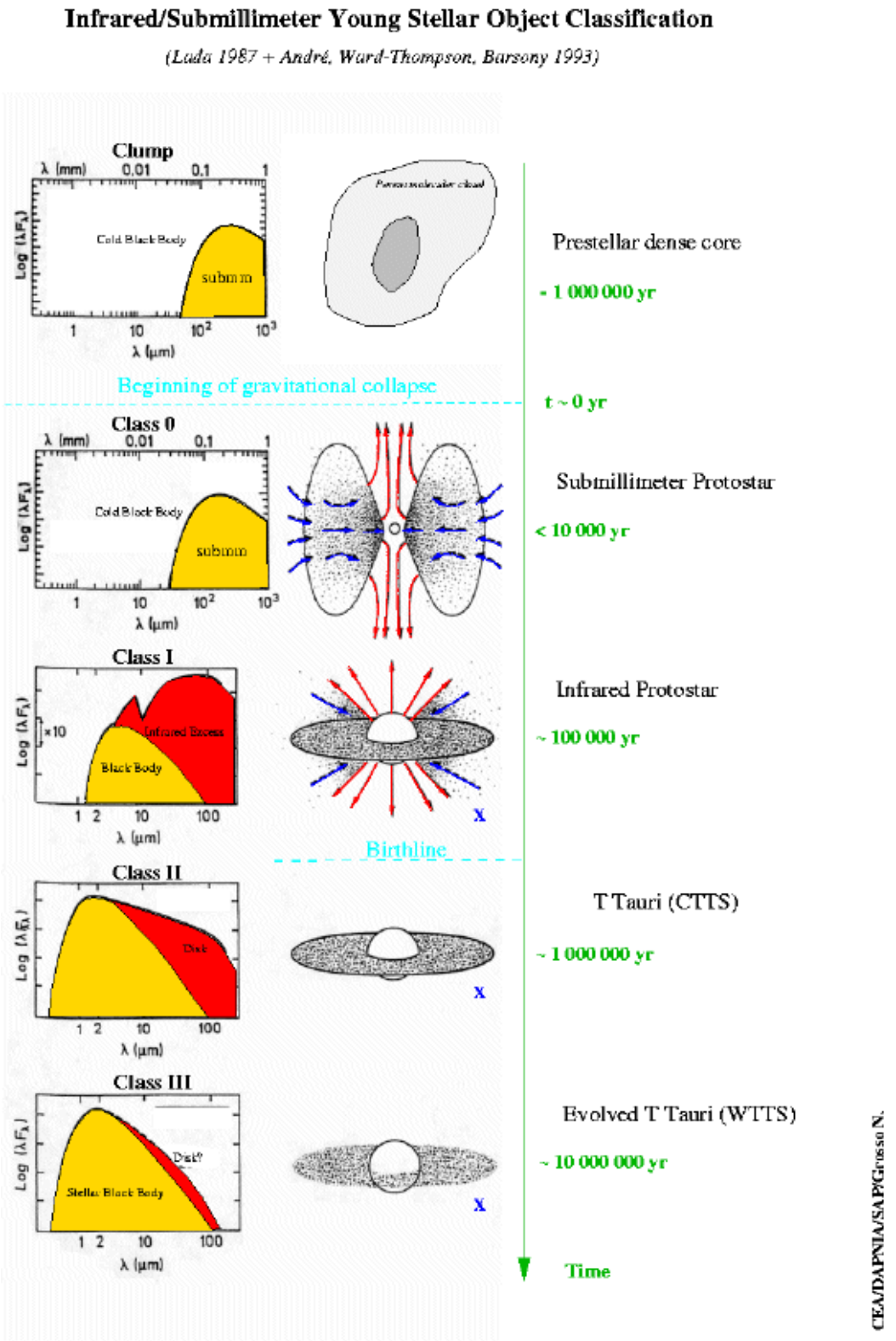

Figure 1.2: Infrared classification of YSOs. The different classes are presented, with a view of their correspondent SED morphology. Fig. from Lada 1987.

1.2 Act I - Transitional disks as cradles of planets

When studying the formation of exoplanets there is a first, crucial decision to make: where to begin? One can start from the very beginning, and focus the interest on the primordial molecular cloud, where stars are born. Another approach would be to study the distribution and properties of protoplanetary disks, paying attention to their chemistry, dynamics and evolution. Or maybe to select known evolved planetary systems and elaborate on their structure, multiplicity, distribution of masses, of radii, of transiting periods...etc. The objects selected as starting points on the evolution of planet formation are transitional disks. These objects are considered one of the evolutionary steps in the process of disk evolution, but present enough unique and particular features as to be treated as independent objects on their own right. As such, they will be the main characters of this first act.

Transitional disks (TD) were first identified by Strom et al. 1989b. Using *IRAS* photometry, they noticed some protoplanetary disks which presented infrared excesses at long wavelengths ($\lambda \geq 10$ μm) but little to none in the near-infrared ($\lambda \leq 10$ μm). This was interpreted as a lack of dust in the inner regions of the disk, assuming that wavelength traces dust temperature, which is roughly proportional to the distance from the host star. This could have been caused by photoevaporation or dust clearance by a companion, possibly of planetary origin. This discovery was understood as an evolutionary step of protoplanetary disks, and meant the identification of the missing link between young circumstellar disks and planetary systems (Calvet et al. 2002; Calvet et al. 2005; Espaillat et al. 2012).

This definition of TD, though, is a simple explanation for what is actually a quite complex kind of object. There are several different kinds of TD, analogously similar to the different kinds of T Tauris defined in the prologue. Cieza et al. 2007 introduced an SED shape classification, based on the slope of the SED from the longest wavelength dominated by the photosphere (usually 4.5 - 8 μm) and 24 μm (Muzerolle et al. 2010; Sicilia-Aguilar et al. 2010). Fig. 1.3 shows an example of each type. All of them share the large excesses at far-infrared wavelengths. The differences are found on the presence of excesses on the near- and mid- infrared regions. Classical TD present only excess at mid-infrared wavelengths and beyond (Muzerolle et al. 2010); anemic or weak-excess TD have flux decrement at mid-infrared ranges (Lada et al. 2006); cold disks present sharp rises at mid-infrared ranges (Brown et al. 2007; Merín et al. 2010); and pre-transitional disks show near-infrared excess, suggesting the presence of warm dust, optically thick, near the star

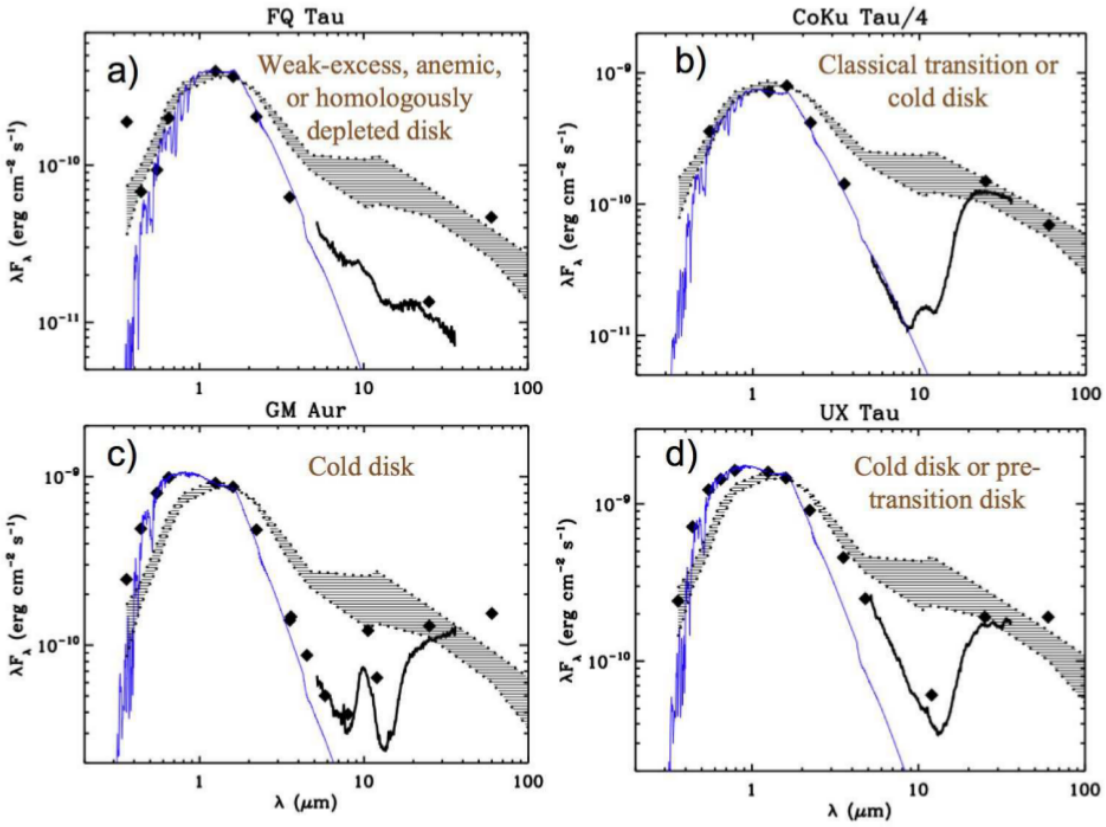

Figure 1.3: Classification of transitional disks, attending to the SED distribution. Four examples are shown, one of each type. Photometric points, *Spitzer* spectra, typical T Tauri SED and photosphere are shown. Real examples of (a) anemic disk, (b) classical TD, (c) cold disk, and (d) pre-transitional disk are shown. Fig. from Williams and Cieza 2011.

(Espaillat et al. 2007; Espaillat et al. 2010). These classifications do not account for geometric observational bias. Similarly to protoplanetary disks, the angle of observation plays a key role in the determination of the category, and has to be taken into account (Merín et al. 2010).

The next step in the analysis of TD is to derive how common they are. Determining the incidence of TD on the overall populations of protoplanetary disks suggests the time that a disk stays on this stage, and, thus, helps to set constrains on the timescales of planet formation. In the case of low-mass YSOs with disks, (Cieza et al. 2007) found a ∼10% occurrence of TD compared to the total disk sample, while Hernández et al. 2006; Hernández et al. 2007; Uzpen et al. 2009 found a lower incidence in the case of larger mass YSOs. In particular, Uzpen et al. 2009 found a ∼1% incidence of TD in a sample of intermediate-mass YSOs. This could

indicate a different evolutionary path between low-mass and large-mass YSOs. Nevertheless, be them low or large mass, the low incidence of TD found in the samples of known protoplanetary disks suggests that this stage is either uncommon, or very rapid when compared to the overall lifetime of disks (Alexander et al. 2014). If we assume the latter, disk clearing should happen in a very short time (Habing et al. 2001; Mamajek et al. 2004), with timescales from an optically thick disk to a thin one of ∼0.1 Myr (Kenyon and Hartmann 1995; Andrews and Williams 2005), ∼0.3 Myr (Skrutskie et al. 1990), or ∼0.4 Myr (Cieza et al. 2007). Fig. 1.4 presents a scheme of the general life times of protoplanetary disks, while Fig. 1.5 shows a representation of the typical life times of transitional disks. Nevertheless, these results should be taken with care. There is an inherent uncertainty in the estimation of the age of these regions, and the varied definitions of transitional disks also introduce biases in some of these identifications.

The dispersal of protoplanetary disks is crucial on the appearance of any potential planet. It is usually driven by photoevaporation of the disk at different distances and accretion of gas from the disk onto the star, but also stellar winds and close stellar encounters may play an important part in the process (Hollenbach et al. 2000; Dullemond et al. 2007; Königl and Salmeron 2011; Alexander et al. 2014). In the early stages of disk evolution, accretion dominates the dispersion of gas in the inner parts of the disk (Hartmann 1998). Fig. 1.6 shows a scheme of these processes.

But in the case of transitional disks, these dispersal processes remain unsatisfactory to explain the observations. Grain-growth, mass accretion or stellar or sub-stellar companions can not explain the observed features of transitional disks (Najita et al. 2007; Espaillat et al. 2012; Birnstiel et al. 2012; Cieza et al. 2012). Only photoevaporation and clearing by a planetary body remain as the viable options (Cieza et al. 2007; Espaillat et al. 2012; Cieza et al. 2013). And, in the case of large inner holes, photoevaporation can not account for all the mass dissipation (Owen et al. 2011). Thus, the presence of a planet of sufficient mass remains as the most plausible explanation (Espaillat et al. 2012).

Once it has been settled that the dispersion of the inner region of the disk in TDs is most probably caused by planet formation, the last key feature is to analyze the sizes of this gap, and check if they are compatible with the sizes of planetary systems. These gaps span from a few to tens of AU (Skrutskie et al. 1990; Cieza et al. 2007; Sicilia-Aguilar et al. 2010; Andrews et al. 2011; Khalafinejad et al. 2016). In particular, (Kim et al. 2009) and (Kim et al. 2013) obtained inner disk gaps of sizes ranging from ∼4 to ∼150AU, by fitting *Spitzer* IRS to different disk

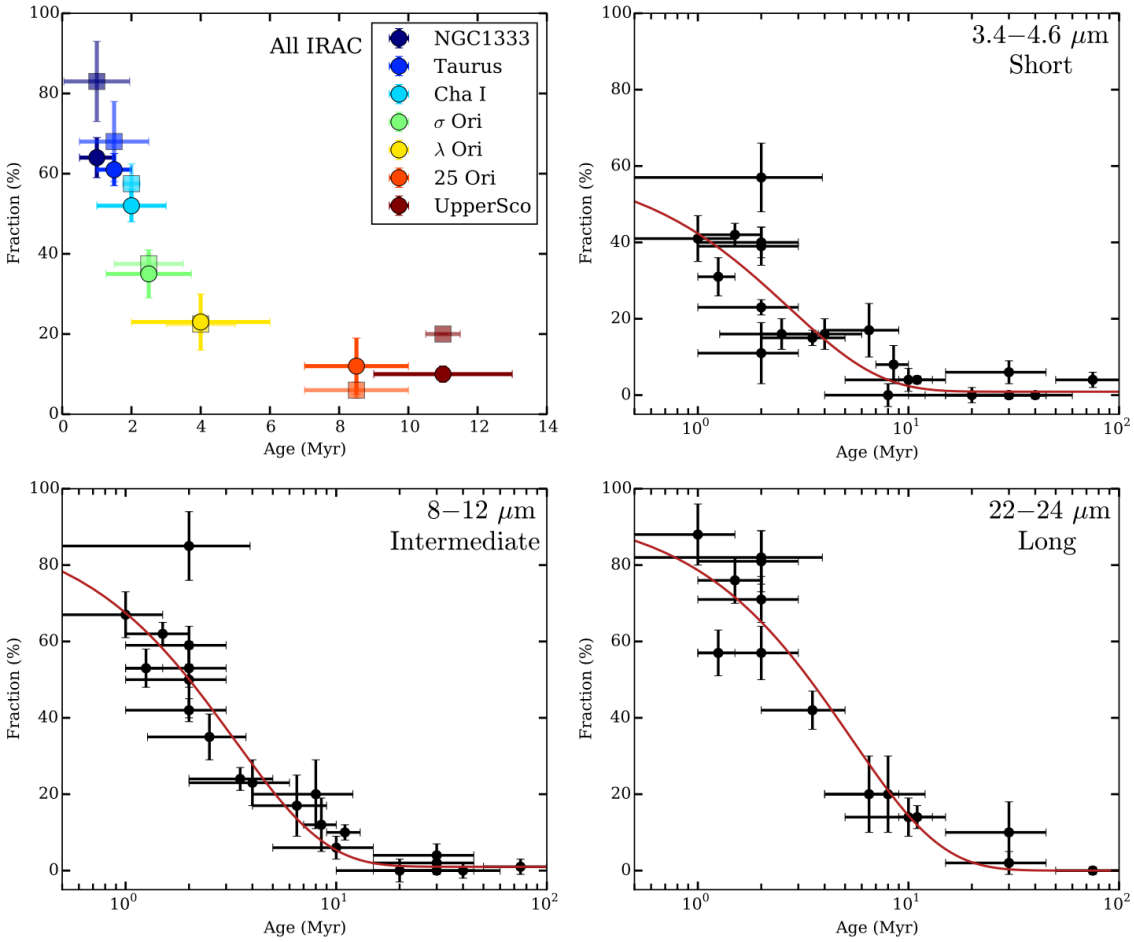

Figure 1.4: Upper left panel: disks fractions versus age, on several star-forming regions. Rest of the panels: disks fractions versus age, for the same regions, at near-, mid- and long-infrared wavelengths. An exponential law, representing the disk lifetimes behavior, is included. Fig. from Ribas et al. 2014.

models.

Albeit recent observations of transitional disks suggesting ongoing planet formation, detecting exoplanets around young optically thick protoplanetary disks, at the timescales when the planets are thought to be formed, remains elusive. The tracers of this process can be detected, though, via perturbations on the disk caused by the planet in formation, like dust traps, gas gaps and cavities in the disk. (Kraus and Ireland 2012; van der Marel et al. 2013; van der Marel et al. 2016) (Fig. 1.7). The planet can sculpt the disk and play a role in the evolution of dust grains and gas dispersion.

Now the story jumps forward in time, towards the next step: the identification

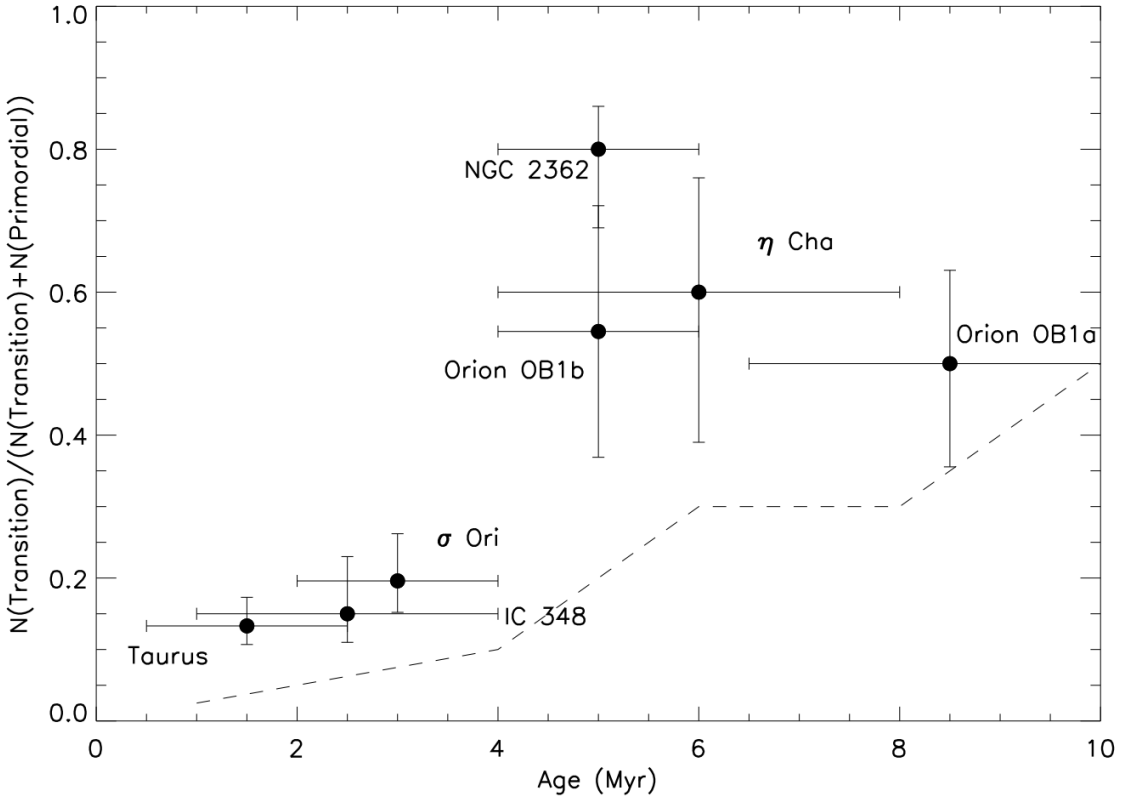

Figure 1.5: Frequency of transitional disks versus time, for several star-forming regions, for stars between 0.5-1.4 $M_{\odot}$. The dashed line represent the theoretical frequency predictions by Armitage 2009, assuming a transitional timescale of 0.5Myr. The higher frequency observed for all clusters suggests a larger transitional timescale. Fig. from Currie 2010.

of exoplanets around young disk-less stars.

1.3 Act II - Young exoplanets, the missing link

There is still much to know about exoplanets during the first years after their formation and possible migration (see Armitage 2009 for a review on the topic). Detecting new young planetary bodies provides constraints on the theories of planet formation, migration and evolution. The most widely spread way of detecting planets is the transit method (Fig. 1.8). But the cool dust surrounding the star in circumstellar systems makes it difficult to differentiate the eclipses caused by a transiting exoplanet from those of the disk. For this reason, the next best option is to look for planets around young stars, but those whose protoplanetary disk have

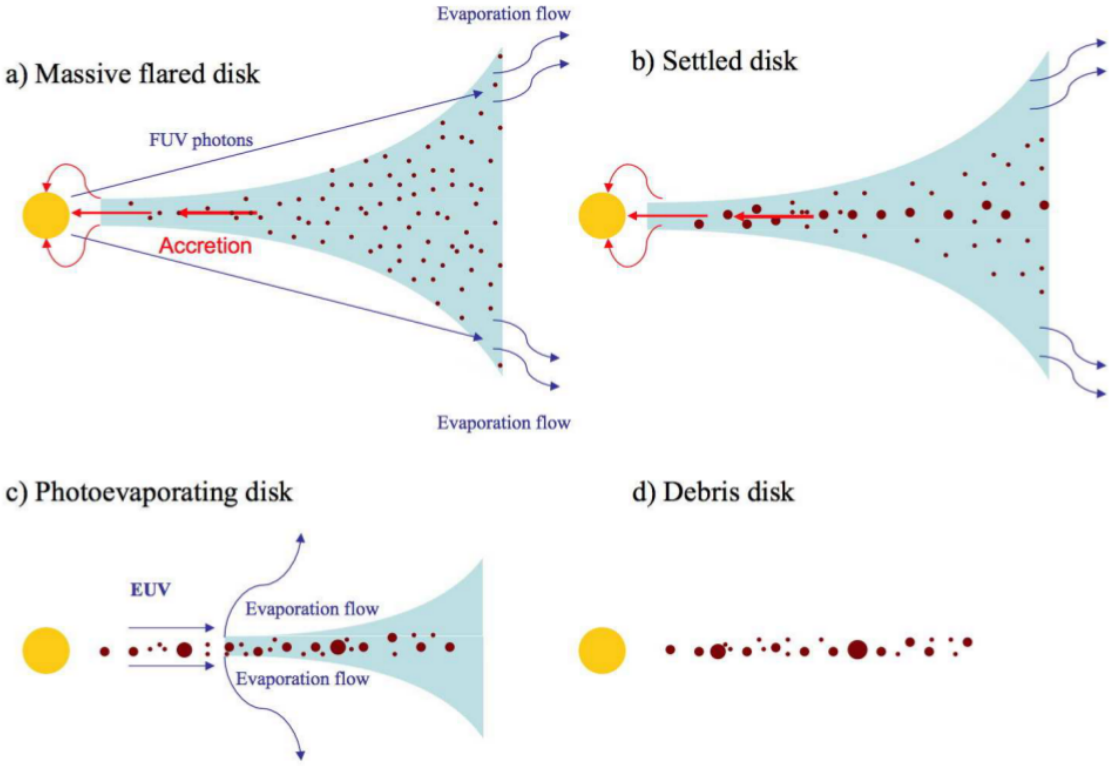

Figure 1.6: Dispersal an evolution processes of protoplanetary disks. Brown dots represent dust and blue region represent gas. During the first stages of the disk, the accretion processes dominates the dispersion of the disk, and FUV evaporates the outer layers. Then the grains starts to coalesce, and settle mid-plane. As it settles, photoevaporation in the EUV takes count of the inner part of the disk, that starts to give way. Finally, the gas has photoevaporated and a debris disk formed by the larger dust grains remains. Fig. from Williams and Cieza 2011.

already dissipated. These objects are related with the previously defined WTTS and Class III protoplanetary disk. Thus, our Verona has changed: from the dusty star-forming regions of Act I, to the evolved free of dust ones of Act II, where we try to find our new Romeos and Juliets: exoplanets around young disk-less stars.

A note has to be made, though, to address the nomenclature of these objects. The name 'debris disks' attends to any kind of star that presents any weak warm dust. This definition not only refers to young pre-main sequence stars, but also includes more evolved objects, even Gyr old. They are thought to be analogs to the Kuiper belt of the solar system (Moro-Martín et al. 2008), and were first identified with IRAS around Vega (Aumann et al. 1984), and then found by the hundreds in many other regions (Oudmaijer et al. 1992; Mannings and Barlow 1998; Trilling et al.

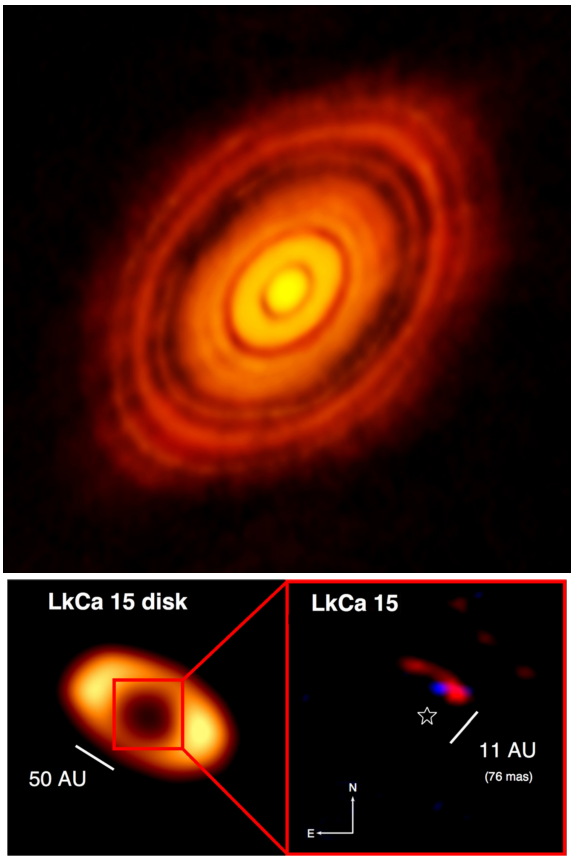

Figure 1.7: Images from HL Tau by ALMA (top) and LkCa 15 (bottom) transitional disks. Several gaps, suggesting the presence of planets, can be seen in HL Tau, and an inner exoplanet candidate in formation was identified inside the inner hole of LkCa 15 TD. Figs. from ALMA (NRAO/ESO/NAOJ) and Kraus and Ireland 2012.

2008; Eiroa et al. 2013). This warm dust is consider to be caused by planetesimal collisions (Wyatt 2008), although in the case of younger sources, it is also considered as the remnants of the protoplanetary disk. When talking about 'debris disks' in this work, it is referred to these young ($\leq$10Myr) sources, analogs to WTTS and Class III protoplanetary disks.

The search of planets around young disk-less stars, though, is still elusive. Several attempts have yielded inconclusive results (Hebb et al. 2007). Just a few exoplanets candidates have been detected, in fact, around young T Tauri stars, either by photometric transits or radial velocity variations. In some cases, even not fully confirmed.

van Eyken et al. 2012 found a transiting close exoplanet candidate around the

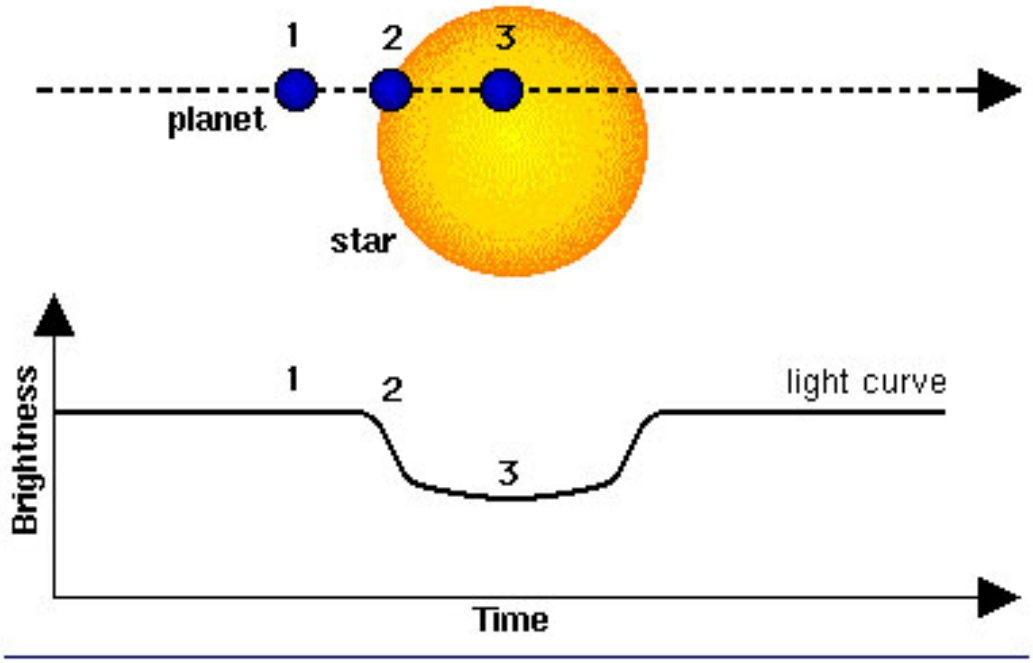

Figure 1.8: Transit of a planet orbiting around a star. When the orbital plane is aligned with the line of observation, the planet shadows the star when it crosses in front of it, diminishing the light from the host, which can be observed to identify the exoplanet.

WTTS CVSO 30 (∼7-10Myr), located in the 25-Ori association, under the frame of the Palomar Transient Factory Orion project (see below). They derived a period of 0.448 days, and a mass of less than 5.5 M_{Jup}.

Mann et al. 2016 discovered a super-Neptune sized planet around a late-type PMS star located on Upper Scorpius, from the Zodiacal Exoplanets in Time program, with a period of 5.425 days, and a system age of ∼11Myr,.

Donati et al. 2016 detected a Hot Jupiter around the magnetically active young (∼2Myr) WTTS V830 Tau, in the Taurus-Auriga star-forming region, via radial velocity variations, with a period of 4.93 days, not related with the star intrinsic variability.

Johns-Krull et al. 2016a pointed to a possible planetary candidate around CI Tau (∼2Myr), using infrared radial velocity measures. A period of ∼9 days was derived , although cool and hot spots, or reflection of the stellar spectrum off the inner disk, could also explain the infrared signal.

David 2016 observed a Neptune type planet around the 5-10 Myr old star USco 161014.75-191909.3, under the K2 program, using radial velocity and photometric variability, located in the Upper Scorpius OB association, and derived a period of 5.4 days.

In the case of van Eyken et al. 2012 and Johns-Krull et al. 2016a the planetary nature of the systems is still in debate. But the other four planets are confirmed. The distribution of periods and ages from the previous examples points towards two distinctive possibilities in the paradigm of planet formation. Finding giant planets with close-in orbits around young PMS stars can only happen if either the planets are formed in those orbits, or they migrate to the observed orbits on a timescale equal or lower than that of disk dissipation. But with such low number of detections, these explanations remain uncertain.

Young disk-less stars are found on evolved star-forming regions, such as the 25-Ori association (Briceño et al. 2007, ∼7-10Myr), the Upper-Scorpius OB association (Pecaut et al. 2012; Rizzuto et al. 2016, ∼11Myr), the Taurus-Auriga molecular cloud (Kenyon et al. 2008, ∼0-5Myr), or TW Hya association (Zuckerman and Song 2004, ∼5-10Myr), among others. These regions have the expected age of disk dispersal for low-mass young stars (Hillenbrand 2008, ∼5-10Myr). Another key feature of these regions is the low interstellar extinction found on them. At these ages, the molecular cloud has started to dissipate. When looking for transiting exoplanets, to get the best signal possible, the clearer the sky, the better.

The plot has twisted. Young planets are found, but not where they should be. As the curtain falls, before the next Act starts, one final question remains to be answered: why?

1.4 Act III - Planet migration, the first steps

The paradigm of planet formation was established in the mid-1990s, and was based on the idea that planets originate from the coagulation of smaller solids (Safronov and Zvjagina 1969) (Hayashi et al. 1985; Lissauer 1993), although this coalescence idea was developed much earlier (Chamberlin 1916). Planets would surge from the material of the protoplanetary disk surrounding their host star, with nominal low eccentricity and inclination (Cresswell et al. 2007; Xiang-Gruess and Papaloizou 2013). In the case of giant planets, they should form beyond the "snow line", that is, the distance from the star beyond which the water would be found in solid form. There, the ice is incorporated into solid bodies that are in the process

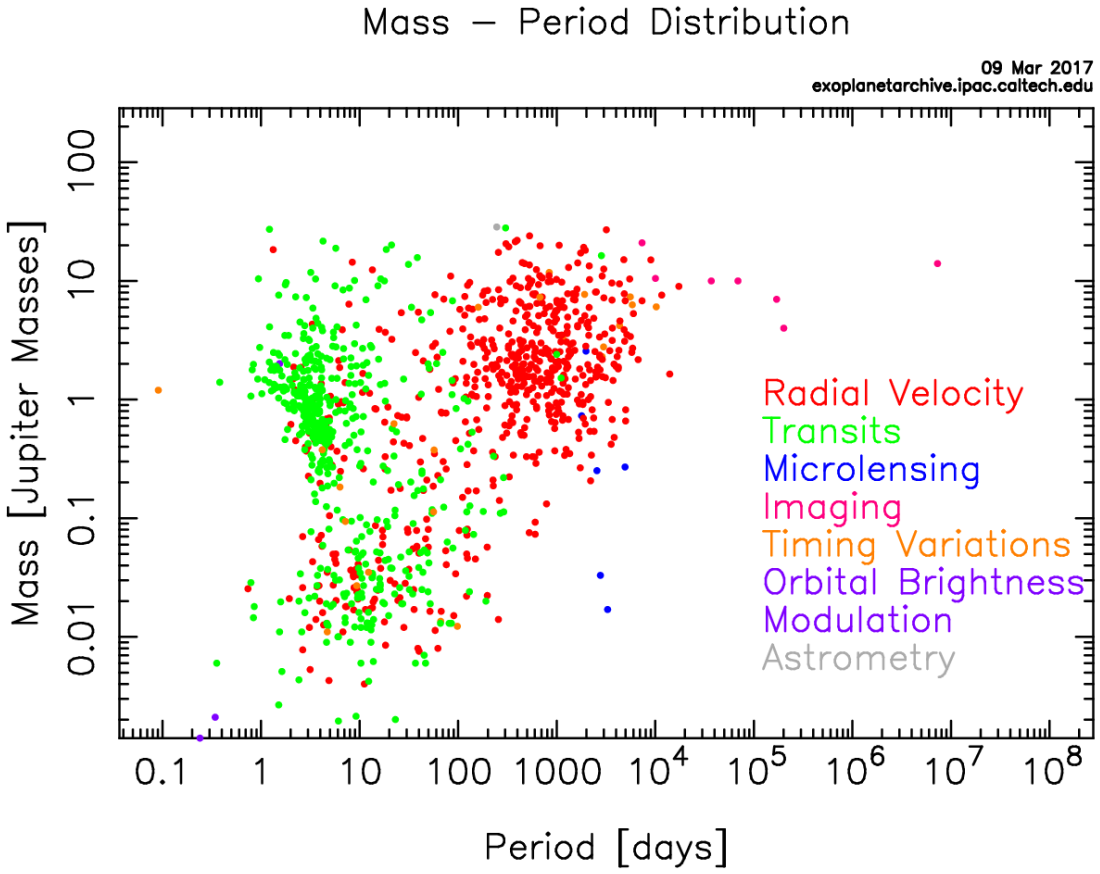

Figure 1.9: Mass-Period distribution of confirmed exoplanets. The different colors correspond to the different identification methods used. As can be seen, the transit method favors close, giant planets (Hot Jupiters). Fig. from NASA Exoplanet Archive (http://exoplanetarchive.ipac.caltech.edu/).

of planetesimal formation. This boundary is located some AU away from the host star (∼5AU for the solar nebula condition), depending on the stellar type (Banzatti et al. 2017). But the formation of planets in that position comes in contradiction with the distribution of giant planets identified so far.

As seen in Fig. 1.9, a large population of these giant planets are found in close orbits to the star, where theoretically it would be impossible for them to form. These planets are denominated Hot Jupiters, and the only possible explanation for their observable situation is that they have suffered a displacement from where they were born in the protoplanetary disk, to finally end on that position. More so, in Fig. 1.9 it can also be seen how the transit method favors the identification of planets on close-in orbits, whether for larger ones other methods are needed.

Migration is a consequence of disk-planet tidal interactions (Ward 1997; Nelson

et al. 2000). The angular momentum exchange for this long-distance displacements of jovian-sized planets is considerable, and only the protoplanetary disks provides a big enough reservoir of angular momentum as to be considered the main contributor for migration (Papaloizou 2003). Depending on the mass of the protoplanet, three different types of migration are found: Types I, II and III.

Type I (dynamical friction) corresponds to planets in the M⊕ range (Ward and Hahn 2000). In this case, the planet navigates through the disk without perturbing its structure. The differences between the torques they exert to the material inwards and outwards away from the planet account for their migration. Numerical models yield a migration timescale of ∼1Myr (Tanaka et al. 2002), much shorter than the expected building timescale of planets with this mass range (Papaloizou and Nelson 2005). In theses cases, low-mass planets would be lost into the star before the disk has dissipated. But terrestrial planets are still found. Disk turbulences and magnetic interactions with the protoplanet could account for these discrepancies (Terquem 2003).

Type II (coevolution) migration (Lin and Papaloizou 1986; Ward 1997; Ward and Hahn 2000), on the other hand, accounts for protoplanets in the Jupiter-size mass range. In these cases, as the planet migrates, the larger mass produces shock perturbations in its vicinity, pushing material away from the planet, and creating a gap (Lin and Papaloizou 1993; Bryden et al. 1999; Crida et al. 2006). The planet exerts a negative torque on the inner disc, which pushes it away towards the star, and a positive torque on the outer disk, which pushes it away from the star (Crida et al. 2006) (Fig. 1.10). This way the protoplanet is dragged along the evolving disk, inwards. The timescale of this migration and accretion process is of the order of 0.1Myr (Nelson et al. 2000). If the planet is not too massive, it behaves as a particle on the accreting disk, and thus it migrates inwards at the same rate of the disk (Lin and Papaloizou 1986); but if it is massive enough, the displacement rate decreases due to the larger inertia of the planet (Syer and Clarke 1995; Ivanov et al. 1999).

Type III migration is applied to intermediate-mass protoplanets (Neptune-to-Jupiter mass), which create a partial gap in the disk, and which changes the orbits of the planets dramatically in a very short amount of time (Lin and Papaloizou 2010; Baruteau et al. 2014), and, interestingly, it can be inwards or outwards away from the star (Pepliński et al. 2008; Masset and Papaloizou 2003; Masset 2008).

Thus, it is most probable that the close-in orbits found for Hot Jupiters are caused by Type II migration (Baruteau et al. 2014). Nevertheless, this processes

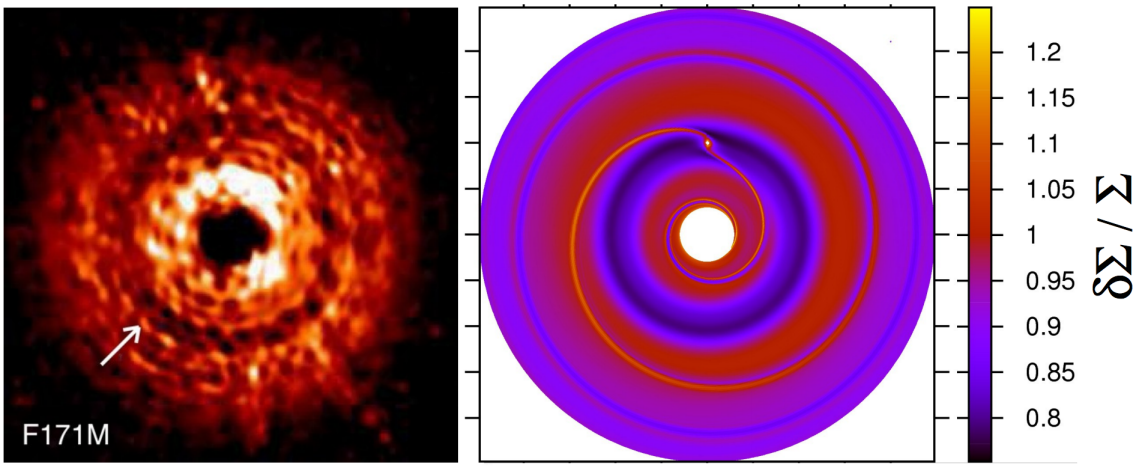

Figure 1.10: *Left*: Image from *HST* of the disk around TW Hya. The gap created from a potential giant exoplanet in migration is clearly identified (Debes et al. 2013). *Right*: Type II migration model, showing the perturbation of the giant planet on the protoplanetary disk (Baruteau et al. 2014).

apply to evolved exoplanetary systems and, thus, the question still remains: is this the case for recently formed exoplanets?

1.5 Finale - This thesis

As the curtain falls one last time, the answer to the original question remains unanswered. The link that unites the formation of planetary systems and young stellar objects is still uncertain, mostly for one reason: more observations and data are needed. And there is where this work comes into scene.

In June 2013 the *Herschel* Space Observatory (Pilbratt et al. 2010) was deactivated and ended its service life. But that was not, by any extent, the end of its usefulness. An unparalleled amount of infrared and sub-mm images and spectra was left as its legacy, ready to be processed and analyzed. The wavelength coverage of its instruments, PACS (Photodetecting Array Camera and Spectrometer) (Poglitsch et al. 2010) and SPIRE (Spectral and Photometric Imaging Receiver) (Griffin et al. 2010), ranging from 70μm to 500μm, opened the possibility to observe protoplanetary disks as never before. In particular, in the case of transitional disks, *Herschel* complemented the wavelength coverage of *Spitzer*. The latter allowed for the identification of inner disk holes, while the former, with the farthest regions of the disk now available, was able to give crucial information about the size and composition of

the inner and outer disk structure. This implied the direct surveillance of the inner gap, between star and disk, where planets were potentially being formed, offering constraints on young planetary systems sizes (Fig. 1.11).

One of the key aspects of the evolution of a PMSs is the higher X-ray rate observed, when comparing it with nominal main sequence stars irradiation. This feature may play a key role in the early evolution of planetary atmospheres, as the high energetic photons could ionize, and even evaporate, the young atmosphere of any potential exoplanet. Thus, analyzing its processes is of the utmost importance in the study of exoplanet occurrences and, eventually, habitability. This high energetic irradiation is intimately related with the accretion processes of gas onto the stellar photosphere. The potency of the *Chandra* X-ray Observatory allows us to observe the densest and the most clustered star-forming regions, and thus measure the X-ray fluxes of these early objects. This, summed to the optical capabilities of the *Hubble* Space Telescope, which allows to identify the tracers needed to measure accretion rates in young T Tauri stars, offers the opportunity of studying the inherent relationship between these two key features of early star evolution.

Finally, the most effective technique of exoplanet detection is the transit method. Astonishing advances and discoveries have been made by the space telescopes commended to that task (*CoRoT*, *Kepler*). But ground-based observations play also a crucial role in this regard. As such, a program was developed as part of the Palomar Transient Factory (PTF) (Law et al. 2010), denominated PTF Orion (van Eyken et al. 2011). The main objective of the program was the detection of young transiting exoplanets around WTTS in the 25-Ori association. The age of the region, which coincide with that of protoplanetary disk dispersal, made it an ideal spot for this. If an exoplanet were to be found, giving the young age of the association, it would suppose a key piece in the puzzle of planet formation and migration.

This thesis follows the thread that unifies these ideas, and tries to answer the following main questions: what is the incidence of transitional disks in young star-forming regions? How does the larger wavelength coverage of the *Herschel* Space Observatory assists in the identification and analysis of transitional disks? What inherent relations can be found between the higher X-ray emission of T Tauri stars and their accretion rates? Does the environment play some role in these properties? How do the periods of Hot Jupiters reconcile with their theoretical formation location beyond the snow line? Does migration accounts for it? Or is it feasible for a giant planet to form closer to its host star?

To answer these questions, an observational and archival enterprise was carried

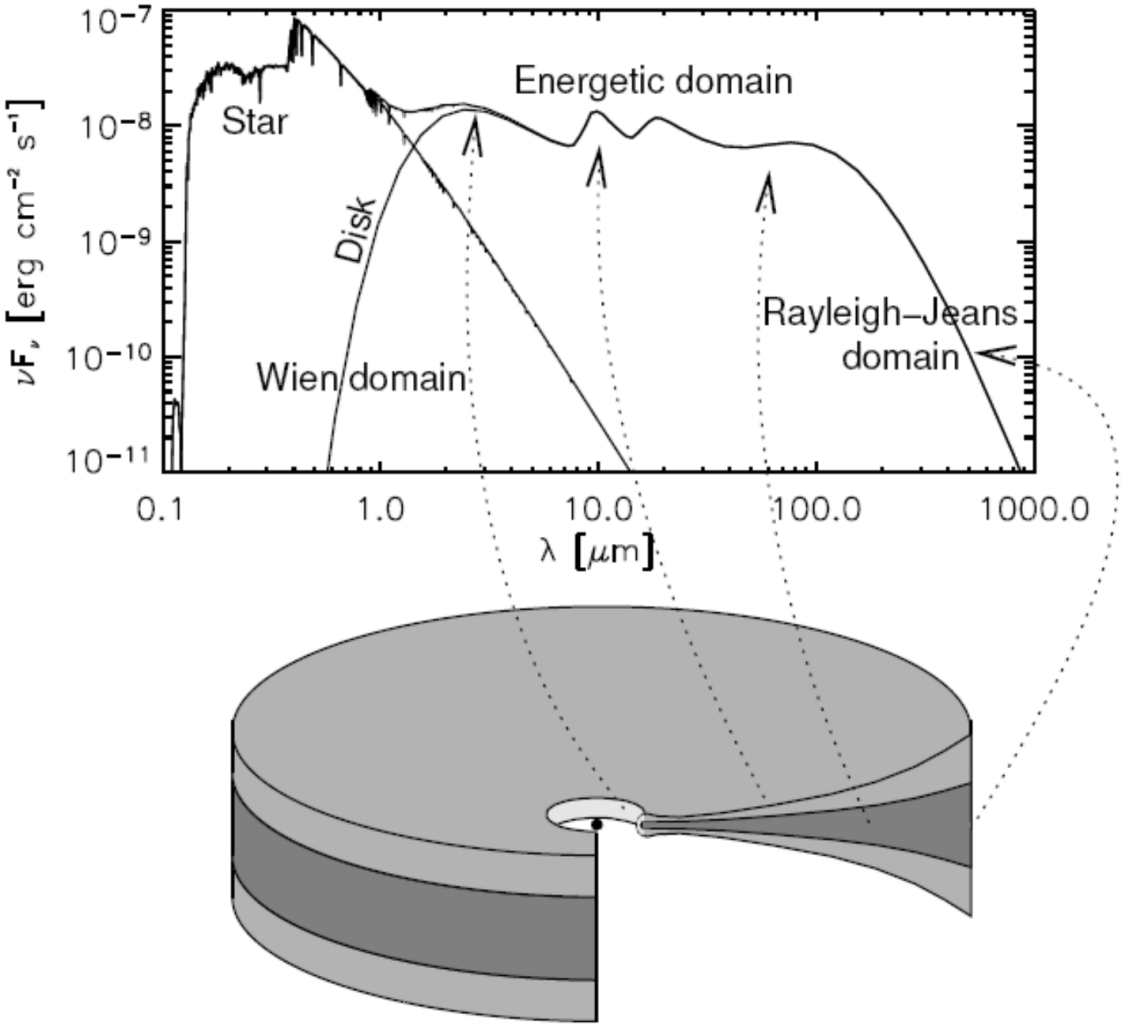

Figure 1.11: Diagram of the different contributors of the disk to the SED photometry. With the larger infrared wavelength coverage from *Herschel*, the furthest regions od the disk are observable.

out. Data from several different programs were needed, as the inquiries span several fields of study. Thus, observations in the optical, near-, mid- and far-infrared and sub-mm were used, as well as X-ray information and photometric data. Four articles comprise the efforts performed. These projects are the contribution of this work to the overall picture of star and planet formation. They are included in the following chapters. A summary of them is given below, for reference.

- Chapter 2 - **Identification of new transitional disk candidates in Lupus with Herschel**. This project was elaborated using *Herschel* data, as part of the *Herschel* Gould Belt Survey (HGBS) (André et al. 2010). The *Lupus Molecular Clouds* is one of the closest (< 200pc) star forming regions to the Sun (Comerón 2008). The aim was the identification of transitional disks by analyzing the SED of the YSOs in the regions. From those sources with clear detections in the *Herschel* maps, the SED method was applied. Ribas et al. 2013 elaborated a similar tool for the identification of transitional disks than that elaborated in Act I. Instead of accounting for one unique spectral index, two are used: α_{K_S-12} and α_{12-70}. This way the separation between Class II objects and TD is clearer (Fig. 1.12).

- Chapter 3 - **Infrared study of transitional disks in Ophiuchus with Herschel**. Analogously to the project carried out in Lupus and described in Chapter 1, a similar enterprise was elaborated in Ophiuchus. The Ophiucus cloud is also one of the closest star-forming regions to the Sun (∼130pc) (Wilking et al. 2008). Using *Herschel* observations, and with a sample of spectroscopically known members of the cloud, an spectral index analysis was carried out to identify transitional disk candidates.

- Chapter 4 - **X-ray deficiency on strongly accreting T Tauri stars. Comparing Orion with Taurus**. It focuses on the interactions between the protoplanetary disk and the host star. One of these features is the presence of a higher X-ray emission on PMS stars than that found on main-sequence stars. X-ray emission is related with the rotational period in main-sequence sources (Pizzolato et al. 2003), but that is not the case of PMSs (Preibisch et al. 2005). Thus, another mechanism should play a role in these events. And one of the characteristic mechanisms of CTTS is the accretion of gas onto the star, which produces shock spectrum and excesses in the luminosity of the young object (Calvet and Gullbring 1998). In this project, the relation

between the accretion rates and X-ray emission from a sample of CTTS in the Orion Nebula Cluster (ONC) was analyzed, and compared with results of a similar study in the Taurus Molecular Complex (TMC) (Telleschi et al. 2007).

- Chapter 5 - **Optical variability in the young PTF Orion project. Identification of transiting exoplanets and classification of sources of interest**. The main objective of this project was the identification of transiting exoplanet candidates around young WTTS in the 25-Ori association. Under the frame of the Palomar Transient Factory in Orion project (PTFO), ∼116,000 lightcurves were visually inspected looking for transiting features. Also, a membership analysis to the 25-Ori association of the exoplanet host candidates identified and of all the variable sources observed was carried out.

In Chapter 6 a summary of the results of this project, as well as the prospects of future work, is shown. Also, the conclusions of the thesis (both in English and Spanish) are elaborated.

Finally, in Chapter 7 three articles published in *Astronomy & Astrophysics* (corresponding to Chapters 2, 3 and 4) are included, in the form of an appendix. The fourth article (corresponding to Chapter 5) was submitted to the journal, but not yet accepted. Because of this, it has not been included in this appendix.

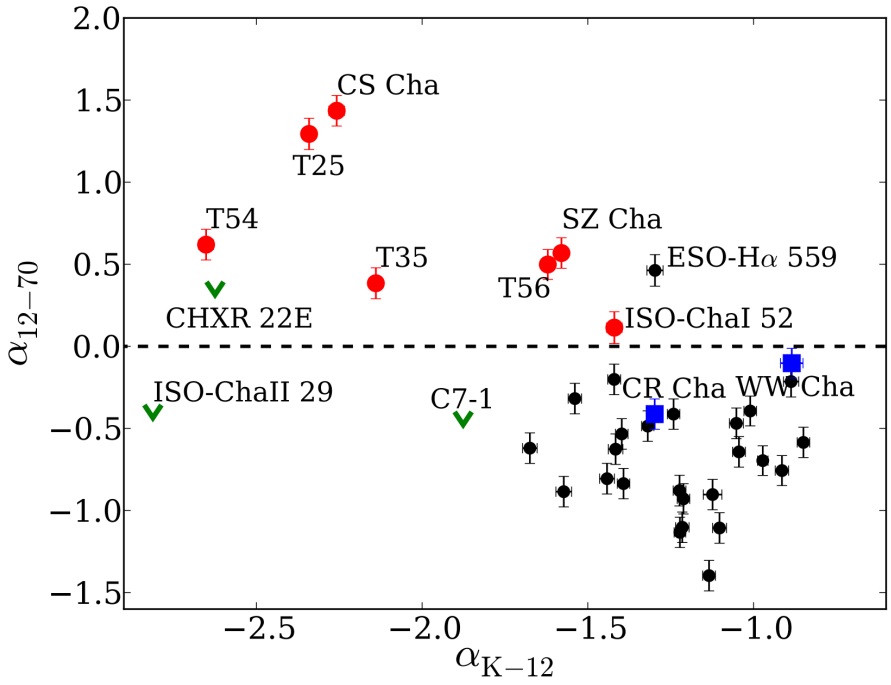

Figure 1.12: Spectral indexes α_{K_S-12} versus α_{12-70} diagram for a sample of transitional disks in Chameleon. Red dots represent transitional disks, black squares are Class II objects and blue squares pre-transitional disks. A separation is clear between TD and Class II objects. An edge-on Class II presents $\alpha_{K_S-12} > 0$. Fig. from Ribas et al. 2013.

Chapter 2

Identification of new transitional disk candidates in Lupus with *Herschel*

Bustamante, I.; Merín, B.; Ribas, Á.; Bouy, H.;Prusti, T.; Pilbratt, G. L.; André, Ph.

Identification of new transitional disk candidates in Lupus with Herschel. 2015, Astronomy & Astrophysics, 578, A23

Abstract

New data from the *Herschel* Space Observatory are broadening our understanding of the physics and evolution of the outer regions of protoplanetary disks in star-forming regions. In particular they prove to be useful for identifying transitional disk candidates. The goals of this work are to complement the detections of disks and the identification of transitional disk candidates in the Lupus clouds with data from the *Herschel* Gould Belt Survey. We extracted photometry at 70, 100, 160, 250, 350, and 500 μm of all spectroscopically confirmed Class II members previously identified in the Lupus regions and analyzed their updated spectral energy distributions. We have detected 34 young disks in Lupus in at least one *Herschel* band, from an initial sample of 123 known members in the observed fields. Using recently defined criteria, we have identified five transitional disk candidates in the region. Three of them are new to the literature. Their PACS 70 μm fluxes are systematically higher than those of normal T Tauri stars in the same associations, as already found in T Cha and in the transitional disks in the Chamaeleon molecular cloud. *Herschel* efficiently complements mid-infrared surveys for identifying transitional disk candidates and confirms that these objects seem to have substantially different outer disks than the T Tauri stars in the same molecular clouds.

2.1 Introduction

Transitional disks link the studies of planet formation and disk evolution around young stars. They are protoplanetary disks around young stars, optically thick and gas rich, with astronomical unit-scale inner disk clearings or radial gaps evident in their spectral energy distributions (SED). They lack excess emission at short-mid infrared (typically around 8-12 μm), but present considerable emission at longer wavelengths (Muzerolle et al. 2010). Since their discovery by Strom et al. (1989b) with IRAS data, the *Spitzer* Space Telescope (Werner et al. 2004) allowed the identification of a much larger population of these objects (Cieza et al. 2010; Merín et al. 2010; Espaillat et al. 2014). It was possible to use the mid-infrared data to make good estimates of the dust distribution in the inner few astronomical units of the disks around T Tauri stars in nearby star-forming regions (e.g.,Calvet et al. (2005), Lada et al. (2006)).

The *Herschel* Space Observatory (Pilbratt et al. 2010) grants us access to the outer disk region of these objects. Recent studies suggest that the outer disks, as detected in far-infrared emission, undergo substantial transformations in the transitional disk phase (Cieza et al. 2011; Ribas et al. 2013). However, *Herschel* data are still lacking for most known transitional disks.

The main objective of this article is to revisit and extend our knowledge of known Class II objects in the Lupus dark clouds, and to identify transitional disk candidates in the region using *Herschel* photometry, complemented with photometry from previous studies from the optical to the mid-infrared. With *Herschel* we have the opportunity to study objects with large inner holes, reaching the farthest regions of their disks that *Spitzer* was unable to access with the required sensitivity (IRAC and IRS had different wavelength ranges, 3.5 - 8.0 μm and 5 - 35 μm, respectively, and the sensitivity of MIPS, with pass bands between 24 and 160 μm, was limited). Therefore, we are not only able to study the outer regions of known transitional disks, but also to detect new candidates, with larger cavities and outer disks.

This work is organized as follows. Section 2.2 describes the *Herschel* observations and data reduction and the procedure applied to identify and extract the fluxes for the known objects. In § 2.3 we identify new transitional disk candidates, describe the procedure to build the SEDs, and discuss some objects with certain peculiarities. In § 2.4 we discuss the properties of the newly found transitional disk candidates, and in § 2.5 we present the conclusions of this work.

2.2 Observations and data reduction

The Lupus dark clouds were observed by *Herschel* as part of the *Herschel* Gould Belt Survey (HGBS,André et al. (2010)). It is one of the star-forming regions located within 150 to 200 pc from the Sun and has a mean age of a few Myrs (Comerón (2008), for a review on the region). It contains four main regions, with one of them, Lupus III, being a rich T Tauri association. Located in the Scorpius-Centaurus OB association, the massive stars in the region are likely to have played a significant role in its evolution.

By employing the PACS (Poglitsch et al. 2010) and SPIRE (Griffin et al. 2010) photometers in parallel mode, *Herschel* has the capability for large scale mapping of star-forming regions in the far-infrared range. Early *Herschel* observations of Lupus from the HGBS were already published by Rygl et al. (2013), where the observing strategy and main results are described.

We produced our maps using *Scanamorphos* (Roussel 2012) version 21.0 for the PACS maps and version 18.0 for the SPIRE maps. The identification numbers of the Lupus *Herschel* parallel mode observations processed for this work are (1342-)189880, 189881, 203070, 2203071, 2203087, 2203088, 2213182, and 2213183 from program KPGT_pandre_1. The observations were made in parallel mode for 70, 160, 250, 350, and 500 μm, and in prime mode for 100 μm (Rygl et al. 2013), which is why some of the sources do not have images at 100 μm in Fig. 2.4.

A complete census of the sources detected with *Herschel* will be published by the *Herschel* Gould Belt Survey consortium in an upcoming paper (Benedettini et al., in prep.).

2.2.1 Point source photometry

Our first objective was to detect and classify sources in the images obtained with PACS and SPIRE. We used coordinates of spectroscopically confirmed Class II members from different sources, compiling a list of 217 targets. This compilation was developed by Ribas et al. (2014), and these objects were selected for having known extinction values and spectral types from optical spectroscopy. Of this sample of 217 objects, only 123 are found in the fields observed by *Herschel*.

We applied the *sourceExtractorSussextractor* algorithm in our maps, with the *Herschel Interactive Processing Environment* (HIPE), version 12.0, using a detection threshold of S/N> 3. We then cross-matched the resulting list of detected objects with our pre-selected targets, using a search radius between 5" and 10". We selected

only those objects with detections in PACS. After this process, we found 37 objects with at least one detection in one PACS band, 35 in the 70 μm maps, and 2 in the 100 μm maps. We then validated all of them by visual inspection. This way we were able to double-check our detections. The background emission becomes more significant at longer wavelengths, where detections are in general less frequent, or false detections appear, due to bright filaments and ridges. This is the reason why we selected only PACS-detected objects. The combination of quantitative and qualitative analysis was essential to produce reliable detections and photometry. After this process we discarded four objects as not having clear detections in the maps and added two objects that were found by visual inspection. They are flagged in Table 2.5. After this process, 35 objects in the list had one clean detection in at least one *Herschel* PACS or SPIRE band.

We applied the *sourceExtractorDaophot* algorithm to extract the photometry for PACS, and the *annularSkyAperturePhotometry* task for SPIRE. All point-source fluxes were aperture corrected with the recommended aperture corrections for both instruments (see the PACS Photometer Point Spread Function Technical Note from April 2012, and Sect. 6.7.1 of the SPIRE Data Reduction Guide of HIPE 12.0). Table 2.1 shows the set of aperture, inner, and outer sky radii for each *Herschel* band, as well as the corresponding aperture corrections.

Table 2.1: Aperture, inner, and outer radii used in the photometry extraction process for each band, with their corresponding aperture corrections.

Band	$R_{aperture}$ (")	R_{inner} (")	R_{outer} (")	Correction
PACS 70	6	25	35	1.5711
PACS 100	6	25	35	1.6804
PACS 160	12	25	35	1.4850
SPIRE 250	22	60	90	1.2796
SPIRE 350	30	60	90	1.2396
SPIRE 500	42	60	90	1.2937

Table 2.2 shows the sensitivity limit for each *Herschel* band, as stated in the SPIRE/PACS Parallel Mode Observers' Manual (Sect. 2.3). The values correspond to a nominal scan direction and a scan speed of 60"/s.

Upper limits for non-detections were derived by adding scaled synthetic point spread functions (PSFs) at the expected position of the sources until the *sussExtractor* detection algorithm did not recover them. In most cases visual inspection

Table 2.2: Sensitivity limits for each *Herschel* band in parallel mode at 60"/s, as stated in the PACS/SPIRE Parallel Mode Observers' Manual.

Filter	Sensitivity (mJy/beam)
PACS 70	21.0
PACS 100	24.7
PACS 160	47.0
SPIRE 250	12.6
SPIRE 350	10.5
SPIRE 500	15.0

was applied. The calibration errors for PACS and SPIRE are 5% and 7% (as stated in their observer manuals), respectively. To ensure consistency with Ribas et al. (2013) we chose a more conservative estimation, 20% for SPIRE as error values, taking into account that the background emission becomes increasingly stronger at longer wavelengths. In the case of PACS, after comparing several photometric extraction algorithms (*sussExtractor*, *Daophot*, *annularSkyAperturePhotometry*, and *Hyper*,Traficante et al. (2015)), and extraction apertures with the MIPS70 fluxes of a subsample of clean sources, we selected a conservative error value of 25% of the flux to account for the different flux values obtained. Table 2.5 gives the stellar parameters of these detected sources as given in the literature, and Table 2.6 presents their *Herschel* point source fluxes and upper limits. As stated before, at least one point source was detected for at least one wavelength of the *Herschel* instruments for all objects in Table 2.6 (see Fig. 2.4).

We then looked for bright *Spitzer* 24 μm and 70 μm sources around the targets to check for possible contamination from other nearby mid-infrared sources. We used a radius of 42", as this was the value we used for the largest wavelength band when extracting the *Herschel* photometry (which corresponds to SPIRE 500 μm). The results of this analysis are shown in Tables 2.3 and 2.4.

In the cases where MIPS70 sources were found near our sources we inspected the PACS 70 images of the targets. Except for sources Sz65, Sz66, Sz103, Sz104, and 2MASSJ16085373-3914367 (as explained below), we did not find evidence of the presence of extra sources inside the matching radius (see Fig. 2.4). This means that *Herschel* did not detect them, so we assume that the full contribution to the flux measured at PACS 70 comes from our target sources, and not from contaminants. In Table 2.4 we maintain all the sources with possible contamination for reference.

Objects Sz65 and Sz66 form a pair, as is explained in Sect. 2.3.3.6, and this is taken into account in their photometry extraction. The MIPS excesses seen for objects Sz103 are associated with object Sz104, and vice versa. We only flagged objects with potential contaminations in case they were detected (see Table 2.6). When they are not detected and upper limits are calculated instead, we do not take into account the possible contaminations.

The nearby source near object 2MASSJ16085373-3914367 presented significantly larger MIPS24 and MIPS70 fluxes than our target. In this case, we concluded that the infrared excesses measured in the *Herschel* image corresponded to this other object instead of our target, and thus we discarded object 2MASSJ16085373-3914367 because its *Herschel* photometry could not be unequivocally associated with it. The other object is a known young stellar object (YSO) candidate, SSTc2d J160853.2-391440. It is probably another member of the Lupus region, yet not confirmed spectroscopically and therefore not included in our study.

In other cases other contaminant sources were found, but with sufficiently weaker MIPS24 and MIPS70 fluxes so as not to affect our measurements. These sources are marked in Table 2.3. In these cases we assumed that the *Herschel* fluxes measured correspond to our targets as the major contributors.

Another interesting object is Sz108B, which presents two possible contaminants that could affect its photometry. The one farthest away, at 38.8", has larger MIPS24 flux. The closest one, at 9.7", has a higher MIPS70 flux. Thus, the *Herschel* photometry of Sz108B could be contaminated by the closest one and therefore it is flagged as unreliable in Table 2.4.

After this analysis, our final set of sources decreased to 34. We maintain the image of object 2MASSJ16085373-3914367 in Fig. 2.4 for completeness.

2.3 Results

2.3.1 Identification of transitional disk candidates

To identify transitional disk candidates we applied the procedure developed in Ribas et al. (2013), which defines a transitional disk candidate as having $\alpha_{K-12} < 0$ and $\alpha_{12-70} > 0$, where $\alpha_{\lambda_1-\lambda_2}$ is defined as $\alpha_{\lambda_1-\lambda_2} = \frac{log(\lambda_1 F_{\lambda_1}) - log(\lambda_2 F_{\lambda_2})}{log(\lambda_1) - log(\lambda_2)}$, and λ is measured in μm and F_λ in erg $\cdot$ s^{-1} $\cdot$ cm^{-2}.

The K-band flux comes from 2MASS (Skrutskie et al. 2006), the 12 μm flux from WISE and the 70 μm flux from PACS. Some exceptions to this rule were applied

Table 2.3: Targets with possible contamination within the used apertures in MIPS24. The second column shows the fraction of total MIPS24 flux in the aperture with that of the target.

Object	F_{source}/F_{aper}	N	Companion distance (")	Band
Sz65[1]	0.4	1	6.5	PACS 70
Sz66[1]	2.9	1	6.2	PACS 70
Sz100[3]	0.2	1	23.4	SPIRE 350
Sz103[2]	0.8	10	41.2	SPIRE 500
Sz104[2]	2.7	10	36.4	SPIRE 500
Sz108B	1.4	3	38.8	SPIRE 500
2MASSJ16085373-3914367*	9.3	1	6.9	PACS 70
Sz112	0.5	4	31.9	SPIRE 500
SSTc2dJ161029.4-392215[3]	0.1	2	7.4	PACS 70
SSTc2dJ160002.4-422216[3]	0.4	2	39.8	SPIRE 500
SSTc2dJ160111.6-413730[3]	0.2	1	24.2	SPIRE 350

Notes. [1] The MIPS24 contamination affecting Sz65 is caused by Sz66, and vice-versa, as can be seen in Fig. 2.4. This is taken into account in the photometry analysis.
[2] The MIPS24 contamination affecting Sz103 is caused by Sz104, and vice versa, as can be seen in Fig. 2.4. This is taken into account in the photometry analysis.
[3] Objects with sufficiently low contamination from nearby sources so as to not affect our *Herschel* measurements.
* This is the only object that has been removed from the list of detected sources because its *Herschel* photometry cannot be unequivocally associated with it.

when these fluxes were unavailable for certain objects; for example, Sz95 has no flux at 70 μm, so we used PACS 100 μm instead. We did the same for 2MASS J1608149. An exceptional case is object SSTc2dJ160111.6-413730, discussed later in Sect. 2.3.3.5, as no PACS flux was available, and therefore could not be classified.

With this procedure we detected five objects that satisfy the transitional disk candidate criteria: SSTc2dJ161029.6-392215, Sz91, Sz111, Sz123, and 2MASS J1608149. In Fig. 2.1 we show the objects that fulfilled our selection criteria. Objects Sz91 and Sz111 were previously known transitional disks from *Spitzer* data (Merín et al. 2008), and they occupy a different region in the diagram than the others. They present little to no excess at 12 μm and a steep rise between 12 and 70 μm in their

Table 2.4: Same as Table 2.3, but with MIPS70 possible contamination.

Object	F_{source}/F_{aper}	N	Companion distance (")	Band
Sz66	$468.^{mJy}$	1	6.2	PACS 70
Sz98[2]	0.2	1	26.3	SPIRE 350
Sz100[2]	0.7	1	32.3	SPIRE 500
Sz103[1]	1.4	1	23.2	SPIRE 350
Sz104[1]	0.7	1	23.2	SPIRE 350
Sz108B	$212.^{mJy}$	1	9.7	PACS 70
2MASSJ16085373-3914367*	119.0^{mJy}	1	6.9	PACS 70
Sz112[2]	0.7	1	28.6	SPIRE 350

Notes. [1] The MIPS70 contamination in Sz103 is caused by Sz104, and vice versa, as can be seen in Fig. 2.4. This is taken into account in the photometry analysis.
[2] Objects with sufficiently low contamination from nearby sources so as to not affect our *Herschel* measurements.
* This is the only object that has been removed from the list of detected sources, because its *Herschel* photometry cannot be unequivocally associated with it.
^{mJy} In these cases the MIPS photometry of the target was not available, but that of the companions was. Therefore, we present the actual flux of the objects inside the search radius instead of the percentage.

SEDs (see Fig. 2.2). This could be indicative of a large cavity in both cases, mostly empty of small dust grains. In the case of Sz91, a resolved image of this inner hole has already been obtained in the submillimeter with SMA (Tsukagoshi et al. 2014), being one of the largest imaged so far (∼65 AU) in a T Tauri disk. Sz111 is likely to have a similarly large and empty cavity.

The rest of the objects present excesses at intermediate wavelengths, and fulfill our color criteria (see Fig. 2.2 for a representation of their SEDs). Object 2MASS J1608149 is a special case, as is explained in Sect. 2.3.3.3.

In Fig. 2.1 three additional objects present error bars falling in the transitional disk detection criteria: SSTc2dJ160703.9-391112, RXJ1608.6-3922, and Sz108B. Their SEDs present far-infrared excesses, but mid-infrared ones as well. As they do not strictly fulfill our selection criteria, they are not to be considered transitional disk candidates in this work, yet they deserve attention.

Analysis of the remaining sample of T Tauris in the Lupus regions is outside the scope of this work, although special cases are discussed in some detail in § 2.3.3.

2.3.2 Spectral energy distributions

To construct the SEDs we used ancillary data from ground-based optical, near-infrared, *Spitzer* and *WISE* data (Mortier et al. 2011; Comerón 2008; Allen et al. 2007; Krautter et al. 1997). These photometric data provide continuous wavelength coverage between 0.4 and 500 μm. Figs. 2.2 and 2.3 show the SEDs of the transitional disk candidates and the rest of the detected objects. We used the interstellar extinction law of Weingartner and Draine (2001). The A_V values were extracted from Mortier et al. (2011) and Merín et al. (2008), except in seven sources, identified with an asterisk in Table 2.6, for which we derived the values from the observed optical and near-infrared photometry and their spectral types.

We inspected all the images in 2MASS band J of the entire sample of detected objects. All of them were confirmed as point sources except those marked in Table 2.5 with a *j*, where minor extended emission cannot be discarded.

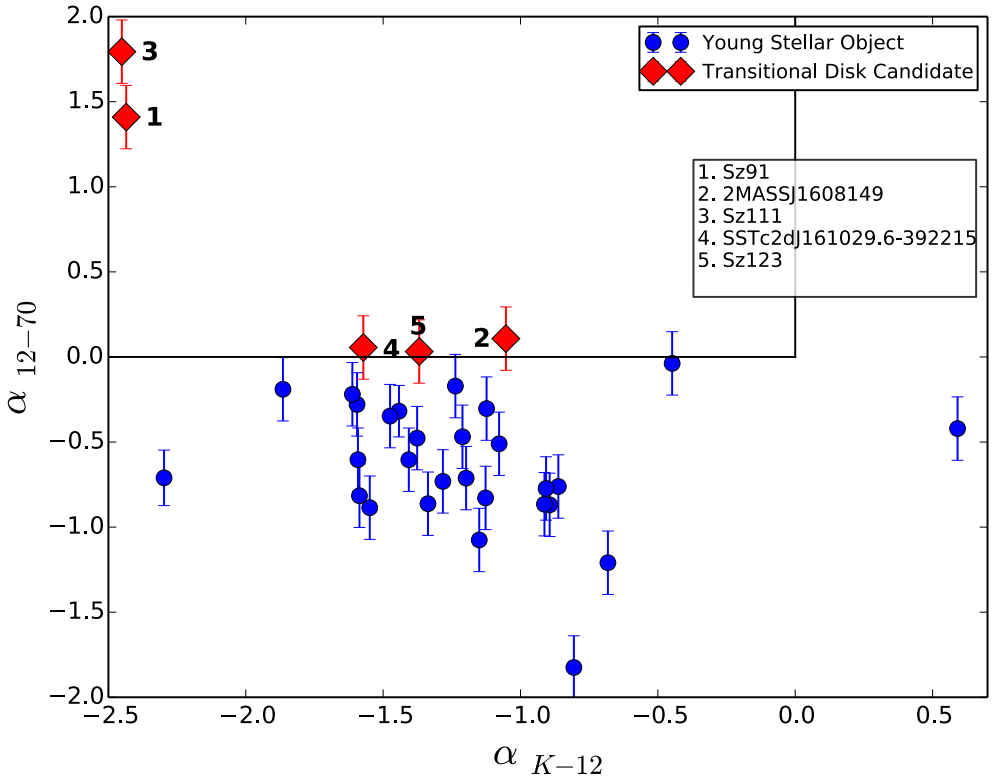

Figure 2.1: Identification of transitional disk candidates applying the color criteria from Ribas et al. (2013) to the Lupus *Herschel* data.

2.3.3 Individual objects of interest

2.3.3.1 Sz91 and Sz111

Sz91 and Sz111 had been previously identified as potential transitional disks based on *Spitzer* data in Merín et al. (2008) and have large Hα equivalent widths of 95.9 and 145.2 (Hughes et al. 1994), which indicate youth and active gas accretion to the stars.

The optical images of Sz91 reveal a known companion at approximately 8″ (Ghez et al. 1997), which corresponds to a distance of 1200 - 1600 AU from the star. However, the centroids of all the *Herschel*-detected sources match the coordinates of the primary source, Sz91 (see Fig. 2.4), so we assume no contribution from the companion to the measured fluxes.

2.3.3.2 SSTc2dJ161029.6-392215 and Sz123

Objects SSTc2dJ161029.6-392215 and Sz123 present SEDs characteristic of transitional disks,[moved comma] but with narrow gaps instead of the wide ones found at Sz91 and Sz111. They also present small excesses at near-infrared wavelengths (3-10 μm), that could signal the presence of an inner optically thick disk.

2.3.3.3 2MASS J1608149-3857145

Since object 2MASS J1608149 was not detected on the PACS 70 band, we used the PACS 100 band to classify it. The target then fulfilled the transitional disk detection criteria. As its SED shows 2.2, the *Herschel* far-infrared excess is not significant enough to classify the object as a transitional disk with absolute certainty. A further analysis including modeling could reveal the true nature of this object. Nevertheless, in this work we assume that object 2MASS J1608149 is a transitional disk candidate.

2.3.3.4 Sz68

Fig. 2.4 shows an extended feature at all wavelengths to the north of the Sz68 object. This is an already known Herbig-Haro object driven by Sz68 (Moreno-Corral et al. 1995). Interestingly, its emission dominates at wavelengths longer than 100 μm, which probably contaminates the SED of this object with unrelated flux to the star itself. A similar effect was discovered around the star T54 in Chamaeleon

I (Matrà et al. 2012), which had been erroneously classified as a transitional disk owing to nearby extended emission (see also Lestrade et al. (2012)).

2.3.3.5 SSTc2dJ160111.6-413730

SSTc2dJ160111.6-413730 has a very peculiar SED (see Fig. 2.3) with no excess at any wavelengths between optical and 160 μm, but substantial potential excesses at 250 - 500 μm associated with a clear point source in the images (see Fig. 2.4). The low 70 μm upper limit is nevertheless consistent with the sensitivity limit of the observations.

Previous claims of such extreme types of objects have been made in the context of the DUNES *Herschel* Key Programme, who named these objects "cold disks" because of their extreme nature (Krivov et al. 2013). Other authors have suggested background galaxies as the possible explanation (Gáspár and Rieke 2014). This object did not fulfill our classification criteria as transitional disk candidate.

2.3.3.6 Sz65 and Sz66

Objects Sz65 and Sz66 form a binary system, with a separation of 6.4" (Lommen et al. 2010), unresolved by *Herschel* (see Fig. 2.4). We inspected their SEDs to select the main contributor. We deduce that the primary source is Sz65 by studying the contour diagram of the image. The contour lines were centered at the position of source Sz65. Their MIPS24 and MIPS70 fluxes support this association. Then we set the *Herschel* fluxes of Sz66 as upper limits in Table 2.6 and in Fig. 2.3.

2.4 Discussion

2.4.1 Detection statistics

From an initial sample of 217 known Class II sources with spectroscopic membership confirmation in the Lupus clouds, 123 objects fell in at least one of the fields observed by the *Herschel* Gould Belt Survey. In particular, 92 and 98 were in the PACS and SPIRE Lupus III maps, respectively; 12 and 15 were found in Lupus I PACS and SPIRE mosaics; and 10 objects were observed in Lupus IV with both instruments. From these sources we detected 35 objects, 32 in PACS 70, two in PACS 100, and one in SPIRE. We then discarded one, 2MASSJ16085373-3914367, as we could not unequivocally assign its *Herschel* photometry to the target.

Compared with a similar study in Chamaeleon (Ribas et al. 2013), here we report a *Herschel* detection rate of $\sim$ 28% of the previously known objects in the region, comparable with the percentage in that work ($\sim$30%). The small differences in the distances to the regions ($\sim$ 150 pc for Chamaeleon vs $\sim$ 200 pc to Lupus III) might account for the small difference in the detection rate. Further analysis of the detection statistics of known and new sources in these regions with the HGBS data will be presented by Benedittini et al. (in prep.).

2.4.2 Incidence of transitional disks in Lupus

We report the detection of five transitional disk candidates in the Lupus molecular clouds based on *Herschel* and previous data of all spectroscopically confirmed Class II members of the association. Two transitional disks were known from previous works (Sz91 and Sz111), but the other three are new to the literature.

The Spitzer study of the Lupus clouds found a global disk fraction of 50 - 60% (Ribas et al. 2014), compatible with a relatively young age for the region of 1 - 2 Myrs (Comerón 2008). However, the total sample in Merín et al. (2008) included objects without spectroscopic membership confirmation so it could have a certain level of contamination from background galaxies and/or old dusty AGB stars (for a spectroscopic survey of Spitzer selected candidate members in Lupus see Mortier et al. (2011)). This work, however, uses an input target list where all objects have spectroscopic membership confirmation and is therefore not affected.

The observed fraction of transitional disks in Lupus based on our *Herschel* detected sample is $\sim$15%, which is comparable to the fractions measured in other such young and nearby regions (Espaillat et al. 2014). This corrects a surprisingly low incidence of this type of objects from the Spitzer sample reported in Merín et al. (2008), where only two objects were identified as transitional out of a photometric sample of 139 Class II and III sources. This demonstrates how *Herschel* efficiently complements mid-infrared surveys for the specific study of transitional disks.

2.4.3 Brighter PACS 70 fluxes in transitional disks

Recent studies have reported brighter 70 μm fluxes in transitional disks as compared with the median SED of standard T Tauri stars in the same regions (Cieza et al. 2011; Ribas et al. 2013). To check whether this phenomenon is dependent on the conditions of certain molecular clouds, we compared the SEDs of the detected disks in Lupus with the median SED of T Tauri stars in the region. Figs. 2.2 and

2.3 show the median SED normalized to the dereddened J-band flux for comparison, and Table 2.7 shows the fluxes of this median SED.

As shown in Fig. 2.2 most transitional disk candidates identified in Sect. 2.3.1 show the same phenomenon: the PACS fluxes are systematically above the median SED of the T Tauri stars. Therefore, the result has been confirmed around the isolated transitional disk T Cha (Cieza et al. 2011), in the Chamaeleon I cloud (Ribas et al. 2013), and in the Lupus molecular clouds (this work).

The interpretation of this phenomenon requires detailed SED modeling with radiative transfer disk models. However, the higher PACS fluxes compared with the median SED of the T Tauri stars suggests that the inner and outer disks of these objects follow different evolutionary paths by the time the inner gaps or holes are formed in the inner disks. Thus, the evolution of both inner and outer disk regions might not be dynamically decoupled.

2.4.4 SED population analysis

Merín et al. (2008) classified the YSO population in Lupus by studying the shape of their SEDs, and comparing the median SED of the CTTS from Taurus with their data. They grouped the objects into four categories, based on whether their slopes decay like a classical accreting optically thick disk around a low-mass star (T-Type), or if they present infrared excess clearly weaker (L-Type) or stronger (H-Type) than the median SED or where no excess is detected (E-Type). They also introduced a category that they called *cold disks* (LU-Type), which corresponds to our criteria for transitional disks. In their work, they made use of *Spitzer* and ground based photometry.

We did the same analysis for the 34 objects detected by *Herschel*, but now also taking into account the photometry we extracted. For simplification, we used a different nomenclature, grouping our objects into three categories that reveal their evolutionary state: higher infrared excess than the median values (H), indicating an early evolutionary stage; weaker (W), showing a more evolved stage; and transitional candidate (T). The results can be found in Table 2.5, where we also compare our classification to the aforementioned work by Merín et al. (2008). Another difference is that instead of using the Taurus median SED, we have used the Lupus value/values.

Apart from the transitional nature for the three new objects found in this work ($\sim$ 10%), we find that by adding the *Herschel* photometry to the SEDs we can

update the type found in Merín et al. (2008) for another nine objects ($\sim$ 27%). The final population for our sample is then classified as follows: $\sim$ 56% *primordial* disks (this groups T Tauri types and stronger infrared excesses), $\sim$ 29% *evolved* disks, and $\sim$ 15% transitional disk candidates. This compares well to the 67%, 26%, and 7% found for the same types of objects from the *Spitzer*-only study. Table 2.5 shows the *Spitzer*-only and *Spitzer*+*Herschel* classifications. The relative overall fractions have not changed substantially, except on the larger fraction of transitional disk candidates.

2.5 Conclusions

We have detected 34 objects in the Lupus cloud using *Herschel* and broadened the study of the YSOs in the association. Having confirmed that our *Herschel* data enable improved characterization of the outer regions of protoplanetary disks, we have identified additional transitional disks in our sample. The fraction of transitional disks detected in our study, comparable in size to Ribas et al. (2013), corrects the relatively low value from *Spitzer* detections. In addition, we find that all of these objects have 70 μm fluxes brighter than the median SED, showing perhaps another possible intrinsic property. Finally, we have carried out a population analysis by studying the SED shapes of the detections, and updated the morphological type of several sources. Further studies and modeling will give us more information on [about] these objects.

Table 2.5: Class II objects detected by *Herschel* in the Lupus clouds. The object types are higher than the median infrared excess (H), weaker (W), and transitional disk candidates (T). See text for details.

Object	R.A.$_{J2000}$	Dec$_{J2000}$	A_V (mag)	SpT	Type (*Spitzer***)	Type (This Work)	References^r
			Lupus I				
Sz65	15:39:27.8	-34:46:17.1	1.0	M0	H	H	2
Sz66^v	15:39:28.3	-34:46:18.0	2.0	M3	H	H	2
Sz68	15:45:12.9	-34:17:30.6	1.5	K2	H	H	2
Sz69	15:45:17.4	-34:18:28.3	4.0	M1	W	W	2
			Lupus III				
SSTc2dJ160703.9-391112	16:07:03.8	-39:11:11.3	2.2	M5.5	-	H	1
Sz90	16:07:10.1	-39:11:03.3	5.0*	K8	W	H	2, 5
Sz91	16:07:11.6	-39:03:47.5	1.0	M0.5	T	T	2
Sz95	16:07:52.3	-38:58:05.9	1.0	M1.5	W	W	2
Sz96	16:08:12.6	-39:08:33.5	1.4	M2	H	W	1
2MASSJ1608149-3857145	16:08:14.9	-38:57:14.6	7.0*	M4.7	H	T	3, 5
Sz98	16:08:22.5	-39:04:46.5	2.5	K5	H	H	1
Sz100	16:08:25.8	-39:06:01.2	1.2	M4.5	H	H	1
Sz102	16:08:29.7	-39:03:11.0	2.5	K2	-	H	1
Sz103	16:08:30.3	-39:06:11.2	1.0	M4.5	H	H	1
Sz104	16:08:30.8	-39:05:48.9	0.7	M5.5	H	H	1
HR5999	16:08:34.3	-39:06:18.2	1.0*	A7	H	W	2, 5
RXJ1608.6-3922	16:08:36.2	-39:23:02.5	3.0*	K6	-	H	4, 5
Sz108B	16:08:42.9	-39:06:14.4	0.8	M5.5	W	W	1
Sz110	16:08:51.6	-39:03:17.7	0.2	M3	H	H	1
Sz111	16:08:54.6	-39:37:43.1	0.0	M1.5	T	T	2
Sz112^j	16:08:55.5	-39:02:33.9	1.0	M4	W	W	2
SSTc2dJ160901.4-392512	16:09:01.4	-39:25:11.9	0.6	M3.5	H	H	1
Sz114^j	16:09:01.9	-39:05:12.4	1.3	M4	H	H	1
Sz117	16:09:44.4	-39:13:30.1	1.0	M2	H	W	2
Sz118^j	16:09:48.7	-39:11:16.9	2.6	K7	H	H	1
SSTc2dJ161029.6-392215	16:10:29.6	-39:22:14.5	0.0	M5.5	H	T	1
Sz123	16:10:51.6	-38:53:13.8	0.0	M3	W	T	2
			Lupus IV				
SSTc2dJ160002.4-422216	16:00:02.4	-42:22:14.6	2.0*	M3.5	H	H	1, 5
IRAS15567-4141^j	16:00:07.4	-41:49:48.4	2.0	M6.5	W	W	1
Sz130^j	16:00:31.1	-41:43:36.9	0.60	M2	H	W	1
F403^j	16:00:44.5	-41:55:31.0	2.0	K0	W	H	2
Sz131^j	16:00:49.4	-41:30:03.9	0.0	M2	H	H	2
SSTc2dJ160111.6-413730^v	16:01:11.5	-41:37:29.9	0.0	M8.5	W	W	1
Sz133^j	16:03:29.4	-41:40:01.8	10.0*	K2	H	H	1

Notes. $^{(r)}$ References for the spectral type and A_V: (1) Mortier et al. (2011), (2) Comerón (2008), (3) Allen et al. (2007), (4) Krautter et al. (1997), and (5) this work.
$^{(j)}$ The objects marked with j presented potential small extended emission at J band. Nevertheless, all of them have spectroscopic confirmation of being young stellar objects.
$^{(v)}$ These objects were missed by our detection method and were detected in the visual inspection.
$^{(*)}$ Extinction values denoted with an asterisk indicate that they were computed in this work either because they were not available in the literature or the ones found did not provide appropriate fits to the model photospheres.
$^{(**)}$ Merín et al. (2008).

Table 2.6: *Herschel* photometry for the 34 YSOs detected in the maps. When no source was detected at a certain band, an upper limit is provided.

Object	$F_{70\mu m}$ (Jy)	$F_{100\mu m}$ (Jy)	$F_{160\mu m}$ (Jy)	$F_{250\mu m}$ (Jy)	$F_{350\mu m}$ (Jy)	$F_{500\mu m}$ (Jy)
Lupus I						
Sz65	0.47±0.12	-	0.55±0.14	0.77±0.15	0.95±0.19	<1.59
Sz66	0.45±0.11	-	0.55±0.14	0.81±0.16	0.98±0.20	<1.63
Sz68	3.01±0.75	3.80±0.95	11.77±2.94	13.06±2.61	10.22±2.04	6.74±1.35
Sz69	0.12±0.03	0.19±0.05	<0.31	<1.59	<0.88	<2.13
Lupus III						
SSTc2dJ160703.9-391112	0.07±0.02	0.10±0.02	0.19±0.05	<0.33	<0.44	<0.43
Sz90	0.36±0.09	0.37±0.09	0.26±0.07	0.51±0.10	0.50±0.10	<0.61
Sz91	0.51±0.13	0.68±0.17	0.72±0.18	0.86±0.17	0.62±0.12	0.38±0.08
Sz95	<0.05	0.05±0.01	0.09±0.02	<0.28	<0.30	<0.25
Sz96	0.14±0.03	0.12±0.03	0.10±0.02	<1.49	<1.87	<1.96
2MASSJ1608149-3857145	<0.08	0.07±0.02	<0.11	<0.48	<0.25	<0.21
Sz98	0.64±0.16	0.58±0.14	0.50±0.12	0.93±0.19	1.14±0.23	<2.12
Sz100	0.17±0.04	0.23±0.06	0.29±0.07	0.59±0.12	<1.99	<1.33
Sz102	0.34±0.09	0.37±0.09	0.22±0.06	<3.25	<4.07	<4.37
Sz103	0.11±0.03	0.16±0.04	<0.23	<2.13	<1.64	<1.20
Sz104	0.10±0.02	0.18±0.04	<0.19	<2.08	<1.97	<2.13
HR5999	4.25±1.06	3.20±0.80	1.60±0.40	0.92±0.18	0.47±0.09	<3.26
RXJ1608.6-3922	0.40±0.10	0.69±0.17	1.36±0.34	2.55±0.51	2.83±0.57	2.40±0.48
Sz108B	0.20±0.05	0.21±0.05	<0.61	<5.81	<9.68	<8.85
Sz110	0.13±0.03	0.09±0.02	<0.26	<0.57	<0.48	<0.76
Sz111	1.16±0.29	-	1.73±0.43	1.31±0.26	0.94±0.19	0.58±0.12
Sz112	0.10±0.03	0.04±0.01	<0.16	<0.33	<0.27	<0.38
SSTc2dJ160901.4-392512	0.08±0.02	0.09±0.02	0.12±0.03	0.15±0.03	0.13±0.03	0.07±0.01
Sz114	0.28±0.07	0.26±0.06	0.13±0.03	<0.53	<0.51	<1.11
Sz117	0.06±0.02	0.11±0.03	0.17±0.04	<0.82	<0.70	<0.65
Sz118	0.35±0.09	0.46±0.11	0.37±0.09	0.49±0.10	0.56±0.11	<0.98
SSTc2dJ161029.6-392215	0.07±0.02	0.10±0.02	<0.13	<0.29	<0.27	<0.26
Sz123	0.27±0.07	0.37±0.09	0.45±0.11	0.17±0.03	0.12±0.02	0.08±0.02
Lupus IV						
SSTc2dJ160002.4-422216	0.10±0.02	0.20±0.05	0.21±0.05	0.22±0.04	0.23±0.05	0.17±0.03
IRAS15567-4141	0.11±0.03	0.05±0.01	<0.11	<0.38	<0.34	<0.22
Sz130	0.11±0.03	0.12±0.03	0.05±0.01	<0.39	<0.34	<0.34
F403	1.04±0.26	1.26±0.31	1.57±0.39	1.33±0.27	0.93±0.19	0.58±0.12
Sz131	0.11±0.03	-	<0.10	<0.24	<0.35	<0.25
SSTc2dJ160111.6-413730	<0.05	-	<0.09	0.11±0.02	0.07±0.01	<0.16
Sz133	0.21±0.05	0.38±0.10	0.32±0.08	0.37±0.07	0.30±0.06	0.20±0.04

Table 2.7: Normalized flux densities of the median SED, lower SED (first quartile), and upper SED (fourth quartile) of the Class II objects in Lupus I, III, and IV. The number of detections in each band is also included. The transitional disk candidates are excluded from this count. All values are normalized to J band.

Band(μm)	Median	First Quartile	Fourth Quartile	Detections
		(F_λ arbitrary units)		
J 1.25	1.000	1.000	1.000	28
H 1.62	1.048	0.982	1.186	28
K 2.15	0.761	0.673	1.015	28
IRAC 3.6	0.331	0.260	0.501	23
IRAC 4.5	0.259	0.182	0.385	24
IRAC 5.8	0.193	0.143	0.284	24
IRAC 8.0	0.167	0.111	0.223	25
MIPS 23.68	0.090	0.054	0.122	27
PACS 70	0.049	0.025	0.074	25
PACS 100	0.042	0.018	0.056	25
PACS 160	0.028	0.023	0.066	18
SPIRE 250	0.023	0.015	0.045	15
SPIRE 350	0.017	0.013	0.036	11
SPIRE 500	0.011	0.007	0.019	6

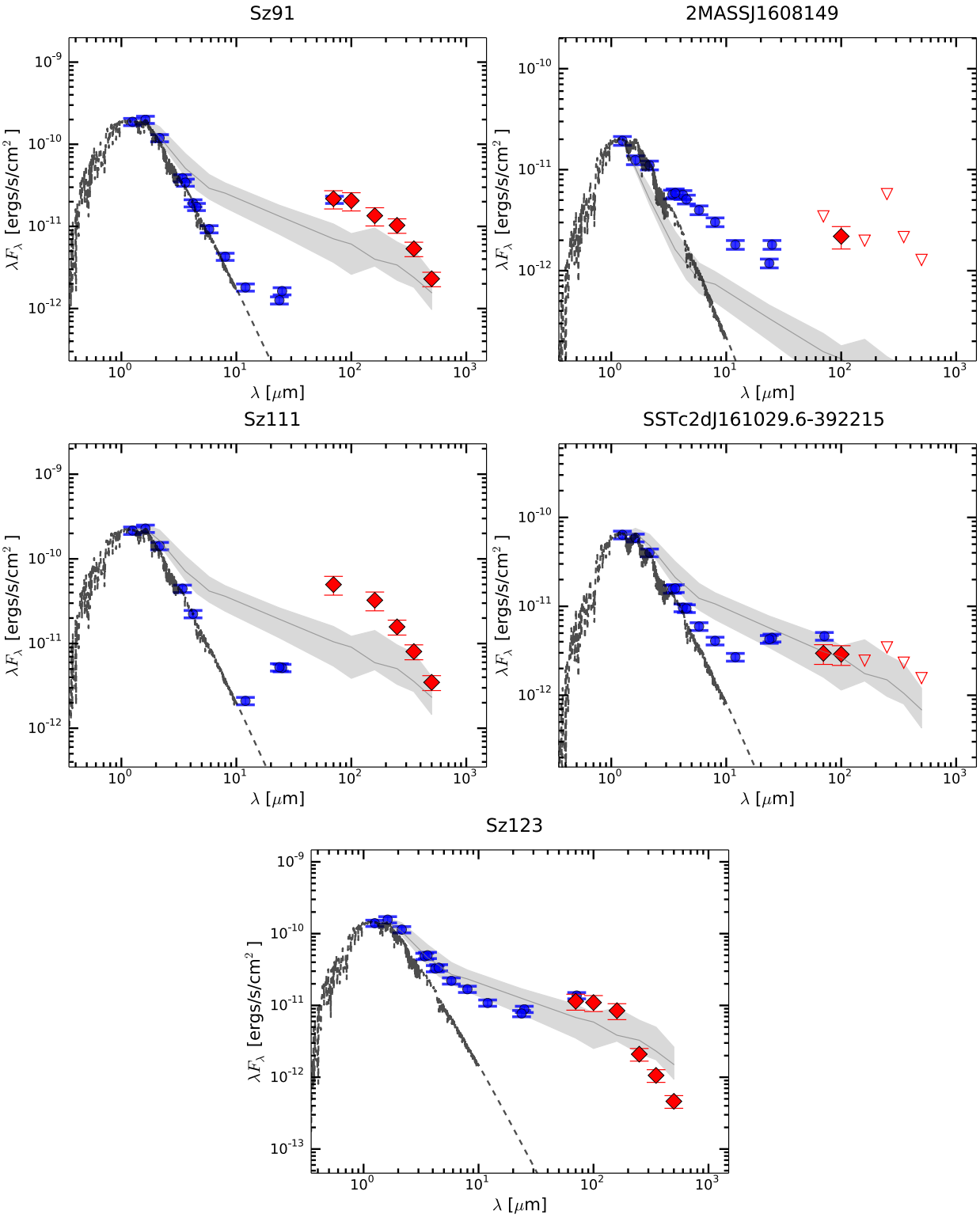

Figure 2.2: Spectral energy distributions of the five transitional disk candidates identified with *Herschel*. Blue dots represent the dereddened ancillary data from the literature from previous studies. The red diamonds are the clear detections with *Herschel*, and the red triangles the upper limits wherever no clear detection in the maps was found. The gray solid line is the median SED from the Lupus sample of the 29 non-transitional disks in the region, and the gray shaded area the first and fourth quartiles. See Table 2.7 for more information. The dashed lines are the photospheric NextGen models from Allard et al. (2012).

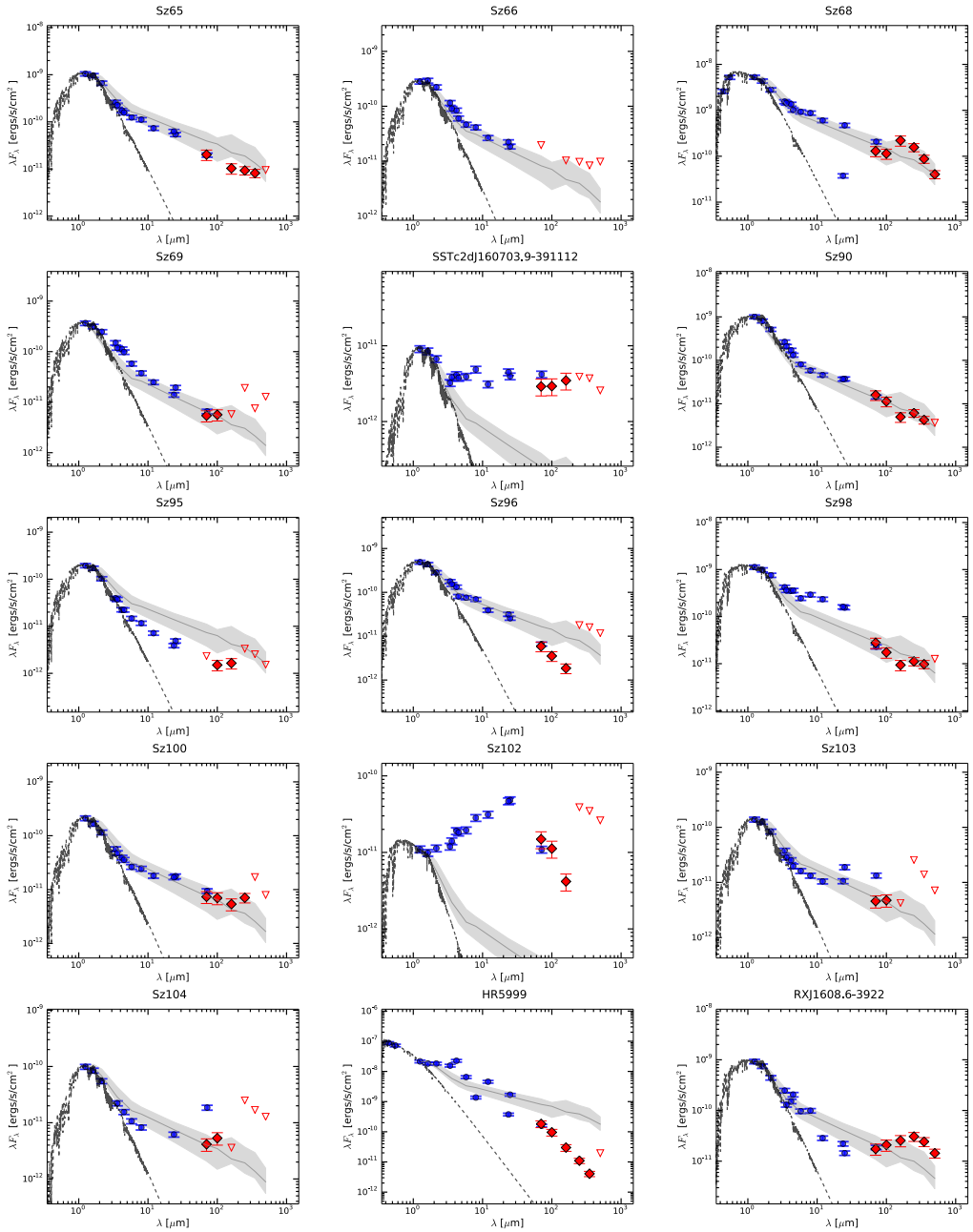

Figure 2.3: Spectral energy distributions of the 29 YSOs with *Herschel* detections that do not fulfill our transitional disk selection criteria

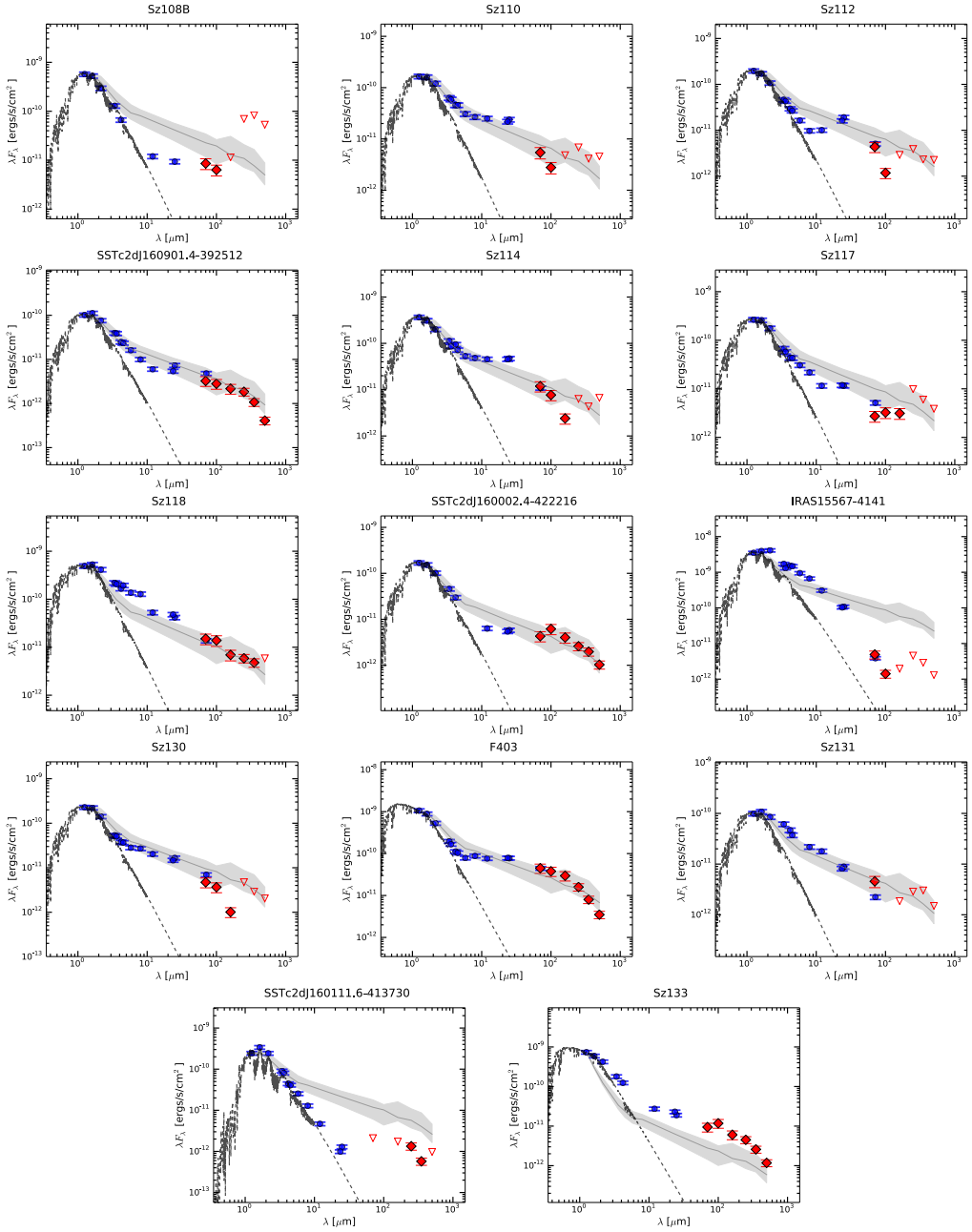
Sz108B
Sz110
Sz112
SSTc2dJ160901.4-392512
Sz114
Sz117
Sz118
SSTc2dJ160002.4-422216
IRAS15567-4141
Sz130
F403
Sz131
SSTc2dJ160111.6-413730
Sz133
λ [μm]
λF_λ [ergs/s/cm²]

(Fig. 2.3 cont.)

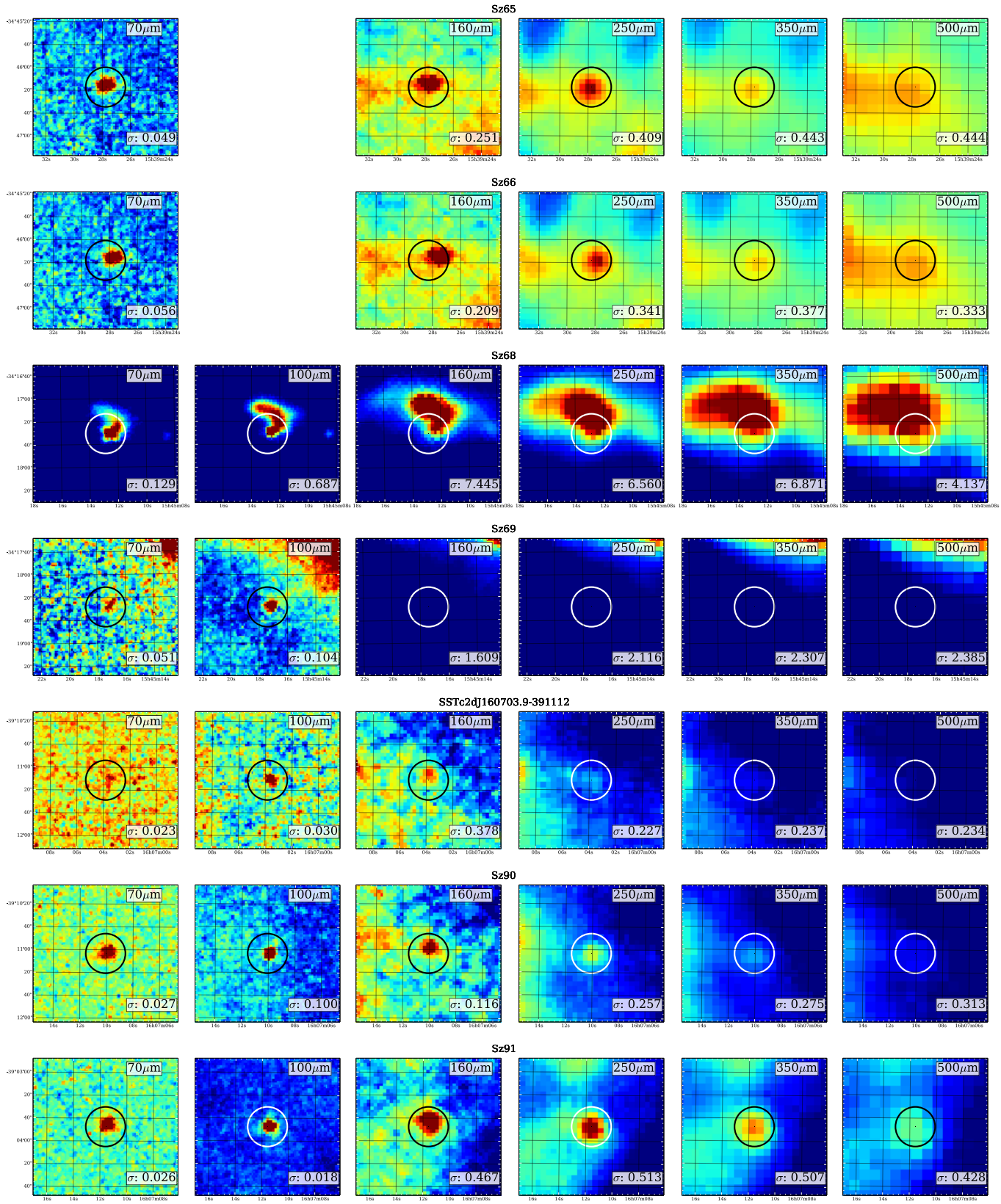

Figure 2.4: Images of each of the 34 sources with at least one point source detected by *Herschel*, plus object 2MASSJ16085373-3914367, added for completeness. The images correspond to a box of 120" x 120" in size. Coordinates are given in Table 2.5. The color scale is defined with the RMS of the pixel values (as background level) and this number plus three times the standard deviation (as maximum level). North is up and east is left. A circle indicates the expected position of the target. The standard deviation computed around the sources is shown for each image (bottom right)

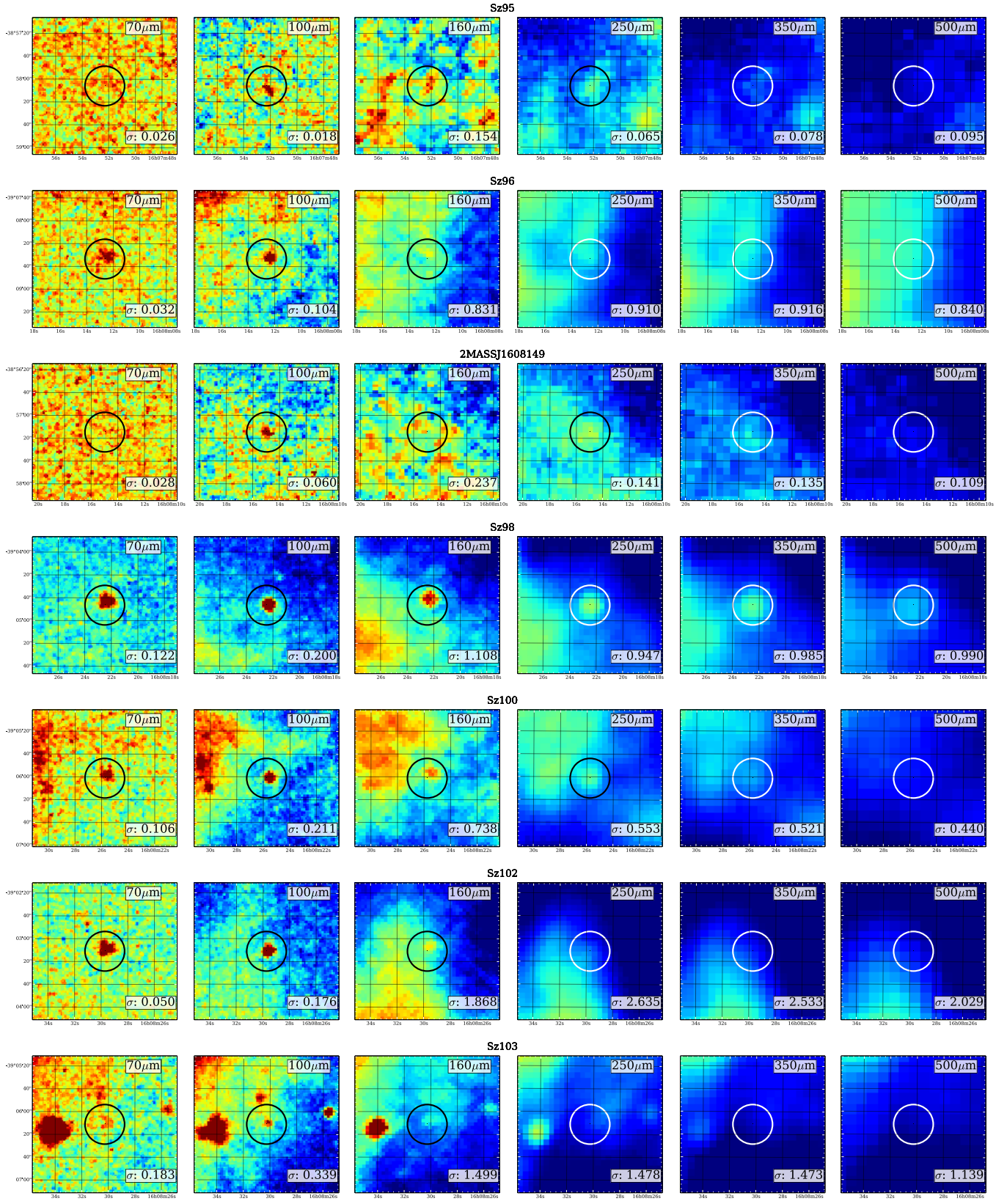
Sz95
70μm σ: 0.026
100μm σ: 0.018
160μm σ: 0.154
250μm σ: 0.065
350μm σ: 0.078
500μm σ: 0.095
Sz96
70μm σ: 0.032
100μm σ: 0.104
160μm σ: 0.831
250μm σ: 0.910
350μm σ: 0.916
500μm σ: 0.840
2MASSJ1608149
70μm σ: 0.028
100μm σ: 0.060
160μm σ: 0.237
250μm σ: 0.141
350μm σ: 0.135
500μm σ: 0.109
Sz98
70μm σ: 0.122
100μm σ: 0.200
160μm σ: 1.108
250μm σ: 0.947
350μm σ: 0.985
500μm σ: 0.990
Sz100
70μm σ: 0.106
100μm σ: 0.211
160μm σ: 0.738
250μm σ: 0.553
350μm σ: 0.521
500μm σ: 0.440
Sz102
70μm σ: 0.050
100μm σ: 0.176
160μm σ: 1.868
250μm σ: 2.635
350μm σ: 2.533
500μm σ: 2.029
Sz103
70μm σ: 0.183
100μm σ: 0.339
160μm σ: 1.499
250μm σ: 1.478
350μm σ: 1.473
500μm σ: 1.139

(Fig. 2.4 cont.)

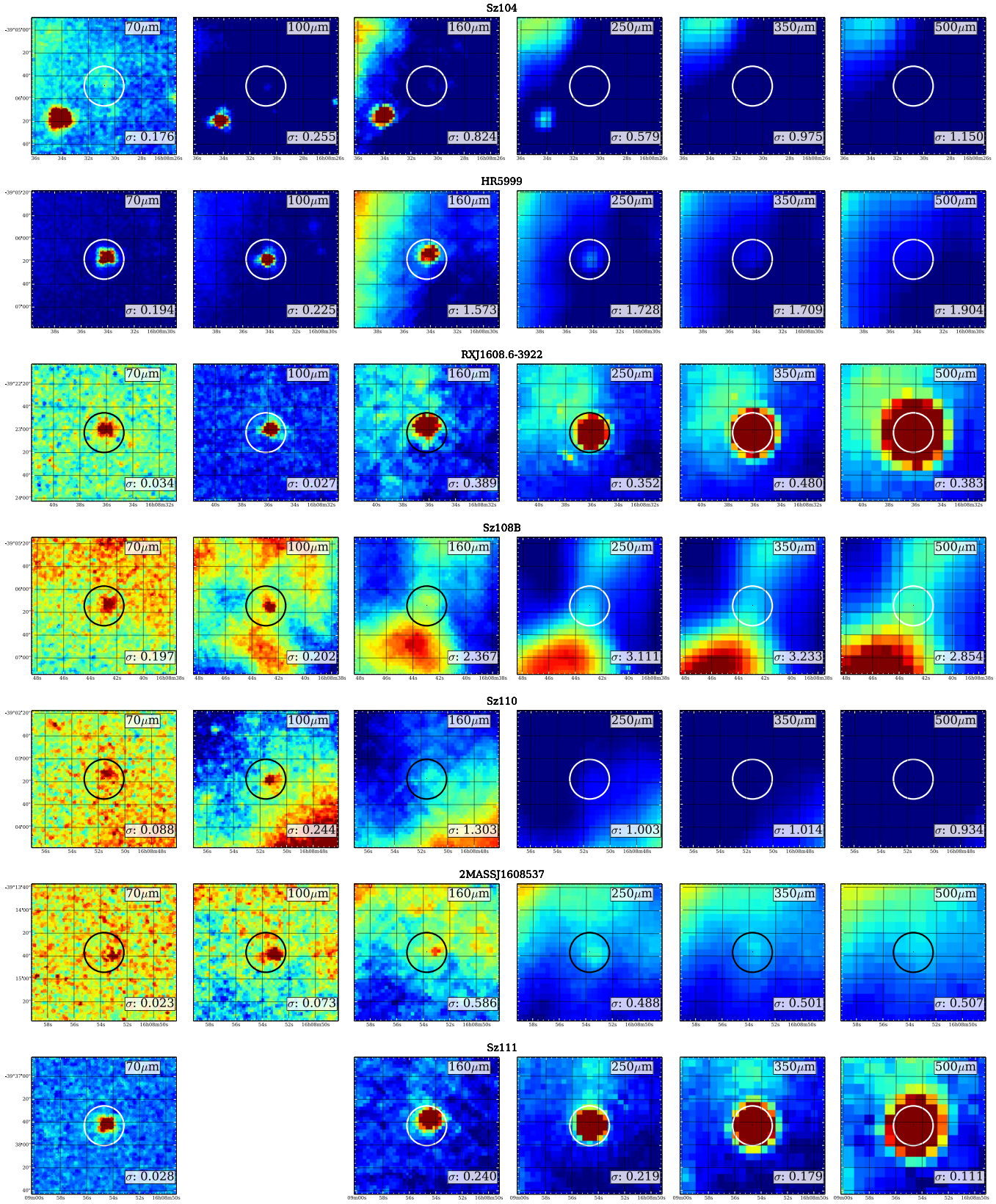
Sz104
70μm σ: 0.176
100μm σ: 0.255
160μm σ: 0.824
250μm σ: 0.579
350μm σ: 0.975
500μm σ: 1.150
HR5999
70μm σ: 0.194
100μm σ: 0.225
160μm σ: 1.573
250μm σ: 1.728
350μm σ: 1.709
500μm σ: 1.904
RXJ1608.6-3922
70μm σ: 0.034
100μm σ: 0.027
160μm σ: 0.389
250μm σ: 0.352
350μm σ: 0.480
500μm σ: 0.383
Sz108B
70μm σ: 0.197
100μm σ: 0.202
160μm σ: 2.367
250μm σ: 3.111
350μm σ: 3.233
500μm σ: 2.854
Sz110
70μm σ: 0.088
100μm σ: 0.244
160μm σ: 1.303
250μm σ: 1.003
350μm σ: 1.014
500μm σ: 0.934
2MASSJ1608537
70μm σ: 0.023
100μm σ: 0.073
160μm σ: 0.586
250μm σ: 0.488
350μm σ: 0.501
500μm σ: 0.507
Sz111
70μm σ: 0.028
160μm σ: 0.240
250μm σ: 0.219
350μm σ: 0.179
500μm σ: 0.111

(Fig. 2.4 cont.)

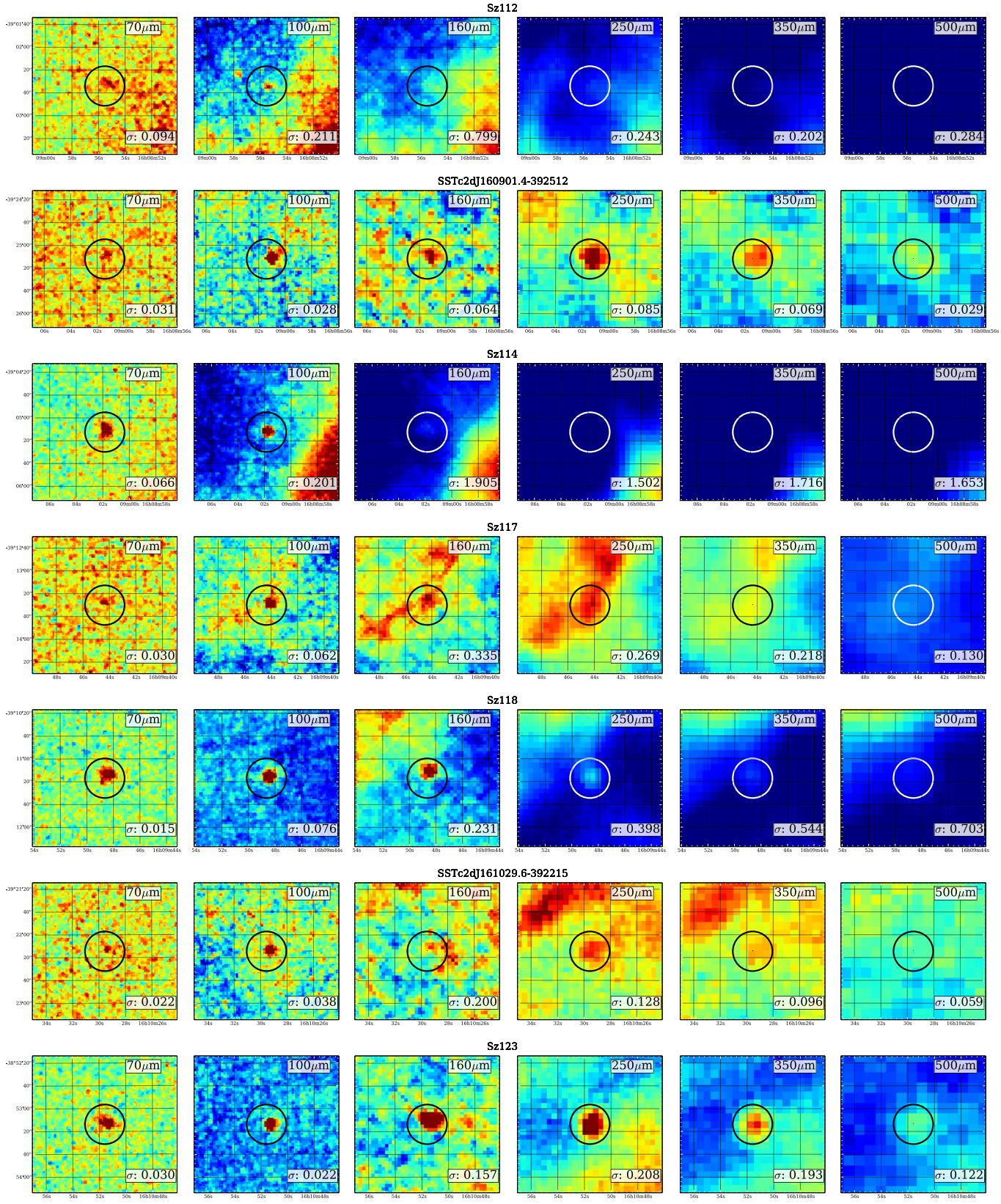
Sz112
70μm σ: 0.094
100μm σ: 0.211
160μm σ: 0.799
250μm σ: 0.243
350μm σ: 0.202
500μm σ: 0.284
SSTc2dJ160901.4-392512
70μm σ: 0.031
100μm σ: 0.028
160μm σ: 0.064
250μm σ: 0.085
350μm σ: 0.069
500μm σ: 0.029
Sz114
70μm σ: 0.066
100μm σ: 0.201
160μm σ: 1.905
250μm σ: 1.502
350μm σ: 1.716
500μm σ: 1.653
Sz117
70μm σ: 0.030
100μm σ: 0.062
160μm σ: 0.335
250μm σ: 0.269
350μm σ: 0.218
500μm σ: 0.130
Sz118
70μm σ: 0.015
100μm σ: 0.076
160μm σ: 0.231
250μm σ: 0.398
350μm σ: 0.544
500μm σ: 0.703
SSTc2dJ161029.6-392215
70μm σ: 0.022
100μm σ: 0.038
160μm σ: 0.200
250μm σ: 0.128
350μm σ: 0.096
500μm σ: 0.059
Sz123
70μm σ: 0.030
100μm σ: 0.022
160μm σ: 0.157
250μm σ: 0.208
350μm σ: 0.193
500μm σ: 0.122

(Fig. 2.4 cont.)

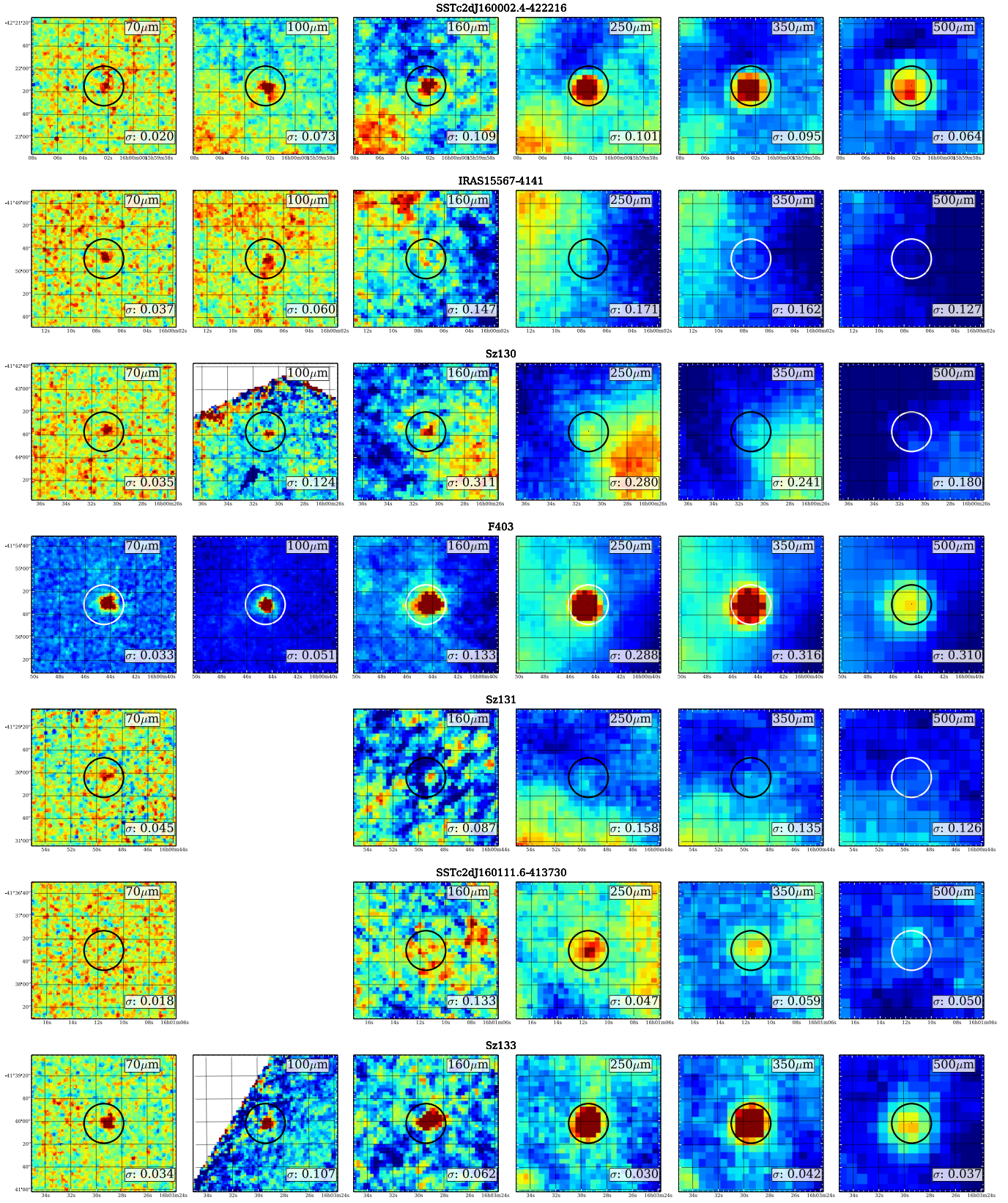
SSTc2dJ160002.4-422216
70μm σ: 0.020
100μm σ: 0.073
160μm σ: 0.109
250μm σ: 0.101
350μm σ: 0.095
500μm σ: 0.064
IRAS15567-4141
70μm σ: 0.037
100μm σ: 0.060
160μm σ: 0.147
250μm σ: 0.171
350μm σ: 0.162
500μm σ: 0.127
Sz130
70μm σ: 0.035
100μm σ: 0.124
160μm σ: 0.311
250μm σ: 0.280
350μm σ: 0.241
500μm σ: 0.180
F403
70μm σ: 0.033
100μm σ: 0.051
160μm σ: 0.133
250μm σ: 0.288
350μm σ: 0.316
500μm σ: 0.310
Sz131
70μm σ: 0.045
160μm σ: 0.087
250μm σ: 0.158
350μm σ: 0.135
500μm σ: 0.126
SSTc2dJ160111.6-413730
70μm σ: 0.018
160μm σ: 0.133
250μm σ: 0.047
350μm σ: 0.059
500μm σ: 0.050
Sz133
70μm σ: 0.034
100μm σ: 0.107
160μm σ: 0.062
250μm σ: 0.030
350μm σ: 0.042
500μm σ: 0.037

(Fig. 2.4 cont.)

Chapter 3

Infrared study of transitional disks in Ophiuchus with *Herschel*

Rebollido, I; Merín, B; Ribas, Á; Bustamante, I; Bouy, H; Riviere-Marichalar, P; Prusti, T; Pilbratt, G.L.; André, P; Ábrahám, P

Infrared study of transitional disks in Ophiuchus with Herschel. 2015, Astronomy & Astrophysics, 581, A30

Abstract

Observations of nearby star-forming regions with the *Herschel* Space Observatory complement our view of the protoplantary disks in Ophiuchus with information about the outer disks. The main goal of this project is to provide new far-infrared fluxes for the known disks in the core region of Ophiuchus and to identify potential transitional disks using data from *Herschel*. We obtained PACS and SPIRE photometry of previously spectroscopically confirmed young stellar objects (YSO) in the region and analysed their spectral energy distributions. From an initial sample of 261 objects with spectral types in Ophiuchus, we detect 49 disks in at least one *Herschel* band. We provide new far-infrared fluxes for these objects. One of them is clearly a new transitional disk candidate. The data from *Herschel* Space Observatory provides fluxes that complement previous infrared data and that we use to identify a new transitional disk candidate.

3.1 Introduction

Protoplanetary disks around young stars are objects of major interest as they lead us to a better understanding of star and planet formation. Transitional disks are key in this study since they appear to have an unusual radial structure. They have been proposed as the environment for planet formation (Marsh and Mahoney 1992) and have other proposed formation mechanisms, such as photo-evaporation by ultraviolet light emitted by the central star (Clarke et al. 2001), grain growth (Dullemond and Dominik 2005), and gravitational instabilities (see Espaillat et al. (2014) for a recent review on transitional disks). Recently, Kim et al. (2013) studied accretion towards transitional disks in Orion A and concluded that planet formation was the most likely explanation for their observations. What characterizes a transitional disk is a lack of excess in the near- or mid-IR region (usually around 8 or 10 μm) and typical Class-II excesses in mid- to far-IR. This lack of near- and mid-IR excess denotes an inner disk opacity hole, which is related to the dust distribution in the surroundings of the star and reveals inner holes. These objects are thought to be an intermediate stage between Class II objects (optically thick disks) and Class III objects (smaller amount of material in the disk).

The first transitional disks were reported by Strom et al. (1989b). Since that time, the known population of these objects has grown substantially thanks to data from *Spitzer* Space Telescope (Werner et al. 2004). The study of these objects has improved with new and more powerful telescopes, such as the *Herschel* Space Obsevatory (Pilbratt et al. 2010), which provides a wider range of wavelengths. *Herschel* also represents an improvement *Spitzer*'s sensitivity and spatial resolution at long wavelengths, which allows for a reduction in the noise level of measurements at these wavelengths. Studies in the millimetric and sub-millimetric range allowed for the imaging and direct measurement of hole sizes, such as those made by Andrews et al. (2011) with the Sub-Millimeter Array (Ho et al. 2004). Recent work with ALMA (Wootten and Thompson 2009) has achieved new results in the field as seen in works by van der Marel et al. (2013) and the recent study on the transitional disk HL Tauri (ALMA Partnership et al. 2015).

The aim of this work is to study the young stellar objects (YSOs) in the Ophiuchus star-forming region. *Herschel* data provide us with accurate fluxes of the detected objects, and enables the construction of the spectral energy distributions (SEDs) along with other multi-wavelength photometric data, collected by Ribas et al. (2014). The study of the SEDs also allows us to classify the transitional disks

in the region by identifying the previously mentioned lack of excess in near and/or mid-IR region.

The structure of this work is as follows: Sect. 2 describes the *Herschel* observations and data reduction, explaining the source detection and photometry extraction processes. In Sect. 3 we explain the results obtained from the data reduction, both with the method described in Ribas et al. (2013) and with the analysis of the SED of each individual object. In Sect. 4 we discuss the detection statistics and compare them with other similar studies. In Sect. 5 we present the conclusions of this work.

3.2 Observations and data reduction

The Ophiuchus cloud complex was observed by *Herschel* as part of the *Herschel* Gould Belt Survey (André et al. 2010) and by a deeper PACS survey (Alves de Oliveira et al. 2013). It is one of the closest star-forming regions, located at an estimated distance of 130 pc and with an age between 2 and 5 Myr, although it has been suggested that it is younger (for a review on the region see Wilking et al. (2008)). Apart from its proxmity, most significant characteristic of this cloud is its dense core, which is the focus of our study. The cloud itself appears as a large scale structure with complex filaments, heated by B-type stars, and is strongly emitting at infrared wavelengths. We might consider the cloud itself as a possible source of contamination. Fig. 3.1 shows the region with the objects in the sample overplotted and marked differently according to their state of non-detected, detected, or transitional.

The maps used to examine this region were obtained from two sets of observations, using the parallel mode of both PACS (Poglitsch et al. 2010) and SPIRE (Griffin et al. 2010) on board the *Herschel* Space Observatory. For SPIRE maps (250 μm, 350 μm and 500 μm) the parallel mode was used, with a speed of 60″/s (program $KPGT\_pandre\_1$), but for the PACS maps (70 μm and 160 μm) the scan mapping mode was used, with a cross-scan speed of 20″/s (program $OT1\_pabraham\_3$). We used this later PACS data because it goes deeper, as shown by the sensitivity limits given in the SPIRE/PACS Observers' Manual and in Table 3.1 in this work. In both cases (PACS and SPIRE), a single pair of scan and cross-scan was obtained. The obsids for the SPIRE maps are (1342-) 205093 & 205094, and for PACS maps (1342-) 238816 & 238817.

The maps were produced using Scanamorphos (Roussel 2012), an IDL software designed to process *Herschel* maps. Version 24.0 was used for PACS maps, with

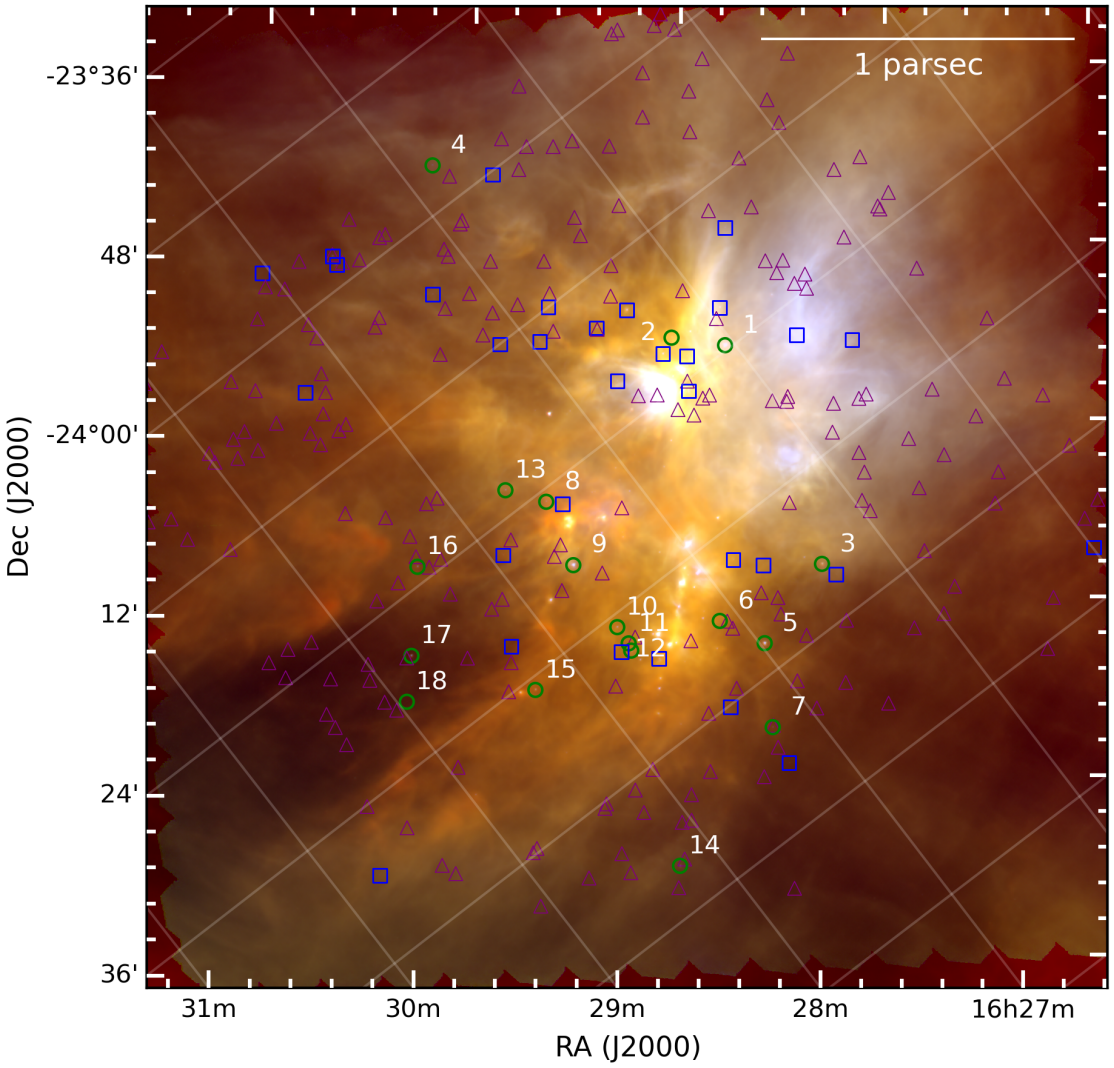

Figure 3.1: RGB image (PACS 70 in blue, PACS 100 in green, and PACS 160 in red) of the observed Ophiuchus region with the marked objects. Transitional disks are marked with green circles. The blue squares mark the detected objects, and the purple triangles mark the rest of the sample of known young stars in the region.

Table 3.1: Sensitivity of the *Herschel* observations used in this study

	$F_{70}\,[mJy]$	$F_{160}\,[mJy]$	$F_{250}\,[mJy]$	$F_{350}\,[mJy]$	$F_{500}\,[mJy]$
Sensitivity per scan	12.2	14.3	12.6	10.5	15.0
Effective Sensitivity	2	2.4	6.3	5.2	7.5
Minimum Flux Detected	20	50	70	10	30

calibration file version 65, and version 22.0 for SPIRE maps, with calibration files version 12.3.

3.2.1 Sample selection and point source photometry

The objective of this work is to determine the nature of the sources detected in the maps produced with PACS and SPIRE observations and to obtain fluxes in the mid- to far-IR regions when detected. The YSO candidates were selected from the work of Ribas et al. (2014) (which for Ophiuchus contains objects from Natta et al. (2002), Wilking et al. (2005), Alves de Oliveira et al. (2010) and Erickson et al. (2011)), for having known spectral type from spectroscopy, making a list of 258 sources, all of them located in the core of the cloud. For a more complete study, the objects from Cieza et al. (2010) contained in the region of interest were also considered. The final sample consists of 261 objects. We used photometry from the 2MASS K-band (Skrutskie et al. 2006) and WISE4 (Wright et al. 2010) to classify the disks according to the method described by Lada (1987). The only object that does not fulfill the criteria is IRS 48, which has a positive slope that is almost flat. This object cannot be classified as Class I and remains Class II in the final classificaiton because of the lack of strong emission in mid- and far-IR.

To determine whether our candidates are transitional disks or not, the first step was to detect sources in our maps and extract the photometry from them. We used the algorithm *Sussextractor* in the *Herschel Interactive Processing Environment* (HIPE), version 12.1, with a threshold of S/N > 3. Additionally, visual inspection was applied to all sources. Only sources clearly separated from filaments and distinguishable from the background were selected as valid detections.

We extracted aperture photometry for these sources using the sourceExtractorDaophot task in HIPE (Ott 2010). The fluxes were aperture corrected to account for the shape of the PSF and they are listed in Table 3.4. Those corrections were obtained from Balog et al. (2014) for PACS and from the SPIRE Observers' Manual (now named SPIRE Handbook) version 2.5. In Table 3.4, objects marked with an asterisk suffered from high nearby background emission and, in those cases, we used a special sky estimate from a rectangular area identified after visual inspection. The set of apertures and the corrections applied to the photometry extracted are shown in Table 3.2. We tested several point-source extraction algorithms, including Sussextractor, Daophot, AnnularSkyAperturePhotometry, and Hyper (Traficante et al. 2015), and different apertures. The combination above provides the best fit to the

Table 3.2: Aperture photometry parameters

Band	FWHM (")	Radius (")	Inner Annulus (")	Outer Annulus (")	Aperture Correction Factors
PACS-70	5.4	6	25	35	1.5711
PACS-160	10.5	12	25	35	1.4850
SPIRE-250	18	22	60	90	1.2584
SPIRE-350	24	30	60	90	1.2242
SPIRE-500	36	42	60	90	1.1975

MIPS70 (Rieke and Su 2004) fluxes of clean selected sources in the field.

At the end of the process, we had 49 successfully detected sources in at least one PACS band, and 19 in a SPIRE band; PACS also detected all of these. Images of the detected objects can be found in Fig. 3.6, for visual inspection.

The calibration errors for PACS and SPIRE are 5% and 7% (as stated in the PACS Observer's Manual, version 2.3 and in the SPIRE Observer's Manual version 2.5), however, as a more conservative estimation, we used 25% for both. These measurement uncertainties account for the high variations in the results of the different extraction methods and apertures listed above.

In Table 3.3 we show the parameters of the detected sources, as given in the literature, and for an easier reference we list the identification numbers (I.D.) used in this work as seen in Fig. 3.1. From now on, the I.D. number is referenced in parenthesis for its respective source. Table 3.4 gives the fluxes measured with *Herschel* for each source.

3.2.2 Sensitivity and non-detections

The high background present in the region increases the sensitivity limit of these observations, and affects the number of detections. In Table 3.1 we present the sensitivities given in the SPIRE/PACS Parallel Mode Observers' Manual v2.1 (section 2.3), and the minimum flux detected for each band. Also, the effective sensitivity is calculated taking the number of scans made per map into account; this includes six for the PACS maps and two for the SPIRE maps. We also report a lower value of fluxes in the cleanest areas of the map, which agrees with the fact that the extended emission from the molecular cloud reduces the effective sensitivity.

Another study took into account the sources detected by *Spitzer* and catalogued by c2d (Evans et al. 2009) in each of the apertures defined per band and per detected source to estimate possible contamination due to *Herschel* resolution. The flux in MIPS-24 band of each of this c2d sources was used to extrapolate via the median

Table 3.3: Parameters of detected sources as extracted from the literature. Also, we give the I.D. number used to identify the transitional disks.

I.D.	Name	R.A. (deg)	Dec (deg)	SpT	A_v*	References
-	2MASSJ16245974-2456008	16 : 24 : 59.63	−24 : 55 : 59.32	M3.5	0.10	1
-	V*V852Oph	16 : 25 : 24.38	−24 : 29 : 43.77	M4.5	0.21	2
-	2MASSJ16253673-2415424	16 : 25 : 36.73	−24 : 15 : 42.32	K4	0.10	1
-	2MASSJ16253958-2426349	16 : 25 : 39.58	−24 : 26 : 34.27	M2	0.13	2
-	V*V2058Oph	16 : 25 : 56.18	−24 : 20 : 47.77	K4.5	0.61	1
1	Haro1-6	16 : 26 : 03.02	−24 : 23 : 36.04	K1	5.70	4
-	2MASSJ16261684-2422231	16 : 26 : 16.83	−24 : 22 : 23.32	K6	0.11	1
2	DoAr24	16 : 26 : 17.08	−24 : 20 : 21.47	K4.5	0.13	2
-	2MASSJ16262189-2444397	16 : 26 : 21.88	−24 : 44 : 39.67	M8	0.10	2
-	DoAr24E	16 : 26 : 23.28	−24 : 20 : 59.37	G6	0.10	2
3	DoAr25	16 : 26 : 23.68	−24 : 43 : 13.57	K5	0.21	2
-	GSS32	16 : 26 : 24.03	−24 : 24 : 48.32	K5	0.63	1
-	2MASSJ16262407-2416134	16 : 26 : 24.08	−24 : 16 : 13.27	K5.5	0.19	2
-	2MASSJ16263297-2400168	16 : 26 : 32.98	−24 : 00 : 16.77	M4.5	0.09	2
-	2MASSJ16263682-2415518	16 : 26 : 36.93	−24 : 15 : 52.32	M0	0.55	1
-	$[GY92]93$	16 : 26 : 41.28	−24 : 40 : 17.87	M5	0.09	2
-	2MASSJ16264285-2420299	16 : 26 : 42.83	−24 : 20 : 30.32	M1	0.11	1
-	2MASSJ16264643-2412000	16 : 26 : 46.48	−24 : 11 : 59.97	G3.5	0.10	2
4	WSB40	16 : 26 : 48.58	−23 : 56 : 34.57	K5.5	0.09	2
-	WL18	16 : 26 : 48.98	−24 : 38 : 25.07	K6.5	0.59	2
-	2MASSJ16265677-2413515	16 : 26 : 56.68	−24 : 13 : 51.47	K7	0.11	2
5	SR24S	16 : 26 : 58.48	−24 : 45 : 36.67	K1	0.18	2
6	2MASSJ16270659-2441488	16 : 27 : 06.68	−24 : 41 : 49.07	M5.5	0.09	2
-	2MASSJ16270907-2412007	16 : 27 : 09.03	−24 : 12 : 01.32	M2.5	0.11	1
7	WSB46	16 : 27 : 15.08	−24 : 51 : 38.77	M2	0.09	2
-	$[WMR2005]4-10$	16 : 27 : 17.48	−24 : 05 : 13.67	M3.5	0.10	2
-	2MASSJ16271836-2454537	16 : 27 : 18.38	−24 : 54 : 52.77	M3.75	0.16	2
-	WSB49	16 : 27 : 22.98	−24 : 48 : 07.07	M4.25	0.09	2
-	2MASSJ16272658-2425543	16 : 27 : 26.58	−24 : 25 : 54.47	M8	0.14	2
8	2MASSJ16273084-2424560	16 : 27 : 30.88	−24 : 24 : 56.37	M3.25	0.12	2
-	2MASSJ16273311-2441152	16 : 27 : 33.13	−24 : 41 : 14.32	K6	0.50	1
9	IRS48	16 : 27 : 37.23	−24 : 30 : 34.32	A0	0.76	1
10	IRS49	16 : 27 : 38.28	−24 : 36 : 58.67	K5.5	0.15	2
-	2MASSJ16273832-2357324	16 : 27 : 38.28	−23 : 57 : 32.97	K6	0.14	2
11	2MASSJ16273863-2438391	16 : 27 : 38.60	−24 : 38 : 39.00	M6	0.24	3
-	2MASSJ16273901-2358187	16 : 27 : 38.98	−23 : 58 : 19.17	K5.5	0.15	2
12	WSB52	16 : 27 : 39.48	−24 : 39 : 15.87	K5	0.09	2
13	SR9	16 : 27 : 40.28	−24 : 22 : 04.37	K5	0.17	2
-	2MASSJ16274270-2438506	16 : 27 : 42.68	−24 : 38 : 51.27	M2	0.11	2
-	V*V2059Oph	16 : 27 : 55.58	−24 : 26 : 18.27	M2	0.11	2
-	2MASSJ16280256-2355035	16 : 28 : 02.58	−23 : 55 : 03.61	M3	4.30	4
-	2MASSJ16281379-2432494	16 : 28 : 13.83	−24 : 32 : 49.32	M4	0.10	1
14	2MASSJ16281385-2456113	16 : 28 : 13.83	−24 : 56 : 10.32	M0	0.10	1
15	WSB60	16 : 28 : 16.58	−24 : 36 : 58.57	M4.5	0.11	2
-	2MASSJ16281673-2405142	16 : 28 : 16.83	−24 : 05 : 15.32	K6	0.08	1
16	SR20W	16 : 28 : 23.38	−24 : 22 : 40.87	K5	0.50	2
17	SR13	16 : 28 : 45.28	−24 : 28 : 19.27	M3.75	0.20	2
18	2MASSJ16285694-2431096	16 : 28 : 57.03	−24 : 31 : 09.32	M5.5	0.13	1
-	2MASSJ16294427-2441218	16 : 29 : 44.28	−24 : 41 : 21.80	M4	0.80	4

Notes. References: 1) Erickson et al. (2011), 2) Wilking et al. (2005), 3) Natta et al. (2002), 4) Cieza et al. (2010)

* All A_v are calculated according to Ribas et al. (2014)

Table 3.4: Point source fluxes of each of the 49 sources detected

I.D.	Name	$F_{70}\,[Jy]$	$F_{160}\,[Jy]$	$F_{250}\,[Jy]$	$F_{350}\,[Jy]$	$F_{500}\,[Jy]$
-	2MASSJ16245974-2456008	0.05 ± 0.01	-	-	-	-
-	V*V852Oph	0.73 ± 0.18	-	-	-	-
-	2MASSJ16253673-2415424	0.74 ± 0.18	-	-	-	-
-	2MASSJ16253958-2426349	0.92 ± 0.23	-	-	-	-
-	V*V2058Oph	3.86 ± 0.97	3.77 ± 0.94	12.56 ± 3.14	-	-
1	Haro1-6	10.70 ± 2.68	7.48 ± 1.87	-	-	-
-	2MASSJ16261684-2422231	0.20 ± 0.05	-	-	-	-
2	DoAr24	0.50 ± 0.12	-	-	-	-
-	2MASSJ16262189-2444397	0.10 ± 0.02	-	-	-	-
-	DoAr24E	4.17 ± 1.04	3.91 ± 0.98	-	-	-
3	DoAr25	1.39 ± 0.35	3.52 ± 0.88	4.17 ± 1.04	5.30 ± 1.33	2.05 ± 0.51
-	GSS32	3.70 ± 0.93	-	-	-	-
-	2MASSJ16262407-2416134	3.04 ± 0.76	6.10 ± 1.53	4.73 ± 1.18	2.66 ± 0.66	1.12 ± 0.28
-	2MASSJ16263297-2400168	0.08 ± 0.02	0.13 ± 0.03	-	0.01 ± 0.00	-
-	2MASSJ16263682-2415518*	1.37 ± 0.34	0.72 ± 0.18	0.44 ± 0.11	-	-
-	$[GY92]93$	0.02 ± 0.00	-	-	-	-
-	2MASSJ16264285-2420299	0.65 ± 0.16	-	-	-	-
-	2MASSJ16264643-2412000	0.57 ± 0.14	-	-	-	-
4	WSB40	0.42 ± 0.10	0.29 ± 0.07	-	-	-
-	WL18	0.42 ± 0.10	-	-	-	-
-	2MASSJ16265677-2413515	0.21 ± 0.05	0.79 ± 0.20	-	-	-
5	SR42S	9.70 ± 2.42	7.88 ± 1.97	5.06 ± 1.26	3.02 ± 0.76	1.55 ± 0.39
6	2MASSJ16270659-2441488	0.10 ± 0.02	-	-	-	-
-	2MASSJ16270907-2412007	0.07 ± 0.02	0.23 ± 0.06	-	0.11 ± 0.03	-
7	WSB46	0.25 ± 0.06	0.15 ± 0.04	-	-	-
-	$[WMR2005]4-10$	0.18 ± 0.04	0.32 ± 0.08	0.51 ± 0.13	0.37 ± 0.09	-
-	2MASSJ16271836-2454537*	0.07 ± 0.02	0.05 ± 0.01	0.07 ± 0.02	-	-
-	WSB49	0.04 ± 0.01	-	-	-	-
-	2MASSJ16272658-2425543	0.04 ± 0.01	-	-	-	-
8	2MASSJ16273084-2424560	0.50 ± 0.13	-	-	-	-
-	2MASSJ16273311-2441152	1.27 ± 0.32	0.08 ± 0.02	-	-	-
9	IRS48	37.57 ± 9.39	12.85 ± 3.21	6.48 ± 1.62	2.51 ± 0.63	-
10	IRS49*	1.29 ± 0.32	0.95 ± 0.24	0.07 ± 0.02	0.67 ± 0.17	-
-	2MASSJ16273832-2357324*	0.63 ± 0.16	0.25 ± 0.06	0.52 ± 0.13	0.30 ± 0.07	-
11	2MASSJ16273863-2438391	0.09 ± 0.02	-	-	-	-
-	2MASSJ16273901-2358187	0.44 ± 0.11	0.52 ± 0.13	0.10 ± 0.02	0.09 ± 0.02	0.03 ± 0.01
12	WSB52*	2.37 ± 0.59	2.23 ± 0.56	3.43 ± 0.86	0.76 ± 0.19	0.28 ± 0.07
13	SR9	0.86 ± 0.21	0.22 ± 0.05	-	-	-
-	2MASSJ16274270-2438506	0.02 ± 0.01	-	-	-	-
-	V*V2059Oph	0.06 ± 0.01	-	-	-	-
-	2MASSJ16280256-2355035	0.02 ± 0.01	-	-	-	-
-	2MASSJ16281379-2432494	0.05 ± 0.01	-	-	-	-
14	2MASSJ16281385-2456113	0.74 ± 0.18	0.68 ± 0.17	0.29 ± 0.07	0.19 ± 0.05	0.14 ± 0.03
15	WSB60	0.87 ± 0.22	1.19 ± 0.30	1.26 ± 0.32	1.79 ± 0.45	-
-	2MASSJ16281673-2405142	0.12 ± 0.03	-	-	-	-
16	SR20W	0.89 ± 0.22	0.60 ± 0.15	0.57 ± 0.14	0.46 ± 0.12	0.37 ± 0.09
17	SR13	1.36 ± 0.34	1.32 ± 0.33	0.79 ± 0.20	0.51 ± 0.13	0.20 ± 0.05
18	2MASSJ16285694-2431096	0.02 ± 0.01	-	-	-	-
-	2MASSJ16294427-2441218	0.05 ± 0.01	-	-	-	-

Notes. (*) Sources near bright background emission; sky measurement was done in clean regions.

SED of the Ophiuchus region (see Table 3.5) the expected fluxes at 70 μm. In Table 3.1, we list a sum of all the expected fluxes for this contaminating sources, where it is possible to check whether the expected contamination is lower than the flux error. Notice that this contamination flux is only an estimation, as only the reported object has been detected in the aperture.

3.3 Results

The fluxes of all the detected sources per band are given in Table 3.4, as mentioned above. As expected, the higher flux corresponds to the most known object in the region, IRS 48 (#9). All the objects proposed as transitional disk candidates present relatively high fluxes, being 2MASS J16285694-2431096 (#18) the the candidate with the lower flux at 70 μm (20 mJy). The detection on more than one band for these objects seems to be arbitrary. Less than half of the candidates have been detected either in one band or in all of them. This is probably related to the physical properties of each of the disks rather than to instrumental issues.

3.3.1 Identification of transitional disks

Once we measured the fluxes, we use the criterion by Ribas et al. (2013) to classify transitional disks with *Herschel* photometry. As previously noted, transitional disks display little or no excess at near- to mid-IR, and large excess at long wavelengths, which translates into a change of slope in the SED of the object around 12 μm, i.e. from a negative to positive slope. To proceed with the identification, we defined two indexes , following:

$$\alpha_{\lambda_1-\lambda_2} = \frac{log(\lambda_1 F_{\lambda_1}) - log(\lambda_2 F_{\lambda_2})}{log(\lambda_1) - log(\lambda_2)} \tag{3.1}$$

where λ is measured in μm and F_λ in erg $\cdot$ s^{-1} $\cdot$ cm^{-2}. The first index is defined for the band K acquired from 2MASS and 12 μm acquired from WISE. The second index is defined for the 12 μm band and the 70 μm band acquired from *Herschel*. The criterion to determine whether an object is a transitional disk candidate is $\alpha_{12-70} > 0$, since we define transitional disks as objects with a deficit of excess flux at near to mid-IR fluxes, but standard excesses at longer wavelengths. For DoAr 24(#2), the 12 μm-band was not available and, therefore, we used 8 μm band from *Spitzer/IRAC* (Fazio et al. 2004) instead.

To understand the result of this process, we represent in Fig. 3.2 a slope-slope diagram, which shows the value of the two different slopes in the two axes. The figure shows that we obtained two candidates with a positive slope between 12 μm and 70 μm, clearly separated from the Class II population. These two candidates, 2MASS J16281385-2456113 (#14) and Haro1-6 (#1), clearly fulfil the criteria of having a lack of mid-IR excess since Haro1-6 (#1) is an object previously classified as debris disk in Cieza et al. (2010). The candidate 2MASS J16281385-2456113 (#14), has never been reported before as a transitional disk. The other objects above the threshold do not have this kind of clear 12 μm flux deficit, which is indicative of the presence of a flatter slope in the mid- to far- infrared wavelengths. If we construct the SEDs of those objects (see Fig. 3.4), we see that in general they do not present the characteristic gap expected from a transitional disk. However, as they fulfil the criteria, we classified them here as tentative candidates. Some of these candidates were also classified as transitional disks in previous works. Object WSB 60 (#15) was imaged in Andrews et al. (2009), detecting a small inner hole in dust continuum observations done with the Sub-Millimeter Array (Ho et al. 2004). In the work by Cieza et al. (2010) DoAr 25 (#3) was already suggested as a candidate. We consider objects SR 42 S (#5), WSB 46 (#7), and SR 20 W (#16) as tentative candidates despite they do not fulfill the criteria for their nominal values, but we are considering a high error in PACS photometry. In particular, SR 42 S (#5) has already been classified as transitional disk, and appears in Espaillat et al. (2014) as so. For WSB 46 (#7) and SR 20 W (#16), further study is needed to determine their nature.

3.3.2 Complementary identification with spectral energy distributions

To better analyse the nature of these objects, we built their SEDs using data from optical to mid-infrared from both ground-based and space telescopes (all references for the photometry can be found in section 2.1). We completed these SEDs with the photometry shown in Table 3.2 and extracted from *Herschel* data, therefore, we cover a range between 0.35 to 500 μm. Figs. 3.4 and 3.5 show the obtained SEDs, plus the NextGen atmosphere model for each object (Hauschildt et al. 1999a), which are the best approximation of how a naked photosphere would emit as a function of its spectral type.

We also built the median SED of all the objects detected in the region for com-

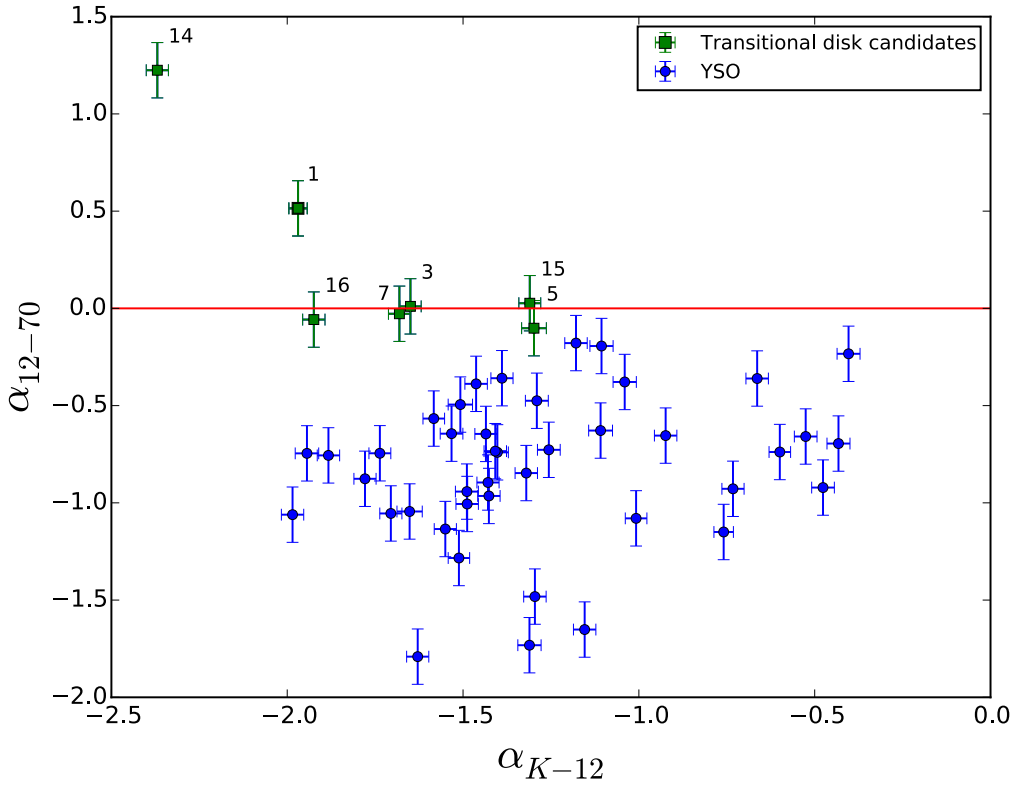

Figure 3.2: SED slope between 12 and 70 μm as a function of the SED slope between the K-band and 12 μm. Transitional disks are marked with green squares.

parison (see Table 3.5), which is plotted along each object's SEDs. Because of the lack of detections for fluxes under the sensitivity limits given in Table 3.4, the median SED might be slightly overestimated, but we assume the efffect in our result is negligible.

To determine the interstellar extinction, we used the procedure in Ribas et al. (2014) and the extinction law from Weingartner and Draine (2001), which uses a model of grains to estimate the interstellar extinction, scattering, and infrared emission. In each plot of Fig. 3.6, the observed fluxes are also shown as empty circles. The de-reddened fluxes, according to the associated interstellar extinction, are shown as filled circles.

When visually inspecting the SEDs, we detect objects with a lack of mid-IR excess that were not classified as transitional disks, according to the criteria of Ribas et al. (2013) described in section 3.1. Some of these objects are well known in the literature, such as IRS 48 (#9). To make a more reliable study of the region, we add

Table 3.5: Median SED of detected disks in Ophiuchus

Band	Median	First Quartile	Third Quartile	Detections
J	1.0000	1.0000	1.0000	49
H	0.6109	0.5664	0.6577	49
K	0.3305	0.3018	0.3662	49
IRAC-3.6	0.0743	0.0628	0.0958	45
IRAC-4.5	0.0380	0.0305	0.0537	47
IRAC-5.8	0.0212	0.0162	0.0293	46
IRAC-8.0	0.0121	0.0088	0.0190	48
MIPS-24	0.0018	0.0013	0.0030	48
PACS-70	0.0003	0.0001	0.0008	49
PACS-160	$8.53 \cdot 10^{-5}$	$5.54 \cdot 10^{-5}$	0.0002	26
SPIRE-250	$3.48 \cdot 10^{-5}$	$2.32 \cdot 10^{-5}$	0.0001	17
SPIRE-350	$9.60 \cdot 10^{-6}$	$5.88 \cdot 10^{-6}$	$1.44 \cdot 10^{-5}$	15
SPIRE-500	$2.62 \cdot 10^{-6}$	$2.12 \cdot 10^{-6}$	$4.18 \cdot 10^{-6}$	8

in this subsection a complementary criterion based on Spitzer data to identify the other transitional disks or transitional disks candidates detected by *Herschel* with a change of slope between 12 μm and 24 μm. Fig. 3.3 shows the new slope-slope diagram.

We detected 17 transitional disks candidates with this criteria. Six of the objects detected with the previous criteria appear now as well, with the exception of SR 24 S (#5), which is a confirmed transitional disk.

Fig. 3.4 shows the SEDs for the 18 transitional disks candidates, where the change of slope is not equally noticeable for all of them. In the case of 2MASS J16281385-2456113 (#14), the change of slope is evident, in agreement with that expected from the slope-slope diagram. In cases such as WSB 60 (#15) or IRS 48 (#9), which are well-known transitional disks, the slope is flatter, and located in a different position in the wavelength axis. For SR 24 S (#5), we see an unexpected behaviour, where we get a discrepancy between MIPS-24 and WISE4 fluxes, but we still see an increase in the far-IR emission with respect to the near-IR. Another object classified as a transitional disk in Cieza et al. (2010) is SR 9 (#13), although it has a continuous decreasing slope, as the criterion shows, and looks more like a Class II SED. The rest of the objects in the sample have been widely studied, but not previously considered transitional disks. The variation in the outputs of both methods illustrates the complexity in defining a selection criteria.

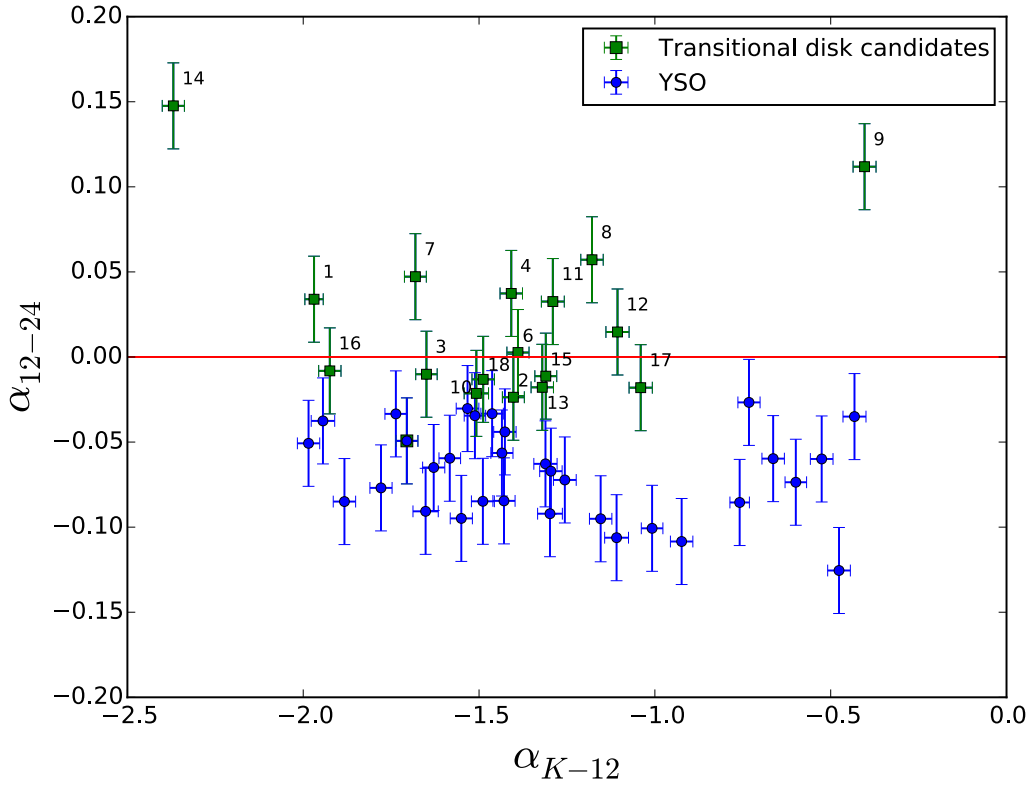

Figure 3.3: SED slope between 12 and 24 μm as a function of the SED slope between the K-band and 12 μm. Transitional disks are marked with green squares.

3.4 Discussion

3.4.1 Detection statistics

The initial sample was composed of 261 YSO objects in the centre of Ophiuchus, with known spectral type from optical spectroscopy and all classified as Class II objects. Our sample is different from that in Evans et al. (2009), since they had photometrically selected objects, including many objects with other classes, while we have only spectroscopically confirmed Class II YSOs. All of these YSOs fell within the coverage of the maps used, and 49 were detected in at least one *Herschel* band, 49 in PACS, and 19 in SPIRE. This leads to a *Herschel* detection rate of 18.77%±2.6%, which is much smaller than the percentage of detections obtained in similar studies in Chamaeleon (Ribas et al. 2013) and Lupus (Bustamante et al. 2015) of around 30 %. Given that Ophiuchus is closer than those regions (150∼200 pc), the low detection rate is probably due to the higher background, which is emitting at mid-

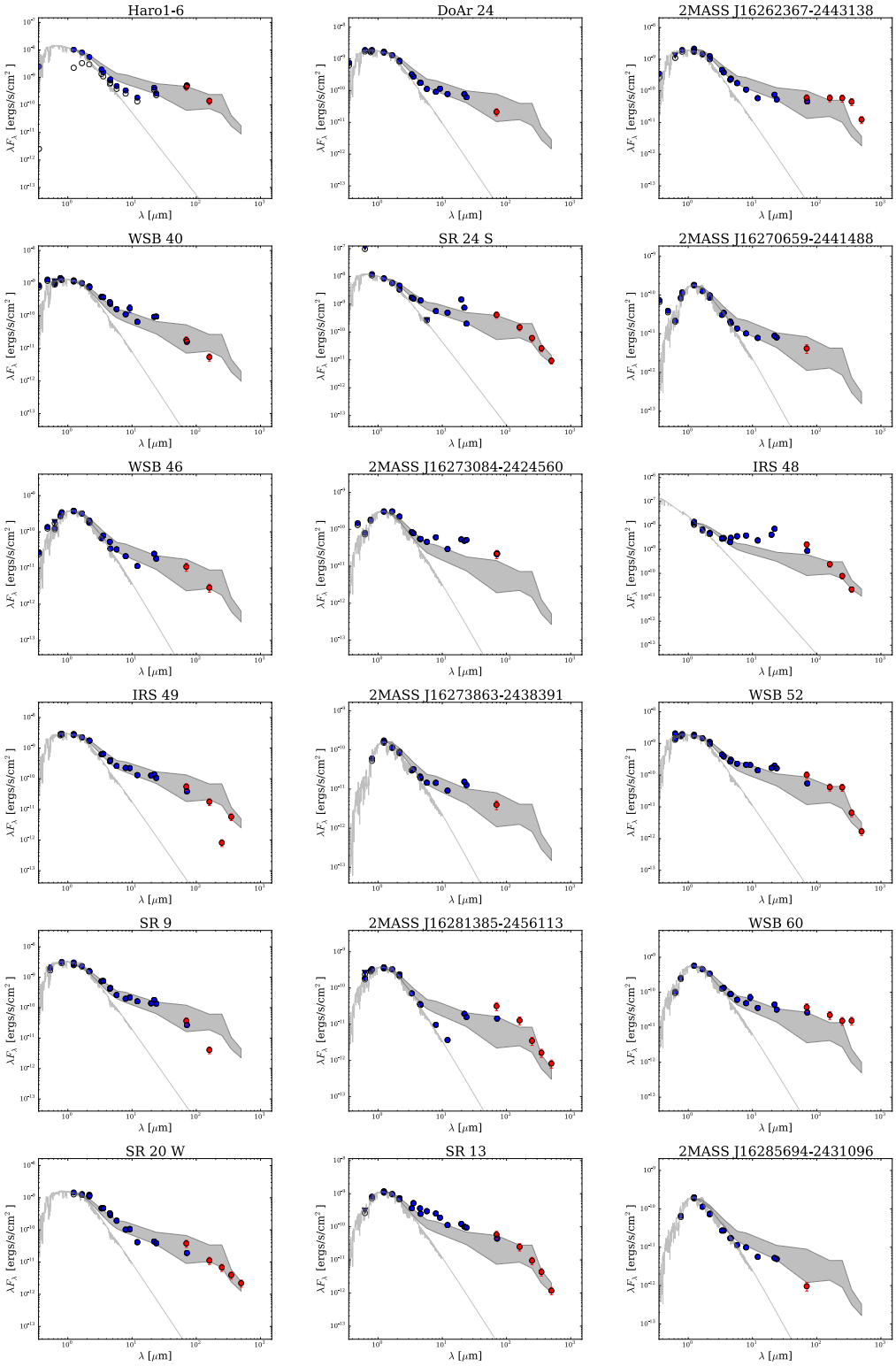

Figure 3.4: Spectral energy distribution (SED) of the sources classified as transitional disks candidates. Blue dots show data acquired from the literature, red dots are photometric fluxes obtained from *Herschel* data. Grey dashed line is the photosphere model according to the spectral type, and the grey shaded area is the filled area between the first and third quartile of all the disk fluxes. Observed fluxes are shown with empty circles and A_v values used are in Table 3.3.

and long-IR wavelengths, and precludes the detection of faint objects.

3.4.2 Incidence of transitional disks in the centre of Ophiuchus

We report here the detection of 18 transitional disk candidates in the cloud complex in the centre of Ophiuchus based on new *Herschel* and previous known data of spectroscopically confirmed YSO sample. Despite the fact that all of these objects fulfil either one or both of the criteria exposed previously, only a few of them have evident changes of slopes in the SEDs. The candidate with the biggest change in slope, 2MASS J16281385-2456113 (#14), is new to the literature.

The fraction of transitional disk candidates observed in Ophiuchus based on our *Herschel* sample, is $37\%^{+7}_{-6}$. We have considered two classification criteria, depending on the change of slope, that is, on the wavelength position of the lack of mid-IR excess. If we only consider our main criteria, the fraction is lower, at $14\%^{+6}_{-4}$, but it is compatible with the fractions measured in other regions with similar ages in previous works (Espaillat et al. 2014). Even though we have identified 18 transitional disks candidates in total, some of them present a relatively flat slope and, in the slope-slope diagram, are represented very close to, or even below, the threshold . Having objects with nearly a Class-II slope explains the high fraction of transitional disks in the region, as many of them might be fulfilling the criteria due to the large error in their PACS fluxes. These objects would need further study for their safe classification. One of the objects close to the threshold, however, namely YLW 58 or WSB 60 (#15), had been imaged with SMA and shows a small but conspicuous inner hole (Andrews et al. 2011). Despite this, most of the objects in the first criterion were also detected by the complementary criterion; SR 42 S (#5) was not, even though it is a confirmed transitional disk (Andrews et al. 2011). The fact that *Herchel* data is including transitional candidates to the sample, confirms the improvement that *Herschel* represents regarding reaching to further regions in disks. The longer wavelengths now accessible allow us to detect wider and larger cavities, which we could not have identified solely with data from *Spitzer* at mid-infrared ranges.

3.4.3 Other interesting objects

Even though we have combined two criteria to identify new candidates, and that these criteria select even very small changes of slope, there might be objects in the

sample with the characteristics of a transitional disk, which are, as previously noted, a lack of excess around 10 μm and normal excesses at mid- to far-IR. If we inspect Figs. 3.2 and 3.3, we observe that several objects present these features. There are two clear cases of objects previously classified as transitional disk candidates: 2MASS J16280256-2355035 and 2MASS J16294427-2441218. Both of these candidates present a lack of excess around 8 μm and excesses in longer wavelengths, but because of the restrictions in the criteria, neither appear as transitional candidates.

The objects V* V852 Oph, 2MASS J16253958-2426349 and 2MASS J16262189-2444397 are similar cases that were never classified as transitional disks, but have a gap in their SED, which could be an indication of a hole in their disks. The object 2MASS J16272658-2425543 also shows a lack of excess around 10 μm with a larger excess in longer wavelengths. This object could also be considered a transitional candidate, despite the fact that it does not fulfil any of the criteria. All of these objects are shown in Table 3.6 along with the previous objects classified as transitional disk candidates.

3.4.4 Study of 70 micron fluxes in transitional disks

For a comparison of the 70 μm flux of both the transitional disk candidates and tentative candidates, we constructed the median SED of all the detected objects in the sample, using the photometric data in Table 3.5. This would show if, apart from a lack of excess in the near mid-IR, transitional disks also show another remarkable characteristic that could be used in classification or, possibly, in disk modelling. The median SED lacks the contribution from the faintest objects, which might remain undetected by *Herschel* or some of the other surveys, and hence is just an upper limit to the true median SED of Ophiuchus.

When we overplot the median SED to the detected fluxes (as a grey shaded area in Figs. 3.4 and 3.5), we only find the 70 μm flux to be higher for some of the objects classified as transitional disks candidates. Hence, we cannot conclude that we have detected a trend in the transitional disk population, such as as has been observed in previous investigations (Bustamante et al. 2015; Ribas et al. 2013). We also find the case of 2MASS J16285694-2431096 (#18), where the 70 μm flux is not only lower than the median SED, but lower than the third quartile. Because of the lack of large excess in mid- to far-IR and the fact that this object presents a slightly smaller flux in the 70 μm band than the rest of transitional disks candidates, it needs further study to clarify its nature.

3.5 Conclusions

We have detected 49 objects in the central region of Ophiuchus in at least one PACS band and 19 in at least one SPIRE band. We obtained accurate photometric fluxes for the detected objects by means of aperture photometry.

Seven of the detected objects were classified as transitional disk candidates by the criterion in Ribas et al. (2013), and 11 more were classified according to the complementary criterion, generating a total sample of 18 transitional disk candidates. Some of these candidates were already imaged in previous works, and hence, confirmed. Six more objects are added to the final classification of candidates that have transitional features in their SEDs, rather than fulfilling any of the criterion. All of the transitional disk candidates are shown in Table 3.6 along with their classification criteria. This large difference between the identification methods can be due to the different nature or evolutionary stages of the disks, creating different geometries and leading to a large diversity of SEDs.

Several of the objects classified as transitional disks candidates have not been considered candidates before, but 2MASSJ16281385-2456113 (#14) appears to be an attractive object for follow-up because of its prominent change of slope when compared to the rest of the sample, including previously imaged disks, such as IRS 48 (#9).

So far, *Herschel* data has proved to be very useful to improve the characterization of the outer regions of protoplanetary systems because of its long-wavelength coverage, unattainable until now, and its improved sensitivity and spatial resolution compared with previous IR missions. A study of the SED population of the disk sample detected with *Herschel* should give us more information on the true nature of these disks, but this study is outside the scope of this work.

Table 3.6: Summary of all transitional disk candidates in Ophiuchus

I.D.	Name	Classification Criteria
1	Haro1-6	$12-70$*
2	DoAr24	$12-24$
3	DoAr25	$12-70$*
4	WSB40	$12-24$
5	SR42S	$12-70$
6	2MASSJ16270659-2441488	$12-24$
7	WSB46	$12-70$*
8	2MASSJ16273084-2424560	$12-24$
9	IRS48	$12-24$
10	IRS49	$12-24$
11	2MASSJ16273863-2438391	$12-24$
12	WSB52	$12-24$
13	SR9	$12-24$
14	2MASSJ16281385-2456113 †	$12-70$*
15	WSB60	$12-70$*
16	SR20W	$12-70$*
17	SR13	$12-24$
18	2MASSJ16285694-2431096	$12-24$
-	V*V852Oph	SED
-	2MASSJ16253958-2426349	SED
-	2MASSJ16262189-2444397	SED
-	2MASSJ16272658-2425543	SED
-	2MASSJ16280256-2355035	SED
-	2MASSJ16294427-2441218	SED

Notes. *These objects have also been classified with the complementary criterion of 12-24
† This transitional disk candidate is new to the literature.

Table 3.7: Estimation of contaminating flux contained in the aperture for each band, according to the median SED extrapolation.

I.D.	Name	$F_{70}\,[Jy]$ (6")	$F_{160}\,[Jy]$ (12")	$F_{250}\,[Jy]$ (22")	$F_{350}\,[Jy]$ (30")	$F_{500}\,[Jy]$ (42")
-	2MASSJ16245974-2456008	-	$2.66 \cdot 10^{-5}$	$2.94 \cdot 10^{-4}$	$9.00 \cdot 10^{-5}$	$2.77 \cdot 10^{-5}$
-	V*V852Oph	-	$1.44 \cdot 10^{-4}$	$1.48 \cdot 10^{-4}$	$4.96 \cdot 10^{-5}$	$6.11 \cdot 10^{-5}$
-	2MASSJ16253673-2415424	-	-	$4.47 \cdot 10^{-5}$	$1.23 \cdot 10^{-5}$	$3.17 \cdot 10^{-5}$
-	2MASSJ16253958-2426349	-	-	$9.65 \cdot 10^{-4}$	$4.60 \cdot 10^{-4}$	$3.15 \cdot 10^{-4}$
-	V*V2058Oph	$3.34 \cdot 10^{-2}$	$1.12 \cdot 10^{-2}$	$5.29 \cdot 10^{-3}$	$1.46 \cdot 10^{-3}$	$3.97 \cdot 10^{-4}$
1	Haro1-6	$5.85 \cdot 10^{-2}$	$1.55 \cdot 10^{-2}$	$7.64 \cdot 10^{-3}$	$2.15 \cdot 10^{-3}$	$6.09 \cdot 10^{-4}$
-	2MASSJ16261684-2422231	-	-	$1.01 \cdot 10^{-5}$	$1.15 \cdot 10^{-5}$	$1.48 \cdot 10^{-5}$
2	DoAr24	$4.51 \cdot 10^{-3}$	$9.56 \cdot 10^{-4}$	$4.50 \cdot 10^{-4}$	$1.32 \cdot 10^{-4}$	$4.03 \cdot 10^{-5}$
-	2MASSJ16262189-2444397	$5.90 \cdot 10^{-3}$	$1.27 \cdot 10^{-3}$	$5.98 \cdot 10^{-4}$	$2.07 \cdot 10^{-4}$	$7.49 \cdot 10^{-5}$
-	DoAr24E	-	-	-	$1.41 \cdot 10^{-4}$	$3.85 \cdot 10^{-5}$
3	DoAr25	-	$1.23 \cdot 10^{-4}$	$8.50 \cdot 10^{-5}$	$3.09 \cdot 10^{-5}$	$2.91 \cdot 10^{-5}$
-	GSS32	-	$3.76 \cdot 10^{-2}$	$1.77 \cdot 10^{-2}$	$5.67 \cdot 10^{-3}$	$1.61 \cdot 10^{-3}$
-	2MASSJ16262407-2416134	-	-	-	$6.89 \cdot 10^{-5}$	$2.34 \cdot 10^{-5}$
-	2MASSJ16263297-2400168	-	-	$1.32 \cdot 10^{-5}$	$1.86 \cdot 10^{-5}$	$1.06 \cdot 10^{-5}$
-	2MASSJ16263682-2415518	-	$1.39 \cdot 10^{-3}$	$6.68 \cdot 10^{-4}$	$2.07 \cdot 10^{-4}$	$6.18 \cdot 10^{-5}$
-	$[GY92]93$	-	-	$1.36 \cdot 10^{-5}$	$1.12 \cdot 10^{-5}$	$1.59 \cdot 10^{-5}$
-	2MASSJ16264285-2420299	-	-	-	$2.40 \cdot 10^{-4}$	$1.60 \cdot 10^{-4}$
-	2MASSJ16264643-2412000	-	$3.32 \cdot 10^{-4}$	$1.65 \cdot 10^{-4}$	$4.94 \cdot 10^{-5}$	$1.69 \cdot 10^{-5}$
4	WSB40	$2.09 \cdot 10^{-2}$	$4.43 \cdot 10^{-3}$	$2.09 \cdot 10^{-3}$	$5.86 \cdot 10^{-4}$	$1.65 \cdot 10^{-4}$
-	WL18	-	-	$4.75 \cdot 10^{-6}$	$5.77 \cdot 10^{-6}$	$5.37 \cdot 10^{-6}$
-	2MASSJ16265677-2413515	$1.59 \cdot 10^{-3}$	$3.36 \cdot 10^{-4}$	$1.58 \cdot 10^{-4}$	$5.43 \cdot 10^{-5}$	$2.13 \cdot 10^{-5}$
5	SR24S	$3.92 \cdot 10^{-1}$	$8.29 \cdot 10^{-2}$	$3.91 \cdot 10^{-2}$	$1.08 \cdot 10^{-2}$	$2.95 \cdot 10^{-3}$
6	2MASSJ16270659-2441488	-	$2.93 \cdot 10^{-5}$	$2.17 \cdot 10^{-5}$	$1.28 \cdot 10^{-5}$	$1.23 \cdot 10^{-5}$
-	2MASSJ16270907-2412007	-	-	$2.68 \cdot 10^{-5}$	$1.86 \cdot 10^{-5}$	$8.30 \cdot 10^{-6}$
7	WSB46	-	$4.76 \cdot 10^{-5}$	$2.46 \cdot 10^{-5}$	$1.65 \cdot 10^{-5}$	$8.68 \cdot 10^{-6}$
-	$[WMR2005]4-10$	$5.65 \cdot 10^{-4}$	$1.20 \cdot 10^{-4}$	$7.63 \cdot 10^{-5}$	$5.06 \cdot 10^{-5}$	$2.52 \cdot 10^{-5}$
-	2MASSJ16271836-2454537	-	-	$7.27 \cdot 10^{-6}$	$3.56 \cdot 10^{-6}$	$3.40 \cdot 10^{-6}$
-	WSB49	-	-	$1.78 \cdot 10^{-5}$	$6.58 \cdot 10^{-6}$	$4.63 \cdot 10^{-6}$
-	2MASSJ16272658-2425543	-	-	$4.66 \cdot 10^{-5}$	$3.35 \cdot 10^{-5}$	$1.53 \cdot 10^{-5}$
8	2MASSJ16273084-2424560	-	-	$1.72 \cdot 10^{-5}$	$1.30 \cdot 10^{-5}$	$5.67 \cdot 10^{-6}$
-	2MASSJ16273311-2441152	-	-	-	$3.20 \cdot 10^{-6}$	$5.10 \cdot 10^{-6}$
9	IRS48	-	-	-	$1.20 \cdot 10^{-4}$	$4.42 \cdot 10^{-5}$
10	IRS49	-	-	$6.90 \cdot 10^{-6}$	$7.97 \cdot 10^{-6}$	$6.54 \cdot 10^{-6}$
-	2MASSJ16273832-2357324	-	-	$7.64 \cdot 10^{-4}$	$2.19 \cdot 10^{-4}$	$6.12 \cdot 10^{-5}$
11	2MASSJ16273863-2438391	$6.27 \cdot 10^{-3}$	$1.62 \cdot 10^{-3}$	$5.83 \cdot 10^{-5}$	$3.59 \cdot 10^{-5}$	$1.51 \cdot 10^{-3}$
-	2MASSJ16273901-2358187	-	-	$1.51 \cdot 10^{-4}$	$5.32 \cdot 10^{-5}$	$2.76 \cdot 10^{-5}$
12	WSB52	$1.45 \cdot 10^{-3}$	$3.08 \cdot 10^{-4}$	$1.56 \cdot 10^{-4}$	$1.61 \cdot 10^{-5}$	$1.25 \cdot 10^{-4}$
13	SR9	-	-	$1.70 \cdot 10^{-5}$	$1.59 \cdot 10^{-5}$	$1.02 \cdot 10^{-5}$
-	2MASSJ16274270-2438506	-	-	$5.44 \cdot 10^{-6}$	$4.54 \cdot 10^{-6}$	$6.99 \cdot 10^{-6}$
-	V*V2059Oph	-	-	-	$8.23 \cdot 10^{-6}$	$7.76 \cdot 10^{-6}$
-	2MASSJ16280256-2355035	-	-	$6.06 \cdot 10^{-8}$	$5.08 \cdot 10^{-6}$	$5.56 \cdot 10^{-6}$
-	2MASSJ16281379-2432494	-	-	$5.82 \cdot 10^{-6}$	$4.25 \cdot 10^{-6}$	$7.35 \cdot 10^{-6}$
14	2MASSJ16281385-2456113	-	-	$1.02 \cdot 10^{-4}$	$2.94 \cdot 10^{-5}$	$1.63 \cdot 10^{-5}$
15	WSB60	-	$2.13 \cdot 10^{-4}$	$1.10 \cdot 10^{-5}$	$1.00 \cdot 10^{-5}$	$6.31 \cdot 10^{-6}$
-	2MASSJ16281673-2405142	-	-	-	$7.31 \cdot 10^{-6}$	$8.51 \cdot 10^{-6}$
16	SR20W	-	-	$4.36 \cdot 10^{-6}$	$5.78 \cdot 10^{-6}$	$6.48 \cdot 10^{-6}$
17	SR13	-	-	-	$4.01 \cdot 10^{-5}$	$1.51 \cdot 10^{-5}$
18	2MASSJ16285694-2431096	-	-	$4.67 \cdot 10^{-6}$	$1.83 \cdot 10^{-5}$	$7.36 \cdot 10^{-6}$
-	2MASSJ16294427-2441218	-	-	$1.75 \cdot 10^{-5}$	$1.35 \cdot 10^{-5}$	$7.44 \cdot 10^{-6}$

Notes. The contaminating flux has been calculated extrapolating the MIPS-24 flux obtained from the Spitzer c2d catalogue (Evans et al. 2009) to the median SED for each source contained in the different apertures for each band.

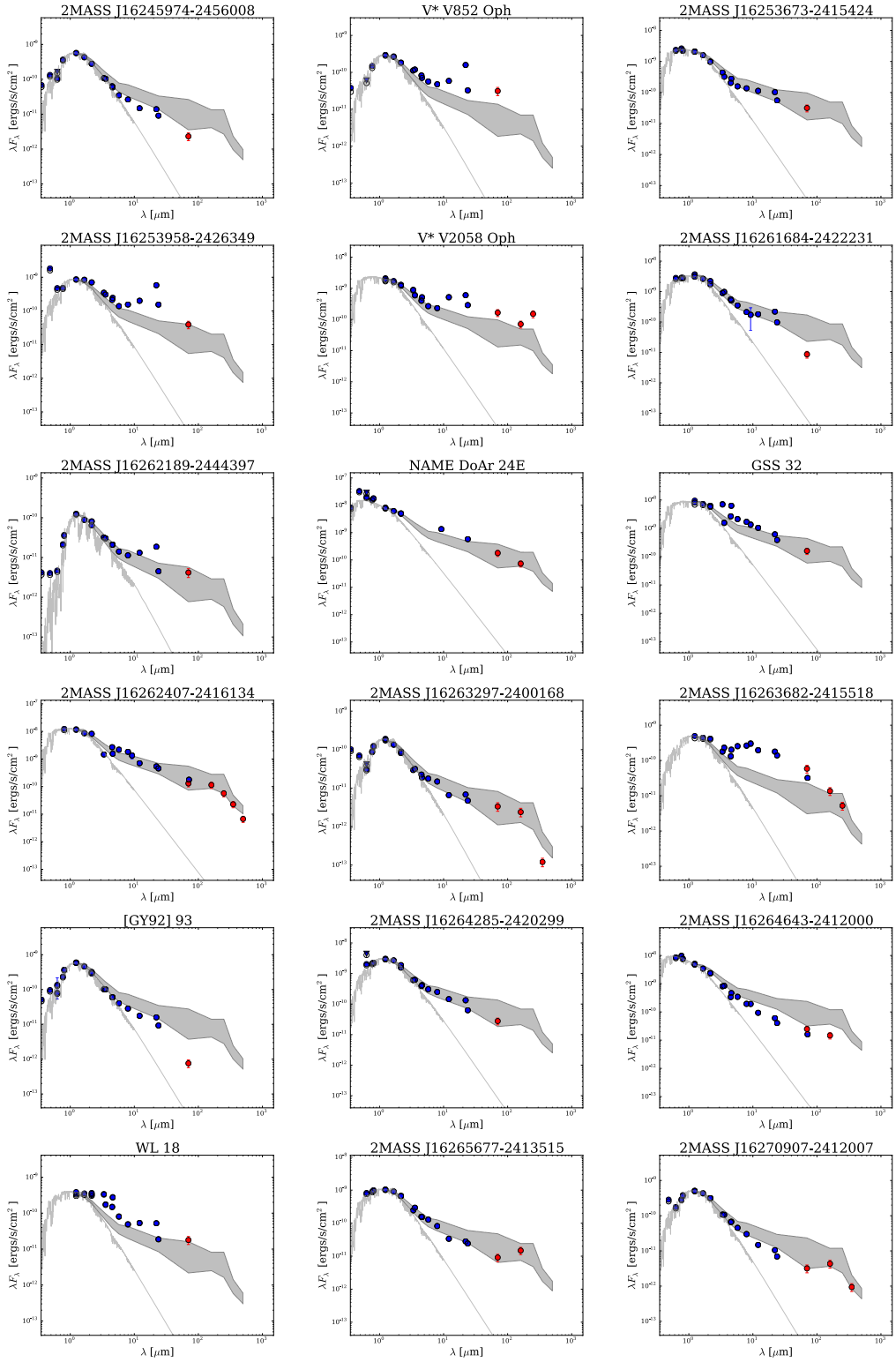

Figure 3.5: Spectral energy distribution (SED's) of the sources detected in at least one band by *Herschel* and classified as non-transitional. Blue dots show data acquired from the literature, red dots are photometric fluxes obtained from *Herschel* data. Grey dashed line is the photosphere model according to the spectral type, and the grey shaded area is the filled area between the first and third quartile of all the disk fluxes. Observed fluxes are shown with empty circles and A_v values used are in Table 3.3.

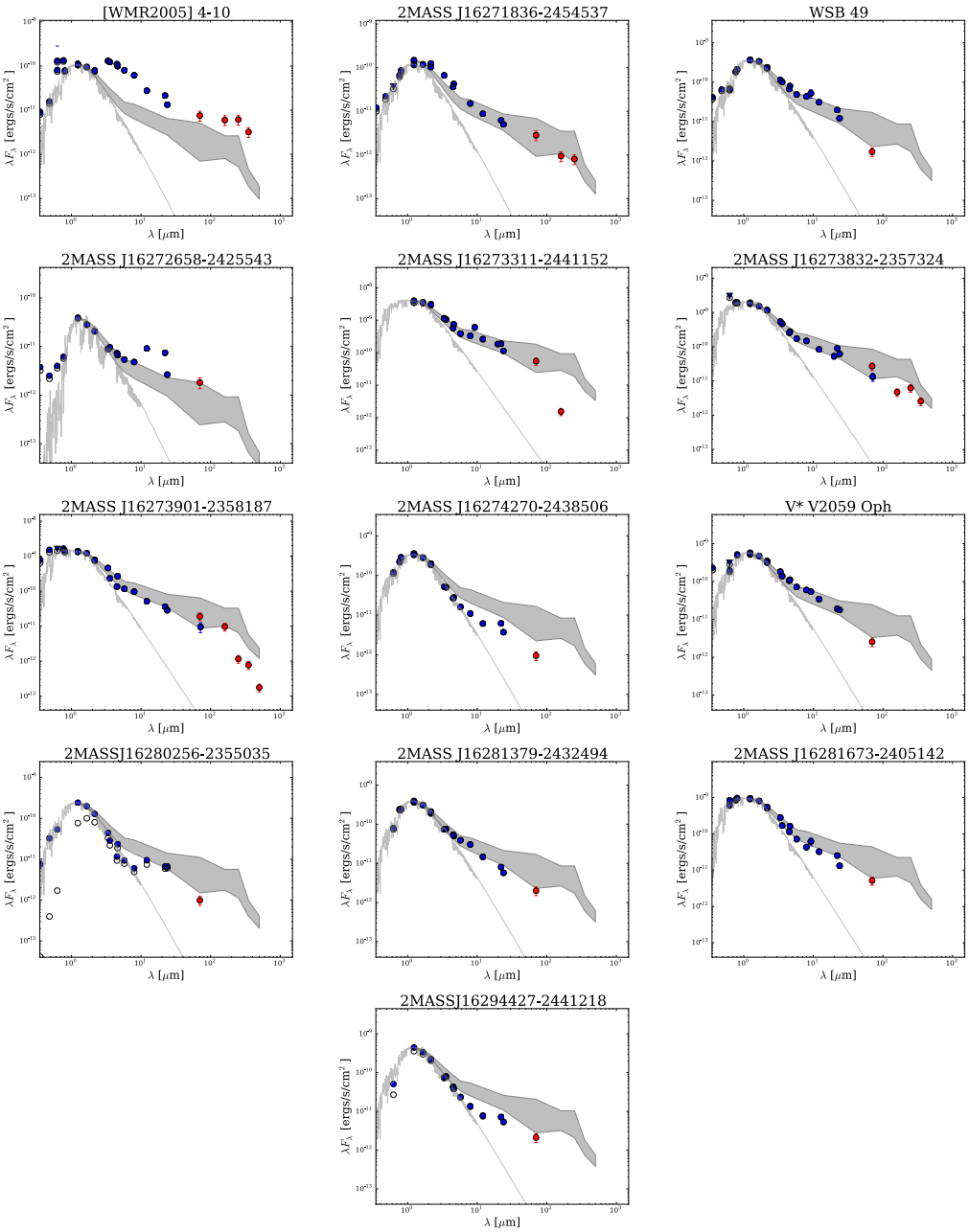
[WMR2005] 4-10
2MASS J16271836-2454537
WSB 49
2MASS J16272658-2425543
2MASS J16273311-2441152
2MASS J16273832-2357324
2MASS J16273901-2358187
2MASS J16274270-2438506
V* V2059 Oph
2MASSJ16280256-2355035
2MASS J16281379-2432494
2MASS J16281673-2405142
2MASSJ16294427-2441218
λ [μm]
λF_λ [ergs/s/cm²]

(Fig. 3.5 cont.)

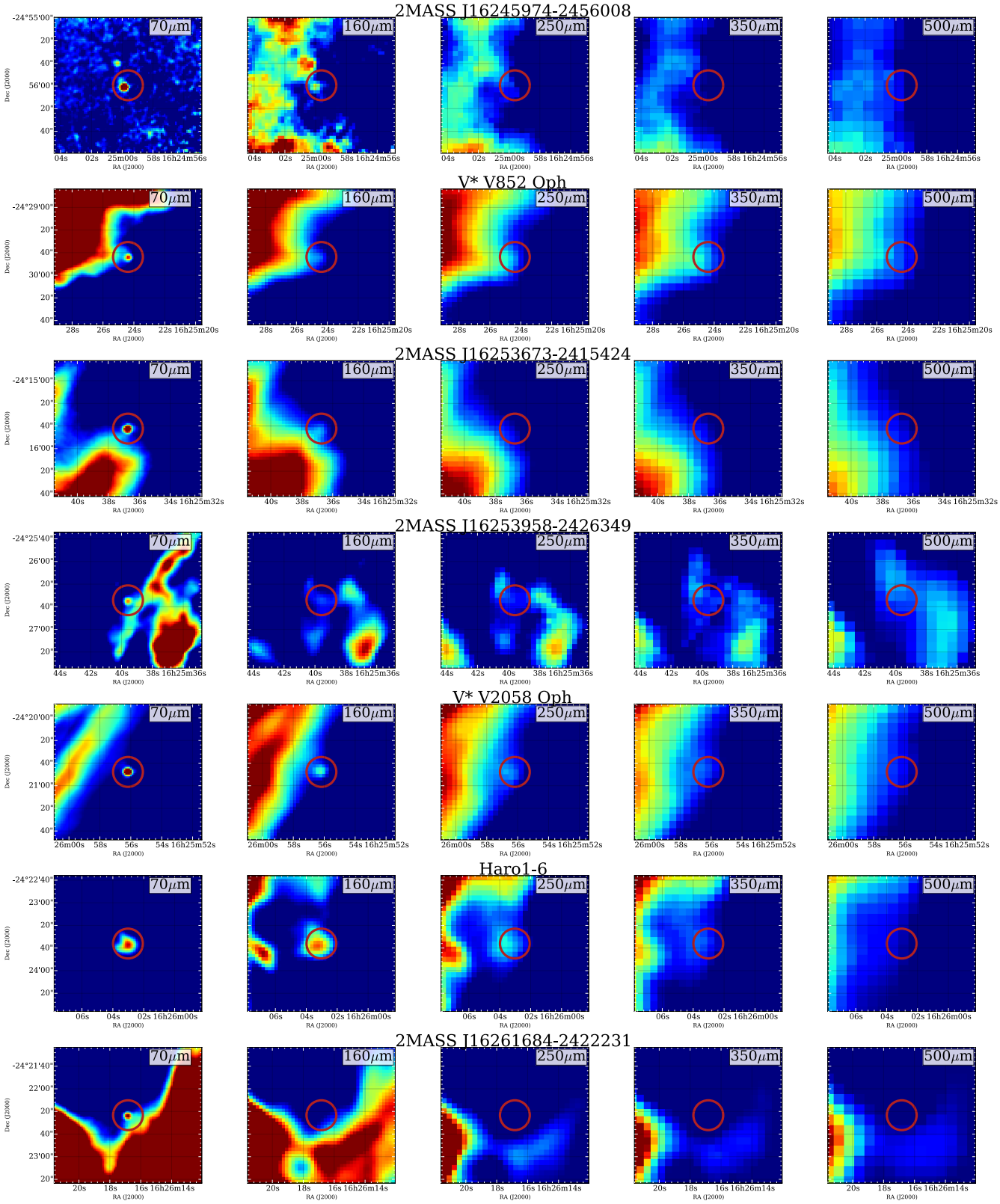

Figure 3.6: Thumbnail images of each of the 46 sources with at least one point source detected by *Herschel*. All images are 60 ″x 60 ″with north up and east to the left. The cut levels are set to the RMS of the background for the minimum and three times that value for the maximum with linear stretch.

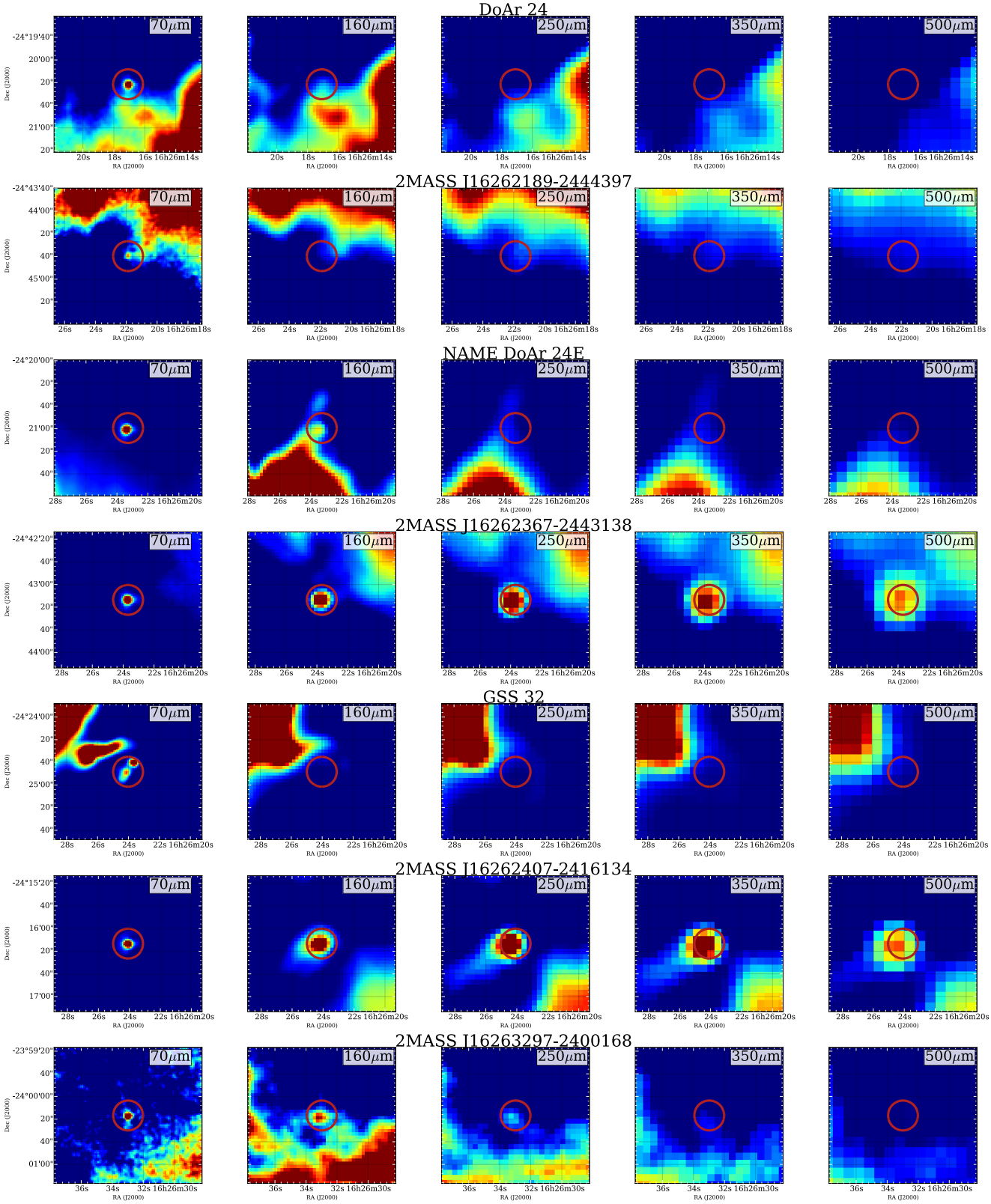
DoAr 24
70μm
160μm
250μm
350μm
500μm
2MASS J16262189-2444397
NAME DoAr 24E
2MASS J16262367-2443138
GSS 32
2MASS J16262407-2416134
2MASS J16263297-2400168
Dec (J2000)
RA (J2000)

(Fig. 3.6 cont.)

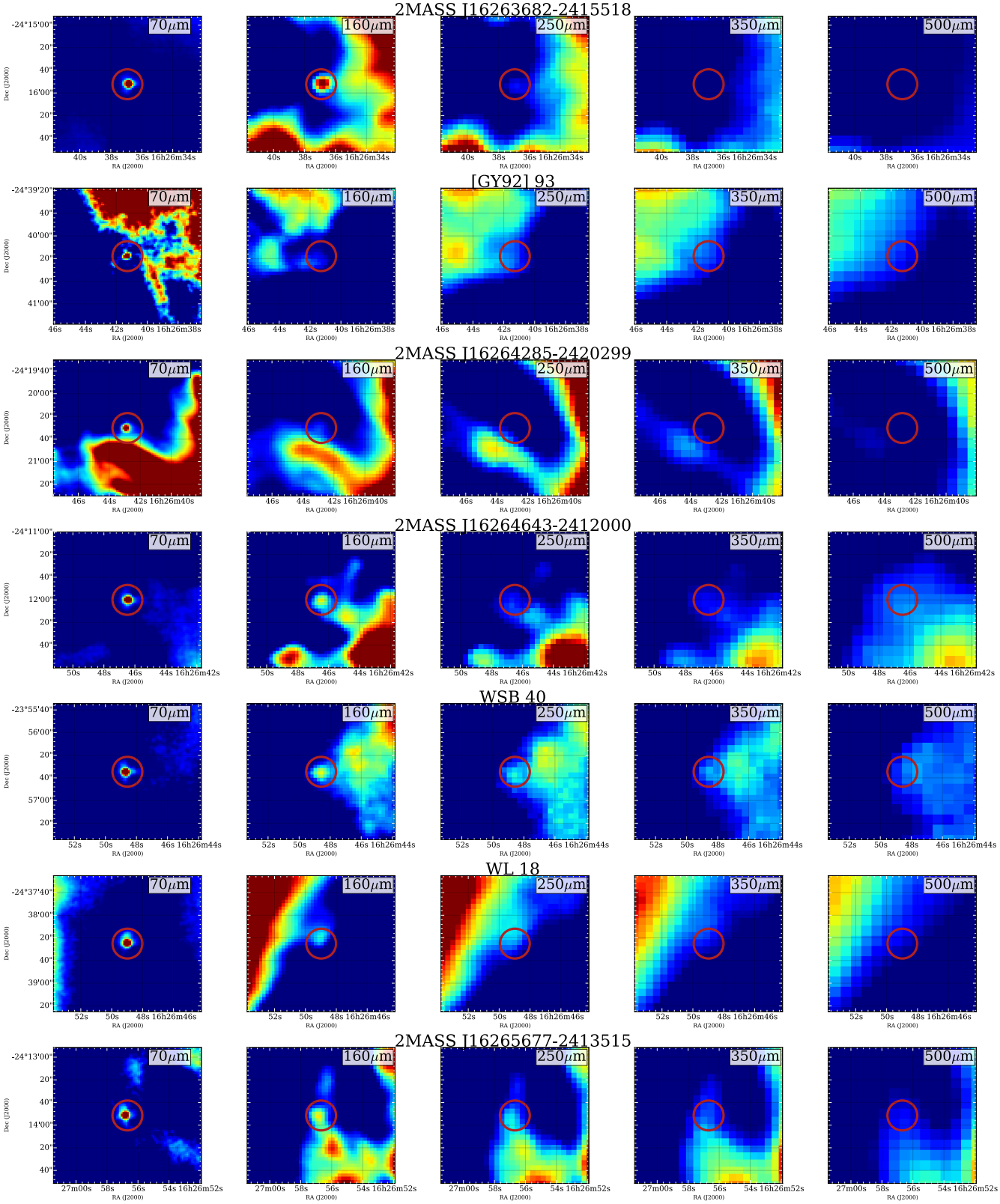
2MASS J16263682-2415518
[GY92] 93
2MASS J16264285-2420299
2MASS J16264643-2412000
WSB 40
WL 18
2MASS J16265677-2413515
70μm
160μm
250μm
350μm
500μm
Dec (J2000)
RA (J2000)

(Fig. 3.6 cont.)

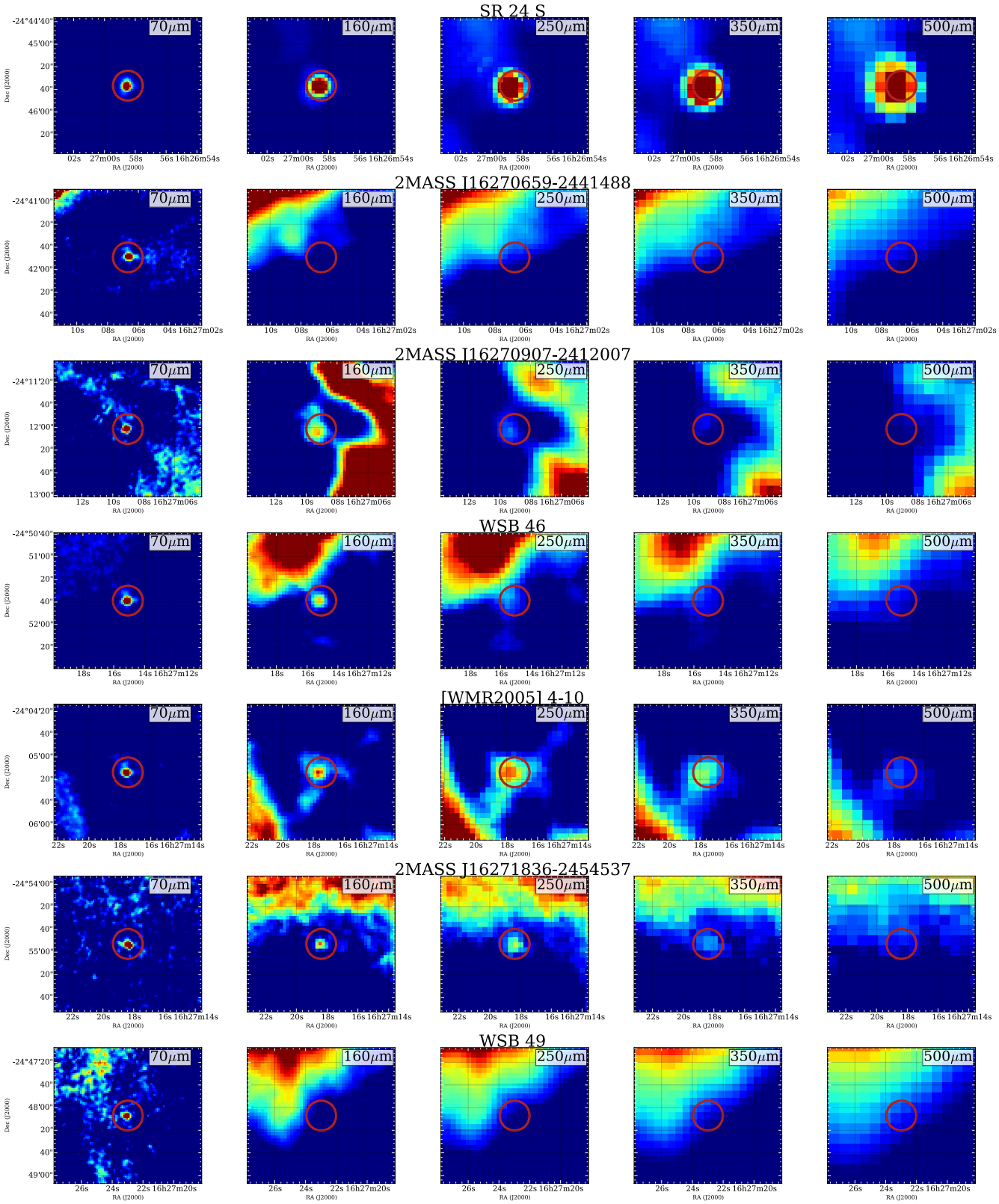
SR 24 S
2MASS J16270659-2441488
2MASS J16270907-2412007
WSB 46
[WMR2005] 4-10
2MASS J16271836-2454537
WSB 49
70μm
160μm
250μm
350μm
500μm
Dec (J2000)
RA (J2000)

(Fig. 3.6 cont.)

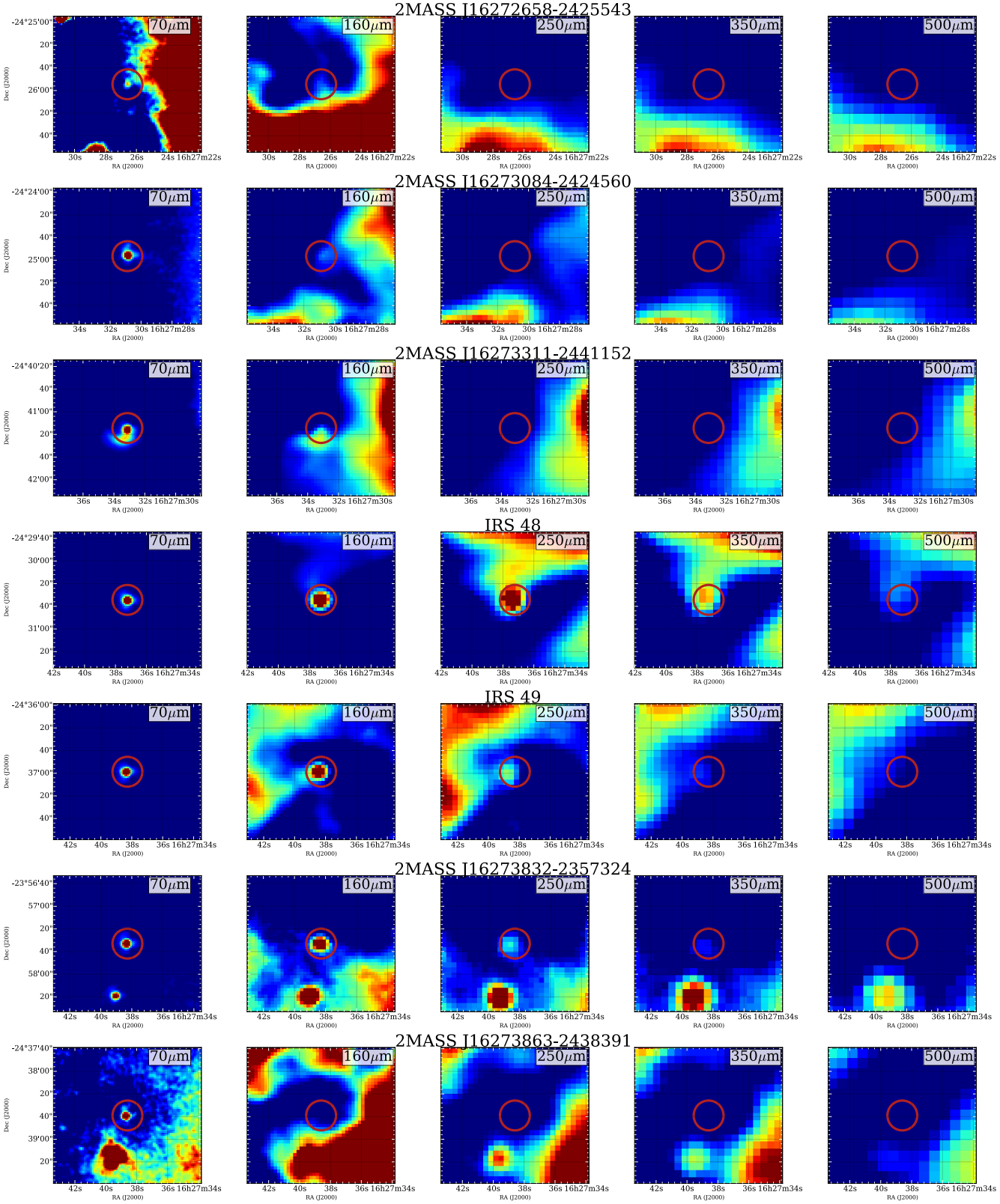
2MASS J16272658-2425543
2MASS J16273084-2424560
2MASS J16273311-2441152
IRS 48
IRS 49
2MASS J16273832-2357324
2MASS J16273863-2438391
70μm
160μm
250μm
350μm
500μm
Dec (J2000)
RA (J2000)

(Fig. 3.6 cont.)

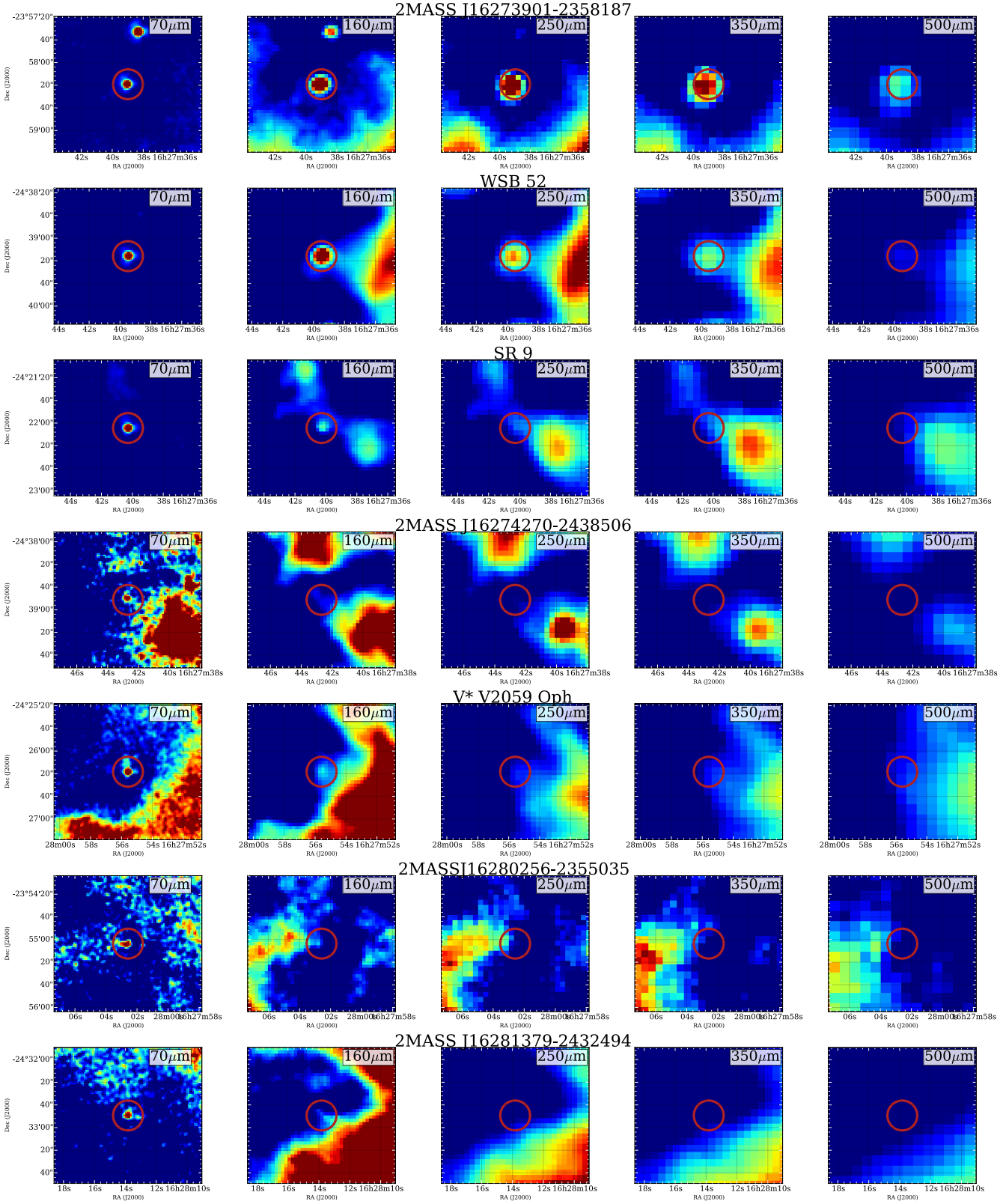
2MASS J16273901-2358187
70μm
160μm
250μm
350μm
500μm
WSB 52
SR 9
2MASS J16274270-2438506
V* V2059 Oph
2MASSJ16280256-2355035
2MASS J16281379-2432494
RA (J2000)
Dec (J2000)

(Fig. 3.6 cont.)

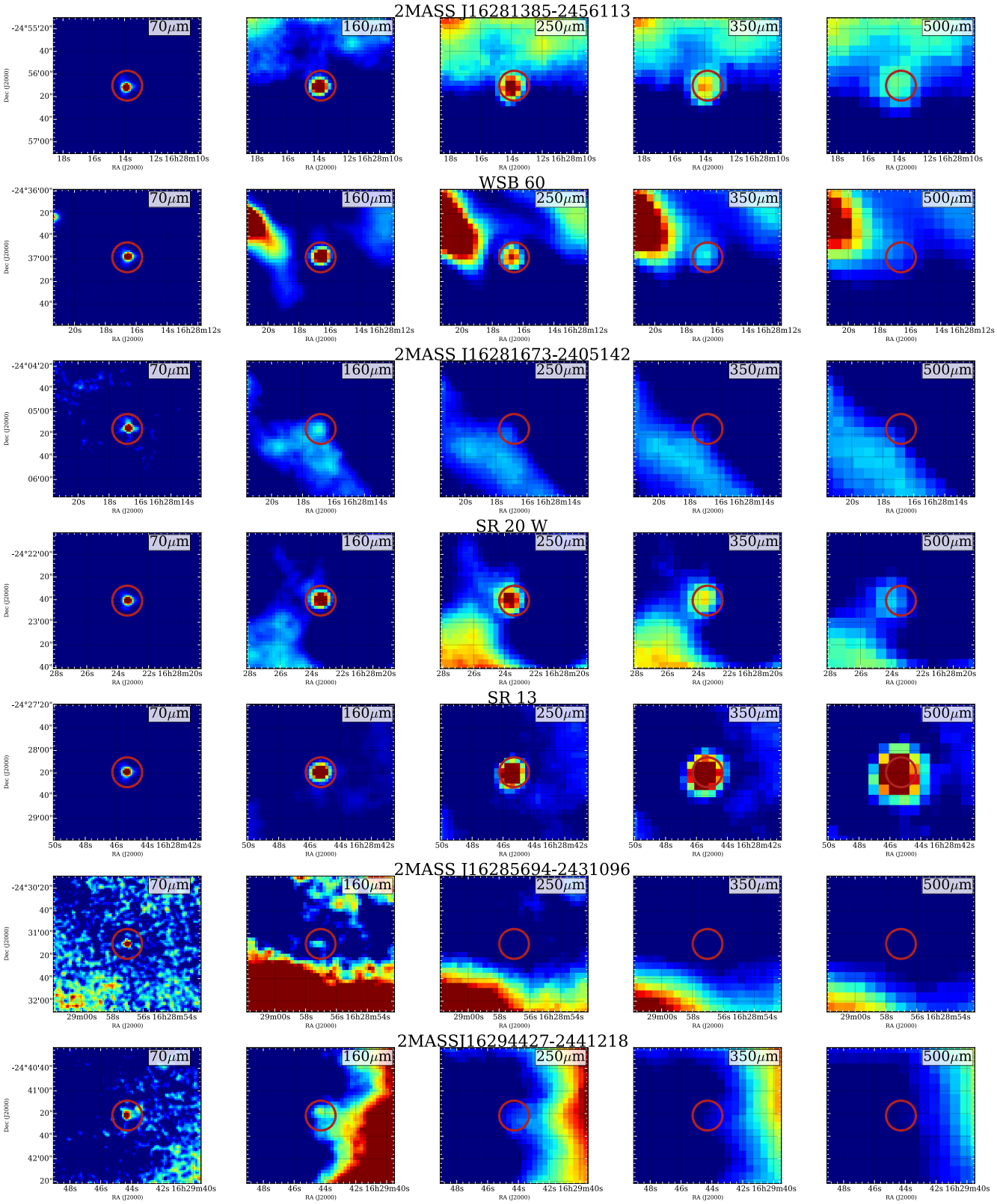
2MASS J16281385-2456113
70μm
160μm
250μm
350μm
500μm
WSB 60
2MASS J16281673-2405142
SR 20 W
SR 13
2MASS J16285694-2431096
2MASSJ16294427-2441218
Dec (J2000)
RA (J2000)

(Fig. 3.6 cont.)

Chapter 4

X-ray deficiency on strongly accreting T Tauri stars. Comparing Orion with Taurus

Bustamante, I.; Merín, B.; Bouy, H.; Manara, C. F.; Ribas, Á.; Riviere-Marichalar, P.

X-ray deficiency on strongly accreting T Tauri stars. Comparing Orion with Taurus. 2016, Astronomy & Astrophysics, 587, A81

Abstract

Depending on whether a T Tauri star accretes material from its circumstellar disk or not, different X-ray emission properties can be found. The accretion shocks produce cool heating of the plasma, contributing to the soft X-ray emission from the star. Using X-ray data from the *Chandra Orion Ultra-deep Project* and accretion rates that were obtained with the *Hubble Space Telescope*/WFPC2 photometric measurements in the Orion Nebula Cluster, we studied the relation between the accretion processes and the X-ray emissions of a coherent sample of T Tauri sources in the region. We performed regression and correlation analyses of our sample of T Tauri stars between the X-ray parameters, stellar properties, and the accretion measurements. We find that a clear anti-correlation is present between the residual X-ray luminosity and the accretion rates in our samples in Orion that is consistent with that found on the *XMM-Newton Extended Survey of the Taurus molecular cloud* (XEST) study. A considerable number of classified non-accreting sources show accretion rates comparable to those of classical T Tauri Stars (CTTS). Our data do not allow us to confirm the classification between classical and weak-line T Tauri stars (WTTS), and the number of WTTS in this work is small compared to the complete samples. Thus, we have used the entire samples as accretors in our analysis. We provide a catalog with X-ray luminosities (corrected from distance) and accretion measurements of an Orion Nebula Cluster (ONC) T Tauri stars sample. Although Orion and Taurus display strong differences in their properties (total gas and dust mass, star density, strong irradiation from massive stars), we find that a similar relation between the residual X-ray emission and accretion rate is present in the Taurus molecular cloud and in the accreting samples from the Orion Nebula Cluster. The spread in the data suggests dependencies of the accretion rates and the X-ray luminosities other than the stellar mass, but the similarity between Orion and Taurus hints at the environment not being one of them. The anti-correlation between the residual X-ray luminosity and mass accretion rate is inherent to the T Tauri stars in general, independent of their birthplace and environment, and intrinsic to early stellar evolution.

4.1 Introduction

The interaction between the central star and its surrounding disk in young stellar objects (YSOs) could be one the most important processes in the evolution of young stars, proto-planetary disks, and planetary system formation but, paradoxically, one of the least understood. Ultraviolet and X-ray irradiation from the star affects the dispersal and evolution of its surroundings (Owen et al. 2010), and the magnetic activity of the star has an important role in the mass-accretion rate from the disk onto the central object. The X-ray emission from the central star should photo-ionize the circumstellar material (Gorti and Hollenbach 2009), affecting its chemical composition, accreting processes (Alexander et al. 2014), outflows, and potential planetary atmospheres.

T Tauri stars present X-ray luminosities (L_X) near the saturation limit ($\log(L_X/L_{bol})$ = -3) found for main-sequence (MS) stars, $L_X/L_{bol} \sim 10^{-3.5}$, i.e., sometimes orders of magnitude higher than more evolved stars. For MS stars the X-ray activity is highly related with the rotation period, a relation given by the power law $L_X/L_{bol} \propto P_{rot}^{-2.6}$ (Pizzolato et al. 2003). But this relation has not been found for T Tauri stars (Preibisch et al. 2005). Several reasons have been postulated: the totally convective nature of young stars could be generating a different magnetic activity than that of MS stars (solar-like dynamo); a possible star magnetic field that is coupling with its surrounding disk; or the X-ray emission from accretion shocks could be altering the total amount of X-ray luminosity (Preibisch et al. 2005).

In the accretion process, material from the disk falls onto the stellar photosphere, generating a characteristic shock spectrum and an excess emission (L_{acc}), which can be measured with spectroscopic or photometric methods (Calvet and Gullbring 1998). This accretion luminosity can be linked to the mass accretion rate, $\dot{M}_{acc}$, through the relation: $\dot{M}_{acc} = L_{acc}R_*/0.8GM_*$, with R_*, and M_* being the radius and the mass of the star, respectively, and 0.8 being the factor that accounts for the assumption that the infall originates at a magnetospheric radius of R_m = 5 (Gullbring et al. 1998). The excess emission is mostly seen in the blue part of the spectrum (*U-band* excess) and in the emission lines ($H\alpha$ equivalent width) (Hartmann 1998).

The accretion processes were thought to play an important role in the X-ray activity of these stars, although several studies have found that strong accretors present lower L_X (Preibisch et al. 2005). Different explanations have been elaborated, such as disk opaqueness to certain L_X energies (Güdel et al. 2007b), thermalization and

absorption of the soft component of the X-ray luminosity (∼5 keV) (Calvet and Gullbring 1998) or changes in the coronal magnetic field activity provoked by the accretion processes (Telleschi et al. 2007). Also, a higher magnetic activity of the young star would result in highly energetic flares, showing large enough peaks in the X-ray measurements to even connect the inner disk to the star's photosphere (Aarnio et al. 2010).

Several studies have been carried out regarding the relation between mass accretion rates and X-ray emission. One of these is the anti-correlation found between the residual L_X and the $\dot{M}_{acc}$ by Telleschi et al. (2007), using data part of the *XMM-Newton Extended Survey of the Taurus molecular cloud* (XEST). Our main objective is to compare the mass accretion rates - X-ray emission relation found in that article (Telleschi et al. 2007) for the low mass T-association of the Taurus Molecular Cloud (TMC) with data on the Orion Nebula Cluster (ONC), and to look for any possible environmental effect. We used the X-ray emission data from the *Chandra Orion Ultra-deep Project* (COUP) (Getman et al. 2005b; Preibisch et al. 2005) and the accretion measurements from Manara et al. (2012), which use data from the *Hubble Space Telescope* (*HST*) Treasury Program on the Orion Nebula Cluster (Robberto et al. 2013).

This article is organized as follows: Sect. 4.2 describes the different datasets we use in our study and the cross-matching procedure. Sect. 4.3 illustrates the selection of the sub-samples we use. In Sect. 4.4 we explain the relation between X-ray emission and accretion processes we want to analyze and the correlation results we obtained, which are fully discussed in Sect. 4.5. In Section 4.6, we summarize the conclusions of this work.

4.2 X-rays and accretion in the ONC

4.2.1 Taurus and Orion comparison

The TMC is the nearest largest (distance ∼140 pc, Loinard et al. (2005)) star-forming region known. It is composed of several loosely associated molecular clouds, each of them producing small numbers of YSOs. Its small star density (1-10 stars pc^{-2}, Gomez et al. (1993)) prevents a notable influence from gravitational effects, outflows, or strong UV radiation fields, which creates a calm evolutionary environment, compared to other star-forming regions.

Although several other X-ray studies have been carried out in the region, the

XEST project provided the most sensitive and complete sample of X-ray detections (Telleschi et al. 2007; Güdel et al. 2007a). The X-ray emission of TTS is usually between $L_X \sim 10^{29}$ - 10^{31} erg s^{-1}, clearly higher than the instrument detection limit of $L_X \sim 10^{28}$ erg s^{-1}, for typical integration times. In fact, the XEST presents X-ray detection statistics consistent with near-completeness: 126 out of 152 TMC members are detected in X-rays (Güdel et al. 2007a). Out of a this sample, 55 are classified as strong accretors (or classical T Tauri stars) and 45 as weak accretors (or weak-line T Tauri stars), a classification that is based on the equivalent width of the Hα line. We refer to Telleschi et al. (2007) for a complete description of their sample selection and analyses.

In contrast, the ONC presents a much denser picture, with a distance of ∼414 pc (Menten et al. 2007). This massive cluster of young stars ($\sim 10^6$ yr) located in the Orion Molecular Cloud is illuminated by two O-type stars (Θ^1 Ori C and Θ^2 Ori A), has a star population of ∼1600 optically visible sources, and is recognized as a benchmark laboratory for star and planet formation, and the closest massive cluster to the Sun. It represents a coherent and homogeneous group of pre-main sequence (PMS) stars (Hillenbrand 1997; Da Rio et al. 2010; Da Rio et al. 2012), and a perfect bench test for a comparison with the TMC. Table 4.1 summarizes some key characteristics of both regions.

4.2.2 X-ray emission in the ONC - COUP

We use the data available from the COUP (Preibisch et al. 2005; Getman et al. 2005a), or more precisely, from the *Chandra* Orion Ultra-deep Point Source Catalog (http://heasarc.gsfc.nasa.gov/W3Browse/chandra/coup.html).

The COUP was a deep observation of the ONC using the Advanced CCD Imaging Spectrometer (ACIS) mounted on the *Chandra* X-ray telescope. This was a continuous 838 ks exposure program over a period of 13.2 days in January 2003. It detected 1 616 individual X-ray sources, with typical positional uncertainties of <0."3. This observation of the ONC (Getman et al. 2005b) resulted in the detection of ∼1400 X-ray-emitting PMS and is the richest source of X-ray data ever obtained for the ONC. We refer to Getman et al. (2005a) and Getman et al. (2005b) for a full review of the program.

4.2.3 Accretion data

For the accretion measurements, we used the data of Manara et al. (2012) on the ONC, in which they use the photometric catalog from the *HST* Treasury Program of Robberto et al. (2013). This program observed the ONC for 104 HST orbits of *HST* time with the Advanced Camera for Surveys (ACS), the Wide-Field/Planetary Camera 2 (WFCP2), and the Near-Infrared Camera and Multi-Object Spectrograph (NICMOS), using 11 filters in total that range from the U to the H band. With the data obtained from WFPC2, Manara et al. (2012) calculate the mass accretion rates of almost ∼600 PMS stars. Here we summarize the key aspects of their work and briefly discuss the two methodologies they use to determine the accretion rates. In the following, we divide the discussion on this dataset using two subsamples that were created by the method used to determine the accretion rates: the *U-band* excess and the $H\alpha$ line flux. For a complete analysis of the data selection and procedure, we refer to their article.

Manara et al. (2012) construct a two-color diagram (2CD) with the *UBI* photometric measurements, and simultaneously obtain an estimate of the extinction, A_V, and accretion luminosity, L_{acc}/L_{tot}. They assume that the displacement of the observed sources from the theoretical isochrone on the 2CD is caused by a combination of these two processes. They assume spectral types from the literature for all their targets.

U-band excess - From the 2CD that they converted they derive L_{acc}/L_{tot} into $L_{acc}/L_{\odot}$, taking into consideration the stellar luminosities with the relation $L_{acc}/L_{\odot}$ = $(L_{acc}/L_{tot})/(1\text{-}L_{acc}/L_{tot})$ * $L_*/L_{\odot}$ (L_* being the stellar luminosity).

Hα line - Manara et al. (2012) also use the $H\alpha$ luminosity as an accretion tracer. With the $H\alpha$ photometry available from the WFPC2 catalog (more precisely, the photometry from the *F656N* filter), they measure the excess with respect to the photospheric ($H\alpha$ - I) color for each star, which is dependent on T_{eff}. They then convert this $H\alpha$ excess into equivalent width. They consider the sources that fulfill the condition 3 Å < $\mathrm{EW}_{H\alpha}$ < 1000 Å as accretors. Finally, they derive the accretion luminosity L_{acc} from the $H\alpha$ luminosity $L_{H\alpha}$ with the relation $\log(L_{acc}/L_{\odot}) = (1.31 \pm 0.03)\log(L_{H\alpha}/L_{\odot})+(2.63 \pm 0.13)$. The $L_{acc}-L_{H\alpha}$ relation was calibrated using the *U-excess* data. The masses of the stars were computed with an evolutionary model interpolation of the position of them on the Hertzprung-Russel diagram (HRD).

Manara et al. (2012) obtain accretion rates for 244 objects using the *U-excess* method, and for 486 using the $H\alpha$ one. These subsamples are independent of one another. The excess in the U-band is a direct proxy of accretion, while the $L_{H\alpha}$ is

an indirect one. Thus, the accretion rate measurements of the *U-excess* subsample are more reliable than those of the $H\alpha$ one.

Manara et al. (2012) discard close binaries and visual proplyds (Ricci et al. 2008) from their sample. Thus, our subsamples are cleansed of these objects too. Consequently, our catalogs are only composed of young accreting stars. We will refer to these catalogs as the *U-excess* and the $H\alpha$ subsamples, respectively.

4.2.4 Cross-matching

The first step in our analysis was to find the COUP X-ray counterparts for the sources in the *HST* sub-samples. Using the nearest neighbors method, we made a first cross-match with the sky positions of the sources of the COUP catalog and those of the *Manara2012* subsamples, using a matching distance of 1" as a first approximation. We chose this distance taking into account the astrometric accuracy of *Chandra*: the 99% limit on positional accuracy is 0.8", in the worst case being an offset of 1.1" [1]. With this matching distance, we obtained 170 pairings with the *U-excess* group, and 322 pairings with the $H\alpha$ one.

We wanted to check if a systematic offset in the positions of both catalogs was present. Thus, we calculated the median differences in the right ascension and declination of this first set. As can be seen in Fig. 4.1, we found $\delta RA_{U-excess} = +0.274$" and $\delta DEC_{U-excess} = +0.036$", and $\delta RA_{H\alpha} = +0.228$", and $\delta DEC_{H\alpha} = +0.026$". We then corrected the COUP sources' right ascension and declination with these median offset values to refine the search of *HST* counterparts, and did a new cross-match with these new coordinates. For the *U-excess* sub-sample we found one less source, obtaining a sub-sample of 169 matches, whereas for the $H\alpha$ sub-sample we gained two more, obtaining 324 pairings.

As an extra control measure, we also performed the cross-match with the possibility of various pairings instead of just the nearest one. Not one of the *HST* sources in our *Manara2012* subsamples had more than one COUP counterpart nearby. Table 4.2 shows the parameters from this procedure.

[1] http://cxc.harvard.edu/cal/ASPECT/celmon/

4.3 Sample selection

4.3.1 Spectral type and low mass

To study the mass accretion rates and the X-ray luminosities as a function of T_{eff}, we only kept sources with a known spectral type. This left us with 281 sources in the case of the $H\alpha$ subsample, and 164 in the *U-excess* one. Spectral types were derived from Hillenbrand (1997), Luhman et al. (2000), and Lucas et al. (2001). For some sources, the spectral type was recalculated in Hillenbrand et al. (2013). In these cases, we use the latest spectral type available.

The X-ray emission of high-mass stars is non-coronal in origin, or comes from a different kind of corona, or originates in unresolved lower mass companions (Flaccomio et al. 2012). Because of this, we limited our study to stars with $M_* < 2$ $M_\odot$. With this selection, the numbers decreased to 277 sources for the $H\alpha$ subsample and 163 for the *U-excess* subsample.

Some sources did not have defined uncertainties for the mass accretion rates. We only used sources with valid mass accretion values and uncertainties, discarding the invalid ones. Thus, the *U-excess* subsample was reduced to 154 sources. The $H\alpha$ remained the same. This selection criteria is similar to that in Telleschi et al. (2007).

4.3.2 Classical T Tauri stars and weak-line T Tauri stars

The T Tauri family is divided into classical T Tauri stars (CTTS) and weak-line T Tauri stars (WTTS). This division takes into account the value of some accretion tracers to classify the objects into accretors or non-accretors. Several studies use this classification when studying the accretion properties of star-forming regions. For example, Preibisch et al. (2005) and Flaccomio et al. (2003) use the Ca_{II} infrared triplet lines ($\lambda = 8542$Å) equivalent width to classify their sample, as do Hillenbrand et al. (1998); and in Telleschi et al. (2007) they use the $H\alpha$ line ($\lambda = 6563$Å), as in Güdel et al. (2007a).

In our case, different classifications were possible. From the COUP data we accessed the values of the Ca_{II} line for both of our subsamples. Furthermore, for the $H\alpha$ subsample, the $H\alpha$ line equivalent width was also available. Thus, a second classification analysis could be carried out for this subsample.

Table 4.3 shows the mean accretion values for both subsamples. We note that, although both subsamples were classified using the Ca_{II} method, not every object

in them was included in the analysis. The classification method only selects objects with $EW(Ca_{II})$ < -1Å (CTTS) and $EW(Ca_{II})$ > 1Å (WTTS) (Preibisch et al. 2005). Thus, objects with -1Å < $EW(Ca_{II})$ < 1Å are not included in the classification. In the case of the $H\alpha$ subsample, we used 108 sources for these analyses, and for the *U-excess* subsample we used 56 sources.

Several objects that we classified as WTTS have stronger accretion rate measurements than the mean value of the total CTTS, and several CTTS have lower accretion rate values than the mean WTTS value. As a result, the mean $\dot{M}_{acc}$ values of the WTTS and CTTS sources for both subsamples differ by less than 3-σ.

The excess emission in $H\alpha$ (and probably in *U band*) present in WTTS may be due to cromospheric emission and not only to accretion. There have been studies that measure how strong this effect is and, in general, it is below the observed accretion rates (Ingleby et al. 2011; Stelzer et al. 2013; Manara et al. 2013a). Accreting PMS with values of logL_{acc} ≤ -3 log$L_{\odot}$ should be treated with caution because the line emission may be dominated by the contribution of chromospheric activity (Manara et al. 2013b). In our case, none of the WTTS with strong accretion measurements had logL_{acc} values lower than -3 log$L_{\odot}$, so we assume no significant cromospheric dependence for their accretion-rate measurements.

Our data do not allow us to classify our subsamples between CTTS and WTTS clearly. Medium-high resolution spectra would be needed for that analysis. Thus, in this work, we do not use the classical and weak-lined T Tauri division.

4.4 Relations between X-ray luminosity, stellar mass, and accretion rate

For the characterization of the X-ray properties, we used the following data from the COUP catalog: the total X-ray luminosity L_X (corrected for interstellar absorption), which corresponds to the total 0.5 - 8.0 keV energy band, with units of *erg* s^{-1}, and the equivalent width values of the Ca_{II} line for the T Tauri classification, in units of Å (see previous section). Importantly, Manara et al. (2012) formulate their analyses using a distance of 414 pc to the ONC, while the data in the COUP catalog assumes a distance of 450 pc. We corrected the latter with the distance of the former, using the equation used in the COUP catalog: L = $4\pi D^2$F, with F being the X-ray flux and D being the distance in parsecs. We used a value of 0.39 dex for the uncertainty of L_X.

These X-ray parameters are selected as in Preibisch et al. (2005). The main difference with that work is the spectral type classification (we updated the spectral types of several objects with the information from Hillenbrand et al. (2013)) and the sample selection (we used only objects with $M_* < 2$ $M_\odot$).

The rest of the stellar parameters were gathered from Manara et al. (2012): the stellar masses M_*, in units of $M_\odot$, were obtained from D'Antona and Mazzitelli (1994) models and the accretion rates, with units of $M_\odot yr^{-1}$, were derived from that paper, using photometric data from the *HST Treasury Program* (see Sect. 4.2).

In Table 4.4 we present the final catalog with all these parameters for both subsamples.

4.4.1 Least-square fit and outlier rejection study

In this work the regression analyses were carried out using two methods: a least-square approximation and an outlier rejection fit.

For the first, we used a classical *ordinary least square* (OLS) algorithm using the *scipy's orthogonal distance regression* (ODR) package on *Python* (Jones et al. 2001; Boggs et al. 1988). The ODR package allowed us to feed the uncertainties of our parameters into the analysis and take them into account to acquire the fit. Moreover, it also produced the errors of the fitted coefficients, which we used to compute the uncertainties in our results.

Because of the large spread of our data, we decided to include a Bayesian outlier rejection algorithm with *Monte Carlo Markov Chain* (MCMC), using the *astroML* package of *Python* (Vanderplas et al. 2012). The points, which are identified by this method as not part of the fit with a probability greater than 99.7% (3-σ confidence), are selected as outliers. This method uses models that marginalizes over the probability that each point is an outlier. The MCMC is used for this marginalization process. Then, from the sets of maximum a posteriori likelihoods for the slope and intercept values, we selected the median values for both parameters as the best-fit results.

This method relies heavily on the measurement uncertainty. A few good points might have been rejected if their uncertainties were underestimated. But since the sample and measurements come from the same homogeneous survey, these errors should not bias our result significantly.

The Spearman correlation analysis was used to test the relation between the parameters in our study, because it is less sensitive to outliers than other correlation

analyses, such as Kendall τ or Pearson ρ.

4.4.2 Stellar mass dependencies

Many studies have shown that there is an inherent relation between the mass of the young star and its X-ray emission (Flaccomio et al. 2003; Preibisch et al. 2005; Telleschi et al. 2007; Ercolano et al. 2014) and between the stellar mass and the mass accretion rates (Calvet et al. 2004; Muzerolle et al. 2003; Muzerolle et al. 2005; Mohanty et al. 2005; Natta et al. 2006; Manara et al. 2012; Alcalá et al. 2014). We want to test these results with our data.

Stellar mass and accretion rates - Fig. 4.2 and Table 4.5 show the correlation study between the mass of the star and its mass accretion rate. Important differences can be found for both subsamples. Strong correlation coefficients are found for the *U-excess* subsample, with a relation of $\log\dot{M} = (1.94\pm0.23)\times\log M_* - (7.95\pm0.12)$ using the minimum-square fit analysis. This result is consistent with previous studies, $\log\dot{M} = 2\times\log M_* - 7.5$, which is used in the Telleschi et al. (2007) study of the TMC. But we can see how this is not the case for the $H\alpha$ subsample. The relation for this subsample is $\log\dot{M} = (1.57\pm0.23)\times\log M_* - (7.60\pm0.15)$, but with weaker correlation coefficients. This discrepancy suggests that *U-band excess* is a better accretion tracer than the $H\alpha$ line equivalent width (Venuti et al. 2014), and calls for a word of caution when using $H\alpha$ to derive accretion rates. In the case of the outlier rejection analysis, a steeper slope is found for the *U-excess* subsample, $\log\dot{M} = (3.29\pm0.25)\times\log M_* - (7.37\pm0.15)$, as well as for the $H\alpha$ subsample, $(3.19\pm0.21)\times\log M_* - (7.09\pm0.16)$. In Sect. 4.5 we address this difference.

Stellar mass and X-ray emission - Fig. 4.3 shows the relations between the stellar mass and L_X, for both subsamples. The regression and correlation parameters of the different subsamples are summarized in Table 4.5. For the *U-excess* subsample, stronger correlations are present between these parameters than those found for the $H\alpha$ one, a similar result to that on the $\dot{M}_{acc}$ - M_* study. In Sect. 4.5 we explain this critical difference.

4.4.2.1 Selection bias

Ercolano et al. (2014) study whether the $\dot{M}_{acc}$ - M_* relation found for different samples of YSO can be a consequence of a selection bias or detection threshold. Apart for finding similar relations to our subsamples, they find that it is not affected by a selection bias.

The *Manara2012* sample we used is almost complete down to the hydrogen-burning limit. Thus, we conclude that selection effects are not present in our $\dot{M}_{acc} - M$ relations. And given the X-ray detection limit of the *Chandra* telescope, which is lower than our lowest X-ray luminosity value, we also deduce that our $L_X - M$ relations are also not affected by a selection bias owing to undetected sources.

4.4.3 Accretion rate and X-ray luminosity

We now focus on our primary objective: study the accretion processes of the PMS objects in the ONC and their relation with the X-ray emissions of the central stars. This interaction has also been studied in different works, such as Preibisch et al. (2005) and Drake et al. (2009) in Orion, or Telleschi et al. (2007) in Taurus. Here we want to reformulate the results obtained in these works, using different accretor tracers and measurements. In particular, we want to compare the analysis of Telleschi et al. (2007) in the TMC with our results in the ONC, and see if similar relations can be inferred.

In our work we are not interested in studying the differences between accretors and non-accretors. That classification is no longer appropriate for our study, as seen in Sect. 4.3. This is why we study the direct dependences and relations of the measured mass accretion rates and the X-ray luminosities. We take an approach similar to that of Telleschi et al. (2007). Here they study the L_X - $\dot{M}_{acc}$ relation, taking into account the inherent dependences of these properties with the mass of the star. Class II objects show a direct relation between $\dot{M}_{acc}$ and M. Using different evolutionary tracks, Muzerolle et al. (2003) and Muzerolle et al. (2005) found $\dot{M} \propto M^2$ and $\dot{M} \propto M^{2.1}$, respectively, so in Telleschi et al. (2007) they adopted the relation $\log\dot{M} \approx 2\log M$ - 7.5. They also compute a relation between $\log L_X$ and $\log M$ with their data. Finally, they relate the L_X with the $\dot{M}_{acc}$ with the equation $\log L_X(\dot{M}) = 0.85 \times \log(\dot{M}) + 36.67$.

Taking the same approach, we used the $\dot{M}_{acc}$ - M_* and the L_X - M_* relations we found for both our subsamples and derived L_X as a function of $\dot{M}_{acc}$. By using both the *OLS* and the *outlier detection and rejection* methods, different regression results and, consequently, $L_X(\dot{M}_{acc})$ equations, are obtained for each subsample. These results are shown in Table 4.6. With them, we computed the expected L_X given the $\dot{M}_{acc}$ of the sources in our catalog. We called this our *theoretical* $L_X(\dot{M}_{acc})$. This relation could define the L_X - $\dot{M}_{acc}$ in Orion if both parameters were to only depend on the stellar mass.

Finally, we computed what we called the *residual* L_X. This parameter was obtained by dividing the observed L_X by the *theorethical* L_X, given by our derived equations, for a given $\dot{M}_{acc}$. In Table 4.4 we include the different residual L_X values of each source that has been computed this way, for both subsamples. This residual X-ray luminosity compares the observed L_X with the expected value if both the L_X and the $\dot{M}_{acc}$ were to only depend on the stellar mass. It represents the excess (or deficit) of X-ray luminosities that are dependent on the $\dot{M}_{acc}$. In Fig. 4.4 we plot this value against the $\dot{M}_{acc}$. If this ratio were determined only by the L_X - M_* and $\dot{M}_{acc}$ - M_* relations, then the values would scatter around a constant. As can be seen in the figure, they present a large scatter, pointing towards more dependencies, in addition to the stellar mass, for L_X and $\dot{M}_{acc}$.

Again, we used both the *OLS* and the *outlier detection and rejection* methods for these final plots. Table 4.5 summarizes all the regression results obtained for all the possible combinations of data and methods. The values under *"Least square algorithm"* in Table 4.5 correspond to the regression results that were obtained using the OLS methodology, whilst the ones under *"Outlier rejection algorithm"* correspond to the results obtained using the named method. The four top rows present the results of the regressions that were found directly from the data, whilst the bottom four show the regression results from the derived *residual X-ray luminosity*. This last parameter is computed using what we defined here as the *theoretical X-ray luminosity*, $L_X(\dot{M})$, which in turn depends on the first relations. Thus, depending on the methodology used to derive the first relations on the top four rows (OLS or outlier rejection), different $L_X(\dot{M})$ are obtained. This is represented in the four bottom rows. The top two present the results from the $L_X(\dot{M})$ derived from the OLS methodology, while the bottom two represent the $L_X(\dot{M})$ derived from the outlier rejection analysis.

4.5 Discussion

We will now discuss the correlations and trends found in the previous section. The main objective is to compare the residual X-ray luminosity - mass accretion rate relations from both Taurus, obtained in Telleschi et al. (2007), and Orion, obtained in this work, which we do in Sect. 4.5.1. Different methods yield different results, which we address in Sects. 4.5.2 and 4.5.3. In Sect. 4.5.4, we interpret these results.

4.5.1 Comparing Taurus and Orion - OLS method regression results

Telleschi et al. (2007) find the following results when studying the X-ray emission differences between CTTS and WTTS: i) CTTS present smaller L_X than WTTS, on average; ii) they also present smaller L_X/L_*; iii) and a correlation is found between the electron temperature and the total L_X for WTTS, but not for CTTS (where the temperatures are higher than those in the WTTS). Their results point towards a magnetic coronal source for the X-ray emissions in TTS. Also, they suggest that the lower L_X emission from CTTS is caused by coronal heating from an accretion disk and accretion processes. Denser accreting material from CTTS would cause a decreased heated plasma from the reconnection events, accounting for the lower measurements of L_X in accreting systems than in WTTS. The cool plasma may also reorganize the magnetic loops after entering them, stretching and causing them not to reconnect (diminishing the X-ray emission therefore); or by just lowering their temperature because they are colder than them; or inducing radiative losses and more rapid cooling.

One of their main results regarding the accretion processes and the L_X luminosities was the relation between the residual L_X and the $\dot{M}_{acc}$ they they found for their CTTS sample. The main difference to their work can be found in the subsamples we gathered for the Orion YSOs, which yield different results in each case.

4.5.2 OLS method regression results

As can be seen in Figs. 4.2 and 4.3, the spread in the data is considerable, over orders of magnitude. For the $H\alpha$ subsample, in fact, this spread is large enough to produce ineffective correlation results as can be seen in the low Spearman ρ coefficient for the $\dot{M}_{acc}$ - M_* relation in Table 4.5. This spread may be caused by hidden variables that affect our data.

The *U-excess* subsample presents a stronger correlation between these parameters, pointing towards more coherent measurement of the mass accretion rates of the sources (Venuti et al. 2014). The process to derive the accretion rate, which uses the equivalent width of the $H\alpha$ line, is more complex than the one with the excess emission of the *U band*. More factors enter into play in the former, leading to more uncertainties in the final data, which maybe explains the larger spread in the plots for this subsample.

This is why we cannot assert the reliability of the rest of the results from the

$H\alpha$ sample from this conclusion onward. The low ρ coefficient in the $\dot{M}_{acc}$ - M_* relation means the derived L_X - $\dot{M}_{acc}$ one is not sufficiently reliable. Therefore, our analyses will focus on the *U-excess* subsample from now on. Nevertheless, we report the results from the other subsample as a reference and when making a comparison with the *U-excess* data.

The *U-excess* subsample presents moderate/strong correlations between our four main parameters, M_*, $\dot{M}_{acc}$, L_X, and the residual L_X. In fact, this is very similar to those found in Telleschi et al. (2007). The relation between M_* and $\dot{M}_{acc}$, $\dot{M}_{acc} \propto M_*^{1.94\pm0.23}$ given by the *least-square* method is totally compatible with that found in many previous studies. Also, the $L_X \propto M_*^{1.72\pm0.17}$ relation is compatible with that found in Preibisch et al. (2005) for the same region. We still find considerable spreads in the data but the results we find are consistent with those on Taurus in Telleschi et al. (2007).

We find that the final relation between the residual X-ray luminosity and the mass accretion rate for the *U-excess* subsample, $L_X/\ L_X(\dot{M}) \propto \dot{M}^{-0.53\pm0.05}$, is very compatible with the relation found in Taurus in Telleschi et al. (2007), $L_X/\ L_X(\dot{M}) \propto \dot{M}^{-0.48\pm0.15}$.

4.5.3 Outlier method regression results

To test the robustness of our fits, we used an *outlier detection algorithm*. The problem with this method, as stated before, is that it is very sensitive to uncertainties in the dependent variable, in this case, $\dot{M}_{acc}$, L_X, and $L_X/\ L_X(\dot{M})$. Several sources present sufficiently small errors as to be selected as outliers, although their position in the plot is consistent with the best-regression fit. Thus, the results obtained using this method should be taken cautiously.

The parameters we are working with (stellar mass, mass accretion rate, and X-ray luminosity) are not measured directly, but obtained indirectly from other measurements (i.e., the equivalent width of the $H\alpha$ line or the excess in the *U band* for the $\dot{M}_{acc}$, or the flux of the objects, which is obtained by measuring the photons that arrive to the X-ray detector, for the L_X). Consequently, the uncertainties should represent this process.

As mentioned in the previous section, the relation obtained between the residual X-ray luminosity and the mass accretion rate using the *OLS* method for the *U-excess* subsample agrees considerably well with the results found by Telleschi et al. (2007) in Taurus. On the other hand, using the outliers detection method, the results on

Orion differ considerably from those in Taurus.

The relations obtained with the *outliers detection* method between M_* and $\dot{M}_{acc}$ in both subsamples have considerably steeper slopes compared to those found in the literature: $\dot{M}_{acc} \propto M_*^{3.19\pm0.21}$ for the $H\alpha$ subsample and $\dot{M}_{acc} \propto M_*^{3.29\pm0.25}$ for the *U-excess* one. This represents a difference of more than 3-σ from the ones obtained using the *OLS* method. In the case of the L_X - M_* relation, the results differ from one subsample to another. The *U-excess* subsample presents compatible regression results between both methods, and between the relation found in Preibisch et al. (2005). But the ones found for the $H\alpha$ subsample are considerably different, by a factor larger than 3-σ.

In Table 4.5 all the final $L_X/L_X(\dot{M}_{acc})$ - $\dot{M}_{acc}$ relations are shown, and Fig. 4.4 presents the final plots. Using both methods, we obtain eight different results: two plots for the $H\alpha$ subsample, each with two different regression results, depending on whether we used the *OLS* or the *outliers detection* method to derive the regressions between L_X or $\dot{M}_{acc}$ and M_* and between $L_X/L_X(\dot{M}_{acc})$ - $\dot{M}_{acc}$; and the same in the case of the *U-excess* subsample.

Out of these eight results, and taking into account the aforementioned issues with each subsample and methodology, we decided that only two of them were compatible with Taurus: the one from the *U-excess* subsample that uses the *OLS* method between the M_* - L_X and M_* - $\dot{M}_{acc}$ relations and between the $L_X/L_X(\dot{M}_{acc})$ - $\dot{M}_{acc}$ final relation, and the one from the $H\alpha$ subsample that uses the *outliers detection* method for the initial relations and the *OLS* analysis for the $L_X/L_X(\dot{M}_{acc})$ - $\dot{M}_{acc}$ final relation.

The uncertainties shown in Table 4.5 for Orion are far narrower than those found in Telleschi et al. (2007) for Taurus. The 1-σ range for the slope from Telleschi et al. (2007) is *-0.33* to *-0.63*, which is compatible with three more results from our analysis if we add the uncertainties from them (slopes *-0.35* $\pm$ *0.07*, *-0.67* $\pm$ *0.06,* and *-0.68* $\pm$ *0.13*). With these, our final interpretation of the results, as stated in Section 4.5.4, becomes stronger. Nevertheless, we urge caution, given the issues we explained before.

One important result to point out is that the regression results obtained using the *OLS* method are recovered using the *outliers detection* method when the uncertainties on the dependent variables are increased sufficiently (1-σ, 2-σ, 3-σ...).

The accretion processes present an important variability in time, which we disregard. Applying an outliers detection and rejection method to these kind of data, without taking this characteristic into account may seem risky, as some sources could

be an order of magnitude off its quiescent value and be selected as outliers when, in fact, they are not. This is another reason why the results of the outliers analysis must be taken with caution. Nevertheless, given the numbers in our data, this issue is not so critical.

4.5.4 Results

Our main result is the anti-correlation found between the residual L_X and the $\dot{M}_{acc}$. We deduce two interpretations from these results.

The first is that for higher accretion rates there is a deficit in the observed L_X, compared with the *theoretical* one. This implies that, for stronger accretors, the observed L_X is weaker. That is, the accretion processes seem to "cover" the emission of X-ray radiation from the YSOs. This result is also found in Telleschi et al. (2007).

The second is with regard to the scatter in the values on these plots. If the L_X and $\dot{M}_{acc}$ are only dependent on the stellar mass of the YSOs, as we have assumed, these values would scatter around a constant value of one. But the higher scatter and the negative slope points towards other dependencies for these parameters (e.g., stellar rotation, Rossby number, magnetic field intensity). What is interesting is the similarity between the $L_X/L_X(\dot{M}_{acc})$ - $\dot{M}_{acc}$ relation on Taurus and Orion. This suggests that the environment where the T Tauri stars are born is not one of the parameters that affects the $L_X/L_X(\dot{M}_{acc})$ - $\dot{M}_{acc}$ relation.

As a result, we can conclude that this anti-correlation between the residual L_X and the mass accretion rate is independent of the region and environment; its arbitrary appearance both in the TMC and in the ONC, shows reasonably well how it is an inherent property of accreting systems. Similar analyses in other star-forming regions could reinforce this result.

4.6 Conclusions

We have gathered a sample of T Tauri stars in the Orion Nebula Cluster with known X-ray detections and mass accretion rates. Using the classification criteria in Telleschi et al. (2007), we have divided our sample in CTTS and WTTS, finding that several WTTS have accretion rates comparable or even higher to those of CTTS. Since our data do not allow us to confirm these classifications and the number of WTTS in this work is small compared to the whole catalog, we have used all the

subsamples for our analysis.

Two subsamples have been used in this work, depending on the method used to calculate the accretion rates of the sources. The $H\alpha$ sample used the equivalent width of this spectral line, and the *U-excess* subsample, the color excess compared to the nominal values.

Because of the large spread in our data, two regression analyses were carried out. First, we used a *least-square* regression analysis, using the *ODRPACK* of *Scipy* on Python, obtaining results compatible with those in the literature and with Telleschi et al. (2007) for one of our subsamples. Then, we detected and rejected outliers from our samples using the *astroML MCMC* package of Python. This method is very sensitive to the uncertainties from the dependent variables and some sources were rejected as outliers as a result of too small error values, which thus affect the final regression-fit results. Using this method, only one more result was compatible with that from Taurus in Telleschi et al. (2007). By enlarging the uncertainties in the dependent variables, the *OLS* regression results were recovered.

We find that a clear anti-correlation between the residual X-ray luminosity and the accretion rates is present in both subsamples, although we cannot assert the reliability of the $H\alpha$ results because of the weak correlation found between its previous parameters. In the case of the *U-excess* subsample, our results are consistent with those found in the Taurus Molecular Cloud. This result, independent of the environment studied, points towards an inherent property in these type of YSOs; the accretion processes causes a decrease in the emission of X-rays. Different theories have been postulated for this situation, such as thermalization by the X-rays of the stream being accreted, which causes a reduction in the X-ray measurements.

Table 4.1: Key parameter comparison between the TMC and the ONC.

Region	X-ray Program[1]	Distance (pc)[2]	Age (Myr)[3]	N_{total}[4]
Orion Nebula Cluster	COUP	414	~ 2	277/163
Taurus Molecular Cloud	XEST	150	$\sim$ 1-2	105

Notes. [1] Name of the program from where the data were extracted (ONC Ref. Preibisch et al. (2005);TMC Ref. Telleschi et al. (2007) and Güdel et al. (2007a)).
[2] Distance to the star-forming region (ONC Ref. Menten et al. (2007); TMC Ref. Telleschi et al. (2007)).
[3] Mean log stellar age (ONC Ref. data from COUP and Reggiani et al. (2011); TMC Ref. Telleschi et al. (2007)).
[4] Number of sources used in the TMC analyses (Ref. Telleschi et al. (2007)) and in the analyses of the ONC. (Ref. Preibisch et al. (2005), this wok). In the case of the ONC, the different numbers correspond to the sizes of each subsample studied.

Table 4.2: Cross-matching coordinates and parameters before and after the offset corrections.

	Mean $\Delta(")^1$	Mean$\Delta\alpha(")^2$	Mean$\Delta\delta(")^2$	Mean $\Delta(")^1$	Mean$\Delta\alpha(")^2$	Mean$\Delta\delta(")^2$
(Subsample)		(*Halpha*)			(*U-excess*)	
Before correction	0.320	+0.248	+0.026	0.337	+0.274	+0.036
After correction	0.208	+0.130e-3	+0.011	0.199	+0.007	+0.003

Notes. [1] Mean position offset between X-ray COUP sources and both *HST* Manara et al. (2012) subsamples.
[2] Mean right ascension and declination offsets for both sub-samples.

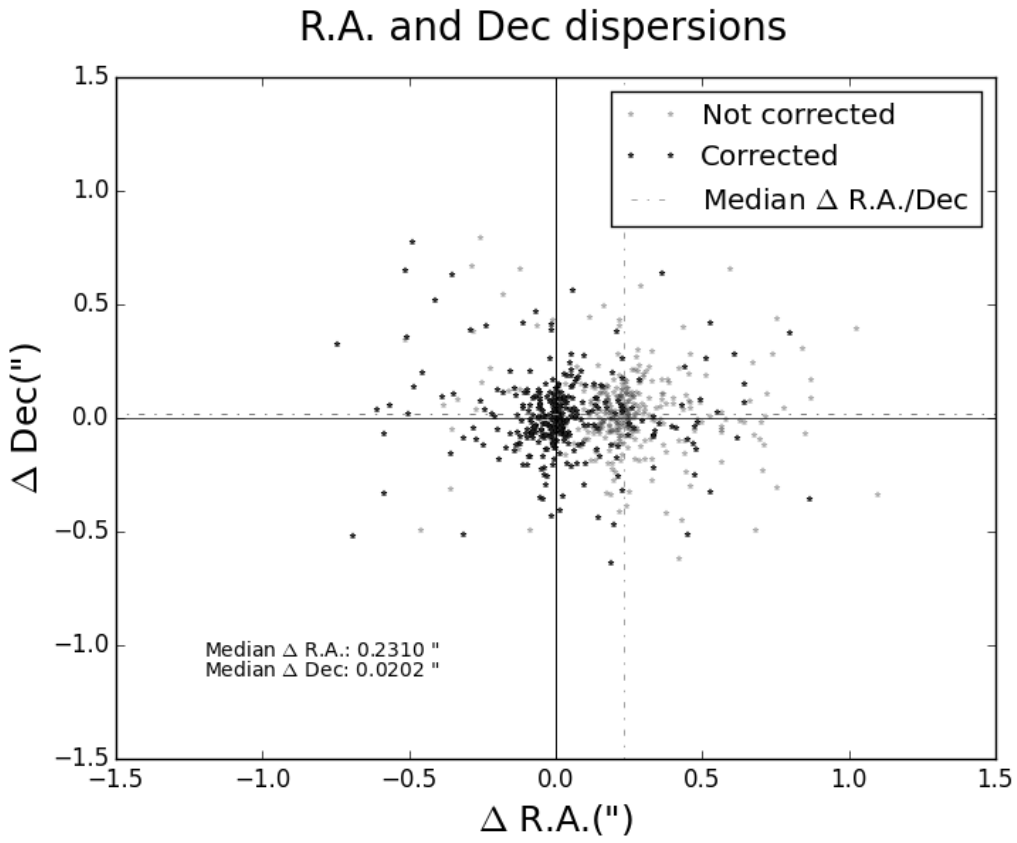

Figure 4.1: Right ascension and declination offsets between the *HST* $H\alpha$ sources and the COUP sample, before and after correction.

Table 4.3: Mean values of $\log(\dot{M}_{acc})$ for both CTTS and WTTS classified with the different accretion tracers. The standard deviation is used as the uncertainty.

	$Mean_{\dot{M}_{acc}}$ CTTS $\pm\ \sigma$	$Mean_{\dot{M}_{acc}}$ WTTS $\pm\ \sigma$	$Mean_{\dot{M}_{acc}}$ CTTS $\pm\ \sigma$	$Mean_{\dot{M}_{acc}}$ WTTS $\pm\ \sigma$
(Subsample)	(*Halpha*)		(*U-excess*)	
Ca_{II} method	- 7.99 ± 0.94	- 8.84 ± 0.98	- 7.78 ± 0.80	- 9.00 ± 0.80
Hα method	- 8.11 ± 0.79	- 9.56 ± 0.68	-	-
Barrado method	- 8.30 ± 0.91	- 9.00 ± 1.01	-	-

Table 4.4: X-ray and stellar parameter information for both subsamples.

Coup id[1]	RA_{COUP}[2] (deg)	DEC_{COUP}[2] (deg)	$\log(L_X)$[3] (erg s^{-1})	OM id[1]	RA_{Manara}[2] (deg)	DEC_{Manara}[2] (deg)	$\log(M_*)$ (M_O)	$\log(\dot{M}_{acc})$ (M_O yr^{-1})	SpT	$\log(L_X/L_X(\dot{M}_{acc}))$[4] *OLS* method	$\log(L_X/L_X(\dot{M}_{acc}))$[4] *Outlier* method
					Hα						
11	83.670400	-5.378410	30.29±0.17	101	83.670246	-5.378431	-0.40±0.05	-6.60±0.36	M1	-1.22±0.78	-1.05±0.42
14	83.673400	-5.399380	28.69±0.17	108	83.673392	-5.399303	-0.82±0.01	-10.02±0.43	M5	1.31±0.37	0.21±0.15
16	83.674400	-5.363780	28.53±0.17	117	83.674233	-5.363750	-0.92±0.01	-10.60±0.59	M7	1.85±0.34	0.54±0.18
29	83.694200	-5.390450	29.75±0.17	144	83.693996	-5.390442	-0.51±0.07	-7.78±0.36	M2	-0.34±0.45	-0.60±0.30
37	83.699800	-5.394550	28.03±0.17	153	83.699687	-5.394536	-0.80±0.01	-9.78±0.36	M5	0.36±0.38	-0.65±0.18
28	83.693400	-5.408840	30.79±0.17	157	83.693308	-5.408869	-0.35±0.05	-9.13±0.66	M0	2.34±0.42	1.57±0.40
40	83.700700	-5.377370	28.90±0.17	158	83.700454	-5.377372	-0.89±0.01	-9.77±0.42	M3	1.22±0.31	0.21±0.13
117	83.737300	-5.368430	29.53±0.17	185	83.737183	-5.368425	-0.52±0.01	-8.79±0.32	M3	0.67±0.15	0.02±0.15
133	83.746700	-5.385510	28.78±0.17	194	83.746587	-5.385497	-0.89±0.01	-9.48±0.47	M4	0.75±0.16	-0.15±0.21
137	83.748200	-5.400080	29.15±0.17	199	83.748138	-5.400053	-0.64±0.01	-8.32±0.30	M4	-0.28±0.22	-0.75±0.18
...											
					U-excess						
1	83.622700	-5.393730	29.74±0.17	70	83.622692	-5.393733	-0.74±0.00	-11.04±0.34	M5	1.90±0.44	0.77±0.27
43	83.703500	-5.388330	30.24±0.17	146	83.703458	-5.388329	-0.49±0.07	-8.92±0.26	M1	0.53±0.16	0.16±0.15
55	83.710600	-5.393160	29.17±0.17	167	83.710400	-5.393148	-0.57±0.01	-8.37±0.20	M1	-1.03±0.22	-1.20±0.14
89	83.726200	-5.359870	29.59±0.17	174	83.726037	-5.359843	-0.48±0.08	-7.94±0.11	M0	-0.99±0.22	-1.00±0.16
65	83.716800	-5.405220	29.46±0.17	175	83.716704	-5.405229	-0.64±0.01	-8.82±0.08	M3	-0.34±0.24	-0.67±0.24
71	83.719200	-5.401070	30.17±0.17	177	83.719104	-5.401034	-0.44±0.06	-9.43±0.20	M1	0.91±0.25	0.36±0.22
107	83.733300	-5.386970	31.32±0.17	178	83.733208	-5.386923	0.04±0.09	-7.45±0.30	K2	0.31±0.48	0.47±0.24
118	83.737600	-5.383360	28.82±0.17	189	83.737512	-5.383354	-0.70±0.01	-10.38±0.31	M4	0.40±0.34	-0.49±0.24
122	83.740800	-5.380900	30.09±0.17	191	83.740746	-5.380872	-0.70±0.01	-8.05±0.11	M3	-0.39±0.20	-0.44±0.16
228	83.770100	-5.377450	28.34±0.17	224	83.770043	-5.377404	-0.70±0.01	-8.76±0.08	M4	-1.52±0.23	-1.82±0.24
...											
...											

Notes. [1] Source ids as in the COUP catalog and in the Manara et al. (2012) samples. [2] Source coordinates as in the COUP catalog and in the Manara et al. (2012) samples. [3] Logarithmic value of the X-ray luminosity, computed at a distance of 414pc. [4] Residual X-ray luminosities, computed using the regression results from the extitOLS method in the first case and from the *outlier detection and rejection* algorithm in the second.

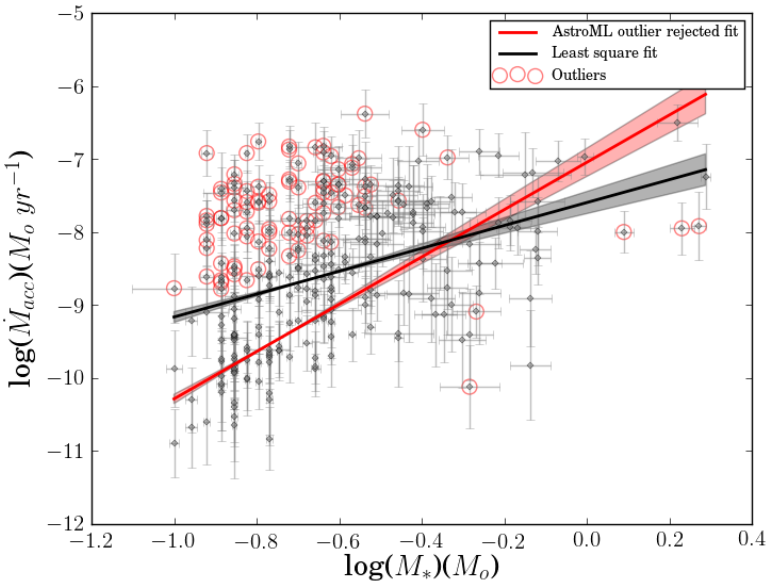

4.2.a: Hα sample.

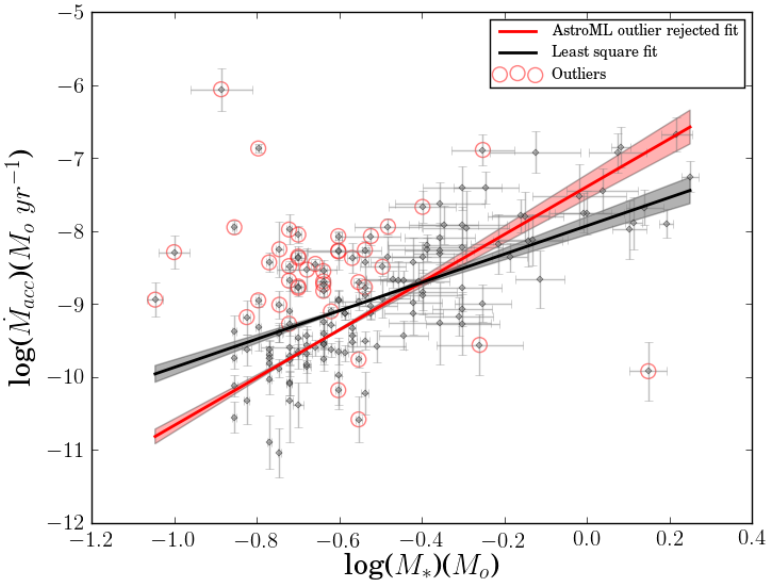

4.2.b: U-excess sample.

Figure 4.2: Stellar mass vs. mass accretion rates for both subsamples. The plot on the left corresponds to the *Hα* subsample, and the one on the right to the *U-excess* subsample. Regression lines (straight) are plotted with their respective errors in the slope (shaded areas) for the OLS regression analysis (black) and the outlier rejection regression method (red).

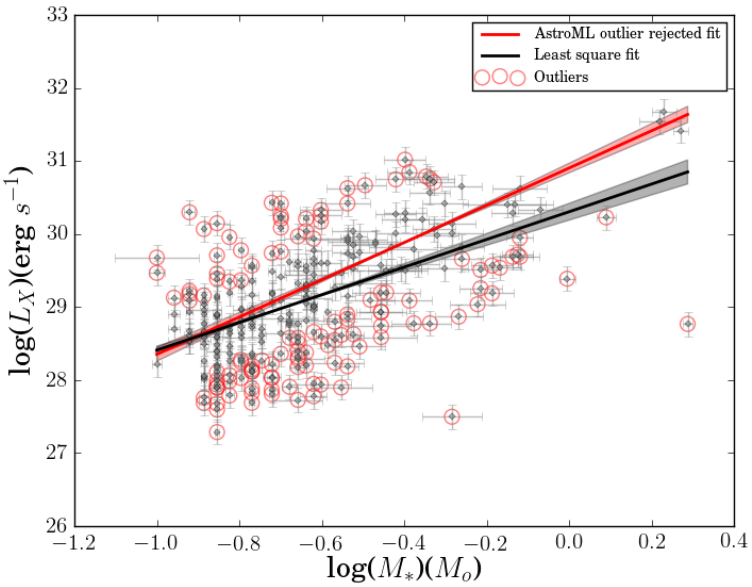

4.3.a: Hα sample.

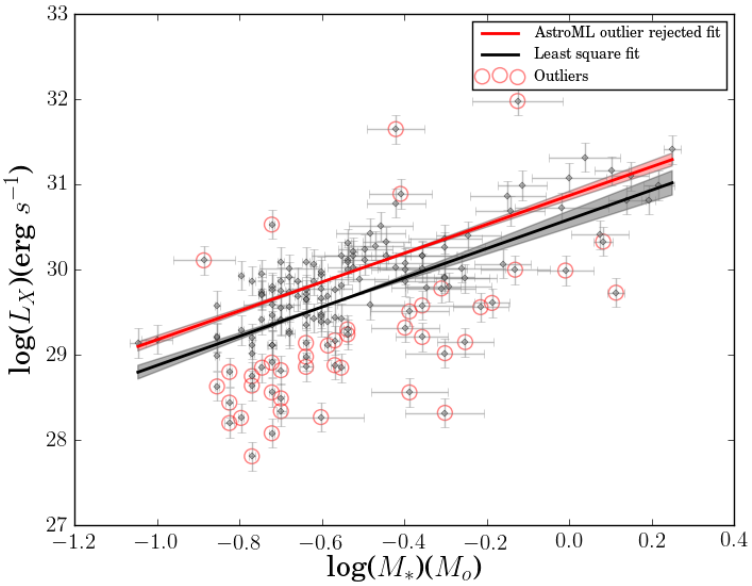

4.3.b: U-excess sample.

Figure 4.3: X-ray luminosities vs. the mass of the sources. The plot on the left corresponds to the *Hα* subsample, and the one on the right to the *U-excess* subsample. Regression lines (straight) are plotted with their respective errors in the slope (shaded areas) for the OLS regression analysis (black) and the outlier rejection regression method (red).

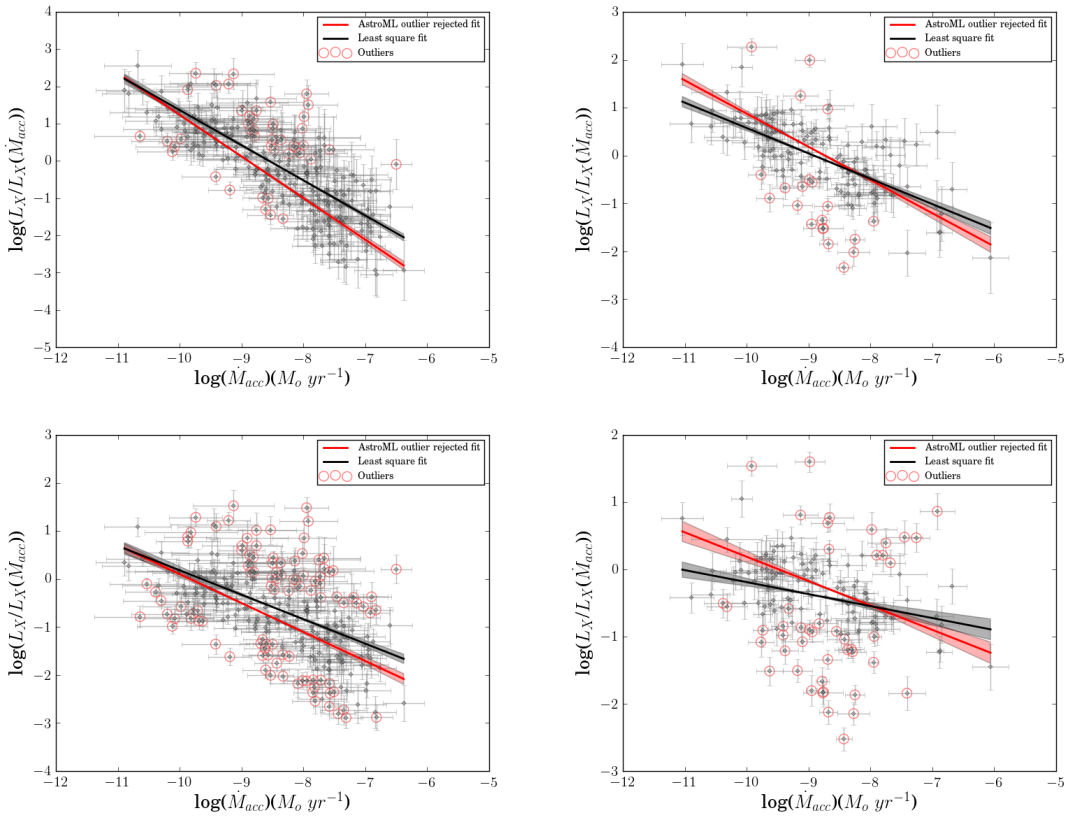

Figure 4.4: Residual X-ray luminosity, after normalization with the M - L_X and M - $\dot{M}$ relations, as a function of the mass accretion rate. Left figures correspond to the $H\alpha$ subsample. Right figures correspond to the *U-excess* subsample. The top plots present the results using the OLS method for the initial regression analyses between M_*, L_X and $\dot{M}_{acc}$. The bottom ones when using the outlier rejection method for those same analyses. Regression lines (straight), with their respective errors in the slope (shaded areas), are shown for the OLS (black) and outlier rejection (red) final regression results.

Table 4.5: Summary of results of the different correlations analyses. The relations correspond to the logarithmic equation of the parameters.

Correlation[1]	Subsample[2]	N[3]	Least square algorithm [4]		Outlier rejection algorithm [4]		Spearman Parameters	
			a	b	a	b	ρ[5]	g[6]
$\dot{M}$ vs. M	Hα	277	1.57 ± 0.23	-7.60 ± 0.15	3.19 ± 0.21	-7.09 ± 0.16	0.38	Weak
$\dot{M}$ vs. M	*U-excess*	154	1.94 ± 0.23	-7.93 ± 0.12	3.29 ± 0.25	-7.37 ± 0.15	0.55	Moderate
L_X vs. M	Hα	277	1.90 ± 0.17	30.33 ± 0.12	2.72 ± 0.17	30.89 ± 0.09	0.52	Moderate
L_X vs. M	*U-excess*	154	1.72 ± 0.17	30.59 ± 0.10	1.75 ± 0.12	30.89 ± 0.07	0.61	Strong
Residual L_X determined using minimum-square fit analysis [7]								
$L_X/\ L_X(\dot{M})$ vs. $\dot{M}$	Hα	277	-0.94 ± 0.05	-8.07 ± 0.40	-1.09 ± 0.04	-9.65 ± 0.39	-0.78	Strong
$L_X/\ L_X(\dot{M})$ vs. $\dot{M}$	*U-excess*	154	-0.53 ± 0.05	-4.72 ± 0.43	-0.67 ± 0.06	-5.85 ± 0.53	-0.63	Strong
Residual L_X determined using MCMC outlier rejection fit analysis [7]								
$L_X/\ L_X(\dot{M})$ vs. $\dot{M}$	Hα	277	-0.59 ± 0.05	-5.50 ± 0.43	-0.68 ± 0.13	-6.51 ± 1.22	-0.55	Moderate
$L_X/\ L_X(\dot{M})$ vs. $\dot{M}$	*U-excess*	154	-0.19 ± 0.05	-2.04 ± 0.47	-0.35 ± 0.07	-3.28 ± 0.58	-0.29	Weak

Notes. [1] Parameters to analyze.

[2] Subsample from which the data are referred.

[3] Number of objects in the subsample.

[4] a stands for the slope of the linear regression and b for the intercept. Errors for the least square analyses are the standard deviation as given in the ODR algorithm. Errors for the outlier analyses are the standard deviation of all the values computed in the MCMC algorithm for each parameter.

[5] Spearman's ρ rank correlation coefficient.

[6] Goodness-of-fit as given by ρ.

[7] Different regression methods between M_*, L_X and $\dot{M}_{acc}$ yield different $L_X(\dot{M})$ equations. Rows five and six show the regression results between $L_X/L_X(\dot{M})$ and $\dot{M}_{acc}$ when the OLS method was used for the first regressions, while rows seven and eight, when the outlier rejection methodology was applied.

Table 4.6: L_X vs. $\dot{M}_{acc}$ equations for each subsample. Each one is computed using the regression results of L_X, M_* and $\dot{M}_{acc}$. The ones using the results from the minimum-square analysis are shown on top, and the ones using the outlier detection and rejection analysis are shown below.

Sample	L_X - $\dot{M}_{acc}$
Using minimum-square fit analysis	
$H\alpha$	$\log L_X = (1.21\pm0.28)\log\dot{M} + (39.49\pm2.09)$
U-excess	$\log L_X = (0.89\pm0.19)\log\dot{M} + (37.60\pm1.51)$
Using MCMC outlier rejection fit analysis	
$H\alpha$	$\log L_X = (0.85\pm0.11)\log\dot{M} + (36.93\pm0.74)$
U-excess	$\log L_X = (0.53\pm0.08)\log\dot{M} + (34.81\pm0.55)$

Chapter 5

Optical variability in the young PTF Orion project. New young transiting exoplanets candidates and variable stars.

Bustamante, I.; van Eyken, J. C.; Ciardi, D.; Merín, B.; Christiansen, J.; Rebull, L.; Stauffer, J.; Schlieder, J. E.; Bouy, H.; Alfonso-Garzón, J.; Riviere-Marichalar, P.

Optical variability in the young PTF Orion project. New young transiting exoplanets candidates and variable stars.. 2017, Astronomy & Astrophysics, (submitted, April 2017)

Abstract

The identification of young transiting exoplanets in young star-forming regions is a key step in understanding the process of planet formation. With an estimated age of ∼7-10 Myr, the 25-Ori association harbors young pre-main sequence stars which circumstellar disks have started to dissipate. The Palomar Transient Factory Orion (PTF Orion) project was developed to search for transiting exoplanets around these young stars. Confirmation of transiting exoplanets could help to establish constraints in planetary formation and migration theories. We aim to mine the complete set of observations of the PTF Orion survey, searching for transiting exoplanets and establishing membership status of the 25-Ori association of those candidates. Furthermore, we aim to identify other variable objects, classify them by light curve morphology, and assess their 25-Ori membership. We visually inspected the complete set of light curves looking for features of transiting exoplanets. The periodicity of the candidates was determined using a Plavchan periodogram. We derived the spectral types of the host stars by fitting archival PAN-STARRS, 2MASS and WISE photometry to NEXTGEN models, assuming dwarf cool stars. We gauged the likelihood of an exoplanet presence by comparing eclipse depths with stellar temperature and periodicity of the transit events. Finally, we provided a degree of membership of the 25-Ori association by looking for youth tracers in the sources, such as stellar variability, flare presence, position in color-color/color-magnitude diagrams, infrared excess in the spectral energy distributions and X-ray detections. We found 37 sources showing exoplanet transit-like events, sixteen of them being potential young low-mass stars. Nine of them show youth tracers compatible with membership of the 25-Ori association. Furthermore, a catalog of 858 variable stars was produced, composed of the aforementioned planet candidates, plus 177 eclipsing binaries (82 of which were previously identified); 31 classical T Tauri stars (16 previously identified); 30, 112 and 96 sources showing short-, intermediate- or long-term periodic behavior, respectively; 11 and 240 sources showing short or long term non-periodic variability, respectively; and 144 sources presenting flare activity. Approximately 52% of these sources show signs of youth, making them potential young members of the 25-Ori association. We have accomplished the main goal of the PTF Orion program, identifying young transiting exoplanet candidates suitable for follow-up. Our catalog also incorporates disk-bearing pre-main sequence stars, active weak-lined T Tauris, young eclipsing binaries, and several older pulsating sources, enabling diverse ancillary science in stellar formation and evolution.

5.1 Introduction

The Palomar Transient Factory Orion (PTF Orion) project was a photometric monitoring campaign of the region surrounding 25-Ori and the OB1a association. Its main goal was to detect transits that could point towards the presence of exoplanets orbiting the young stars of the region. Given the young age of the association, $\sim$ 7 - 10 Myr (Briceño et al. 2007), any exoplanet candidate found could potentially give crucial information on planetary formation theories. Few young ($\leq$ 10 Myr) confirmed planets have been identified (David 2016; Mann et al. 2016; Donati et al. 2016; Johns-Krull et al. 2016b), and little is known about the first stages of planetary evolution. Thus detecting new candidates presents an ideal opportunity to improve our knowledge of these systems.

The presence of circumstellar material around young pre-main sequence (PMS) stars, birthplace and cradle of exoplanets, makes it difficult to detect these objects in this early stage via photometric means. That is why this region was selected. Its age corresponds to the time scale of disk dissipation of $\sim$5-10 Myr (Haisch et al. 2001; Hillenbrand 2008; Mamajek 2009; Ribas et al. 2015), making it possible to find exoplanets at the stages in which the disk-planet interaction and photometric disk contamination would be minimal.

Our group has published two previous studies using the PTF Orion data. The first one, van Eyken et al. (2011), focused on the search and identification of eclipsing binaries (EB) and young stellar objects (YSOs), looking at the most clearly variable stars in the sample. As such, 82 EB and 16 YSOs were identified. Some of these sources were identified as candidate 25-Ori or OB1a association members. The complete description of the reduction pipeline of the PTF Orion data can be found in that work. The second paper, van Eyken et al. (2012), reported the identification of a young transiting exoplanet candidate around a weak-lined T Tauri star (WTTS) in the PTF Orion sample. The candidate planet, labeled PTFO 8-8695b, where the host star is also known as CVSO 30 (Briceño et al. 2007), has an orbital period of 0.448413 $\pm$ 0.000040 days (van Eyken et al. 2012). Radial velocity measures and adaptive optics imaging suggests that the system is not an eclipsing binary. The status of this system is still unclear, though (Yu et al. 2015; Koen 2015; Howarth 2016; Onitsuka et al. 2017). Further data acquisition and follow up has been carried out to ascertain the nature of this system (Barnes et al. 2013; Ciardi et al. 2015; Kamiaka et al. 2015; Raetz et al. 2016; Johns-Krull et al. 2016a)

The main goal of this work is to identify any other potential transiting exoplanet

candidates. For that purpose, we visually inspected the light curves for sources that presented any transits, looking for those consistent with a planet presence. Using archival photometry from the Panoramic Survey Telescope and Rapid Response System (Pan-STARRS) PS1 catalog (Chambers et al. 2016), the 2MASS All-Sky Catalog (Skrutskie et al. 2006) and the WISE All-Sky Release Catalog (Wright et al. 2010), we produced the spectral energy distributions (SEDs) of the candidates, and determined estimates of their spectral types photometrically. As a last step, we conducted membership analysis of our targets to the young association known to spread through the field of view of the PTF Orion project.

During the search for the transit events, the complete set of light curves of the PTF Orion was studied. Photometric variability can be used to track and identify eclipsing binaries, stellar activity, flares, classical and weak T Tauri stars and pulsating sources. As such, we constructed a catalog of all variable stars that we identified in the PTF Orion project. We also established membership status in the 25-Ori association for these sources, following the same criteria as for the transiting exoplanet candidates sample.

Finally, we validated our membership analysis results by comparing with previous works carried out in the region (Briceño et al. 2005; McGehee 2006; Briceño et al. 2007; Hernández et al. 2007; Downes et al. 2015).

This work is organized as follows. Section 5.2 shows a summary of the data reduction and processing pipeline (a complete description can be found in van Eyken et al. (2011)). In Section 5.3 we explain the methodology we used, detailing the variability identification, periodicity assessment, 25-Ori membership tracers analysis, and elaborating on the different works carried out in the region. In Section 5.4 we describe the criteria used to select our transiting exoplanet candidates, list all the sources classified as such, and assess their membership likelihood of the 25-Ori association. Section 5.5 presents the final variable catalog, explains the classification method we used, and shows which of them are suitable 25-Ori member candidates. In Section 5.6 we analyze these results and, finally, the summary and conclusions of this work can be found in Section 5.7.

5.2 Data

5.2.1 The 25-Orionis region

The observations were carried out around the early-B star 25-Ori, in the Orion OB1a sub-association. This region has low interstellar reddening ($A_V = 0.29$, Briceño et al. (2007)), and high but not overcrowded source count density ($\sim$4.4 sources/$arcmin^2$). It has been relatively well characterized by other studies (Briceño et al. 2005; Briceño et al. 2007; Briceño 2008; Briceño et al. 2011; Franciosini et al. 2011), and it has an estimated age of $\sim$ 7-10 Myr (Briceño et al. 2007). This age corresponds to the dissipation time of the circumstellar disk around pre-main sequence stars (Hillenbrand 2008), making it possible to observe the photometric variability of the star without it being dominated by effects from the disk, such as accretion or circumstellar extinction.

5.2.2 PTF Orion observations

The PTF survey was carried out using the wide-field mosaic camera on the Samuel Oschin 48 inch telescope on the Palomar Observatory. The camera consists of a mosaic of 12 CCDs (one of them non-functional), with 1″ pixels, spanning a field of view of $\sim 3^\circ.5$ x $2^\circ.3$. The observations are centered at approximately $\alpha = 05^h26^m46^s$, $\delta = +01^\circ50'50''$ (J2000).

Two observing runs were carried out as part of the PTF Orion project, with the observations consisting of a single pointing. The first run, in the winter of 2009, was comprised of 40 nights of observations, 14 (non-consecutive) yielding usable data, with 4486 exposures obtained during the run. The exposures were 30 s long, with a cadence between 70 and 90 s. The 2010 winter run was comprised of 20 nights, out of which seven consecutive nights were usable. This run was observed in a similar fashion as to the 2009 one. But due to clearer weather and no fogging effects in the CCDs (van Eyken et al. 2011; Ofek et al. 2012) (see Sec. 5.3.1.2 below), the 2010 data present a better rms noise floor for the brightest sources ($\sim$3 to $\sim$4 mmag) than the 2009 one, and fewer systematic effects. The 2010 data were used only in the exoplanet candidate discovery paper; as a result, the 2010 data remain mostly unanalyzed, even though the data quality is better than the 2009 data.

After the differential photometry process, all data points are checked and flagged following certain criteria: flags are set for multiple source detections or references within the FWHM, low number of detections, high variations in right ascension/de-

clination on time for an individual source, saturated objects, proximity to optical ghosts or contamination within the photometry aperture. In van Eyken et al. (2011) a complete description of the PTF Orion reduction pipeline can be found, and we refer to Ofek et al. (2012) for a description of the general PTF data reduction pipeline.

5.3 Methodology

After the data reduction and the differential photometry processes, the sample was composed of 116,285 light curves for each year of observation. The first step was to look for transit events in these light curves, and to do so, we started by looking for sources that presented any optical variability features.

5.3.1 Variability identification

We used two different approaches for identifying variable sources: visual inspection of the complete sample and a Stetson variability index analysis (Stetson 1996).

5.3.1.1 Visual inspection

Developing an automatic variability-detection algorithm proved inefficient. Systematic errors in the light curve and photometric outliers introduced a prohibitively high number of false positives with automatic detection algorithms. Several kinds of systematic effects were found: saturated sources ($R_{med} < 12$mag) presented similar high amplitude ($\sim$ 1mag) stochastic variability, not related to any physical process; systematic drops and rises in flux after gaps in several of the light curves were found, unaccounted for by any astrophysical explanation.

Most of these systematic effects were flagged as bad data points, using the criteria listed before, and could have been identified as such and rejected automatically. But other sources presenting flagged photometric points showed real variability features (e.g., sources 0-769, 0-3542, 0-5197 or 0-9653). This is why we decided not to omit these sources from the variability analysis using an automatic detection and rejection algorithm.

Moreover, some sources with low signal to noise ratios were not selected as variables with the automatic detection algorithm, even though clear variability could be seen in their light curves.

We decided to visually inspect the entire sample of the PTF Orion, for both years, which yielded a total of 232,570 light curves to examine. Despite being a tedious process, the identification of structures in the light curves done by eye proved to be the most efficient way to detect objects of interest and to discard false positives. Photometric systematic errors and outliers were easily identified visually. We identified as variable sources those that showed a specific feature in the light curve, like sinusoid shapes or transits, sources with flaring events, objects with slow trends through a single night's observation and sources that showed stochastic variability.

Although this process proved efficient and robust, its downside is its inherent subjectiveness; visual identification of variability strongly depends on the observer.

From this first selection process, we identified 1,376 sources of interest. These sources showed some kind of variability in the 2009 data, in the 2010 data, or in both.

This first identification was meant to detect any kind of variability in the light curves. Minor structures were taken into account, including some systematic errors not identified as such at first glance. Because of that, a second visual inspection of the 1,376 initial variable sources was performed.

After this second vetting, we discounted 532 sources as having negligible variability or as being a false identification due to previously unidentified systematic errors. This yielded a total of 844 sources of interest.

5.3.1.2 Fogging effect

In the 2009 run there is a trend that appears in the differential photometry due to fogging of the detector window during the observations (Law et al. 2010; van Eyken et al. 2011). This effect was caused by slow deposition of oil contaminants in the dry air supply used to prevent condensation on the CCD window. In some areas of the detector this causes a long-term variation of almost ~ 0.2 mags on the light curves, easy to detect once the sources have been folded. Fig. 5.1 shows one example of this effect.

5.3.1.3 Stetson variability index

For a more quantitative and less subjective approach to identifying variable sources, we used the Stetson variability index (Stetson 1996). This index measures the correlation of the different points in a light curve.

The J index is defined, in Stetson (1996), as:

$$J = \frac{\sum_{k=1}^{n} \omega_k sgn(P_k)\sqrt{|P_k|}}{\sum_{k=1}^{n} \omega_k}$$

Where:

- n: the number of pairs of observations defined.
- ω_k: the weight for the kth pair
- P_k: the product of *magnitude residuals*, $\delta_{i(k)}$, defined as:
  - $P_k = \delta_{i(k)}\delta_{j(k)}$, if i $\neq$ j
  - $P_k = \delta_{i(k)}^2$ - 1, if i = j
- sgn(P_k): the sign, positive or negative, of P_k

The magnitude residuals δ are defined as:

$$\delta = \sqrt{\frac{n}{n-1}}\left(\frac{\upsilon - \tilde{\upsilon}}{\sigma_\upsilon}\right)$$

Where υ is the measured magnitude of the observation, $\tilde{\upsilon}$ is the mean magnitude over all observations and σ_υ is the individual error of the observed magnitude. (Note: In our case, given the presence of systematic errors and outliers in the light curves, instead of the mean $\tilde{\upsilon}$ we used the median.)

The procedure works as follows. A certain period of time, t, is selected to create the pairs for a certain photometric point, i. All the j points that fulfill JD_j - $JD_i < t$, where JD is the Julian date of that point, are paired with it (including itself), and the correlation index is computed. This procedure is repeated using all the points in the light curve. The higher the J index is, the higher the degree of variability of the source.

We selected different values of t to test the detection results. The shorter the value of t, the larger the number of short-term variables detected, and vice versa. We tested this procedure with values of t of 60, 30, 10 and 1 minutes, recovering 69%, 70%, 72% and 68% (for the 2009 data) and 66%, 68%, 70% and 64% (for the 2010 data) out of the 844 sources classified as variables by the visual inspection, respectively. The best results where the largest fraction of visual variables is recovered come from t=10 mins.

Sources with Stetson index >1 were selected as variables. This threshold value refers to the J value acquired for known variables stars in our sample, identified as detached binaries or CTTS, in van Eyken et al. (2011) (see Fig. 5.2).

Not all the sources identified as variables by the visual inspection are detected with this method. For example, some sources with real variability features but high uncertainties presented a J index lower than expected, and were classified by this approach as non-variable, but we retain them in the variable sample.

Finally, 14 sources missed in the visual inspection analysis and detected as variables by the Stetson index were added to the sample, making a total of 858 variable stars. This means we find a fraction of variable stars of ∼0.74%, similar to the fraction found in all-sky surveys, such as the All Sky Automated Survey (Pojmanski 2003) (0.4%) and the Robotic Optical Transient Search Experiment variability survey (Akerlof et al. 2000) (0.8%), but considerably lower than the fraction found in the CIDA Variability survey (Briceño et al. 2005) (6.1%). This large difference may be due to the method applied of detecting variable stars in Briceño et al. (2005); where we visually inspected and selected only identifiable variable sources, they applied an statistical approach, using a χ^2 test on the normalized magnitudes. This method does not get rid of false positives; in that work they relied on spectroscopic data to reject contaminants.

The sample of 858 variable stars comprised the core result of our study, which we will refer from now on as the *PTF Orion variable catalog*.

5.3.2 Periodicity identification

One of the key aspects of exoplanetary analysis is the periodicity of the eclipses found in the light curves. Stable periodic transits are a necessary condition to determine the size of the companion of an eclipsing light curve. Furthermore, we can use the periodic behavior of the sources in the *PTF Orion variable catalog* as an initial classification method.

The period, P, was obtained calculating the Plavchan periodogram (Plavchan et al. 2008), using a standalone version of the periodogram service of the NASA / IPAC / NExScI Star and Exoplanet Database [1] (Akeson et al. 2013). The maximum period of the periodogram was selected as half of the time range of the observations, so as to be able to get two cycles in the folded light curves. This value depends on the length of each set of observations: 40 and seven days for the 2009 and 2010

[1] http://exoplanetarchive.ipac.caltech.edu

data, respectively. The sources were folded to the 20 periods with the highest peaks in the periodogram, and then visually inspected to select the best value, and make sure it was not half or a multiple of another period. If a source was correctly folded with one of these periods, it was identified as periodic and the uncertainty was set as the FWHM of a Gaussian fit to the corresponding peak of the periodogram.

The sources which had not been folded correctly with any of the 20 highest periods were not automatically rejected as periodic. In some cases, the Plavchan periodogram did not detect the observable feature we had identified in the visual inspection and had not assigned a correct period for it. This was the case for many of the transit candidate events we had observed, due to larger-scale out-of-transit variability in the light curve. We identified those sources and manually searched for a correct period for those features.

5.3.3 Membership analysis

The last step of our analysis was to assess the 25 Ori association membership status of the variable sources. The following youth tracers were used as an indicator of membership: infrared excess in the SEDs, position in color-color and color-magnitude diagrams, X-ray emission detection and flare occurrences. Furthermore, we cross-correlated our sample with archival catalogs comprised of known members of the OB1a and 25-Ori associations to validate some of our results.

We acquired the following archival catalogs: the Pan-STARRS PS1 catalog (Chambers et al. 2016), the AllWISE Source Catalog (Wright et al. 2010), the 2MASS All-Sky Point Source Catalog (Skrutskie et al. 2006), and a source list from an *XMM-Newton* observation on the field around 25-Ori (Franciosini et al. 2011). The Pan-STARRS DR1 catalog provides Sloan $grzi$ photometry and y-band photometry. This survey used a 1.8 meter ground-based telescope to image the sky in these bands. From the 2MASS All-Sky catalog we obtained near-infrared photometry in J, H and K_S bands. The WISE All-Sky Release catalog provides mid-infrared [3.5], [4.6], [12] and [22] μm bands. We visually inspected all images from the 2MASS and WISE catalogs for the cross-matched sources to validate detections, using the NASA/IPAC Infrared Science Archive (IRSA) [2] imaging tools for both catalog images, and flagged each photometric point accordingly (detection, blended sources, non detection).

We also included the median R magnitude from our own light curves as another

[2]http://irsa.ipac.caltech.edu/frontpage/

photometric point

Finally, we obtained samples in the region from Briceño et al. (2005), Briceño et al. (2007), Hernández et al. (2006), Hernández et al. (2007), McGehee (2006), Downes et al. (2014) and Downes et al. (2015) and compared their results with ours. We used a closest-neighbor approach with a 5 arcsecs searching radius.

5.3.3.1 Color-color and color-magnitude diagrams

We used 2MASS JHK_S color-color diagrams and R-K_S color-magnitude diagrams to determine whether a source presented colors consistent with low-mass stars or PMS stars, respectively. We assigned an homogeneous extinction value of $A_V = 0.29$ mag (Briceño et al. 2007) for all our sources. This assumed value corresponds to extinctions of ΔR = 0.22, ΔJ = 0.082, ΔH = 0.055 and $\Delta K_S = 0.033$, applied to each source, following the Cardelli et al. (1989) extinction law. We only applied this method to the sources which presented good quality 2MASS photometry, and clear visible detections in those bands. Using the main sequence disposition and isochrones for 1, 5 and 10 Myr from Siess et al. (2000) models, assuming a distance of 330 pc to the association, we were able to identify young variable sources.

With this method we identified 531 sources from our catalog of 858 as potential pre-main sequence stars.

5.3.3.2 SED analysis

We obtained NEXTGEN photospheric models (Hauschildt et al. 1999b; Allard et al. 2012) and fit the photospheric points available in our data (g, r, z, i, y, R, J, H and K_S) to those models, using a minimum chi square algorithm. Fixing the extinction to the value above, we derived estimates of the spectral types for our sources by selecting the best fit NEXTGEN model. In most cases, no near-infrared excess is expected given the age of the association. Nevertheless, taking into account the results from van Eyken et al. (2011) and Downes et al. (2014), where they found several sources with infrared excesses indicative of protoplanetary disks, we normalized each source independently to fit the SED, depending on whether some infrared excess was present in the 2MASS and WISE photometric points or not.

We only applied this method to sources with clear JHK_S detections. The evolutionary state of our sources was unknown initially. Using NEXTGEN models as fits for the complete sample would be inaccurate for some of the potentially evolved field sources. Because of this reason, this SED fitting method was only considered

robust enough for the sources with PMS disposition in the color-magnitude diagram identified in Sec. 5.3.3.1, as well as for sources that showed infrared excess, and for all the planets identified as transiting exoplanet host candidates. The estimated type uncertainty, by comparing with spectral types from previous works (5.3.4), is of ±two subtypes. For the rest of the sources, no spectral type was assigned this way. Estimations with a color-color diagram were applied in these last cases.

Finally, any source presenting any WISE detection was flagged as an *infrared source*. Furthermore, if that excess was higher than the corresponding continuum derived with the SED fitting by 3-σ or more, it was flagged as having *infrared excess*. In these last cases, the presence of a circumstellar disk was assumed whenever more than one WISE photometric point presented this excess.

5.3.3.3 Binary systems and spectral type determination

Some of our sources were classified as eclipsing binaries. In these cases, both sources contribute to the photometry used for the SED fitting analysis and further spectral type identification. Contact W Uma sources usually share a uniform surface temperature of the common envelope, and are of similar spectral type, but Algol and β Lyrae binaries can present many different combinations of spectral types. Because of this reason using only one photosphere model to fit the SED of these sources would be an over- or under- estimation of one of the components. That is why we used a grid of two combined photosphere models in these cases. This way we can account for the contribution of two sources to the overall photometry of the system. As a result, we indicate not one, but two different spectral types for these sources.

5.3.3.4 X-ray detections

Franciosini et al. (2011) observed the region around 25-Ori with the *XMM-Newton* telescope, using the EPIC cameras (OBSID = 0554610101, March 1-2, 2009, Fig. 5.3). Their goal was to study the X-ray luminosities of the known cluster members and compare them with other younger clusters (λ Ori and σ Ori). As such, 187 sources were detected, 62 of which corresponded with previously known members and 19 had consistent color memberships from 2MASS photometry. We used this catalog to find X-ray counterparts of our variable sources and add this information to the membership analysis. Fig. 5.4 shows the field of view (FOV) of the *XMM-Newton* observation compared with that of the PTF Orion. It can

be seen how the *XMM-Newton* FOV is much smaller than ours, introducing a bias with respect to the overall sample, but it still adds important information about the sources closer to 25-Ori, and we use it as a tracer of youth for that sub-sample.

5.3.3.5 Photospheric activity - flares

One of the main characteristics of YSOs, and in particular of T Tauri stars, is the strong magnetic activity they exhibit (Gahm 1990; Preibisch et al. 2005). The interaction between the circumstellar disk and the star in CTTS produces accretion streams that can be detected as flaring events in the X-ray or optical regimes, due to the high energies involved (Getman et al. 2008b). WTTS also present these high-energy features (Gahm 1990; Getman et al. 2008a). The presence of high energy flares observed in the X-ray regime can sometimes be related with optical flares (Kenyon and Hartmann 1987; Guenther and Ball 1998; Montes et al. 2005). As such, optical flares could point towards high energetic flares, which could point towards strong magnetic activity, which could be a signpost of youth. Because of this, we include this variability feature as a youth tracer in our analysis.

5.3.3.6 Degree of membership

We defined the degree of membership (DoM) as an indicator of how likely a source is to be part of the young 25-Ori association. It is a list of flags indicating which youth tracers assigned to the source. A higher number of positive flags results in higher DoM and a higher membership likelihood. The flags correspond to:

- (1) X-ray counterpart
- (2) infrared excess in the SED
- (3) flare presence in the light curves
- (4) PMS location in the color-magnitude diagram
- (5) counterpart with van Eyken et al. (2011) binaries
- (6) counterpart with van Eyken et al. (2011) CTTS
- (7) counterpart with Briceño et al. (2005) or Briceño et al. (2007) YSO catalog members
- (8) counterpart with Hernández et al. (2006) or Hernández et al. (2007) debris disks and 25-Ori T Tauri catalogs
- (9) counterpart with McGehee (2006) catalog of low-mass YSOs
- (10) counterpart with Downes et al. (2014) and Downes et al. (2015) catalogs of brown dwarfs and low-mass members of 25-Ori.

Some sources presented infrared detections, but without excess with respect to the photosphere. These detections do not suggest presence of disks. Nevertheless, we indicate it by flagging these sources adding an asterisk to the infrared flag (2*).

If a source presented a PMS disposition in the color-magnitude diagram it was automatically selected as potential 25-Ori member candidate. Then, depending on the presence of flares or infrared excess, a higher likelihood was selected. If these three conditions (PMS, flares and infrared excess) were met, the source was selected as a strong 25-Ori candidate member.

We also used X-ray counterparts as indicators of youth, but the smaller field of view of that observation introduced a bias in the membership statistics of the cluster. Because of that, we indicated that a source is more likely to be a part of the 25-Ori association if it has X-ray emissions, but did not include this indicator in the overall statistical analysis.

Counterparts with the van Eyken et al. (2011) binaries and CTTS catalogs are only shown for reference. If conditions (7), (8), (9) or (10), that is, counterparts in catalogs of known 25-Ori members, are fulfilled, the sources were selected as members of the association.

5.3.4 Description of previous studies on the region

As indicated in Sec. 5.3.3, we acquired several catalogs from other works carried out in the region to compare with our results.

Briceño et al. (2005) conducted a census of young variable stars from a large-scale multi-epoch survey around the Ori OB1a and Ori OB1b regions. They used optical variability and infrared color-magnitude diagrams to select candidate members, and then spectral analysis to confirm the nature of these candidates. They found a clear distinction between the two regions, identifying a larger fraction of disk bearing stars in Ori OB1b than in Ori OB1a; this is not surprising, giving the difference in age between the regions, ∼5 Myr and ∼7-10 Myr, respectively. Thus, Ori OB1b, being older, would harbor a smaller number of CTTS than Ori OB1a.

Briceño et al. (2005) selected as variables a sample of 20,729 stars, from which they identified 3744 as PMS sources from a color-magnitude diagram. They could spectroscopically confirm the T Tauri nature of 197 objects from a sub-sample of 1403 of these PMS sources, which yields a ratio of ∼14% young stars identified.

Briceño et al. (2007) studied the 25-Ori association specifically, treating it as an independent group from Ori OB1b. They expanded the number of spectroscopically

confirmed TTS, and studied the kinematics of the sample. They established that 78 sources had consistent radial velocities with 25-Ori, and thus deduced a common origin between the B2 star and those young TTS. They also derived an estimated age for the 25-Ori group of 7-10 Myr.

Hernández et al. (2006) reported the identification of several debris disks located in the fields of OB1a and OB1b. Using IRAC and 2MASS observations and optical spectra, they studied the properties of these disks around early type B, A, and F stars, and found, not surprisingly, that the occurrence of these objects is higher in the older OB1a association than in the younger OB1b. This is in agreement with the fact that debris disks are thought to be an evolution of protoplanetary disks (Rieke and Su 2004; Williams and Cieza 2011), and thus they would be found more frequently in more evolved associations. We did not find any counterpart with this work in our variable catalog.

Hernández et al. (2007) studied the disks around low-mass members of 25-Ori. Using *Spitzer* IRAC and MIPS, they observed 115 confirmed members and 41 photometric candidates in OB1a, and 106 members and 65 candidates in OB1b, and found a larger disk occurrence rate in the younger (OB1b) association than in the older one (OB1a), similar to Briceño et al. (2005).

McGehee (2006) studied the low-mass population of 25-Ori, establishing with multi-epoch photometry from the Sloan Digital Sky Survey that the association was unbound from the rest of the OB1a complex, and deriving a CTTS fraction of $\sim$10% for the association.

Downes et al. (2014) used optical (CIDA) (Briceño et al. 2005) and infrared (VISTA) (Emerson et al. 2004) photometry, as well as low resolution spectra to identify a sample of low-mass and brown dwarf members of 25-Ori. Using color-magnitude diagram locus and spectral confirmation, they presented a catalog of 75 association members, classifying them according to spectral signatures. Downes et al. (2015) included a census of 15 confirmed brown dwarf members of 25-Ori, and studied the disk fraction in this sample.

We compared the results from Briceño et al. (2005), McGehee (2006), Briceño et al. (2007), Hernández et al. (2007) and Downes et al. (2014) with the spectral type determination and physical type classification from our analysis, wherever any counterpart was found in our catalog.

5.4 Transiting exoplanet candidates

5.4.1 Identification

We selected as transiting exoplanet candidates those sources which presented clear dips in any portion of the light curve, with depths equal to or smaller than 0.1 magnitudes. A Jupiter-size planet would produce a $0.1 > \Delta m > 0.02$, $0.02 > \Delta m > 0.01$, and $\Delta m < 0.01$ for stars of M, K, and G spectral types, respectively. For earlier spectral types, a shallower Δm would be needed.

To accurately determine the period of the transiting events we whitened their light curves. We isolated the variations caused by the eclipses from the rest of the stellar variability, if present, selecting by hand the positions of the potential transits and removing those data points from the light curves. After that, we smoothed the remaining points with a Savitzky-Golay filter (Savitzky and Golay 1964), interpolating the empty regions where the transits were found. Finally, we normalized this interpolated function to the the original light curve, in flux space, obtaining the whitened functions with the eclipses as the only source of variability.

The downside of this approximation is the identification of the transit event in stars with high stellar variability. In these cases some transits could be mistaken for spot modulation, or vice-versa. Thus, we repeated this analysis in those cases where stellar variability could be a cause of misinterpretation, choosing different eclipse candidates until we obtained consistent whitened light curves.

In some cases, the orbital periodicity of the systems could not be computed, given that not enough eclipses were present in the light curves. The planetary nature of these systems is, thus, unlikely.

5.4.2 Results

The main criteria we have used thus far to identify exoplanet-candidates is based on the depth of the eclipses and the spectral types derived with the SED fitting algorithm.

We identified 37 sources showing exoplanet-transit-like events. A stellar period was derived for 33 of these 37 sources. Fig. 5.5 shows the folded light curves of these 33 sources. In some cases, the stellar periodicity is coupled with the transit periodicity, and the eclipse is clearly identified; in others, this variability makes it difficult to spot the eclipses on the folded light curves.

From this sample of 37 candidates, fifteen sources (0-7220, 2-1144, 4-5444, 5-3045,

5-11919, 6-3001, 6-3938, 7-2844, 8-3311, 8-4176, 8-8695, 8-9088, 8-9555, 9-2156 and 10-10911) have a PMS position in the color-magnitude diagram, and all of them also have a low-mass location in the color-color diagram (Fig. 5.9). We derived their spectral types as explained in Sec. 5.3.3.2, obtaining a distribution of twelve M0 to M6 stars, two K9 and one K6. We included three non-PMS sources to this sample, given the depth and shapes of their eclipses (4-2953, 7-2919 and 8-3886). This yields a sample of 18 potential transiting exoplanet candidates.

After analyzing this sample, we ruled out three as unlikely exoplanet host candidates: source 0-7220 is classified as an Algol detached binary in van Eyken et al. (2011), and has an spectral type of K6, possibly too hot for the depth threshold we used; source 5-11919 presents no eclipses in the 2010 observations and thus no clear period was determined; source 8-4176 presents small dips in flux, with periods of stability, compatible with an Algol detached binary.

From the remaining sources that showed exoplanet-transit-like events, we re-classified 21 as potential Algol detached binaries (0-4407, 0-7220, 1-146, 2-1875, 2-1925, 2-4281, 4-2781, 4-2831, 4-5261, 4-6325, 4-9497, 7-882, 7-5967, 7-8191, 8-1336, 8-4176, 8-4549, 8-9356, 8-9435, 8-10585 and 9-11713). One other source is ruled out as planet and re-classified as a potential WTTS (5-11919).

Thus, we present a final sample of fifteen transiting exoplanet candidates. After whitening their light curves, as explained in the previous section, a period for the transiting events was derived for ten of them. Fig. 5.6 shows the whitened light curves of these ten candidates. In Table 5.1 we show the derived stellar and planetary parameters, based on the spectral type of the host star and the transit depth. Stellar effective temperature, absolute V magnitude and radius were obtained from Gray and Corbally (2009), Appendix B, from the derived spectral types, assuming our sources are dwarf stars. We also provide the planet periods acquired for the whitened light curves for each run, and for the combined data of both years. With these values we computed a first approximation of the radius of the planet with the relation *depth* $= R_p^2 \ / \ R_*^2$, and with a Jupiter radius of 0.102719 $R_\odot$. Additionally, sources with good or strong 25-Ori membership candidacy are also flagged in Table 5.1 with asterisks. These results serve as a first approximation to the actual values of the planets radii. Radial velocity measures and spectral confirmation should be carried out to assess the reliability of these results.

From the fifteen candidates, we could not derive any period for the transit events for five sources: 5-3045, 6-3001, 8-3311 (in these cases, for presenting only one unique eclipse) and sources 8-9088 and 9-2156. We maintain them in Table 5.1, without a

period value, as reference. The planet hypothesis in these cases is not discarded, as we may not be sensitive to their orbital period with our data.

Summarizing, after these analysis, we obtained a sample of **15 transiting exoplanet host candidates**. Fig. 5.7 summarizes this selection process.

Source 8-8695 is included in this sample. This candidate was already identified in van Eyken et al. (2012), and thoroughly studied since then (Barnes et al. 2013; Ciardi et al. 2015; Yu et al. 2015; Koen 2015; Kamiaka et al. 2015; Raetz et al. 2016; Howarth 2016; Johns-Krull et al. 2016b; Onitsuka et al. 2017). The planetary nature of this source is still under debate. Nevertheless, we include it here as a potential transiting candidate, as it fulfills our own criteria.

Regarding the other youth tracers, none of the sources presents any excess compatible with the presence of a protoplanetary disk. Six sources present flares in their light curves (4-5444, 5-3045, 7-2884, 8-3311, 8-9088 and 9-2156). Two of them (7-2884, 8-3311) showing a high number of flares, which is not unexpected, as their light curves have a shape consistent with the presence of spots in the photosphere, and thus stellar activity, probably an indicator of youth. Three have counterparts within the *XMM-Newton* X-ray observation (8-8965, 8-9088 and 8-9555).

Two sources, 6-3938 and 8-8695, are classified as WTTS in Briceño et al. (2005) and Briceño et al. (2007), with ids CVSO-11 and CVSO-30, respectively. Source 8-8695 has, as well, a counterpart in the Hernández et al. (2007) catalog of low-mass disk-bearers, and it is classified as a class III disk-less star, which corresponds to our analysis, and that of van Eyken et al. (2012). Also, other two sources (2-1144 and 8-9088) have counterparts with the low-mass Downes et al. (2015) sample, one of them (8-9088) having also a Hernández et al. (2007) disk-less class III counterpart.

Table 5.2 shows the median R values from the light curves, the periods for both the 2009 and 2010 runs separated and also concatenated, as well as the period derived for the transit events (when available), the infrared colors, youth tracer flags, degree of membership and possible physical interpretation for the 15 transiting exoplanet candidates identified. Table 5.3 presents the same information, but for the 22 rejected exoplanet candidates. We present the periods obtained for each of the sources, as well as the infrared colors, degree of membership and possible physical interpretation.

We discuss in some detail here the 15 sources presented in Table 5.1, comprised of the 10 transiting exoplanet candidates plus the 5 sources with no derived transit periods.

2-1144 - This source was identified in van Eyken et al. (2011) as a detached

Algol type binary. But we identified it as a potential candidate given the depth of the eclipses, compatible with our criteria. This M5 star presents spot modulation, only primary eclipses with depths $\sim$ 0.1 mags, and has a PMS position in the color-magnitude diagram. As such, it is a good 25-Ori member candidate. The spot modulation does not vary appreciably between both years. This source has a counterpart in the Downes et al. (2014) low-mass catalog.

4-2953 - The 2009 data shows detector fogging. Nevertheless, the source presents a very stable out-of-transit flux. Clear periods can be derived for the primary eclipse in both years, consistent with one another. The depth of the transits ($\sim$ 0.05 mags) remains constant over time. With a spectral type of K3, this source is unlikely to host a planet, though spectral analysis should be carried out to reject it. We flagged it as an interesting source for follow-up.

4-5444 - detector fogging affects the light curve from 2009, clearly seen when folding and comparing both years of data. Small flares of 0.5 - 0.6 mags are seen in the 2009 data, and short stochastic variability is present in both years, pointing towards spot modulation, suggesting the young evolutionary state of this source. This is supported by the PMS location of the source in the color-magnitude diagram. The M0 spectral type derived by the SED fitting makes this source a good 25-Ori member candidate. The period of the transit seems to match the period of the overall variability, pointing towards a coupling between the potential planet and the star rotation.

5-3045 - The depth of the potential eclipse, 0.01 magnitudes, opens the possibility of it being caused by a planetary companion. Flares, infrared detections, PMS position in the color-magnitude diagram and stellar variability consistent with spot modulation make this a good 25-Ori member candidate. The period given in Table 5.2 for this source reflects this stellar variability. Just one unique eclipse is found in each year's light curve, and thus an orbital period could not be derived.

6-3001 - Global variations of $\sim$0.3 mags are present in both the 2009 and 2010 light curves, in phase with the transit events. The eclipses are $\sim$0.05 mags in depth, situated on the peak of the general variation. This stable position of the eclipses in the light curves points towards a planet orbit and star modulation coupling. This variability, with a PMS distribution, makes this source a young candidate member of the 25-Ori association. But the stable general variability could be produced by causes other than spots.

6-3938 - General variations are present in both years, comparable in depth to the candidate eclipses ($\sim$0.05 mags). When folded, these variations appear to be

periodic, pointing towards the presence of star spots. It also has a PMS position in the color-magnitude diagram. Thus, this would be a good 25-Ori member candidate.

7-2884 - Stellar variability is found in this source, stable in amplitude over both years. It is difficult to distinguish between the eclipses and this general variability, and thus the period derived for this source is uncertain. A large number of flares is found in both light curves. This, added to the overall variability, a PMS position in the color-magnitude diagram and a spectral type of M5 derived in the SED fitting analysis make this source another good young 25-Ori member candidate.

7-2919 - This source has one of the most peculiar light curves in the complete catalog. It shows clear flat-bottom transits of ∼0.1 magnitudes in depth in both years, with a very stable period. Also, general variability is seen in both years. It is consistent with that of a contact W Uma binary, although there is a difference in between both years' folded light curves. The 2010 data presents two bumps at either side of the flat-bottom transit, whether in the 2009 data there is only one. This change in the light curve could point towards spot modulation, rather than a contact binary. Be that as it may, the depth of the eclipse and the derived spectral type of K4 for this source weakens the planetary companion possibility.

8-3311 - This source presents a light curve similar to 6-3001. General variation is found for both years, though the difference between both sets of data points towards spot modulation in this case. One single eclipse in the 2009 data is found, with a depth of ~ 0.02 magnitudes, easily mistaken with the general stellar variability. The general stellar variability is joined by intense flaring activity and PMS position in the color-magnitude diagram, making this source a strong 25-Ori member candidate.

8-3886 - Clear flat-bottom transits are found in the 2009 light curves, but none in 2010. Thus, just one period was derived. The depth of the transit (∼0.05 mags) and the flat-bottom points towards a planetary scenario, although the K7 spectral type derived weakens that possibility. The stability of the light curve and the lack of youth tracers suggests this is a field star.

8-8695 - Detected in van Eyken et al. (2012) as one of the youngest transiting exoplanet candidates yet discovered, several additional studies have been carried out for this source. We refer to those for a thorough analysis of the system (Barnes et al. 2013; Ciardi et al. 2015; Yu et al. 2015; Koen 2015; Kamiaka et al. 2015; Raetz et al. 2016; Howarth 2016; Johns-Krull et al. 2016b; Onitsuka et al. 2017).

8-9088 - Similar to 6-3938, apparent stochastic variability can be seen in both light curves, that once folded, present a periodic behavior. The candidate eclipses have a depth <0.1 mags, which with the M4 spectral type classification makes this

a strong planet candidate. It also presents flaring activity, PMS colors and even an X-ray detection, thus making it a good young 25-Ori member candidate. Also, this source has a counterpart in the low-mass catalog from Downes et al. (2014). Not a certain orbital period was derived for this source.

8-9555 - Spot modulation is seen in both years, with one flat-bottom primary eclipse. Taking into account the depth of the eclipse (<0.1 mags) and the derived spectral type of M0, this source is a good candidate for the planetary scenario. Also, X-ray detections and PMS colors suggests that this source is a good young 25-Ori young member candidate.

9-2156 - Flares, PMS colors, and general variability probably caused by spots make this a strong young 25-Ori candidate. Also, a depth of less than 0.05 magnitudes in the transits, with an estimated spectral type of M0, strengthen the planetary scenario, making this a very suitable source for follow-up. Nevertheless, the shallow depth of the eclipse makes the derivation of an orbital period difficult.

10-10911 - This source presents stable flux outside of the transit events, which have ∼0.1 mags in depth. With an M6 spectral type, and PMS colors, this is a good planet candidate for follow-up.

5.5 PTF Orion variable catalog

Classifying optical variable sources by physical nature can be challenging, given that different processes can display similar features in the light curves. The General Catalog of Variable Stars (Samus et al. 2010) lists different variability types (eruptive, pulsating, rotating, cataclysmic, eclipsing binary systems, intense variable X-ray sources, and other types not classified in the previous categories), and even so that classification is not perfect, as sources can present different kinds of variability and belong to different categories at the same time. In some cases, the morphology of the light curve is enough to point towards a certain physical explanation, such as eclipsing binaries or eruptive stars, but in most cases this analysis is not enough. Cody et al. (2014) classified a sample of CTTS of the NGC 2264 cluster members, using both infrared (*Spitzer*) and optical (*CoRoT*) light curves, based on curve morphology, and then trying to correlate these properties with physical processes. Christiansen et al. (2008) developed a catalog of variable stars using data from the UNSW Extrasolar Planet Search, classifying them morphologically as eclipsing binaries, pre-main sequence stars, long-period variables, etc, but using color-color diagrams to assess the physical processes of several sources.

We followed an approach similar to those papers, consisting of three steps. First we determined the periodicity, or lack thereof, for each source. For the periodic sources, we used the morphology of the folded light curves to place a source in a certain category or add them to a general variable group. Finally, for some sources in these last groups, we used color-color and color-magnitude diagrams to point towards possible physical explanations. The nature of some of the sources could be identified just by the light curve morphology. Spectroscopic follow-up would be needed to ascertain the nature of these sources.

5.5.1 Classification

5.5.1.1 Periodic sources

If a source was categorized as periodic, we folded the light curve to the best fit period and classified it according to its light curve morphology, when possible. Here we list the classifications we used:

Contact binaries: or W Uma-type objects, where both components fill their Roche lobes. It is impossible to identify the precise moments of end of eclipse and onset, and the primary and secondary minima are almost identical (Kopal 1959), caused by nearly uniform surface temperature of the common envelope. They usually have short periods, between 0.25 and 1.2 days.

Close binaries: also called β Lyrae-type stars, they present no clear distinction between in- and out- of transit in the light curve, making the moments of end of eclipse and onset impossible to ascertain. The light changes continuously and the primary and secondary eclipses are usually identifiable (Huang 1963). Both stars can have very different evolutionary states, and the light curve presents ellipsoidal components due to tidal distortions. The periods are usually larger than half a day.

Detached binaries: also known as Algol (β Persei)-type systems. The moments of ingress/egress are clear in the light curve, and the flux remains constant between eclipses (Giuricin et al. 1983). They present extremely large ranges of periods, from hours to thousands of days.

Fig. 5.10 shows the distributions of periods for each category of eclipsing binaries. The periods of sources labeled as contact and close binaries fall between 0.1 to 1.0 days, while the detached binaries have a wider distribution, as expected. Given that the value of the period was not used as a differentiating factor between eclipsing binaries, this result suggests consistency in our categorization.

Close and contact binaries present similar light curve morphologies. To distin-

guish between them, we used the difference in depths between primary and secondary eclipses. If a source presents a difference between primary and secondary eclipses smaller than 0.1 mags, it was identified as contact binary; if it was larger, it was labeled as close binary. Spectroscopic analysis would validate these categorizations.

Fig. 5.11 shows the folded light curves of a sub-sample of eclipsing binaries, as reference.

Other periodic stars: sources showing some kind of periodicity and not introduced in other categories are labeled as periodic. Fig. 5.12 shows the distributions of periods of this category. We identified three distributions in them, depending on the period. We sub-categorized the sources as *short-*, *intermediate-* and *long*-period sources, depending whether they have periods shorter than 0.1 days, between 0.1 and 1.0 days and between 1.0 and 3.5 days, respectively. This upper limit of 3.5 days was selected as being half of the time baseline of the 2010 observations.

We used these period values as divisions based on the General Catalog of Variable Stars (GCVS) (Samus et al. 2010). Several categories in the GCVS use these values to subcategorize one type of variable from another: *Rapidly oscillating Alpha CVn variables* rotate with periods between 0.004 to 0.01 days, while the threshold for *Short β Cephei types* is between 0.015 to 0.04 days; *β Cephei types* present radial-velocity variations in a range of 0.1 to 0.6 days; *PV Telescopii type* pulsate with periods in the range of 0.1 to one day; *RR Lyrae* present periods between 0.3 to 1.2 days (RRAB) or 0.2 to 0.5 days (RRC); standard *Cepheid* stars pulsate with a period larger than one day; *Orion Eruptive variables* are named differently if their period is smaller or larger than one day; *Long Pulsating B stars* have periods exceeding one day, ... and so on. All this, plus the distribution shown in Fig. 5.12, supports our decision to divide our category using these thresholds. Furthermore, in Section 5.5.2.2 we show how this distinction is supported by the distribution of these sources in the color-color and color-magnitude diagrams, and the different physical explanations that this entails for each sub-category.

Fig. 5.13 shows the folded light curves of a sub-sample of periodic variables from the *PTF Orion variable catalog*.

5.5.1.2 Non-periodic sources

The non-periodic sources were classified according to the following categories:

Flares: Sources showing *only* flaring activity, without any other kind of variability. In the GCVS they are denominated UV Ceti variables. In this category we include all the stable non-variable stars of our sample which just show some flaring

activity. In the case of a variable star in any other category and showing flares, we use a flag (see Sec. 5.3.3.6) to indicate this circumstance, but do not include them in the *Flares* category.

Long-term variables: Sources displaying low ($\leq$ 1.0 mag) variability with a base time larger than one observing night. For some of these sources, a period was identified in the Plavchan analysis, but with values larger than 3.5 days, or with a significant difference between the 2009 and 2010 runs. In these cases we are unable to confidently ensure their periodic nature, and include them in this category.

Short-term irregular variables: Sources with non-periodic variability, with timescales smaller than one night, and not selected for any of the previous categories.

5.5.1.3 CTTS

Classical T Tauri stars: Sources exhibiting large ($\geq$ 1.0 mag) and irregular brightness modulation were selected as young classical T Tauri stars. These variations are thought to be related to photospheric spots, accretion streams or occultation by a circumstellar disk. Briceño et al. (2007) identified 40 CTTS in the region, and van Eyken et al. (2011) identified 14 CTTS candidates from the PTF Orion 2009 run. We compared our identification to those in Briceño et al. (2007) and van Eyken et al. (2011). Several of these CTTS candidates display infrared photometric excesses (see Sect. 5.3.3), suggesting the presence of a circumstelar disk. Nevertheless, these sources should be considered as CTTS candidates; spectroscopic follow up to confirm their nature would be needed.

We found periods for some of the sources in this category, but not for others. That is why we treat this sample as independent from the periodic/non-periodic division.

Fig. 5.15 shows the complete lightcurves of the 31 sources classified as CTTS, and Fig. 5.14 shows the folded light curves for those sources for which a period was identified.

Sources 4-2953, 4-2814, 5-3639 and 5-3461 from our catalog presented the fogging anomaly, as explained in Sect. 5.3.1.2. Thus, it has to be taken into account that the trends observed there are not caused by natural effects, but by instrumental systematics.

5.5.2 Results

Tables 5.4 to 5.12 summarize the *PTF Orion variable catalog* results. Each table corresponds to one of the categories defined in the previous section. In each of the tables we present the PTF Orion identification, J2000 coordinates, median R magnitude, periods (when available), infrared colors (when available), spectral type (or types, in the case of binary systems) derived from the SED analysis, the degree of membership and the possible physical interpretation we assumed after the analysis of each source. A sample of the results is shown in the tables as reference. The complete catalog will be available online.

We will discuss the results for each category in this section, paying attention to some sources of interest.

The association membership or youth analysis is based on Figures 5.16, 5.17, and 5.18, where we show the SEDs of all the sources presenting infrared excesses compatible with disk presence, the color-color diagrams for each category and the color-magnitude diagrams for each category, respectively.

5.5.2.1 Eclipsing binaries

We have identified 157 eclipsing binaries, 82 of them already known from van Eyken et al. (2011), comprised of 11, 81 and 65 close, contact, and detached binaries, respectively. After the analysis of the 37 planet candidates in the previous section, and the re-classification of 20 of them as potential Algol-type binaries, we increase the number of Algol-types to 85 sources. We treat them as detached binaries for the rest of this analysis.

Color-magnitude/color-color diagrams distribution - Sources 0-4757, 2-1066, 4-5331, 5-3088, 5-3670, 5-6432, 5-12446, 5-12712, 6-8645, 7-121, 7-5291, 7-7604, 8-756, 10-10597, 11-1065 and 11-5402 present positions in the color-magnitude diagram and color-color diagram corresponding to young low-mass stars. Reclassified sources 0-7220 and 8-4176 also present PMS dispositions. We derived spectral types photometrically for this sample, obtaining a combination of K and M types. We indicate two spectral types for each source, as explained in Sec. 5.3.3.3.

Infrared excess - Sources 0-9653, 1-8098, 2-1066, 4-2642, 4-5331, 5-3913, 5-5387, 5-5767, 5-12712 and 7-121 present clear infrared excesses. Furthermore, sources 0-9653, 2-1066 and 5-5387 show a change in the slope between WISE [12.0] and [22.0], indicating the possibility of these sources having a transitional disk (Strom et al. 1989b; Calvet et al. 2002). Fourteen more sources present infrared detections, but

not large enough to be associated with the presence of a disk.

These 10 circumbinary disk candidates yield a ∼5.7% occurrence of disks in the sample of 177 binaries, lower than the ∼7.9% of remaining non-binary disk bearing sources in the catalog (54 non-binary sources with disk indicators out of a total of 681 non-binary sources). In theory, the presence of a companion in a disk-bearing system should truncate the disk and shorten the dissipation time of the material, as indicated in Artymowicz and Lubow (1994). Cieza et al. (2009) deduced, using *Spitzer* observations, that there is a correlation between the separation of the binary components of the system and the presence of an inner disk. It is also argued that multiplicity does not affect the lifetime of disks (Armitage et al. 2003; Monin et al. 2007; Pascucci et al. 2008). Given that we identify our circumbinary disk candidates only with WISE infrared excess, we can not assert whether our sample is consistent with one or the other result. Spectral analysis of the sample should validate or discard our identifications, and thus point towards one scenario of disk dissipation or another.

Flaring activity - Four sources show flaring activity in the lightcurves: 0-4757 and 7-5291 (β lyrae), 2-1066 (Algol) and 7-7604 (W Uma). Reclassified source 0-7220 also presents flaring activity. In particular, 7-7604 is one of the most active stars of our sample, showing up to four flares in the 2009 data and two in the 2010 one. This agrees with the fact that W Uma stars, sharing a convective envelope and rotating fast, could have strong magnetic activity (Qian et al. 2014), and thus present higher flaring activity.

X-ray counterparts - No X-ray counterparts were found for the binary sample.

With the previous results at hand, we can point out that eight binary sources present good 25-Ori membership candidacy: 0-4757, 0-7220, 2-1066 4-5331, 5-12712, 7-121, 7-5291 and 7-7604, all of them showing a combination of disk presence, flaring activity, low-mass and young disposition in the color-magnitude diagram. In particular, source 2-1066 shows all these youth indicators, making it the strongest binary member candidate.

From this sample, five of the sources (0-7220, 2-1066, 4-5331, 7-5291 and 7-7604) were already identified as good young 25-Ori member candidates in van Eyken et al. (2011). The rest are new to the literature.

5.5.2.2 Other periodic stars

We classified 238 sources as simply *periodic*, comprised of 96 *long-period variable stars*, 112 *intermediate-period variable stars* and 30 *short-period variable stars*.

Color-magnitude/color-color diagrams distribution - almost ∼79% of the *long-period stars* present a pre-main sequence age in the diagrams, compared with the ∼55% of the *intermediate-period* sample. The spectral types derived in these cases range between K2-K9 and M0-M6. None of the *short-period* sources have PMS colors. All of them are distributed in the instability region in the color-color-diagram.

Infrared excess - Five *long-period* sources show infrared excesses compatible with disk presence (0-8545, 1-3797, 2-2440, 7-1740 and 8-9153), while only a single one of the *intermediate-period* sample, 2-3586, does. This last source presents a difference in the SED slope between WISE [12] and [22], indicative of a possible transition disk. None of the *short-period stars* present any kind of disk indicator.

Furthermore, 48, 29 and three sources of the *long*, *intermediate* and *short* categories, respectively, show infrared detections, although not high enough to be flagged as disk-bearers.

Flaring activity - ∼41% of the *long-period stars* present some flaring event, two of them, 7-479 and 11-8358, having the highest number of flares in the *PTF Orion variable catalog* (seven and eight, respectively). On the other hand, ∼38% of the *intermediate-period stars* show flaring events, one of them, 7-7326 with one of the largest flare recorded in the catalog, up to 2.0 magnitudes in flux rise. No sources classified as *short-period* presents flaring activity.

X-ray counterparts - eight of the *long-period stars* (7-7675, 8-8565, 8-8987, 8-9153, 8-9221, 8-10164, 8-10397 and 8-11126) have counterparts with the *XMM-Newton* observation around 25-Ori, while three of the *intermediate-period* ones (8-9020, 8-10817 and 8-11586) do too. No sources classified as *short-period* have X-ray counterpart.

With these results, we are now in a position to shed some light on the nature of these categories. First, one possible explanation for the high rates of young candidates found in the *long-period stars* sample would be that these long period sources correspond to WTTS with periodic photospheric variations produced by atmospheric spots, that we have detected as long term variability. The entire subsample of *long-period* flaring sources present pre-main sequence disposition in the color-magnitude diagram. T Tauri stars present higher magnetic activity, and show larger X-ray fluxes than main-sequence stars (Getman et al. 2008b; Preibisch et al. 2005; Preibisch 2007), causing a potential higher presence of flaring activity (Gahm 1990; Guenther and Emerson 1997; Guenther and Ball 1998; Barrado y Navascués and Martín 2003). Thus we conclude that the subsample of ∼41% *long-period stars* presenting flaring activity are potential young weak-lined T Tauri stars with the

majority of their disk already dissipated, consistent with the age of the cluster, and thus good 25-Ori member candidates.

Similar to the *long-period* sample, we consider that the *intermediate-period stars* of our catalog that show flaring events and have a PMS disposition in the color-magnitude diagram are WTTS, and we consider them good 25-Ori member candidates.

Using the GCVS morphological description and periodic sampling, we observed that some of the light curves in the *long-period* and *intermediate-period* categories presented features compatible with pulsating sources. These stars present a quite distinct morphology (Percy 2011), with periodic fast rises in magnitude followed by slower decreases (see Fig. 5.19). Depending on whether this period is larger or smaller than one day, they are identified as Cepheids or RR Lyraes, respectively. These are usually massive, evolved stars; we used the location on the color-color and color-magnitude diagrams of these sources to identify them, as well as the light curve morphology. With this methodology, we identified two Cepheids and 21 RR Lyrae candidates.

Finally, all of the 30 sources classified as *short-period stars*, with periods lower than 0.1 days, fall into the instability regime region in the color-color diagram. They present a disposition in the color-magnitude diagram compatible with evolved stars. All these indicators suggest that this group is formed, too, by an homogeneous sample of pulsating stars (Percy 2011).

5.5.2.3 CTTS

We selected 31 sources as CTTS with the light curve morphological analysis.

Color-magnitude/color-color diagrams distribution - As expected of the young evolutionary state of these objects, all of them present PMS positions in the color-magnitude diagram (except one, 2-4707), and they all present low-mass disposition in the color-color diagram. The derived spectral types for the young ones range between K5 to M9 types.

Infrared excess - As expected, most of the sources classified as CTTS show mid-infrared excess consistent with the presence of a protoplanetary disk. In particular, sources 1-970, 8-10259, 8-11085, 9-3485, 9-6886 and 11-8549 present dips in flux between WISE [12] and [22] consistent with the possibility of a transitional disk (Strom et al. 1989b; Calvet et al. 2002). The rest show large excesses indicating Class II YSOs (Williams and Cieza 2011). It is also interesting to point out that two of the CTTS classified sources (1-955 and 6-1391) only present infrared detections,

no excesses, and five (1-4056, 2-4707, 4-8623, 9-3150 and 9-11604) present no infrared excess whatsoever.

Flaring activity - Ten sources present flaring activity, with one source with the highest number of flares in the catalog (9-11604, nine flares in total), and another with one of the largest (8-4545, 1.5 mags rise in flux).

X-ray counterparts - Four sources have counterparts within the *XMM-Newton* X-ray observation: 2-556, 8-10259, 8-10691 and 8-11085. These sources present some of the highest infrared excess in their SEDs, pointing towards their Class II YSO nature (Williams and Cieza 2011), and consistent with the fact that these young disk-bearing objects exhibit a higher X-ray flux than more evolved stars (Feigelson and Montmerle 1999; Flaccomio et al. 2012).

The previous analysis suggests that all the sources in the entire sample of CTTS are strong 25-Ori young member candidates. The exception is source 2-4707, which does not show colors corresponding to a pre-main sequence object, and has no near or mid infrared detection. Thus, its CTTS nature is doubtful, even though it presents clear stochastic optical variability in the light curve, similar to the other CTTS in this category.

5.5.2.4 Flares

Several sources in our catalog showed flaring activity in addition to other kind of variability, and thus were included in one or another section. But we also found 144 stable sources which showed flares, and thus included them in this separate category.

Color-magnitude/color-color diagrams distribution - most of them (123 out of 144) present PMS colors in the color-magnitude diagram. This is consistent with the fact that these sources are most likely active young stars members of the 25-Ori association. The majority of these PMS flaring sources are M0 to M9 sources, except three of them: 2-3647 (K8), 8-2118 (K8) and 9-10080 (K9). All of them are clustered in the low-mass region in the color-color diagram, except one, 0-4745.

Infrared excess - four flaring stars (2-3647, 2-5865, 4-5538 and 8-2809) have infrared excess consistent with the presence of a circumstellar disk, and 19 more present infrared detections.

Flaring activity - all the sources in this sample present flaring activity, ranging from 0.02 to 3.0 magnitudes in flux variation. From this last type, 22 have flux variations larger than 1.0 magnitude, five (1-4545, 2-1560, 2-3192, 7-759 and 10-9696) larger than 2.0 magnitudes and one (2-4089) of 3.0 magnitudes. It is interesting to note the inverse relation in number of flares and the change in magnitude; the larger

the magnitude of the flares present in the light curve, the fewer of them there are, as shown in Fig. 5.20.

X-ray counterparts -11 sources (8-8317, 8-8345, 8-8647, 8-9494, 9-9938, 8-10068, 8-10485, 8-10672, 8-10837, 8-11082 and 8-11580) had counterparts with the X-ray sample.

Young stellar objects exhibit magnetic fields several orders of magnitude stronger that those in main sequence stars (Preibisch et al. 1993; Guenther and Emerson 1997). This, in turn, causes a higher rate of flaring (Gahm 1990; Guenther and Ball 1998; Getman et al. 2008a). These flares, mostly detected in the X-ray regime (Guenther and Emerson 1997) can also be related with optical events (Guenther and Ball 1998). The large number of flaring sources in our sample with a PMS disposition in the color-magnitude diagram is, therefore, not surprising, given that flaring is a common occurrence in young stars. This activity decays with age (Gahm 1990), and as such it can be use as a clear signpost of youth.

It is important to differentiate between WTTS and CTTS flare activity. Flares found in the former objects would mostly be related to magnetic activity of the young star, whether the ones found in the latter objects can be also related to accretion events from the surrounding disk onto the host star (Guenther and Ball 1998). From our analysis we cannot differentiate between these; spectral identification should be carried out. Nevertheless we can use the presence of an infrared excess as a first approximation. Thus, we established the following categorization in this sample: flaring sources with PMS colors, M spectral types and without infrared excess consistent with disk-bearing object are classified as WTTS candidates; sources fulfilling the same conditions, but with infrared excesses, are classified as CTTS candidates. With these criteria at hand, we classified 117 sources as potential WTTS, three (2-5865, 4-5538 and 8-2809) as potential CTTS, and 24 as undetermined flaring sources.

5.5.2.5 Long and short-term variable sources

Finally, sources showing any kind of variability and not included in any previous category were classified as variables. This sample is comprised of 251 sources, eleven of which have short term variability, on scales of hours, and the rest long term variations with scales of days. In this last category, some periods were found during the Plavchan periodogram analysis, but with periods larger than the maximum timebase of 3.5 days. Thus, even though in some cases the periods looked stable, we discarded them and treated these sources as just variables.

Color-magnitude/color-color diagrams distribution - 201 of the 251 sources of the long term variable sample have PMS colors, compared to nine out of eleven on the short term one. The derived spectral types range from K3 to M9 sources, and all of them are clustered on the low-mass region on the color-color diagram.

Infrared excess - two sources in the short term variable sub-sample (7-4494 and 9-4358) have infrared excess consistent with disk presence, while eleven of the long term variables (2-225, 2-361, 2-9365, 4-10830, 5-6464, 5-6536, 7-5290, 7-7728, 7-8419, 8-9156 and 9-6035) do too. Fig. 5.16 shows how in the case of sources 4-10830 and 7-8419 this excess is high enough to reclassify them as Class II CTTS.

Flaring activity - more than ∼40% (97 sources) of the long term variables present flaring activity, and ∼37% (4 sources) on the short term sample also do. Only two sources of the long term sample have flux increases higher than 1.0 magnitude (0-8819 and 4-2514).

X-ray counterparts - 21 long term variable sources have counterparts with the X-ray *XMM-Newton* observation. None of the short term variables do. It is interesting to note that all of the X-ray counterparts, except one (8-10439), have PMS colors.

With these results at hand, we can now deduce that this sample behaves similarly to the *long-period* and *intermediate-period* ones. The presence of the high rate of PMS stars, flares, X-ray counterparts and late M's and K's indicates that these sources are most likely potential active young WTTS, with some potential CTTS as well, and thus strong 25-Ori member candidates.

Specifically, we find that 95 out of the 240 long term variables have PMS colors and flaring activity, and as such label them as 25-Ori member candidates. From this sample, four sources (2-225, 2-9365, 4-10830 and 8-9156) present protoplanetary disks, and thus are most likely CTTS, and the rest are most likely WTTS, in particular ten sources with X-ray counterparts (7-7339, 7-7353, 7-7580, 7-8307, 8-8634, 8-8783, 8-9701, 8-9949, 8-10295 and 8-11414).

5.6 Discussion

5.6.1 Transiting exoplanet host candidates

From our sample of 15 transiting exoplanet host candidates, we were able to derive orbital periods for 10 of them. There were not enough eclipses on the light curves of sources 5-3045, 6-3001 and 8-3311 to derive an orbital period; and for sources 8-9088 and 9-2156, albeit having enough eclipses, we were not able to derive

an orbital period. Nevertheless, given the depth of the eclipses, we maintain them as candidates, even though the lack of a consistent period could potentially rule them out.

In some cases the periods are equal or very similar to the ones found for the stellar variation, as can be seen in Table 5.2. Figure 5.8 shows the distribution of planetary radii versus the orbital period, with data from Table 5.1. We also include the planetary parameters derived for 8-8695 in van Eyken et al. (2011), for reference.

The sample of 12 exoplanet candidates is clustered in the top left region of the diagram, that is, large radii with low orbits. This region is the only one we are sensitive to, so any potential candidates found would be located in here. Two different explanations can account for this behavior.

In the first case, the fact that these sources present radii similar to Jupiter does not automatically identify them as exoplanets. Brown dwarfs have Jupiter-size radii (Basri and Brown 2006). If this were the case, these systems could be binary stars, with one component being a low-mass star and the other a brown dwarf. They would have been formed simultaneously from the same parental cloud. There is a lack of brown dwarf companions at small orbital radii (the so-called 'brown dwarf desert' (Kraus et al. 2008; Kraus et al. 2011; Evans et al. 2012; Cheetham et al. 2015)), which suggests it is unusual to find brown dwarfs this close to the host star. But this absence of close brown dwarfs is is seen in evolved systems. The youth of the association could account for their presence.

On the other hand, if we assume they are actually exoplanets, their position and radii suggest a migration event in the timescale of disk dissipation (Lin and Papaloizou 1986; Ward 1997; Ward and Hahn 2000). None of the sources present infrared excess, so we assume an absence of disk. The large radii observed could be caused by the inflation of the atmosphere due to high and close stellar irradiation, given their close-in orbits. In particular, three sources have X-ray detections in the *XMM-Newton* observation: 8-8695, 8-9088 and 8-9555. In these cases, the planet could be in the process of evaporating due to high-energetic irradiation. Interestingly, these three sources are also spatially adjacent, close to 25-Ori, and good candidate members of the association. Their youth could also be the reason of a potentially inflated atmosphere.

Be it as it may, our observations limit the range of potential exoplanets to identify. With our period cut-off at 3.5 days, we would only be capable of detecting close-in companions. Also, the sensitivity of our data constrains our detections in favor of giant planets. Further follow-up data is needed to assess the nature of these

candidates and discard that they may be blended field binaries or star spots.

5.6.2 25-Ori members

After analyzing the complete set of sources in the *PTF Orion variable catalog*, we are now in a position to establish some quantitative values regarding overall membership status with respect to the 25-Ori association.

From the total sample of 858 variable sources, 350 show flaring activity in their light curves, and 288 (∼34%) have infrared detections, 57 (∼7%) of which are strong enough to indicate the presence of a protoplanetary disk (the percentages refer to the total sample of 858 variable stars).

Out of our 531 sources classified as PMS candidates, and thus, with photometrically derived spectral types, 398 (∼75%) have late spectral type of M0 to M9, while 133 (∼25%) have spectral types K0 to K9.

As indicated in Sec. 5.3.3.6, we assumed sources with pre-main sequence distribution in the color-magnitude diagrams to be the most likely to be members of the 25-Ori association. Thus, we use this sample of 531 stars as our baseline of member candidates. Out of this young sub-sample, we select the sources with flaring activity *or* infrared detections as potential 25-Ori member candidates. This yielded a sub-group of potential 25-Ori candidate members of 310 sources.

We then selected sources from the PMS sub-sample with *both* flares and infrared detections, constituting a sub-sample of 134 sources. This sample comprised the sources with the highest likelihood of membership of the 25-Ori association. 34 of them have estimated K0 to K9 spectral types and 100 have estimated M0 to M9 spectral types. Based on our final physical classification, there are: four planet candidates, two Algol detached binaries, 17 CTTS, 93 WTTS, two sources with spot modulation, one flaring unclassified source, six intermediate-period unclassified sources, three long-period unclassified sources, and seven long term variable unclassified sources. This sample of 134 sources yields a ratio of ∼16% 25-Ori member candidates over the complete variable catalog.

The reliability of these results is supported by the fact that the sources with a higher likelihood of being part of the young 25-Ori association appear to be clustered around 25-Ori, as can be seen in Fig. 5.21. In this figure we represent the spatial distribution of sources showing any youth tracer, that is: presence of flares, infrared excess or PMS colors. We also show the distribution of the complete *PTF Orion variable catalog* based on the degree of membership. We note that not only sources

presenting any of the youth tracers mentioned above appear to be clustered over the young association, but also that the higher the degree of membership (that is, the higher number of youth tracers found in a source), the more clustered the sources are. This result adds consistency to our conclusion.

5.6.3 Physical interpretation - T Tauri stars

With the information from the infrared excesses, spectral types, flare activity and PMS colors, we identified several sources as WTTS or CTTS candidates based on the following criteria:

1) The clearest signpost of CTTS is the presence of a primordial disk. Thus, if a source was found to show infrared excess consistent with this feature, it was labeled as a CTTS candidate (CTTS* in Tables 5.4 to 5.13). The exception to this condition would be the classification of the source in another physical category (for example, an eclipsing binary). Fig. 5.16 shows the SEDs of all the sources that fulfill this condition. We also include in this category of CTTS the ones identified as such by the optical variability in their light curves.

2) WTTS are young low-mass sources, with no clear signs of a disk and with an active photosphere. Thus, sources with PMS colors and one of the active photosphere tracer (infrared detections, flare activity or counterparts in the Franciosini et al. (2011) X-ray sample) were labeled as WTTS candidates (WTTS* in Tables 5.4 to 5.13). If the source had PMS colors and two or more of the youth tracers, it was identified as a strong WTTS candidate (WTTS in Tables 5.4 to 5.13). Note that sources fulfilling the previous criteria would be selected as potential 25-Ori member candidates as well.

Thus, we identified 64 sources as potential disk bearing objects; six detached Algol-type binaries, four contact W Ursa-type binaries and 54 potential CTTS stars. This yields a $\sim$8% presence of protoplanetary disks in our sample of variable stars. On the other hand, from the sample of 531 PMS candidates, we found 376 potential WTTS. This means a total of 430 T Tauri stars identified in our sample of variable stars, which yields a $\sim$50% occurrence.

It is important to note that we have included in this analysis the X-ray detections as a tracer of T Tauri identification. We did not include it in the 25-Ori analysis, due to the spatial distribution bias explained in Sec. 5.3.3.4. This is why the percentages of sources classified as T-Tauris and the ones as potential 25-Ori member candidates differ.

5.6.4 Validation with previous works

We acquired a sample of 264 (Briceño et al. 2005; Briceño et al. 2007), 328 (Hernández et al. 2006; Hernández et al. 2007), 506 (McGehee 2006) and 90 (Downes et al. 2014; Downes et al. 2015) sources observed in the region, 115 of which had counterparts with our *PTF Orion variable catalog*, all of them classified as PMS stars by our color-magnitude analysis. From these 115, 65 present infrared excess *or* flare activity, making them potential 25-Ori candidates by our analysis, and 34 present infrared excess *and* flare activity, making them strong 25-Ori candidates. The remaining 16 sources are a mix of long-term variables and long/intermediate-period sources; seven of them classified as Class III diskless sources in Hernández et al. (2007), and one CTTS and three WTTS in McGehee (2006).

Table 5.14 shows the comparison of our analysis with the 115 matches with previous works carried out in the region, as explained in Sec. 5.3.4. We present, for each source, the PTF Orion identification, initial light curve morphological type, estimated spectral type (when available), physical interpretations after the previous analysis, and comparison with previous works: identification, spectral type, T Tauri type and membership flag from Briceño et al. (2007); identificator and disk type from Hernández et al. (2007); identifier and disk type from McGehee (2006); and identificator and spectral type from Downes et al. (2014).

We compared our estimated spectral types with those of Briceño et al. (2007) and Downes et al. (2014), acquired spectroscopically, for 46 of our sources with counterparts in those catalogs. Only seven of our sources (7-8338, 8-6444, 8-6538, 8-9133, 8-10691, 9-9777 and 10-9685) had a difference of spectral type larger than two sub spectral types, but never larger than five, when compared with the ones in those works. This implies an $\sim$85% concordance between our photometric approximation and the spectroscopic derivation for the sub sample of counterparts. Thus, we are confident with the precision of our derived spectral types. Nevertheless, spectroscopic analysis confirmation would be needed to validate them completely.

Four exoplanet candidates have counterparts with previous works. Three of them (6-3938, 8-8695, and 8-9088) are identified as WTTS in those works, and our youth analysis supports it. Because of this, they are flagged as good 25-Ori association member candidates, but we maintain their transiting exoplanet candidate classification.

Finally, eleven CTTS of the catalog have counterparts with previous works. Six were classified as CTTS in those works. On the other hand, for our 90 classified WTTS with counterparts in previous works, 80 were also identified in the previous

works. This yields a ∼55% and ∼89% match between our results and theirs, respectively. Source 8-10259, identified in this work as a potential transitional disk, is also classified as such in Hernández et al. (2007). This adds credence to our youth tracers membership and physical interpretation method. Nevertheless, spectral analysis is still needed to validate the results presented here.

5.7 Conclusions

We found a sample of 15 potential transiting exoplanet host candidates. Assuming dwarf radii for the stellar hosts, we calculated the potential radii of these exoplanets, based on the depth of the transits. 12 of them show some tracer of youth, making them potential 25 Ori-members. If the planetary nature of these systems, via radial velocity measurements, and the association membership, were to be confirmed, it would make this sample the perfect benchmark for young exoplanet studies. Thus, we mark them as suitable candidates for follow-up.

After the complete analysis of the PTF Orion observations, we have produced a catalog of 858 variable stars from the Palomar Transient Factory Orion project. Based on our final physical interpretation, the catalog is comprised of:

- 10 transiting exoplanet host candidates with derived orbital periods
- 5 transiting exoplanet host candidates without derived orbital periods
- 86 detached Algol-type binaries
- 11 close β Lyrae-type binaries
- 82 W Uma-type contact binaries
- 55 potential classical T Tauri stars
- 376 potential weak-lined T Tauri stars
- 2 potential Cepheid pulsating stars
- 21 potential RR Lyrae pulsating stars
- 30 short period pulsating stars
- 180 undetermined variables (showing flares, long- and intermediate-period, or long- or short- term variability)

From this catalog, 310 sources present potential 25-Ori membership, and 134 sources present strong 25-Ori membership. ∼50% of the variable sources present T-Tauri signs, validated with the results from previous works carried out in the region.

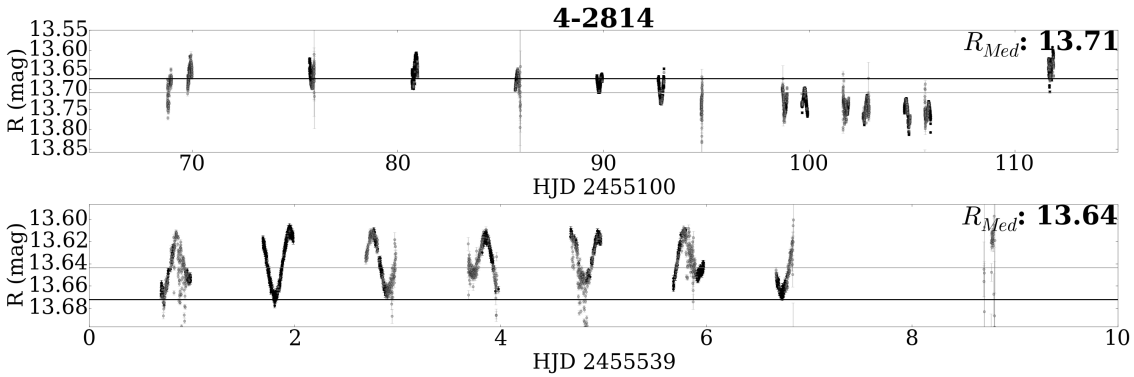

Figure 5.1: Fogging effect example. Top and bottom figures correspond to the 2009 and 2010 light curves, respectively, for the same source. It can be clearly seen how the fogging effect causes a systematic diminishing of the flux in the 2009 photometry, that is corrected the last day, when the instrument was cleaned. The 2010 data shows no such effect.

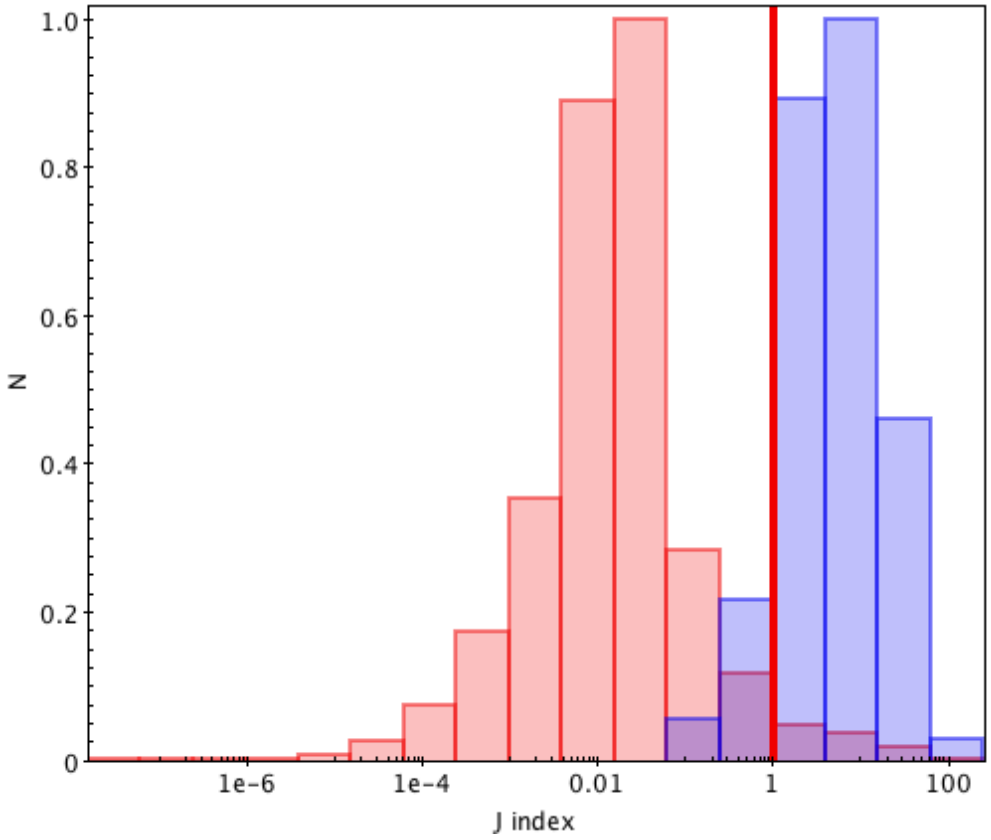

Figure 5.2: Normalized histogram with the different distributions of Stetson index for the total PTF Orion sample (red bars) and sources classified as binaries or CTTS in the van Eyken et al. (2011) catalog (blue bars), that is, known variable stars. The vertical red line indicates the threshold we used as limit for variability detection. Any source with a J index larger than this value is identified as variable. This threshold is derived from the distribution of the variable sources in van Eyken et al. (2011).

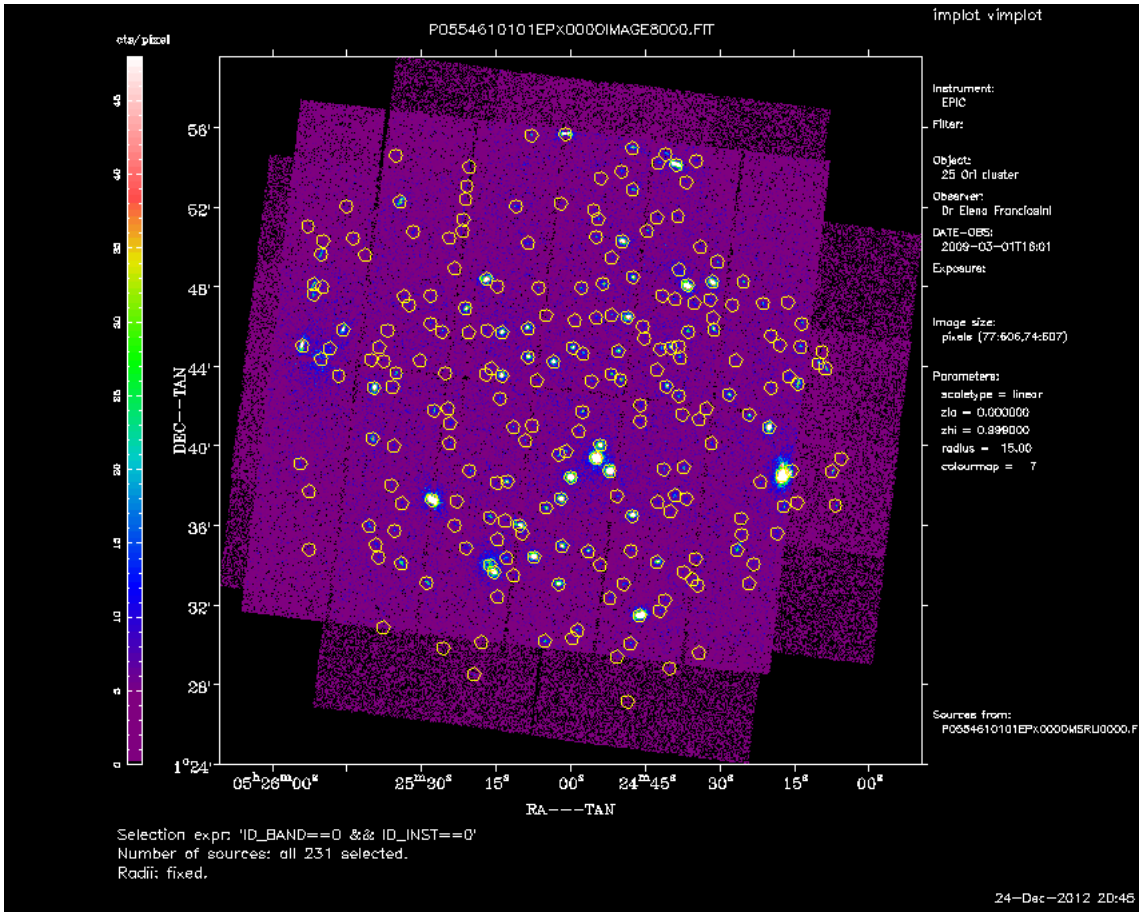

Figure 5.3: X-ray observation from Franciosini et al. (2011), pointing out the detections on the field of view.

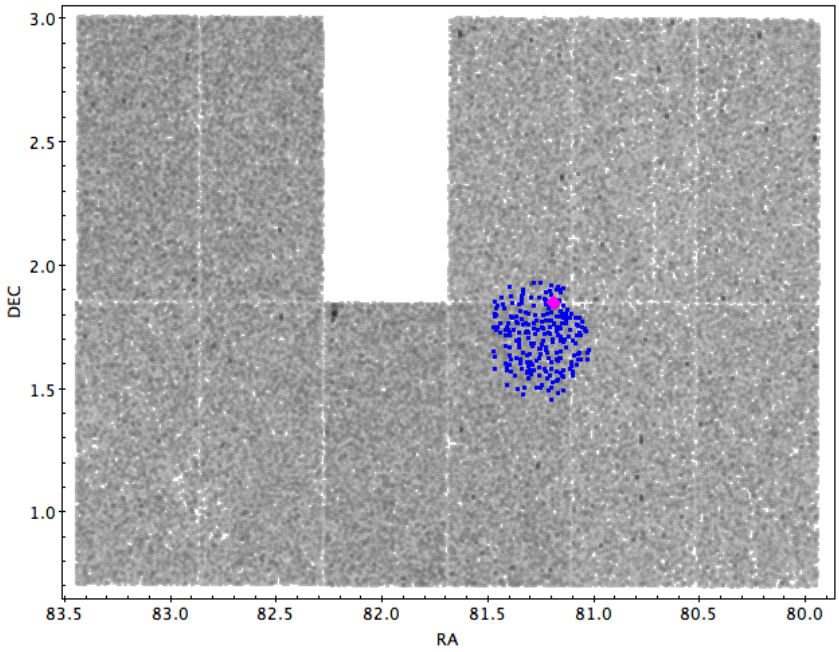

Figure 5.4: This figure shows the PTF Orion field of view with all the observed stars in grey, the 11 CCD chips, and in blue the positions of the X-ray detections from the *XMM-Newton* observations. The pink diamond represents the position of 25-Ori.

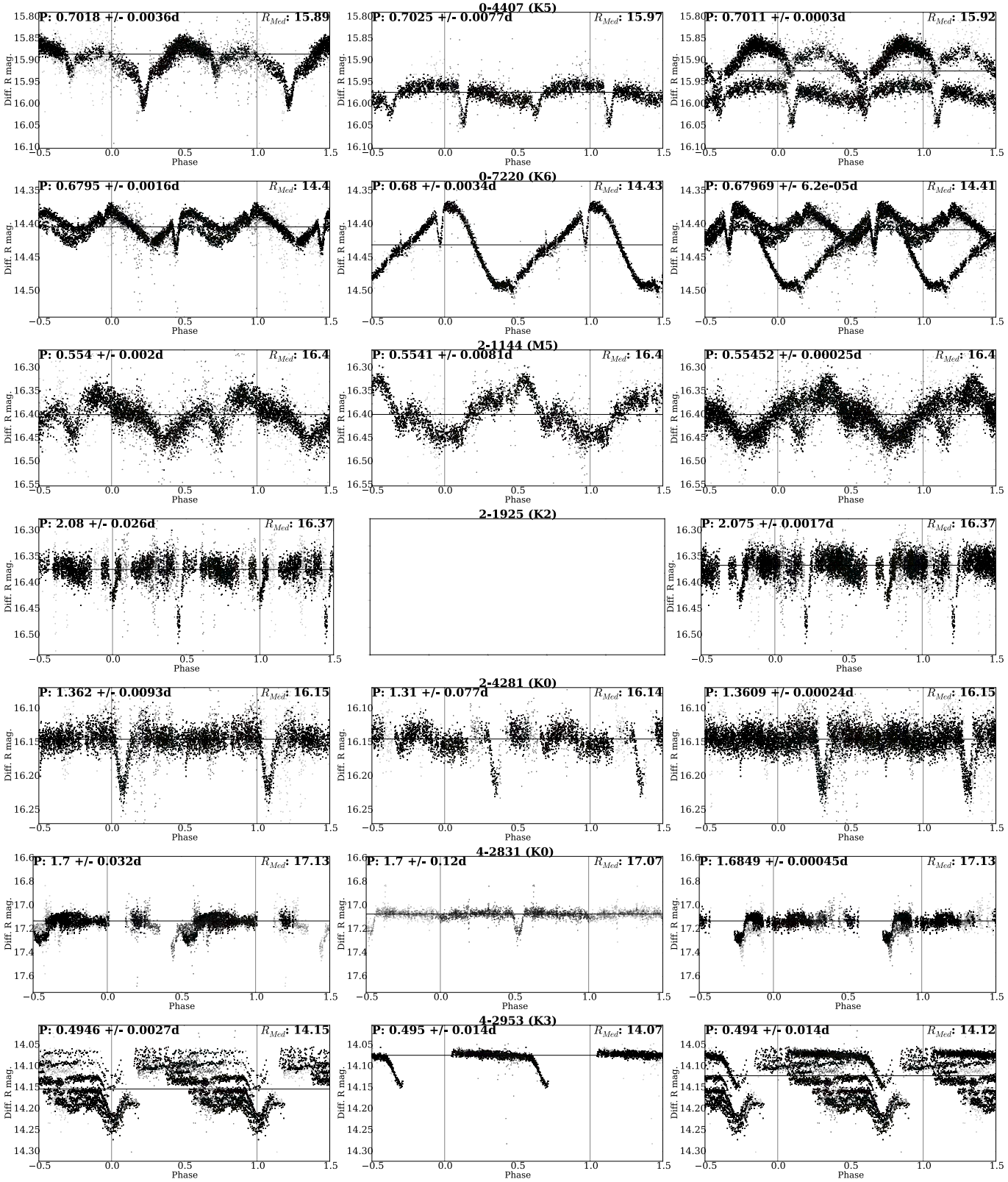

Figure 5.5: Folded light curves of sources classified as planet candidates. For each source we show the 2009 folded lightcurve (left), the 2010 one (center) and the one with both sets of data (right). Whenever a period was not found for one set of data, no plot was included. The different colors represent each day of observation in both runs. The PTF Orion id, spectral type derived, the period and the median R magnitude for each year is indicated. Error bars have been omitted for clarity.

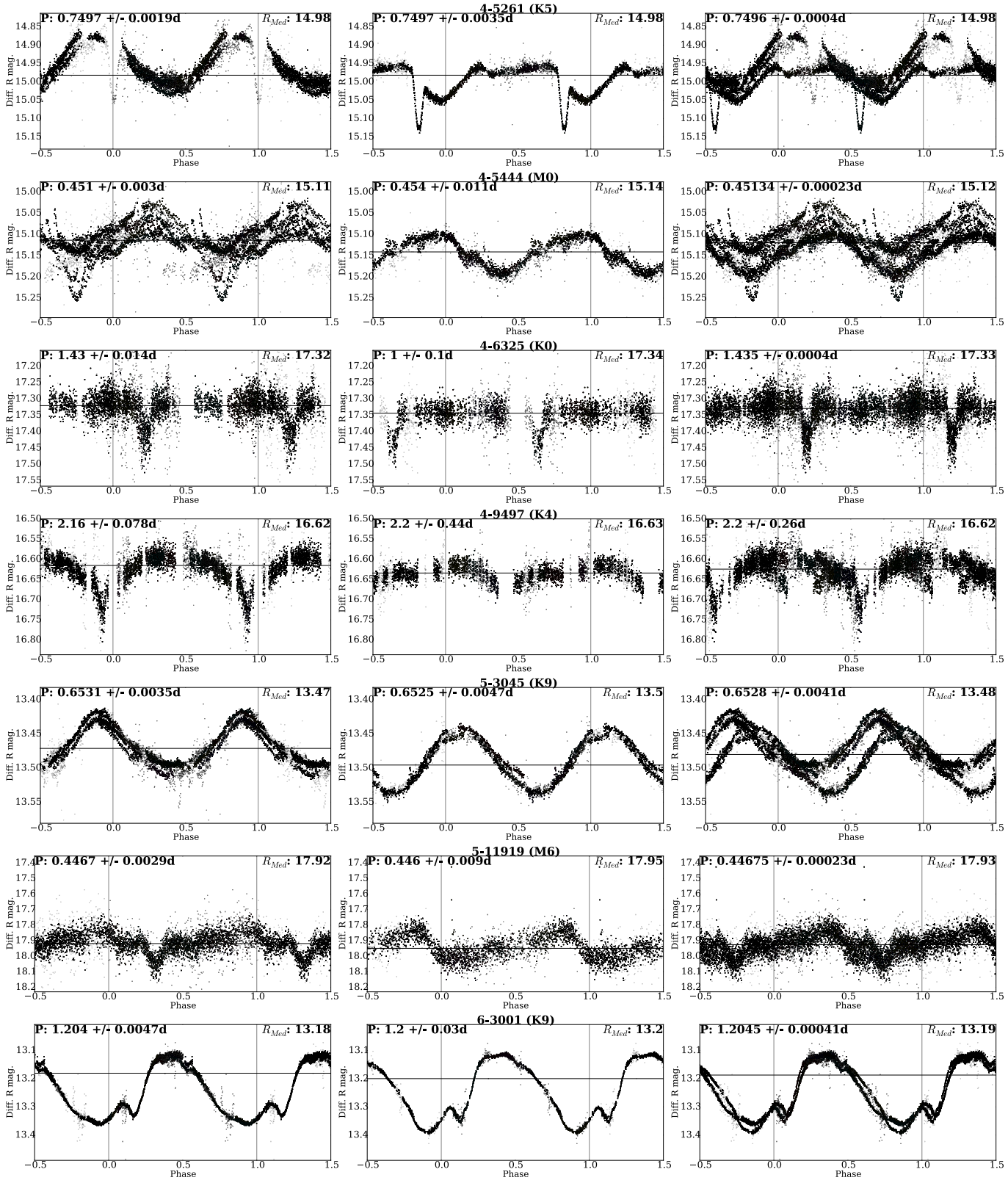
4-5261 (K5)
P: 0.7497 +/- 0.0019d
R_{Med}: 14.98
P: 0.7497 +/- 0.0035d
R_{Med}: 14.98
P: 0.7496 +/- 0.0004d
R_{Med}: 14.98
4-5444 (M0)
P: 0.451 +/- 0.003d
R_{Med}: 15.11
P: 0.454 +/- 0.011d
R_{Med}: 15.14
P: 0.45134 +/- 0.00023d
R_{Med}: 15.12
4-6325 (K0)
P: 1.43 +/- 0.014d
R_{Med}: 17.32
P: 1 +/- 0.1d
R_{Med}: 17.34
P: 1.435 +/- 0.0004d
R_{Med}: 17.33
4-9497 (K4)
P: 2.16 +/- 0.078d
R_{Med}: 16.62
P: 2.2 +/- 0.44d
R_{Med}: 16.63
P: 2.2 +/- 0.26d
R_{Med}: 16.62
5-3045 (K9)
P: 0.6531 +/- 0.0035d
R_{Med}: 13.47
P: 0.6525 +/- 0.0047d
R_{Med}: 13.5
P: 0.6528 +/- 0.0041d
R_{Med}: 13.48
5-11919 (M6)
P: 0.4467 +/- 0.0029d
R_{Med}: 17.92
P: 0.446 +/- 0.009d
R_{Med}: 17.95
P: 0.44675 +/- 0.00023d
R_{Med}: 17.93
6-3001 (K9)
P: 1.204 +/- 0.0047d
R_{Med}: 13.18
P: 1.2 +/- 0.03d
R_{Med}: 13.2
P: 1.2045 +/- 0.00041d
R_{Med}: 13.19
Diff. R mag.
Phase

(Fig. 5.5 cont.)

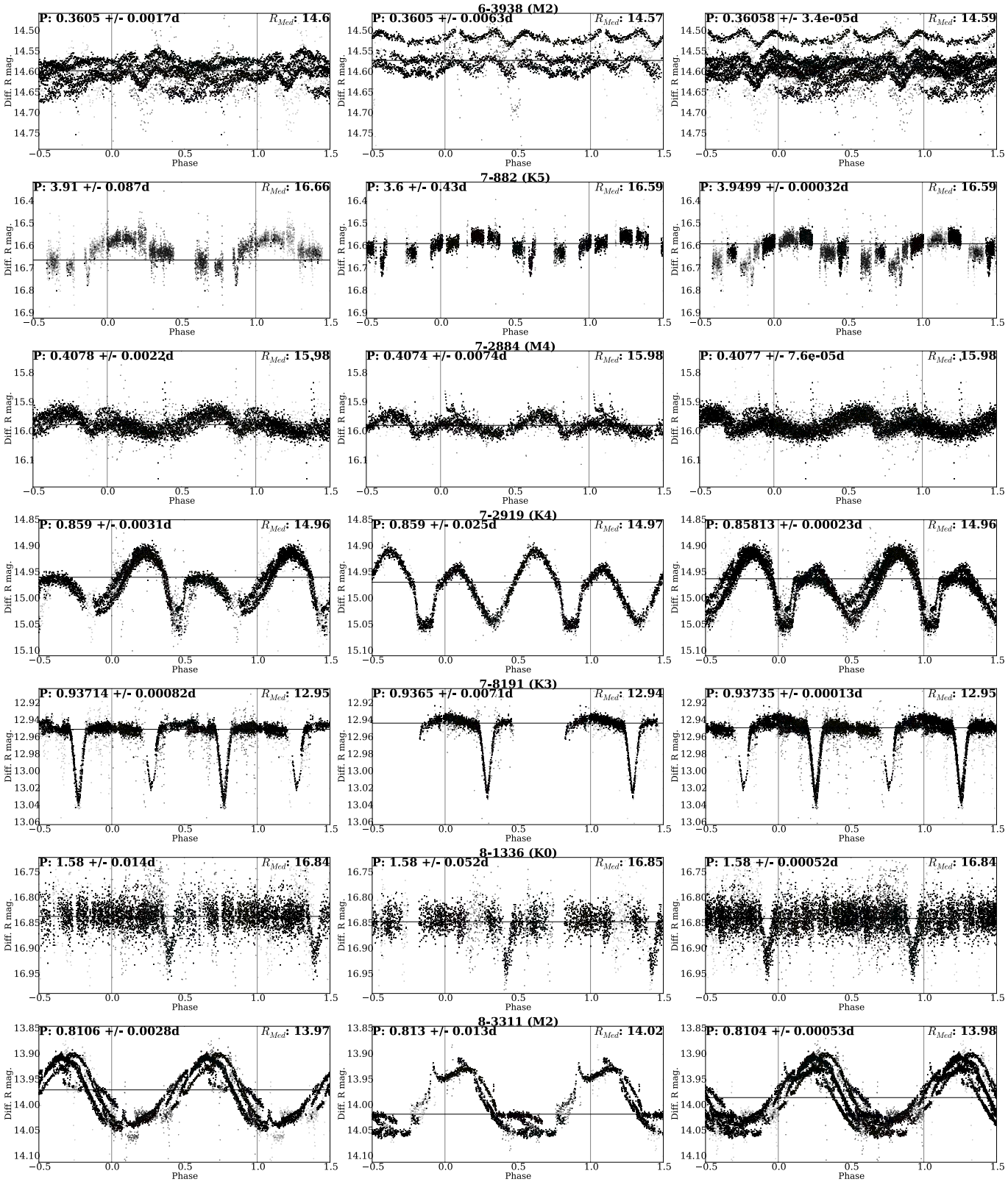
6-3938 (M2)
P: 0.3605 +/- 0.0017d
R_{Med}: 14.6
P: 0.3605 +/- 0.0063d
R_{Med}: 14.57
P: 0.36058 +/- 3.4e-05d
R_{Med}: 14.59
7-882 (K5)
P: 3.91 +/- 0.087d
R_{Med}: 16.66
P: 3.6 +/- 0.43d
R_{Med}: 16.59
P: 3.9499 +/- 0.00032d
R_{Med}: 16.59
7-2884 (M4)
P: 0.4078 +/- 0.0022d
R_{Med}: 15.98
P: 0.4074 +/- 0.0074d
R_{Med}: 15.98
P: 0.4077 +/- 7.6e-05d
R_{Med}: 15.98
7-2919 (K4)
P: 0.859 +/- 0.0031d
R_{Med}: 14.96
P: 0.859 +/- 0.025d
R_{Med}: 14.97
P: 0.85813 +/- 0.00023d
R_{Med}: 14.96
7-8191 (K3)
P: 0.93714 +/- 0.00082d
R_{Med}: 12.95
P: 0.9365 +/- 0.0071d
R_{Med}: 12.94
P: 0.93735 +/- 0.00013d
R_{Med}: 12.95
8-1336 (K0)
P: 1.58 +/- 0.014d
R_{Med}: 16.84
P: 1.58 +/- 0.052d
R_{Med}: 16.85
P: 1.58 +/- 0.00052d
R_{Med}: 16.84
8-3311 (M2)
P: 0.8106 +/- 0.0028d
R_{Med}: 13.97
P: 0.813 +/- 0.013d
R_{Med}: 14.02
P: 0.8104 +/- 0.00053d
R_{Med}: 13.98
Diff. R mag.
Phase

(Fig. 5.5 cont.)

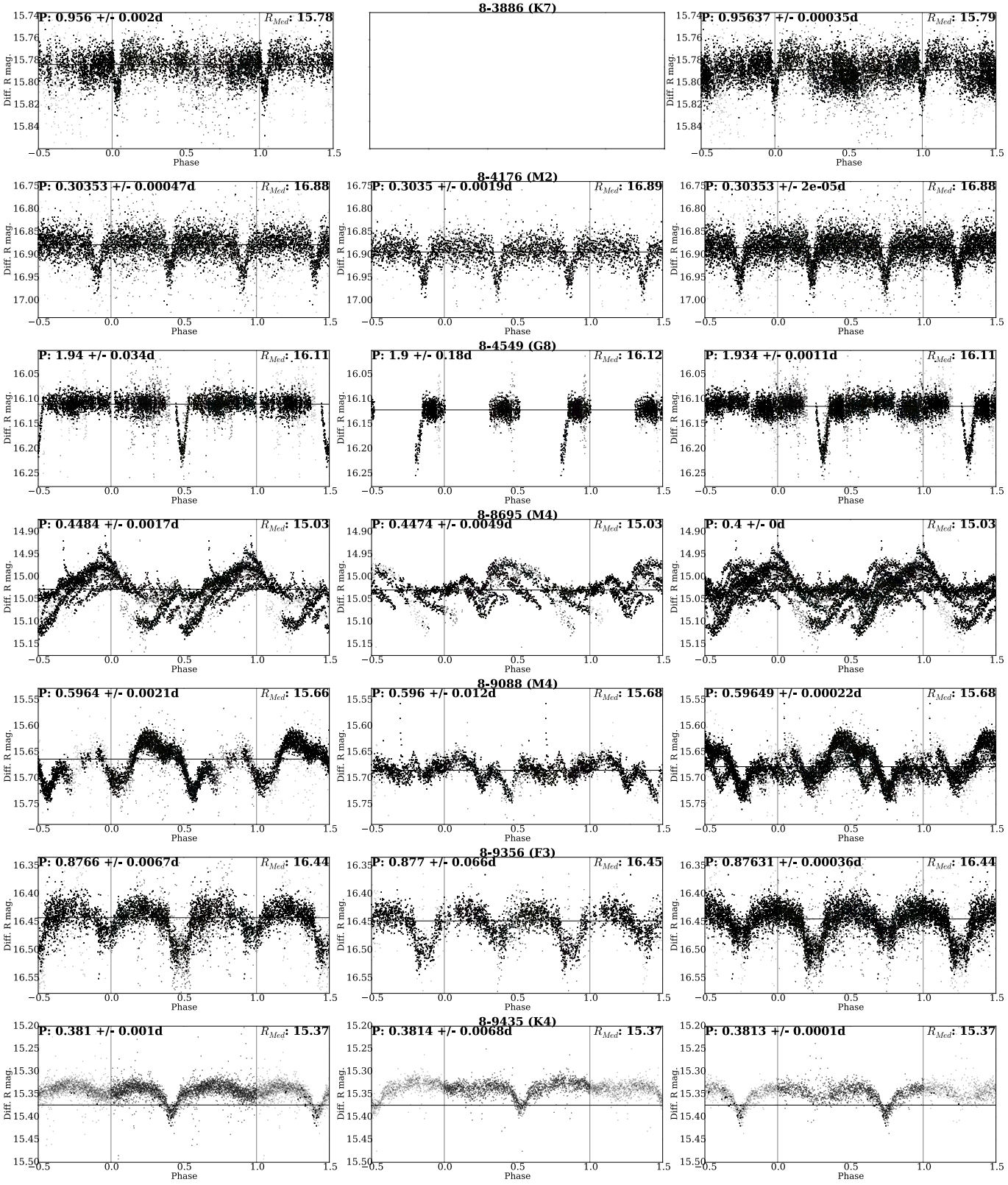
8-3886 (K7)
P: 0.956 +/- 0.002d
R_{Med}: 15.78
P: 0.95637 +/- 0.00035d
R_{Med}: 15.79
8-4176 (M2)
P: 0.30353 +/- 0.00047d
R_{Med}: 16.88
P: 0.3035 +/- 0.0019d
R_{Med}: 16.89
P: 0.30353 +/- 2e-05d
R_{Med}: 16.88
8-4549 (G8)
P: 1.94 +/- 0.034d
R_{Med}: 16.11
P: 1.9 +/- 0.18d
R_{Med}: 16.12
P: 1.934 +/- 0.0011d
R_{Med}: 16.11
8-8695 (M4)
P: 0.4484 +/- 0.0017d
R_{Med}: 15.03
P: 0.4474 +/- 0.0049d
R_{Med}: 15.03
P: 0.4 +/- 0d
R_{Med}: 15.03
8-9088 (M4)
P: 0.5964 +/- 0.0021d
R_{Med}: 15.66
P: 0.596 +/- 0.012d
R_{Med}: 15.68
P: 0.59649 +/- 0.00022d
R_{Med}: 15.68
8-9356 (F3)
P: 0.8766 +/- 0.0067d
R_{Med}: 16.44
P: 0.877 +/- 0.066d
R_{Med}: 16.45
P: 0.87631 +/- 0.00036d
R_{Med}: 16.44
8-9435 (K4)
P: 0.381 +/- 0.001d
R_{Med}: 15.37
P: 0.3814 +/- 0.0068d
R_{Med}: 15.37
P: 0.3813 +/- 0.0001d
R_{Med}: 15.37
Diff. R mag.
Phase

(Fig. 5.5 cont.)

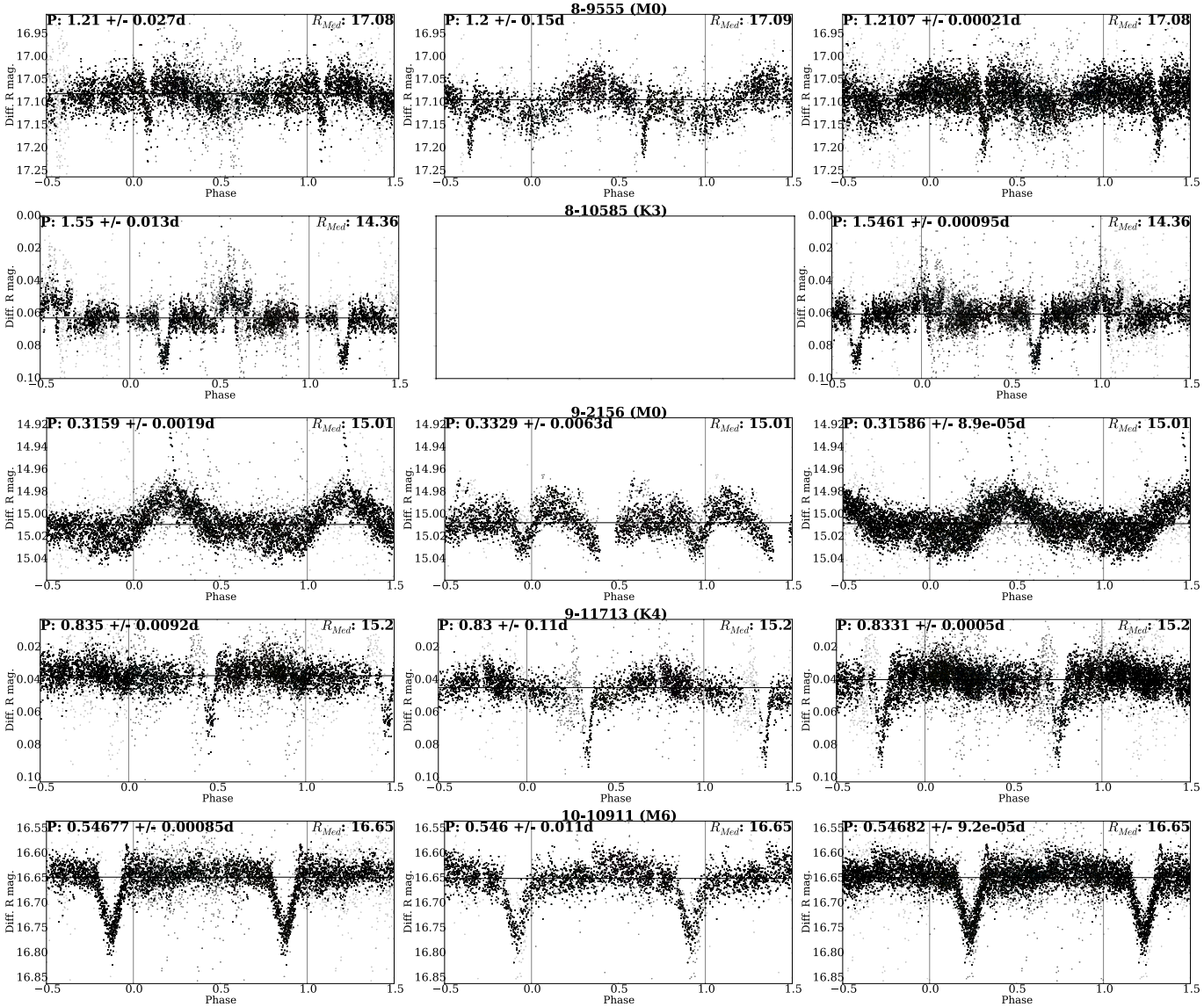
8-9555 (M0)
P: 1.21 +/- 0.027d
R_{Med}: 17.08
P: 1.2 +/- 0.15d
R_{Med}: 17.09
P: 1.2107 +/- 0.00021d
R_{Med}: 17.08
8-10585 (K3)
P: 1.55 +/- 0.013d
R_{Med}: 14.36
P: 1.5461 +/- 0.00095d
R_{Med}: 14.36
9-2156 (M0)
P: 0.3159 +/- 0.0019d
R_{Med}: 15.01
P: 0.3329 +/- 0.0063d
R_{Med}: 15.01
P: 0.31586 +/- 8.9e-05d
R_{Med}: 15.01
9-11713 (K4)
P: 0.835 +/- 0.0092d
R_{Med}: 15.2
P: 0.83 +/- 0.11d
R_{Med}: 15.2
P: 0.8331 +/- 0.0005d
R_{Med}: 15.2
10-10911 (M6)
P: 0.54677 +/- 0.00085d
R_{Med}: 16.65
P: 0.546 +/- 0.011d
R_{Med}: 16.65
P: 0.54682 +/- 9.2e-05d
R_{Med}: 16.65
Diff. R mag.
Phase

(Fig. 5.5 cont.)

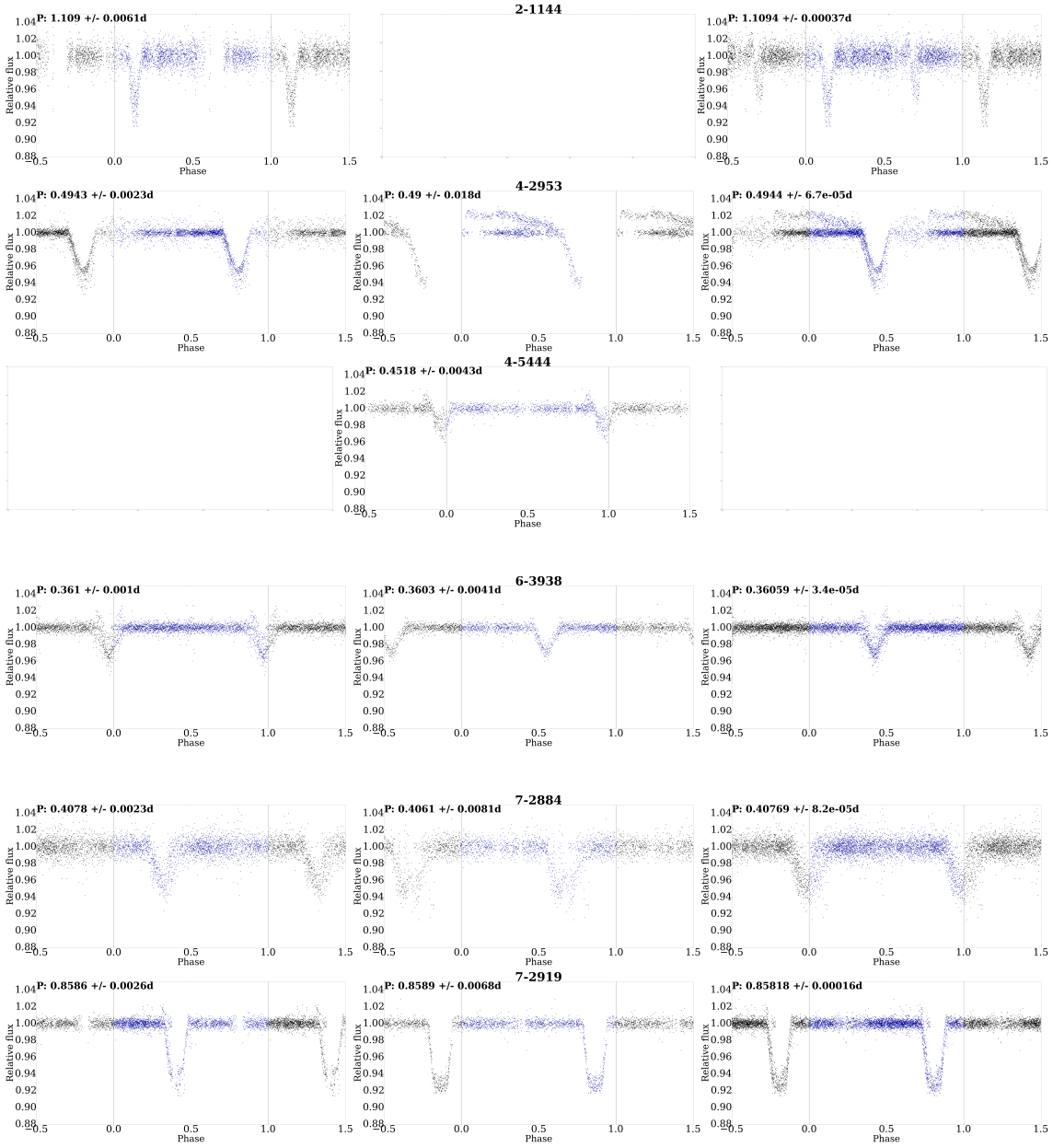

Figure 5.6: Folded light curves of the potential planetary candidates, with out-of-transit flux normalized to unity. Stellar variability has been removed with a Savitzky-Golay filter. Three light curves are shown for each source, corresponding to the 2009, 2010 and combined epochs. The depth of the eclipses is calculated by subtracting the minimum value to the mean in each epoch. The final value of the depth used to compute the planet radius is the median of the depths of 2009 and 2010. Sources 5-3045, 6-3001 and 8-3311 only presented one unique eclipse in the light-curve, so we do not include their whitened light curves in this figure. Additionally, for sources 8-9088 and 9-2156 no clear period was found, even with several eclipses in the light curves, so we omit them too in this figure.

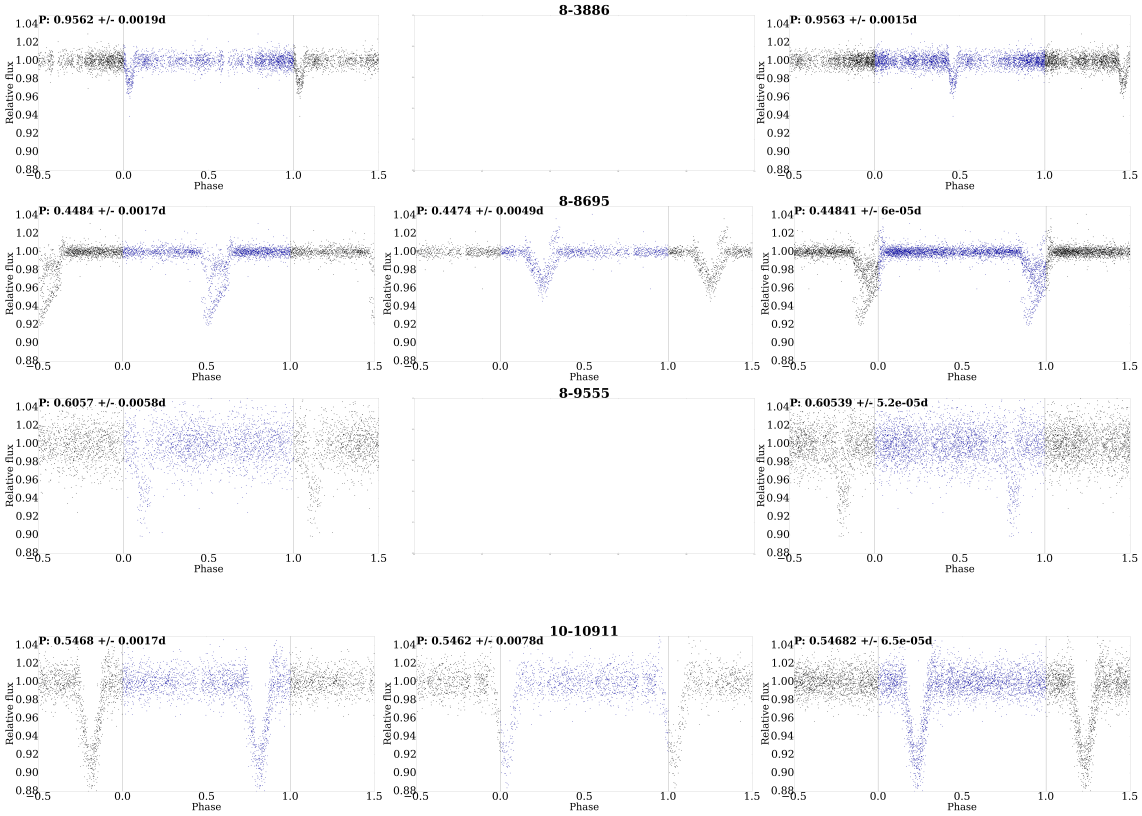
8-3886
P: 0.9562 +/- 0.0019d
P: 0.9563 +/- 0.0015d
8-8695
P: 0.4484 +/- 0.0017d
P: 0.4474 +/- 0.0049d
P: 0.44841 +/- 6e-05d
8-9555
P: 0.6057 +/- 0.0058d
P: 0.60539 +/- 5.2e-05d
10-10911
P: 0.5468 +/- 0.0017d
P: 0.5462 +/- 0.0078d
P: 0.54682 +/- 6.5e-05d
Relative flux
Phase

(Fig. 5.6 cont.)

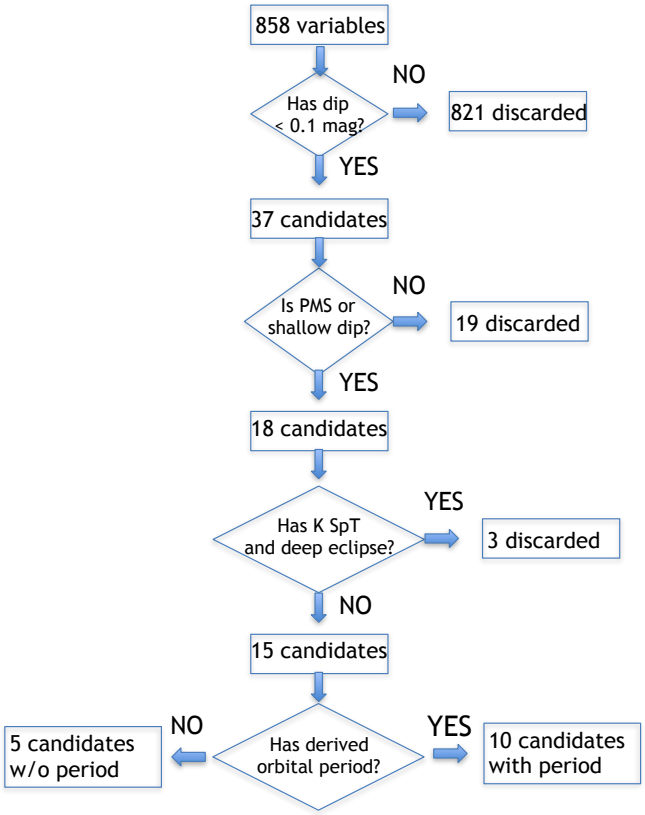

Figure 5.7: Workflow diagram used for the selection criteria of the transiting exoplanet host candidates.

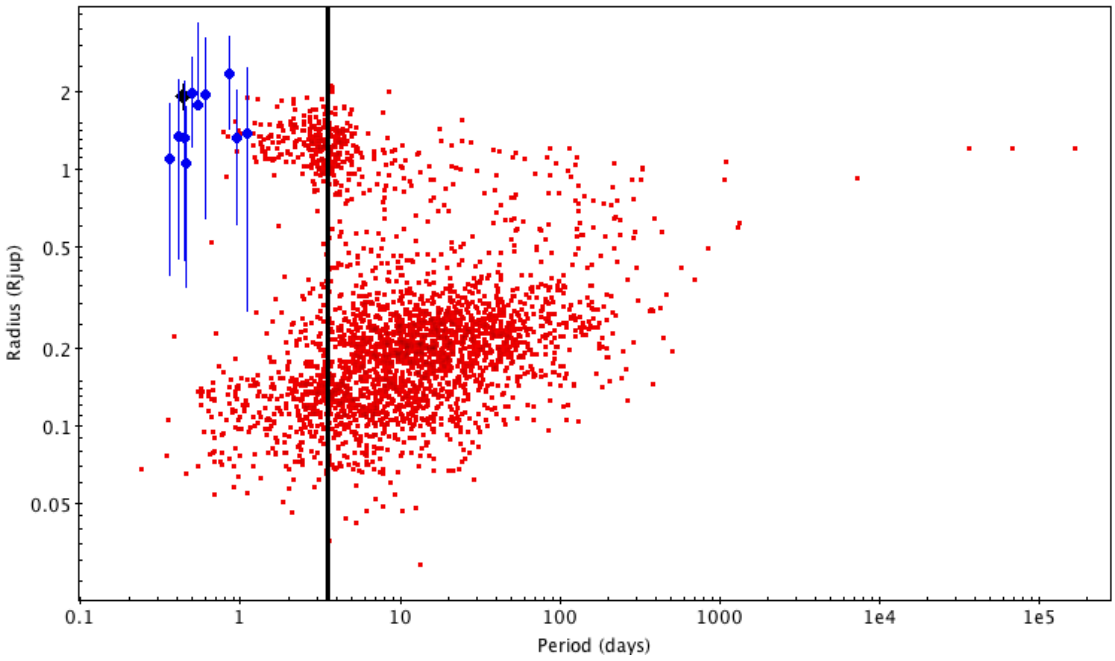

Figure 5.8: Orbital period vs planet radius diagram of the 12 transiting exoplanet candidates with valid periods. Blue dots (with error bars) correspond to our sample, while red dots correspond to confirmed exoplanets from the NASA Exoplanet Archive. The black line indicates our maximum period cut-off. The black dot shows the position of 8-8695 with van Eyken et al. (2012) data.

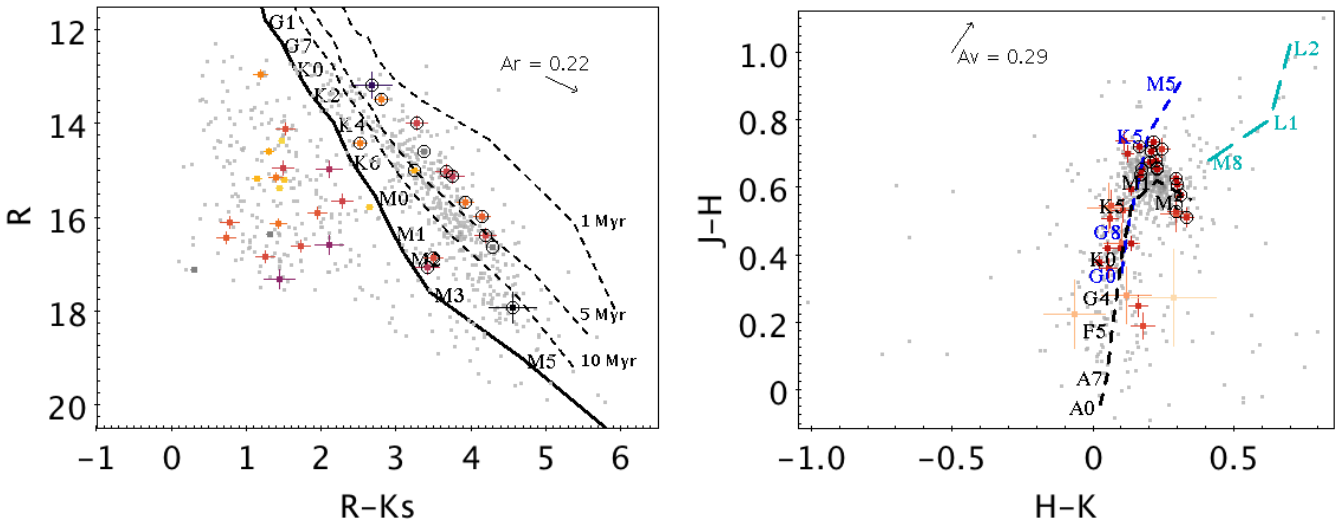

5.9.a: Color-magnitude diagram.

5.9.b: Color-color diagram.

Figure 5.9: (a) 2MASS J-H vs H-K color-color diagram and (b) $R - K_S$ color-magnitude diagram for the transiting exoplanet host candidates identified. Grey dots mark the positions of the entire *PTFO variable catalog*, red dots show the position for the candidates. Intensity of the colors marks the degree of uncertainty of the JHK_S values in (a) and of R in (b): the larger the uncertainty, the fainter the source. The main sequence is shown by a straight line in (a), with the spectral types positions indicated, as well as the isochrones for 1, 5 and 10 Myrs, all of them obtained from the models of Siess et al. (2000), as well as the redenning vector for $A_R = 0.22$ is indicated as well. Black, blue and green dashed lines in (b) indicate the main sequence, giant branch, and the L-dwarf regime regions, respectively, with the locus of some spectral types, as reference, and the assume redenning of $A_V = 0.29$ is also indicated.

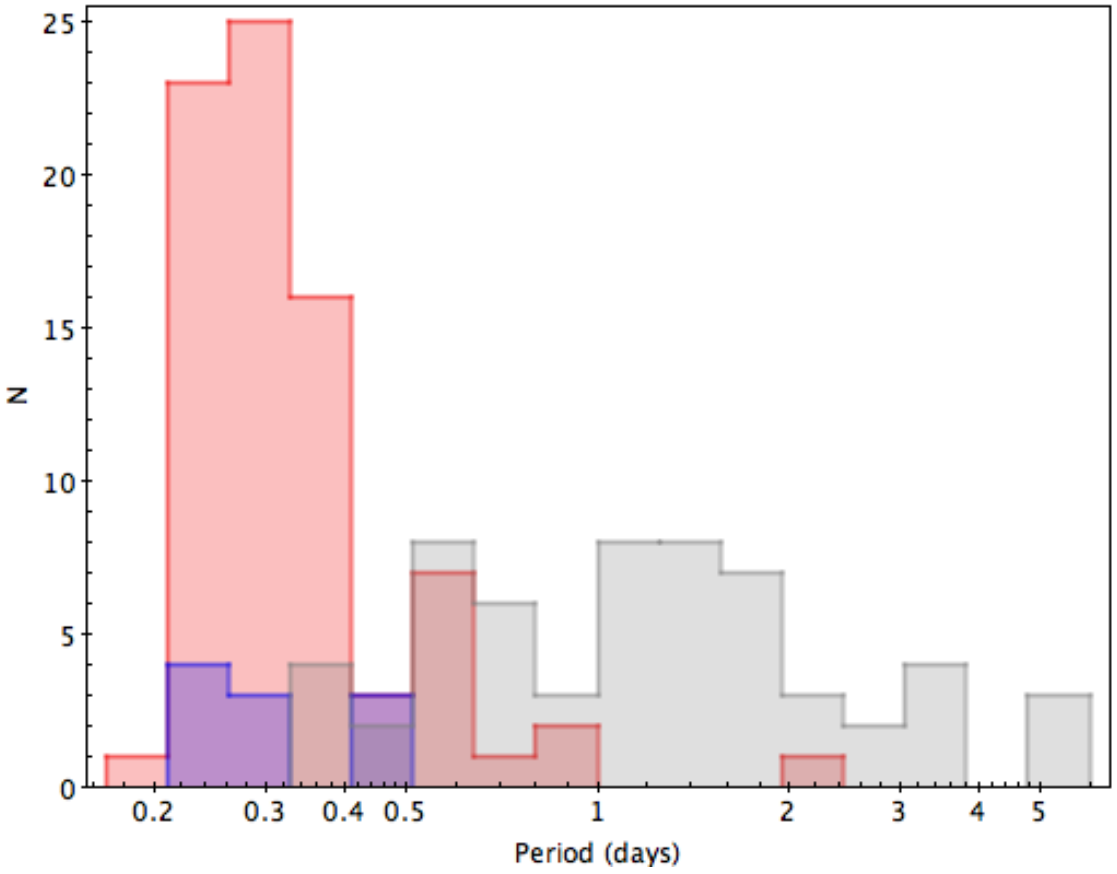

Figure 5.10: Distribution of periods for the sources in the *Eclipsing binaries* category. Red, blue and gray correspond to contact, close and detached eclipsing binaries, respectively.

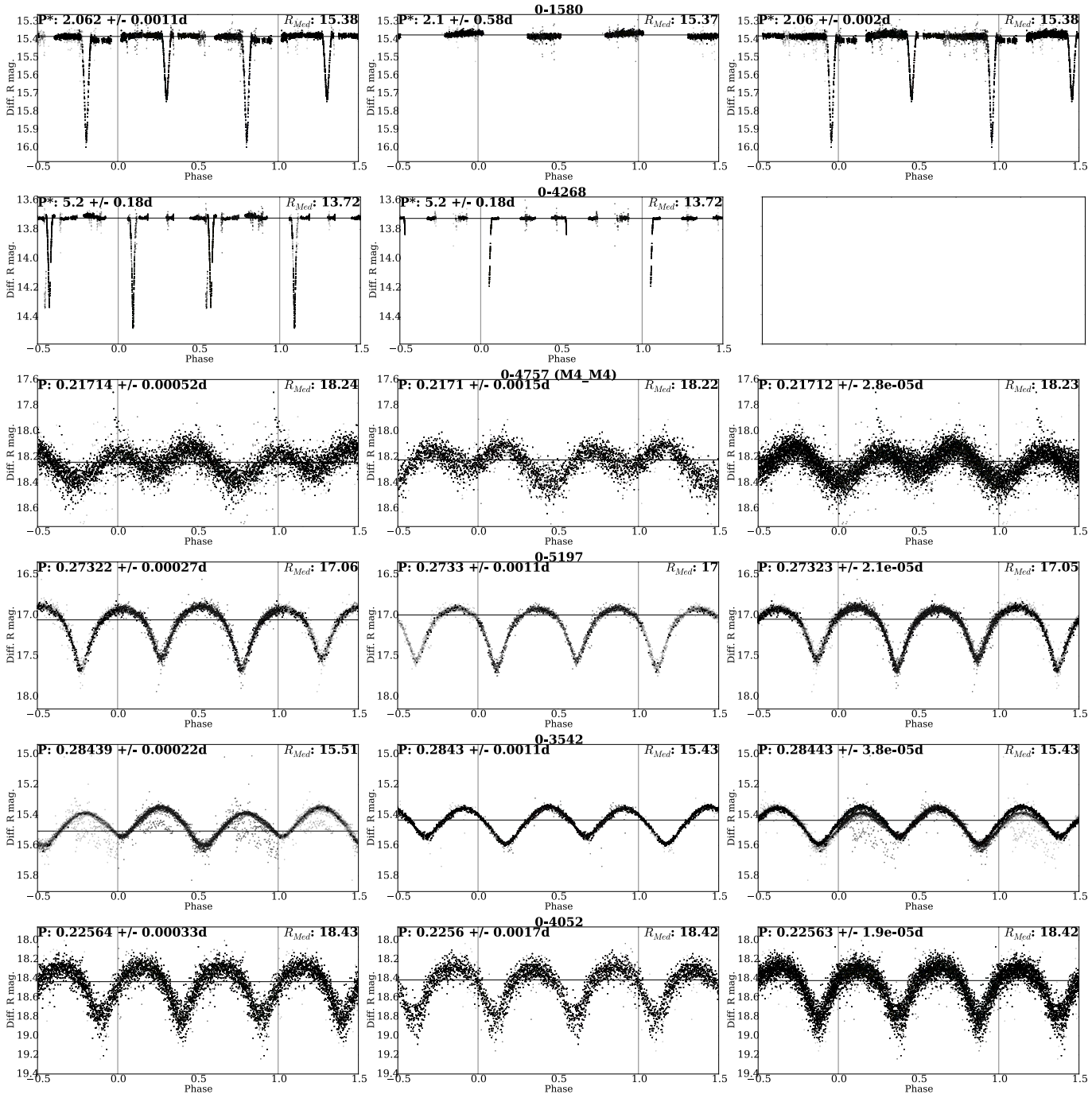

Figure 5.11: Folded light curves of detached (top two rows), close (mid two rows) and contact (bottom two rows) binaries. The different colors represent different days of observation in both runs. The PTF Orion id, spectral types derived for the PMS sources, the period and the median R magnitude for each year is indicated. Error bars have been omitted for clarity. Left, middle and right plots correspond to 2009, 2010 and combined data, respectively.

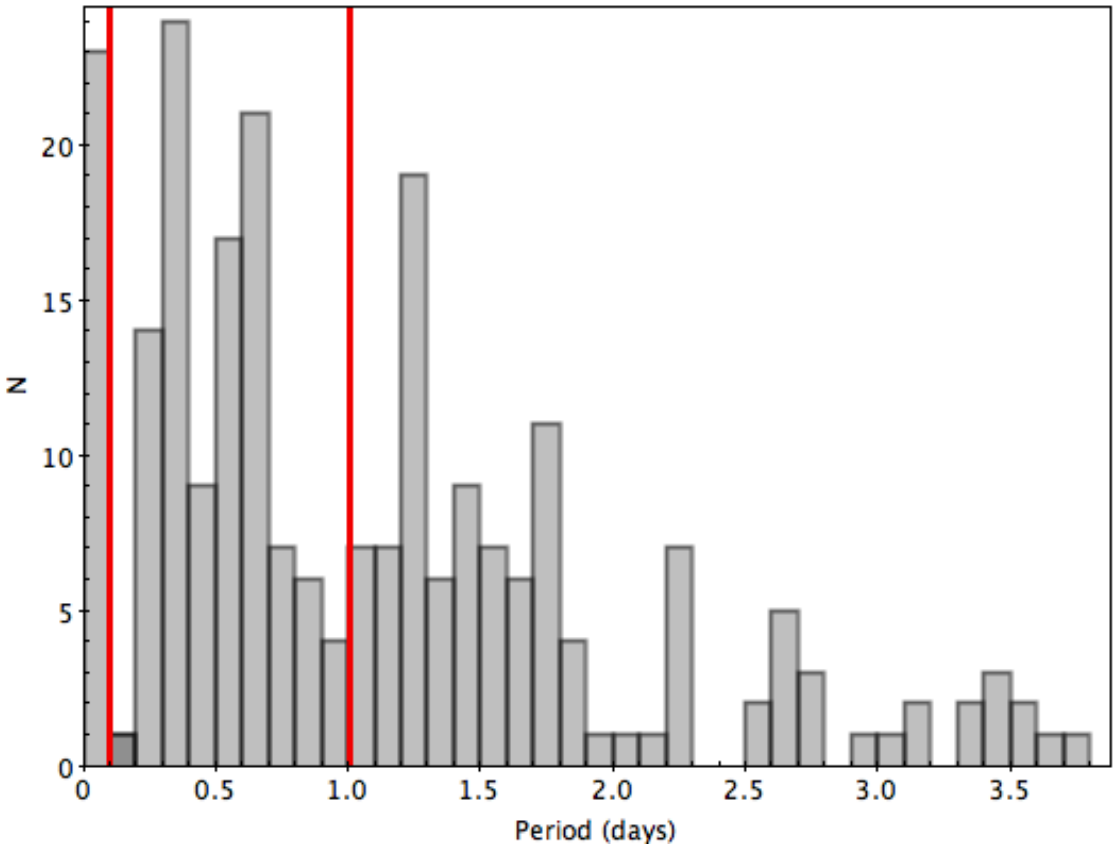

Figure 5.12: Distribution of periods for the sources in the *Periodic stars* category. Red vertical lines separate the three regions we identify in this category, using 0.1 and 1.0 days as thresholds.

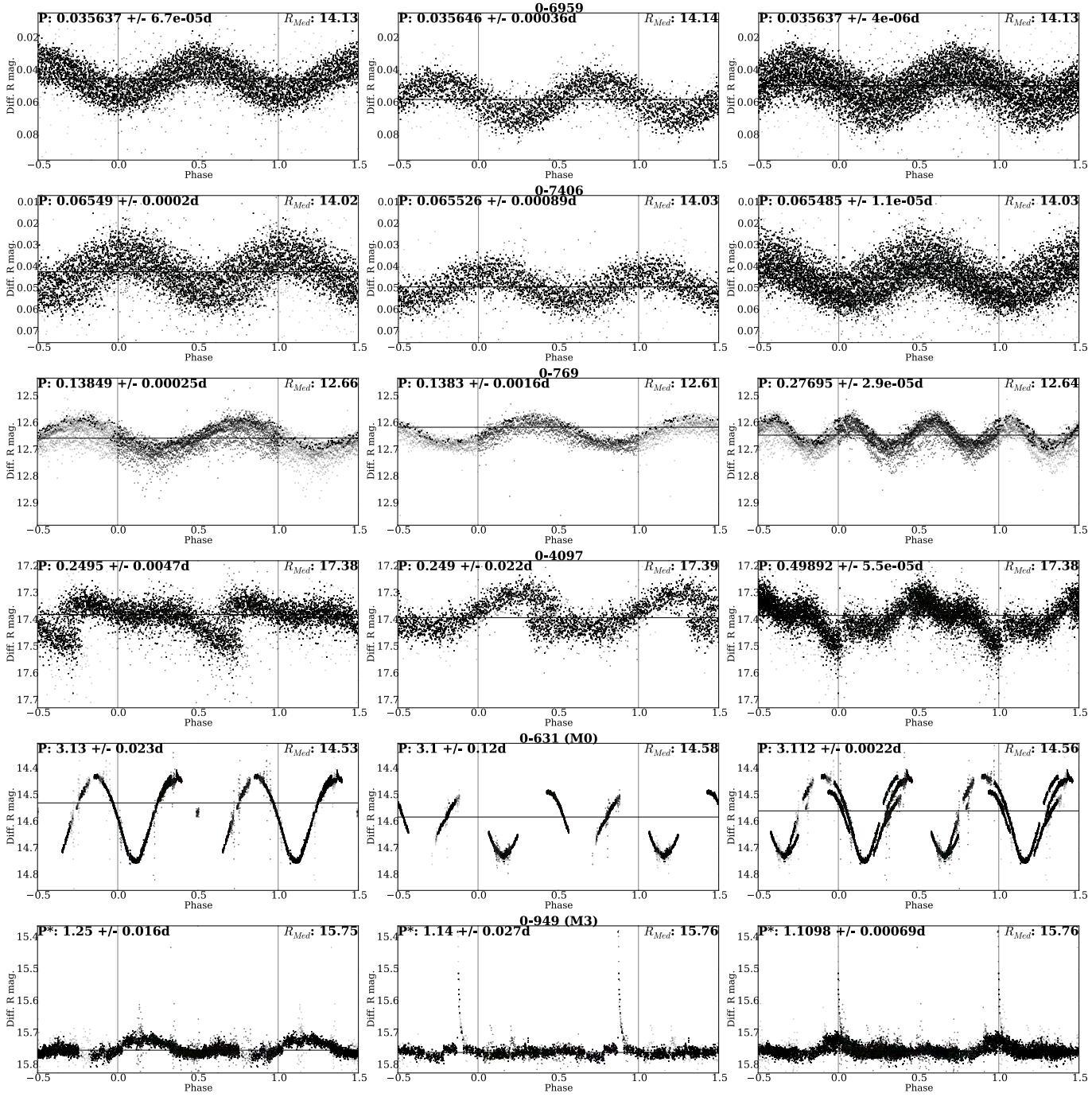

Figure 5.13: Folded light curves of short- (top two rows), intermediate- (mid two rows) and long- (bottom two rows) period sources. The different colors represent different days of observation in both runs. The PTF Orion id, spectral type derived for the PMS sources, the period and the median R magnitude for each year is indicated. Error bars have been omitted for clarity. Left, middle and right plots correspond to 2009, 2010 and combined data, respectively.

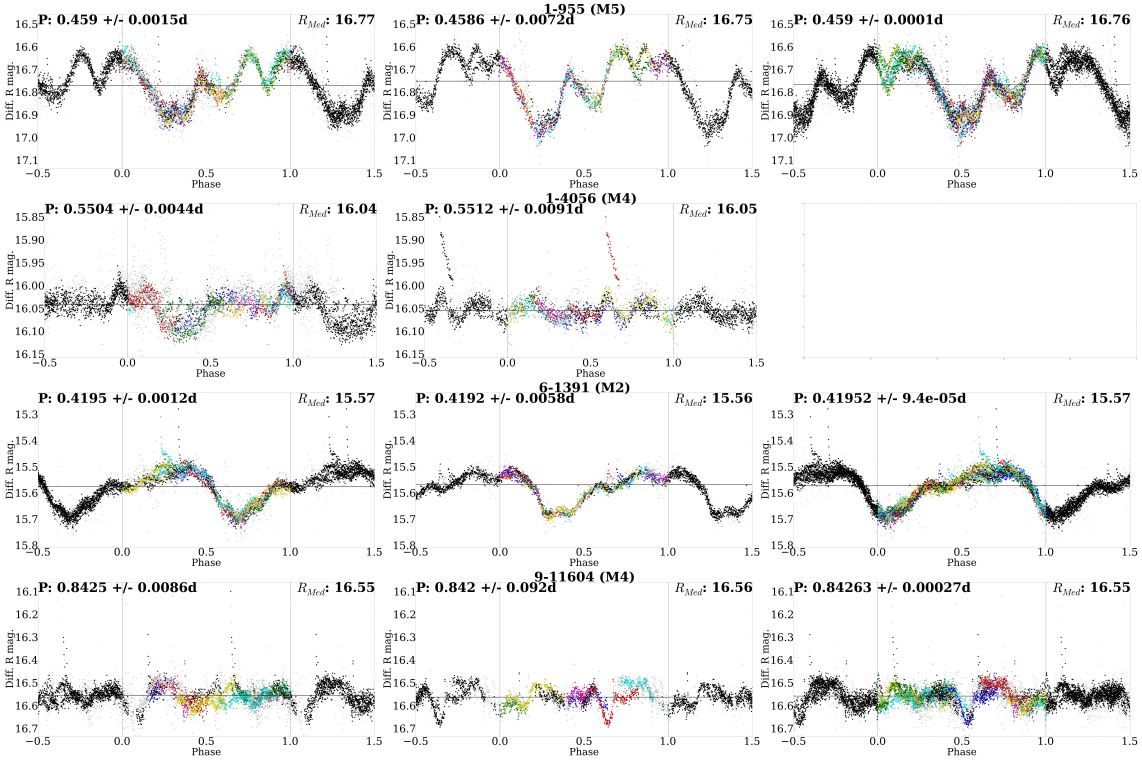

Figure 5.14: Folded light curves of CTTS with periods found with the Plavchan algorithm. The different colors represent each day of observation in both runs. The PTF Orion id, spectral type derived for the PMS sources, the period and the median R magnitude for each year is indicated. Error bars have been omitted for clarity. Left, middle and right plots correspond to 2009, 2010 and combined data, respectively.

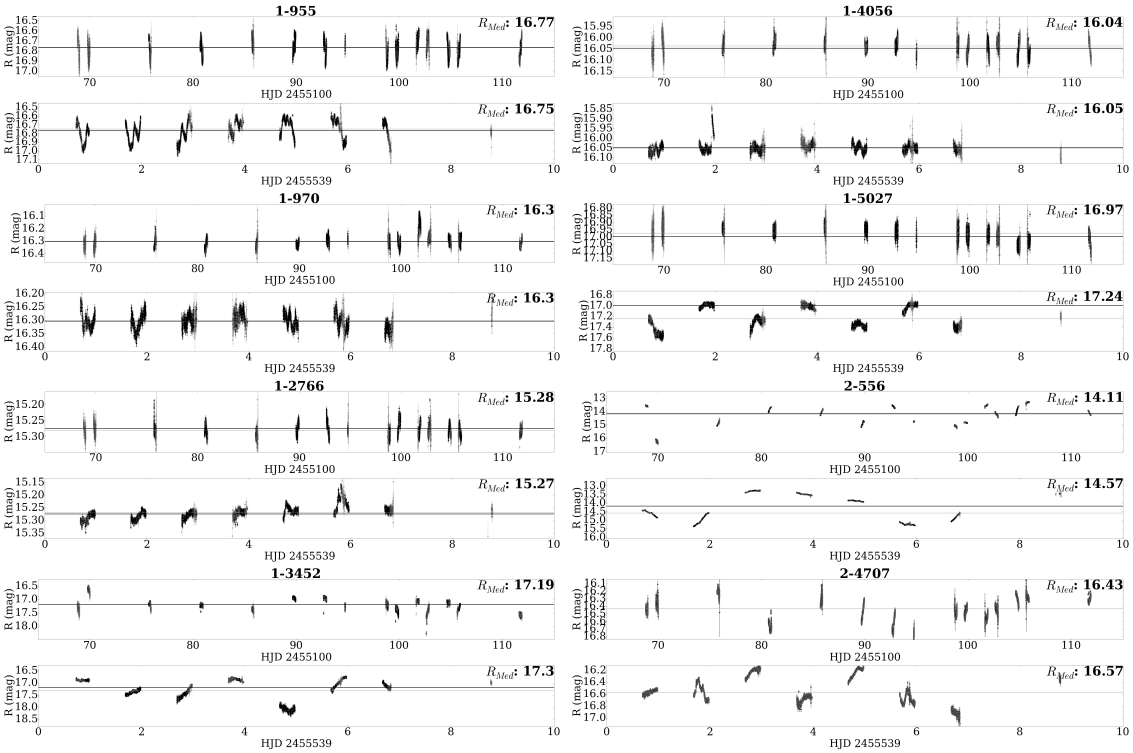

Figure 5.15: Complete light curves of the sources classified as CTTS. We present the 2009 observations on top and the 2010 observations below. Black dots correspond to unflagged photometric points, while gray correspond to flagged photometric points. The black horizontal line indicates the median R magnitude for both years (indicated in the header of the plot), while the gray ones indicate the median for that particular year (indicated in the top right corner of each year).

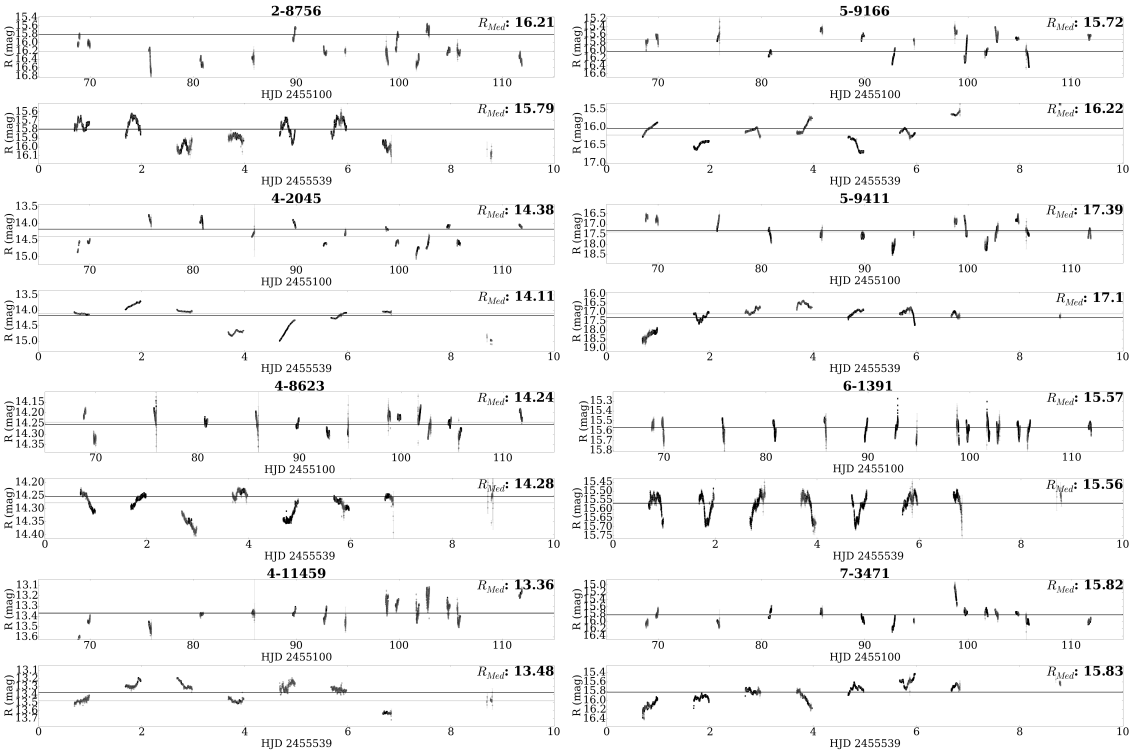
2-8756
R_{Med}: 16.21
R_{Med}: 15.79
5-9166
R_{Med}: 15.72
R_{Med}: 16.22
4-2045
R_{Med}: 14.38
R_{Med}: 14.11
5-9411
R_{Med}: 17.39
R_{Med}: 17.1
4-8623
R_{Med}: 14.24
R_{Med}: 14.28
6-1391
R_{Med}: 15.57
R_{Med}: 15.56
4-11459
R_{Med}: 13.36
R_{Med}: 13.48
7-3471
R_{Med}: 15.82
R_{Med}: 15.83
R (mag)
HJD 2455100
HJD 2455539

(Fig. 5.15 cont.)

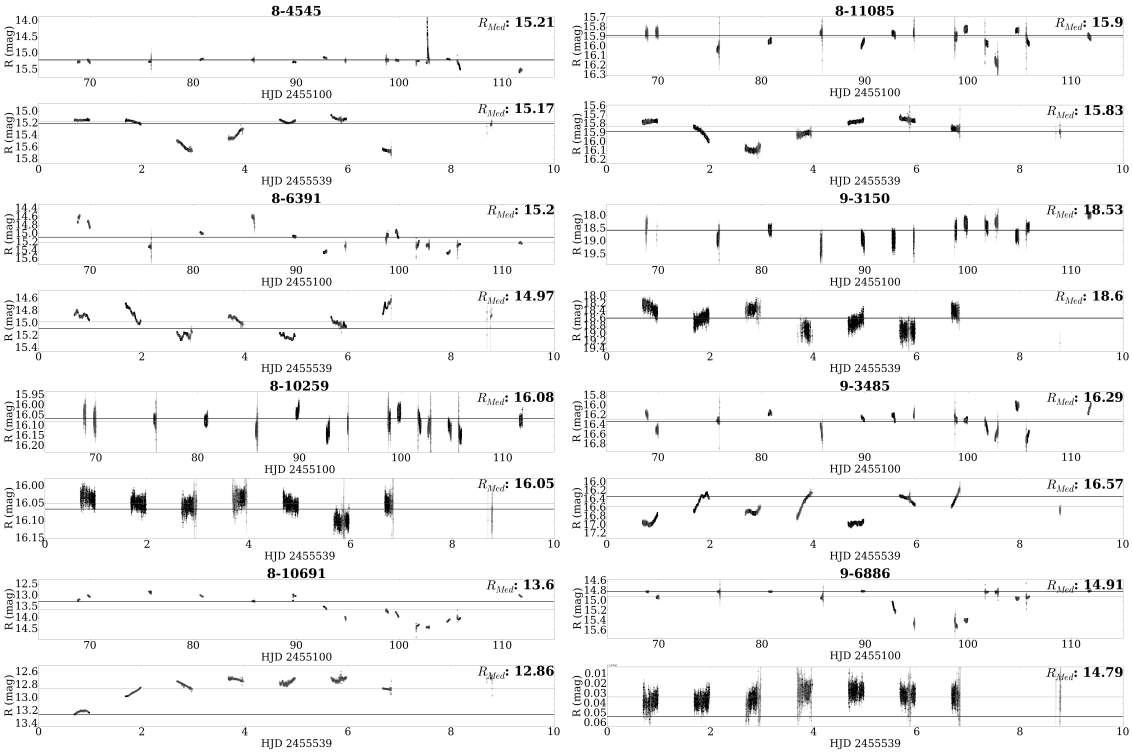
8-4545
R_{Med}: 15.21
R_{Med}: 15.17
8-11085
R_{Med}: 15.9
R_{Med}: 15.83
8-6391
R_{Med}: 15.2
R_{Med}: 14.97
9-3150
R_{Med}: 18.53
R_{Med}: 18.6
8-10259
R_{Med}: 16.08
R_{Med}: 16.05
9-3485
R_{Med}: 16.29
R_{Med}: 16.57
8-10691
R_{Med}: 13.6
R_{Med}: 12.86
9-6886
R_{Med}: 14.91
R_{Med}: 14.79
R (mag)
HJD 2455100
HJD 2455539

(Fig. 5.15 cont.)

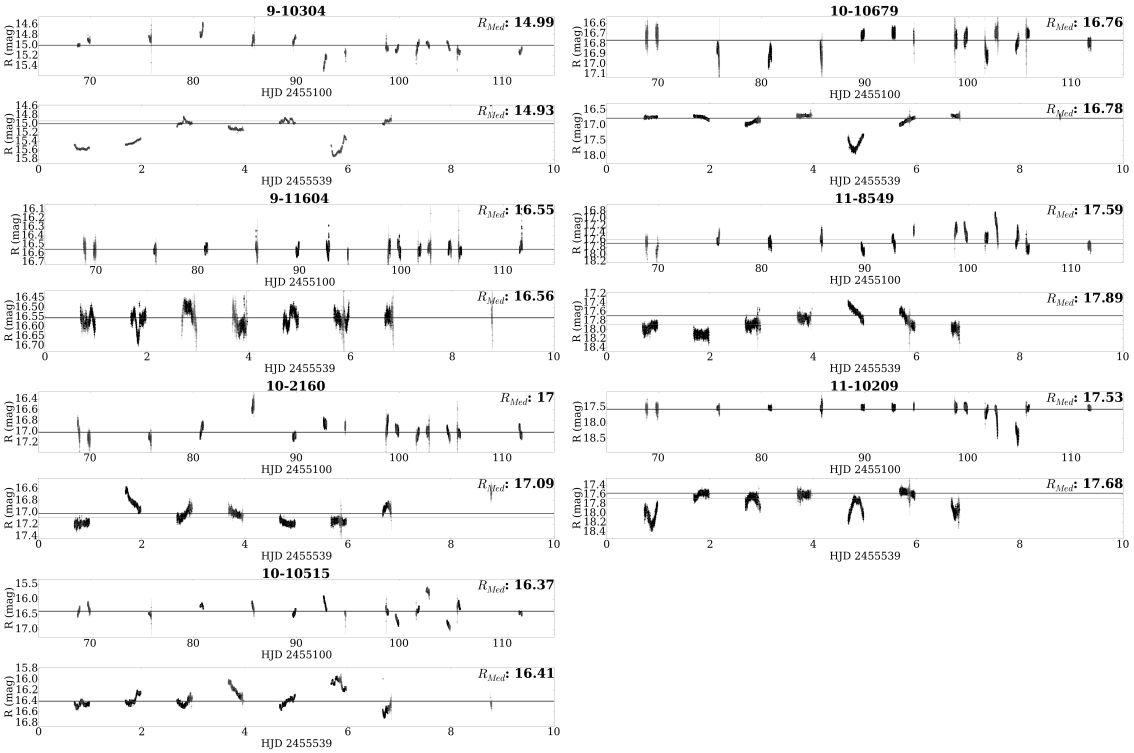
9-10304
R_{Med}: 14.99
R_{Med}: 14.93
9-11604
R_{Med}: 16.55
R_{Med}: 16.56
10-2160
R_{Med}: 17
R_{Med}: 17.09
10-10515
R_{Med}: 16.37
R_{Med}: 16.41
10-10679
R_{Med}: 16.76
R_{Med}: 16.78
11-8549
R_{Med}: 17.59
R_{Med}: 17.89
11-10209
R_{Med}: 17.53
R_{Med}: 17.68
R (mag)
HJD 2455100
HJD 2455539

(Fig. 5.15 cont.)

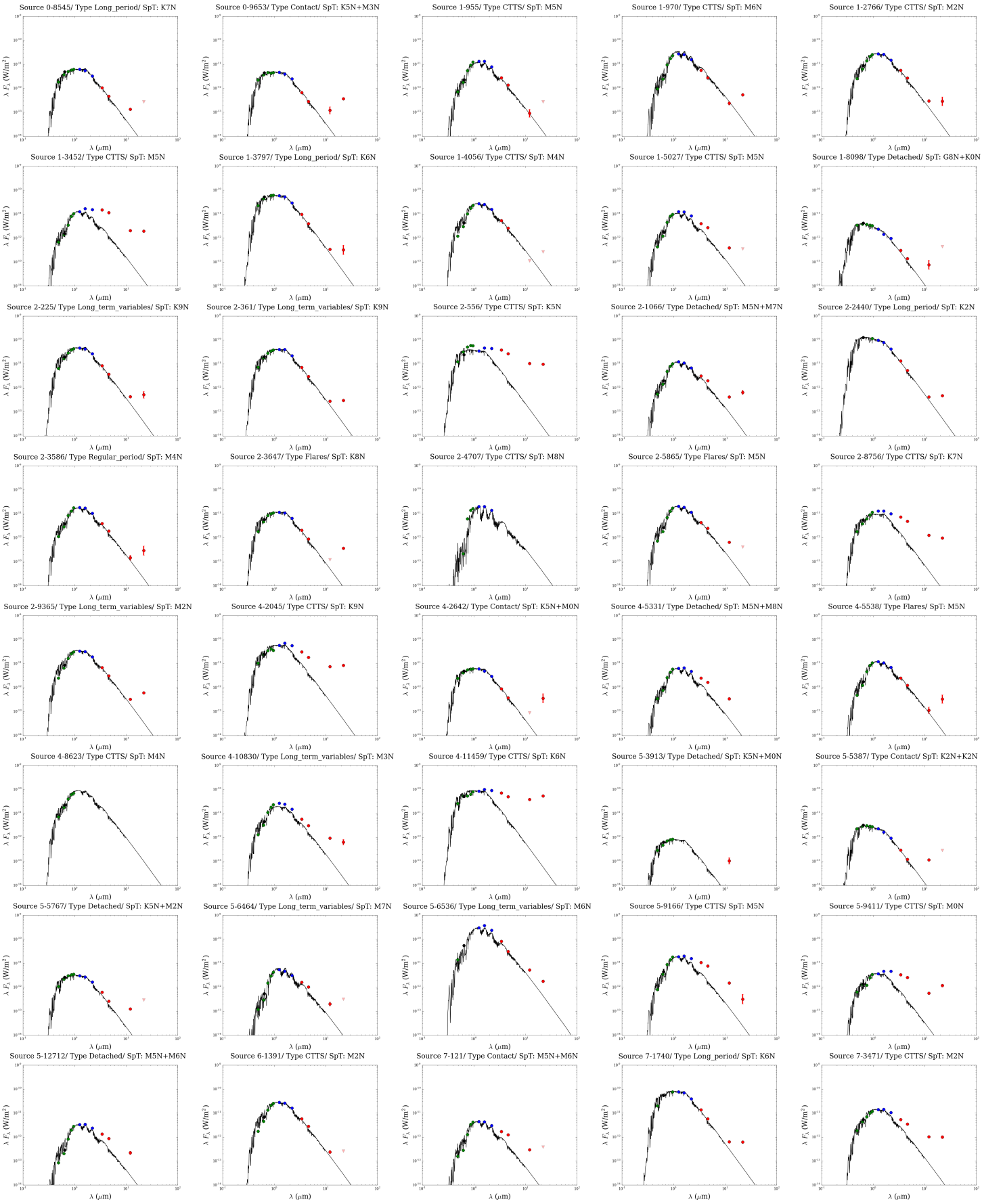

Figure 5.16: Spectral energy distributions for sources with infrared excesses higher than the photospheric flux. Green dots correspond to the Pan-STARRS *grziy* photometry, the black dot to the median R magnitude from our light curves, the blue dots correspond to 2MASS near infrared [J, H, K] and the red ones to WISE [3.35], [4.6], [11.6] and [22.1] μm bands, respectively. Triangles represent upper limits, color coded as the photometric points. The grey line represents the NEXTGEN photosphere of the best spectral type acquired during the SED fitting analysis. We also indicate the variable type of each source, as reference.

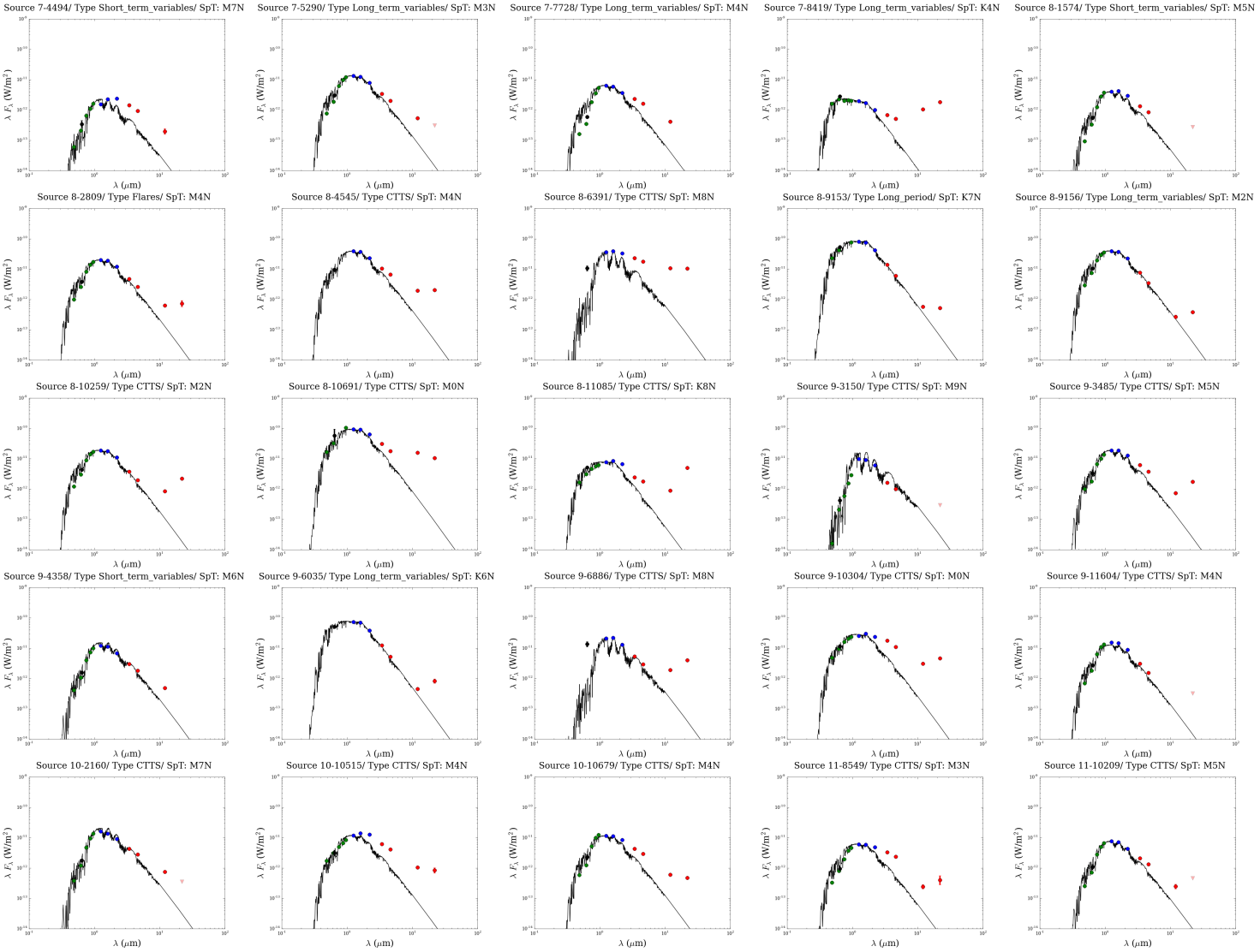
Source 7-4494/ Type Short_term_variables/ SpT: M7N
Source 7-5290/ Type Long_term_variables/ SpT: M3N
Source 7-7728/ Type Long_term_variables/ SpT: M4N
Source 7-8419/ Type Long_term_variables/ SpT: K4N
Source 8-1574/ Type Short_term_variables/ SpT: M5N
Source 8-2809/ Type Flares/ SpT: M4N
Source 8-4545/ Type CTTS/ SpT: M4N
Source 8-6391/ Type CTTS/ SpT: M8N
Source 8-9153/ Type Long_period/ SpT: K7N
Source 8-9156/ Type Long_term_variables/ SpT: M2N
Source 8-10259/ Type CTTS/ SpT: M2N
Source 8-10691/ Type CTTS/ SpT: M0N
Source 8-11085/ Type CTTS/ SpT: K8N
Source 9-3150/ Type CTTS/ SpT: M9N
Source 9-3485/ Type CTTS/ SpT: M5N
Source 9-4358/ Type Short_term_variables/ SpT: M6N
Source 9-6035/ Type Long_term_variables/ SpT: K6N
Source 9-6886/ Type CTTS/ SpT: M8N
Source 9-10304/ Type CTTS/ SpT: M0N
Source 9-11604/ Type CTTS/ SpT: M4N
Source 10-2160/ Type CTTS/ SpT: M7N
Source 10-10515/ Type CTTS/ SpT: M4N
Source 10-10679/ Type CTTS/ SpT: M4N
Source 11-8549/ Type CTTS/ SpT: M3N
Source 11-10209/ Type CTTS/ SpT: M5N
λ (μm)
λ F_λ (W/m²)

(Fig. 5.16 cont.)

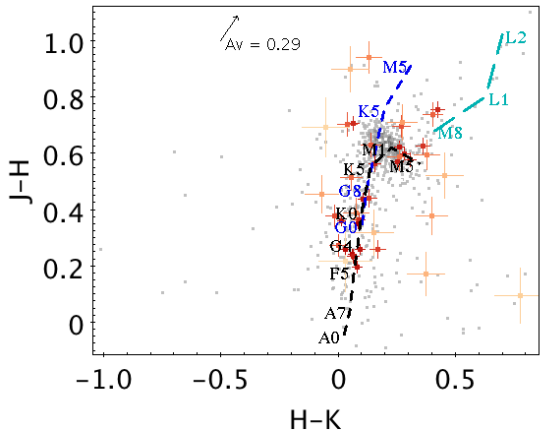

5.17.a: Detached binaries.

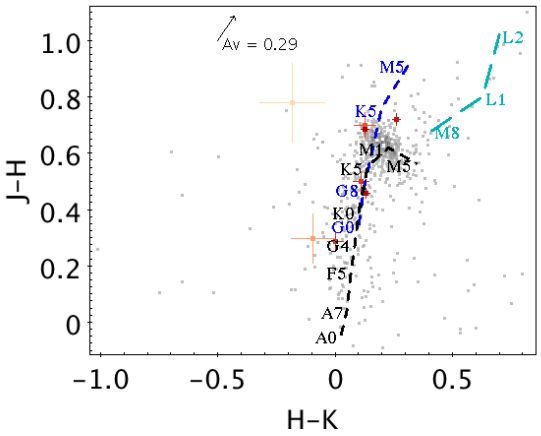

5.17.b: Close binaries.

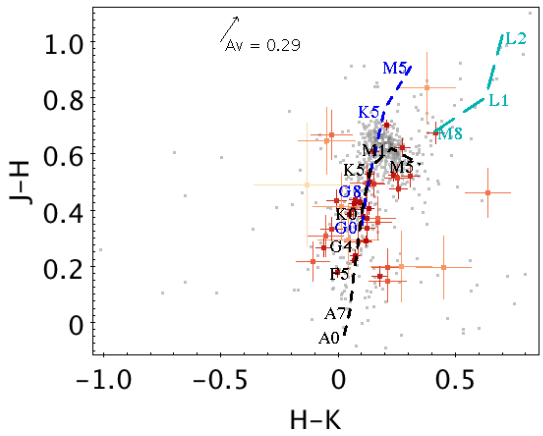

5.17.c: Contact binaries.

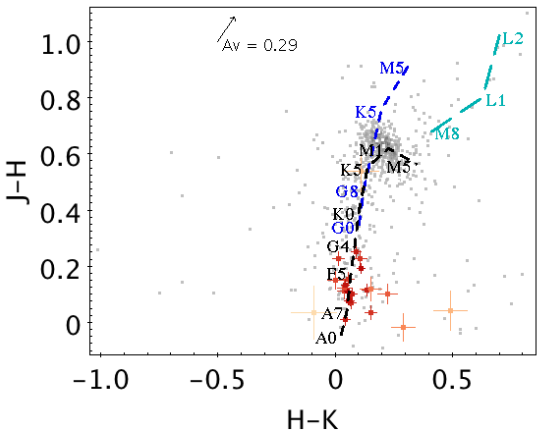

5.17.d: Short period.

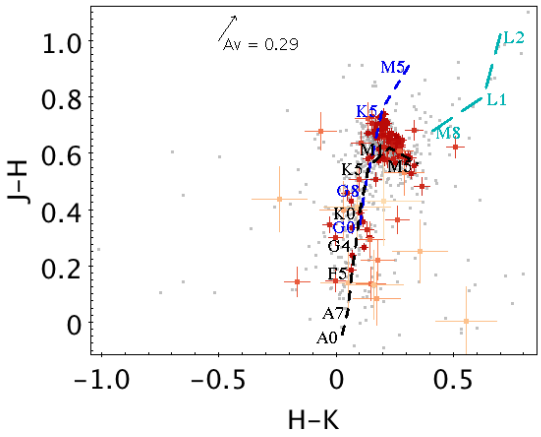

5.17.e: Regular period.

Figure 5.17: 2MASS J-H vs H-K Color-color diagrams for the different categories in Section 5.5 for the *PTF Orion variable catalog*. Black, blue and green dashed lines indicate the main sequence, giant branch and the L-dwarf regime regions, respectively, with the locus of some spectral types, as reference. The assume redenning of $A_V = 0.29$ is indicated. Grey dots mark the positions of the entire variable catalog, while red dots show the position for the sources in each category. Intensity of the colors marks the degree of uncertainty of the JHK_S values: the fainter, the larger the uncertainty.

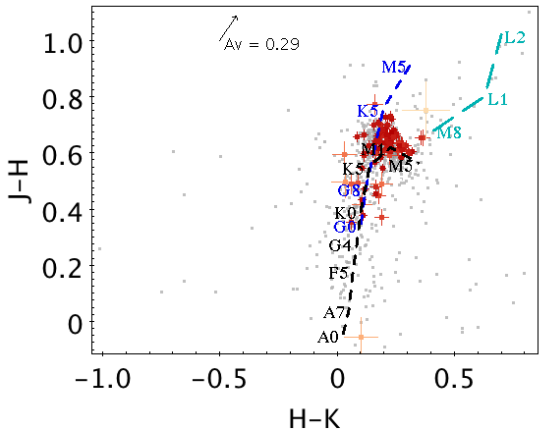

5.18.a: Long period.

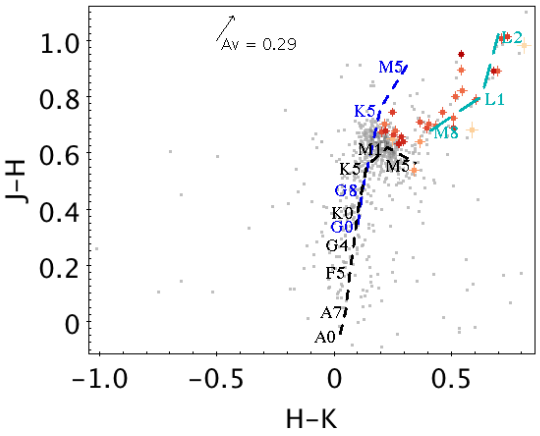

5.18.b: CTTS.

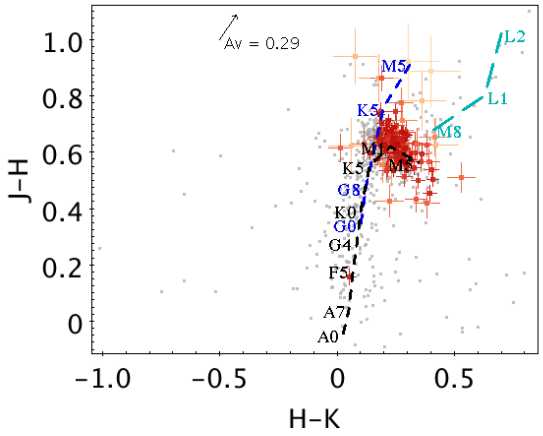

5.18.c: Flares.

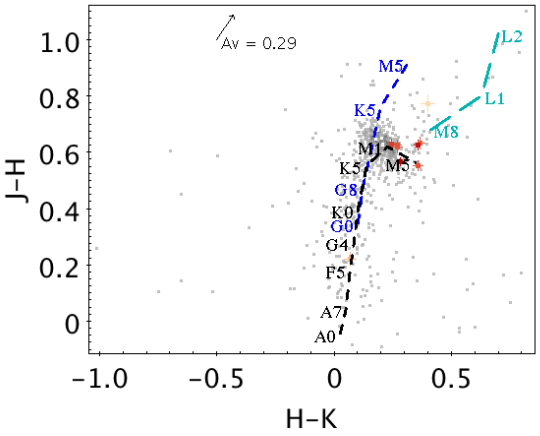

5.18.d: Short variables.

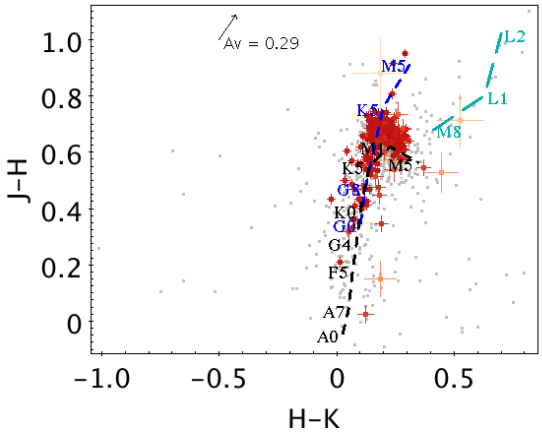

5.18.e: Long variables.

(Fig. 5.17 cont.)

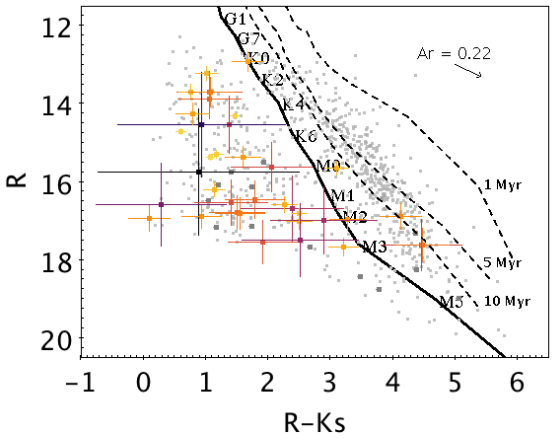

5.18.f: Detached binaries.

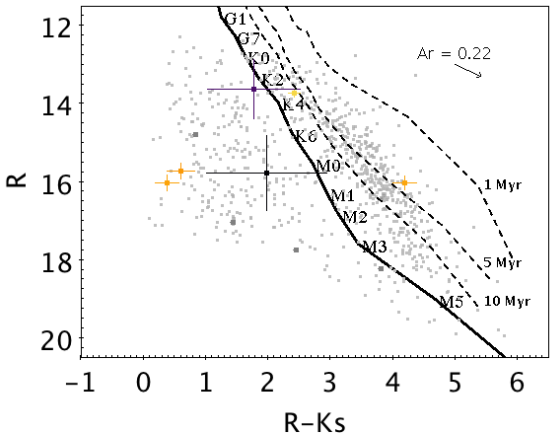

5.18.g: Close binaries.

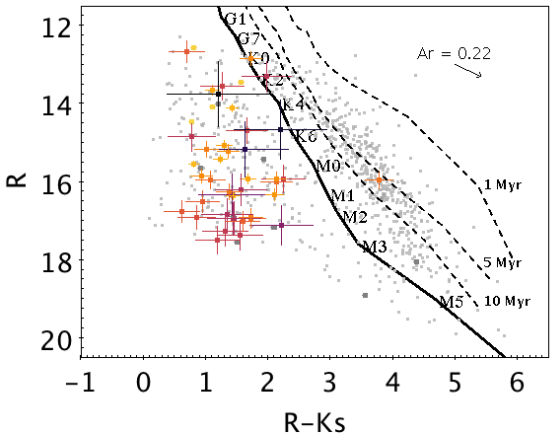

5.18.h: Contact binaries.

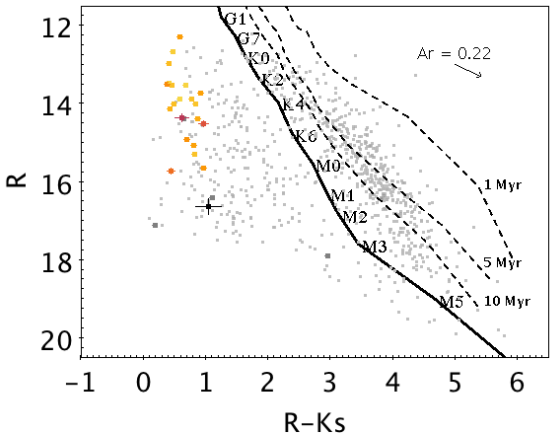

5.18.i: Short period.

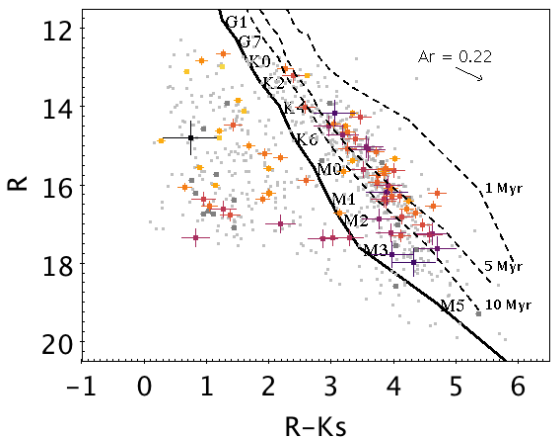

5.18.j: Regular period.

Figure 5.18: Color-magnitude diagrams for every category in Section 5.5 the *PTF Orion variable catalog*, based on the median R value (in both the 2009 and 2010 photometric points) and 2MASS K_S. Grey dots show the distribution of the entire catalog, and red dots the ones for each category. Intensity of the colors marks the degree of uncertainty of the R values: the fainter, the smaller the uncertainty. The main sequence is shown by a straight line, with the spectral types positions indicated, as well as the isochrones for 1, 5 and 10 Myrs, all of them obtained from the models of Siess et al. (2000). The redenning vector for $A_R = 0.22$ is indicated as well.

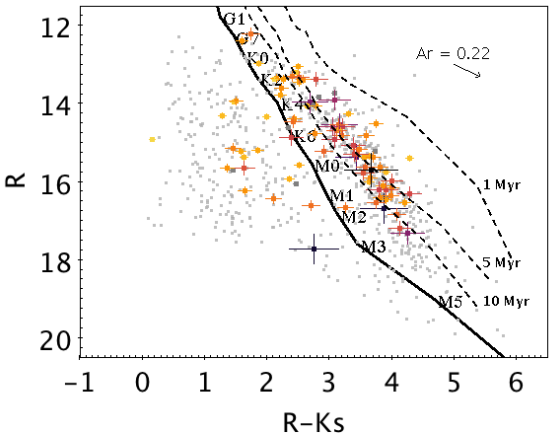

5.19.a: Long period.

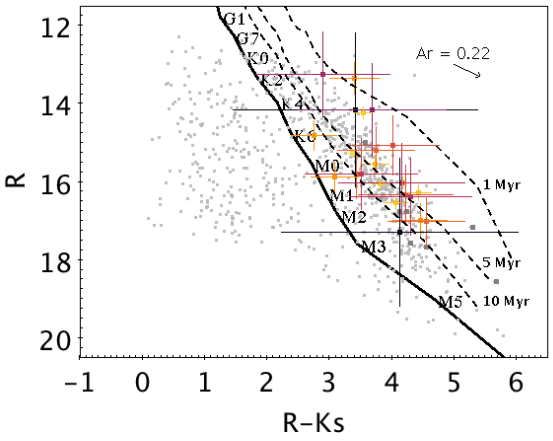

5.19.b: CTTS.

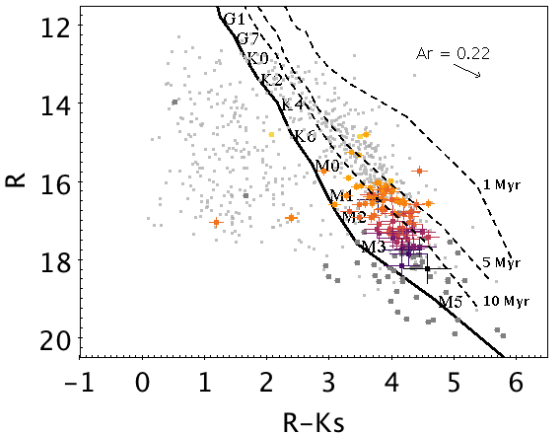

5.19.c: Flares.

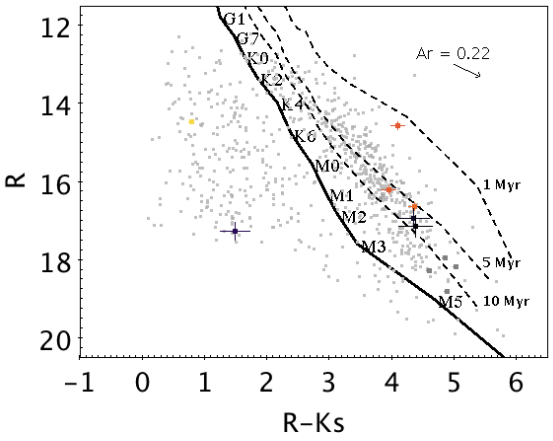

5.19.d: Short variables.

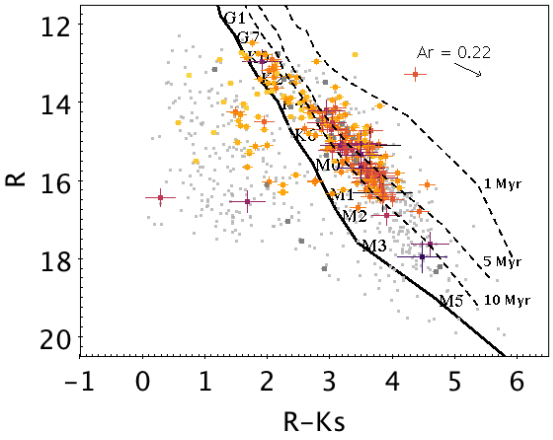

5.19.e: Long variables.

(Fig. 5.18 cont.)

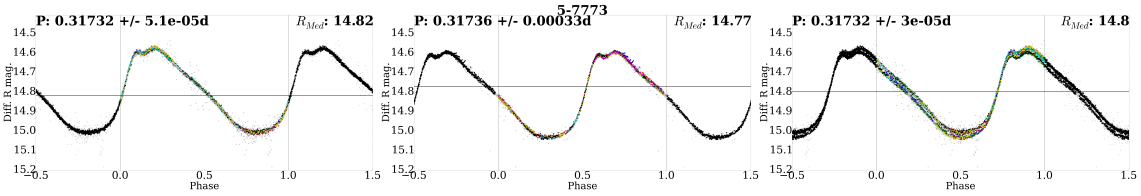

Figure 5.19: Example of a light curve of an RR Lyrae.

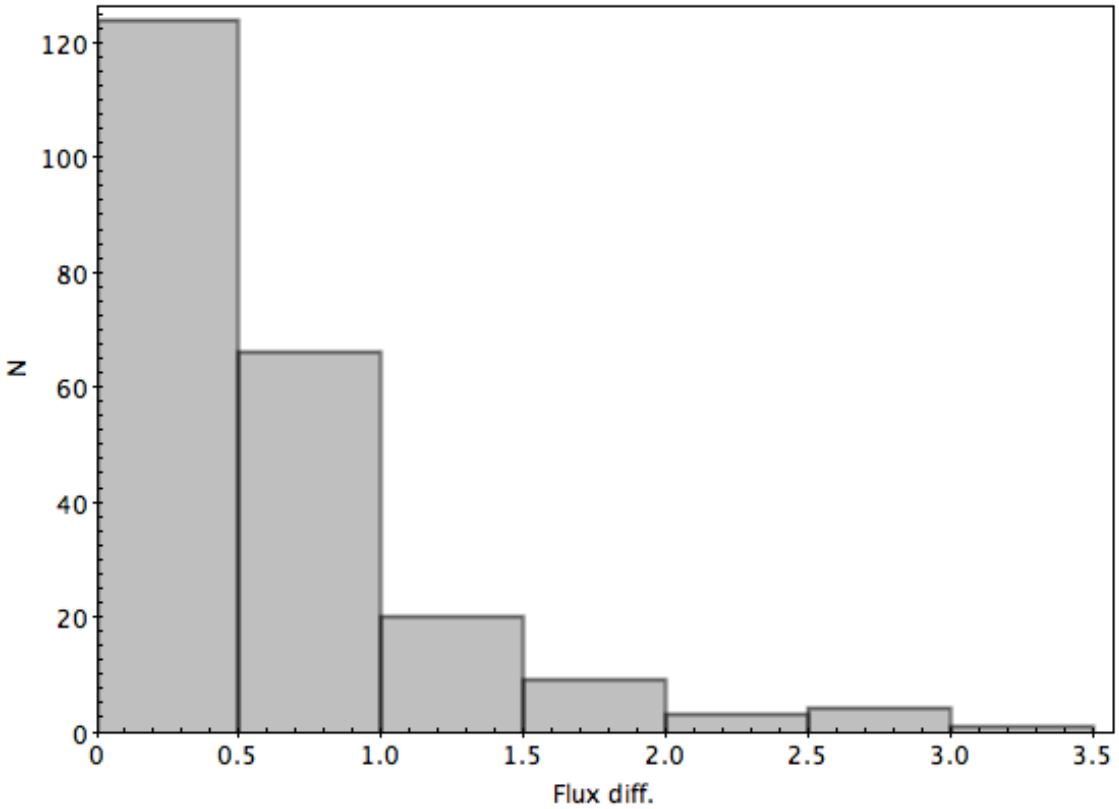

Figure 5.20: Distributions of flare flux differences. It can be seen how the larger the difference in flux, the fewer number of flares are present in the source.

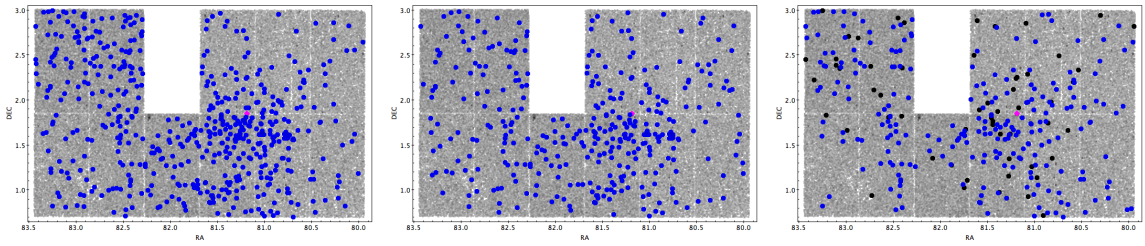

5.21.a: PMS

5.21.b: Flares

5.21.c: Infrared

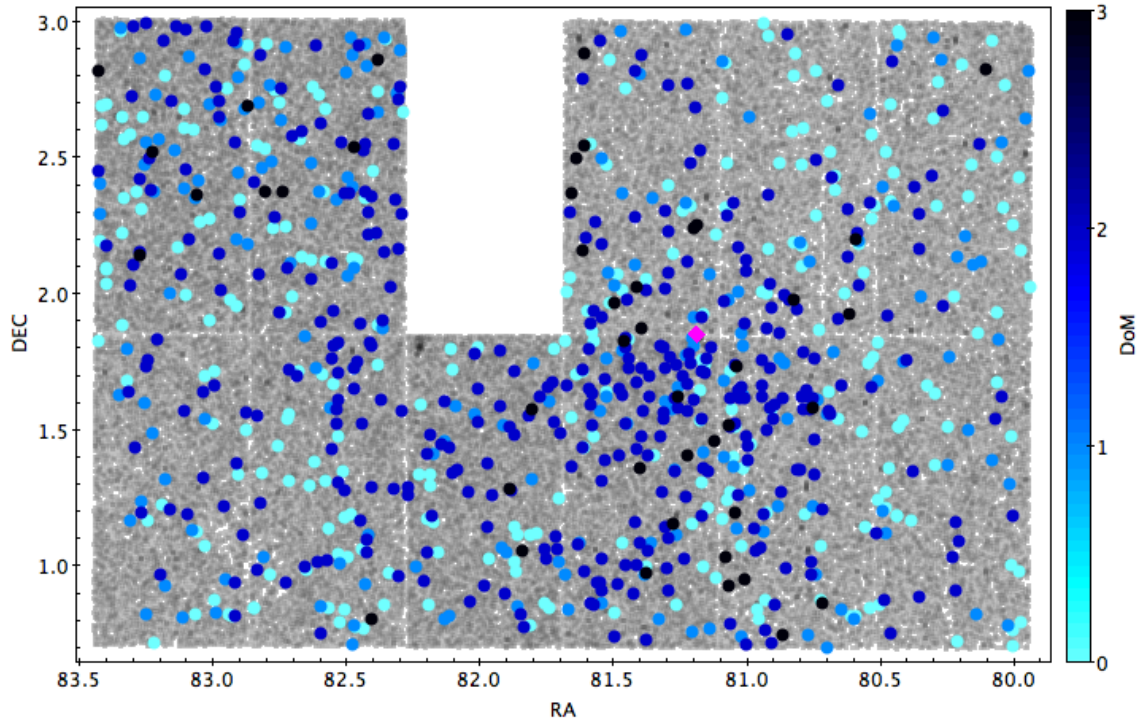

5.21.d: Degree of membership

Figure 5.21: Spatial distributions of the *PTF Orion variable catalog* sources based on indicators of youth such as (a) pre-main sequence colors in the color-magnitude diagram, (b) presence of flares in the light curves or (c) infrared excesses. Blue dots represent the sources of our catalog in each category, gray dots corresponds to the entire ∼100,000 PTF Orion detections and the pink diamond shows the position of 25-Ori. In plot (c), black dots indicate sources with infrared excess consistent with disk-bearing objects, and blue dots sources with infrared detections. Plot (d) shows the distribution of sources based on their degree of membership, that is, the number of youth tracers they have (flares, pms colors or infrared excess), color coded by that number. The clustering around 25-Ori is clearly observable in all the plots, pointing towards association membership.

Table 5.1: Stellar parameters for the planetary candidates, derived from the spectral type assuming they are dwarf stars. We provide the PTF Orion identifier, spectral type derived, effective temperature, absolute magnitude given their luminosity class, stellar radius derived with the previous information, depth of the transit and planetary radius derived. The uncertainty in the stellar radii is the difference in radii derived between spectral types ±2 sub-types from the nominal one. Uncertainty in planetary radii is derived by error propagation of the equation used, assuming a depth uncertainty of 10% and using the aforementioned stellar radius uncertainty. We also provide the periods for each year and for the combined years. We also indicate those sources which are potential 25-Ori members (with an asterisk). Sources 5-3045, 6-3001, 8-3311, 8-9088 and 9-2156 had no derived orbital period.

ID	SpT	T_{eff}	M_V	R_*	Depth	R_P	P_{2009}	P_{2010}	P_{total}
-	-	K	mags	$R_\odot$	%	R_{Jup}	days	days	days
2-1144*	M5	3095	14.5	0.51±0.079	7.73	1.4±1.1	1.1092±0.0061	-	1.1094±0.0004
4-2953	K3	4700	6.9	0.81±0.14	6.22	2±0.75	0.4943±0.0023	0.4897±0.0184	0.4944±0.0001
4-5444*	M0	3760	9.2	0.6±0.11	3.23	1±0.7	-	0.4518±0.0043	-
5-3045*	K9	3884	9.0	0.63±0.12	0.851	0.57±0.37	-	-	-
6-3001*	K9	3884	9.0	0.63±0.12	1.89	0.85±0.55	-	-	-
6-3938*	M2	3490	10.6	0.55±0.079	4.17	1.1±0.71	0.3607±0.0010	0.3603±0.0041	0.3606±0.0001
7-2884*	M4	3220	12.9	0.52±0.066	7.04	1.3±0.89	0.4078±0.0023	0.4061±0.0081	0.4077±0.0001
7-2919	K4	4550	7.4	0.79±0.13	9.31	2.3±0.91	0.8586±0.0026	0.8589±0.0068	0.8582±0.0002
8-3311*	M2	3490	10.6	0.55±0.079	1.96	0.75±0.49	-	-	-
8-3886	K7	4130	8.5	0.69±0.13	3.82	1.3±0.71	0.9562±0.0019	-	0.9563±0.0015
8-8695*	M4	3220	12.9	0.52±0.066	6.84	1.3±0.88	0.4484±0.0017	0.4474±0.0049	0.4484±0.0001
8-9088*	M4	3220	12.9	0.52±0.066	4.3	1±0.7	-	-	-
8-9555*	M0	3760	9.2	0.6±0.11	11	1.9±1.3	0.6057±0.0058	-	0.6054±0.0001
9-2156*	M0	3760	9.2	0.6±0.11	2.3	0.88±0.59	-	-	-
10-10911*	M6	2950	16.1	0.49±0.1	13.7	1.8±1.9	0.5468±0.0017	0.5462±0.0078	0.5468±0.0001

Table 5.2: PLANET CANDIDATES table. We provide the PTFO identification number; J2000 coordinates; total median R magnitude; general stellar periods of the 2009 and 2010 runs, separated, and the period of the concatenated data; orbital periods of the transits for both runs and the concatenated data, when available; J-H and H-K infrared colors; spectral type derived; and degree of membership (DoM) for each source. The numbers in this last column indicate the following: (1) for X-ray counterpart in Franciosini et al. (2011) observation; (2) for infrared excess present in the SED; (3) for flares found in the light curve; (4) for sources with pre-main sequence positions in the CMD; (5) and (6) for counterparts in the van Eyken et al. (2011) binaries or CTTS samples, respectively; (7), (8) (9) and (10) for counterparts in the catalogs from Briceño et al. (2005, Briceño et al. (2007), Hernández et al. (2007), McGehee (2006) or Downes et al. (2014), respectively. *Class* indicates the physical interpretation we have derived for some of the sources during our analysis. We show here the complete sample of planet candidates; in the rest of the categories just ten sources are shown, as reference. The complete tables are available in digital format. We also indicate those sources which are potential 25-Ori members (with an asterisk).

ID	RA	DEC	R_{median}	P_{2009} $P_{transit-2009}$	P_{2010} $P_{transit-2010}$	P_{total} $P_{transit-total}$	[J-H]	[H-K]	SpT	DoM	Class
-	deg	deg	mag	days	days	days	mag	mag	-	-	
2-1144*	81.4516	1.9745	16.40 ± 0.03	0.554 ± 0.002	0.5541 ± 0.0081	0.55452 ± 0.00025	0.66 ± 0.05	0.23 ± 0.06	M5	2* 4 5 10	Planet candidate
				1.109 ± 0.0061	-	1.1094 ± 0.00037					
4-2953	82.6675	2.1351	14.12 ± 0.05	0.4946 ± 0.0027	0.495 ± 0.014	0.494 ± 0.014	0.42 ± 0.05	0.05 ± 0.05	K3	-	Planet candidate
				0.4943 ± 0.0023	0.49 ± 0.018	0.4944 ± 6.7e-05					
4-5444*	82.4898	2.3685	15.12 ± 0.04	0.451 ± 0.003	0.454 ± 0.011	0.45134 ± 0.00023	0.68 ± 0.04	0.22 ± 0.04	M0	2* 3 4	Planet candidate
				-	0.4518 ± 0.0043	-					
5-3045*	83.2750	2.1423	13.48 ± 0.03	0.6531 ± 0.0035	0.6525 ± 0.0047	0.6528 ± 0.0041	0.65 ± 0.04	0.17 ± 0.04	K9	2* 3 4	Planet candidate
				-	-	-					
6-3001*	80.2069	1.0878	13.19 ± 0.09	1.204 ± 0.0047	1.2 ± 0.03	1.2045 ± 0.00041	0.71 ± 0.04	0.21 ± 0.04	K9	2* 4	Planet candidate
				-	-	-					
6-3938*	80.4928	1.2040	14.59 ± 0.04	0.3605 ± 0.0017	0.3605 ± 0.0063	0.36058 ± 3.4e-05	0.65 ± 0.05	0.23 ± 0.05	M2	2* 4 7	Planet candidate
				0.361 ± 0.001	0.3603 ± 0.0041	0.36059 ± 3.4e-05					
7-2884*	80.9471	1.0672	15.98 ± 0.03	0.4078 ± 0.0022	0.4074 ± 0.0074	0.4077 ± 7.6e-05	0.58 ± 0.05	0.31 ± 0.04	M4	3 4	Planet candidate
				0.4078 ± 0.0023	0.4061 ± 0.0081	0.40769 ± 8.2e-05					
7-2919	80.7211	1.0711	14.96 ± 0.04	0.859 ± 0.0031	0.859 ± 0.025	0.85813 ± 0.00023	0.42 ± 0.05	0.10 ± 0.07	K4	-	Planet candidate
				0.8586 ± 0.0026	0.8589 ± 0.0068	0.85818 ± 0.00016					
8-3311*	81.5429	1.0249	13.98 ± 0.05	0.8106 ± 0.0028	0.813 ± 0.013	0.8104 ± 0.00053	0.73 ± 0.05	0.21 ± 0.04	M2	2* 3 4	Planet candidate
				-	-	-					
8-3886	81.4687	1.0831	15.79 ± 0.01	0.956 ± 0.002	-	0.95637 ± 0.00035	0.70 ± 0.06	0.12 ± 0.06	K7	-	Planet candidate
				0.9562 ± 0.0019	-	0.9563 ± 0.0015					
8-8695*	81.2814	1.5735	15.03 ± 0.04	0.4484 ± 0.0017	0.4474 ± 0.0049	0.4 ± 0	0.67 ± 0.05	0.20 ± 0.04	M4	1 2* 4 7 8	Planet candidate
				0.4484 ± 0.0017	0.4474 ± 0.0049	0.44841 ± 6e-05					
8-9088*	81.2711	1.6149	15.68 ± 0.03	0.5964 ± 0.0021	0.596 ± 0.012	0.59649 ± 0.00022	0.62 ± 0.05	0.30 ± 0.04	M4	1 2* 3 4 8 10	Planet candidate
				-	-	-					
8-9555*	81.2609	1.6590	17.08 ± 0.03	1.21 ± 0.027	1.2 ± 0.15	1.2107 ± 0.00021	0.71 ± 0.09	0.25 ± 0.08	M0	1 4	Planet candidate
				0.6057 ± 0.0058	-	0.60539 ± 5.2e-05					
9-2156*	81.9093	0.8988	15.01 ± 0.01	0.3159 ± 0.0019	0.3329 ± 0.0063	0.31586 ± 8.9e-05	0.72 ± 0.04	0.17 ± 0.04	M0	3 4	Planet candidate
				-	-	-					
10-10911*	82.6581	1.8436	16.65 ± 0.04	0.54677 ± 0.00085	0.546 ± 0.011	0.54682 ± 9.2e-05	0.61 ± 0.05	0.30 ± 0.05	M6	2* 4	Planet candidate
				0.5468 ± 0.0017	0.5462 ± 0.0078	0.54682 ± 6.5e-05					

Table 5.3: DISCARDED PLANET CANDIDATES table. Same as in Table 5.2 but for those transiting planet candidates discarded after the analysis. Most are flagged as Algol detached binaries.

ID	RA	DEC	R_{median}	P_{2009}	P_{2010}	P_{total}	[J-H]	[H-K]	SpT	DoM	Class
				$P_{transit-2009}$	$P_{transit-2010}$	$P_{transit-total}$					
-	deg	deg	mag	days	days	days	mag	mag	-	-	
0-4407	80.1731	2.3552	15.92 ± 0.05	0.7018 ± 0.0036	0.7025 ± 0.0077	0.7011 ± 0.0003	0.53 ± 0.07	0.11 ± 0.10	K5	5	Alg
				0.7018 ± 0.0022	0.7025 ± 0.0078	0.70186 ± 7.5e-05					
0-7220	80.2664	2.6743	14.41 ± 0.03	0.6795 ± 0.0016	0.68 ± 0.0034	0.67969 ± 6.2e-05	0.64 ± 0.04	0.17 ± 0.04	K6	2* 3 4 5	Alg
				0.6797 ± 0.0018	0.679 ± 0.005	0.67969 ± 6.2e-05					
1-146	80.7269	1.8667	15.17 ± 0.01	-	-	-	0.19 ± 0.08	0.18 ± 0.12	K0	-	Alg
				-	-	-					
2-1875	81.3751	2.0533	14.59 ± 0.01	-	-	-	0.36 ± 0.06	0.06 ± 0.08	K0	-	Alg
				-	-	-					
2-1925	81.6642	2.0594	16.37 ± 0.02	2.08 ± 0.026	-	2.075 ± 0.0017	0.28 ± 0.17	0.12 ± 0.27	K2	-	Alg
				-	-	-					
2-4281	81.2125	2.3237	16.15 ± 0.02	1.362 ± 0.0093	1.31 ± 0.077	1.3609 ± 0.00024	0.43 ± 0.14	0.10 ± 0.18	K0	-	Alg
				1.362 ± 0.0047	-	1.3609 ± 0.00025					
4-2781	82.5766	2.1188	15.16 ± 0.05	-	-	-	0.25 ± 0.07	0.16 ± 0.09	K3	-	Alg
				-	-	-					
4-2831	82.4617	2.1238	17.13 ± 0.05	1.7 ± 0.032	1.7 ± 0.12	1.6849 ± 0.00045	-	-	K0	-	Alg
				1.69 ± 0.044	2 ± 0.1	1.6851 ± 0.00041					
4-5261	82.4297	2.3500	14.98 ± 0.04	0.7497 ± 0.0019	0.7497 ± 0.0035	0.7496 ± 0.0004	0.59 ± 0.05	0.13 ± 0.06	K5	-	Alg
				0.7498 ± 0.0046	0.7495 ± 0.0087	0.75015 ± 9.6e-05					
4-6325	82.3993	2.4511	17.33 ± 0.04	1.43 ± 0.014	1 ± 0.1	1.435 ± 0.0004	-	-	K0	-	Alg
				1.435 ± 0.0077	1.4 ± 0.08	1.4351 ± 0.00032					
4-9497	82.3818	2.7394	16.62 ± 0.03	2.16 ± 0.078	2.2 ± 0.44	2.2 ± 0.26	0.54 ± 0.14	0.06 ± 0.20	K4	-	Alg
				-	-	-					
5-11919	83.1835	2.9289	17.93 ± 0.07	0.4467 ± 0.0029	0.446 ± 0.009	0.44675 ± 0.00023	0.51 ± 0.07	0.33 ± 0.08	M6	3 4	WTTS
				0.4467 ± 0.0016	-	0.44697 ± 0.00026					
7-882	80.6097	0.8186	16.59 ± 0.04	3.91 ± 0.087	3.6 ± 0.43	3.9499 ± 0.00032	0.52 ± 0.12	0.30 ± 0.16	K5	-	Alg
				-	-	1.1233 ± 0.00032					
7-5967	80.9863	1.4465	15.67 ± 0.03	-	-	-	0.74 ± 0.05	0.11 ± 0.08	K6	-	Alg
				-	-	-					
7-8191	81.0607	1.7167	12.95 ± 0.02	0.93714 ± 0.00082	0.9365 ± 0.0071	0.93735 ± 0.00013	0.38 ± 0.04	0.02 ± 0.05	K3	5	Alg
				0.9373 ± 0.0024	0.93 ± 0.07	0.93735 ± 0.00014					
8-1336	81.4944	0.8300	16.84 ± 0.03	1.58 ± 0.014	1.58 ± 0.052	1.58 ± 0.00052	-	-	K0	-	Alg
				1.58 ± 0.027	-	1.58 ± 0.00048					
8-4176	81.2624	1.1135	16.88 ± 0.03	0.30353 ± 0.00047	0.3035 ± 0.0019	0.30353 ± 2e-05	0.53 ± 0.08	0.29 ± 0.08	M2	4	Alg
				0.30353 ± 0.00047	0.3035 ± 0.0024	0.30353 ± 1.4e-05					
8-4549	81.2058	1.1522	16.11 ± 0.02	1.94 ± 0.034	1.9 ± 0.18	1.934 ± 0.0011	0.22 ± 0.18	-0.07 ± 0.32	G8	-	Alg
				1.96 ± 0.052	1.94 ± 0.064	1.9663 ± 0.00042					
8-9356	81.5285	1.6401	16.44 ± 0.03	0.8766 ± 0.0067	0.877 ± 0.066	0.87631 ± 0.00036	0.27 ± 0.35	0.29 ± 0.46	F3	-	Alg
				0.877 ± 0.0086	0.883 ± 0.051	0.87636 ± 0.00023					
8-9435	81.1735	1.6469	15.37 ± 0.02	0.381 ± 0.001	0.3814 ± 0.0068	0.3813 ± 0.0001	0.54 ± 0.10	0.07 ± 0.12	K4	1 2*	Alg
				0.3812 ± 0.0018	0.3823 ± 0.0066	0.38129 ± 0.00011					
8-10585	81.1671	1.7543	14.36 ± 0.01	1.55 ± 0.013	-	1.5461 ± 0.00095	0.43 ± 0.06	0.13 ± 0.07	K3	-	Alg
				1.55 ± 0.032	-	1.5464 ± 0.00073					
9-11713	82.1092	1.7988	15.20 ± 0.01	0.835 ± 0.0092	0.83 ± 0.11	0.8331 ± 0.0005	0.51 ± 0.07	0.06 ± 0.08	K4	-	Alg
				0.8346 ± 0.0079	0.83 ± 0.11	0.8351 ± 0.0001					

Table 5.4: Similar to Table 5.2 for DETACHED BINARIES.

ID	RA	DEC	R_{median}	P_{2009}	P_{2010}	P_{total}	[J-H]	[H-K]	SpT	DoM	Class
-	deg	deg	mag	days	days	days	mag	mag	-	-	
0-1580	79.9413	2.0266	15.38 ± 0.08	2.062 ± 0.0011	2.1 ± 0.58	2.06 ± 0.002	0.44 ± 0.07	0.13 ± 0.09	-	5	Alg
0-4268	80.4615	2.3390	13.72 ± 0.11	5.2 ± 0.18	5.2 ± 0.18	-	-	-	-	5	Alg
0-5673	80.0640	2.5029	15.76 ± 0.05	0.54324 ± 0.00043	0.542 ± 0.013	0.54315 ± 5.8e-05	0.51 ± 0.08	0.06 ± 0.11	-	5	Alg
0-8036	80.0366	2.7629	17.93 ± 0.17	0.5974 ± 0.0016	0.5982 ± 0.0061	0.59747 ± 8.5e-05	-	-	-	5	Alg
0-9559	80.0790	2.9304	18.44 ± 0.10	-	-	-	0.52 ± 0.17	0.45 ± 0.23	-	-	Alg
1-1223	80.9458	2.0064	15.77 ± 0.35	1.252 ± 0.0046	1.25 ± 0.017	1.2522 ± 0.00017	0.45 ± 0.12	-0.07 ± 0.20	-	5	Alg
1-2592	80.7947	2.1758	16.22 ± 0.04	2.5 ± 0.044	-	2.5 ± 0.001	0.32 ± 0.16	0.15 ± 0.24	-	-	Alg
1-2659	80.8017	2.1855	16.54 ± 0.13	0.9596 ± 0.0073	0.96 ± 0.012	0.96197 ± 9.6e-05	0.09 ± 0.29	0.78 ± 0.35	-	2* 5	Alg
1-3638	81.0822	2.3140	16.49 ± 0.08	-	-	-	0.22 ± 0.19	0.03 ± 0.32	-	5	Alg
1-4581	80.6682	2.4316	15.30 ± 0.02	1.871 ± 0.0057	-	1.871 ± 0.0019	0.38 ± 0.07	-0.01 ± 0.11	-	5	Alg
1-5838	80.8290	2.5932	13.72 ± 0.08	1.9 ± 0.015	2 ± 0.1	1.896 ± 0.0026	0.20 ± 0.06	0.08 ± 0.06	-	-	Alg
1-6862	80.6978	2.7085	18.28 ± 0.08	-	-	-	-	-	-	-	Alg
1-8098	81.0921	2.8533	16.09 ± 0.03	-	-	-	0.17 ± 0.18	0.38 ± 0.25	-	2	Alg
2-822	81.5964	1.9389	16.68 ± 0.16	0.9206 ± 0.0016	0.92 ± 0.05	0.92042 ± 0.00011	0.59 ± 0.13	0.38 ± 0.15	-	5	Alg
2-1066	81.4980	1.9666	16.89 ± 0.09	-	-	-	0.60 ± 0.06	0.28 ± 0.06	M5-M7	2 3 4 5	Alg
2-4114	81.2384	2.3049	16.80 ± 0.08	3.5 ± 0.13	3.5 ± 0.33	3.5194 ± 0.00073	-	-	-	5	Alg
2-5622	81.5270	2.4709	17.17 ± 0.05	1000 ± 0.0072	1.9 ± 0.12	-	-	-	-	-	Alg
4-5331	82.4063	2.3569	17.63 ± 0.13	-	-	-	0.76 ± 0.07	0.43 ± 0.08	M5-M8	2 4 5	Alg
4-7397	82.8369	2.5455	16.13 ± 0.10	0.46613 ± 0.00018	0.466 ± 0.0016	-	-	-	-	-	Alg
4-8678	82.2856	2.6666	16.82 ± 0.03	-	-	-	0.70 ± 0.09	0.04 ± 0.12	-	-	Alg
4-9418	82.6047	2.7325	19.88 ± 0.33	0.5713 ± 0.0021	0.5718 ± 0.0035	0.5711 ± 0.00012	-	-	-	-	Alg
4-11668	82.3548	2.9317	17.55 ± 0.12	-	1.25 ± 0.018	-	-	-	-	5	Alg
5-961	82.9103	1.9510	13.71 ± 0.11	1.332 ± 0.0039	1.33 ± 0.022	1.3312 ± 0.00021	0.26 ± 0.05	0.03 ± 0.06	-	5	Alg
5-1825	83.3973	2.0328	18.17 ± 0.15	0 ± 0.013	1.33 ± 0.018	-	-	-	-	-	Alg
5-3088	82.9782	2.1458	17.63 ± 0.09	1.15 ± 0.013	1.15 ± 0.067	1.148 ± 0.00032	0.58 ± 0.06	0.31 ± 0.07	M5-M5	2* 4	Alg
5-3670	82.9129	2.1997	17.34 ± 0.00	-	-	-	0.57 ± 0.06	0.25 ± 0.07	M6-M6	4	Alg
5-3913	83.3412	2.2210	18.13 ± 0.10	0.522 ± 0.0016	0.523 ± 0.016	0.52192 ± 8.1e-05	-	-	-	2	Alg
5-4481	83.0149	2.2723	18.43 ± 0.13	0.5488 ± 0.0031	0.5497 ± 0.0061	0.5489 ± 0.0001	-	-	-	-	Alg
5-5592	83.2842	2.3715	16.91 ± 0.06	-	-	2.2014 ± 0.00076	-	-	-	-	Alg
5-5767	83.1095	2.3861	16.59 ± 0.05	1.052 ± 0.0026	-	1.05 ± 0.001	0.59 ± 0.12	0.26 ± 0.14	-	2 5	Alg

Table 5.5: Similar to Table 5.2 for CLOSE BINARIES.

ID	RA	DEC	R_{median}	P_{2009}	P_{2010}	P_{total}	[J-H]	[H-K]	SpT	DoM	Class
-	deg	deg	mag	days	days	days	mag	mag	-	-	
0-4757	80.3731	2.3942	18.23 ± 0.10	0.21714 ± 0.00052	0.2171 ± 0.0015	0.21712 ± 2.8e-05	0.70 ± 0.08	0.13 ± 0.12	M4-M4	3 4	βLy
0-5197	80.4524	2.4466	17.05 ± 0.21	0.27322 ± 0.00027	0.2733 ± 0.0011	0.27323 ± 2.1e-05	0.78 ± 0.24	-0.18 ± 0.36	-	5	βLy
5-295	83.3409	1.8864	16.04 ± 0.05	0.42249 ± 0.00073	0.4224 ± 0.0031	0.42243 ± 4.3e-05	-	-	-	5	βLy
5-9211	83.3973	2.6921	15.79 ± 0.27	0.24398 ± 8.6e-05	0.244 ± 0.0004	0.24396 ± 7.4e-06	0.50 ± 0.08	0.11 ± 0.10	-	5	βLy
5-12287	83.3473	2.9614	13.63 ± 0.21	0.28711 ± 9e-05	0.287 ± 0.00054	0.28709 ± 7.6e-06	0.46 ± 0.05	0.13 ± 0.05	-	5	βLy
6-4502	80.4785	1.2735	18.75 ± 0.16	0.3264 ± 0.0014	0.3266 ± 0.0061	0.32632 ± 6.2e-05	-	-	-	-	βLy
6-5196	80.4669	1.3563	15.74 ± 0.06	0.42526 ± 0.00063	0.4251 ± 0.0034	0.42526 ± 4.3e-05	0.30 ± 0.14	-0.09 ± 0.26	-	5	βLy
7-5291	80.8017	1.3543	13.74 ± 0.03	3.62 ± 0.099	3.4 ± 0.62	3.642 ± 0.0026	0.68 ± 0.04	0.13 ± 0.04	K9-M0	3 4 5	βLy
8-756	81.1418	0.7722	16.05 ± 0.04	0.3974 ± 0.0085	0.3974 ± 0.0085	0.3974 ± 0.0085	0.72 ± 0.06	0.26 ± 0.05	M4-M4	4	βLy
10-3070	82.5328	1.0413	17.76 ± 0.11	0.21857 ± 0.00046	0.2184 ± 0.0022	0.21854 ± 2.6e-05	-	-	-	-	βLy
11-10141	83.4273	1.8244	14.80 ± 0.05	0.45611 ± 0.00056	0.4563 ± 0.0026	0.45606 ± 3.6e-05	0.29 ± 0.07	0.00 ± 0.09	-	5	βLy

Table 5.6: Similar to Table 5.2 for CONTACT BINARIES.

ID	RA	DEC	R_{median}	P_{2009}	P_{2010}	P_{total}	[J-H]	[H-K]	SpT	DoM	Class
-	deg	deg	mag	days	days	days	mag	mag	-	-	
0-3542	80.0020	2.2544	15.43 ± 0.07	0.28439 ± 0.00022	0.2843 ± 0.0011	0.28443 ± 3.8e-05	-	-	-	5	Wur
0-4052	80.0375	2.3150	18.42 ± 0.19	0.22564 ± 0.00033	0.2256 ± 0.0017	0.22563 ± 1.9e-05	-	-	-	-	Wur
0-5453	80.1562	2.4756	17.95 ± 0.11	0.4945 ± 0.0026	0.4946 ± 0.0095	0.49447 ± 0.00012	-	-	-	-	Wur
0-8177	80.2822	2.7777	16.94 ± 0.06	0.30442 ± 0.00054	0.3044 ± 0.0026	0.30443 ± 3.5e-05	-	-	-	5	Wur
0-9653	80.2995	2.9387	16.02 ± 0.08	0.9107 ± 0.0031	0.914 ± 0.038	0.91101 ± 0.00042	0.52 ± 0.09	0.31 ± 0.10	-	2 5	Wur
0-9790	80.4245	2.9530	16.95 ± 0.12	0.32632 ± 0.00044	0.326 ± 0.002	0.32631 ± 2.8e-05	0.20 ± 0.23	0.27 ± 0.36	-	5	Wur
1-1187	80.6370	2.0017	18.11 ± 0.18	0.28796 ± 0.00051	0.288 ± 0.0026	0.28797 ± 3.1e-05	-	-	-	-	Wur
1-1822	80.5626	2.0781	19.52 ± 0.25	0.2752 ± 0.0006	0.2749 ± 0.0034	0.27525 ± 4.3e-05	-	-	-	-	Wur
1-6009	80.7892	2.6099	17.53 ± 0.10	0.31655 ± 0.00076	0.3166 ± 0.0039	0.31652 ± 4.3e-05	-	-	-	-	Wur
1-6477	80.5404	2.6609	14.10 ± 0.01	0.7791 ± 0.0066	0.781 ± 0.019	0.77978 ± 0.00025	0.24 ± 0.06	0.08 ± 0.07	-	2* 5	Wur
1-7793	80.7414	2.8173	19.35 ± 0.24	0.24373 ± 0.00043	0.2434 ± 0.0031	0.2437 ± 3.2e-05	-	-	-	-	Wur
1-8053	81.0777	2.8481	18.59 ± 0.15	0.27034 ± 0.00072	0.2702 ± 0.0038	0.27037 ± 4e-05	-	-	-	-	Wur
2-1063	81.5164	1.9660	19.17 ± 0.24	0.21888 ± 0.00039	0.2188 ± 0.0022	0.21887 ± 2.3e-05	-	-	-	-	Wur
2-1985	81.4870	2.0681	16.33 ± 0.17	0.30344 ± 0.00017	0.30332 ± 0.00086	0.30345 ± 1.2e-05	0.14 ± 0.15	0.21 ± 0.24	-	5	Wur
4-267	82.3814	1.8820	19.00 ± 0.15	0.26159 ± 0.00081	0.2616 ± 0.0038	0.2616 ± 4.1e-05	-	-	-	-	Wur
4-827	82.7265	1.9305	13.56 ± 0.11	0.32224 ± 0.00034	0.3222 ± 0.00089	0.32224 ± 1.9e-05	-	-	-	5	Wur
4-2642	82.7078	2.1089	15.93 ± 0.10	0.2316 ± 0.00027	0.23171 ± 0.00054	0.23161 ± 2e-05	0.48 ± 0.08	0.26 ± 0.10	-	2	Wur
4-2814	82.6320	2.1223	13.67 ± 0.05	-	0.5479 ± 0.0061	-	0.38 ± 0.04	0.05 ± 0.05	-	-	Wur
4-3811	82.4108	2.2163	18.96 ± 0.14	0.25377 ± 0.00076	0.254 ± 0.0035	0.25375 ± 4e-05	-	-	-	-	Wur
4-4080	82.7728	2.2419	18.77 ± 0.17	0.25588 ± 0.00065	0.2559 ± 0.0031	0.25584 ± 3.5e-05	-	-	-	-	Wur
4-7558	82.6728	2.5640	16.22 ± 0.13	0.25833 ± 0.00015	0.2583 ± 0.00065	0.25834 ± 1.2e-05	0.36 ± 0.12	0.17 ± 0.17	-	5	Wur
4-8796	82.5808	2.6770	16.95 ± 0.13	0.39717 ± 0.00049	0.397 ± 0.0023	0.39714 ± 3.3e-05	-	-	-	5	Wur
4-9573	82.7673	2.7471	17.13 ± 0.15	0.26463 ± 0.00024	0.2647 ± 0.0011	0.26462 ± 1.6e-05	-	-	-	5	Wur
4-11500	82.8000	2.9167	16.76 ± 0.08	0.6174 ± 0.0022	0.6178 ± 0.0084	0.61756 ± 9.5e-05	-	-	-	-	Wur
5-2476	83.4012	2.0906	17.18 ± 0.09	0.35496 ± 0.00033	0.3549 ± 0.0014	-	-	-	-	-	Wur
5-2483	83.4015	2.0912	17.18 ± 0.08	0.35498 ± 0.00037	0.3549 ± 0.0015	-	-	-	-	-	Wur
5-4382	83.0506	2.2629	17.72 ± 0.17	0.30328 ± 0.00038	0.3034 ± 0.0019	0.30326 ± 2.3e-05	-	-	-	5	Wur
5-5387	83.0662	2.3533	16.38 ± 0.03	0.25712 ± 0.00057	0.2568 ± 0.0028	0.25708 ± 3.2e-05	0.37 ± 0.16	0.17 ± 0.22	-	2	Wur
5-5669	83.2187	2.3765	13.46 ± 0.02	0.5103 ± 0.0015	0.5107 ± 0.0073	0.5103 ± 0.0001	0.43 ± 0.04	0.09 ± 0.05	-	2* 5	Wur
5-8209	83.1066	2.6059	16.35 ± 0.04	0.29575 ± 0.00059	0.2957 ± 0.0024	0.29574 ± 3.3e-05	0.49 ± 0.10	0.15 ± 0.13	-	5	Wur

Table 5.7: Similar to Table 5.2 for LONG PERIODIC sources.

ID	RA	DEC	R_{median}	P_{2009}	P_{2010}	P_{total}	[J-H]	[H-K]	SpT	DoM	Class
-	deg	deg	mag	days	days	days	mag	mag	-	-	
0-631	80.4758	1.9175	14.56 ± 0.10	3.13 ± 0.023	3.1 ± 0.12	3.112 ± 0.0022	0.68 ± 0.04	0.24 ± 0.04	M0	2* 3 4 7	WTTS
0-949	80.2658	1.9524	15.76 ± 0.02	1.25 ± 0.016	1.14 ± 0.027	1.1098 ± 0.00069	0.66 ± 0.05	0.19 ± 0.06	M3	2* 3 4	WTTS
0-1290	80.3473	1.9916	13.96 ± 0.01	1.07 ± 0.017	1.07 ± 0.092	-	0.44 ± 0.04	0.11 ± 0.04	-	2*	-
0-8545	79.9451	2.8198	15.94 ± 0.02	1.23 ± 0.041	1.2 ± 0.17	1.225 ± 0.0014	0.59 ± 0.07	0.22 ± 0.09	-	2	CTTS*
1-39	80.8786	1.8554	13.96 ± 0.09	1.24 ± 0.0046	1.24 ± 0.018	1.24 ± 0.0005	0.70 ± 0.05	0.16 ± 0.05	K9	2* 3 4 8	WTTS
1-57	81.0234	1.8566	16.42 ± 0.03	1.46 ± 0.021	1.4 ± 0.13	1.44 ± 0.0005	0.64 ± 0.05	0.17 ± 0.06	M5	4 10	-
1-1410	80.5827	2.0275	13.05 ± 0.02	2.79 ± 0.049	2.7 ± 0.18	2.798 ± 0.0026	0.63 ± 0.04	0.16 ± 0.04	M2	2* 4	WTTS*
1-1467	80.9144	2.0335	16.16 ± 0.02	1.61 ± 0.042	1.63 ± 0.049	1.6114 ± 0.00059	0.64 ± 0.06	0.23 ± 0.05	M5	2* 3 4	WTTS
1-2180	81.0012	2.1246	15.64 ± 0.03	2.2 ± 0.052	2.3 ± 0.19	2.206 ± 0.0028	0.67 ± 0.05	0.25 ± 0.04	M4	2* 3 4	WTTS
1-2261	80.6237	2.1349	13.45 ± 0.03	3.37 ± 0.072	3.3 ± 0.45	3.228 ± 0.0053	0.58 ± 0.04	0.19 ± 0.04	K9	2* 3 4	WTTS
1-3797	80.5374	2.3341	13.35 ± 0.03	2.53 ± 0.044	2.7 ± 0.22	2.557 ± 0.0031	0.60 ± 0.05	0.15 ± 0.05	K6	2 4	CTTS*
1-5242	80.6852	2.5180	16.06 ± 0.03	1.05 ± 0.011	1 ± 0.14	1.045 ± 0.0014	0.61 ± 0.07	0.26 ± 0.08	-	-	-
1-6353	80.9892	2.6491	15.58 ± 0.02	3.4 ± 0.13	3.3 ± 0.75	3.437 ± 0.0016	0.65 ± 0.05	0.18 ± 0.06	-	2*	-
1-8335	80.8205	2.8802	16.43 ± 0.05	1.57 ± 0.033	1.6 ± 0.11	1.553 ± 0.0039	0.59 ± 0.10	0.03 ± 0.14	-	2*	-
2-2440	81.2229	2.1180	12.39 ± 0.03	2.752 ± 0.0084	2.7 ± 0.24	2.758 ± 0.0012	0.47 ± 0.05	0.12 ± 0.04	K2	2 4	CTTS*
2-2816	81.6164	2.1579	14.07 ± 0.03	1.58 ± 0.015	1.58 ± 0.049	1.596 ± 0.0027	0.62 ± 0.05	0.22 ± 0.04	K8	2* 3 4	WTTS
2-3036	81.5441	2.1833	15.34 ± 0.02	1.41 ± 0.031	1.4 ± 0.099	-	0.64 ± 0.05	0.20 ± 0.05	M2	2* 3 4	WTTS
2-3909	81.4212	2.2803	13.22 ± 0.02	2.59 ± 0.047	2.6 ± 0.21	2.586 ± 0.0039	0.64 ± 0.05	0.18 ± 0.04	K6	2* 4	WTTS*
2-4934	81.2957	2.3953	13.94 ± 0.02	1.22 ± 0.0045	1.2 ± 0.12	1.22 ± 0.001	0.38 ± 0.04	0.11 ± 0.05	-	-	-
4-2212	82.4933	2.0667	13.38 ± 0.03	1.47 ± 0.019	1.46 ± 0.095	-	0.55 ± 0.04	0.19 ± 0.04	K6	2* 4	WTTS*
4-3265	82.3031	2.1635	14.39 ± 0.04	1.3 ± 0.01	1.27 ± 0.036	1.278 ± 0.0011	0.66 ± 0.05	0.11 ± 0.05	K6	3 4	WTTS*
4-4143	82.7278	2.2470	18.37 ± 0.38	1.24 ± 0.012	1.24 ± 0.062	1.2376 ± 0.00079	-	-	-	-	-
4-5199	82.3172	2.3434	14.70 ± 0.05	1.15 ± 0.011	1.15 ± 0.054	-	0.68 ± 0.04	0.18 ± 0.04	K9	2* 4	WTTS*
4-5493	82.5829	2.3727	16.62 ± 0.05	1.44 ± 0.026	1 ± 0.2	1.437 ± 0.0028	0.77 ± 0.07	0.16 ± 0.09	-	-	-
4-5505	82.6001	2.3733	14.78 ± 0.02	2.55 ± 0.025	2.5 ± 0.41	-	0.71 ± 0.04	0.18 ± 0.05	K9	4	-
4-5869	82.8498	2.4062	15.39 ± 0.04	1.61 ± 0.093	1.7 ± 0.22	1.623 ± 0.0023	0.67 ± 0.05	0.24 ± 0.05	M3	2* 3 4	WTTS
4-7310	82.4713	2.5371	14.59 ± 0.06	1.93 ± 0.011	1.9 ± 0.11	1.929 ± 0.0012	0.69 ± 0.05	0.21 ± 0.05	K7	2* 3 4	WTTS
4-7493	82.5171	2.5551	14.82 ± 0.04	1.1 ± 0.01	1.13 ± 0.033	1.1447 ± 0.00085	0.64 ± 0.04	0.22 ± 0.05	M4	2* 3 4	WTTS
4-11236	82.3004	2.8929	15.08 ± 0.06	1.59 ± 0.012	1.59 ± 0.097	1.582 ± 0.0029	0.66 ± 0.05	0.22 ± 0.05	M3	2* 4	WTTS*
4-11530	82.4290	2.9196	16.21 ± 0.05	2.3 ± 0.07	2.2 ± 0.23	2.313 ± 0.0072	0.67 ± 0.05	0.23 ± 0.04	M4	4	-

Table 5.8: Similar to Table 5.2 for INTERMEDIATE PERIODIC sources.

ID	RA	DEC	R_{median}	P_{2009}	P_{2010}	P_{total}	[J-H]	[H-K]	SpT	DoM	Class
-	deg	deg	mag	days	days	days	mag	mag	-	-	
0-769	80.0645	1.9327	12.64 ± 0.04	0.27697 ± 0.00025	0.2766 ± 0.0016	0.27695 ± 2.9e-05	0.27 ± 0.04	0.12 ± 0.04	-	2*	RR Lyr*
0-4097	80.2907	2.3206	17.38 ± 0.05	0.499 ± 0.0047	0.498 ± 0.022	0.49892 ± 5.5e-05	0.72 ± 0.11	0.13 ± 0.15	-	-	-
1-589	80.6156	1.9260	15.44 ± 0.01	0.347 ± 0.0041	0.342 ± 0.012	-	0.65 ± 0.04	0.25 ± 0.04	M5	2* 3 4	WTTS
1-962	81.0703	1.9748	16.33 ± 0.03	0.4037 ± 0.0027	0.403 ± 0.016	0.40367 ± 0.00019	0.64 ± 0.04	0.22 ± 0.05	M4	2* 4	WTTS*
1-2647	80.5833	2.1836	14.99 ± 0.03	0.7917 ± 0.0043	0.793 ± 0.028	0.79144 ± 0.00044	0.46 ± 0.06	0.05 ± 0.07	-	-	RR Lyr*
1-2672	80.8229	2.1874	17.32 ± 0.06	0.17405 ± 0.00051	0.174 ± 0.0027	0.17404 ± 3.1e-05	-	-	-	-	-
1-2940	80.5864	2.2248	15.63 ± 0.04	0.5157 ± 0.0075	0.522 ± 0.023	0.5155 ± 0.00068	0.61 ± 0.04	0.26 ± 0.04	M4	2* 3 4	WTTS
1-4924	81.0774	2.4770	14.58 ± 0.06	0.20303 ± 0.00023	0.20314 ± 0.00088	0.20301 ± 1.6e-05	0.30 ± 0.07	-0.00 ± 0.08	-	-	RR Lyr*
1-7315	80.6610	2.7640	14.49 ± 0.02	0.6001 ± 0.0037	0.601 ± 0.011	0.60007 ± 0.00019	0.70 ± 0.05	0.17 ± 0.04	M0	3 4	WTTS
1-8886	80.9179	2.9476	15.31 ± 0.04	0.311 ± 0.001	0.311 ± 0.0034	0.31111 ± 5.3e-05	0.58 ± 0.07	0.22 ± 0.07	-	2*	-
1-9274	80.9359	2.9915	15.89 ± 0.05	0.28785 ± 0.00086	0.2877 ± 0.0048	0.28783 ± 5.9e-05	0.08 ± 0.18	0.17 ± 0.29	-	-	RR Lyr*
2-103	81.5816	1.8610	16.36 ± 0.04	0.5516 ± 0.0065	0.557 ± 0.013	0.5541 ± 0.0039	0.00 ± 0.30	0.56 ± 0.42	-	-	-
2-1483	81.3808	2.0104	16.37 ± 0.05	0.857 ± 0.012	0.869 ± 0.039	0.8557 ± 0.0045	-	-	M5	3 4	WTTS
2-1651	81.4961	2.0307	16.30 ± 0.04	0.645 ± 0.0068	0.647 ± 0.026	0.6448 ± 0.00033	0.65 ± 0.05	0.28 ± 0.04	M5	4 10	-
2-3586	81.1974	2.2425	16.19 ± 0.08	0.6226 ± 0.0035	0.624 ± 0.028	0.62226 ± 0.00029	0.65 ± 0.05	0.26 ± 0.04	M4	2 3 4	CTTS
2-8151	81.4533	2.7521	18.49 ± 0.09	0.1702 ± 0.0025	0.17 ± 0.011	0.17013 ± 8.5e-05	-	-	-	-	-
2-8612	81.4027	2.8033	12.99 ± 0.01	0.1501 ± 0.00058	0.1503 ± 0.0026	0.14986 ± 0.00012	0.30 ± 0.06	0.14 ± 0.05	-	2*	RR Lyr*
2-9134	81.5158	2.8579	18.31 ± 0.09	0.1501 ± 0.00049	0.1503 ± 0.0022	0.15008 ± 2.8e-05	-	-	-	-	-
2-10187	81.4727	2.9647	17.97 ± 0.07	0.2996 ± 0.0023	0.3 ± 0.009	0.29942 ± 0.00011	0.66 ± 0.06	0.21 ± 0.08	M5	4	-
2-10227	81.2318	2.9694	16.23 ± 0.03	0.573 ± 0.002	0.579 ± 0.016	-	0.51 ± 0.08	0.10 ± 0.12	-	3	-
4-1416	82.7050	1.9875	14.62 ± 0.03	0.17307 ± 0.00045	0.173 ± 0.0017	0.17307 ± 2.6e-05	0.34 ± 0.07	-0.03 ± 0.08	-	-	RR Lyr*
4-2868	82.4786	2.1271	17.10 ± 0.07	0.14448 ± 0.00033	0.1446 ± 0.0013	-	0.41 ± 0.27	0.09 ± 0.40	-	-	RR Lyr*
4-3839	82.4209	2.2186	17.31 ± 0.04	0.383 ± 0.011	0.387 ± 0.024	0.3829 ± 0.00056	0.58 ± 0.06	0.25 ± 0.07	M4	3 4	WTTS
4-5441	82.5106	2.3684	15.11 ± 0.09	0.805 ± 0.0053	0.804 ± 0.012	0.805 ± 0.061	0.70 ± 0.04	0.20 ± 0.04	M3	2* 4	WTTS*
4-6632	82.6311	2.4779	17.65 ± 0.05	0.3955 ± 0.0044	0.397 ± 0.012	0.39619 ± 2.8e-05	0.59 ± 0.07	0.28 ± 0.08	M5	4	-
4-7692	82.7050	2.5761	15.93 ± 0.04	0.33 ± 0.0037	0.333 ± 0.0097	0.3308 ± 0.0016	0.70 ± 0.05	0.21 ± 0.05	M4	3 4	WTTS
4-8330	82.7473	2.6339	14.27 ± 0.05	0.6305 ± 0.0041	0.618 ± 0.027	0.63003 ± 0.00034	0.66 ± 0.04	0.26 ± 0.04	M3	2* 4	WTTS*
4-9491	82.3104	2.7387	16.83 ± 0.04	0.24 ± 0.68	0.2436 ± 0.0021	0.244 ± 0.00026	0.57 ± 0.05	0.30 ± 0.04	M4	2* 4	WTTS*
4-9736	82.6261	2.7603	14.47 ± 0.04	0.18161 ± 0.00045	0.1815 ± 0.0015	-	-	-	-	-	RR Lyr*
4-9827	82.7899	2.7673	16.73 ± 0.02	0.2261 ± 0.0012	0.226 ± 0.005	0.22601 ± 6.5e-05	0.73 ± 0.08	0.15 ± 0.09	M0	4	-

Table 5.9: Similar to Table 5.2 for SHORT PERIODIC sources.

ID	RA	DEC	R_{median}	P_{2009}	P_{2010}	P_{total}	[J-H]	[H-K]	SpT	DoM	Class
-	deg	deg	mag	days	days	days	mag	mag	-	-	
0-6959	80.3010	2.6451	14.13 ± 0.01	0.035637 ± 6.7e-05	0.035646 ± 0.00036	0.035637 ± 4e-06	0.11 ± 0.06	0.04 ± 0.08	-	-	Pulsating
0-7406	80.4627	2.6948	14.03 ± 0.01	0.06549 ± 0.0002	0.065526 ± 0.00089	0.065485 ± 1.1e-05	0.19 ± 0.04	0.11 ± 0.05	-	-	Pulsating
0-8720	80.1933	2.8399	13.90 ± 0.01	-	-	-	0.11 ± 0.05	0.14 ± 0.06	-	-	Pulsating
1-2487	80.9197	2.1635	13.49 ± 0.01	-	-	-	0.01 ± 0.05	0.04 ± 0.07	-	-	Pulsating
1-3355	80.5319	2.2767	16.64 ± 0.06	0.051155 ± 5.8e-05	0.05115 ± 0.0003	0.051152 ± 3.6e-06	-	-	-	-	Pulsating
1-3688	80.5232	2.3199	12.69 ± 0.01	-	0.07451 ± 0.0013	-	0.08 ± 0.04	0.06 ± 0.04	-	-	Pulsating
1-4164	80.6692	2.3787	18.47 ± 0.09	0.050605 ± 0.00011	0.05064 ± 0.00057	0.050601 ± 5.9e-06	-	-	-	-	Pulsating
1-4897	80.7927	2.4738	13.53 ± 0.01	-	0.03947 ± 0.0006	-	0.07 ± 0.05	0.07 ± 0.06	-	-	Pulsating
1-6922	81.0913	2.7170	14.40 ± 0.01	0.073495 ± 0.00032	0.0736 ± 0.0027	0.073492 ± 2e-05	0.15 ± 0.08	0.00 ± 0.10	-	-	Pulsating
1-7636	80.8257	2.8004	15.65 ± 0.01	0.050474 ± 0.00011	0.050482 ± 0.00092	0.050477 ± 6.3e-06	0.04 ± 0.15	0.49 ± 0.21	-	-	Pulsating
2-1459	81.6767	2.0077	17.91 ± 0.09	0.08 ± 1.5	0.078 ± 0.78	0.078348 ± 1.3e-05	0.54 ± 0.17	0.11 ± 0.23	-	2*	Pulsating
2-1520	81.4692	2.0144	13.89 ± 0.01	-	0.079 ± 0.96	-	0.15 ± 0.05	0.06 ± 0.08	-	-	Pulsating
2-2702	81.2756	2.1468	14.37 ± 0.03	0.10231 ± 7.3e-05	0.10226 ± 0.00035	0.10231 ± 8.5e-06	0.12 ± 0.07	0.04 ± 0.08	-	-	Pulsating
4-9040	82.7499	2.6993	13.73 ± 0.02	0.034 ± 0.92	0.03 ± 4.6	0.033901 ± 4e-06	0.25 ± 0.05	0.09 ± 0.06	-	-	Pulsating
5-4920	83.2714	2.3104	14.39 ± 0.02	-	-	-	0.23 ± 0.07	0.11 ± 0.08	-	-	Pulsating
5-7304	83.1424	2.5235	14.53 ± 0.03	0.07 ± 1.2	0.067 ± 0.61	0.066616 ± 5.1e-06	0.23 ± 0.07	0.01 ± 0.08	-	2*	Pulsating
5-7973	83.3122	2.5821	15.31 ± 0.01	-	-	-	-0.02 ± 0.12	0.29 ± 0.16	-	-	Pulsating
5-8312	83.4165	2.6164	17.13 ± 0.03	0.07 ± 2.7	0.07 ± 1.8	0.066619 ± 1e-05	-	-	-	-	Pulsating
5-10403	83.1818	2.8003	13.54 ± 0.01	0.03 ± 1.5	0.04 ± 8.1	0.036004 ± 4.8e-06	0.10 ± 0.05	0.07 ± 0.07	-	-	Pulsating
6-6461	80.4315	1.5076	13.51 ± 0.01	0.036 ± 0.77	0.04 ± 0.5	0.036386 ± 3.8e-06	0.08 ± 0.05	0.06 ± 0.06	-	-	Pulsating
7-3777	81.0912	1.1745	18.22 ± 0.10	0.05 ± 1.6	0.05 ± 1.1	0.052921 ± 5.5e-06	-	-	-	-	Pulsating
7-3903	80.7841	1.1882	12.97 ± 0.01	-	-	-	0.13 ± 0.05	0.04 ± 0.05	-	-	Pulsating
7-4349	81.0729	1.2405	18.88 ± 0.16	0.06 ± 1.3	0.05563 ± 0.0005	0.05563 ± 7.6e-06	-	-	-	-	Pulsating
8-6961	81.3492	1.4038	14.94 ± 0.01	0.053799 ± 3.3e-05	0.051 ± 0.78	-	0.12 ± 0.08	0.15 ± 0.13	-	-	Pulsating
9-4863	82.1755	1.1614	15.07 ± 0.01	0.06 ± 1.1	0.063 ± 0.81	0.06334 ± 1.3e-05	0.10 ± 0.09	0.22 ± 0.13	-	-	Pulsating
9-9442	82.2227	1.5930	16.42 ± 0.02	0.033592 ± 0.00014	0.034 ± 0.88	0.033601 ± 2.5e-06	-	-	-	-	Pulsating
10-4356	82.5084	1.1793	18.02 ± 0.07	0.04 ± 1.6	0.042 ± 0.98	0.042149 ± 6.3e-06	-	-	-	-	Pulsating
10-5467	82.6363	1.2969	12.29 ± 0.01	0.066 ± 0.63	0.065712 ± 0.00062	0.065636 ± 8.8e-06	0.11 ± 0.04	0.05 ± 0.05	-	2*	Pulsating
11-8926	83.0291	1.6955	15.73 ± 0.02	0.043 ± 0.97	0.04 ± 0.6	-	0.04 ± 0.16	-0.09 ± 0.28	-	-	Pulsating
11-9097	82.9956	1.7143	14.01 ± 0.01	0.032 ± 29	0.034 ± 0.52	-	0.03 ± 0.06	0.15 ± 0.08	-	-	Pulsating

Table 5.10: Similar to Table 5.2 for CTTS sources. As these sources are not periodic, we omit the 2009 and 2010 period columns, present in the other tables.

ID	RA	DEC	R_{median}	P_{2009}	P_{2010}	P_{total}	[J-H]	[H-K]	SpT	DoM	Class
-	deg	deg	mag	days	days	days	mag	mag	-	-	
1-955	81.0856	1.9740	16.76 ± 0.10	0.459 ± 0.0015	0.4586 ± 0.0072	0.459 ± 0.0001	0.70 ± 0.04	0.22 ± 0.06	M5	2* 3 4 10	CTTS
1-970	80.8231	1.9762	16.30 ± 0.05	-	-	-	0.63 ± 0.04	0.28 ± 0.04	M6	2 3 4	CTTS
1-2766	80.5919	2.2009	15.27 ± 0.02	-	-	-	0.67 ± 0.05	0.20 ± 0.05	M2	2 3 4	CTTS
1-3452	81.0759	2.2889	17.19 ± 0.32	-	-	-	1.01 ± 0.04	0.72 ± 0.05	M5	2 4	CTTS
1-4056	80.9226	2.3649	16.05 ± 0.03	0.5504 ± 0.0044	0.5512 ± 0.0091	-	0.63 ± 0.05	0.28 ± 0.04	M4	3 4	CTTS
1-5027	80.7421	2.4911	17.00 ± 0.17	-	-	-	0.69 ± 0.05	0.39 ± 0.05	M5	2 4	CTTS
2-556	81.1710	1.9108	14.17 ± 0.66	-	-	-	1.01 ± 0.05	0.74 ± 0.04	K5	1 2 4 8	CTTS
2-4707	81.4683	2.3681	-	-	-	-	0.70 ± 0.05	0.43 ± 0.05	-	3	CTTS
2-8756	81.4216	2.8184	15.80 ± 0.14	-	-	-	0.72 ± 0.06	0.51 ± 0.05	K7	2 4	CTTS
4-2045	82.6318	2.0515	14.17 ± 0.33	-	-	-	0.95 ± 0.04	0.54 ± 0.04	K9	2 4	CTTS
4-8623	82.4196	2.6610	14.25 ± 0.04	-	-	-	-	-	M4	3 4	CTTS
4-11459	82.4516	2.9132	13.37 ± 0.12	-	-	-	0.89 ± 0.04	0.68 ± 0.04	K6	2 4	CTTS
5-9166	82.8733	2.6883	16.04 ± 0.30	-	-	-	0.80 ± 0.05	0.52 ± 0.05	M5	2 3 4	CTTS
5-9411	82.9747	2.7086	17.31 ± 0.48	-	-	-	0.98 ± 0.09	0.81 ± 0.08	M0	2 4	CTTS
6-1391	80.3565	0.8865	15.57 ± 0.06	0.4195 ± 0.0012	0.4192 ± 0.0058	0.41952 ± 9.4e-05	0.64 ± 0.04	0.29 ± 0.04	M2	2* 3 4	CTTS
7-3471	80.9754	1.1370	15.82 ± 0.18	-	-	-	0.74 ± 0.05	0.46 ± 0.05	M2	2 4	CTTS
8-4545	81.2780	1.1520	15.20 ± 0.15	-	-	-	0.68 ± 0.05	0.26 ± 0.05	M4	2 3 4	CTTS
8-6391	81.2695	1.3476	15.08 ± 0.21	-	-	-	0.79 ± 0.05	0.61 ± 0.04	M8	2 4	CTTS
8-10259	81.4448	1.7250	16.07 ± 0.04	-	-	-	0.66 ± 0.05	0.29 ± 0.04	M2	1 2 4 8 10	CTTS
8-10691	81.4411	1.7638	13.26 ± 0.56	-	-	-	0.70 ± 0.06	0.41 ± 0.05	M0	1 2 4 7 8	CTTS
8-11085	81.4578	1.8000	15.88 ± 0.10	-	-	-	0.82 ± 0.07	0.55 ± 0.05	K8	1 2 4	CTTS
9-3150	82.2389	0.9953	18.58 ± 0.28	-	-	-	0.64 ± 0.06	0.37 ± 0.06	M9	4	CTTS
9-3485	81.7504	1.0270	16.33 ± 0.27	-	-	-	0.71 ± 0.04	0.37 ± 0.05	M5	2 4 9	CTTS
9-6886	82.0843	1.3545	14.81 ± 0.22	-	-	-	0.75 ± 0.04	0.25 ± 0.04	M8	2 4	CTTS
9-10304	81.7308	1.6728	15.00 ± 0.16	-	-	-	0.89 ± 0.06	0.54 ± 0.05	M0	2 4 8	CTTS
9-11604	81.9247	1.7915	16.55 ± 0.04	0.8425 ± 0.0086	0.842 ± 0.092	0.84263 ± 0.00027	0.66 ± 0.04	0.25 ± 0.04	M4	3 4	CTTS
10-2160	82.7271	0.9412	17.02 ± 0.14	-	-	-	0.54 ± 0.06	0.34 ± 0.06	M7	2 4	CTTS
10-10515	82.5516	1.8058	16.40 ± 0.25	-	-	-	0.89 ± 0.05	0.70 ± 0.04	M4	2 4	CTTS
10-10679	82.4131	1.8208	16.77 ± 0.24	-	-	-	0.69 ± 0.04	0.51 ± 0.05	M4	2 4	CTTS
11-8549	82.9925	1.6605	17.69 ± 0.25	-	-	-	0.68 ± 0.07	0.59 ± 0.07	M3	2 4	CTTS
11-10209	83.2116	1.8304	17.57 ± 0.24	-	-	-	0.65 ± 0.06	0.25 ± 0.06	M5	2 4	CTTS

Table 5.11: Similar to Table 5.10 for FLARING sources.

ID	RA	DEC	R_{median}	[J-H]	[H-K]	SpT	DoM	Class
-	deg	deg	mag	mag	mag	-	-	
0-2250	80.1528	2.1043	16.95 ± 0.02	0.62 ± 0.07	0.01 ± 0.13	-	3	-
0-2362	80.1226	2.1185	16.92 ± 0.02	0.63 ± 0.08	0.12 ± 0.13	-	3	-
0-2526	80.2117	2.1373	18.05 ± 0.05	-	-	-	3	-
0-3127	80.1824	2.2082	18.44 ± 0.08	-	-	-	3	-
0-3856	80.3564	2.2912	18.83 ± 0.11	0.68 ± 0.15	0.25 ± 0.19	M6	2* 3 4	WTTS
0-4089	80.4473	2.3193	18.53 ± 0.08	-	-	-	3	-
0-4745	80.4929	2.3927	13.96 ± 0.01	0.16 ± 0.06	0.05 ± 0.09	-	3	-
0-9382	80.4365	2.9131	18.15 ± 0.06	0.62 ± 0.18	0.06 ± 0.26	-	3	-
1-202	80.9242	1.8742	17.88 ± 0.06	0.60 ± 0.08	0.33 ± 0.07	M4	3 4 8 10	WTTS
1-781	80.9096	1.9498	16.93 ± 0.03	0.57 ± 0.07	0.26 ± 0.08	M3	3 4	WTTS
1-1131	80.8587	1.9944	19.55 ± 0.28	0.51 ± 0.14	0.53 ± 0.17	M7	3 4	WTTS
1-2529	81.0359	2.1686	17.22 ± 0.04	0.62 ± 0.06	0.26 ± 0.06	M5	2* 3 4	WTTS
1-4545	80.6813	2.4271	19.59 ± 0.26	0.63 ± 0.24	0.42 ± 0.28	M6	3 4	WTTS
1-8899	80.8497	2.9494	16.15 ± 0.03	0.62 ± 0.05	0.28 ± 0.05	M0	2* 3 4	WTTS
2-790	81.5716	1.9357	17.37 ± 0.03	0.58 ± 0.06	0.27 ± 0.07	M5	3 4 8	WTTS
2-1560	81.3063	2.0186	19.81 ± 0.24	0.68 ± 0.09	0.21 ± 0.11	M7	3 4	WTTS
2-2087	81.2931	2.0777	16.83 ± 0.03	0.65 ± 0.06	0.24 ± 0.06	M4	2* 3 4 10	WTTS
2-2350	81.4187	2.1063	18.08 ± 0.06	0.65 ± 0.18	0.42 ± 0.20	-	3	-
2-3192	81.6059	2.2031	19.95 ± 0.67	0.57 ± 0.11	0.39 ± 0.14	M6	3 4	WTTS
2-3647	81.1865	2.2491	15.74 ± 0.03	0.65 ± 0.05	0.24 ± 0.06	K8	2 3 4	CTTS*
2-4074	81.6663	2.3004	17.31 ± 0.04	0.74 ± 0.07	0.25 ± 0.07	M0	3 4	WTTS
2-4089	81.3047	2.3020	19.91 ± 0.64	0.87 ± 0.20	0.18 ± 0.23	M7	3 4	WTTS
2-5683	81.2090	2.4785	16.58 ± 0.04	0.60 ± 0.05	0.27 ± 0.07	M0	3 4	WTTS
2-5846	81.5420	2.4961	17.73 ± 0.04	-	-	-	3	-
2-5865	81.6402	2.4984	16.60 ± 0.05	0.62 ± 0.05	0.27 ± 0.05	M5	2 3 4	CTTS
2-7507	81.1924	2.6809	16.17 ± 0.02	0.60 ± 0.06	0.23 ± 0.06	M3	2* 3 4	WTTS
2-8253	81.2959	2.7638	17.23 ± 0.04	0.63 ± 0.06	0.24 ± 0.07	M3	3 4	WTTS
2-8497	81.6182	2.7907	16.82 ± 0.04	0.65 ± 0.06	0.18 ± 0.06	M4	3 4	WTTS
2-9833	81.5526	2.9309	16.54 ± 0.02	0.60 ± 0.05	0.25 ± 0.05	M4	3 4	WTTS
4-382	82.4499	1.8918	17.86 ± 0.06	0.63 ± 0.07	0.22 ± 0.10	M4	3 4	WTTS

Table 5.12: Similar to Table 5.10 for LONG TERM VARIABLE sources.

ID	RA	DEC	R_{median}	[J-H]	[H-K]	SpT	DoM	Class
-	deg	deg	mag	mag	mag	-	-	
0-39	80.1363	1.8529	16.32 ± 0.03	0.66 ± 0.06	0.13 ± 0.09	-	2*	-
0-1285	80.2216	1.9908	13.31 ± 0.01	0.21 ± 0.05	0.01 ± 0.05	-	-	-
0-2691	79.9716	2.1559	15.67 ± 0.03	0.51 ± 0.06	0.17 ± 0.08	-	-	-
0-2762	80.3542	2.1658	15.87 ± 0.04	0.68 ± 0.04	0.25 ± 0.04	M3	3 4	WTTS
0-5009	79.9782	2.4252	16.44 ± 0.07	-	-	-	-	-
0-5095	80.3053	2.4347	14.80 ± 0.03	0.68 ± 0.04	0.23 ± 0.04	M2	2* 3 4	WTTS
0-5861	80.4782	2.5220	16.03 ± 0.03	0.55 ± 0.07	0.12 ± 0.10	-	-	-
0-6131	80.1271	2.5507	15.70 ± 0.04	0.74 ± 0.04	0.21 ± 0.05	M3	3 4	WTTS
0-6192	80.0437	2.5560	16.01 ± 0.04	0.69 ± 0.05	0.18 ± 0.06	K6	2* 4	WTTS*
0-6933	79.9583	2.6419	13.74 ± 0.02	0.54 ± 0.04	0.13 ± 0.04	K5	2* 4	WTTS*
0-8583	80.1069	2.8241	15.05 ± 0.03	0.68 ± 0.06	0.29 ± 0.06	M3	2* 3 4	WTTS
0-8819	80.4577	2.8500	16.30 ± 0.08	0.64 ± 0.05	0.21 ± 0.04	M5	3 4	WTTS
0-8867	80.2696	2.8561	16.69 ± 0.04	0.61 ± 0.05	0.28 ± 0.05	M2	4	-
0-9906	80.4301	2.9645	14.37 ± 0.02	0.60 ± 0.05	0.04 ± 0.05	-	-	-
1-332	81.0094	1.8895	15.35 ± 0.05	0.68 ± 0.04	0.21 ± 0.05	M0	2* 3 4 8	WTTS
1-460	80.6589	1.9069	14.03 ± 0.02	0.73 ± 0.05	0.13 ± 0.04	M4	2* 4	WTTS*
1-732	80.8107	1.9448	16.23 ± 0.03	0.68 ± 0.05	0.26 ± 0.05	M4	2* 4	WTTS*
1-974	80.8410	1.9763	14.70 ± 0.03	0.70 ± 0.05	0.19 ± 0.04	K9	2* 4	WTTS*
1-1168	80.9265	1.9993	18.27 ± 0.07	0.88 ± 0.30	0.19 ± 0.33	-	-	-
1-1217	81.0320	2.0059	14.62 ± 0.03	0.50 ± 0.05	0.04 ± 0.06	-	2*	-
1-1884	81.0029	2.0845	16.29 ± 0.02	0.65 ± 0.05	0.29 ± 0.05	M3	3 4	WTTS
1-1981	80.7943	2.0973	15.03 ± 0.02	0.35 ± 0.06	0.19 ± 0.08	-	-	-
1-2114	80.7662	2.1161	15.94 ± 0.08	0.65 ± 0.05	0.23 ± 0.06	M3	2* 4	WTTS*
1-2730	80.5815	2.1954	12.95 ± 0.02	0.53 ± 0.04	0.17 ± 0.04	K7	2* 4	WTTS*
1-3455	80.7431	2.2891	14.27 ± 0.02	0.47 ± 0.05	0.08 ± 0.05	-	-	-
1-3601	80.6216	2.3083	12.96 ± 0.10	0.56 ± 0.04	0.09 ± 0.04	K5	2* 4	WTTS*
1-3815	81.0526	2.3359	15.15 ± 0.04	0.67 ± 0.05	0.18 ± 0.05	M4	2* 3 4	WTTS
1-4928	80.8789	2.4774	14.32 ± 0.03	0.41 ± 0.06	0.13 ± 0.06	-	-	-
2-225	81.3933	1.8723	14.42 ± 0.03	0.61 ± 0.05	0.29 ± 0.05	K9	1 2 3 4 8	CTTS*
2-361	81.5857	1.8886	14.38 ± 0.05	0.70 ± 0.05	0.15 ± 0.05	K9	2 4 8	CTTS*

Table 5.13: Similar to Table 5.10 for SHORT TERM VARIABLE sources.

ID	RA	DEC	R_{median}	[J-H]	[H-K]	SpT	DoM	Class
-	deg	deg	mag	mag	mag	-	-	
1-5777	80.5329	2.5847	14.48 ± 0.01	0.22 ± 0.05	0.07 ± 0.07	-	-	-
4-7889	82.6685	2.5932	18.17 ± 0.08	0.63 ± 0.06	0.37 ± 0.06	M6	3 4	WTTS
6-384	80.4601	0.7508	16.94 ± 0.06	0.62 ± 0.04	0.36 ± 0.04	M5	2* 4	WTTS*
7-4494	81.0301	1.2569	18.81 ± 0.30	1.13 ± 0.16	0.84 ± 0.13	M7	2 4	CTTS*
7-4657	80.9912	1.2765	14.57 ± 0.02	0.57 ± 0.05	0.28 ± 0.04	M5	2* 4	WTTS*
8-332	81.3786	0.7288	16.22 ± 0.03	0.63 ± 0.05	0.24 ± 0.05	M4	3 4	WTTS
8-1574	81.5755	0.8541	18.30 ± 0.15	0.77 ± 0.08	0.40 ± 0.09	M5	2 3 4 9	CTTS*
9-4358	81.7164	1.1100	17.14 ± 0.07	0.62 ± 0.04	0.27 ± 0.05	M6	2 4	CTTS*
9-4985	82.1989	1.1735	17.28 ± 0.05	-	-	-	-	-
10-411	82.5998	0.7520	17.96 ± 0.07	0.55 ± 0.05	0.36 ± 0.06	M6	3 4	WTTS
11-4719	83.2673	1.2369	16.64 ± 0.02	0.62 ± 0.05	0.27 ± 0.05	M6	4	-

Table 5.14: Counterparts with previous works developed in the region. We provide the PTF Orion identifier, spectral type derived by the SED fit analysis, morphological light curve classification, physical interpretation, Briceño et al. (2007) identifier, spectral type, source type and membership flag, Downes et al. (2014) identifier and spectral type, Hernández et al. (2007) identifier and disk type, and McGehee (2006) identifier and disk type. The spectral types, object classifications and membership in Briceño et al. (2007) were derived using low resolution spectroscopy with the code SPTCALSS developed by Centro de Inevestigación De Astronomía (CIDA). They classified their sources in CTTS (C) or WTTS (W). The spectral types in Downes et al. (2014) were acquired comparing sixteen spectral features typical of M stars with models of Kirkpatrick et al. (1999). Disk types in Hernández et al. (2007) were identified using optical spectra and analyzing the presence of $Li_I\lambda6707$ and Hα line in emission, and classified in class I, II and III (CI, CII and CIII), evolved (EV), transitional disks (TD) and disk excess at 8 μm (disk[8]?). Disk types in McGehee (2006) were determined using multi band variability, and classified as CTTS (C) or WTTS (W).

ID	SpT	Type	Class	Briceño et al. (2007)				Downes et al. (2014)		Hernández et al. (2007)		McGehee (2006)	
				ID	SpT	Type	Memb.	ID	SpT	ID	DType	ID	DType
0-631	M0	Long-period	WTTS	10	M0	W	1a						
1-39	K9	Long-period	WTTS							294	CIII		
1-57	M5	Long-period	Long-period					1279	M3.5				
1-202	M4	Flares	WTTS					1284	M4.5	359	CIII		
1-332	M0	Long variables	WTTS							489	CIII		
1-955	M5	CTTS	CTTS					1297	M4				
2-225	K9	Long variables	CTTS							1121	EV		
2-361	K9	Long variables	CTTS							1407	CIII		
2-556	K5	CTTS	CTTS							776	CII		
2-585	M2	Long variables	WTTS							1348	CIII		
2-592	M3	Long variables	Long variables							834	CIII		
2-790	M5	Flares	WTTS							1389	CIII		
2-1144	M5	Planet candidate	Planet candidate					1319	M4.25				
2-1651	M5	Intermediate-period	Intermediate-period					1322	M3.75				
2-2087	M4	Flares	WTTS					1311	M4				
6-3938	M2	Planet candidate	Planet candidate	11	M2	W	1a						
7-1902	K9	Long variables	WTTS	23	M0	W	1a						
7-3942	M0	Long variables	WTTS									J052410.49+011138.0	C
7-4176	M0	Long variables	Long variables									J052332.70+011317.1	W
7-4609	M3	Long variables	WTTS									J052329.50+011612.2	W
7-5148	M0	Long variables	WTTS	15	M1	W	1a						
7-5640	M0	Long variables	Long variables					1261	M1				
7-6076	M5	Flares	WTTS							84	CIII		
7-6170	M3	Long variables	WTTS							477	CIII		
7-6701	M0	Long variables	WTTS							328	CIII		
7-6928	M5	Flares	WTTS							9	CIII		
7-6989	M2	Long variables	WTTS							152	CIII		
7-7025	M3	Flares	WTTS							346	CIII		
7-7151	M0	Long variables	WTTS	20	M1	W	1a			324	CIII		
7-7265	M3	Long-period	Spot modulation							64	CIII		
7-7339	M3	Long variables	WTTS							517	CIII		
7-7351	M2	Intermediate-period	WTTS	22	M2	W	1a			481	CIII		
7-7384	M2	Long variables	WTTS	17	M3	W	1a			121	CIII		
7-7387	M5	Flares	WTTS							160	CIII		
7-7423	M4	Intermediate-period	Intermediate-period					1266	M4				
7-7580	M2	Long variables	WTTS							523	CIII		
7-7604	M3-M4	Contact	W Ursa							131	CIII		
7-7876	M2	Long variables	Long variables							613	CIII		
7-8257	M4	Flares	WTTS					1277	M3.5	347	CIII		
7-8307	M3	Long variables	WTTS					1242	M3.5	532	CIII		
7-8338	K6	Long variables	Long variables	25	M0	W	1a			542	CIII		
7-8477	K6	Long variables	Long variables							400	CIII		
7-8554	M0	Flares	WTTS							80	CIII		
7-8566	M3	Long variables	Long variables	19	M3	W	1a			293	CIII		
7-8757	M3	Intermediate-period	WTTS							158	CIII		

(Table 5.14 cont.)

ID	SpT	Type	Class	Briceño et al. (2007)				Downes et al. (2014)		Hernández et al. (2007)		McGehee (2006)	
				ID	SpT	Type	Memb.	ID	SpT	ID	DType	ID	DType
7-8937	M0	Long variables	Long variables	24	M2	W	1a			499	CIII		
8-641	K9	Long variables	Long variables									J052449.37+004537.3	W
8-1574	M5	Short variables	CTTS									J052618.12+005114.8	C
8-1991	M3	Flares	WTTS									J052542.40+005345.2	W
8-2118	K8	Flares	Flares									J052611.22+005425.9	W
8-2755	M2	Long variables	Long variables									J052532.56+005813.0	W
8-2831	M0	Long variables	WTTS									J052625.73+005835.8	W
8-3319	M6	Flares	WTTS									J052455.89+010133.8	W
8-4058	M3	Intermediate-period	Intermediate-period									J052510.11+010608.6	W
8-4598	M4	Long variables	WTTS									J052540.77+010930.4	W
8-4824	M6	Intermediate-period	WTTS					1382	M5				
8-6032	M4	Intermediate-period	WTTS					1370	M3.75				
8-6444	M0	Long-period	Spot modulation					1383	M3.5				
8-6486	M3	Long-period	WTTS					1374	M3				
8-6538	K7	Long variables	Long variables					1253	M0.5				
8-6549	M0	Long variables	WTTS					1365	M2				
8-7246	M0	Long variables	WTTS							1156	CIII		
8-7655	K8	Long variables	Long variables							1128	CIII		
8-8634	M2	Long variables	WTTS							872	CIII		
8-8647	M4	Flares	WTTS					1400	M4	1119	CIII		
8-8695	M4	Planet candidate	Planet candidate	30	M3	W	1a			962	CIII		
8-8783	M3	Long variables	WTTS							930	CIII		
8-8987	M5	Long-period	Long-period							998	CIII		
8-9020	M2	Intermediate-period	WTTS	28	M1	W	1a			833	CIII		
8-9088	M4	Planet candidate	Planet candidate					1252	M3.5	951	CIII		
8-9133	K7	Long-period	Spot modulation	38	M2	W	1a			1317	CIII		
8-9153	K7	Long-period	CTTS							1088	CIII		
8-9156	M2	Long variables	CTTS	29	M2	W	1a	1232	M3	931	disk[8]?		
8-9221	M3	Long-period	Long-period							1240	CIII		
8-9285	M3	Flares	WTTS							1396	CIII		
8-9468	M4	Intermediate-period	WTTS	39	M2	W	1a	1347	M3	1418	CIII		
8-9494	M2	Flares	WTTS							1253	CIII		
8-9596	M2	Long variables	WTTS							1548	CIII		
8-9651	K7	Long variables	Long variables							873	CIII		
8-9701	M4	Long variables	WTTS							1160	CIII		
8-9863	M2	Long-period	WTTS							1326	CIII		
8-9938	M4	Flares	WTTS					1283	M4	896	CIII		
8-9949	M4	Long variables	WTTS							1087	CIII		
8-10068	M5	Flares	WTTS							750	CIII		
8-10164	M4	Long-period	Long-period							774	CIII		
8-10259	M2	CTTS	CTTS					1330	M3.5	1200	TD		
8-10262	K9	Long variables	Long variables							1002	CIII		
8-10295	M2	Long variables	WTTS							1126	CIII		
8-10397	K9	Long-period	Long-period							948	CIII		
8-10672	M3	Flares	WTTS					1280	M3.5	736	CIII		
8-10679	M2	Long variables	Long variables							1316	CIII		
8-10691	M0	CTTS	CTTS	35	K7	C	1a			1192	CII		
8-10706	K7	Long variables	Long variables							971	CIII		
8-10837	M5	Flares	WTTS					1295	M4.75	862	CIII		
8-11011	M2	Long variables	Long variables							1235	CIII		
8-11070	M3	Long variables	WTTS							1417	CIII		
8-11126	K5	Long-period	Long-period							699	CIII		
8-11151	M4	Flares	WTTS							1029	CIII		
8-11414	M2	Long variables	WTTS	36	M3	W	1a			1222	disk[8]?		
8-11580	M4	Flares	WTTS					1328	M4.5	1217	CIII		
9-810	M5	Intermediate-period	WTTS									J052720.93+004623.1	W
9-1649	K9	Long variables	Long variables									J052725.93+005107.7	C
9-3371	M3	Intermediate-period	Intermediate-period									J052649.69+010056.2	W
9-3485	M5	CTTS	CTTS									J052700.12+010136.8	W
9-4678	M5	Intermediate-period	WTTS									J052753.54+010831.9	W
9-8309	M6	Intermediate-period	WTTS					1358	M4.5				
9-9236	K9	Long-period	WTTS							1755	CIII		
9-9556	M2	Long variables	Long variables							1658	CIII		
9-9777	M0	Long variables	WTTS	43	K5	W	1a			1716	CIII		
9-10104	M4	Flares	WTTS					1349	M4	1663	CIII		
9-10304	M0	CTTS	CTTS							1630	CII		
9-10741	K9	Intermediate-period	Intermediate-period	46	M0	W	1a			1861	CIII		
9-11024	K6	Long-period	Long-period	44	K6	W	1a			1744	CIII		
10-2854	M3	Intermediate-period	WTTS									J053026.54+010057.8	C
10-9685	M0	Long-period	Long-period	77	K6	W	1a						

Chapter 6

Outlook

6.1 Results

The main results from each chapter are summarized here.

- Chapter 2 - Five transitional disk candidates were identified in the Lupus Molecular Clouds, from a sample of 34 *Herschel* detections. Two of them, Sz91 and Sz111 had been already identified before. In fact, Sz91 was modeled (Tsukagoshi et al. 2014) and imaged (Canovas et al. 2016), finding an inner and outer disk radius of 65 and 170 AU, respectively, confirming the efficiency and robustness of our identification method based only on photometric properties. The other three were new to the literature. These five transitional disks identified yield a ∼15% incidence when compared with the overall disk population detected with *Herschel*. This transitional disk frequency comes to agreement with what would be expected, given the age of the association (1-2Myrs), when comparing it with the TD frequency VS association age diagram from Currie (2010).

- Chapter 3 - A sample of 49 *Herschel* detections in ρ Ophiuchi was analyzed, from a catalog of 261 confirmed members (Ribas et al. 2014), finding 18 transitional disk candidates by the criteria from Ribas et al. (2013), confirming several of the ones that were previously identified and discovering a new one. These 18 transitional disks yield an incidence ratio of ∼37% when compared with all the *Herschel* detections in the region. Given the age of the region (∼2-5Myr by Wilking et al. (2008), or 3.1Myr by Erickson et al. (2011)), this frequency of transitional disks is higher than what would be expected by Currie (2010) or Espaillat et al. (2014). Follow-up observations would confirm the transitional nature of these candidates, and ascertain these results.

- Chapter 4 - X-ray emissions from sources on the Orion Nebula Cluster (ONC) from the *Chandra* Orion Ultra-deep Project (COUP) was obtained, as well as accretion rates from several sources of the ONC from Manara et al. (2012) (calculated from UV excesses and Hα luminosities). After cross-matching these samples, a catalog of 431 PMS was elaborated, and an anti-correlation between the X-ray luminosities (normalized to the theoretical luminosities independent of mass) and mass accretion rates was found, similar to that found in the Taurus Molecualr Cloud (TMC) by Telleschi et al. (2007). Given the differences in the environments of the ONC and the TMC, this result could point towards an inherent property of PMS stars with ongoing accretion processes.

- Chapter 5 - From a sample of 858 variable stars identified in the region surrounding 25 Ori, 15 presented eclipsing transits consistent with a planetary scenario. We derived stellar and potentially orbital periods, and derived the radii of the potential planet based on the depth of the eclipses and the radii of the stars. Twelve were identified as low-mass PMS based on color-magnitude and color-color diagrams. Their radii suggest Jupiter-size companions, and their periods a close-in orbit (Hot Jupiters). Radial velocity measures are needed to confirm their nature. The rest of the variable sources were classified according to periodicity, light curve morphology, binarity, among other factors. These sources conformed the *PTF Orion variable catalog*. Using a Plavchan algorithm (Plavchan et al. 2008) the periodicity of the variable catalog was asserted or discarded. Finally, a membership analysis to the 25-Ori association was carried out, using different youth tracers. Approximately ∼50% of the sources showed potential membership status to the young 25-Ori association.

6.2 Future work

This thesis has focused on the identification of new sources of interest. The next sensible step would be to analyze in all their detail such sources. Here we describe some approaches to that goal.

The first and most important next step to be carried out would be to confirm or discard the planetary nature of the 15 good exoplanet host candidates on Chapter 5. Follow up spectral data would allow for radial velocity measures, which would help discard the possibility of the eclipses being caused by spots in the photosphere. Then, with that same data, the masses of the system can be derived, so as to finally identify them as planets or brown dwarfs. Given the lack of young exoplanets confirmed in the literature, these candidates would add a crucial amount of data on the formation of young exoplanetary systems.

The transitional disks identified in Chapters 2 and 3 could be modeled using an SED fitting algorithm (*Hyperion*, for example [Robitaille 2011]), similarly to Sz 91 in Tsukagoshi et al. (2014). With this process, the inner and outer radii of the disk could be measured and compared with the sizes of known planetary systems.

The *PTFO variable catalog* is a peach ripe for the taking. Several sources of interest have been identified, their youth status assessed. Here we indicate some interesting avenues to pursue.

A study of the disk population of this young region could be carried out with the

SED information in Chapter 5. Also, two *Herschel* observations of the region were obtained. Thus, a similar study than that in Chapters 2 and 3 can be carried out (in a first approximation, with *2MASS* and *WISE* photometry, some transitional disk candidates are identified in Chapter 5).

X-ray emissions can be acquired from the *XMM-Newton* observation around 25-Ori, and compare the high-energy emission of sources that had just dissipated their disk, with those younger that still have circumstelar material around them. Furthermore, this would be crucial for three of the exoplanetary candidates with X-ray counterparts, as the X-ray emissions from the host star play a key part in the evolution of the planetary atmospheres.

An analysis of the T Tauri population in the catalog would help set constraints on the evolution of the association, and make comparison with other less evolved regions.

Other approaches not related with this thesis:

- A thorough analysis of the young eclipsing binary population, complementary to that found in van Eyken et al. (2011), would give crucial data on the evolution of early binary systems, as well as in the field of circumbinary disks, and extremely important measurements of stellar radii and dynamical masses to calibrate the evolutionnary models at young ages.

- The X-ray emission excess in PMS stars is not yet fully understood. The data from the young members of the association with counterparts on the *XMM-Newton* observation could be analyzed, by studying the period-X-ray emission relations for the periodic sources.

As can be seen, even more data would be needed to tackle all these approaches, another proof in favor of these observational enterprises.

Conclusions

Here we elaborate on a summary of the outlook of this thesis, as closure. Nevertheless, each chapter presents its own conclusions.

Throughout this work we have focused on the early stages of planetary formation, a field that has just recently started to sprout with new exciting results. The imaging of potential planetary systems in formation inside their protoplanetary disks hosts (HL Tau), the detection of exoplanets around young active WTTS (V830b), or the identification of planets inside the transitional disk cavity (LkCa 15), proves that the field is entering a golden age, thanks mostly to the capabilities of state of the art instruments and telescopes (ALMA, *Kepler*), and the prospects for the future could not be more promising (James Webb Space Telescope, ELT, PLATO, ...).

In this work we have tried to link the processes of planetary formation by observing and identifying some of the different kind of objects that regulate this mechanism. As such, identifying transitional disks opens the door towards the analysis of the early stages of planetary systems. This identification is a first step, followed by the measurement of the disk properties. After their discoveries, the measurement of the properties of the disk (see Sect. 6.2) automatically follows, in particular its morphology, as well as the size of the inner hole, the composition of the outer ring, or the accretion rates, among others. The identification of the transitional disks in Lupus and Ophiucus in Chapters 2 and 3 opens the door to future analysis, in some cases already carried out. For example, the inner size of the gap of one of the detected transitional disks in Lupus, Sz 91, was measured by Tsukagoshi et al. (2014). With a size of $\sim$65 AU, this system could not only harbor a young exoplanet inside, but a complete planetary system (using the Solar System for reference, $\sim$100AU). Thus, the objects identified in this work are perfect candidates for further follow-up.

This last feature, the accretion rate from the disk to the star, is also intimately related to the evolution of the disk and potential planetary system. The young protoplanetary disk harboring stars accretes gas from it, a process that contributes to the emission of highly energetic photons, in the form of X-rays or UV. This emissions, in turn, interact with the disk, modifying its evolution. This creates a circular relation, between disk-star-X-ray-disk, which effects are crucial for the evolution of an early exoplanetary system: these X-ray photons play an essential role in the evolution of early planetary atmospheres. Analyzing these interactions and the processes that rule them, then, is of the utmost importance on the study of early exoplanet atmospheres. The accretion-X-ray relation derived in Chapter 4 demonstrates how the environment plays a key role in many of the processes of

the evolution of early stellar systems, but not in all of them. The anti-correlation between X-ray and mass accretion rate would be counter-intuitive at first sight, given the fact that the accreted gas produces X-ray emission as it collides with the stellar photosphere: the more the gas accreted, the more the X-ray. But that is not the case. One possibility, as stated in Chapter 4, is that the stream of gas that is producing the X-ray emission is the one blocking it afterwards. This could play a crucial role in the evolution of the potential planetary atmospheres: an orbiting exoplanet in a system that is showing ongoing accretion processes could be shielded, by the accreted stream, of the high energetic photons from the early processes of star formation, and thus, its atmosphere would evolve 'protected' from these X-ray emissions. Thus, it is key to find young exoplanet candidates in PMSs with observable accretion processes.

The last step on the analysis of young planet formation is to actually identify such young objects. The astonishing number of confirmed exoplanets identified these last years, although key in the understanding of our place in the universe, is not totally suitable for explaining the early formation and evolution of these systems, due to a simple reason: over time, the planetary systems evolve and change their configuration dramatically (migration, ejections, bombardment, interactions with nearby stellar neighbors,...). After not so a long time (few tens of Myrs), any tracer of the early stages of the System are not quite directly observable. Thus, identifying evolved exoplanetary systems ($\leq$1Gyr old) can not help us in the study of the early formation of exoplanets. Looking for these objects in young star forming-regions is key for our field of study. And there is where Chapter 5 enters into play. The 15 exoplanet host candidates identified in the region are the last piece of the puzzle we have been constructing during this thesis. Their planetary nature should be confirmed first, but if we assume they are, indeed, exoplanets, and not brown dwarf binary systems, or spots in the photosphere (as discussed in Chapter 5), their close-in orbits would suggest a Type II migration scenario. They would be Hot Jupiters, with large radii and close to their host stars, in some cases even in the process of evaporating. Given the age of the association, and the lack of infrared excess pointing to the presence of a cirumstellar disk around the host stars, the most plausible scenario could be a disk-planet interaction during the $\sim$10 Myr age of the association which ended up pushing the candidates closer to their stellar hosts. But these close orbits open one question: have these disk systems go trough a transitional phase? How would a planet migrate so close to the star if there is not a disk close to the host to be able to displace it? In these cases, a possible scenario would be

a late transitional phase, once the planet has migrated to that position, or even a 'planetary triggered' transitional phase (Alexander and Armitage 2009).

Several objects, key in the process of stellar and planetary formation have been identified, more data to be taken into account in the overall picture. If their nature were to be confirmed, they would point towards some possible scenarios in the field of planet formation. But as stated before, they are just the first step. Now, more data is needed about them, to confirm their nature, to establish more constraints on the theories. Their discovery and identification has opened the door, show us the way.

Now we just need to follow it.

Conclusiones

A continuación se presenta un resumen de esta tesis, como cierre. No obstante, cada capítulo presenta sus propias conclusiones.

A lo largo de este trabajo nos hemos centrado en las primeras etapas de la formación planetaria, un campo que recientemente ha empezado a surgir con nuevos y emocionantes resultados. La obtención de imágenes de potenciales sistemas planetarios en formación dentro de sus discos protoplanetarios anfitriones (HL Tau), la detección de exoplanetas alrededor de WTTS jóvenes y activos (V830b) o la identificación de planetas dentro de las cavidades de discos de transición (LkCa 15) demuestran que el campo está entrando en una época dorada, gracias sobre todo a las capacidades de instrumentos y telescopios punteros (ALMA, Kepler), y las perspectivas para el futuro no podrían ser más prometedoras (Telescopio Espacial James Webb, ELT, PLATO, ...).

En este trabajo hemos tratado de vincular los procesos de formación planetaria observando e identificando algunos de los diferentes tipos de objetos que regulan este mecanismo. Como tal, la identificación de los discos de transición abre la puerta al análisis de las primeras etapas de los sistemas planetarios. Esta identificación es el primer paso, seguido de la medida de las propiedades del disco. Una vez descubiertos, el siguiente paso es la medición de las propiedades del disco (véase la sección 6.3), en particular su morfología, así como el tamaño del agujero interior, la composición del anillo exterior o las tasas de acreción, entre otros. La identificación de los discos de transición en Lupus y Ophiucus en los Capítulos 2 y 3 abre la puerta a futuros análisis, en algunos casos ya realizados. Por ejemplo, el tamaño interno del agujero de uno de los discos de transición detectados en Lupus, Sz 91, fue medido por Tsukagoshi et al. (2014). Con un tamaño de $\sim$ 65 AU, este sistema podría no sólo albergar un joven exoplaneta en su interior, sino un sistema planetario completo (usando el Sistema Solar como referencia, $\sim$100AU). Por lo tanto, los objetos identificados en este trabajo son perfectos candidatos para seguimiento adicional.

Esta última característica, la tasa de acreción desde el disco a la estrella, está a su vez íntimamente relacionada con la evolución del disco y del potencial sistema planetario. La estrella albergando el joven disco protoplanetario acreta gas de él, un proceso que contribuye a la emisión de fotones altamente energéticos, en forma de rayos X o UV. Estas emisiones, a su vez, interactúan con el disco, modificando su evolución. Esto crea una relación circular entre disco-estrella-rayos-x-disco, cuyos efectos son cruciales para la evolución del joven sistema exoplanetario: estos fotones de rayos X desempeñan un papel esencial en la evolución de las atmósferas plane-

tarias primordiales. Analizar estas interacciones y los procesos que las gobiernan, entonces, es de suma importancia en el estudio de dichas atmósferas exoplanetas. La relación entre acreción y rayos X obtenida en el Capítulo 4 demuestra cómo el medio ambiente desempeña un papel clave en muchos de los procesos de la evolución de los primeros sistemas estelares, pero no en todos ellos. La anti-correlación entre la tasa de rayos X y la tasa de acreción es contraintuitiva a primera vista, dado el hecho de que el gas acretado produce emisión de rayos X cuando interacciona con la fotosfera estelar: cuanto más se acrete gas, más rayos X son emitidos. Pero ese no es el caso. Una posibilidad, como se indica en el Capítulo 4, es que la corriente de gas que está produciendo la emisión de rayos X es la que la bloquea después. Esto podría jugar un papel crucial en la evolución de las potenciales atmósferas planetarias: un exoplaneta en órbita en un sistema que está mostrando procesos de acreción en curso podría estar siendo protegido por la corriente de acreción de los fotones energéticos de los primeros procesos de la formación estelar y, por lo tanto, su atmósfera evolucionaría "protegida" de estas emisiones de rayos X. Por lo tanto, encontrar candidatos de exoplanetas jóvenes con procesos de acreción observables es clave.

El último paso en el análisis de la formación del joven planeta es identificar estos objetos jóvenes. El asombroso número de exoplanetas identificados estos últimos años, aunque clave en la comprensión de nuestro lugar en el universo, no es totalmente adecuado para explicar la formación y evolución temprana de estos sistemas, debido a una simple razón: a lo largo del tiempo, los sistemas planetarios evolucionan y cambian su configuración dramáticamente (migración, expulsiones, bombardeo, interacciones con vecinos estelares cercanos, ...). Después de no mucho tiempo (pocas decenas de Myrs), cualquier trazador de las primeras etapas del sistema no es observable directamente. Por ello, la identificación de sistemas exoplanetarios evolucionados ($\leq$1Gyr de edad) no puede ayudarnos en el estudio de la formación temprana de exoplanetas. La búsqueda de estos objetos en la regiones de formación de estrellas jóvenes es clave para nuestro campo de estudio. Y allí es donde el Capítulo 5 entra en juego. Los 15 candidateos a exoplanetas anfitriones identificados en la región son la última pieza del rompecabezas que hemos estado construyendo durante esta tesis. Su naturaleza planetaria debe ser confirmada en primer lugar, pero si asumimos que son, de hecho, exoplanetas y no sistemas binarios de enanas marrones, o manchas en la fotosfera (como se discutió en el Capítulo 5), sus órbitas cercanas sugerirían una migración de Tipo II. Serían Júpiter Calientes, con radios grandes y cercanos a sus estrellas anfitrionas, en algunos casos incluso

en proceso de evaporación. Dada la edad de la asociación y la ausencia de excesos infrarrojos, que apuntaría a la presencia de un disco cirumestelar alrededor de las estrellas anfitrionas, el escenario más plausible podría ser una interacción disco-planeta durante la edad de ∼10 Myr de la asociación, que terminó empujando a los candidatos más cerca de sus estrellas anfitrionas. Pero estas órbitas cercanas abren una pregunta: ¿han pasado estos sistemas por una fase de transición? ¿Cómo migraría un planeta tan cerca de la estrella si no hay un disco cerca de la anfitriona para poder desplazarlo? En estos casos, un posible escenario sería una fase de transición tardía, una vez que el planeta haya migrado a esa posición, o incluso una fase de transición desencadenada por el propio planeta Alexander and Armitage 2009.

Se han identificado varios objetos, clave en el proceso de formación estelar y planetaria, constituyendo más datos a tener en cuenta en la imagen general. Si su naturaleza es confirmada, señalarían hacia algunos posibles escenarios en el campo de la formación planetaria. Pero como se ha indicado antes, son sólo el primer paso. Ahora son necesarios más datos, para confirmar su naturaleza, para establecer más restricciones sobre las teorías. Su descubrimiento e identificación han abierto la puerta, nos muestran el camino.

Ahora sólo tenemos que seguirlo.

Chapter 7

Appendix

A&A 578, A23 (2015)
DOI: 10.1051/0004-6361/201424073

Astronomy & Astrophysics

Identification of new transitional disk candidates in Lupus with *Herschel*⋆,⋆⋆

I. Bustamante[1,2,3], B. Merín[1], Á. Ribas[1,2,3], H. Bouy[2], T. Prusti[4], G. L. Pilbratt[4], and Ph. André[5]

[1] European Space Astronomy Centre (ESA), PO Box, 78, 28691 Villanueva de la Cañada, Madrid, Spain
e-mail: ibustamante@cab.inta-csic.es
[2] Centro de Astrobiología, INTA-CSIC, PO Box – Apdo. de correos 78, 28691 Villanueva de la Cañada Madrid, Spain
[3] ISDEFE – ESAC, PO Box 78, 28691 Villanueva de la Cañada, Madrid, Spain
[4] ESA Science Support Office, ESTEC/SRE-S, Keplerlaan 1, 2201 AZ Noordwijk, The Netherlands
[5] Laboratoire AIM Paris, Saclay, CEA/DSM, CNRS, Université Paris Diderot, IRFU, Service d'Astrophysique, Centre d'Études de Saclay, Orme des Merisiers, 91191 Gif-sur-Yvette, France

Received 25 April 2014 / Accepted 15 January 2015

ABSTRACT

Context. New data from the *Herschel* Space Observatory are broadening our understanding of the physics and evolution of the outer regions of protoplanetary disks in star-forming regions. In particular they prove to be useful for identifying transitional disk candidates.
Aims. The goals of this work are to complement the detections of disks and the identification of transitional disk candidates in the Lupus clouds with data from the *Herschel* Gould Belt Survey.
Methods. We extracted photometry at 70, 100, 160, 250, 350, and 500 μm of all spectroscopically confirmed Class II members previously identified in the Lupus regions and analyzed their updated spectral energy distributions.
Results. We have detected 34 young disks in Lupus in at least one *Herschel* band, from an initial sample of 123 known members in the observed fields. Using recently defined criteria, we have identified five transitional disk candidates in the region. Three of them are new to the literature. Their PACS-70 μm fluxes are systematically higher than those of normal T Tauri stars in the same associations, as already found in T Cha and in the transitional disks in the Chamaeleon molecular cloud.
Conclusions. *Herschel* efficiently complements mid-infrared surveys for identifying transitional disk candidates and confirms that these objects seem to have substantially different outer disks than the T Tauri stars in the same molecular clouds.

Key words. stars: pre-main sequence – protoplanetary disks – planetary systems

1. Introduction

Transitional disks link the studies of planet formation and disk evolution around young stars. They are protoplanetary disks around young stars, optically thick and gas rich, with astronomical unit-scale inner disk clearings or radial gaps evident in their spectral energy distributions (SEDs). They lack excess emission at short-mid infrared (typically around 8–12 μm), but present considerable emission at longer wavelengths (Muzerolle et al. 2010). Since their discovery by Strom et al. (1989) with IRAS data, the *Spitzer* Space Telescope (Werner et al. 2004) allowed the identification of a much larger population of these objects (Cieza et al. 2010; Merín et al. 2010; Espaillat et al. 2014). It was possible to use the mid-infrared data to make good estimates of the dust distribution in the inner few astronomical units of the disks around T Tauri stars in nearby star-forming regions (e.g. Calvet et al. 2005; Lada et al. 2006).

The *Herschel* Space Observatory (Pilbratt et al. 2010) grants us access to the outer disk region of these objects. Recent studies suggest that the outer disks, as detected in far-infrared emission, undergo substantial transformations in the transitional disk phase (Cieza et al. 2011; Ribas et al. 2013). However, *Herschel* data are still lacking for most known transitional disks.

The main objective of this article is to revisit and extend our knowledge of known Class II objects in the Lupus dark clouds, and to identify transitional disk candidates in the region using *Herschel* photometry, complemented with photometry from previous studies from the optical to the mid-infrared. With *Herschel* we have the opportunity to study objects with large inner holes, reaching the farthest regions of their disks that *Spitzer* was unable to access with the required sensitivity (IRAC and IRS had different wavelength ranges, 3.5–8.0 μm and 5–35 μm, respectively, and the sensitivity of MIPS, with pass bands between 24 and 160 μm, was limited). Therefore, we are not only able to study the outer regions of known transitional disks, but also to detect new candidates, with larger cavities and outer disks.

This work is organized as follows. Section 2 describes the *Herschel* observations and data reduction and the procedure applied to identify and extract the fluxes for the known objects. In Sect. 3 we identify new transitional disk candidates, describe the procedure to build the SEDs, and discuss some objects with certain peculiarities. In Sect. 4 we discuss the properties of the newly found transitional disk candidates, and in Sect. 5 we present the conclusions of this work.

2. Observations and data reduction

The Lupus dark clouds were observed by *Herschel* as part of the *Herschel* Gould Belt Survey (HGBS; André et al. 2010). It is one of the star-forming regions located within 150 to 200 pc

⋆ *Herschel* is an ESA space observatory with science instruments provided by European-led Principal Investigator consortia and with important participation from NASA.
⋆⋆ Tables 5–7 and Figs. 3 and 4 are available in electronic form at http://www.aanda.org

from the Sun and has a mean age of a few Myr (see Comerón 2008, for a review of the region). It contains four main regions, with one of them, Lupus III, being a rich T Tauri association. Located in the Scorpius-Centaurus OB association, the massive stars in the region are likely to have played a significant role in its evolution.

By employing the PACS (Poglitsch et al. 2010) and SPIRE (Griffin et al. 2010) photometers in parallel mode, *Herschel* has the capability for large scale mapping of star-forming regions in the far-infrared range. Early *Herschel* observations of Lupus from the HGBS were already published by Rygl et al. (2013), where the observing strategy and main results are described.

We produced our maps using Scanamorphos (Roussel 2012) version 21.0 for the PACS maps and version 18.0 for the SPIRE maps. The identification numbers of the Lupus *Herschel* parallel mode observations processed for this work are (1342-)189880, 189881, 203070, 2203071, 2203087, 2203088, 2213182, and 2213183 from program KPGT_pandre_1. The observations were made in parallel mode for 70, 160, 250, 350, and 500 μm, and in prime mode for 100 μm (Rygl et al. 2013), which is why some of the sources do not have images at 100 μm in Fig. 4.

A complete census of the sources detected with *Herschel* will be published by the HGBS consortium in an upcoming paper (Benedettini et al., in prep.).

2.1. Point source photometry

Our first objective was to detect and classify sources in the images obtained with PACS and SPIRE. We used coordinates of spectroscopically confirmed Class II members from different sources, compiling a list of 217 targets. This compilation was developed by Ribas et al. (2014), and these objects were selected for having known extinction values and spectral types from optical spectroscopy. Of this sample of 217 objects, only 123 are found in the fields observed by *Herschel*.

We applied the sourceExtractorSussextractor algorithm in our maps, with the *Herschel* interactive processing environment (HIPE), version 12.0, using a detection threshold of $S/N > 3$. We then cross-matched the resulting list of detected objects with our pre-selected targets, using a search radius between 5″ and 10″. We selected only those objects with detections in PACS. After this process, we found 37 objects with at least one detection in one PACS band, 35 in the 70 μm maps, and 2 in the 100 μm maps. We then validated all of them by visual inspection. This way we were able to double-check our detections. The background emission becomes more significant at longer wavelengths, where detections are in general less frequent, or false detections appear, due to bright filaments and ridges. This is the reason why we selected only PACS-detected objects. The combination of quantitative and qualitative analysis was essential to produce reliable detections and photometry. After this process we discarded four objects as not having clear detections in the maps and added two objects that were found by visual inspection. They are flagged in Table 5. After this process, 35 objects in the list had one clean detection in at least one *Herschel* PACS or SPIRE band.

We applied the sourceExtractorDaophot algorithm to extract the photometry for PACS, and the annularSkyAperturePhotometry task for SPIRE. All point-source fluxes were aperture corrected with the recommended aperture corrections for both instruments (see the PACS photometer point spread function technical note from April 2012, and Sect. 6.7.1 of the SPIRE Data Reduction Guide of HIPE 12.0). Table 1 shows the set of aperture, inner, and outer sky radii for each *Herschel* band, as well as the corresponding aperture corrections.

Table 1. Aperture, inner, and outer radii used in the photometry extraction process for each band, with their corresponding aperture corrections.

Band	$R_{\rm aperture}$ (″)	$R_{\rm inner}$ (″)	$R_{\rm outer}$ (″)	Correction
PACS70	6	25	35	1.5711
PACS100	6	25	35	1.6804
PACS160	12	25	35	1.4850
SPIRE250	22	60	90	1.2796
SPIRE350	30	60	90	1.2396
SPIRE500	42	60	90	1.2937

Table 2. Sensitivity limits for each *Herschel* band in parallel mode at 60″/s, as stated in the PACS/SPIRE Parallel Mode Observers' Manual.

Filter	Sensitivity (mJy/beam)
PACS 70	21.0
PACS 100	24.7
PACS 160	47.0
SPIRE 250	12.6
SPIRE 350	10.5
SPIRE 500	15.0

Table 2 shows the sensitivity limit for each *Herschel* band, as stated in the SPIRE/PACS Parallel Mode Observers' Manual (Sect. 2.3). The values correspond to a nominal scan direction and a scan speed of 60″/s.

Upper limits for non-detections were derived by adding scaled synthetic point spread functions (PSFs) at the expected position of the sources until the sussExtractor detection algorithm did not recover them. In most cases visual inspection was applied. The calibration errors for PACS and SPIRE are 5% and 7% (as stated in their observer manuals), respectively. To ensure consistency with Ribas et al. (2013) we chose a more conservative estimation, 20% for SPIRE as error values, taking into account that the background emission becomes increasingly stronger at longer wavelengths. In the case of PACS, after comparing several photometric extraction algorithms (sussExtractor, Daophot, annularSkyAperturePhotometry, and Hyper, Traficante et al. 2015), and extraction apertures with the MIPS70 fluxes of a subsample of clean sources, we selected a conservative error value of 25% of the flux to account for the different flux values obtained. Table 5 gives the stellar parameters of these detected sources as given in the literature, and Table 6 presents their *Herschel* point source fluxes and upper limits. As stated before, at least one point source was detected for at least one wavelength of the *Herschel* instruments for all objects in Table 6 (see Fig. 4).

We then looked for bright *Spitzer* 24 μm and 70 μm sources around the targets to check for possible contamination from other nearby mid-infrared sources. We used a radius of 42″, as this was the value we used for the largest wavelength band when extracting the *Herschel* photometry (which corresponds to SPIRE 500 μm). The results of this analysis are shown in Tables 3 and 4.

In the cases where MIPS70 sources were found near our sources we inspected the PACS70 images of the targets. Except for sources Sz65, Sz66, Sz103, Sz104, and 2MASSJ1608537 (as explained below), we did not find evidence of the presence of extra sources inside the matching radius (see Fig. 4). This means

Table 3. Targets with possible contamination within the used apertures in MIPS24.

Object	F_{source}/F_{aper}	N	Companion distance ($''$)	Band
Sz65[1]	0.4	1	6.5	PACS70
Sz66[1]	2.9	1	6.2	PACS70
Sz100[3]	0.2	1	23.4	SPIRE350
Sz103[2]	0.8	10	41.2	SPIRE500
Sz104[2]	2.7	10	36.4	SPIRE500
Sz108B	1.4	3	38.8	SPIRE500
2MASSJ1608537*	9.3	1	6.9	PACS70
Sz112	0.5	4	31.9	SPIRE500
SSTc2dJ161029.4-392215[3]	0.1	2	7.4	PACS70
SSTc2dJ160002.4-422216[3]	0.4	2	39.8	SPIRE500
SSTc2dJ160111.6-413730[3]	0.2	1	24.2	SPIRE350

Notes. The second column shows the fraction of total MIPS24 flux in the aperture with that of the target. (1) The MIPS24 contamination affecting Sz65 is caused by Sz66, and vice versa, as can be seen in Fig. 4. This is taken into account in the photometry analysis. (2) The MIPS24 contamination affecting Sz103 is caused by Sz104, and vice versa, as can be seen in Fig. 4. This is taken into account in the photometry analysis. (3) Objects with sufficiently low contamination from nearby sources so as to not affect our *Herschel* measurements. (*) This is the only object that has been removed from the list of detected sources because its *Herschel* photometry cannot be unequivocally associated with it.

Table 4. Same as Table 3, but with MIPS70 possible contamination.

Object	F_{source}/F_{aper}	N	Companion distance ($''$)	Band
Sz66	468.^{mJy}	1	6.2	PACS70
Sz98[2]	0.2	1	26.3	SPIRE350
Sz100[2]	0.7	1	32.3	SPIRE500
Sz103[1]	1.4	1	23.2	SPIRE350
Sz104[1]	0.7	1	23.2	SPIRE350
Sz108B	212.^{mJy}	1	9.7	PACS70
2MASSJ1608537*	119.0^{mJy}	1	6.9	PACS70
Sz112[2]	0.7	1	28.6	SPIRE350

Notes. (1) The MIPS70 contamination in Sz103 is caused by Sz104, and vice versa, as can be seen in Fig. 4. This is taken into account in the photometry analysis. (2) Objects with sufficiently low contamination from nearby sources so as to not affect our *Herschel* measurements. (*) This is the only object that has been removed from the list of detected sources, because its *Herschel* photometry cannot be unequivocally associated with it. (mJy) In these cases the MIPS photometry of the target was not available, but that of the companions was. Therefore, we present the actual flux of the objects inside the search radius instead of the percentage.

that *Herschel* did not detect them, so we assume that the full contribution to the flux measured at PACS70 comes from our target sources, and not from contaminants. In Table 4 we maintain all the sources with possible contamination for reference.

Objects Sz65 and Sz66 form a pair, as is explained in Sect. 3.3.6, and this is taken into account in their photometry extraction. The MIPS excesses seen for objects Sz103 are associated with object Sz104, and vice versa. We only flagged objects with potential contaminations in case they were detected (see Table 6). When they are not detected and upper limits are calculated instead, we do not take into account the possible contaminations.

The nearby source near object 2MASSJ1608537 presented significantly larger MIPS24 and MIPS70 fluxes than our target. In this case, we concluded that the infrared excesses measured in the *Herschel* image corresponded to this other object instead of our target, and thus we discarded object 2MASSJ1608537 because its *Herschel* photometry could not be unequivocally associated with it. The other object is a known young stellar object (YSO) candidate, SSTc2d J160853.2-391440. It is probably another member of the Lupus region, yet not confirmed spectroscopically and therefore not included in our study.

In other cases other contaminant sources were found, but with sufficiently weaker MIPS24 and MIPS70 fluxes so as not to affect our measurements. These sources are marked in Table 3. In these cases we assumed that the *Herschel* fluxes measured correspond to our targets as the major contributors.

Another interesting object is Sz108B, which presents two possible contaminants that could affect its photometry. The one farthest away, at 38.8$''$, has larger MIPS24 flux. The closest one, at 9.7$''$, has a higher MIPS70 flux. Thus, the *Herschel* photometry of Sz108B could be contaminated by the closest one and therefore it is flagged as unreliable in Table 4.

After this analysis, our final set of sources decreased to 34. We maintain the image of object 2MASSJ1608537 in Fig. 4 for completeness.

3. Results

3.1. Identification of transitional disk candidates

To identify transitional disk candidates we applied the procedure developed in Ribas et al. (2013), which defines a transitional disk candidate as having $\alpha_{K-12} < 0$ and $\alpha_{12-70} > 0$, where $\alpha_{\lambda_1-\lambda_2}$ is defined as $\alpha_{\lambda_1-\lambda_2} = \frac{\log(\lambda_1 F_{\lambda_1})-\log(\lambda_2 F_{\lambda_2})}{\log(\lambda_1)-\log(\lambda_2)}$, and λ is measured in μm and F_λ in erg s^{-1} cm^{-2}.

The K-band flux comes from 2MASS (Skrutskie et al. 2006), the 12 μm flux from WISE and the 70 μm flux from PACS. Some exceptions to this rule were applied when these fluxes

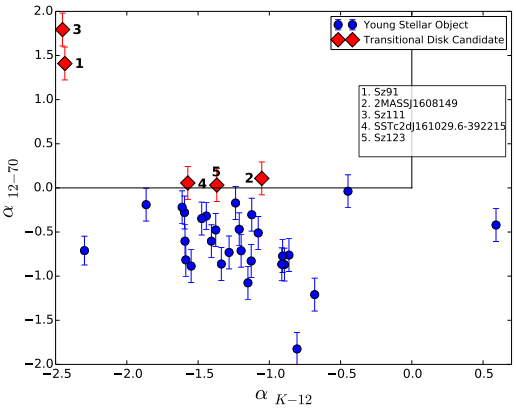

Fig. 1. Identification of transitional disk candidates applying the color criteria from Ribas et al. (2013) to the Lupus *Herschel* data.

were unavailable for certain objects; for example, Sz95 has no flux at 70 μm, so we used PACS100 μm instead. We did the same for 2MASS J1608149. An exceptional case is object SSTc2dJ160111.6-413730, discussed later in Sect. 3.3.5, as no PACS flux was available, and therefore could not be classified.

With this procedure we detected five objects that satisfy the transitional disk candidate criteria: SSTc2dJ161029.6-392215, Sz91, Sz111, Sz123, and 2MASS J1608149. In Fig. 1 we show the objects that fulfilled our selection criteria. Objects Sz91 and Sz111 were previously known transitional disks from *Spitzer* data (Merín et al. 2008), and they occupy a different region in the diagram than the others. They present little to no excess at 12 μm and a steep rise between 12 and 70 μm in their SEDs (see Fig. 2). This could be indicative of a large cavity in both cases, mostly empty of small dust grains. In the case of Sz91, a resolved image of this inner hole has already been obtained in the submillimeter with SMA (Tsukagoshi et al. 2014), being one of the largest imaged so far (~65 AU) in a T Tauri disk. Sz111 is likely to have a similarly large and empty cavity.

The rest of the objects present excesses at intermediate wavelengths, and fulfill our color criteria (see Fig. 2 for a representation of their SEDs). Object 2MASS J1608149 is a special case, as is explained in Sect. 3.3.3.

In Fig. 1 three additional objects present error bars falling in the transitional disk detection criteria: SSTc2dJ160703.9-391112, RXJ1608.6-3922, and Sz108B. Their SEDs present far-infrared excesses, but mid-infrared ones as well. As they do not strictly fulfill our selection criteria, they are not to be considered transitional disk candidates in this work, yet they deserve attention.

Analysis of the remaining sample of T Tauris in the Lupus regions is outside the scope of this work, although special cases are discussed in some detail in Sect. 3.3.

3.2. Spectral energy distributions

To construct the SEDs we used ancillary data from ground-based optical, near-infrared, *Spitzer* and WISE data (Mortier et al. 2011; Comerón 2008; Allen et al. 2007; Krautter et al. 1997). These photometric data provide continuous wavelength coverage between 0.4 and 500 μm. Figures 2 and 3 show the SEDs of the transitional disk candidates and the rest of the detected objects. We used the interstellar extinction law of Weingartner & Draine (2001). The A_V values were extracted from Mortier et al. (2011) and Merín et al. (2008), except in seven sources, identified with an asterisk in Table 6, for which we derived the values from the observed optical and near-infrared photometry and their spectral types.

We inspected all the images in 2MASS band J of the entire sample of detected objects. All of them were confirmed as point sources except those marked in Table 5 with a j, where minor extended emission cannot be discarded.

3.3. Individual objects of interest

3.3.1. Sz91 and Sz111

Sz91 and Sz111 had been previously identified as potential transitional disks based on *Spitzer* data in Merín et al. (2008) and have large Hα equivalent widths of 95.9 and 145.2 Å (Hughes et al. 1994), which indicate youth and active gas accretion to the stars.

The optical images of Sz91 reveal a known companion at approximately 8″ (Ghez et al. 1997), which corresponds to a distance of 1200–1600 AU from the star. However, the centroids of all the *Herschel* detected sources match the coordinates of the primary source, Sz91 (see Fig. 4), so we assume no contribution from the companion to the measured fluxes.

3.3.2. SSTc2dJ161029.6-392215 and Sz123

Objects SSTc2dJ161029.6-392215 and Sz123 present SEDs characteristic of transitional disks,[moved comma] but with narrow gaps instead of the wide ones found at Sz91 and Sz111. They also present small excesses at near-infrared wavelengths (3–10 μm), that could signal the presence of an inner optically thick disk.

3.3.3. 2MASS J1608149

Since object 2MASS J1608149 was not detected on the PACS70 band, we used the PACS100 band to classify it. The target then fulfilled the transitional disk detection criteria. As its SED shows 2, the *Herschel* far-infrared excess is not significant enough to classify the object as a transitional disk with absolute certainty. A further analysis including modeling could reveal the true nature of this object. Nevertheless, in this work we assume that object 2MASS J1608149 is a transitional disk candidate.

3.3.4. Sz68

Figure 4 shows an extended feature at all wavelengths to the north of the Sz68 object. This is an already known Herbig-Haro object driven by Sz68 (Moreno-Corral et al. 1995). Interestingly, its emission dominates at wavelengths longer than 100 μm, which probably contaminates the SED of this object with unrelated flux to the star itself. A similar effect was discovered around the star T54 in Chamaeleon I (Matrà et al. 2012), which had been erroneously classified as a transitional disk owing to nearby extended emission (see also Lestrade et al. 2012).

3.3.5. SSTc2dJ160111.6-413730

SSTc2dJ160111.6-413730 has a very peculiar SED (see Fig. 3) with no excess at any wavelengths between optical and 160 μm, but substantial potential excesses at 250–500 μm associated with a clear point source in the images (see Fig. 4). The low 70 μm

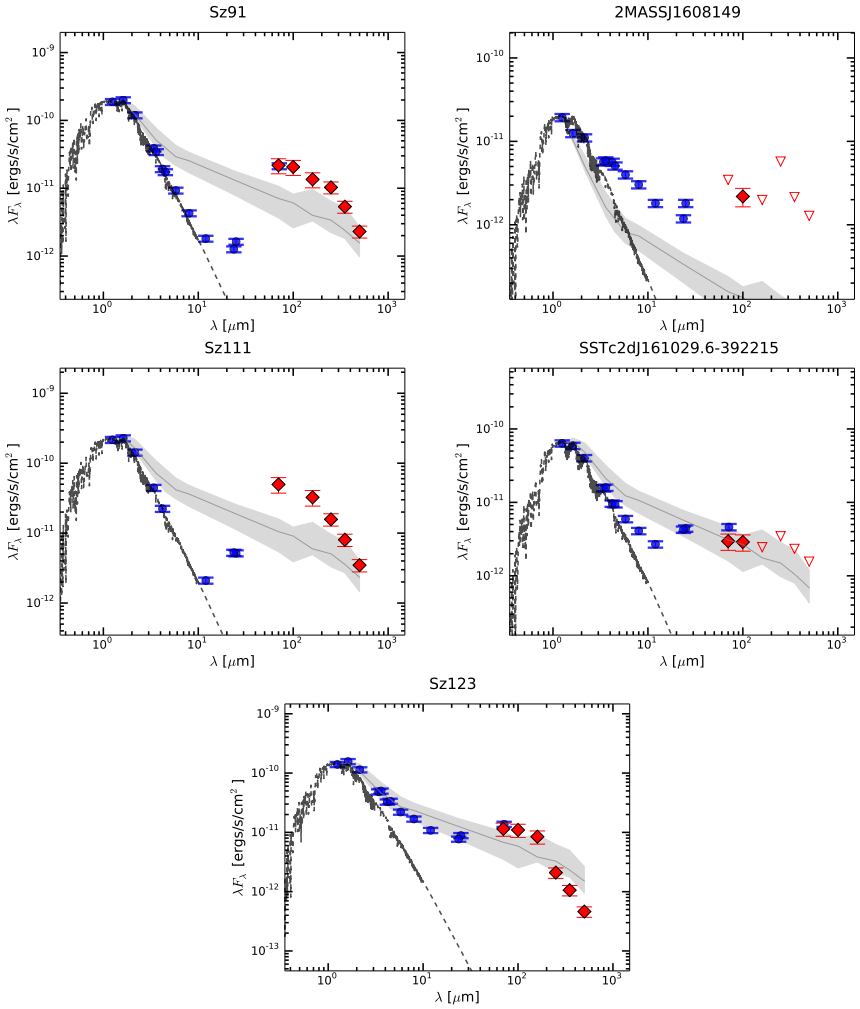

Fig. 2. SEDs of the five transitional disk candidates identified with *Herschel*. Blue dots represent the dereddened ancillary data from the literature from previous studies. The red diamonds are the clear detections with *Herschel*, and the red triangles the upper limits wherever no clear detection in the maps was found. The gray solid line is the median SED from the Lupus sample of the 29 non-transitional disks in the region, and the gray shaded area the first and fourth quartiles. See Table 7 for more information. The dashed lines are the photospheric NextGen models from Allard et al. (2012).

upper limit is nevertheless consistent with the sensitivity limit of the observations.

Previous claims of such extreme types of objects have been made in the context of the DUNES *Herschel* key program, who named these objects "cold disks" because of their extreme nature (Krivov et al. 2013). Other authors have suggested background galaxies as the possible explanation (Gáspár & Rieke 2014). This object did not fulfill our classification criteria as transitional disk candidate.

3.3.6. Sz65 and Sz66

Objects Sz65 and Sz66 form a binary system, with a separation of 6.4″ (Lommen et al. 2010), unresolved by *Herschel* (see Fig. 4). We inspected their SEDs to select the main contributor. We deduce that the primary source is Sz65 by studying the contour diagram of the image. The contour lines were centered at the position of source Sz65. Their MIPS24 and MIPS70 fluxes support this association. Then we set the *Herschel* fluxes of Sz66 as upper limits in Table 6 and in Fig. 3.

4. Discussion

4.1. Detection statistics

From an initial sample of 217 known Class II sources with spectroscopic membership confirmation in the Lupus clouds, 123 objects fell in at least one of the fields observed by the HGBS. In

particular, 92 and 98 were in the PACS and SPIRE Lupus III maps, respectively; 12 and 15 were found in Lupus I PACS and SPIRE mosaics; and 10 objects were observed in Lupus IV with both instruments. From these sources we detected 35 objects, 32 in PACS70, two in PACS100, and one in SPIRE. We then discarded one, 2MASSJ1608537, as we could not unequivocally assign its *Herschel* photometry to the target.

Compared with a similar study in Chamaeleon (Ribas et al. 2013), here we report a *Herschel* detection rate of ∼28% of the previously known objects in the region, comparable with the percentage in that work (∼30%). The small differences in the distances to the regions (∼150 pc for Chamaeleon vs. ∼200 pc to Lupus III) might account for the small difference in the detection rate. Further analysis of the detection statistics of known and new sources in these regions with the HGBS data will be presented by Benedittini et al. (in prep.).

4.2. Incidence of transitional disks in Lupus

We report the detection of five transitional disk candidates in the Lupus molecular clouds based on *Herschel* and previous data of all spectroscopically confirmed Class II members of the association. Two transitional disks were known from previous works (Sz91 and Sz111), but the other three are new to the literature.

The *Spitzer* study of the Lupus clouds found a global disk fraction of 50–60% (Ribas et al. 2014), compatible with a relatively young age for the region of 1–2 Myr (Comerón 2008). However, the total sample in Merín et al. (2008) included objects without spectroscopic membership confirmation so it could have a certain level of contamination from background galaxies and/or old dusty AGB stars (see Mortier et al. 2011, for a spectroscopic survey of *Spitzer* selected candidate members in Lupus). This work, however, uses an input target list where all objects have spectroscopic membership confirmation and is therefore not affected.

The observed fraction of transitional disks in Lupus based on our *Herschel* detected sample is ∼15%, which is comparable to the fractions measured in other such young and nearby regions (Espaillat et al. 2014). This corrects a surprisingly low incidence of this type of objects from the *Spitzer* sample reported in Merín et al. (2008), where only two objects were identified as transitional out of a photometric sample of 139 Class II and III sources. This demonstrates how *Herschel* efficiently complements mid-infrared surveys for the specific study of transitional disks.

4.3. Brighter PACS-70 fluxes in transitional disks

Recent studies have reported brighter 70 μm fluxes in transitional disks as compared with the median SED of standard T Tauri stars in the same regions (Cieza et al. 2011; Ribas et al. 2013). To check whether this phenomenon is dependent on the conditions of certain molecular clouds, we compared the SEDs of the detected disks in Lupus with the median SED of T Tauri stars in the region. Figures 2 and 3 show the median SED normalized to the dereddened J-band flux for comparison, and Table 7 shows the fluxes of this median SED.

As shown in Fig. 2 most transitional disk candidates identified in Sect. 3.1 show the same phenomenon: the PACS fluxes are systematically above the median SED of the T Tauri stars. Therefore, the result has been confirmed around the isolated transitional disk T Cha (Cieza et al. 2011), in the Chamaeleon I cloud (Ribas et al. 2013), and in the Lupus molecular clouds (this work).

The interpretation of this phenomenon requires detailed SED modeling with radiative transfer disk models. However, the higher PACS fluxes compared with the median SED of the T Tauri stars suggests that the inner and outer disks of these objects follow different evolutionary paths by the time the inner gaps or holes are formed in the inner disks. Thus, the evolution of both inner and outer disk regions might not be dynamically decoupled.

4.4. SED population analysis

Merín et al. (2008) classified the YSO population in Lupus by studying the shape of their SEDs, and comparing the median SED of the CTTS from Taurus with their data. They grouped the objects into four categories, based on whether their slopes decay like a classical accreting optically thick disk around a low-mass star (T-Type), or if they present infrared excess clearly weaker (L-Type) or stronger (H-Type) than the median SED or where no excess is detected (E-Type). They also introduced a category that they called *cold disks* (LU-Type), which corresponds to our criteria for transitional disks. In their work, they made use of *Spitzer* and ground based photometry.

We did the same analysis for the 34 objects detected by *Herschel*, but now also taking into account the photometry we extracted. For simplification, we used a different nomenclature, grouping our objects into three categories that reveal their evolutionary state: higher infrared excess than the median values (H), indicating an early evolutionary stage; weaker (W), showing a more evolved stage; and transitional candidate (T). The results can be found in Table 5, where we also compare our classification to the aforementioned work by Merín et al. (2008). Another difference is that instead of using the Taurus median SED, we have used the Lupus value/values.

Apart from the transitional nature for the three new objects found in this work (∼10%), we find that by adding the *Herschel* photometry to the SEDs we can update the type found in Merín et al. (2008) for another nine objects (∼27%). The final population for our sample is then classified as follows: ∼56% *primordial* disks (this groups T Tauri types and stronger infrared excesses), ∼29% *evolved* disks, and ∼15% transitional disk candidates. This compares well to the 67%, 26%, and 7% found for the same types of objects from the *Spitzer*-only study. Table 5 shows the *Spitzer*-only and *Spitzer* + *Herschel* classifications. The relative overall fractions have not changed substantially, except on the larger fraction of transitional disk candidates.

5. Conclusions

We have detected 34 objects in the Lupus cloud using *Herschel* and broadened the study of the YSOs in the association. Having confirmed that our *Herschel* data enable improved characterization of the outer regions of protoplanetary disks, we have identified additional transitional disks in our sample. The fraction of transitional disks detected in our study, comparable in size to Ribas et al. (2013), corrects the relatively low value from *Spitzer* detections. In addition, we find that all of these objects have 70 μm fluxes brighter than the median SED, showing perhaps another possible intrinsic property. Finally, we have carried out a population analysis by studying the SED shapes of the detections, and updated the morphological type of several sources. Further studies and modeling will give us more information on (about) these objects.

Acknowledgements. This work has been possible thanks to the ESAC Science Operations Division research funds with code EXPRO IPL-PSS/GP/gp/44.2014, plus support from the ESAC Space Science Faculty and of the *Herschel*

Science Centre. We thank the referee for valuable comments which have helped to improve the paper. We also acknowledge Isabel Rebollido, Pablo Riviere-Marichalar, Bruno Altieri, Gabor Marton and the members of the *Herschel* Science Centre for discussions and extra checks on the *Herschel*/PACS photometry on large SPIRE/PACS parallel-mode maps of galactic fields. H. Bouy is funded by the Spanish Ramón y Cajal fellowship program number RYC-2009-04497. In the present paper we will be discussing observations performed with the ESA *Herschel* Space Observatory (Pilbratt et al. 2010), in particular employing Herschel's large telescope and powerful science payload to do photometry using the PACS (Poglitsch et al. 2010) and SPIRE (Griffin et al. 2010) instruments. HCSS/HIPE is a joint development by the *Herschel* Science Ground Segment Consortium, consisting of ESA, the NASA *Herschel* Science Center, and the HIFI, PACS and SPIRE consortia. This research has made use of the SIMBAD database, operated at the CDS, Strasbourg, France. This work has made an extensive use of Topcat (TOPCAT http://www.star.bristol.ac.uk/~mbt/topcat/ and STILTS, Taylor 2005, 2006). This work makes use of data from the DENIS Survey. DENIS is the result of a joint effort involving human and financial contributions of several Institutes mostly located in Europe. It has been supported financially mainly by the French Institut National des Sciences de l'Univers, CNRS, and French Education Ministry, the European Southern Observatory, the State of Baden-Wuerttemberg, and the European Commission under networks of the SCIENCE and Human Capital and Mobility programs, the Landessternwarte, Heidelberg and Institut d'Astrophysique de Paris. This publication makes use of data products from the Wide-field Infrared Survey Explorer, which is a joint project of the University of California, Los Angeles, and the Jet Propulsion Laboratory/California Institute of Technology, funded by the National Aeronautics and Space Administration. This research used the facilities of the Canadian Astronomy Data Centre operated by the National Research Council of Canada with the support of the Canadian Space Agency. This publication makes use of data products from the Two Micron All Sky Survey, which is a joint project of the University of Massachusetts and the Infrared Processing and Analysis Center/California Institute of Technology, funded by the National Aeronautics and Space Administration and the National Science Foundation. This work is based in part on observations made with the *Spitzer* Space Telescope, which is operated by the Jet Propulsion Laboratory, California Institute of Technology under a contract with NASA.

References

Allard, F., Homeier, D., & Freytag, B. 2012, IAU Symp. 282, eds. M. T. Richards, & I. Hubeny, 235
Allen, P. R., Luhman, K. L., Myers, P. C., et al. 2007, ApJ, 655, 1095
André, P., Men'shchikov, A., Bontemps, S., et al. 2010, A&A, 518, L102
Calvet, N., D'Alessio, P., Watson, D. M., et al. 2005, ApJ, 630, L185
Cieza, L. A., Schreiber, M. R., Romero, G. A., et al. 2010, ApJ, 712, 925
Cieza, L. A., Olofsson, J., Harvey, P. M., et al. 2011, ApJ, 741, L25
Comerón, F. 2008, The Lupus Clouds, ed. B. Reipurth, 295
Espaillat, C., Muzerolle, J., Najita, J., et al. 2014, Protostars and Planets VI, eds. H. Beuther, R. S. Klessen, C. P. Dullemond, & T. Henning (Tucson: University of Arizona Press), 497
Gáspár, A., & Rieke, G. H. 2014, ApJ, 784, 33
Ghez, A. M., White, R. J., & Simon, M. 1997, ApJ, 490, 353
Griffin, M. J., Abergel, A., Abreu, A., et al. 2010, A&A, 518, L3
Hughes, J., Hartigan, P., Krautter, J., & Kelemen, J. 1994, AJ, 108, 1071
Krautter, J., Wichmann, R., Schmitt, J. H. M. M., et al. 1997, A&AS, 123, 329
Krivov, A. V., Eiroa, C., Löhne, T., et al. 2013, ApJ, 772, 32
Lada, C., Luhman, K., Muench, A., et al. 2006, Spitzer Proposal, 30033
Lestrade, J.-F., Matthews, B. C., Sibthorpe, B., et al. 2012, A&A, 548, A86
Lommen, D. J. P., van Dishoeck, E. F., Wright, C. M., et al. 2010, A&A, 515, A77
Matrà, L., Merín, B., Alves de Oliveira, C., et al. 2012, A&A, 548, A111
Merín, B., Jørgensen, J., Spezzi, L., et al. 2008, ApJS, 177, 551
Merín, B., Brown, J. M., Oliveira, I., et al. 2010, ApJ, 718, 1200
Moreno-Corral, M. A., Chavarria-K., C., & de Lara, E. 1995, in Rev. Mex. Astron. Astrofis. Conf. Ser. 3, eds. M. Pena, & S. Kurtz, 121
Mortier, A., Oliveira, I., & van Dishoeck, E. F. 2011, MNRAS, 418, 1194
Muzerolle, J., Allen, L. E., Megeath, S. T., Hernández, J., & Gutermuth, R. A. 2010, ApJ, 708, 1107
Pilbratt, G. L., Riedinger, J. R., Passvogel, T., et al. 2010, A&A, 518, L1
Poglitsch, A., Waelkens, C., Geis, N., et al. 2010, A&A, 518, L2
Ribas, Á., Merín, B., Bouy, H., et al. 2013, A&A, 552, A115
Ribas, Á., Merín, B., Bouy, H., & Maud, L. T. 2014, A&A, 561, A54
Roussel, H. 2012, Astrophysics Source Code Library [record ascl:1209.012]
Rygl, K. L. J., Benedettini, M., Schisano, E., et al. 2013, A&A, 549, L1
Skrutskie, M. F., Cutri, R. M., Stiening, R., et al. 2006, AJ, 131, 1163
Strom, S. E., Edwards, S., & Strom, K. M. 1989, in The Formation and Evolution of Planetary Systems, eds. H. A. Weaver, & L. Danly (Cambridge: Cambridge University Press), 91
Traficante, A., Fuller, G. A., Pineda, J. E., & Pezzuto, S. 2015, A&A, 574, A119
Tsukagoshi, T., Momose, M., Hashimoto, J., et al. 2014, ApJ, 783, 90
Weingartner, J. C., & Draine, B. T. 2001, ApJ, 548, 296
Werner, M. W., Roellig, T. L., Low, F. J., et al. 2004, ApJS, 154, 1

Pages 8 to 16 are available in the electronic edition of the journal at http://www.aanda.org

Table 5. Class II objects detected by *Herschel* in the Lupus clouds.

Object	RA_{J2000}	Dec_{J2000}	A_V (mag)	SpT	Type (*Spitzer***)	Type (this work)	References[r]
			Lupus I				
Sz65	15:39:27.8	–34:46:17.1	1.0	M0	H	H	2
Sz66[v]	15:39:28.3	–34:46:18.0	2.0	M3	H	H	2
Sz68	15:45:12.9	–34:17:30.6	1.5	K2	H	H	2
Sz69	15:45:17.4	–34:18:28.3	4.0	M1	W	W	2
			Lupus III				
SSTc2dJ160703.9-391112	16:07:03.8	–39:11:11.3	2.2	M5.5	–	H	1
Sz90	16:07:10.1	–39:11:03.3	5.0*	K8	W	H	2, 5
Sz91	16:07:11.6	–39:03:47.5	1.0	M0.5	T	T	2
Sz95	16:07:52.3	–38:58:05.9	1.0	M1.5	W	W	2
Sz96	16:08:12.6	–39:08:33.5	1.4	M2	H	W	1
2MASSJ1608149	16:08:14.9	–38:57:14.6	7.0*	M4.7	H	T	3, 5
Sz98	16:08:22.5	–39:04:46.5	2.5	K5	H	H	1
Sz100	16:08:25.8	–39:06:01.2	1.2	M4.5	H	H	1
Sz102	16:08:29.7	–39:03:11.0	2.5	K2	–	H	1
Sz103	16:08:30.3	–39:06:11.2	1.0	M4.5	H	H	1
Sz104	16:08:30.8	–39:05:48.9	0.7	M5.5	H	H	1
HR5999	16:08:34.3	–39:06:18.2	1.0*	A7	H	W	2, 5
RXJ1608.6-3922	16:08:36.2	–39:23:02.5	3.0*	K6	–	H	4, 5
Sz108B	16:08:42.9	–39:06:14.4	0.8	M5.5	W	W	1
Sz110	16:08:51.6	–39:03:17.7	0.2	M3	H	H	1
Sz111	16:08:54.6	–39:37:43.1	0.0	M1.5	T	T	2
Sz112[j]	16:08:55.5	–39:02:33.9	1.0	M4	W	W	2
SSTc2dJ160901.4-392512	16:09:01.4	–39:25:11.9	0.6	M3.5	H	H	1
Sz114[j]	16:09:01.9	–39:05:12.4	1.3	M4	H	H	1
Sz117	16:09:44.4	–39:13:30.1	1.0	M2	H	W	2
Sz118[j]	16:09:48.7	–39:11:16.9	2.6	K7	H	H	1
SSTc2dJ161029.6-392215	16:10:29.6	–39:22:14.5	0.0	M5.5	H	T	1
Sz123	16:10:51.6	–38:53:13.8	0.0	M3	W	T	2
			Lupus IV				
SSTc2dJ160002.4-422216	16:00:02.4	–42:22:14.6	2.0*	M3.5	H	H	1, 5
IRAS15567-4141[j]	16:00:07.4	–41:49:48.4	2.0	M6.5	W	W	1
Sz130[j]	16:00:31.1	–41:43:36.9	0.60	M2	H	W	1
F403[j]	16:00:44.5	–41:55:31.0	2.0	K0	W	H	2
Sz131[j]	16:00:49.4	–41:30:03.9	0.0	M2	H	H	2
SSTc2dJ160111.6-413730[v]	16:01:11.5	–41:37:29.9	0.0	M8.5	W	W	1
Sz133[j]	16:03:29.4	–41:40:01.8	10.0*	K2	H	H	1

Notes. The object types are higher than the median infrared excess (H), weaker (W), and transitional disk candidates (T). See text for details. [(r)] References for the spectral type and A_V: (1) Mortier et al. (2011); (2) Comerón (2008); (3) Allen et al. (2007); (4) Krautter et al. (1997); and (5) this work. [(j)] The objects marked with *j* presented potential small extended emission at *J*-band. Nevertheless, all of them have spectroscopic confirmation of being young stellar objects. [(v)] These objects were missed by our detection method and were detected in the visual inspection. [(*)] Extinction values denoted with an asterisk indicate that they were computed in this work either because they were not available in the literature or the ones found did not provide appropriate fits to the model photospheres. [(**)] Merín et al. (2008).

Table 6. *Herschel* photometry for the 34 YSOs detected in the maps.

Object	$F_{70\ \mu m}$ (Jy)	$F_{100\ \mu m}$ (Jy)	$F_{160\ \mu m}$ (Jy)	$F_{250\ \mu m}$ (Jy)	$F_{350\ \mu m}$ (Jy)	$F_{500\ \mu m}$ (Jy)
Lupus I						
Sz65	0.47 ± 0.12	–	0.55 ± 0.14	0.77 ± 0.15	0.95 ± 0.19	<1.59
Sz66	0.45 ± 0.11	–	0.55 ± 0.14	0.81 ± 0.16	0.98 ± 0.20	<1.63
Sz68	3.01 ± 0.75	3.80 ± 0.95	11.77 ± 2.94	13.06 ± 2.61	10.22 ± 2.04	6.74 ± 1.35
Sz69	0.12 ± 0.03	0.19 ± 0.05	<0.31	<1.59	<0.88	<2.13
Lupus III						
SSTc2dJ160703.9-391112	0.07 ± 0.02	0.10 ± 0.02	0.19 ± 0.05	<0.33	<0.44	<0.43
Sz90	0.36 ± 0.09	0.37 ± 0.09	0.26 ± 0.07	0.51 ± 0.10	0.50 ± 0.10	<0.61
Sz91	0.51 ± 0.13	0.68 ± 0.17	0.72 ± 0.18	0.86 ± 0.17	0.62 ± 0.12	0.38 ± 0.08
Sz95	<0.05	0.05 ± 0.01	0.09 ± 0.02	<0.28	<0.30	<0.25
Sz96	0.14 ± 0.03	0.12 ± 0.03	0.10 ± 0.02	<1.49	<1.87	<1.96
2MASSJ1608149	<0.08	0.07 ± 0.02	<0.11	<0.48	<0.25	<0.21
Sz98	0.64 ± 0.16	0.58 ± 0.14	0.50 ± 0.12	0.93 ± 0.19	1.14 ± 0.23	<2.12
Sz100	0.17 ± 0.04	0.23 ± 0.06	0.29 ± 0.07	0.59 ± 0.12	<1.99	<1.33
Sz102	0.34 ± 0.09	0.37 ± 0.09	0.22 ± 0.06	<3.25	<4.07	<4.37
Sz103	0.11 ± 0.03	0.16 ± 0.04	<0.23	<2.13	<1.64	<1.20
Sz104	0.10 ± 0.02	0.18 ± 0.04	<0.19	<2.08	<1.97	<2.13
HR5999	4.25 ± 1.06	3.20 ± 0.80	1.60 ± 0.40	0.92 ± 0.18	0.47 ± 0.09	<3.26
RXJ1608.6-3922	0.40 ± 0.10	0.69 ± 0.17	1.36 ± 0.34	2.55 ± 0.51	2.83 ± 0.57	2.40 ± 0.48
Sz108B	0.20 ± 0.05	0.21 ± 0.05	<0.61	<5.81	<9.68	<8.85
Sz110	0.13 ± 0.03	0.09 ± 0.02	<0.26	<0.57	<0.48	<0.76
Sz111	1.16 ± 0.29	–	1.73 ± 0.43	1.31 ± 0.26	0.94 ± 0.19	0.58 ± 0.12
Sz112	0.10 ± 0.03	0.04 ± 0.01	<0.16	<0.33	<0.27	<0.38
SSTc2dJ160901.4-392512	0.08 ± 0.02	0.09 ± 0.02	0.12 ± 0.03	0.15 ± 0.03	0.13 ± 0.03	0.07 ± 0.01
Sz114	0.28 ± 0.07	0.26 ± 0.06	0.13 ± 0.03	<0.53	<0.51	<1.11
Sz117	0.06 ± 0.02	0.11 ± 0.03	0.17 ± 0.04	<0.82	<0.70	<0.65
Sz118	0.35 ± 0.09	0.46 ± 0.11	0.37 ± 0.09	0.49 ± 0.10	0.56 ± 0.11	<0.98
SSTc2dJ161029.6-392215	0.07 ± 0.02	0.10 ± 0.02	<0.13	<0.29	<0.27	<0.26
Sz123	0.27 ± 0.07	0.37 ± 0.09	0.45 ± 0.11	0.17 ± 0.03	0.12 ± 0.02	0.08 ± 0.02
Lupus IV						
SSTc2dJ160002.4-422216	0.10 ± 0.02	0.20 ± 0.05	0.21 ± 0.05	0.22 ± 0.04	0.23 ± 0.05	0.17 ± 0.03
IRAS15567-4141	0.11 ± 0.03	0.05 ± 0.01	<0.11	<0.38	<0.34	<0.22
Sz130	0.11 ± 0.03	0.12 ± 0.03	0.05 ± 0.01	<0.39	<0.34	<0.34
F403	1.04 ± 0.26	1.26 ± 0.31	1.57 ± 0.39	1.33 ± 0.27	0.93 ± 0.19	0.58 ± 0.12
Sz131	0.11 ± 0.03	–	<0.10	<0.24	<0.35	<0.25
SSTc2dJ160111.6-413730	<0.05	–	<0.09	0.11 ± 0.02	0.07 ± 0.01	<0.16
Sz133	0.21 ± 0.05	0.38 ± 0.10	0.32 ± 0.08	0.37 ± 0.07	0.30 ± 0.06	0.20 ± 0.04

Notes. When no source was detected at a certain band, an upper limit is provided.

Table 7. Normalized flux densities of the median SED, lower SED (first quartile), and upper SED (fourth quartile) of the Class II objects in Lupus I, III, and IV.

Band (μm)	Median	First quartile	Fourth quartile	Detections
		(F_λ arbitrary units)		
J 1.25	1.000	1.000	1.000	28
H 1.62	1.048	0.982	1.186	28
K 2.15	0.761	0.673	1.015	28
IRAC 3.6	0.331	0.260	0.501	23
IRAC 4.5	0.259	0.182	0.385	24
IRAC 5.8	0.193	0.143	0.284	24
IRAC 8.0	0.167	0.111	0.223	25
MIPS 23.68	0.090	0.054	0.122	27
PACS 70	0.049	0.025	0.074	25
PACS 100	0.042	0.018	0.056	25
PACS 160	0.028	0.023	0.066	18
SPIRE 250	0.023	0.015	0.045	15
SPIRE 350	0.017	0.013	0.036	11
SPIRE 500	0.011	0.007	0.019	6

Notes. The number of detections in each band is also included. The transitional disk candidates are excluded from this count. All values are normalized to *J*-band.

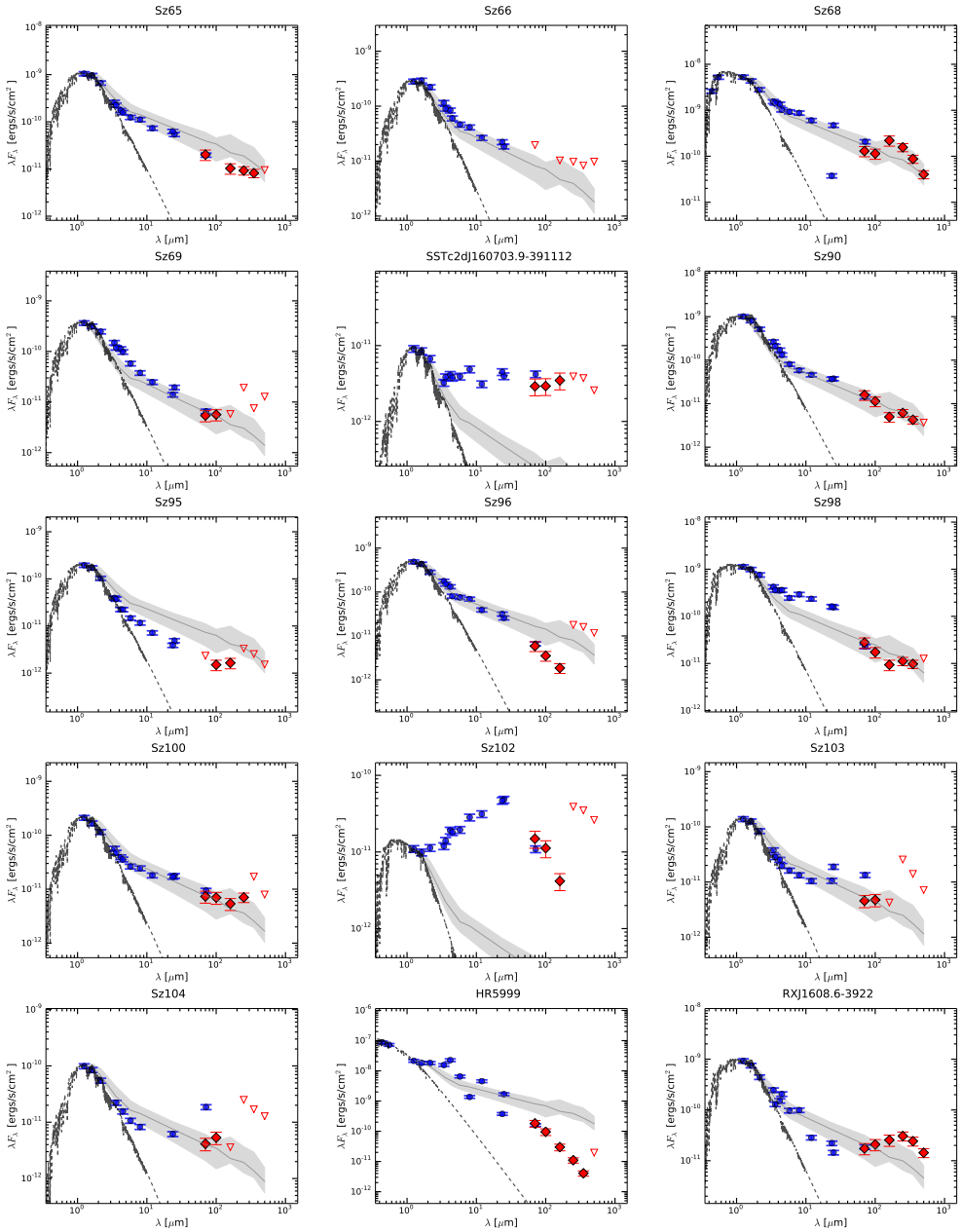

Fig. 3. SEDs of the 29 YSOs with *Herschel* detections that do not fulfill our transitional disk selection criteria.

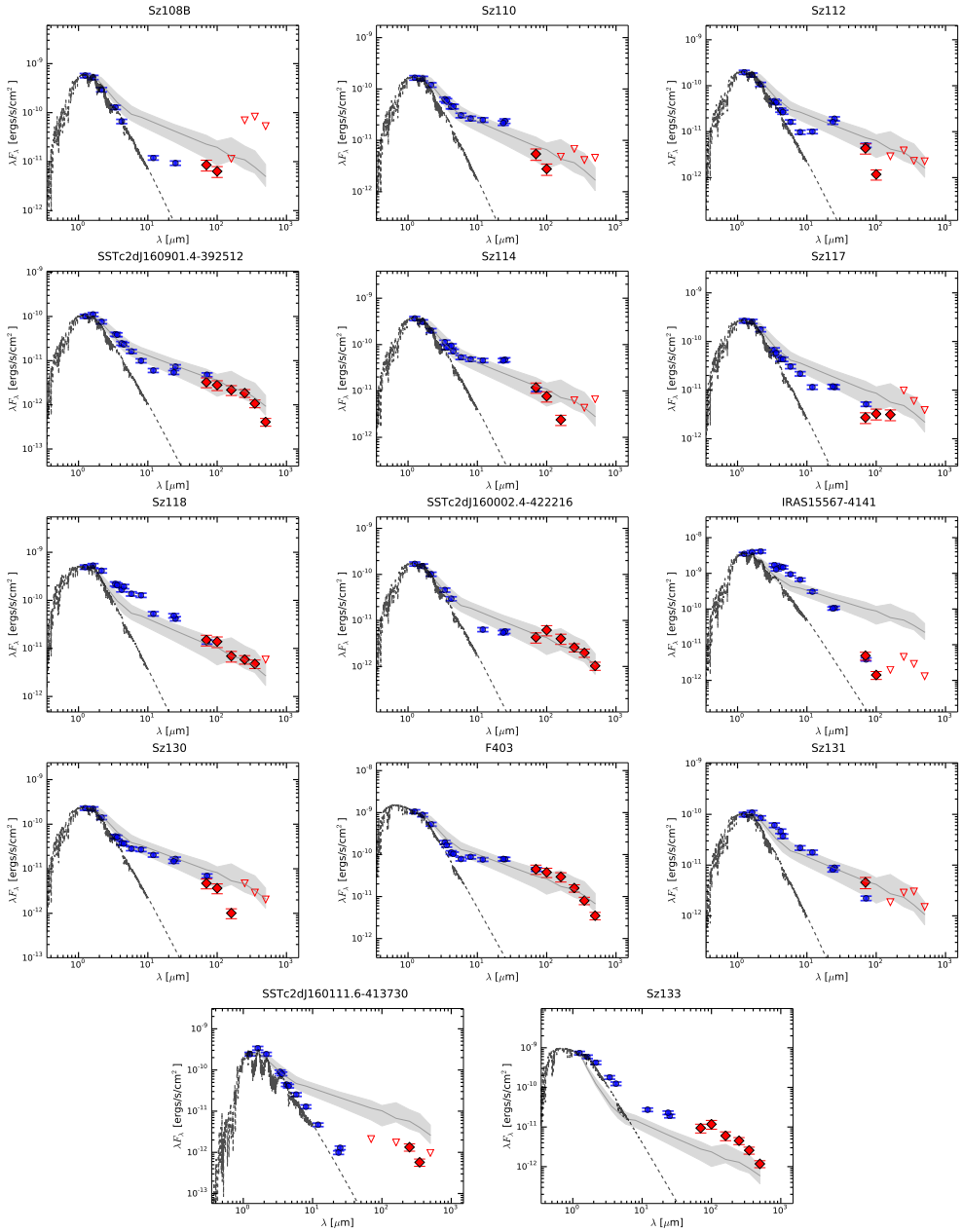

Fig. 3. continued.

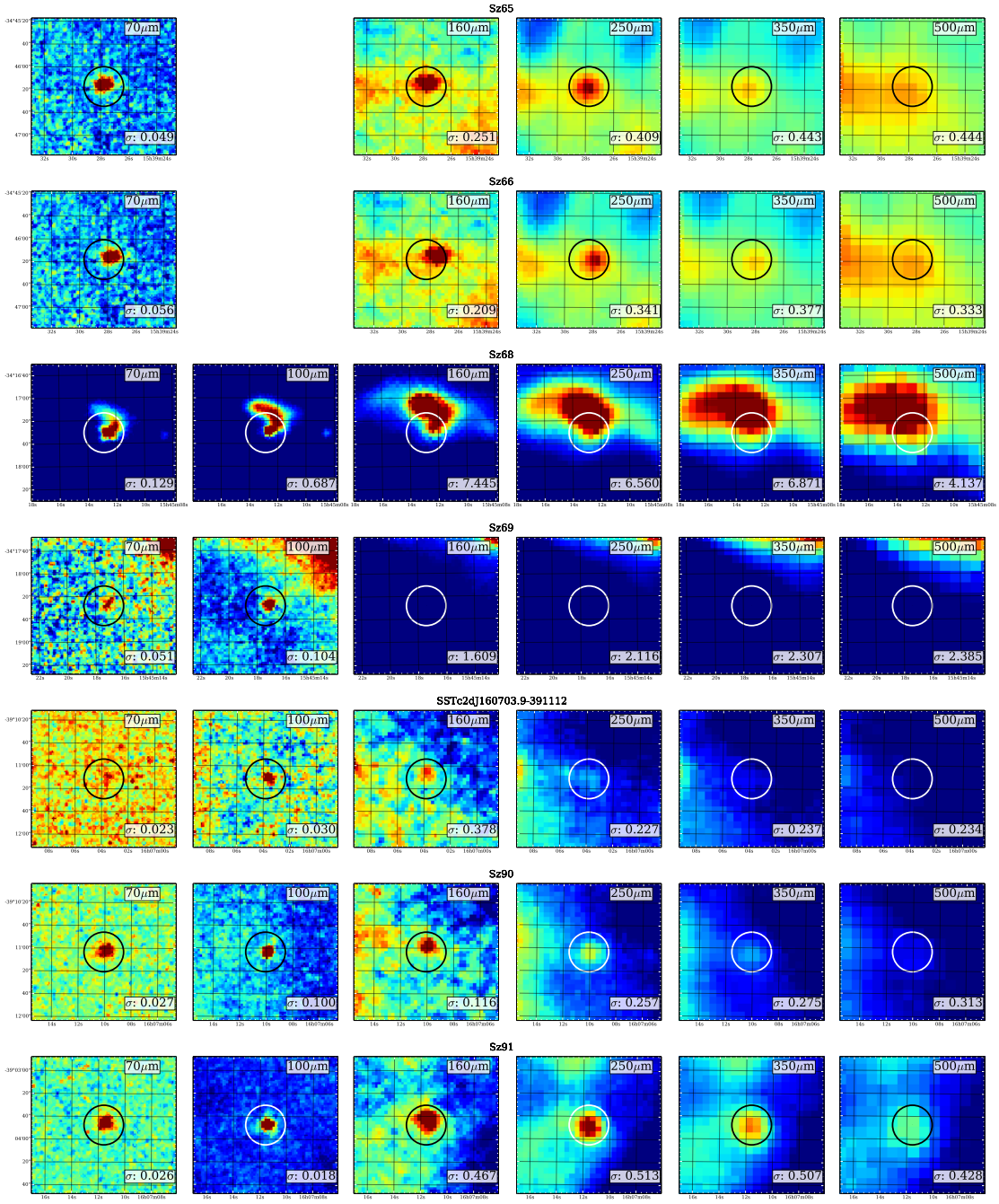

Fig. 4. Images of each of the 34 sources with at least one point source detected by *Herschel*, plus object 2MASSJ1608537, added for completeness. The images correspond to a box of 120″ × 120″ in size. Coordinates are given in Table 5. The color scale is defined with the root-mean square of the pixel values (as background level) and this number plus three times the standard deviation (as maximum level). North is up and east is left. A circle indicates the expected position of the target. The standard deviation computed around the sources is shown for each image (*bottom right*).

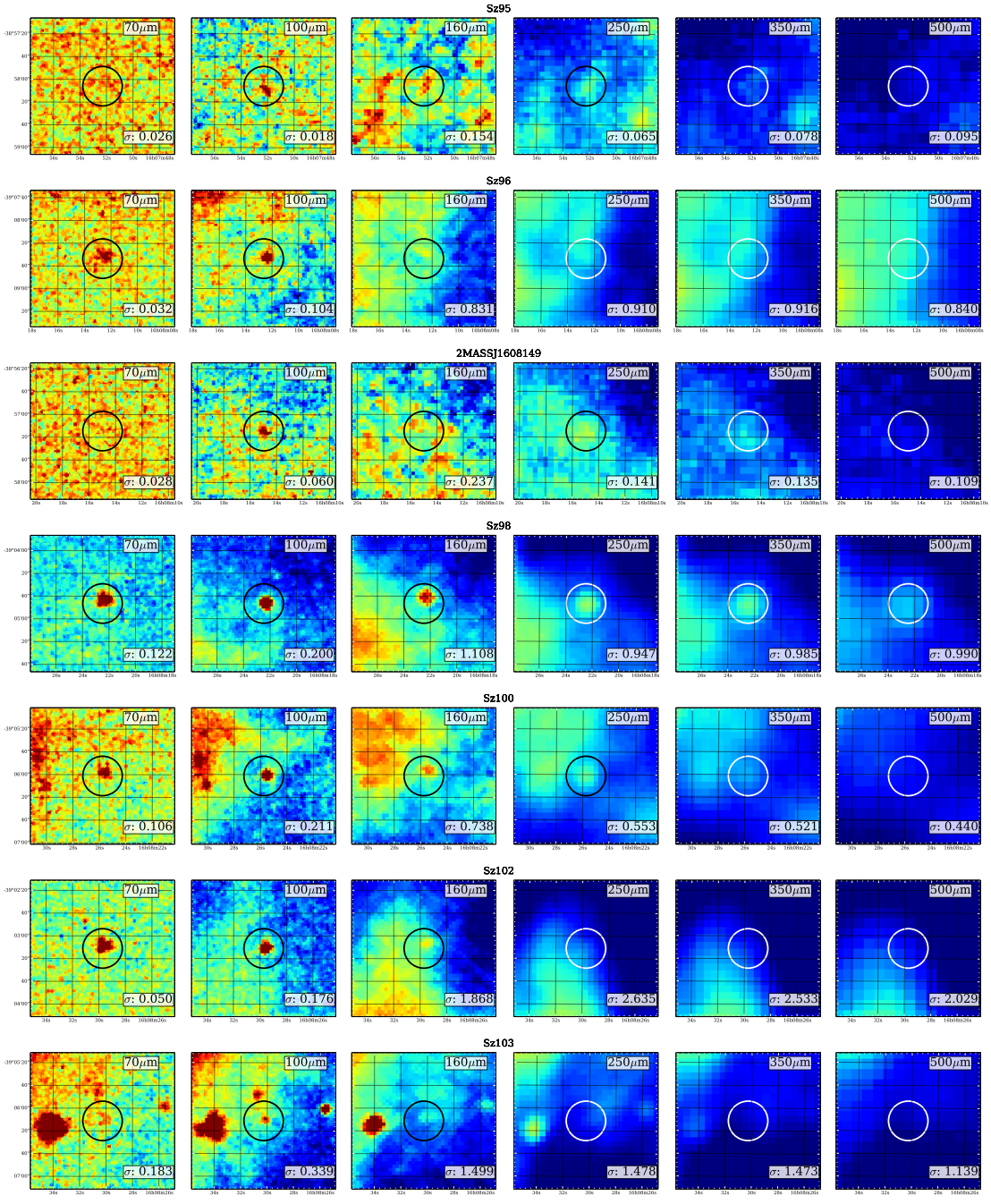

Fig. 4. continued.

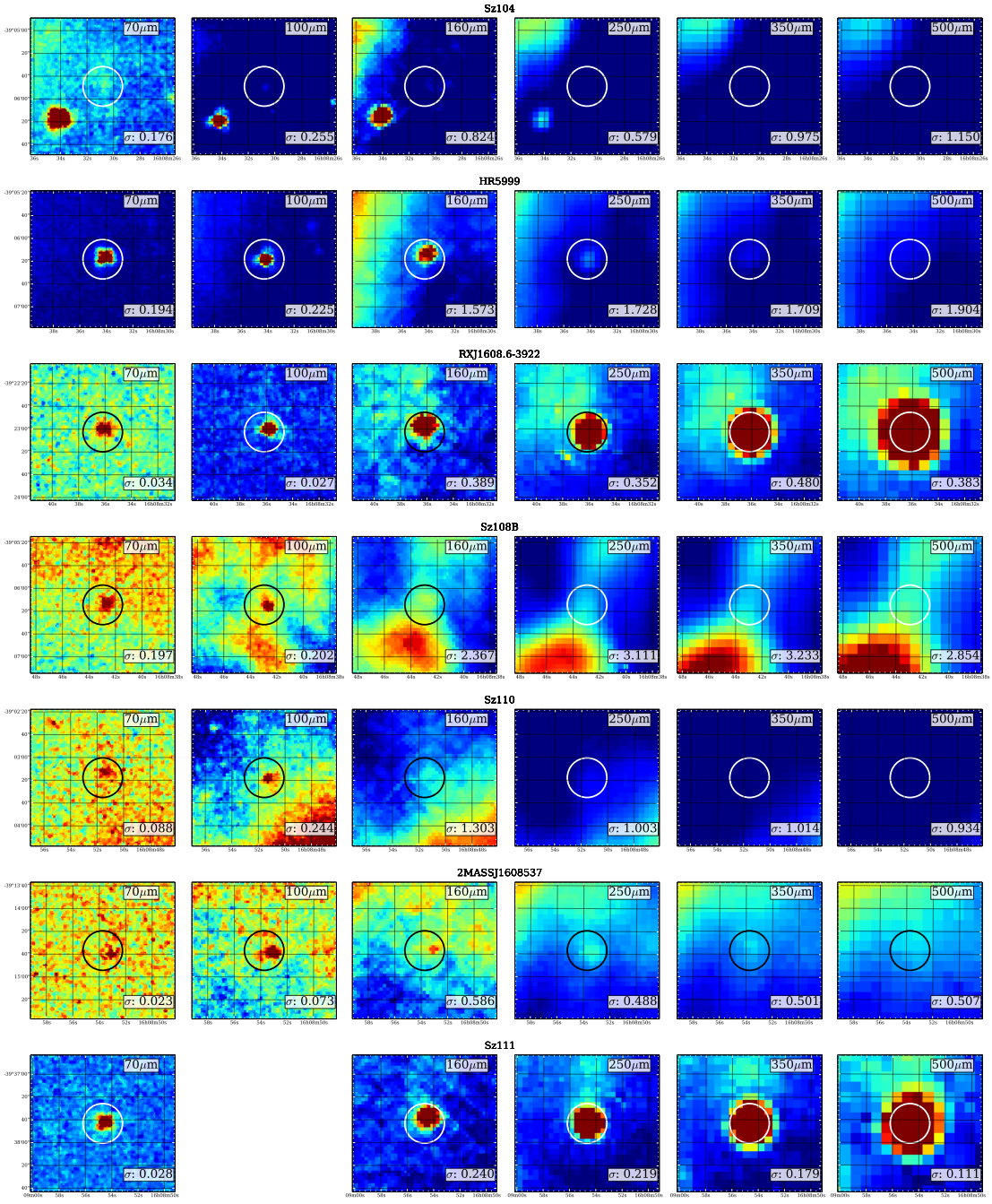

Fig. 4. continued.

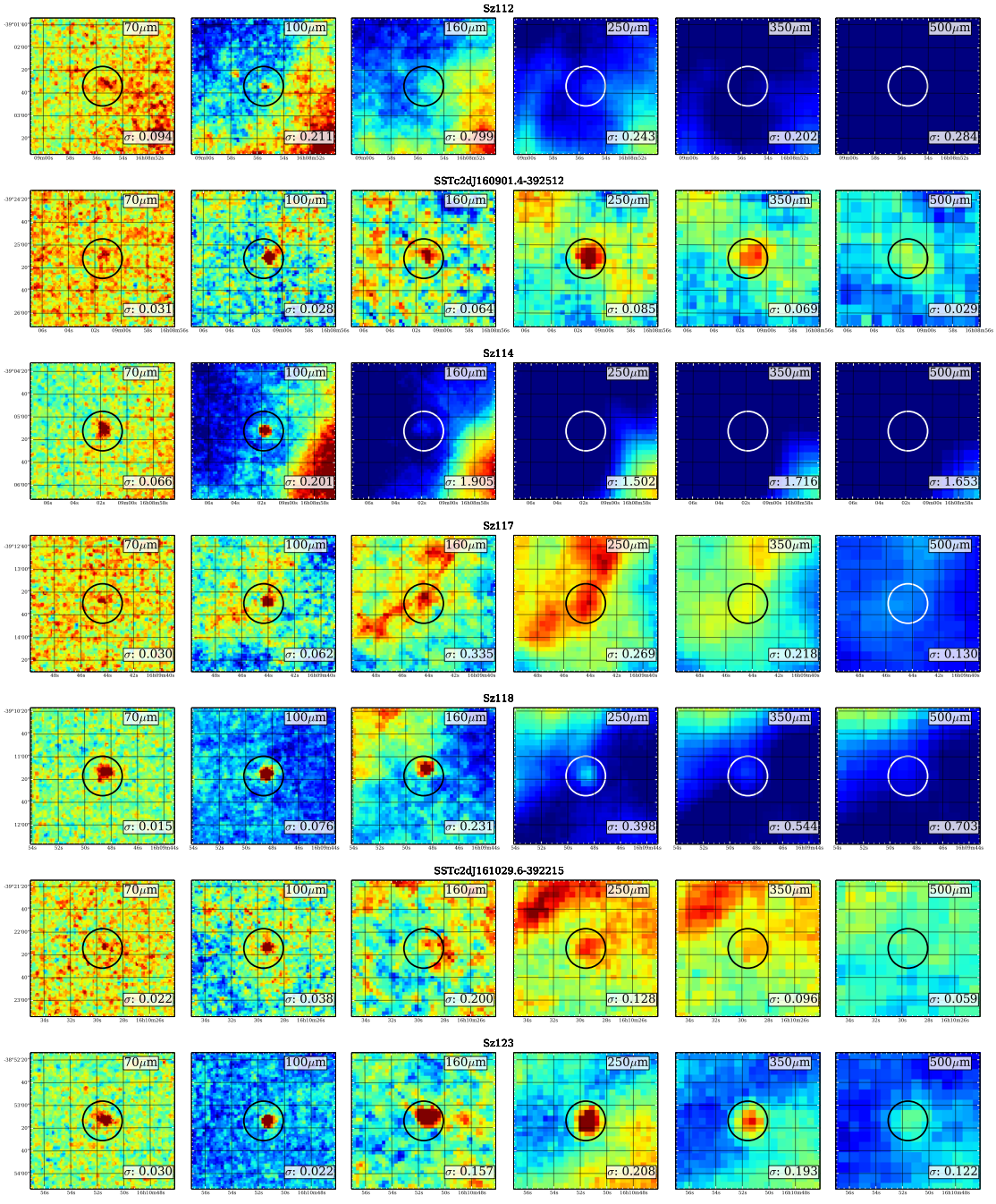

Fig. 4. continued.

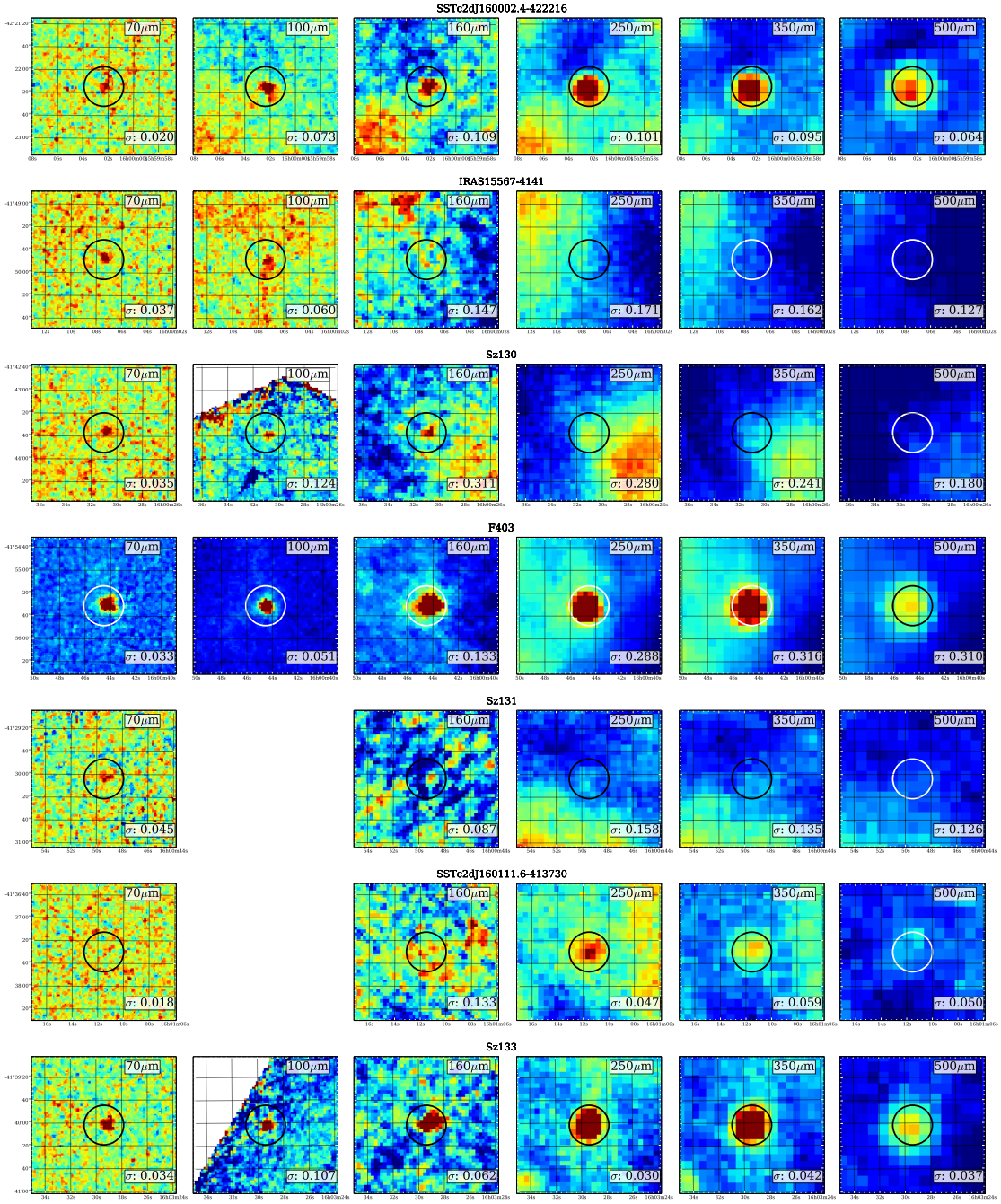

Fig. 4. continued.

A&A 581, A30 (2015)
DOI: 10.1051/0004-6361/201425556

Astronomy & Astrophysics

Infrared study of transitional disks in Ophiuchus with *Herschel*⋆,⋆⋆,⋆⋆⋆,⋆⋆⋆⋆

Isabel Rebollido[1], Bruno Merín[1], Álvaro Ribas[1,2,3], Ignacio Bustamante[1,2,3], Hervé Bouy[2], Pablo Riviere-Marichalar[1], Timo Prusti[4], Göran L. Pilbratt[4], Philippe André[5], and Péter Ábrahám[6]

[1] European Space Astronomy Centre (ESA), PO Box, 78, 28691 Villanueva de la Cañada, Madrid, Spain
e-mail: Isabel.Rebollido@sciops.esa.int
[2] Centro de Astrobiología, INTA-CSIC, PO Box – Apdo. de correos 78, 28691 Villanueva de la Cañada, Madrid, Spain
[3] ISDEFE – ESAC, PO Box, 78, 28691 Villanueva de la Cañada, Madrid, Spain
[4] ESA, Scientific Support Office, Directorate of Science and Robotic Exploration, European Space Research and Technology Centre (ESTEC/SRE-S), Keplerlaan 1, 2201 AZ Noordwijk, The Netherlands
[5] Laboratoire AIM Paris, Saclay, CEA/DSM, CNRS, Université Paris Diderot, IRFU, Service d'Astrophysique, Centre d'Études de Saclay, Orme des Merisiers, 91191 Gif-sur-Yvette, France
[6] Konkoly Observatory, Research Centre for Astronomy and Earth Sciences, Hungarian Academy of Sciences, PO Box 67, 1525 Budapest, Hungary

Received 19 December 2014 / Accepted 2 July 2015

ABSTRACT

Context. Observations of nearby star-forming regions with the *Herschel* Space Observatory complement our view of the protoplanetary disks in Ophiuchus with information about the outer disks.
Aims. The main goal of this project is to provide new far-infrared fluxes for the known disks in the core region of Ophiuchus and to identify potential transitional disks using data from *Herschel*.
Methods. We obtained PACS and SPIRE photometry of previously spectroscopically confirmed young stellar objects (YSO) in the region and analysed their spectral energy distributions.
Results. From an initial sample of 261 objects with spectral types in Ophiuchus, we detect 49 disks in at least one *Herschel* band. We provide new far-infrared fluxes for these objects. One of them is clearly a new transitional disk candidate.
Conclusions. The data from *Herschel* Space Observatory provides fluxes that complement previous infrared data and that we use to identify a new transitional disk candidate.

Key words. stars: formation – stars: pre-main sequence – protoplanetary disks – planets and satellites: formation

1. Introduction

Protoplanetary disks around young stars are objects of major interest as they lead us to a better understanding of star and planet formation. Transitional disks are key in this study since they appear to have an unusual radial structure. They have been proposed as the environment for planet formation (Marsh & Mahoney 1992) and have other proposed formation mechanisms, such as photo-evaporation by ultraviolet light emitted by the central star (Clarke et al. 2001), grain growth (Dullemond & Dominik 2005), and gravitational instabilities (see Espaillat et al. 2014, for a recent review on transitional disks). Recently, Kim et al. (2013) studied accretion towards transitional disks in Orion A and concluded that planet formation was the most likely explanation for their observations. What characterizes a transitional disk is a lack of excess in the near- or mid-IR region (usually around 8 or 10 μm) and typical Class-II excesses in mid- to far-IR. This lack of near- and mid-IR excess denotes an inner disk opacity hole, which is related to the dust distribution in the surroundings of the star and reveals inner holes. These objects are thought to be an intermediate stage between Class II objects (optically thick disks) and Class III objects (smaller amount of material in the disk).

The first transitional disks were reported by Strom et al. (1989). Since that time, the known population of these objects has grown substantially thanks to data from *Spitzer* Space Telescope (Werner et al. 2004). The study of these objects has improved with new and more powerful telescopes, such as the *Herschel* Space Obsevatory (Pilbratt et al. 2010), which provides a wider range of wavelengths. *Herschel* also represents an improvement *Spitzer*'s sensitivity and spatial resolution at long wavelengths, which allows for a reduction in the noise level of measurements at these wavelengths. Studies in the millimetric and sub-millimetric range allowed for the imaging and direct measurement of hole sizes, such as those made

⋆ *Herschel* is an ESA space observatory with science instruments provided by European-led Principal Investigator consortia and with important participation from NASA.
⋆⋆ Final reduced *Herschel* maps are only available at the CDS via anonymous ftp to cdsarc.u-strasbg.fr (130.79.128.5) or via http://cdsarc.u-strasbg.fr/viz-bin/qcat?J/A+A/581/A30
⋆⋆⋆ Appendix A is available in electronic form at http://www.aanda.org
⋆⋆⋆⋆ All tables are also available at the CDS via anonymous ftp to cdsarc.u-strasbg.fr (130.79.128.5) or via http://cdsarc.u-strasbg.fr/viz-bin/qcat?J/A+A/581/A30

Table 1. Sensitivity of the *Herschel* observations used in this study.

	F_{70} [mJy]	F_{160} [mJy]	F_{250} [mJy]	F_{350} [mJy]	F_{500} [mJy]
Sensitivity per scan	12.2	14.3	12.6	10.5	15.0
Effective sensitivity	2	2.4	6.3	5.2	7.5
Minimum flux detected	20	50	70	10	30

by Andrews et al. (2011) with the Sub-Millimeter Array (Ho et al. 2004). Recent work with ALMA (Wootten & Thompson 2009) has achieved new results in the field as seen in works by van der Marel et al. (2013) and the recent study on the transitional disk HL Tauri (ALMA Partnership et al. 2015).

The aim of this work is to study the young stellar objects (YSOs) in the Ophiuchus star-forming region. *Herschel* data provide us with accurate fluxes of the detected objects, and enables the construction of the spectral energy distributions (SEDs) along with other multi-wavelength photometric data, collected by Ribas et al. (2014). The study of the SEDs also allows us to classify the transitional disks in the region by identifying the previously mentioned lack of excess in near and/or mid-IR region.

The structure of this work is as follows: Sect. 2 describes the *Herschel* observations and data reduction, explaining the source detection and photometry extraction processes. In Sect. 3 we explain the results obtained from the data reduction, both with the method described in Ribas et al. (2013) and with the analysis of the SED of each individual object. In Sect. 4 we discuss the detection statistics and compare them with other similar studies. In Sect. 5 we present the conclusions of this work.

2. Observations and data reduction

The Ophiuchus cloud complex was observed by *Herschel* as part of the *Herschel* Gould Belt Survey (André et al. 2010) and by a deeper PACS survey (Alves de Oliveira et al. 2013). It is one of the closest star-forming regions, located at an estimated distance of 130 pc and with an age between 2 and 5 Myr, although it has been suggested that it is younger (see Wilking et al. 2008, for a review on the region). Apart from its proxmity, most significant characteristic of this cloud is its dense core, which is the focus of our study. The cloud itself appears as a large scale structure with complex filaments, heated by B-type stars, and is strongly emitting at infrared wavelengths. We might consider the cloud itself as a possible source of contamination. Figure 1 shows the region with the objects in the sample overplotted and marked differently according to their state of non-detected, detected, or transitional.

The maps used to examine this region were obtained from two sets of observations, using the parallel mode of both PACS (Poglitsch et al. 2010) and SPIRE (Griffin et al. 2010) on board the *Herschel* Space Observatory. For SPIRE maps (250 μm, 350 μm and 500 μm) the parallel mode was used, with a speed of 60″/s (program *KPGT_pandre_*1), but for the PACS maps (70 μm and 160 μm) the scan mapping mode was used, with a cross-scan speed of 20″/s (program *OT*1*_pabraham_*3). We used this later PACS data because it goes deeper, as shown by the sensitivity limits given in the SPIRE/PACS Observers' Manual and in Table 1 in this work. In both cases (PACS and SPIRE), a single pair of scan and cross-scan was obtained. The obsids for the SPIRE maps are (1342-) 205093 and 205094, and for PACS maps (1342-) 238816 and 238817.

The maps were produced using Scanamorphos (Roussel 2013), an IDL software designed to process *Herschel* maps. Version 24.0 was used for PACS maps, with calibration file version 65, and version 22.0 for SPIRE maps, with calibration files version 12.3.

2.1. Sample selection and point source photometry

The objective of this work is to determine the nature of the sources detected in the maps produced with PACS and SPIRE observations and to obtain fluxes in the mid- to far-IR regions when detected. The YSO candidates were selected from the work of Ribas et al. (2014) (which for Ophiuchus contains objects from Natta et al. 2002; Wilking et al. 2005; Alves de Oliveira et al. 2010; Erickson et al. 2011), for having known spectral type from spectroscopy, making a list of 258 sources, all of them located in the core of the cloud. For a more complete study, the objects from Cieza et al. (2010) contained in the region of interest were also considered. The final sample consists of 261 objects. We used photometry from the 2MASS K-band (Skrutskie et al. 2006) and WISE4 (Wright et al. 2010) to classify the disks according to the method described by Lada (1987). The only object that does not fulfill the criteria is IRS 48, which has a positive slope that is almost flat. This object cannot be classified as Class I and remains Class II in the final classificaiton because of the lack of strong emission in mid- and far-IR.

To determine whether our candidates are transitional disks or not, the first step was to detect sources in our maps and extract the photometry from them. We used the algorithm *Sussextractor* in the *Herschel* interactive processing environment (HIPE), version 12.1, with a threshold of $S/N > 3$. Additionally, visual inspection was applied to all sources. Only sources clearly separated from filaments and distinguishable from the background were selected as valid detections.

We extracted aperture photometry for these sources using the sourceExtractorDaophot task in HIPE (Ott 2010). The fluxes were aperture corrected to account for the shape of the PSF and they are listed in Table 4. Those corrections were obtained from Balog et al. (2014) for PACS and from the SPIRE Observers' Manual (now named SPIRE Handbook) version 2.5. In Table 4, objects marked with an asterisk suffered from high nearby background emission and, in those cases, we used a special sky estimate from a rectangular area identified after visual inspection. The set of apertures and the corrections applied to the photometry extracted are shown in Table 2. We tested several point-source extraction algorithms, including Sussextractor, Daophot, AnnularSkyAperturePhotometry, and Hyper (Traficante et al. 2015), and different apertures. The combination above provides the best fit to the MIPS70 (Rieke et al. 2004) fluxes of clean selected sources in the field.

At the end of the process, we had 49 successfully detected sources in at least one PACS band, and 19 in a SPIRE band; PACS also detected all of these. Images of the detected objects can be found in Fig. A.2, for visual inspection.

The calibration errors for PACS and SPIRE are 5% and 7% (as stated in the PACS Observer's Manual, version 2.3 and in the SPIRE Observer's Manual version 2.5), however, as a more conservative estimation, we used 25% for both. These measurement uncertainties account for the high variations in the

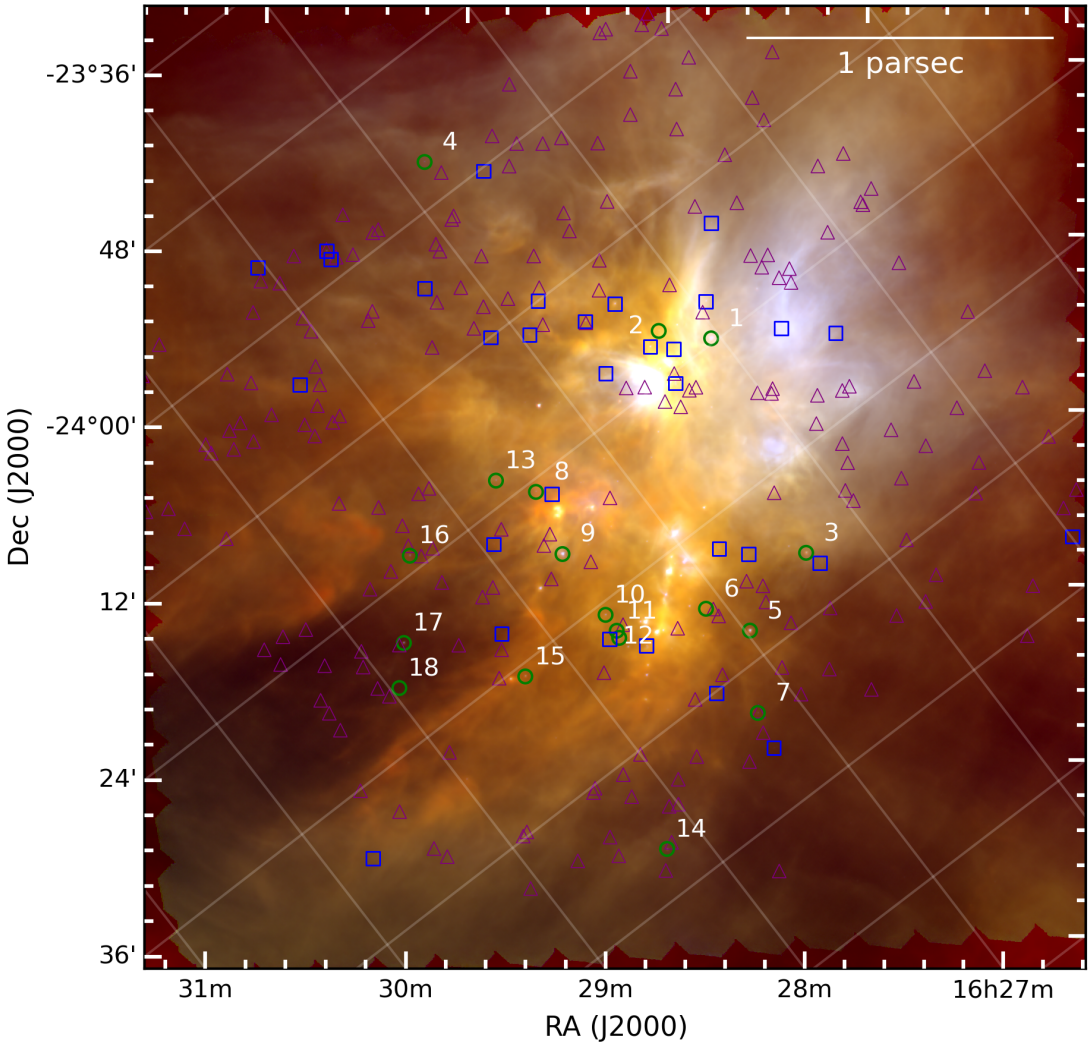

Fig. 1. RGB image (PACS 70 in blue, PACS 100 in green, and PACS 160 in red) of the observed Ophiuchus region with the marked objects. Transitional disks are marked with green circles. The blue squares mark the detected objects, and the purple triangles mark the rest of the sample of known young stars in the region.

results of the different extraction methods and apertures listed above.

In Table 3 we show the parameters of the detected sources, as given in the literature, and for an easier reference we list the identification numbers (ID) used in this work as seen in Fig. 1. From now on, the ID number is referenced in parenthesis for its respective source. Table 4 gives the fluxes measured with *Herschel* for each source.

2.2. Sensitivity and non-detections

The high background present in the region increases the sensitivity limit of these observations, and affects the number of detections. In Table 1 we present the sensitivities given in the SPIRE/PACS Parallel Mode Observers' Manual v2.1 (Sect. 2.3), and the minimum flux detected for each band. Also, the effective sensitivity is calculated taking the number of scans made per map into account; this includes six for the PACS maps and two for the SPIRE maps. We also report a lower value of fluxes in the cleanest areas of the map, which agrees with the fact that the extended emission from the molecular cloud reduces the effective sensitivity.

Another study took into account the sources detected by *Spitzer* and catalogued by c2d (Evans et al. 2009) in each of the apertures defined per band and per detected source to estimate possible contamination due to *Herschel* resolution. The flux in

Table 2. Aperture photometry parameters.

Band	*FWHM* (″)	Radius (″)	Inner annulus (″)	Outer annulus (″)	Aperture correction factors
PACS-70	5.4	6	25	35	1.5711
PACS-160	10.5	12	25	35	1.4850
SPIRE-250	18	22	60	90	1.2584
SPIRE-350	24	30	60	90	1.2242
SPIRE-500	36	42	60	90	1.1975

Table 3. Parameters of detected sources as extracted from the literature.

ID.	Name	RA (deg)	Dec (deg)	SpT	A_v*	References
–	2MASS J16245974-2456008	16:24:59.63	−24:55:59.32	M3.5	0.10	1
–	V*V852Oph	16:25:24.38	−24:29:43.77	M4.5	0.21	2
–	2MASS J16253673-2415424	16:25:36.73	−24:15:42.32	K4	0.10	1
–	2MASS J16253958-2426349	16:25:39.58	−24:26:34.27	M2	0.13	2
–	V*V2058Oph	16:25:56.18	−24:20:47.77	K4.5	0.61	1
1	Haro1-6	16:26:03.02	−24:23:36.04	K1	5.70	4
–	2MASS J16261684-2422231	16:26:16.83	−24:22:23.32	K6	0.11	1
2	DoAr 24	16:26:17.08	−24:20:21.47	K4.5	0.13	2
–	2MASS J16262189-2444397	16:26:21.88	−24:44:39.67	M8	0.10	2
–	DoAr 24E	16:26:23.28	−24:20:59.37	G6	0.10	2
3	DoAr 25	16:26:23.68	−24:43:13.57	K5	0.21	2
–	GSS32	16:26:24.03	−24:24:48.32	K5	0.63	1
–	2MASS J16262407-2416134	16:26:24.08	−24:16:13.27	K5.5	0.19	2
–	2MASS J16263297-2400168	16:26:32.98	−24:00:16.77	M4.5	0.09	2
–	2MASS J16263682-2415518	16:26:36.93	−24:15:52.32	M0	0.55	1
–	[GY92]93	16:26:41.28	−24:40:17.87	M5	0.09	2
–	2MASS J16264285-2420299	16:26:42.83	−24:20:30.32	M1	0.11	1
–	2MASS J16264643-2412000	16:26:46.48	−24:11:59.97	G3.5	0.10	2
4	WSB 40	16:26:48.58	−23:56:34.57	K5.5	0.09	2
–	WL18	16:26:48.98	−24:38:25.07	K6.5	0.59	2
–	2MASS J16265677-2413515	16:26:56.68	−24:13:51.47	K7	0.11	2
5	SR 24 S	16:26:58.48	−24:45:36.67	K1	0.18	2
6	2MASS J16270659-2441488	16:27:06.68	−24:41:49.07	M5.5	0.09	2
–	2MASS J16270907-2412007	16:27:09.03	−24:12:01.32	M2.5	0.11	1
7	WSB 46	16:27:15.08	−24:51:38.77	M2	0.09	2
–	[WMR2005]4 – 10	16:27:17.48	−24:05:13.67	M3.5	0.10	2
–	2MASS J16271836-2454537	16:27:18.38	−24:54:52.77	M3.75	0.16	2
–	WSB 49	16:27:22.98	−24:48:07.07	M4.25	0.09	2
–	2MASS J16272658-2425543	16:27:26.58	−24:25:54.47	M8	0.14	2
8	2MASS J16273084-2424560	16:27:30.88	−24:24:56.37	M3.25	0.12	2
–	2MASS J16273311-2441152	16:27:33.13	−24:41:14.32	K6	0.50	1
9	IRS 48	16:27:37.23	−24:30:34.32	A0	0.76	1
10	IRS 49	16:27:38.28	−24:36:58.67	K5.5	0.15	2
–	2MASS J16273832-2357324	16:27:38.28	−23:57:32.97	K6	0.14	2
11	2MASS J16273863-2438391	16:27:38.60	−24:38:39.00	M6	0.24	3
–	2MASS J16273901-2358187	16:27:38.98	−23:58:19.17	K5.5	0.15	2
12	WSB 52	16:27:39.48	−24:39:15.87	K5	0.09	2
13	SR 9	16:27:40.28	−24:22:04.37	K5	0.17	2
–	2MASS J16274270-2438506	16:27:42.68	−24:38:51.27	M2	0.11	2
–	V*V2059Oph	16:27:55.58	−24:26:18.27	M2	0.11	2
–	2MASS J16280256-2355035	16:28:02.58	−23:55:03.61	M3	4.30	4
–	2MASS J16281379-2432494	16:28:13.83	−24:32:49.32	M4	0.10	1
14	2MASS J16281385-2456113	16:28:13.83	−24:56:10.32	M0	0.10	1
15	WSB 60	16:28:16.58	−24:36:58.57	M4.5	0.11	2
–	2MASS J16281673-2405142	16:28:16.83	−24:05:15.32	K6	0.08	1
16	SR 20W	16:28:23.38	−24:22:40.87	K5	0.50	2
17	SR 13	16:28:45.28	−24:28:19.27	M3.75	0.20	2
18	2MASS J16285694-2431096	16:28:57.03	−24:31:09.32	M5.5	0.13	1
–	2MASS J16294427-2441218	16:29:44.28	−24:41:21.80	M4	0.80	4

Notes. Also, we give the ID number used to identify the transitional disks. (*) All A_v are calculated according to Ribas et al. (2014).
References. 1) Erickson et al. (2011); 2) Wilking et al. (2005); 3) Natta et al. (2002); 4) Cieza et al. (2010).

Table 4. Point source fluxes of each of the 49 sources detected.

ID	Name	F_{70} [Jy]	F_{160} [Jy]	F_{250} [Jy]	F_{350} [Jy]	F_{500} [Jy]
–	2MASS J16245974-2456008	0.05 ± 0.01	–	–	–	–
–	V*V852Oph	0.73 ± 0.18	–	–	–	–
–	2MASS J16253673-2415424	0.74 ± 0.18	–	–	–	–
–	2MASS J16253958-2426349	0.92 ± 0.23	–	–	–	–
–	V*V2058Oph	3.86 ± 0.97	3.77 ± 0.94	12.56 ± 3.14	–	–
1	Haro1-6	10.70 ± 2.68	7.48 ± 1.87	–	–	–
–	2MASS J16261684-2422231	0.20 ± 0.05	–	–	–	–
2	DoAr 24	0.50 ± 0.12	–	–	–	–
–	2MASS J16262189-2444397	0.10 ± 0.02	–	–	–	–
–	DoAr 24E	4.17 ± 1.04	3.91 ± 0.98	–	–	–
3	DoAr 25	1.39 ± 0.35	3.52 ± 0.88	4.17 ± 1.04	5.30 ± 1.33	2.05 ± 0.51
–	GSS32	3.70 ± 0.93	–	–	–	–
–	2MASS J16262407-2416134	3.04 ± 0.76	6.10 ± 1.53	4.73 ± 1.18	2.66 ± 0.66	1.12 ± 0.28
–	2MASS J16263297-2400168	0.08 ± 0.02	0.13 ± 0.03	–	0.01 ± 0.00	–
–	2MASS J16263682-2415518*	1.37 ± 0.34	0.72 ± 0.18	0.44 ± 0.11	–	–
–	[GY92]93	0.02 ± 0.00	–	–	–	–
–	2MASS J16264285-2420299	0.65 ± 0.16	–	–	–	–
–	2MASS J16264643-2412000	0.57 ± 0.14	–	–	–	–
4	WSB 40	0.42 ± 0.10	0.29 ± 0.07	–	–	–
–	WL18	0.42 ± 0.10	–	–	–	–
–	2MASS J16265677-2413515	0.21 ± 0.05	0.79 ± 0.20	–	–	–
5	SR42S	9.70 ± 2.42	7.88 ± 1.97	5.06 ± 1.26	3.02 ± 0.76	1.55 ± 0.39
6	2MASS J16270659-2441488	0.10 ± 0.02	–	–	–	–
–	2MASS J16270907-2412007	0.07 ± 0.02	0.23 ± 0.06	–	0.11 ± 0.03	–
7	WSB 46	0.25 ± 0.06	0.15 ± 0.04	–	–	–
–	[WMR2005]4-10	0.18 ± 0.04	0.32 ± 0.08	0.51 ± 0.13	0.37 ± 0.09	–
–	2MASS J16271836-2454537*	0.07 ± 0.02	0.05 ± 0.01	0.07 ± 0.02	–	–
–	WSB 49	0.04 ± 0.01	–	–	–	–
–	2MASS J16272658-2425543	0.04 ± 0.01	–	–	–	–
8	2MASS J16273084-2424560	0.50 ± 0.13	–	–	–	–
–	2MASS J16273311-2441152	1.27 ± 0.32	0.08 ± 0.02	–	–	–
9	IRS48	37.57 ± 9.39	12.85 ± 3.21	6.48 ± 1.62	2.51 ± 0.63	–
10	IRS49*	1.29 ± 0.32	0.95 ± 0.24	0.07 ± 0.02	0.67 ± 0.17	–
–	2MASS J16273832-2357324*	0.63 ± 0.16	0.25 ± 0.06	0.52 ± 0.13	0.30 ± 0.07	–
11	2MASS J16273863-2438391	0.09 ± 0.02	–	–	–	–
–	2MASS J16273901-2358187	0.44 ± 0.11	0.52 ± 0.13	0.10 ± 0.02	0.09 ± 0.02	0.03 ± 0.01
12	WSB 52*	2.37 ± 0.59	2.23 ± 0.56	3.43 ± 0.86	0.76 ± 0.19	0.28 ± 0.07
13	SR 9	0.86 ± 0.21	0.22 ± 0.05	–	–	–
–	2MASS J16274270-2438506	0.02 ± 0.01	–	–	–	–
–	V*V2059Oph	0.06 ± 0.01	–	–	–	–
–	2MASS J16280256-2355035	0.02 ± 0.01	–	–	–	–
–	2MASS J16281379-2432494	0.05 ± 0.01	–	–	–	–
14	2MASS J16281385-2456113	0.74 ± 0.18	0.68 ± 0.17	0.29 ± 0.07	0.19 ± 0.05	0.14 ± 0.03
15	WSB 60	0.87 ± 0.22	1.19 ± 0.30	1.26 ± 0.32	1.79 ± 0.45	–
–	2MASS J16281673-2405142	0.12 ± 0.03	–	–	–	–
16	SR 20W	0.89 ± 0.22	0.60 ± 0.15	0.57 ± 0.14	0.46 ± 0.12	0.37 ± 0.09
17	SR 13	1.36 ± 0.34	1.32 ± 0.33	0.79 ± 0.20	0.51 ± 0.13	0.20 ± 0.05
18	2MASS J16285694-2431096	0.02 ± 0.01	–	–	–	–
–	2MASS J16294427-2441218	0.05 ± 0.01	–	–	–	–

Notes. (*) Sources near bright background emission; sky measurement was done in clean regions.

MIPS-24 band of each of this c2d sources was used to extrapolate via the median SED of the Ophiuchus region (see Table 5) the expected fluxes at 70 μm. In Table A.1, we list a sum of all the expected fluxes for this contaminating sources, where it is possible to check whether the expected contamination is lower than the flux error. Notice that this contamination flux is only an estimation, as only the reported object has been detected in the aperture.

3. Results

The fluxes of all the detected sources per band are given in Table 4, as mentioned above. As expected, the higher flux corresponds to the most known object in the region, IRS 48 (#9). All the objects proposed as transitional disk candidates present relatively high fluxes, being 2MASS J16285694-2431096 (#18) the candidate with the lower flux at 70 μm (20 mJy). The detection

on more than one band for these objects seems to be arbitrary. Less than half of the candidates have been detected either in one band or in all of them. This is probably related to the physical properties of each of the disks rather than to instrumental issues.

3.1. Identification of transitional disks

Once we measured the fluxes, we use the criterion by Ribas et al. (2013) to classify transitional disks with *Herschel* photometry. As previously noted, transitional disks display little or no excess at near- to mid-IR, and large excess at long wavelengths, which translates into a change of slope in the SED of the object around 12 μm, i.e. from a negative to positive slope. To proceed with the identification, we defined two indexes , following:

$$\alpha_{\lambda_1-\lambda_2} = \frac{\log(\lambda_1 F_{\lambda_1}) - \log(\lambda_2 F_{\lambda_2})}{\log(\lambda_1) - \log(\lambda_2)}, \quad (1)$$

where λ is measured in μm and F_λ in erg s^{-1} cm^{-2}. The first index is defined for the band K acquired from 2MASS and 12 μm acquired from WISE. The second index is defined for the 12 μm band and the 70 μm band acquired from *Herschel*. The criterion to determine whether an object is a transitional disk candidate is $\alpha_{12-70} > 0$, since we define transitional disks as objects with a deficit of excess flux at near- to mid-IR fluxes, but standard excesses at longer wavelengths. For DoAr 24 (#2), the 12 μm-band was not available and, therefore, we used 8 μm band from *Spitzer*/IRAC (Fazio et al. 2004) instead.

To understand the result of this process, we represent in Fig. 2 a slope-slope diagram, which shows the value of the two different slopes in the two axes. The figure shows that we obtained two candidates with a positive slope between 12 μm and 70 μm, clearly separated from the Class II population. These two candidates, 2MASS J16281385-2456113 (#14) and Haro1-6 (#1), clearly fulfil the criteria of having a lack of mid-IR excess since Haro1-6 (#1) is an object previously classified as debris disk in Cieza et al. (2010). The candidate 2MASS J16281385-2456113 (#14), has never been reported before as a transitional disk. The other objects above the threshold do not have this kind of clear 12 μm flux deficit, which is indicative of the presence of a flatter slope in the mid- to far-infrared wavelengths. If we construct the SEDs of those objects (see Fig. 4), we see that in general they do not present the characteristic gap expected from a transitional disk. However, as they fulfil the criteria, we classified them here as tentative candidates. Some of these candidates were also classified as transitional disks in previous works. Object WSB 60 (#15) was imaged in Andrews et al. (2009), detecting a small inner hole in dust continuum observations done with the Sub-Millimeter Array (Ho et al. 2004). In the work by Cieza et al. (2010) DoAr 25 (#3) was already suggested as a candidate. We consider objects SR 42 S (#5), WSB 46 (#7), and SR 20 W (#16) as tentative candidates despite they do not fulfill the criteria for their nominal values, but we are considering a high error in PACS photometry. In particular, SR 42 S (#5) has already been classified as transitional disk, and appears in Espaillat et al. (2014) as so. For WSB 46 (#7) and SR 20 W (#16), further study is needed to determine their nature.

3.2. Complementary identification with spectral energy distributions

To better analyse the nature of these objects, we built their SEDs using data from optical to mid-infrared from both ground-based and space telescopes (all references for the photometry can be found in Sect. 2.1). We completed these SEDs with the photometry shown in Table 2 and extracted from *Herschel* data, therefore, we cover a range between 0.35 to 500 μm. Figures 4 and A.1 show the obtained SEDs, plus the NextGen atmosphere model for each object (Hauschildt et al. 1999), which are the best approximation of how a naked photosphere would emit as a function of its spectral type.

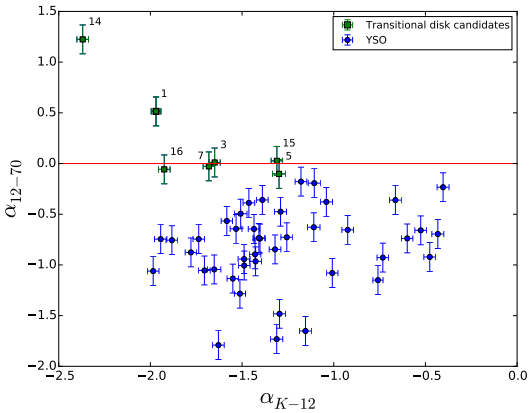

Fig. 2. SED slope between 12 and 70 μm as a function of the SED slope between the K-band and 12 μm. Transitional disks are marked with green squares.

Table 5. Median SED of detected disks in Ophiuchus.

Band	Median	First quartile	Third quartile	Detections
J	1.0000	1.0000	1.0000	49
H	0.6109	0.5664	0.6577	49
K	0.3305	0.3018	0.3662	49
IRAC-3.6	0.0743	0.0628	0.0958	45
IRAC-4.5	0.0380	0.0305	0.0537	47
IRAC-5.8	0.0212	0.0162	0.0293	46
IRAC-8.0	0.0121	0.0088	0.0190	48
MIPS-24	0.0018	0.0013	0.0030	48
PACS-70	0.0003	0.0001	0.0008	49
PACS-160	8.53×10^{-5}	5.54×10^{-5}	0.0002	26
SPIRE-250	3.48×10^{-5}	2.32×10^{-5}	0.0001	17
SPIRE-350	9.60×10^{-6}	5.88×10^{-6}	1.44×10^{-5}	15
SPIRE-500	2.62×10^{-6}	2.12×10^{-6}	4.18×10^{-6}	8

We also built the median SED of all the objects detected in the region for comparison (see Table 5), which is plotted along each object's SEDs. Because of the lack of detections for fluxes under the sensitivity limits given in Table 4, the median SED might be slightly overestimated, but we assume the effect in our result is negligible.

To determine the interstellar extinction, we used the procedure in Ribas et al. (2014) and the extinction law from Weingartner & Draine (2001), which uses a model of grains to estimate the interstellar extinction, scattering, and infrared emission. In each plot of Figs. 4 and A.1, the observed fluxes are also shown as empty circles. The de-reddened fluxes, according to the associated interstellar extinction, are shown as filled circles.

When visually inspecting the SEDs, we detect objects with a lack of mid-IR excess that were not classified as transitional disks, according to the criteria of Ribas et al. (2013) described in Sect. 3.1. Some of these objects are well known in the literature, such as IRS 48 (#9). To make a more reliable study of the region,

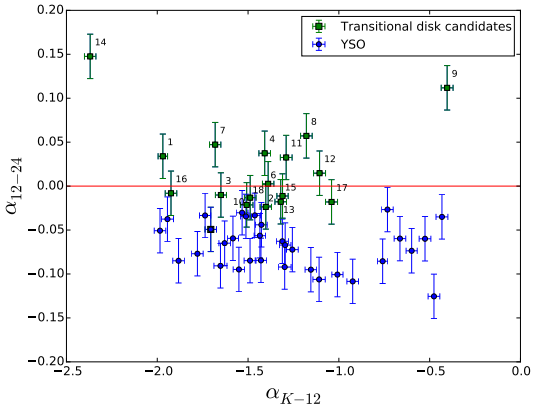

Fig. 3. SED slope between 12 and 24 μm as a function of the SED slope between the K-band and 12 μm. Transitional disks are marked with green squares.

we add in this subsection a complementary criterion based on *Spitzer* data to identify the other transitional disks or transitional disks candidates detected by *Herschel* with a change of slope between 12 μm and 24 μm. Figure 3 shows the new slope-slope diagram.

We detected 17 transitional disks candidates with this criteria. Six of the objects detected with the previous criteria appear now as well, with the exception of SR 24 S (#5), which is a confirmed transitional disk.

Figure 4 shows the SEDs for the 18 transitional disks candidates, where the change of slope is not equally noticeable for all of them. In the case of 2MASS J16281385-2456113 (#14), the change of slope is evident, in agreement with that expected from the slope-slope diagram. In cases such as WSB 60 (#15) or IRS 48 (#9), which are well-known transitional disks, the slope is flatter, and located in a different position in the wavelength axis. For SR 24 S (#5), we see an unexpected behaviour, where we get a discrepancy between MIPS-24 and WISE4 fluxes, but we still see an increase in the far-IR emission with respect to the near-IR. Another object classified as a transitional disk in Cieza et al. (2010) is SR 9 (#13), although it has a continuous decreasing slope, as the criterion shows, and looks more like a Class II SED. The rest of the objects in the sample have been widely studied, but not previously considered transitional disks. The variation in the outputs of both methods illustrates the complexity in defining a selection criteria.

4. Discussion

4.1. Detection statistics

The initial sample was composed of 261 YSO objects in the centre of Ophiuchus, with known spectral type from optical spectroscopy and all classified as Class II objects. Our sample is different from that in Evans et al. (2009), since they had photometrically selected objects, including many objects with other classes, while we have only spectroscopically confirmed Class II YSOs. All of these YSOs fell within the coverage of the maps used, and 49 were detected in at least one *Herschel* band, 49 in PACS, and 19 in SPIRE. This leads to a *Herschel* detection rate of 18.77%±2.6%, which is much smaller than the percentage of detections obtained in similar studies in Chamaeleon (Ribas et al. 2013) and Lupus (Bustamante et al. 2015) of around 30%. Given that Ophiuchus is closer than those regions (150 ∼ 200 pc), the low detection rate is probably due to the higher background, which is emitting at mid- and long-IR wavelengths, and precludes the detection of faint objects.

4.2. Incidence of transitional disks in the centre of Ophiuchus

We report here the detection of 18 transitional disk candidates in the cloud complex in the centre of Ophiuchus based on new *Herschel* and previous known data of spectroscopically confirmed YSO sample. Despite the fact that all of these objects fulfil either one or both of the criteria exposed previously, only a few of them have evident changes of slopes in the SEDs. The candidate with the biggest change in slope, 2MASS J16281385-2456113 (#14), is new to the literature.

The fraction of transitional disk candidates observed in Ophiuchus based on our *Herschel* sample, is $37\%^{+7}_{-6}$. We have considered two classification criteria, depending on the change of slope, that is, on the wavelength position of the lack of mid-IR excess. If we only consider our main criteria, the fraction is lower, at $14\%^{+6}_{-4}$, but it is compatible with the fractions measured in other regions with similar ages in previous works (Espaillat et al. 2014). Even though we have identified 18 transitional disks candidates in total, some of them present a relatively flat slope and, in the slope-slope diagram, are represented very close to, or even below, the threshold . Having objects with nearly a Class-II slope explains the high fraction of transitional disks in the region, as many of them might be fulfilling the criteria due to the large error in their PACS fluxes. These objects would need further study for their safe classification. One of the objects close to the threshold, however, namely YLW 58 or WSB 60 (#15), had been imaged with SMA and shows a small but conspicuous inner hole (Andrews et al. 2011). Despite this, most of the objects in the first criterion were also detected by the complementary criterion; SR 42 S (#5) was not, even though it is a confirmed transitional disk (Andrews et al. 2011). The fact that *Herchel* data is including transitional candidates to the sample, confirms the improvement that *Herschel* represents regarding reaching to further regions in disks. The longer wavelengths now accessible allow us to detect wider and larger cavities, which we could not have identified solely with data from *Spitzer* at mid-infrared ranges.

4.3. Other interesting objects

Even though we have combined two criteria to identify new candidates, and that these criteria select even very small changes of slope, there might be objects in the sample with the characteristics of a transitional disk, which are, as previously noted, a lack of excess around 10 μm and normal excesses at mid- to far-IR. If we inspect Fig. A.1, we observe that several objects present these features. There are two clear cases of objects previously classified as transitional disk candidates: 2MASS J16280256-2355035 and 2MASS J16294427-2441218. Both of these candidates present a lack of excess around 8 μm and excesses in longer wavelengths, but because of the restrictions in the criteria, neither appear as transitional candidates. The objects V* V852 Oph, 2MASS J16253958-2426349 and 2MASS J16262189-2444397 are similar cases that were never classified as transitional disks, but have a gap in their SED, which could be an indication of a hole in their disks. The object 2MASS J16272658-2425543 also shows a lack of excess around 10 μm with a larger excess in

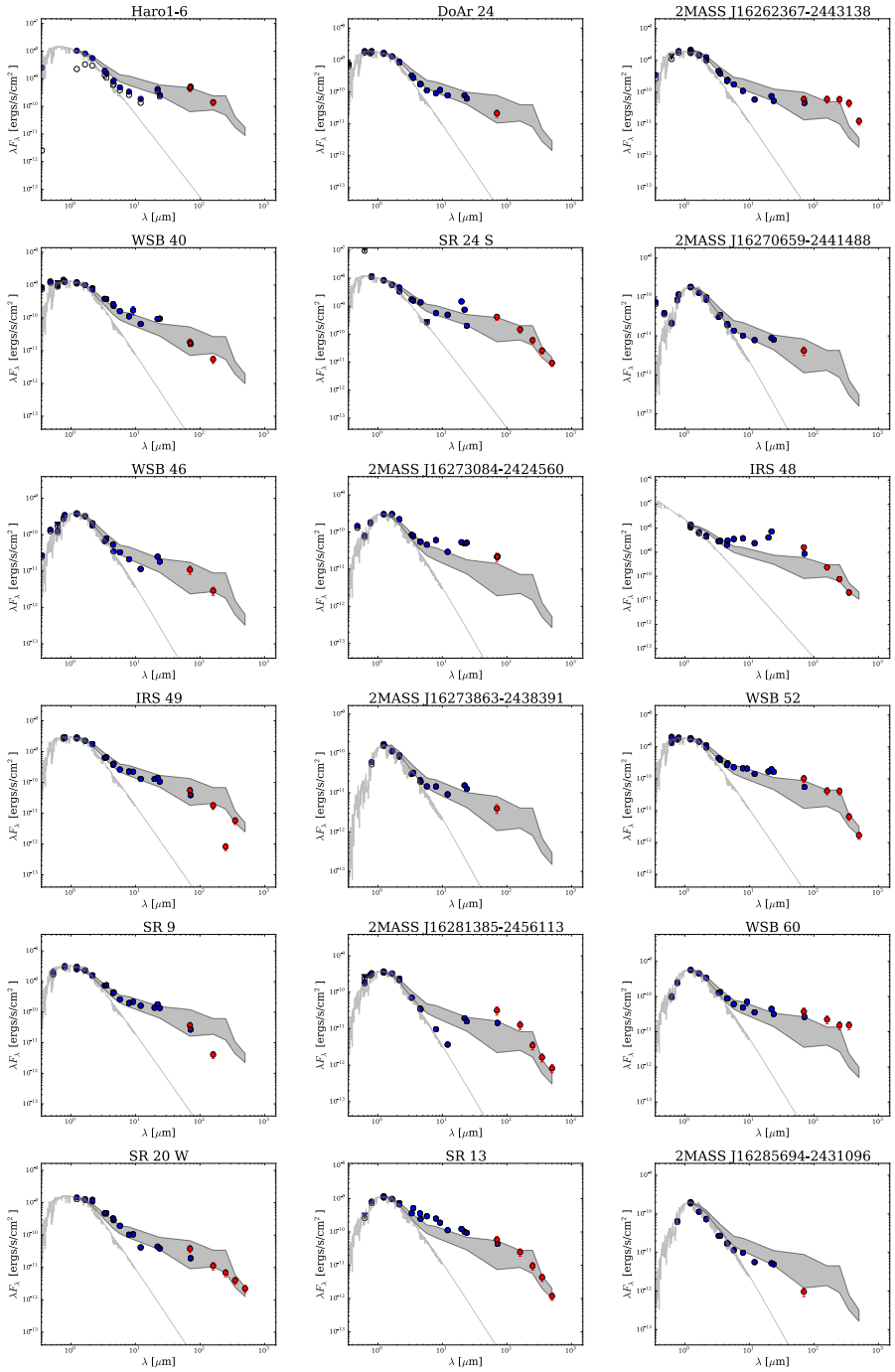

Fig. 4. Spectral energy distribution (SED) of the sources classified as transitional disks candidates. Blue dots show data acquired from the literature, red dots are photometric fluxes obtained from *Herschel* data. Grey dashed line is the photosphere model according to the spectral type, and the grey shaded area is the filled area between the first and third quartile of all the disk fluxes. Observed fluxes are shown with empty circles and A_v values used are in Table 3.

Table 6. Summary of all transitional disk candidates in Ophiuchus.

ID	Name	Classification criteria
1	Haro1-6	12−70*
2	DoAr24	12−24
3	DoAr25	12−70*
4	WSB40	12−24
5	SR42S	12−70
6	2MASS J16270659-2441488	12−24
7	WSB46	12−70*
8	2MASS J16273084-2424560	12−24
9	IRS48	12−24
10	IRS49	12−24
11	2MASS J16273863-2438391	12−24
12	WSB52	12−24
13	SR9	12−24
14	2MASS J16281385-2456113†	12−70*
15	WSB60	12−70*
16	SR20W	12−70*
17	SR13	12−24
18	2MASS J16285694-2431096	12−24
–	V* V852Oph	SED
–	2MASS J16253958–2426349	SED
–	2MASS J16262189–2444397	SED
–	2MASS J16272658–2425543	SED
–	2MASS J16280256–2355035	SED
–	2MASS J16294427-2441218	SED

Notes. (*) These objects have also been classified with the complementary criterion of 12–24. (†) This transitional disk candidate is new to the literature.

longer wavelengths. This object could also be considered a transitional candidate, despite the fact that it does not fulfil any of the criteria. All of these objects are shown in Table 6 along with the previous objects classified as transitional disk candidates.

4.4. Study of 70 micron fluxes in transitional disks

For a comparison of the 70 μm flux of both the transitional disk candidates and tentative candidates, we constructed the median SED of all the detected objects in the sample, using the photometric data in Table 5. This would show if, apart from a lack of excess in the near mid-IR, transitional disks also show another remarkable characteristic that could be used in classification or, possibly, in disk modelling. The median SED lacks the contribution from the faintest objects, which might remain undetected by *Herschel* or some of the other surveys, and hence is just an upper limit to the true median SED of Ophiuchus.

When we overplot the median SED to the detected fluxes (as a grey shaded area in Figs. 4 and A.1), we only find the 70 μm flux to be higher for some of the objects classified as transitional disks candidates. Hence, we cannot conclude that we have detected a trend in the transitional disk population, such as has been observed in previous investigations (Ribas et al. 2013, Bustamante et al. 2015). We also find the case of 2MASS J16285694-2431096 (#18), where the 70 μm flux is not only lower than the median SED, but lower than the third quartile. Because of the lack of large excess in mid- to far-IR and the fact that this object presents a slightly smaller flux in the 70 μm band than the rest of transitional disks candidates, it needs further study to clarify its nature.

5. Conclusions

We have detected 49 objects in the central region of Ophiuchus in at least one PACS band and 19 in at least one SPIRE band. We obtained accurate photometric fluxes for the detected objects by means of aperture photometry.

Seven of the detected objects were classified as transitional disk candidates by the criterion in Ribas et al. (2013), and 11 more were classified according to the complementary criterion, generating a total sample of 18 transitional disk candidates. Some of these candidates were already imaged in previous works, and hence, confirmed. Six more objects are added to the final classification of candidates that have transitional features in their SEDs, rather than fulfilling any of the criterion. All of the transitional disk candidates are shown in Table 6 along with their classification criteria. This large difference between the identification methods can be due to the different nature or evolutionary stages of the disks, creating different geometries and leading to a large diversity of SEDs.

Several of the objects classified as transitional disks candidates have not been considered candidates before, but 2MASS J16281385-2456113 (#14) appears to be an attractive object for follow-up because of its prominent change of slope when compared to the rest of the sample, including previously imaged disks, such as IRS 48 (#9).

So far, *Herschel* data has proved to be very useful to improve the characterization of the outer regions of protoplanetary systems because of its long-wavelength coverage, unattainable until now, and its improved sensitivity and spatial resolution compared with previous IR missions. A study of the SED population of the disk sample detected with *Herschel* should give us more information on the true nature of these disks, but this study is outside the scope of this work.

Acknowledgements. We thank the referee for his/her constructive comments. This work has been possible thanks to the ESAC Space Science Faculty for funding with code ESAC-321, ESAC Traineeship program and of the Herschel Science Centre. We thank Gábor Marton for useful discussions on Herschel data evaluation. This work was partly supported by the Hungarian research grant OTKA 101393, and by the Momentum grant of the MTA CSFK Lendület Disk Research Group. PACS was developed by a consortium of institutes led by MPE (Germany), including UVIE (Austria); KUL, CSL, IMEC (Belgium); CEA, OAMP (France); MPIA (Germany); IFSI, OAP/AOT, OAA/CAISMI, LENS, SISSA (Italy); IAC (Spain). This development has been supported by the funding agencies BMVIT (Austria), ESA-PRODEX (Belgium), CEA/CNES (France), DLR (Germany), ASI (Italy), and CICT/MCT (Spain). SPIRE was developed by a consortium of institutes led by Cardiff Univ. (UK), including Univ. Lethbridge (Canada); NAOC (China); CEA, LAM (France); IFSI, Univ. Padua (Italy); IAC (Spain); Stockholm Observatory (Sweden); Imperial College London, RAL, UCL-MSSL, UKATC, Univ. Sussex (UK); and Caltech, JPL, NHSC, Univ. Colorado (USA). This development has been supported by national funding agencies: CSA (Canada); NAOC (China); CEA, CNES, CNRS (France); ASI (Italy); MCINN (Spain); SNSB (Sweden); STFC (UK); and NASA (USA).This study also makes use of the data products from the Two Micron All Sky Survey (2MASS), a joint project of the University of Massachusetts and IPAC/Caltech, funded by NASA and the National Science Foundation; data products from the Wide-field Infrared Survey Explorer (WISE), a joint project of the University of California, Los Angeles, and the Jet Propulsion Laboratory (JPL)/California Institute of Technology (Caltech); data products from DENIS, a project partly funded by the SCIENCE and the HCM plans of the European Commission under grants CT920791 and CT940627; the NASA Infrared Processing and Analysis Center (IPAC) Science Archive; and the SIMBAD database.

References

ALMA Partnership, Brogan, C. L., Perez, L. M., et al. 2015, ApJ, 808, L3
Alves de Oliveira, C., Moraux, E., Bouvier, J., et al. 2010, A&A, 515, A75
Alves de Oliveira, C., Ábrahám, P., Marton, G., et al. 2013, A&A, 559, A126
André, P., Men'shchikov, A., Bontemps, S., et al. 2010, A&A, 518, L102

Andrews, S. M., Wilner, D. J., Hughes, A. M., Qi, C., & Dullemond, C. P. 2009, ApJ, 700, 1502
Andrews, S. M., Wilner, D. J., Espaillat, C., et al. 2011, ApJ, 732, 42
Balog, Z., Müller, T., Nielbock, M., et al. 2014, Exp. Astron., 37, 129
Bustamante, I., Merín, B., Ribas, Á., et al. 2015, A&A, 578, A23
Cieza, L. A., Schreiber, M. R., Romero, G. A., et al. 2010, ApJ, 712, 925
Clarke, C. J., Gendrin, A., & Sotomayor, M. 2001, MNRAS, 328, 485
Dullemond, C. P., & Dominik, C. 2005, A&A, 434, 971
Erickson, K. L., Wilking, B. A., Meyer, M. R., Robinson, J. G., & Stephenson, L. N. 2011, AJ, 142, 140
Espaillat, C., Muzerolle, J., Najita, J., et al. 2014, in Protostars ans Planets VI, eds. R. S. Klessen, C. P. Dullemond & T. Henning (Tucson: University of Arizona Press), 497
Evans, II, N. J., Dunham, M. M., Jørgensen, J. K., et al. 2009, ApJS, 181, 321
Fazio, G. G., Hora, J. L., Allen, L. E., et al. 2004, ApJS, 154, 10
Griffin, M. J., Abergel, A., Abreu, A., et al. 2010, A&A, 518, L3
Hauschildt, P. H., Allard, F., & Baron, E. 1999, ApJ, 512, 377
Ho, P. T. P., Moran, J. M., & Lo, K. Y. 2004, ApJ, 616, L1
Kim, K. H., Watson, D. M., Manoj, P., et al. 2013, ApJ, 769, 149
Lada, C. J. 1987, in Star Forming Regions, eds. M. Peimbert, & J. Jugaku, IAU Symp., 115, 1
Marsh, K. A., & Mahoney, M. J. 1992, ApJ, 395, L115
Natta, A., Testi, L., Comerón, F., et al. 2002, A&A, 393, 597
Ott, S. 2010, in Astronomical Data Analysis Software and Systems XIX, eds. Y. Mizumoto, K.-I. Morita, & M. Ohishi, ASP Conf. Ser., 434, 139
Pilbratt, G. L., Riedinger, J. R., Passvogel, T., et al. 2010, A&A, 518, L1
Poglitsch, A., Waelkens, C., Geis, N., et al. 2010, A&A, 518, L2
Ribas, Á., Merín, B., Bouy, H., et al. 2013, A&A, 552, A115
Ribas, Á., Merín, B., Bouy, H., & Maud, L. T. 2014, A&A, 561, A54
Rieke, G. H., Young, E. T., Engelbracht, C. W., et al. 2004, ApJS, 154, 25
Roussel, H. 2013, PASP, 125, 1126
Skrutskie, M. F., Cutri, R. M., Stiening, R., et al. 2006, AJ, 131, 1163
Strom, K. M., Strom, S. E., Edwards, S., Cabrit, S., & Skrutskie, M. F. 1989, AJ, 97, 1451
Traficante, A., Fuller, G. A., Pineda, J. E., & Pezzuto, S. 2015, A&A, 574, A119
van der Marel, N., van Dishoeck, E. F., Bruderer, S., et al. 2013, Science, 340, 1199
Weingartner, J. C., & Draine, B. T. 2001, ApJ, 548, 296
Werner, M. W., Roellig, T. L., Low, F. J., et al. 2004, ApJS, 154, 1
Wilking, B. A., Meyer, M. R., Robinson, J. G., & Greene, T. P. 2005, AJ, 130, 1733
Wilking, B. A., Gagné, M., & Allen, L. E. 2008, Star Formation in the ρ Ophiuchi Molecular Cloud, ed. B. Reipurth, 351
Wootten, A., & Thompson, A. R. 2009, IEEE Proc., 97, 1463
Wright, E. L., Eisenhardt, P. R. M., Mainzer, A. K., et al. 2010, AJ, 140, 1868

Pages 11 to 20 are available in the electronic edition of the journal at http://www.aanda.org

Appendix A

Table A.1. Estimation of contaminating flux contained in the aperture for each band, according to the median SED extrapolation.

ID	Name	F_{70} [Jy] (6″)	F_{160} [Jy] (12″)	F_{250} [Jy] (22″)	F_{350} [Jy] (30″)	F_{500} [Jy] (42″)
–	2MASS J16245974-2456008	–	2.66×10^{-5}	2.94×10^{-4}	9.00×10^{-5}	2.77×10^{-5}
–	V*V852Oph	–	1.44×10^{-4}	1.48×10^{-4}	4.96×10^{-5}	6.11×10^{-5}
–	2MASS J16253673-2415424	–	–	4.47×10^{-5}	1.23×10^{-5}	3.17×10^{-5}
–	2MASS J16253958-2426349	–	–	9.65×10^{-4}	4.60×10^{-4}	3.15×10^{-4}
–	V*V2058Oph	3.34×10^{-2}	1.12×10^{-2}	5.29×10^{-3}	1.46×10^{-3}	3.97×10^{-4}
1	Haro1-6	5.85×10^{-2}	1.55×10^{-2}	7.64×10^{-3}	2.15×10^{-3}	6.09×10^{-4}
–	2MASS J16261684-2422231	–	–	1.01×10^{-5}	1.15×10^{-5}	1.48×10^{-5}
2	DoAr 24	4.51×10^{-3}	9.56×10^{-4}	4.50×10^{-4}	1.32×10^{-4}	4.03×10^{-5}
–	2MASS J16262189-2444397	5.90×10^{-3}	1.27×10^{-3}	5.98×10^{-4}	2.07×10^{-4}	7.49×10^{-5}
–	DoAr 24E	–	–	–	1.41×10^{-4}	3.85×10^{-5}
3	DoAr 25	–	1.23×10^{-4}	8.50×10^{-5}	3.09×10^{-5}	2.91×10^{-5}
–	GSS32	–	3.76×10^{-2}	1.77×10^{-2}	5.67×10^{-3}	1.61×10^{-3}
–	2MASS J16262407-2416134	–	–	–	6.89×10^{-5}	2.34×10^{-5}
–	2MASS J16263297-2400168	–	–	1.32×10^{-5}	1.86×10^{-5}	1.06×10^{-5}
–	2MASS J16263682-2415518	–	1.39×10^{-3}	6.68×10^{-4}	2.07×10^{-4}	6.18×10^{-5}
–	[*GY*92]93	–	–	1.36×10^{-5}	1.12×10^{-5}	1.59×10^{-5}
–	2MASS J16264285-2420299	–	–	–	2.40×10^{-4}	1.60×10^{-4}
–	2MASS J16264643-2412000	–	3.32×10^{-4}	1.65×10^{-4}	4.94×10^{-5}	1.69×10^{-5}
4	WSB 40	2.09×10^{-2}	4.43×10^{-3}	2.09×10^{-3}	5.86×10^{-4}	1.65×10^{-4}
–	WL18	–	–	4.75×10^{-6}	5.77×10^{-6}	5.37×10^{-6}
–	2MASS J16265677-2413515	1.59×10^{-3}	3.36×10^{-4}	1.58×10^{-4}	5.43×10^{-5}	2.13×10^{-5}
5	SR 24S	3.92×10^{-1}	8.29×10^{-2}	3.91×10^{-2}	1.08×10^{-2}	2.95×10^{-3}
6	2MASS J16270659-2441488	–	2.93×10^{-5}	2.17×10^{-5}	1.28×10^{-5}	1.23×10^{-5}
–	2MASS J16270907-2412007	–	–	2.68×10^{-5}	1.86×10^{-5}	8.30×10^{-6}
7	WSB 46	–	4.76×10^{-5}	2.46×10^{-5}	1.65×10^{-5}	8.68×10^{-6}
–	[*WMR*2005]4 – 10	5.65×10^{-4}	1.20×10^{-4}	7.63×10^{-5}	5.06×10^{-5}	2.52×10^{-5}
–	2MASS J16271836-2454537	–	–	7.27×10^{-6}	3.56×10^{-6}	3.40×10^{-6}
–	WSB 49	–	–	1.78×10^{-5}	6.58×10^{-6}	4.63×10^{-6}
–	2MASS J16272658-2425543	–	–	4.66×10^{-5}	3.35×10^{-5}	1.53×10^{-5}
8	2MASS J16273084-2424560	–	–	1.72×10^{-5}	1.30×10^{-5}	5.67×10^{-6}
–	2MASS J16273311-2441152	–	–	–	3.20×10^{-6}	5.10×10^{-6}
9	IRS 48	–	–	–	1.20×10^{-4}	4.42×10^{-5}
10	IRS 49	–	–	6.90×10^{-6}	7.97×10^{-6}	6.54×10^{-6}
–	2MASS J16273832-2357324	–	–	7.64×10^{-4}	2.19×10^{-4}	6.12×10^{-5}
11	2MASS J16273863-2438391	6.27×10^{-3}	1.62×10^{-3}	5.83×10^{-5}	3.59×10^{-5}	1.51×10^{-3}
–	2MASS J16273901-2358187	–	–	1.51×10^{-4}	5.32×10^{-5}	2.76×10^{-5}
12	WSB52	1.45×10^{-3}	3.08×10^{-4}	1.56×10^{-4}	1.61×10^{-5}	1.25×10^{-4}
13	SR 9	–	–	1.70×10^{-5}	1.59×10^{-5}	1.02×10^{-5}
–	2MASS J16274270-2438506	–	–	5.44×10^{-6}	4.54×10^{-6}	6.99×10^{-6}
–	V*V2059Oph	–	–	–	8.23×10^{-6}	7.76×10^{-6}
–	2MASS J16280256-2355035	–	–	6.06×10^{-8}	5.08×10^{-6}	5.56×10^{-6}
–	2MASS J16281379-2432494	–	–	5.82×10^{-6}	4.25×10^{-6}	7.35×10^{-6}
14	2MASS J16281385-2456113	–	–	1.02×10^{-4}	2.94×10^{-5}	1.63×10^{-5}
15	WSB 60	–	2.13×10^{-4}	1.10×10^{-5}	1.00×10^{-5}	6.31×10^{-6}
–	2MASS J16281673-2405142	–	–	–	7.31×10^{-6}	8.51×10^{-6}
16	SR 20W	–	–	4.36×10^{-6}	5.78×10^{-6}	6.48×10^{-6}
17	SR 13	–	–	–	4.01×10^{-5}	1.51×10^{-5}
18	2MASS J16285694-2431096	–	–	4.67×10^{-6}	1.83×10^{-5}	7.36×10^{-6}
–	2MASS J16294427-2441218	–	–	1.75×10^{-5}	1.35×10^{-5}	7.44×10^{-6}

Notes. The contaminating flux has been calculated extrapolating the MIPS-24 flux obtained from the *Spitzer* c2d catalogue (Evans et al. 2009) to the median SED for each source contained in the different apertures for each band.

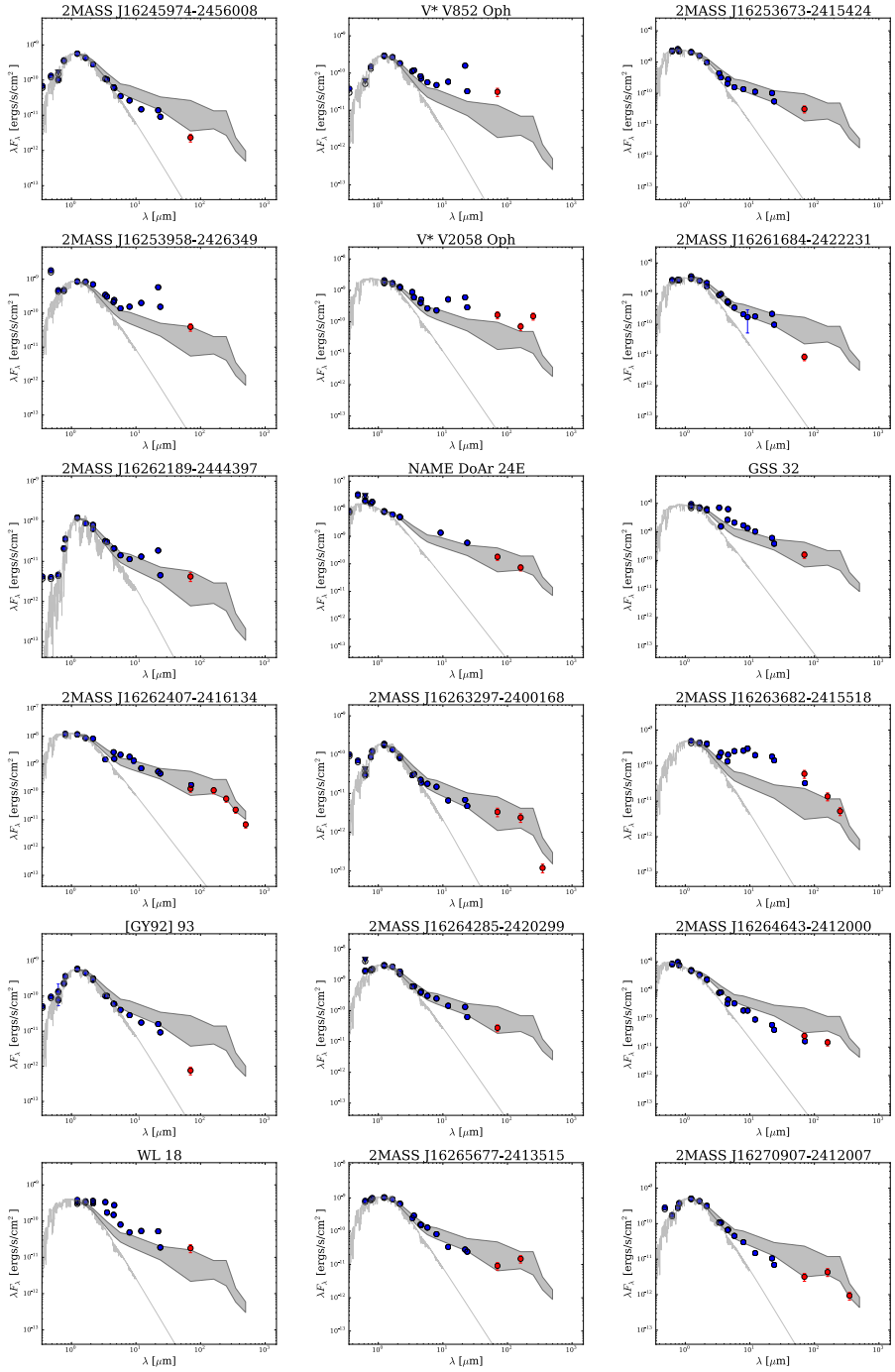

Fig. A.1. Spectral energy distribution (SED) of the sources detected in at least one band by *Herschel* and classified as non-transitional. Blue dots show data acquired from the literature, red dots are photometric fluxes obtained from *Herschel* data. Grey dashed line is the photosphere model according to the spectral type, and the grey shaded area is the filled area between the first and third quartile of all the disk fluxes. Observed fluxes are shown with empty circles and A_v values used are in Table 3.

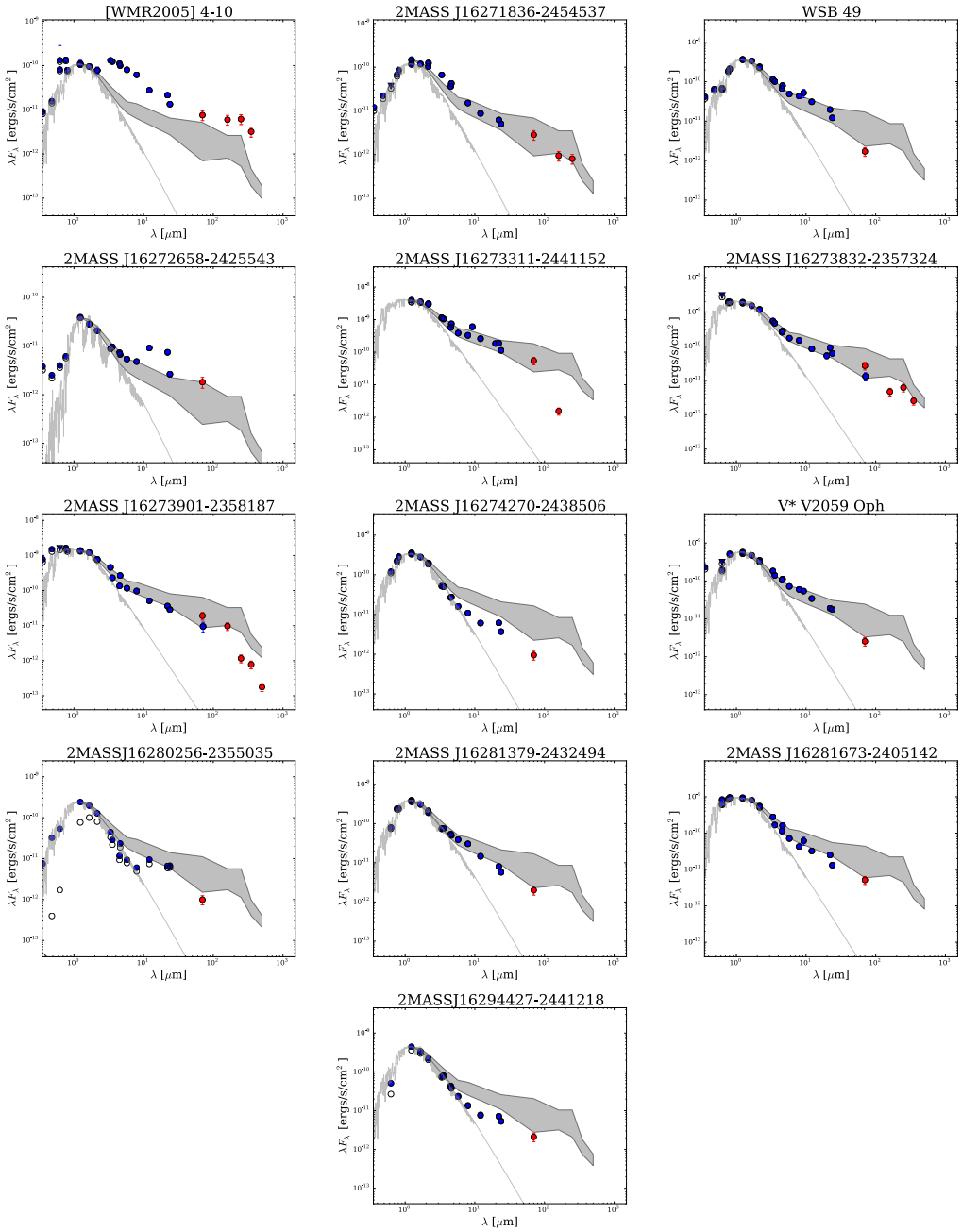

Fig. A.1. continued.

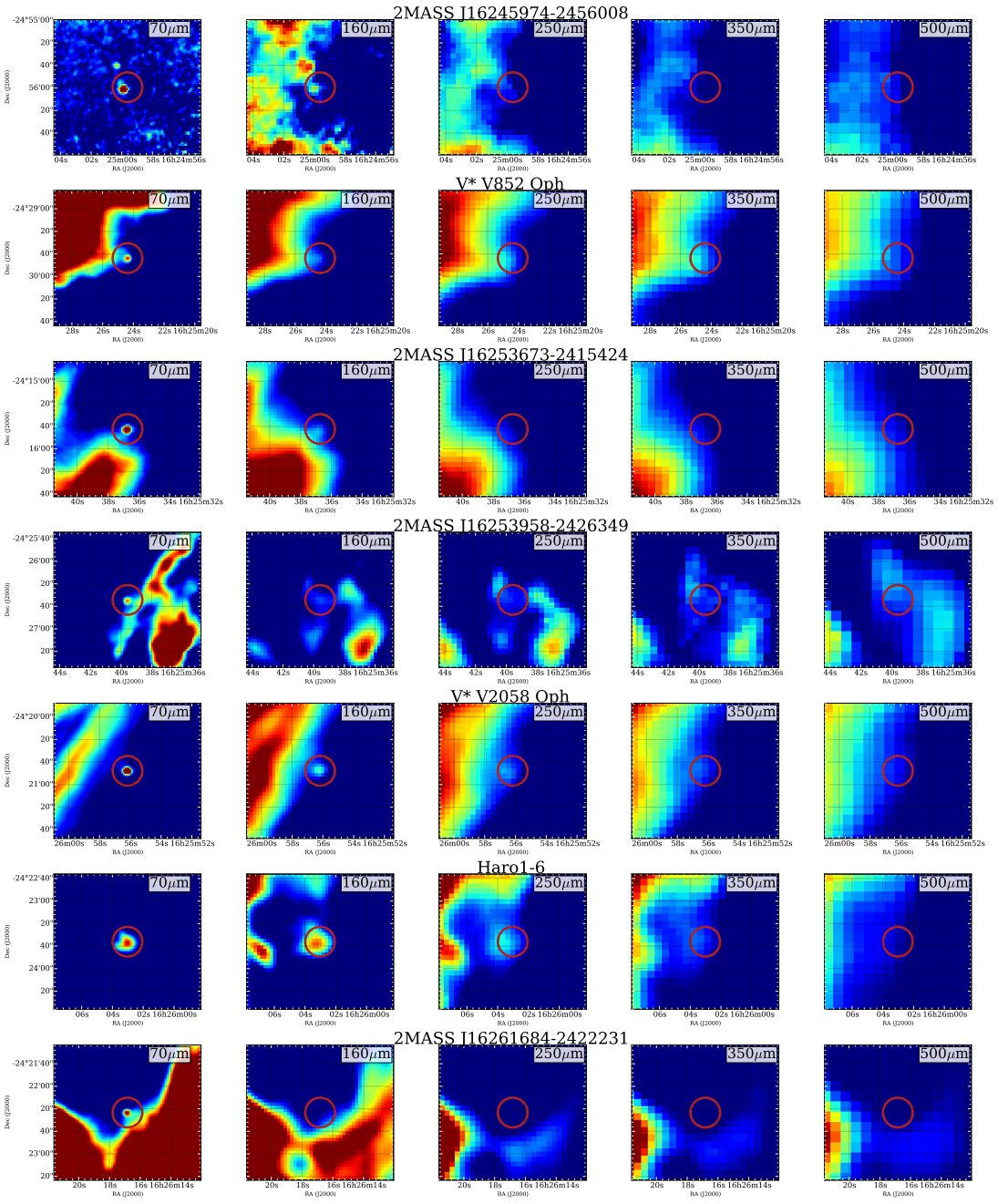

Fig. A.2. Thumbnail images of each of the 46 sources with at least one point source detected by *Herschel*. All images are 60″ ×60″ with north up and east to the left. The cut levels are set to the rms of the background for the minimum and three times that value for the maximum with linear stretch.

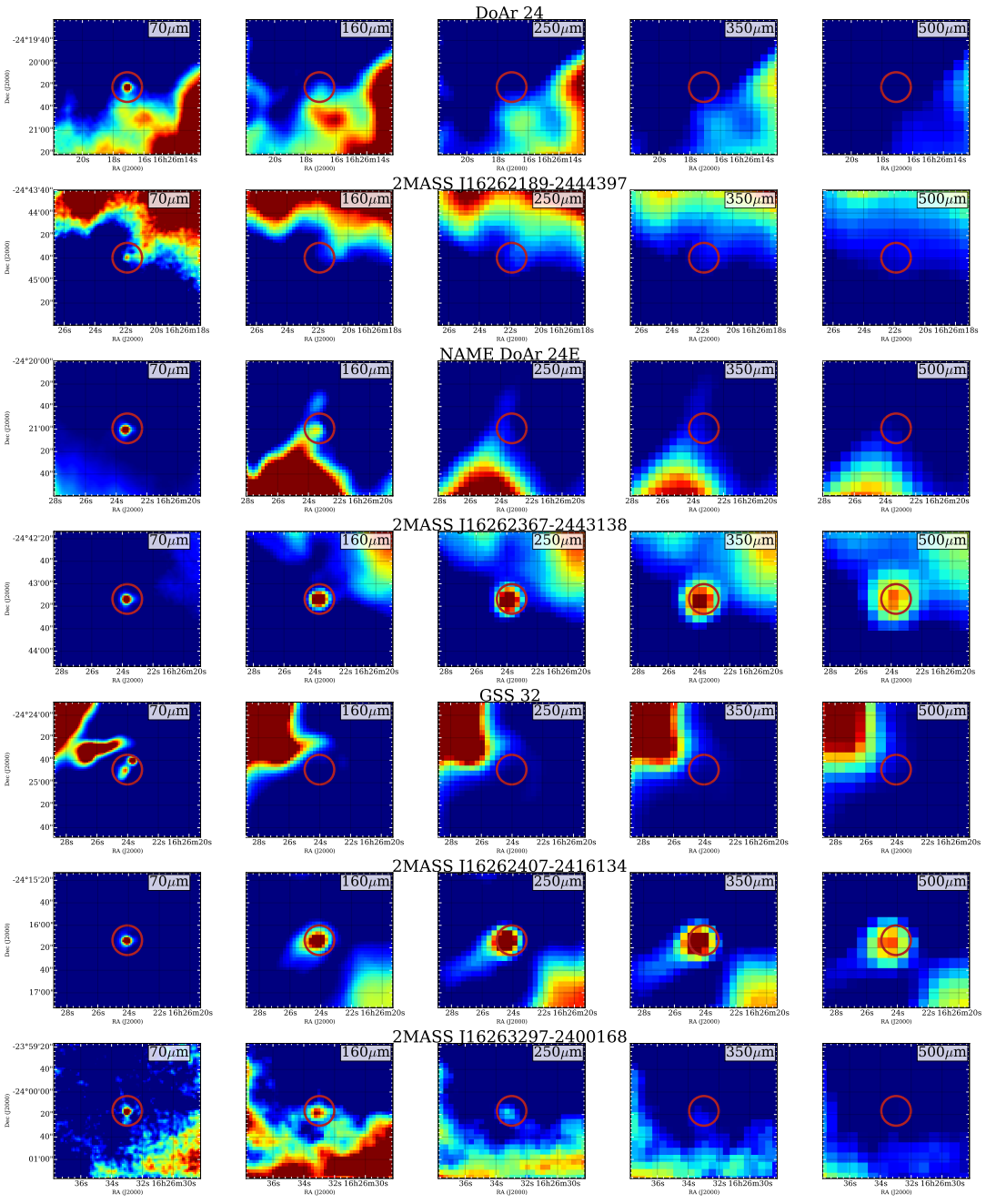

Fig. A.2. continued.

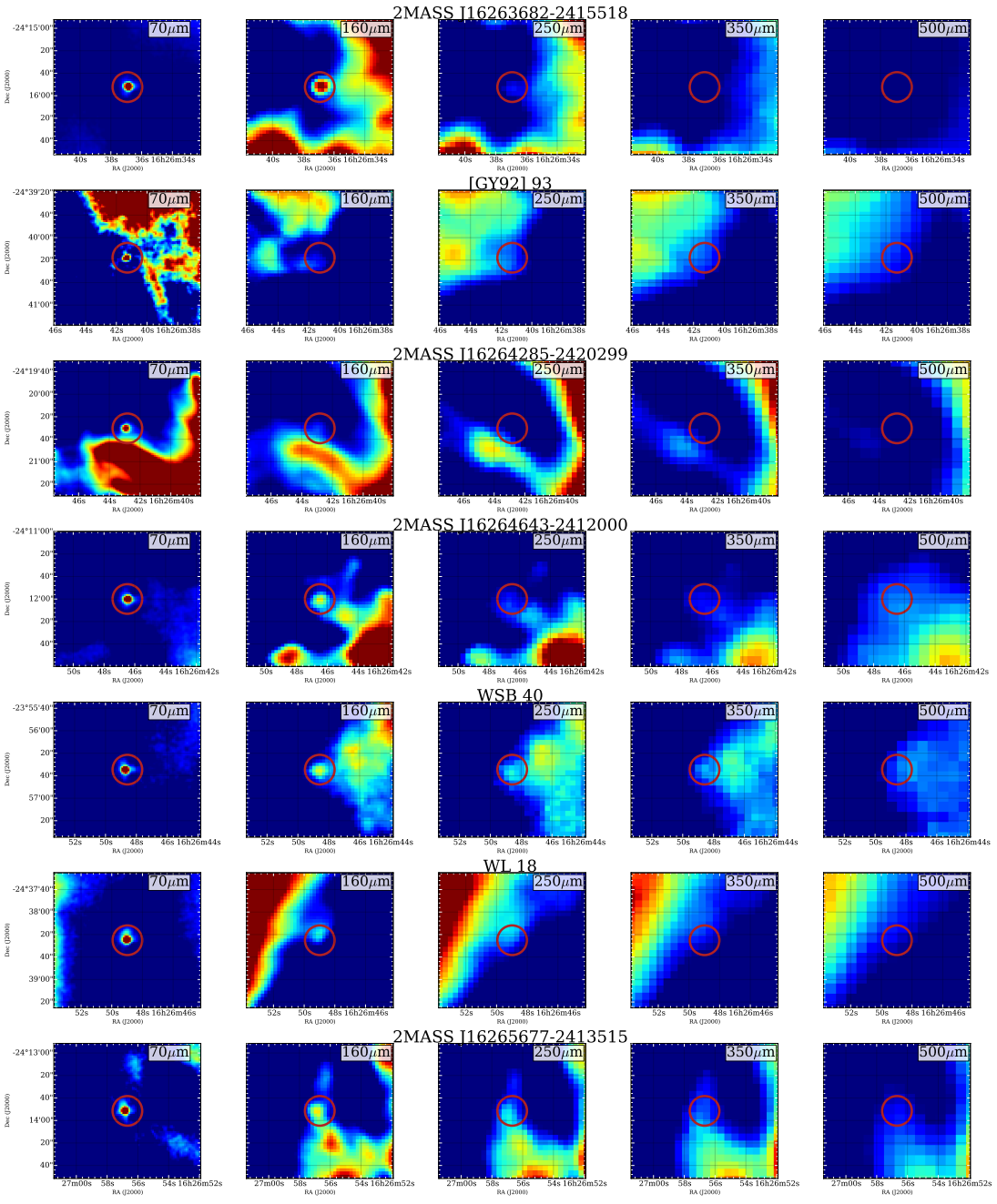

Fig. A.2. continued.

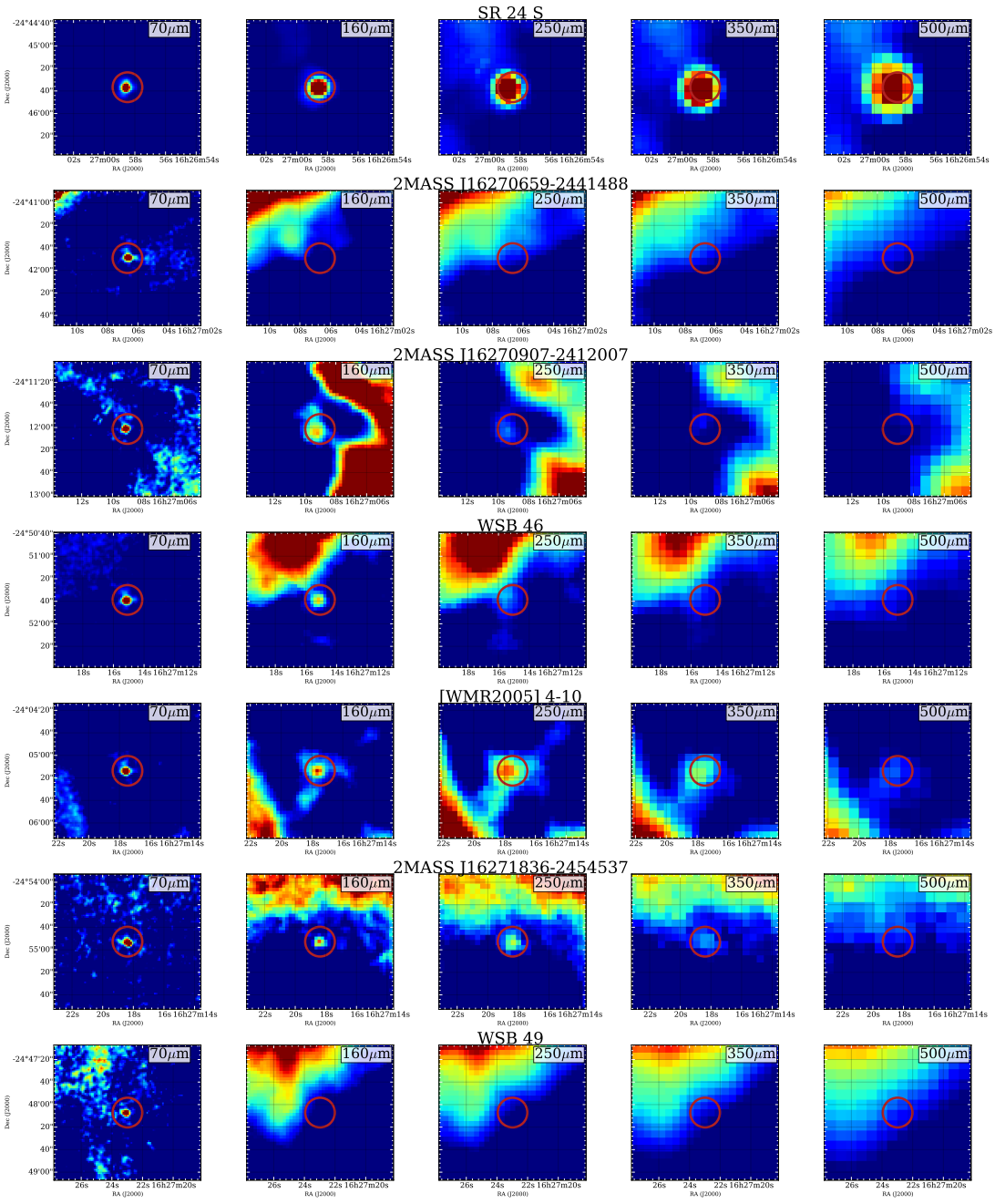

Fig. A.2. continued.

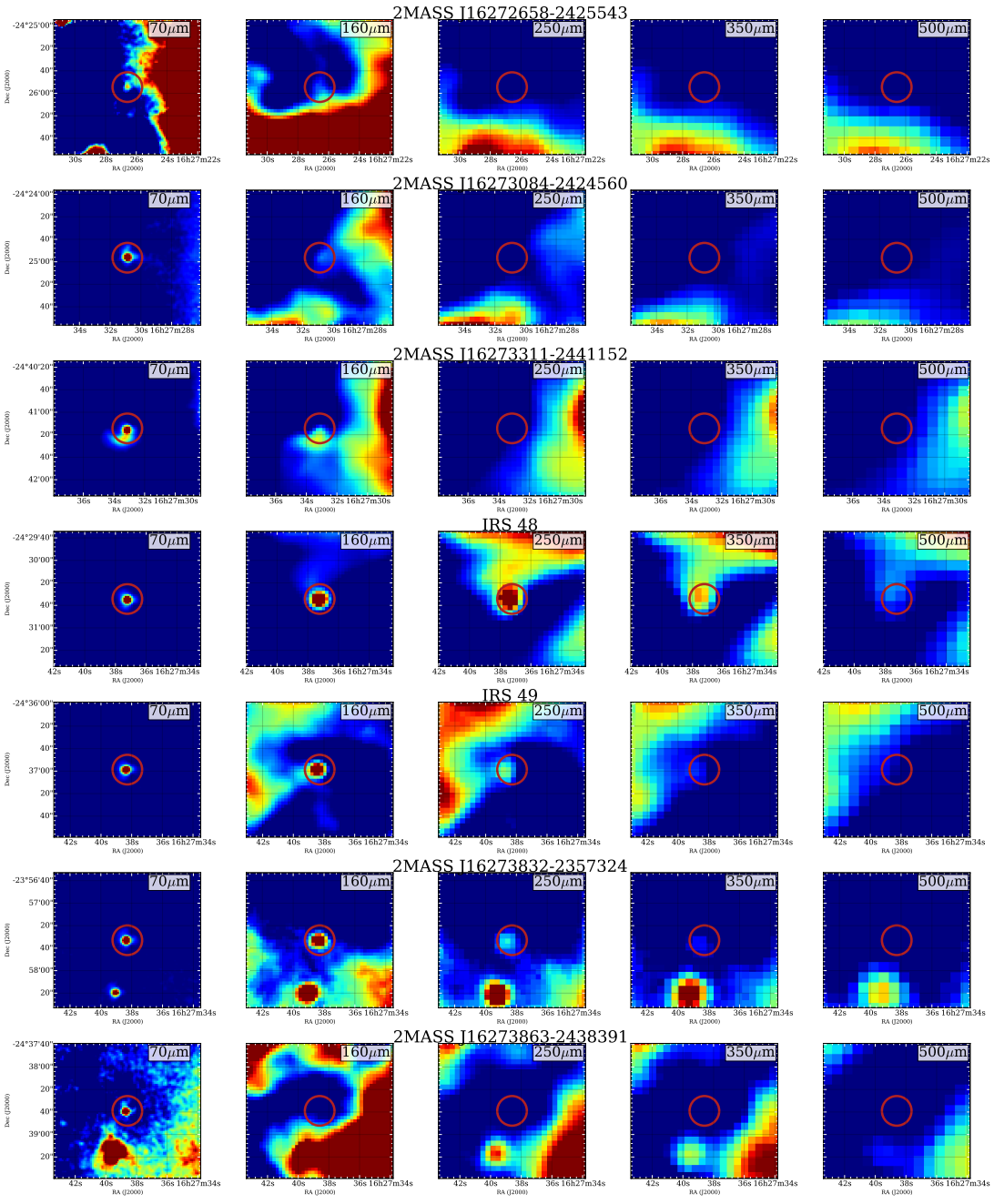

Fig. A.2. continued.

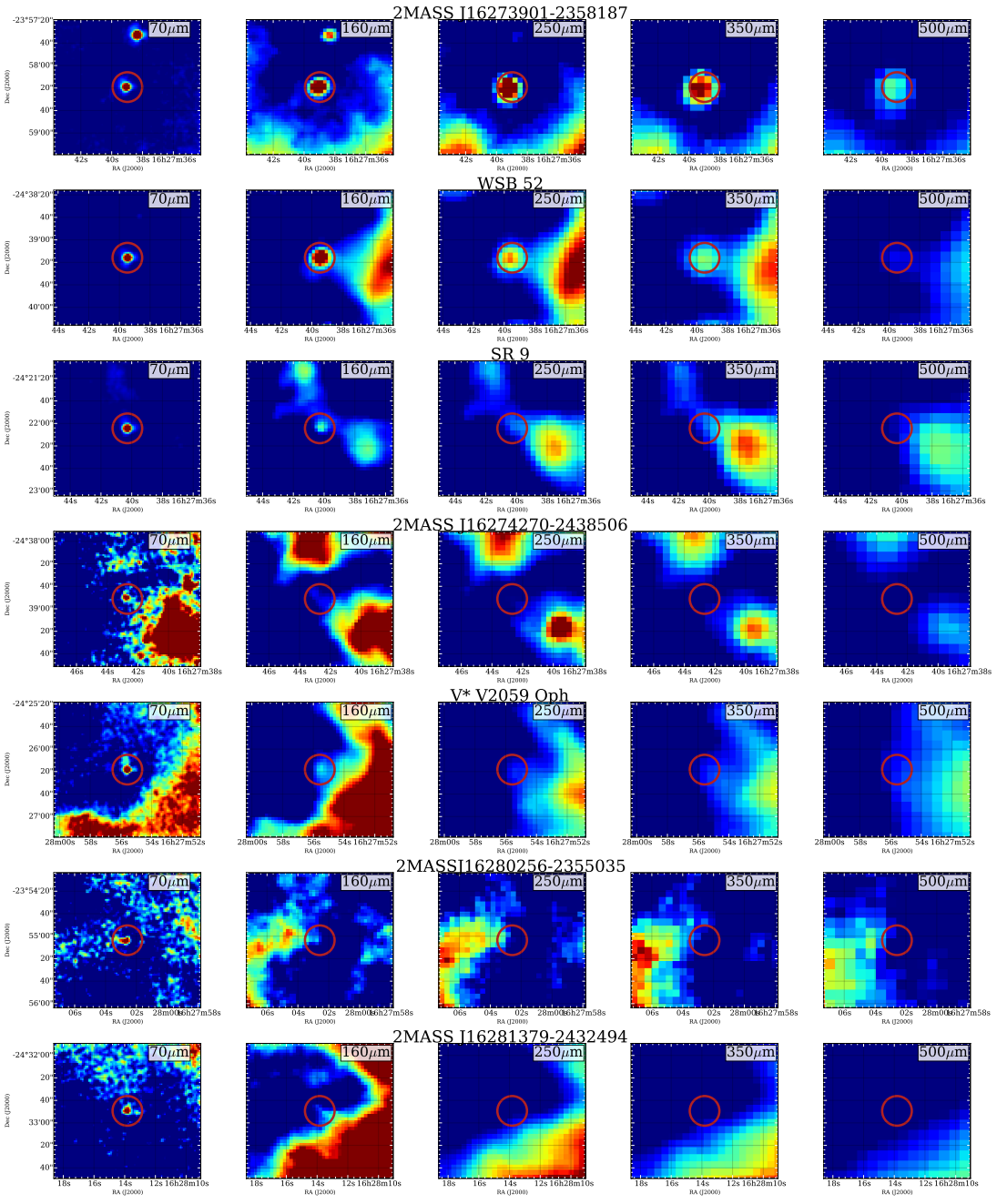

Fig. A.2. continued.

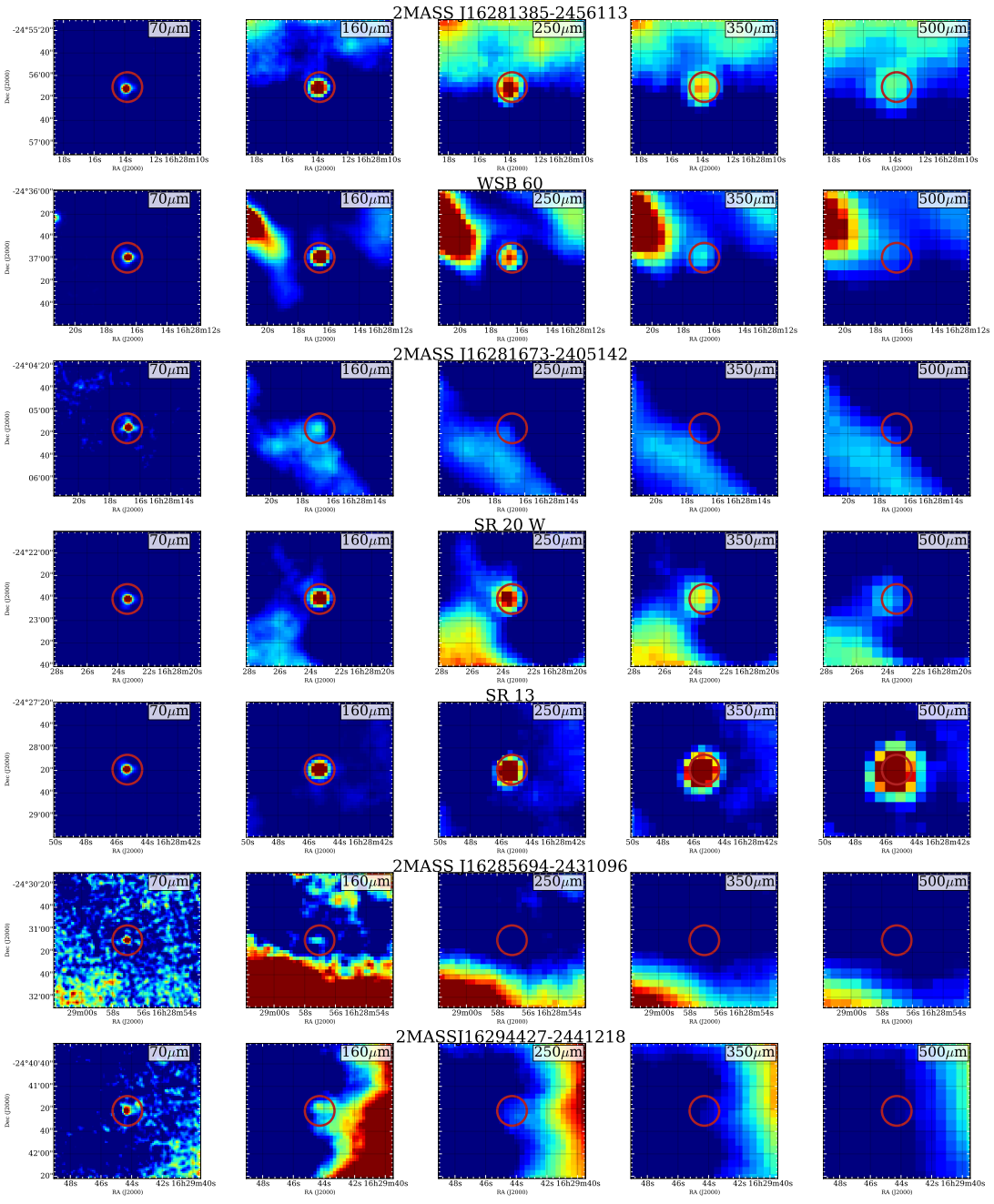

Fig. A.2. continued.

A&A 587, A81 (2016)
DOI: 10.1051/0004-6361/201527383

Astronomy & Astrophysics

X-ray deficiency on strongly accreting T Tauri stars

Comparing Orion with Taurus⋆

I. Bustamante[1,2,3], B. Merín[1], H. Bouy[2], C. F. Manara[4], Á. Ribas[1,2,3], and P. Riviere-Marichalar[1]

[1] European Space Astronomy Centre (ESA), PO Box, 78, 28691 Villanueva de la Cañada, Madrid, Spain
e-mail: ibustamante@cab.inta-csic.es
[2] Centro de Astrobiología, INTA-CSIC, PO Box – Apdo. de correos 78, 28691 Villanueva de la Cañada, Madrid, Spain
[3] ISDEFE – ESAC, PO Box 78, 28691 Villanueva de la Cañada, Madrid, Spain
[4] Scientific Support Office, Directorate of Science and Robotic Exploration, European Space Research and Technology Centre (ESA/ESTEC), Keplerlaan 1, 2201 AZ Noordwijk, The Netherlands

Received 16 September 2015 / Accepted 4 November 2015

ABSTRACT

Context. Depending on whether a T Tauri star accretes material from its circumstellar disk or not, different X-ray emission properties can be found. The accretion shocks produce cool heating of the plasma, contributing to the soft X-ray emission from the star.
Aims. Using X-ray data from the *Chandra* Orion Ultra-deep Project and accretion rates that were obtained with the *Hubble* Space Telescope/WFPC2 photometric measurements in the Orion Nebula Cluster (ONC), we studied the relation between the accretion processes and the X-ray emissions of a coherent sample of T Tauri sources in the region.
Methods. We performed regression and correlation analyses of our sample of T Tauri stars between the X-ray parameters, stellar properties, and the accretion measurements.
Results. We find that a clear anti-correlation is present between the residual X-ray luminosity and the accretion rates in our samples in Orion that is consistent with that found on the *XMM-Newton* Extended Survey of the Taurus molecular cloud (XEST) study. A considerable number of classified non-accreting sources show accretion rates comparable to those of classical T Tauri Stars (CTTS). Our data do not allow us to confirm the classification between classical and weak-line T Tauri stars (WTTS), and the number of WTTS in this work is small compared to the complete samples. Thus, we have used the entire samples as accretors in our analysis. We provide a catalog with X-ray luminosities (corrected from distance) and accretion measurements of an ONC T Tauri stars sample.
Conclusions. Although Orion and Taurus display strong differences in their properties (total gas and dust mass, star density, strong irradiation from massive stars), we find that a similar relation between the residual X-ray emission and accretion rate is present in the Taurus molecular cloud and in the accreting samples from the ONC. The spread in the data suggests dependencies of the accretion rates and the X-ray luminosities other than the stellar mass, but the similarity between Orion and Taurus hints at the environment not being one of them. The anti-correlation between the residual X-ray luminosity and mass accretion rate is inherent to the T Tauri stars in general, independent of their birthplace and environment, and intrinsic to early stellar evolution.

Key words. planetary systems – X-rays: stars – stars: pre-main sequence – protoplanetary disks

1. Introduction

The interaction between the central star and its surrounding disk in young stellar objects (YSOs) could be one the most important processes in the evolution of young stars, proto-planetary disks, and planetary system formation but, paradoxically, one of the least understood. Ultraviolet and X-ray irradiation from the star affects the dispersal and evolution of its surroundings (Owen et al. 2010), and the magnetic activity of the star has an important role in the mass-accretion rate from the disk onto the central object. The X-ray emission from the central star should photo-ionize the circumstellar material (Gorti & Hollenbach 2009), affecting its chemical composition, accreting processes (Alexander et al. 2014), outflows, and potential planetary atmospheres.

T Tauri stars present X-ray luminosities (L_X) near the saturation limit ($\log(L_X/L_{bol}) = -3$) found for main-sequence (MS) stars, $L_X/L_{bol} \sim 10^{-3.5}$, i.e., sometimes orders of magnitude higher than more evolved stars. For MS stars the X-ray activity is highly related with the rotation period, a relation given by the power law $L_X/L_{bol} \propto P_{rot}^{-2.6}$ (Pizzolato et al. 2003). But this relation has not been found for T Tauri stars (Preibisch et al. 2005). Several reasons have been postulated: the totally convective nature of young stars could be generating a different magnetic activity than that of MS stars (solar-like dynamo); a possible star magnetic field that is coupling with its surrounding disk; or the X-ray emission from accretion shocks could be altering the total amount of X-ray luminosity (Preibisch et al. 2005).

In the accretion process, material from the disk falls onto the stellar photosphere, generating a characteristic shock spectrum and an excess emission (L_{acc}), which can be measured with spectroscopic or photometric methods (Calvet & Gullbring 1998). This accretion luminosity can be linked to the mass accretion rate, $\dot{M}_{acc}$, through the relation: $\dot{M}_{acc} = L_{acc}R_*/0.8GM_*$, with R_*, and M_* being the radius and the mass of the star, respectively, and 0.8 being the factor that accounts for the assumption that the infall originates at a magnetospheric radius of $R_m = 5$ (Gullbring et al. 1998). The excess emission is mostly seen in the blue part of the spectrum (U-band excess) and in the emission lines (Hα equivalent width) (Hartmann 1998).

⋆ Full Table 4 is only available at the CDS via anonymous ftp to cdsarc.u-strasbg.fr (130.79.128.5) or via http://cdsarc.u-strasbg.fr/viz-bin/qcat?J/A+A/587/A81

Table 1. Key parameter comparison between the TMC and the ONC.

Region	X-ray program[1]	Distance (pc)[2]	Age (Myr)[3]	$N_{\rm total}$[4]
ONC	COUP	414	~2	277/163
Taurus Molecular Cloud	XEST	150	~1–2	105

Notes. [(1)] Name of the program from where the data were extracted (ONC Ref. Preibisch et al. 2005; TMC Ref. Telleschi et al. 2007; Güdel et al. 2007a). [(2)] Distance to the star-forming region (ONC Ref. Menten et al. 2007; TMC Ref. Telleschi et al. (2007)). [(3)] Mean log stellar age (ONC Ref. data from COUP and Reggiani et al. 2011; TMC Ref. Telleschi et al. 2007). [(4)] Number of sources used in the TMC analyses (Telleschi et al. 2007) and in the analyses of the ONC (Preibisch et al. 2005; this work). In the case of the ONC, the different numbers correspond to the sizes of each subsample studied.

The accretion processes were thought to play an important role in the X-ray activity of these stars, although several studies have found that strong accretors present lower $L_{\rm X}$ (Preibisch et al. 2005). Different explanations have been elaborated, such as disk opaqueness to certain $L_{\rm X}$ energies (Güdel et al. 2007b), thermalization and absorption of the soft component of the X-ray luminosity (~5 keV) (Calvet & Gullbring 1998) or changes in the coronal magnetic field activity provoked by the accretion processes (Telleschi et al. 2007). Also, a higher magnetic activity of the young star would result in highly energetic flares, showing large enough peaks in the X-ray measurements to even connect the inner disk to the star's photosphere (Aarnio et al. 2010).

Several studies have been carried out regarding the relation between mass accretion rates and X-ray emission. One of these is the anti-correlation found between the residual $L_{\rm X}$ and the $\dot{M}_{\rm acc}$ by Telleschi et al. (2007), using data part of the *XMM-Newton* Extended Survey of the Taurus molecular cloud (XEST). Our main objective is to compare the mass accretion rates – X-ray emission relation found in that article (Telleschi et al. 2007) for the low mass T-association of the Taurus Molecular Cloud (TMC) with data on the Orion Nebula Cluster (ONC), and to look for any possible environmental effect. We used the X-ray emission data from the *Chandra* Orion Ultra-deep Project (COUP; Getman et al. 2005b; Preibisch et al. 2005) and the accretion measurements from Manara et al. (2012), which use data from the *Hubble* Space Telescope (HST) Treasury Program on the ONC (Robberto et al. 2013).

This article is organized as follows: Sect. 2 describes the different datasets we use in our study and the cross-matching procedure. Section 3 illustrates the selection of the sub-samples we use. In Sect. 4 we explain the relation between X-ray emission and accretion processes we want to analyze and the correlation results we obtained, which are fully discussed in Sect. 5. In Sect. 6, we summarize the conclusions of this work.

2. X-rays and accretion in the ONC

2.1. Taurus and Orion comparison

The TMC is the nearest largest (distance ~140 pc, Loinard et al. 2005) star-forming region known. It is composed of several loosely associated molecular clouds, each of them producing small numbers of YSOs. Its small star density (1–10 stars pc^{-2}, Gomez et al. 1993) prevents a notable influence from gravitational effects, outflows, or strong UV radiation fields, which creates a calm evolutionary environment, compared to other star-forming regions.

Although several other X-ray studies have been carried out in the region, the XEST project provided the most sensitive and complete sample of X-ray detections (Telleschi et al. 2007; Güdel et al. 2007a). The X-ray emission of TTS is usually between $L_{\rm X} \sim 10^{29}$–10^{31} erg s^{-1}, clearly higher than the instrument detection limit of $L_{\rm X} \sim 10^{28}$ erg s^{-1}, for typical integration times. In fact, the XEST presents X-ray detection statistics consistent with near-completeness: 126 out of 152 TMC members are detected in X-rays (Güdel et al. 2007a). Out of a this sample, 55 are classified as strong accretors (or classical T Tauri stars) and 45 as weak accretors (or weak-line T Tauri stars), a classification that is based on the equivalent width of the Hα line. We refer to Telleschi et al. (2007) for a complete description of their sample selection and analyses.

In contrast, the ONC presents a much denser picture, with a distance of ~414 pc (Menten et al. 2007). This massive cluster of young stars (~10^6 yr) located in the Orion Molecular Cloud is illuminated by two O-type stars (Θ^1 Ori C and Θ^2 Ori A), has a star population of ~1600 optically visible sources, and is recognized as a benchmark laboratory for star and planet formation, and the closest massive cluster to the Sun. It represents a coherent and homogeneous group of pre-main sequence (PMS) stars (Hillenbrand 1997; Da Rio et al. 2010, 2012), and a perfect bench test for a comparison with the TMC. Table 1 summarizes some key characteristics of both regions.

2.2. X-ray emission in the ONC – COUP

We use the data available from the COUP (Preibisch et al. 2005; Feigelson 2005; Getman et al. 2005a), or more precisely, from the *Chandra* Orion Ultra-deep Point Source Catalog[1].

The COUP was a deep observation of the ONC using the Advanced CCD Imaging Spectrometer (ACIS) mounted on the *Chandra* X-ray telescope. This was a continuous 838 ks exposure program over a period of 13.2 days in January 2003. It detected 1 616 individual X-ray sources, with typical positional uncertainties of <0.″3. This observation of the ONC (Getman et al. 2005b) resulted in the detection of ~1400 X-ray-emitting PMS and is the richest source of X-ray data ever obtained for the ONC. We refer to Getman et al. (2005a,b) for a full review of the program.

2.3. Accretion data

For the accretion measurements, we used the data of Manara et al. (2012) on the ONC, in which they use the photometric catalog from the HST Treasury Program of Robberto et al. (2013). This program observed the ONC for 104 HST orbits of HST time with the Advanced Camera for Surveys (ACS), the Wide-Field/Planetary Camera 2 (WFCP2), and the Near-Infrared Camera and Multi-Object Spectrograph (NICMOS),

[1] http://heasarc.gsfc.nasa.gov/W3Browse/chandra/coup.html

using 11 filters in total that range from the U to the H-band. With the data obtained from WFPC2, Manara et al. (2012) calculate the mass accretion rates of almost ~600 PMS stars. Here we summarize the key aspects of their work and briefly discuss the two methodologies they use to determine the accretion rates. In the following, we divide the discussion on this dataset using two subsamples that were created by the method used to determine the accretion rates: the U-band excess and the Hα line flux. For a complete analysis of the data selection and procedure, we refer to their article.

Manara et al. (2012) construct a two-color diagram (2CD) with the *UBI* photometric measurements, and simultaneously obtain an estimate of the extinction, A_V, and accretion luminosity, $L_{\rm acc}/L_{\rm tot}$. They assume that the displacement of the observed sources from the theoretical isochrone on the 2CD is caused by a combination of these two processes. They assume spectral types from the literature for all their targets.

U-band excess – From the 2CD that they converted they derive $L_{\rm acc}/L_{\rm tot}$ into $L_{\rm acc}/L_{\odot}$, taking into consideration the stellar luminosities with the relation $L_{\rm acc}/L_{\odot} = (L_{\rm acc}/L_{\rm tot})/(1 - L_{\rm acc}/L_{\rm tot})* L_*/L_{\odot}$ (L_* being the stellar luminosity).

Hα line – Manara et al. (2012) also use the Hα luminosity as an accretion tracer. With the Hα photometry available from the WFPC2 catalog (more precisely, the photometry from the *F656N* filter), they measure the excess with respect to the photospheric (Hα - I) color for each star, which is dependent on $T_{\rm eff}$. They then convert this Hα excess into equivalent width. They consider the sources that fulfill the condition 3 Å < $EW_{\rm H\alpha}$ < 1000 Å as accretors. Finally, they derive the accretion luminosity $L_{\rm acc}$ from the Hα luminosity $L_{\rm H\alpha}$ with the relation $\log(L_{\rm acc}/L_{\odot}) = (1.31 \pm 0.03)\log(L_{\rm H\alpha}/L_{\odot}) + (2.63 \pm 0.13)$. The $L_{\rm acc} - L_{\rm H\alpha}$ relation was calibrated using the U-excess data. The masses of the stars were computed with an evolutionary model interpolation of the position of them on the Hertzprung-Russel diagram (HRD).

Manara et al. (2012) obtain accretion rates for 244 objects using the U-excess method, and for 486 using the Hα one. These subsamples are independent of one another. The excess in the U-band is a direct proxy of accretion, while the $L_{\rm H\alpha}$ is an indirect one. Thus, the accretion rate measurements of the U-excess subsample are more reliable than those of the Hα one.

Manara et al. (2012) discard close binaries and visual proplyds (Ricci et al. 2008) from their sample. Thus, our subsamples are cleansed of these objects too. Consequently, our catalogs are only composed of young accreting stars. We will refer to these catalogs as the U-excess and the Hα subsamples, respectively.

2.4. Cross-matching

The first step in our analysis was to find the COUP X-ray counterparts for the sources in the HST sub-samples. Using the nearest neighbors method, we made a first cross-match with the sky positions of the sources of the COUP catalog and those of the Manara2012 subsamples, using a matching distance of 1″ as a first approximation. We chose this distance taking into account the astrometric accuracy of *Chandra*: the 99% limit on positional accuracy is 0.8″, in the worst case being an offset of 1.1″[2]. With this matching distance, we obtained 170 pairings with the U-excess group, and 322 pairings with the Hα one.

We wanted to check if a systematic offset in the positions of both catalogs was present. Thus, we calculated the median differences in the right ascension and declination of this first set.

[2] http://cxc.harvard.edu/cal/ASPECT/celmon/

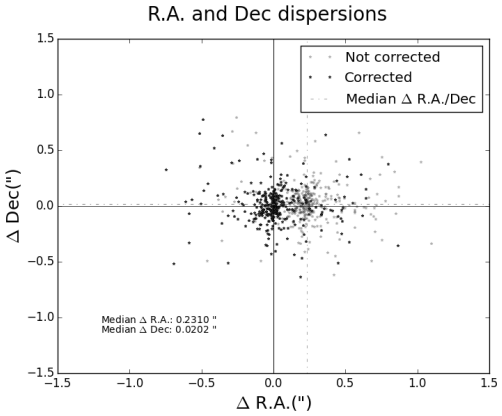

Fig. 1. Right ascension and declination offsets between the HST Hα sources and the COUP sample, before and after correction.

As can be seen in Fig. 1, we found $\delta RA_{U-\rm excess} = +0.274''$ and $\delta DEC_{U-\rm excess} = +0.036''$, and $\delta RA_{\rm H\alpha} = +0.228''$, and $\delta DEC_{\rm H\alpha} = +0.026''$. We then corrected the COUP sources' right ascension and declination with these median offset values to refine the search of HST counterparts, and did a new cross-match with these new coordinates. For the U-excess subsample we found one less source, obtaining a sub-sample of 169 matches, whereas for the Hα sub-sample we gained two more, obtaining 324 pairings.

As an extra control measure, we also performed the cross-match with the possibility of various pairings instead of just the nearest one. Not one of the HST sources in our Manara2012 subsamples had more than one COUP counterpart nearby. Table 2 shows the parameters from this procedure.

3. Sample selection

3.1. Spectral type and low mass

To study the mass accretion rates and the X-ray luminosities as a function of $T_{\rm eff}$, we only kept sources with a known spectral type. This left us with 281 sources in the case of the Hα subsample, and 164 in the U-excess one. Spectral types were derived from Hillenbrand (1997), Luhman et al. (2000), and Lucas et al. (2001). For some sources, the spectral type was recalculated in Hillenbrand et al. (2013). In these cases, we use the latest spectral type available.

The X-ray emission of high-mass stars is non-coronal in origin, or comes from a different kind of corona, or originates in unresolved lower mass companions (Flaccomio et al. 2012). Because of this, we limited our study to stars with $M_* < 2\ M_{\odot}$. With this selection, the numbers decreased to 277 sources for the Hα subsample and 163 for the U-excess subsample.

Some sources did not have defined uncertainties for the mass accretion rates. We only used sources with valid mass accretion values and uncertainties, discarding the invalid ones. Thus, the U-excess subsample was reduced to 154 sources. The Hα remained the same. This selection criteria is similar to that in Telleschi et al. (2007).

3.2. Classical T Tauri stars and weak-line T Tauri stars

The T Tauri family is divided into classical T Tauri stars (CTTS) and weak-line T Tauri stars (WTTS). This division takes into

Table 2. Cross-matching coordinates and parameters before and after the offset corrections.

	Mean $\Delta(")^1$	Mean $\Delta\alpha(")^2$	Mean $\Delta\delta(")^2$	Mean $\Delta(")^1$	Mean $\Delta\alpha(")^2$	Mean $\Delta\delta(")^2$
(Subsample)		(Hα)			(U-excess)	
Before correction	0.320	+0.248	+0.026	0.337	+0.274	+0.036
After correction	0.208	+0.130e-3	+0.011	0.199	+0.007	+0.003

Notes. [(1)] Mean position offset between X-ray COUP sources and both HST Manara et al. (2012) subsamples. [(2)] Mean right ascension and declination offsets for both sub-samples.

Table 3. Mean values of $\log(\dot{M}_{\rm acc})$ for both CTTS and WTTS classified with the different accretion tracers.

	Mean$_{\dot{M}_{\rm acc}}$ CTTS $\pm\,\sigma$	Mean$_{\dot{M}_{\rm acc}}$ WTTS $\pm\,\sigma$	Mean$_{\dot{M}_{\rm acc}}$ CTTS $\pm\,\sigma$	Mean$_{\dot{M}_{\rm acc}}$ WTTS $\pm\,\sigma$
(Subsample)	(Hα)		(U-excess)	
Ca$_{\rm II}$ method	–7.99 ± 0.94	–8.84 ± 0.98	–7.78 ± 0.80	–9.00 ± 0.80
Hα method	–8.11 ± 0.79	–9.56 ± 0.68	–	–
Barrado method	–8.30 ± 0.91	–9.00 ± 1.01	–	–

Notes. The standard deviation is used as the uncertainty.

account the value of some accretion tracers to classify the objects into accretors or non-accretors. Several studies use this classification when studying the accretion properties of star-forming regions. For example, Preibisch et al. (2005) and Flaccomio et al. (2003) use the Ca$_{\rm II}$ infrared triplet lines (λ = 8542 Å) equivalent width to classify their sample, as do Hillenbrand et al. (1998); and in Telleschi et al. (2007) they use the Hα line (λ = 6563 Å), as in Güdel et al. (2007a).

In our case, different classifications were possible. From the COUP data we accessed the values of the Ca$_{\rm II}$ line for both of our subsamples. Furthermore, for the Hα subsample, the Hα line equivalent width was also available. Thus, a second classification analysis could be carried out for this subsample.

Table 3 shows the mean accretion values for both subsamples. We note that, although both subsamples were classified using the Ca$_{\rm II}$ method, not every object in them was included in the analysis. The classification method only selects objects with EW(Ca$_{\rm II}$) < -1 Å (CTTS) and EW(Ca$_{\rm II}$) > 1 Å (WTTS) (Preibisch et al. 2005). Thus, objects with -1 Å $< EW$(Ca$_{\rm II}$) $<$ 1 Å are not included in the classification. In the case of the Hα subsample, we used 108 sources for these analyses, and for the U-excess subsample we used 56 sources.

Several objects that we classified as WTTS have stronger accretion rate measurements than the mean value of the total CTTS, and several CTTS have lower accretion rate values than the mean WTTS value. As a result, the mean $\dot{M}_{\rm acc}$ values of the WTTS and CTTS sources for both subsamples differ by less than 3σ.

The excess emission in Hα (and probably in U-band) present in WTTS may be due to cromospheric emission and not only to accretion. There have been studies that measure how strong this effect is and, in general, it is below the observed accretion rates (Ingleby et al. 2011; Stelzer et al. 2013; Manara et al. 2013a). Accreting PMS with values of $\log L_{\rm acc} \leq -3\ \log L_{\odot}$ should be treated with caution because the line emission may be dominated by the contribution of chromospheric activity (Manara et al. 2013b). In our case, none of the WTTS with strong accretion measurements had $\log L_{\rm acc}$ values lower than $-3\ \log L_{\odot}$, so we assume no significant cromospheric dependence for their accretion-rate measurements.

Our data do not allow us to classify our subsamples between CTTS and WTTS clearly. Medium-high resolution spectra would be needed for that analysis. Thus, in this work, we do not use the classical and weak-lined T Tauri division.

4. Relations between X-ray luminosity, stellar mass, and accretion rate

For the characterization of the X-ray properties, we used the following data from the COUP catalog: the total X-ray luminosity $L_{\rm X}$ (corrected for interstellar absorption), which corresponds to the total 0.5–8.0 keV energy band, with units of erg s^{-1}, and the equivalent width values of the Ca$_{\rm II}$ line for the T Tauri classification, in units of Å (see previous section). Importantly, Manara et al. (2012) formulate their analyses using a distance of 414 pc to the ONC, while the data in the COUP catalog assumes a distance of 450 pc. We corrected the latter with the distance of the former, using the equation used in the COUP catalog: $L = 4\pi D^2 F$, with F being the X-ray flux and D being the distance in parsecs. We used a value of 0.39 dex for the uncertainty of $L_{\rm X}$.

These X-ray parameters are selected as in Preibisch et al. (2005). The main difference with that work is the spectral type classification (we updated the spectral types of several objects with the information from Hillenbrand et al. 2013) and the sample selection (we used only objects with $M_* < 2\ M_{\odot}$).

The rest of the stellar parameters were gathered from Manara et al. (2012): the stellar masses M_*, in units of $M_{\odot}$, were obtained from D'Antona & Mazzitelli (1994) models and the accretion rates, with units of $M_{\odot}\,{\rm yr}^{-1}$, were derived from that paper, using photometric data from the HST Treasury Program (see Sect. 2).

In Table 4 we present the final catalog with all these parameters for both subsamples.

4.1. Least-square fit and outlier rejection study

In this work the regression analyses were carried out using two methods: a least-square approximation and an outlier rejection fit.

For the first, we used a classical ordinary least square (OLS) algorithm using the scipy's orthogonal distance regression (ODR) package on *Python* (Jones et al. 2001; Boggs et al. 1988). The ODR package allowed us to feed the uncertainties of our parameters into the analysis and take them into account to

Table 4. X-ray and stellar parameter information for both subsamples.

Coup id[1]	RA_{COUP}[2] (deg)	DEC_{COUP}[2] (deg)	$\log(L_X)$[3] (erg s^{-1})	OM id[1]	RA_{Manara}[2] (deg)	DEC_{Manara}[2] (deg)	$\log(M_*)$ ($M_\odot$)	$\log(\dot{M}_{acc})$ ($M_\odot$ yr^{-1})	SpT	$\log(L_X/L_X(\dot{M}_{acc}))$[4] OLS method	$\log(L_X/L_X(\dot{M}_{acc}))$[4] Outlier method
					Hα						
11	83.670400	–5.378410	30.29 ± 0.17	101	83.670246	–5.378431	–0.40 ± 0.05	–6.60 ± 0.36	M1	–1.22 ± 0.78	–1.05 ± 0.42
14	83.673400	–5.399380	28.69 ± 0.17	108	83.673392	–5.399303	–0.82 ± 0.01	–10.02 ± 0.43	M5	1.31 ± 0.37	0.21 ± 0.15
16	83.674400	–5.363780	28.53 ± 0.17	117	83.674233	–5.363750	–0.92 ± 0.01	–10.60 ± 0.59	M7	1.85 ± 0.34	0.54 ± 0.18
29	83.694200	–5.390450	29.75 ± 0.17	144	83.693996	–5.390442	–0.51 ± 0.07	–7.78 ± 0.36	M2	–0.34 ± 0.45	–0.60 ± 0.30
37	83.699800	–5.394550	28.03 ± 0.17	153	83.699687	–5.394536	–0.80 ± 0.01	–9.78 ± 0.36	M5	0.36 ± 0.38	–0.65 ± 0.18
28	83.693400	–5.408840	30.79 ± 0.17	157	83.693308	–5.408869	–0.35 ± 0.05	–9.13 ± 0.66	M0	2.34 ± 0.42	1.57 ± 0.40
40	83.700700	–5.377370	28.90 ± 0.17	158	83.700454	–5.377372	–0.89 ± 0.01	–9.77 ± 0.42	M3	1.22 ± 0.31	0.21 ± 0.13
117	83.737300	–5.368430	29.53 ± 0.17	185	83.737183	–5.368425	–0.52 ± 0.01	–8.79 ± 0.32	M3	0.67 ± 0.15	0.02 ± 0.15
133	83.746700	–5.385510	28.78 ± 0.17	194	83.746587	–5.385497	–0.89 ± 0.01	–9.48 ± 0.47	M4	0.75 ± 0.16	–0.15 ± 0.21
137	83.748200	–5.400080	29.15 ± 0.17	199	83.748138	–5.400053	–0.64 ± 0.01	–8.32 ± 0.30	M4	–0.28 ± 0.22	–0.75 ± 0.18
...											
					U-excess						
1	83.622700	–5.393730	29.74 ± 0.17	70	83.622692	–5.393733	–0.74 ± 0.00	–11.04 ± 0.34	M5	1.90 ± 0.44	0.77 ± 0.27
43	83.703500	–5.388330	30.24 ± 0.17	146	83.703458	–5.388329	–0.49 ± 0.07	–8.92 ± 0.26	M1	0.53 ± 0.16	0.16 ± 0.15
55	83.710600	–5.393160	29.17 ± 0.17	167	83.710400	–5.393148	–0.57 ± 0.01	–8.37 ± 0.20	M1	–1.03 ± 0.22	–1.20 ± 0.14
89	83.726200	–5.359870	29.59 ± 0.17	174	83.726037	–5.359843	–0.48 ± 0.08	–7.94 ± 0.11	M0	–0.99 ± 0.22	–1.00 ± 0.16
65	83.716800	–5.405220	29.46 ± 0.17	175	83.716704	–5.405229	–0.64 ± 0.01	–8.82 ± 0.08	M3	–0.34 ± 0.24	–0.67 ± 0.24
71	83.719200	–5.401070	30.17 ± 0.17	177	83.719104	–5.401034	–0.44 ± 0.06	–9.43 ± 0.20	M1	0.91 ± 0.25	0.36 ± 0.22
107	83.733300	–5.386970	31.32 ± 0.17	178	83.733208	–5.386923	0.04 ± 0.09	–7.45 ± 0.30	K2	0.31 ± 0.48	0.47 ± 0.24
118	83.737600	–5.383360	28.82 ± 0.17	189	83.737512	–5.383354	–0.70 ± 0.01	–10.38 ± 0.31	M4	0.40 ± 0.34	–0.49 ± 0.24
122	83.740800	–5.380900	30.09 ± 0.17	191	83.740746	–5.380872	–0.70 ± 0.01	–8.05 ± 0.11	M3	–0.39 ± 0.20	–0.44 ± 0.16
228	83.770100	–5.377450	28.34 ± 0.17	224	83.770043	–5.377404	–0.70 ± 0.01	–8.76 ± 0.08	M4	–1.52 ± 0.23	–1.82 ± 0.24
...											
...											

Notes. [(1)] Source ids as in the COUP catalog and in the Manara et al. (2012) samples. [(2)] Source coordinates as in the COUP catalog and in the Manara et al. (2012) samples. [(3)] Logarithmic value of the X-ray luminosity, computed at a distance of 414 pc. [(4)] Residual X-ray luminosities, computed using the regression results from the OLS method in the first case and from the outlier detection and rejection algorithm in the second.

acquire the fit. Moreover, it also produced the errors of the fitted coefficients, which we used to compute the uncertainties in our results.

Because of the large spread of our data, we decided to include a Bayesian outlier rejection algorithm with Monte Carlo Markov chain (MCMC), using the astroML package of Python (Vanderplas et al. 2012). The points, which are identified by this method as not part of the fit with a probability greater than 99.7% (3σ confidence), are selected as outliers. This method uses models that marginalizes over the probability that each point is an outlier. The MCMC is used for this marginalization process. Then, from the sets of maximum a posteriori likelihoods for the slope and intercept values, we selected the median values for both parameters as the best-fit results.

This method relies heavily on the measurement uncertainty. A few good points might have been rejected if their uncertainties were underestimated. But since the sample and measurements come from the same homogeneous survey, these errors should not bias our result significantly.

The Spearman correlation analysis was used to test the relation between the parameters in our study, because it is less sensitive to outliers than other correlation analyses, such as Kendall τ or Pearson ρ.

4.2. Stellar mass dependencies

Many studies have shown that there is an inherent relation between the mass of the young star and its X-ray emission (Flaccomio et al. 2003; Preibisch et al. 2005; Telleschi et al. 2007; Ercolano et al. 2014) and between the stellar mass and the mass accretion rates (Calvet et al. 2004; Muzerolle et al. 2003, 2005; Mohanty et al. 2005; Natta et al. 2006; Manara et al. 2012; Alcalá et al. 2014). We want to test these results with our data.

Stellar mass and accretion rates – Fig. 2 and Table 5 show the correlation study between the mass of the star and its mass accretion rate. Important differences can be found for both subsamples. Strong correlation coefficients are found for the U-excess subsample, with a relation of $\log\dot{M} = (1.94 \pm 0.23) \times \log M_* - (7.95 \pm 0.12)$ using the minimum-square fit analysis. This result is consistent with previous studies, $\log\dot{M} = 2 \times \log M_* - 7.5$, which is used in the Telleschi et al. (2007) study of the TMC. But we can see how this is not the case for the Hα subsample. The relation for this subsample is $\log\dot{M} = (1.57\pm0.23)\times\log M_* - (7.60\pm0.15)$, but with weaker correlation coefficients. This discrepancy suggests that U-band excess is a better accretion tracer than the Hα line equivalent width (Venuti et al. 2014), and calls for a word of caution when using Hα to derive accretion rates. In the case of the outlier rejection analysis, a steeper slope is found for the U-excess subsample, $\log\dot{M} = (3.29 \pm 0.25) \times \log M_* - (7.37 \pm 0.15)$, as well as for the H$\alpha$ subsample, $(3.19 \pm 0.21) \times \log M_* - (7.09 \pm 0.16)$. In Sect. 5 we address this difference.

Stellar mass and X-ray emission – Fig. 3 shows the relations between the stellar mass and L_X, for both subsamples. The regression and correlation parameters of the different subsamples are summarized in Table 5. For the U-excess subsample, stronger correlations are present between these parameters than those found for the Hα one, a similar result to that on the $\dot{M}_{acc} - M_*$ study. In Sect. 5 we explain this critical difference.

4.2.1. Selection bias

Ercolano et al. (2014) study whether the $\dot{M}_{acc} - M_*$ relation found for different samples of YSO can be a consequence of a selection bias or detection threshold. Apart for finding similar relations to our subsamples, they find that it is not affected by a selection bias.

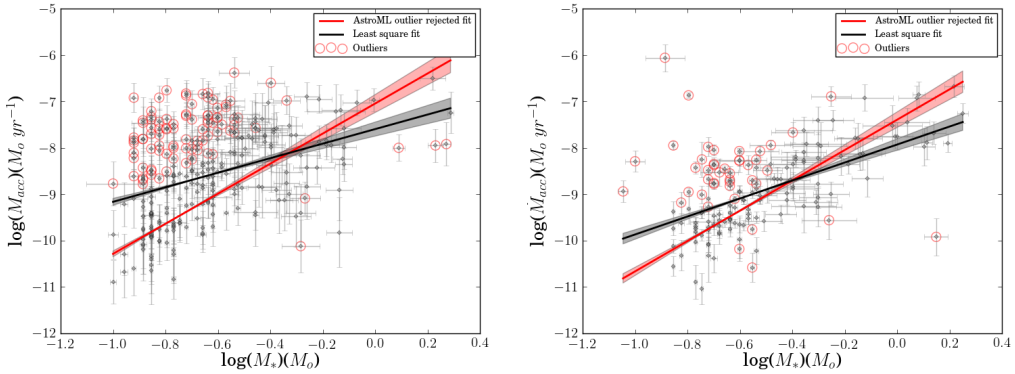

(a) Hα sample. (b) U-excess sample.

Fig. 2. Stellar mass vs. mass accretion rates for both subsamples. The plot on the *left* corresponds to the Hα subsample, and the one on the *right* to the U-excess subsample. Regression lines (straight) are plotted with their respective errors in the slope (shaded areas) for the OLS regression analysis (black) and the outlier rejection regression method (red).

Table 5. Summary of results of the different correlations analyses.

Correlation[1]	Subsample[2]	N[3]	Least square algorithm[4]		Outlier rejection algorithm[4]		Spearman parameters	
			a	b	a	b	ρ[5]	g[6]
$\dot{M}$ vs. M	Hα	277	1.57 ± 0.23	–7.60 ± 0.15	3.19 ± 0.21	–7.09 ± 0.16	0.38	Weak
$\dot{M}$ vs. M	U-excess	154	1.94 ± 0.23	–7.93 ± 0.12	3.29 ± 0.25	–7.37 ± 0.15	0.55	Moderate
L_X vs. M	Hα	277	1.90 ± 0.17	30.33 ± 0.12	2.72 ± 0.17	30.89 ± 0.09	0.52	Moderate
L_X vs. M	U-excess	154	1.72 ± 0.17	30.59 ± 0.10	1.75 ± 0.12	30.89 ± 0.07	0.61	Strong
Residual L_X determined using minimum-square fit analysis[7]								
L_X/ $L_X(\dot{M})$ vs. $\dot{M}$	Hα	277	–0.94 ± 0.05	–8.07 ± 0.40	–1.09 ± 0.04	–9.65 ± 0.39	–0.78	Strong
L_X/ $L_X(\dot{M})$ vs. $\dot{M}$	U-excess	154	–0.53 ± 0.05	–4.72 ± 0.43	–0.67 ± 0.06	–5.85 ± 0.53	–0.63	Strong
Residual L_X determined using MCMC outlier rejection fit analysis[7]								
L_X/ $L_X(\dot{M})$ vs. $\dot{M}$	Hα	277	–0.59 ± 0.05	–5.50 ± 0.43	–0.68 ± 0.13	–6.51 ± 1.22	–0.55	Moderate
L_X/ $L_X(\dot{M})$ vs. $\dot{M}$	U-excess	154	–0.19 ± 0.05	–2.04 ± 0.47	–0.35 ± 0.07	–3.28 ± 0.58	–0.29	Weak

Notes. The relations correspond to the logarithmic equation of the parameters. [(1)] Parameters to analyze. [(2)] Subsample from which the data are referred. [(3)] Number of objects in the subsample. [(4)] a stands for the slope of the linear regression and b for the intercept. Errors for the least square analyses are the standard deviation as given in the ODR algorithm. Errors for the outlier analyses are the standard deviation of all the values computed in the MCMC algorithm for each parameter. [(5)] Spearman's ρ rank correlation coefficient. [(6)] Goodness-of-fit as given by ρ. [(7)] Different regression methods between M_*, L_X and $\dot{M}_{acc}$ yield different $L_X(\dot{M})$ equations. Rows five and six show the regression results between $L_X/L_X(\dot{M})$ and $\dot{M}_{acc}$ when the OLS method was used for the first regressions, while rows seven and eight, when the outlier rejection methodology was applied.

The Manara2012 sample we used is almost complete down to the hydrogen-burning limit. Thus, we conclude that selection effects are not present in our $\dot{M}_{acc} - M$ relations. And given the X-ray detection limit of the *Chandra* telescope, which is lower than our lowest X-ray luminosity value, we also deduce that our $L_X - M$ relations are also not affected by a selection bias owing to undetected sources.

4.3. Accretion rate and X-ray luminosity

We now focus on our primary objective: study the accretion processes of the PMS objects in the ONC and their relation with the X-ray emissions of the central stars. This interaction has also been studied in different works, such as Preibisch et al. (2005) and Drake et al. (2009) in Orion, or Telleschi et al. (2007) in Taurus. Here we want to reformulate the results obtained in these works, using different accretor tracers and measurements. In particular, we want to compare the analysis of Telleschi et al. (2007) in the TMC with our results in the ONC, and see if similar relations can be inferred.

In our work we are not interested in studying the differences between accretors and non-accretors. That classification is no longer appropriate for our study, as seen in Sect. 3. This is why we study the direct dependences and relations of the measured mass accretion rates and the X-ray luminosities. We take an approach similar to that of Telleschi et al. (2007). Here they study the $L_X - \dot{M}_{acc}$ relation, taking into account the inherent dependences of these properties with the mass of the star. Class II objects show a direct relation between $\dot{M}_{acc}$ and M. Using different evolutionary tracks, Muzerolle et al. (2003, 2005) found $\dot{M} \propto M^2$ and $\dot{M} \propto M^{2.1}$, respectively, so in Telleschi et al. (2007) they adopted the relation $\log \dot{M} \approx 2\log M - 7.5$. They also compute a relation between $\log L_X$ and $\log M$ with their data. Finally,

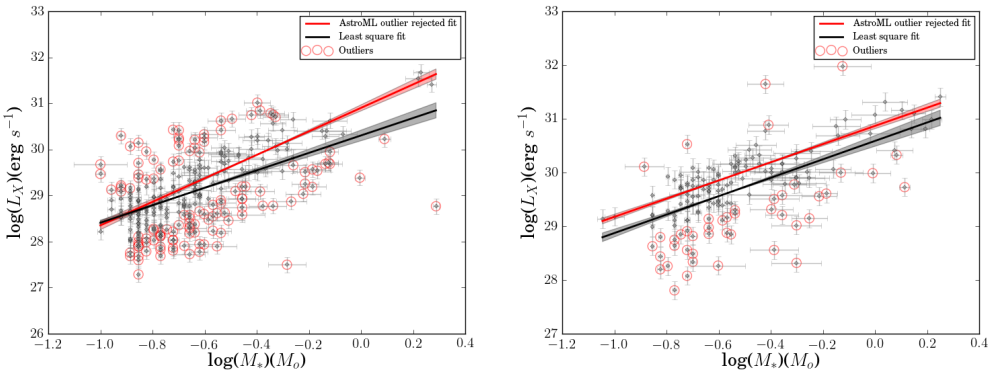

(a) Hα sample. (b) U-excess sample.

Fig. 3. X-ray luminosities vs. the mass of the sources. The plot on the *left* corresponds to the Hα subsample, and the one on the *right* to the U-excess subsample. Regression lines (straight) are plotted with their respective errors in the slope (shaded areas) for the OLS regression analysis (black) and the outlier rejection regression method (red).

Table 6. L_X vs. $\dot{M}_{acc}$ equations for each subsample.

Sample	$L_X - \dot{M}_{acc}$
Using minimum-square fit analysis	
Hα	$\log L_X = (1.21 \pm 0.28)\log\dot{M} + (39.49 \pm 2.09)$
U-excess	$\log L_X = (0.89 \pm 0.19)\log\dot{M} + (37.60 \pm 1.51)$
Using MCMC outlier rejection fit analysis	
Hα	$\log L_X = (0.85 \pm 0.11)\log\dot{M} + (36.93 \pm 0.74)$
U-excess	$\log L_X = (0.53 \pm 0.08)\log\dot{M} + (34.81 \pm 0.55)$

Notes. Each one is computed using the regression results of L_X, M_* and $\dot{M}_{acc}$. The ones using the results from the minimum-square analysis are shown on top, and the ones using the outlier detection and rejection analysis are shown below.

they relate the L_X with the $\dot{M}_{acc}$ with the equation $\log L_X(\dot{M}) = 0.85 \times \log(\dot{M}) + 36.67$.

Taking the same approach, we used the $\dot{M}_{acc} - M_*$ and the $L_X - M_*$ relations we found for both our subsamples and derived L_X as a function of $\dot{M}_{acc}$. By using both the OLS and the outlier detection and rejection methods, different regression results and, consequently, $L_X(\dot{M}_{acc})$ equations, are obtained for each subsample. These results are shown in Table 6. With them, we computed the expected L_X given the $\dot{M}_{acc}$ of the sources in our catalog. We called this our theoretical $L_X(\dot{M}_{acc})$. This relation could define the L_X - $\dot{M}_{acc}$ in Orion if both parameters were to only depend on the stellar mass.

Finally, we computed what we called the residual L_X. This parameter was obtained by dividing the observed L_X by the theorethical L_X, given by our derived equations, for a given $\dot{M}_{acc}$. In Table 4 we include the different residual L_X values of each source that has been computed this way, for both subsamples. This residual X-ray luminosity compares the observed L_X with the expected value if both the L_X and the $\dot{M}_{acc}$ were to only depend on the stellar mass. It represents the excess (or deficit) of X-ray luminosities that are dependent on the $\dot{M}_{acc}$. In Fig. 4 we plot this value against the $\dot{M}_{acc}$. If this ratio were determined only by the $L_X - M_*$ and $\dot{M}_{acc} - M_*$ relations, then the values would scatter around a constant. As can be seen in the figure, they present a large scatter, pointing towards more dependencies, in addition to the stellar mass, for L_X and $\dot{M}_{acc}$.

Again, we used both the OLS and the outlier detection and rejection methods for these final plots. Table 5 summarizes all the regression results obtained for all the possible combinations of data and methods. The values under "Least square algorithm" in Table 5 correspond to the regression results that were obtained using the OLS methodology, whilst the ones under "Outlier rejection algorithm" correspond to the results obtained using the named method. The four top rows present the results of the regressions that were found directly from the data, whilst the bottom four show the regression results from the derived residual X-ray luminosity. This last parameter is computed using what we defined here as the theoretical X-ray luminosity, $L_X(\dot{M})$, which in turn depends on the first relations. Thus, depending on the methodology used to derive the first relations on the top four rows (OLS or outlier rejection), different $L_X(\dot{M})$ are obtained. This is represented in the four bottom rows. The top two present the results from the $L_X(\dot{M})$ derived from the OLS methodology, while the bottom two represent the $L_X(\dot{M})$ derived from the outlier rejection analysis.

5. Discussion

We will now discuss the correlations and trends found in the previous section. The main objective is to compare the residual X-ray luminosity – mass accretion rate relations from both Taurus, obtained in Telleschi et al. (2007), and Orion, obtained in this work, which we do in Sect. 5.1. Different methods yield different results, which we address in Sects. 5.2 and 5.3. In Sect. 5.4, we interpret these results.

5.1. Comparing Taurus and Orion – OLS method regression results

Telleschi et al. (2007) find the following results when studying the X-ray emission differences between CTTS and WTTS: i) CTTS present smaller L_X than WTTS, on average; ii) they also present smaller L_X/L_*; iii) and a correlation is found between the electron temperature and the total L_X for WTTS, but not for CTTS (where the temperatures are higher than those in the

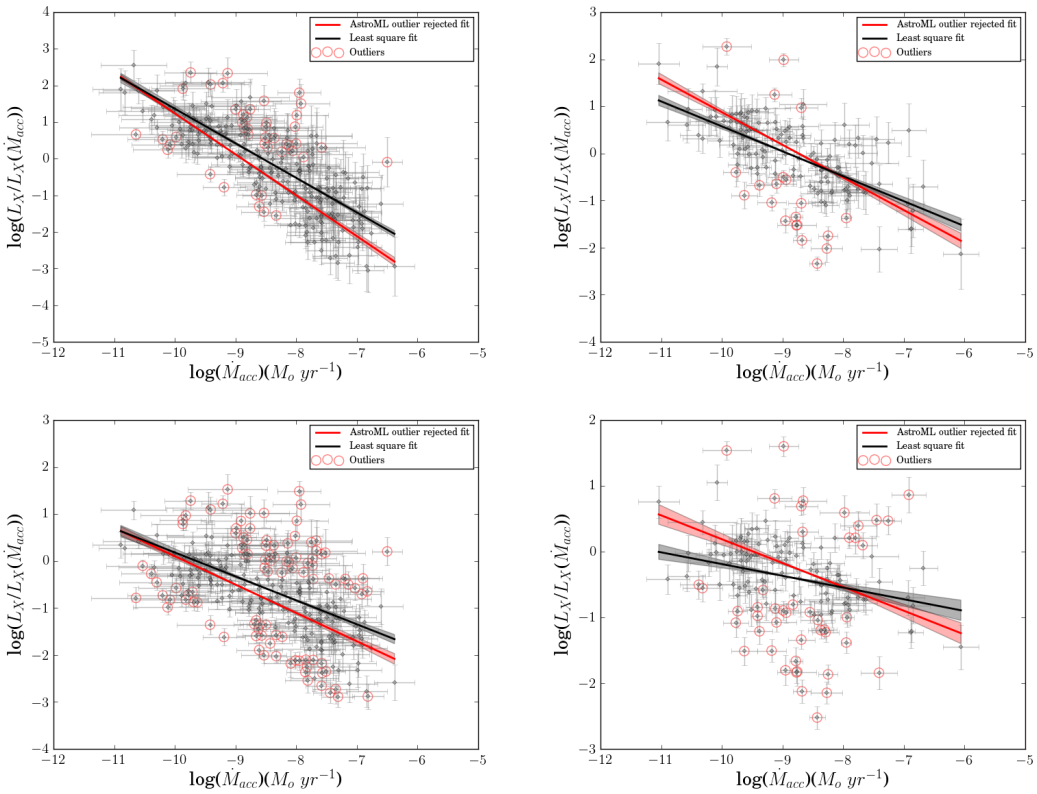

Fig. 4. Residual X-ray luminosity, after normalization with the $M - L_X$ and $M - \dot{M}$ relations, as a function of the mass accretion rate. *Left figures* correspond to the Hα subsample. *Right figures* correspond to the U-excess subsample. The *top plots* present the results using the OLS method for the initial regression analyses between M_*, L_X and $\dot{M}_{acc}$. The *bottom* ones when using the outlier rejection method for those same analyses. Regression lines (straight), with their respective errors in the slope (shaded areas), are shown for the OLS (black) and outlier rejection (red) final regression results.

WTTS). Their results point towards a magnetic coronal source for the X-ray emissions in TTS. Also, they suggest that the lower L_X emission from CTTS is caused by coronal heating from an accretion disk and accretion processes. Denser accreting material from CTTS would cause a decreased heated plasma from the reconnection events, accounting for the lower measurements of L_X in accreting systems than in WTTS. The cool plasma may also reorganize the magnetic loops after entering them, stretching and causing them not to reconnect (diminishing the X-ray emission therefore); or by just lowering their temperature because they are colder than them; or inducing radiative losses and more rapid cooling.

One of their main results regarding the accretion processes and the L_X luminosities was the relation between the residual L_X and the $\dot{M}_{acc}$ they they found for their CTTS sample. The main difference to their work can be found in the subsamples we gathered for the Orion YSOs, which yield different results in each case.

5.2. OLS method regression results

As can be seen in Figs. 2 and 3, the spread in the data is considerable, over orders of magnitude. For the Hα subsample, in fact, this spread is large enough to produce ineffective correlation results as can be seen in the low Spearman ρ coefficient for the $\dot{M}_{acc} - M_*$ relation in Table 5. This spread may be caused by hidden variables that affect our data.

The U-excess subsample presents a stronger correlation between these parameters, pointing towards more coherent measurement of the mass accretion rates of the sources (Venuti et al. 2014). The process to derive the accretion rate, which uses the equivalent width of the Hα line, is more complex than the one with the excess emission of the U-band. More factors enter into play in the former, leading to more uncertainties in the final data, which maybe explains the larger spread in the plots for this subsample.

This is why we cannot assert the reliability of the rest of the results from the Hα sample from this conclusion onward. The low ρ coefficient in the $\dot{M}_{acc} - M_*$ relation means the derived $L_X - \dot{M}_{acc}$ one is not sufficiently reliable. Therefore, our analyses will focus on the U-excess subsample from now on. Nevertheless, we report the results from the other subsample as a reference and when making a comparison with the U-excess data.

The U-excess subsample presents moderate/strong correlations between our four main parameters, M_*, $\dot{M}_{acc}$, L_X, and the residual L_X. In fact, this is very similar to those found

in Telleschi et al. (2007). The relation between M_* and $\dot{M}_{\rm acc}$, $\dot{M}_{\rm acc} \propto M_*^{1.94\pm0.23}$ given by the least-square method is totally compatible with that found in many previous studies. Also, the $L_{\rm X} \propto M_*^{1.72\pm0.17}$ relation is compatible with that found in Preibisch et al. (2005) for the same region. We still find considerable spreads in the data but the results we find are consistent with those on Taurus in Telleschi et al. (2007).

We find that the final relation between the residual X-ray luminosity and the mass accretion rate for the U-excess subsample, $L_{\rm X}/L_{\rm X}(\dot{M}) \propto \dot{M}^{-0.53\pm0.05}$, is very compatible with the relation found in Taurus in Telleschi et al. (2007), $L_{\rm X}/L_{\rm X}(\dot{M}) \propto \dot{M}^{-0.48\pm0.15}$.

5.3. Outlier method regression results

To test the robustness of our fits, we used an outlier detection algorithm. The problem with this method, as stated before, is that it is very sensitive to uncertainties in the dependent variable, in this case, $\dot{M}_{\rm acc}$, $L_{\rm X}$, and $L_{\rm X}/L_{\rm X}(\dot{M})$. Several sources present sufficiently small errors as to be selected as outliers, although their position in the plot is consistent with the best-regression fit. Thus, the results obtained using this method should be taken cautiously.

The parameters we are working with (stellar mass, mass accretion rate, and X-ray luminosity) are not measured directly, but obtained indirectly from other measurements (i.e., the equivalent width of the Hα line or the excess in the U-band for the $\dot{M}_{\rm acc}$, or the flux of the objects, which is obtained by measuring the photons that arrive to the X-ray detector, for the $L_{\rm X}$). Consequently, the uncertainties should represent this process.

As mentioned in the previous section, the relation obtained between the residual X-ray luminosity and the mass accretion rate using the OLS method for the U-excess subsample agrees considerably well with the results found by Telleschi et al. (2007) in Taurus. On the other hand, using the outliers detection method, the results on Orion differ considerably from those in Taurus.

The relations obtained with the outliers detection method between M_* and $\dot{M}_{\rm acc}$ in both subsamples have considerably steeper slopes compared to those found in the literature: $\dot{M}_{\rm acc} \propto M_*^{3.19\pm0.21}$ for the Hα subsample and $\dot{M}_{\rm acc} \propto M_*^{3.29\pm0.25}$ for the U-excess one. This represents a difference of more than 3σ from the ones obtained using the OLS method. In the case of the $L_{\rm X} - M_*$ relation, the results differ from one subsample to another. The U-excess subsample presents compatible regression results between both methods, and between the relation found in Preibisch et al. (2005). But the ones found for the Hα subsample are considerably different, by a factor larger than 3σ.

In Table 5 all the final $L_{\rm X}/L_{\rm X}(\dot{M}_{\rm acc}) - \dot{M}_{\rm acc}$ relations are shown, and Fig. 4 presents the final plots. Using both methods, we obtain eight different results: two plots for the Hα subsample, each with two different regression results, depending on whether we used the OLS or the outliers detection method to derive the regressions between $L_{\rm X}$ or $\dot{M}_{\rm acc}$ and M_* and between $L_{\rm X}/L_{\rm X}(\dot{M}_{\rm acc}) - \dot{M}_{\rm acc}$; and the same in the case of the U-excess subsample.

Out of these eight results, and taking into account the aforementioned issues with each subsample and methodology, we decided that only two of them were compatible with Taurus: the one from the U-excess subsample that uses the OLS method between the $M_* - L_{\rm X}$ and $M_* - \dot{M}_{\rm acc}$ relations and between the $L_{\rm X}/L_{\rm X}(\dot{M}_{\rm acc}) - \dot{M}_{\rm acc}$ final relation, and the one from the Hα subsample that uses the outliers detection method for the initial relations and the OLS analysis for the $L_{\rm X}/L_{\rm X}(\dot{M}_{\rm acc}) - \dot{M}_{\rm acc}$ final relation.

The uncertainties shown in Table 5 for Orion are far narrower than those found in Telleschi et al. (2007) for Taurus. The 1σ range for the slope from Telleschi et al. (2007) is -0.33 to -0.63, which is compatible with three more results from our analysis if we add the uncertainties from them (slopes -0.35 ± 0.07, -0.67 ± 0.06, and -0.68 ± 0.13). With these, our final interpretation of the results, as stated in Sect. 5.4, becomes stronger. Nevertheless, we urge caution, given the issues we explained before.

One important result to point out is that the regression results obtained using the OLS method are recovered using the outliers detection method when the uncertainties on the dependent variables are increased sufficiently (1σ, 2σ, 3σ...).

The accretion processes present an important variability in time, which we disregard. Applying an outliers detection and rejection method to these kind of data, without taking this characteristic into account may seem risky, as some sources could be an order of magnitude off its quiescent value and be selected as outliers when, in fact, they are not. This is another reason why the results of the outliers analysis must be taken with caution. Nevertheless, given the numbers in our data, this issue is not so critical.

5.4. Results

Our main result is the anti-correlation found between the residual $L_{\rm X}$ and the $\dot{M}_{\rm acc}$. We deduce two interpretations from these results.

The first is that for higher accretion rates there is a deficit in the observed $L_{\rm X}$, compared with the theoretical one. This implies that, for stronger accretors, the observed $L_{\rm X}$ is weaker. That is, the accretion processes seem to "cover" the emission of X-ray radiation from the YSOs. This result is also found in (Telleschi et al. 2007).

The second is with regard to the scatter in the values on these plots. If the $L_{\rm X}$ and $\dot{M}_{\rm acc}$ are only dependent on the stellar mass of the YSOs, as we have assumed, these values would scatter around a constant value of one. But the higher scatter and the negative slope points towards other dependencies for these parameters (e.g., stellar rotation, Rossby number, magnetic field intensity). What is interesting is the similarity between the $L_{\rm X}/L_{\rm X}(\dot{M}_{\rm acc}) - \dot{M}_{\rm acc}$ relation on Taurus and Orion. This suggests that the environment where the T Tauri stars are born is not one of the parameters that affects the $L_{\rm X}/L_{\rm X}(\dot{M}_{\rm acc}) - \dot{M}_{\rm acc}$ relation.

As a result, we can conclude that this anti-correlation between the residual $L_{\rm X}$ and the mass accretion rate is independent of the region and environment; its arbitrary appearance both in the TMC and in the ONC, shows reasonably well how it is an inherent property of accreting systems. Similar analyses in other star-forming regions could reinforce this result.

6. Conclusions

We have gathered a sample of T Tauri stars in the ONC with known X-ray detections and mass accretion rates. Using the classification criteria in Telleschi et al. (2007), we have divided our sample in CTTS and WTTS, finding that several WTTS have accretion rates comparable or even higher to those of CTTS. Since our data do not allow us to confirm these classifications and the number of WTTS in this work is small compared to the whole catalog, we have used all the subsamples for our analysis.

Two subsamples have been used in this work, depending on the method used to calculate the accretion rates of the sources. The Hα sample used the equivalent width of this spectral line, and the U-excess subsample, the color excess compared to the nominal values.

Because of the large spread in our data, two regression analyses were carried out. First, we used a least-square regression analysis, using the ODRPACK of Scipy on Python, obtaining results compatible with those in the literature and with Telleschi et al. (2007) for one of our subsamples. Then, we detected and rejected outliers from our samples using the astroML MCMC package of Python. This method is very sensitive to the uncertainties from the dependent variables and some sources were rejected as outliers as a result of too small error values, which thus affect the final regression-fit results. Using this method, only one more result was compatible with that from Taurus in Telleschi et al. (2007). By enlarging the uncertainties in the dependent variables, the OLS regression results were recovered.

We find that a clear anti-correlation between the residual X-ray luminosity and the accretion rates is present in both subsamples, although we cannot assert the reliability of the Hα results because of the weak correlation found between its previous parameters. In the case of the U-excess subsample, our results are consistent with those found in the Taurus Molecular Cloud. This result, independent of the environment studied, points towards an inherent property in these type of YSOs; the accretion processes causes a decrease in the emission of X-rays. Different theories have been postulated for this situation, such as thermalization by the X-rays of the stream being accreted, which causes a reduction in the X-ray measurements.

Acknowledgements. This work has been made possible thanks to the ESAC Science Operations Division research funds, code EXPRO IPL-PSS/GP/gp/44.2014, plus support from the ESAC Space Science Faculty. Pablo Riviere-Marichalar and Carlo Manara acknowledge funding from the ESA Research Fellowship program. H. Bouy is funded by the Spanish Ramn y Cajal fellowship program number RYC-2009- 04497. This research made use of the SIMBAD database, operated at the CDS, Strasbourg, France. This work made extensive use of Topcat (TOPCAT http:// www.star.bristol.ac.uk/~mbt/topcat/ and STILTS, Taylor 2005, 2006). We thank the referee, Manuel Güdel, for his comments and corrections, which help to make this work complete. We would also like to thank Benjamin Montesinos and Nuria Huelamo for their comments and help.

References

Aarnio, A. N., Stassun, K. G., & Matt, S. P. 2010, ApJ, 717, 93
Alcalá, J. M., Natta, A., Manara, C. F., et al. 2014, A&A, 561, A2
Alexander, R., Pascucci, I., Andrews, S., Armitage, P., & Cieza, L. 2014, Protostars and Planets VI, 475
Boggs, P. T., Spiegelman, C. H., Donaldson, J. R., & Schnabel, R. B. 1988, J. Econometrics, 38, 169
Calvet, N., & Gullbring, E. 1998, ApJ, 509, 802
Calvet, N., Muzerolle, J., Briceño, C., et al. 2004, AJ, 128, 1294
D'Antona, F., & Mazzitelli, I. 1994, ApJS, 90, 467
Da Rio, N., Robberto, M., Soderblom, D. R., et al. 2010, ApJ, 722, 1092
Da Rio, N., Robberto, M., Hillenbrand, L. A., Henning, T., & Stassun, K. G. 2012, ApJ, 748, 14
Drake, J. J., Ercolano, B., Flaccomio, E., & Micela, G. 2009, ApJ, 699, L35
Ercolano, B., Mayr, D., Owen, J. E., Rosotti, G., & Manara, C. F. 2014, MNRAS, 439, 256
Feigelson, E. 2005, in Star Formation in the Era of Three Great Observatories, Cambridge Conf., 39
Flaccomio, E., Damiani, F., Micela, G., et al. 2003, ApJ, 582, 398
Flaccomio, E., Micela, G., & Sciortino, S. 2012, A&A, 548, A85
Getman, K. V., Feigelson, E. D., Grosso, N., et al. 2005a, ApJS, 160, 353
Getman, K. V., Flaccomio, E., Broos, P. S., et al. 2005b, ApJS, 160, 319
Gomez, M., Hartmann, L., Kenyon, S. J., & Hewett, R. 1993, AJ, 105, 1927
Gorti, U., & Hollenbach, D. 2009, ApJ, 690, 1539
Güdel, M., Briggs, K. R., Arzner, K., et al. 2007a, A&A, 468, 353
Güdel, M., Telleschi, A., Audard, M., et al. 2007b, A&A, 468, 515
Gullbring, E., Hartmann, L., Briceño, C., & Calvet, N. 1998, ApJ, 492, 323
Hartmann, L. 1998, Accretion Processes in Star Formation (CUP)
Hillenbrand, L. A. 1997, AJ, 113, 1733
Hillenbrand, L. A., Strom, S. E., Calvet, N., et al. 1998, AJ, 116, 1816
Hillenbrand, L. A., Hoffer, A. S., & Herczeg, G. J. 2013, AJ, 146, 85
Ingleby, L., Calvet, N., Bergin, E., et al. 2011, ApJ, 743, 105
Jones, E., Oliphant, T., Peterson, P., et al. 2001, SciPy: Open source scientific tools for Python, http://www.scipy.org
Loinard, L., Mioduszewski, A. J., Rodríguez, L. F., et al. 2005, ApJ, 619, L179
Lucas, P. W., Roche, P. F., Allard, F., & Hauschildt, P. H. 2001, MNRAS, 326, 695
Luhman, K. L., Rieke, G. H., Young, E. T., et al. 2000, ApJ, 540, 1016
Manara, C. F., Robberto, M., Da Rio, N., et al. 2012, ApJ, 755, 154
Manara, C. F., Beccari, G., Da Rio, N., et al. 2013a, A&A, 558, A114
Manara, C. F., Testi, L., Rigliaco, E., et al. 2013b, A&A, 551, A107
Menten, K. M., Reid, M. J., Forbrich, J., & Brunthaler, A. 2007, A&A, 474, 515
Mohanty, S., Basri, G., & Jayawardhana, R. 2005, Astron. Nachr., 326, 891
Muzerolle, J., Hillenbrand, L., Calvet, N., Briceño, C., & Hartmann, L. 2003, ApJ, 592, 266
Muzerolle, J., Luhman, K. L., Briceño, C., Hartmann, L., & Calvet, N. 2005, ApJ, 625, 906
Natta, A., Testi, L., & Randich, S. 2006, A&A, 452, 245
Owen, J. E., Ercolano, B., Clarke, C. J., & Alexander, R. D. 2010, MNRAS, 401, 1415
Pizzolato, N., Maggio, A., Micela, G., Sciortino, S., & Ventura, P. 2003, A&A, 397, 147
Preibisch, T., Kim, Y.-C., Favata, F., et al. 2005, ApJS, 160, 401
Reggiani, M., Robberto, M., Da Rio, N., et al. 2011, A&A, 534, A83
Ricci, L., Robberto, M., & Soderblom, D. R. 2008, AJ, 136, 2136
Robberto, M., Soderblom, D. R., Bergeron, E., et al. 2013, ApJS, 207, 10
Stelzer, B., Frasca, A., Alcalá, J. M., et al. 2013, A&A, 558, A141
Telleschi, A., Güdel, M., Briggs, K. R., Audard, M., & Palla, F. 2007, A&A, 468, 425
Vanderplas, J., Connolly, A., Ivezić, Ž., & Gray, A. 2012, in Proc. Conf. on Intelligent Data Understanding (CIDU), 47
Venuti, L., Bouvier, J., Flaccomio, E., et al. 2014, A&A, 570, A82

Bibliography

Aarnio, A. N., Stassun, K. G., and Matt, S. P.: 2010, ApJ **717**, 93

Akerlof, C., Amrose, S., Balsano, R., Bloch, J., Casperson, D., Fletcher, S., Gisler, G., Hills, J., Kehoe, R., Lee, B., Marshall, S., McKay, T., Pawl, A., Schaefer, J., Szymanski, J., and Wren, J.: 2000, AJ **119**, 1901

Akeson, R. L., Chen, X., Ciardi, D., Crane, M., Good, J., Harbut, M., Jackson, E., Kane, S. R., Laity, A. C., Leifer, S., Lynn, M., McElroy, D. L., Papin, M., Plavchan, P., Ramírez, S. V., Rey, R., von Braun, K., Wittman, M., Abajian, M., Ali, B., Beichman, C., Beekley, A., Berriman, G. B., Berukoff, S., Bryden, G., Chan, B., Groom, S., Lau, C., Payne, A. N., Regelson, M., Saucedo, M., Schmitz, M., Stauffer, J., Wyatt, P., and Zhang, A.: 2013, PASP **125**, 989

Alcalá, J. M., Natta, A., Manara, C. F., Spezzi, L., Stelzer, B., Frasca, A., Biazzo, K., Covino, E., Randich, S., Rigliaco, E., Testi, L., Comerón, F., Cupani, G., and D'Elia, V.: 2014, A&A **561**, A2

Alexander, R., Pascucci, I., Andrews, S., Armitage, P., and Cieza, L.: 2014, *Protostars and Planets VI* pp 475–496

Alexander, R. D. and Armitage, P. J.: 2009, ApJ **704**, 989

Allard, F., Homeier, D., and Freytag, B.: 2012, in M. T. Richards and I. Hubeny (eds.), *IAU Symposium*, Vol. 282 de *IAU Symposium*, pp 235–242

Allen, P. R., Luhman, K. L., Myers, P. C., Megeath, S. T., Allen, L. E., Hartmann, L., and Fazio, G. G.: 2007, ApJ **655**, 1095

ALMA Partnership, Brogan, C. L., Pérez, L. M., Hunter, T. R., Dent, W. R. F., Hales, A. S., Hills, R. E., Corder, S., Fomalont, E. B., Vlahakis, C., Asaki, Y., Barkats, D., Hirota, A., Hodge, J. A., Impellizzeri, C. M. V., Kneissl, R., Liuzzo, E., Lucas, R., Marcelino, N., Matsushita, S., Nakanishi, K., Phillips, N., Richards, A. M. S., Toledo, I., Aladro, R., Broguiere, D., Cortes, J. R., Cortes, P. C., Espada, D., Galarza, F., Garcia-Appadoo, D., Guzman-Ramirez, L.,

Humphreys, E. M., Jung, T., Kameno, S., Laing, R. A., Leon, S., Marconi, G., Mignano, A., Nikolic, B., Nyman, L.-A., Radiszcz, M., Remijan, A., Rodón, J. A., Sawada, T., Takahashi, S., Tilanus, R. P. J., Vila Vilaro, B., Watson, L. C., Wiklind, T., Akiyama, E., Chapillon, E., de Gregorio-Monsalvo, I., Di Francesco, J., Gueth, F., Kawamura, A., Lee, C.-F., Nguyen Luong, Q., Mangum, J., Pietu, V., Sanhueza, P., Saigo, K., Takakuwa, S., Ubach, C., van Kempen, T., Wootten, A., Castro-Carrizo, A., Francke, H., Gallardo, J., Garcia, J., Gonzalez, S., Hill, T., Kaminski, T., Kurono, Y., Liu, H.-Y., Lopez, C., Morales, F., Plarre, K., Schieven, G., Testi, L., Videla, L., Villard, E., Andreani, P., Hibbard, J. E., and Tatematsu, K.: 2015, ApJ **808**, L3

Alves de Oliveira, C., Ábrahám, P., Marton, G., Pinte, C., Kiss, C., Kun, M., Kóspál, Á., André, P., and Könyves, V.: 2013, A&A **559**, A126

Alves de Oliveira, C., Moraux, E., Bouvier, J., Bouy, H., Marmo, C., and Albert, L.: 2010, A&A **515**, A75

André, P., Men'shchikov, A., Bontemps, S., Könyves, V., Motte, F., Schneider, N., Didelon, P., Minier, V., Saraceno, P., Ward-Thompson, D., di Francesco, J., White, G., Molinari, S., Testi, L., Abergel, A., Griffin, M., Henning, T., Royer, P., Merín, B., Vavrek, R., Attard, M., Arzoumanian, D., Wilson, C. D., Ade, P., Aussel, H., Baluteau, J.-P., Benedettini, M., Bernard, J.-P., Blommaert, J. A. D. L., Cambrésy, L., Cox, P., di Giorgio, A., Hargrave, P., Hennemann, M., Huang, M., Kirk, J., Krause, O., Launhardt, R., Leeks, S., Le Pennec, J., Li, J. Z., Martin, P. G., Maury, A., Olofsson, G., Omont, A., Peretto, N., Pezzuto, S., Prusti, T., Roussel, H., Russeil, D., Sauvage, M., Sibthorpe, B., Sicilia-Aguilar, A., Spinoglio, L., Waelkens, C., Woodcraft, A., and Zavagno, A.: 2010, A&A **518**, L102

Andre, P., Ward-Thompson, D., and Barsony, M.: 1993, ApJ **406**, 122

Andrews, S. M. and Williams, J. P.: 2005, ApJ **631**, 1134

Andrews, S. M., Wilner, D. J., Espaillat, C., Hughes, A. M., Dullemond, C. P., McClure, M. K., Qi, C., and Brown, J. M.: 2011, ApJ **732**, 42

Andrews, S. M., Wilner, D. J., Hughes, A. M., Qi, C., and Dullemond, C. P.: 2009, ApJ **700**, 1502

Armitage, P. J.: 2009, in F. Roig, D. Lopes, R. de La Reza, and V. Ortega (eds.), *American Institute of Physics Conference Series*, Vol. 1192 de *American Institute of Physics Conference Series*, pp 3–42

Armitage, P. J., Clarke, C. J., and Palla, F.: 2003, MNRAS **342**, 1139

Artymowicz, P. and Lubow, S. H.: 1994, ApJ **421**, 651

Aumann, H. H., Beichman, C. A., Gillett, F. C., de Jong, T., Houck, J. R., Low, F. J., Neugebauer, G., Walker, R. G., and Wesselius, P. R.: 1984, ApJ **278**, L23

Balog, Z., Müller, T., Nielbock, M., Altieri, B., Klaas, U., Blommaert, J., Linz, H., Lutz, D., Moór, A., Billot, N., Sauvage, M., and Okumura, K.: 2014, *Experimental Astronomy* **37**, 129

Banzatti, A., Pontoppidan, K. M., Salyk, C., Herczeg, G. J., van Dishoeck, E. F., and Blake, G. A.: 2017, ApJ **834**, 152

Barnes, J. W., van Eyken, J. C., Jackson, B. K., Ciardi, D. R., and Fortney, J. J.: 2013, ApJ **774**, 53

Barrado y Navascués, D. and Martín, E. L.: 2003, AJ **126**, 2997

Baruteau, C., Crida, A., Paardekooper, S.-J., Masset, F., Guilet, J., Bitsch, B., Nelson, R., Kley, W., and Papaloizou, J.: 2014, *Protostars and Planets VI* pp 667–689

Basri, G. and Brown, M. E.: 2006, *Annual Review of Earth and Planetary Sciences* **34**, 193

Birnstiel, T., Andrews, S. M., and Ercolano, B.: 2012, A&A **544**, A79

Boggs, P. T., Spiegelman, C. H., Donaldson, J. R., and Schnabel, R. B.: 1988, *Journal of Econometrics* **38(1-2)**, 169

Briceño, C.: 2008, *The Dispersed Young Population in Orion*, p. 838, Handbook of Star Forming Regions, Volume I, Reipurth Bo., ISBN:978-1-58381-670-7

Briceño, C., Calvet, N., Hernández, J., Vivas, A. K., Hartmann, L., Downes, J. J., and Berlind, P.: 2005, AJ **129**, 907

Briceño, C., Hartmann, L., Hernández, J., Calvet, N., Vivas, A. K., Furesz, G., and Szentgyorgyi, A.: 2007, ApJ **661**, 1119

Briceño, C., Mateu, C., Downes, J. J., Vivas, A. K., Hernández, J., and Calvet, N.: 2011, in *Revista Mexicana de Astronomia y Astrofisica Conference Series*, Vol. 40 de *Revista Mexicana de Astronomia y Astrofisica, vol. 27*, pp 225–226

Brown, J. M., Blake, G. A., Dullemond, C. P., Merín, B., Augereau, J. C., Boogert, A. C. A., Evans, II, N. J., Geers, V. C., Lahuis, F., Kessler-Silacci, J. E., Pontoppidan, K. M., and van Dishoeck, E. F.: 2007, ApJ **664**, L107

Bryden, G., Chen, X., Lin, D. N. C., Nelson, R. P., and Papaloizou, J. C. B.: 1999, ApJ **514**, 344

Bustamante, I., Merín, B., Ribas, Á., Bouy, H., Prusti, T., Pilbratt, G. L., and André, P.: 2015, A&A **578**, A23

Calvet, N., D'Alessio, P., Hartmann, L., Wilner, D., Walsh, A., and Sitko, M.: 2002, ApJ **568**, 1008

Calvet, N., D'Alessio, P., Watson, D. M., Franco-Hernández, R., Furlan, E., Green, J., Sutter, P. M., Forrest, W. J., Hartmann, L., Uchida, K. I., Keller, L. D., Sargent, B., Najita, J., Herter, T. L., Barry, D. J., and Hall, P.: 2005, ApJ **630**, L185

Calvet, N. and Gullbring, E.: 1998, ApJ **509**, 802

Calvet, N., Muzerolle, J., Briceño, C., Hernández, J., Hartmann, L., Saucedo, J. L., and Gordon, K. D.: 2004, AJ **128**, 1294

Canovas, H., Caceres, C., Schreiber, M. R., Hardy, A., Cieza, L., Ménard, F., and Hales, A.: 2016, MNRAS **458**, L29

Cardelli, J. A., Clayton, G. C., and Mathis, J. S.: 1989, ApJ **345**, 245

Chamberlin, T. C.: 1916, JRASC **10**, 473

Chambers, K. C., Magnier, E. A., Metcalfe, N., Flewelling, H. A., Huber, M. E., Waters, C. Z., Denneau, L., Draper, P. W., Farrow, D., Finkbeiner, D. P., Holmberg, C., Koppenhoefer, J., Price, P. A., Saglia, R. P., Schlafly, E. F., Smartt, S. J., Sweeney, W., Wainscoat, R. J., Burgett, W. S., Grav, T., Heasley, J. N., Hodapp, K. W., Jedicke, R., Kaiser, N., Kudritzki, R.-P., Luppino, G. A., Lupton, R. H., Monet, D. G., Morgan, J. S., Onaka, P. M., Stubbs, C. W., Tonry, J. L., Banados, E., Bell, E. F., Bender, R., Bernard, E. J., Botticella, M. T., Casertano, S., Chastel, S., Chen, W.-P., Chen, X., Cole, S., Deacon, N., Frenk, C., Fitzsimmons, A., Gezari, S., Goessl, C., Goggia, T., Goldman, B., Grebel, E. K., Hambly, N. C., Hasinger, G., Heavens, A. F., Heckman, T. M., Henderson, R., Henning, T., Holman, M., Hopp, U., Ip, W.-H., Isani, S., Keyes, C. D., Koekemoer, A., Kotak, R., Long, K. S., Lucey, J. R., Liu, M., Martin, N. F., McLean, B., Morganson, E., Murphy, D. N. A., Nieto-Santisteban, M. A., Norberg, P., Peacock, J. A., Pier, E. A., Postman, M., Primak, N., Rae, C., Rest, A., Riess, A., Riffeser, A., Rix, H. W., Roser, S., Schilbach, E., Schultz, A. S. B., Scolnic, D., Szalay, A., Seitz, S., Shiao, B., Small, E., Smith, K. W., Soderblom, D., Taylor, A. N., Thakar, A. R., Thiel,

J., Thilker, D., Urata, Y., Valenti, J., Walter, F., Watters, S. P., Werner, S., White, R., Wood-Vasey, W. M., and Wyse, R.: 2016, *ArXiv e-prints*

Cheetham, A. C., Kraus, A. L., Ireland, M. J., Cieza, L., Rizzuto, A. C., and Tuthill, P. G.: 2015, ApJ **813**, 83

Christiansen, J. L., Derekas, A., Kiss, L. L., Ashley, M. C. B., Curran, S. J., Hamacher, D. W., Hidas, M. G., Thompson, M. R., Webb, J. K., and Young, T. B.: 2008, MNRAS **385**, 1749

Ciardi, D. R., van Eyken, J. C., Barnes, J. W., Beichman, C. A., Carey, S. J., Crockett, C. J., Eastman, J., Johns-Krull, C. M., Howell, S. B., Kane, S. R., . Mclane, J. N., Plavchan, P., Prato, L., Stauffer, J., van Belle, G. T., and von Braun, K.: 2015, ApJ **809**, 42

Cieza, L., Padgett, D. L., Stapelfeldt, K. R., Augereau, J.-C., Harvey, P., Evans, II, N. J., Merín, B., Koerner, D., Sargent, A., van Dishoeck, E. F., Allen, L., Blake, G., Brooke, T., Chapman, N., Huard, T., Lai, S.-P., Mundy, L., Myers, P. C., Spiesman, W., and Wahhaj, Z.: 2007, ApJ **667**, 308

Cieza, L. A., Olofsson, J., Harvey, P. M., Evans, II, N. J., Najita, J., Henning, T., Merín, B., Liebhart, A., Güdel, M., Augereau, J.-C., and Pinte, C.: 2013, ApJ **762**, 100

Cieza, L. A., Olofsson, J., Harvey, P. M., Pinte, C., Merín, B., Augereau, J.-C., Evans, II, N. J., Najita, J., Henning, T., and Ménard, F.: 2011, ApJ **741**, L25

Cieza, L. A., Padgett, D. L., Allen, L. E., McCabe, C. E., Brooke, T. Y., Carey, S. J., Chapman, N. L., Fukagawa, M., Huard, T. L., Noriga-Crespo, A., Peterson, D. E., and Rebull, L. M.: 2009, ApJ **696**, L84

Cieza, L. A., Schreiber, M. R., Romero, G. A., Mora, M. D., Merin, B., Swift, J. J., Orellana, M., Williams, J. P., Harvey, P. M., and Evans, II, N. J.: 2010, ApJ **712**, 925

Cieza, L. A., Schreiber, M. R., Romero, G. A., Williams, J. P., Rebassa-Mansergas, A., and Merín, B.: 2012, ApJ **750**, 157

Clarke, C. J., Gendrin, A., and Sotomayor, M.: 2001, MNRAS **328**, 485

Cody, A. M., Stauffer, J., Baglin, A., Micela, G., Rebull, L. M., Flaccomio, E., Morales-Calderón, M., Aigrain, S., Bouvier, J., Hillenbrand, L. A., Gutermuth, R., Song, I., Turner, N., Alencar, S. H. P., Zwintz, K., Plavchan, P., Carpenter, J., Findeisen, K., Carey, S., Terebey, S., Hartmann, L., Calvet,

N., Teixeira, P., Vrba, F. J., Wolk, S., Covey, K., Poppenhaeger, K., Günther, H. M., Forbrich, J., Whitney, B., Affer, L., Herbst, W., Hora, J., Barrado, D., Holtzman, J., Marchis, F., Wood, K., Medeiros Guimarães, M., Lillo Box, J., Gillen, E., McQuillan, A., Espaillat, C., Allen, L., D'Alessio, P., and Favata, F.: 2014, AJ **147**, 82

Comerón, F.: 2008, *The Lupus Clouds*, p. 295, Handbook of Star Forming Regions, Volume II, Reipurth Bo.; ISBN:978-1-58381-671-4

Cresswell, P., Dirksen, G., Kley, W., and Nelson, R. P.: 2007, A&A **473**, 329

Crida, A., Morbidelli, A., and Masset, F.: 2006, **181**, 587

Currie, T.: 2010

Da Rio, N., Robberto, M., Hillenbrand, L. A., Henning, T., and Stassun, K. G.: 2012, ApJ **748**, 14

Da Rio, N., Robberto, M., Soderblom, D. R., Panagia, N., Hillenbrand, L. A., Palla, F., and Stassun, K. G.: 2010, ApJ **722**, 1092

D'Antona, F. and Mazzitelli, I.: 1994, ApJS **90**, 467

David, T. J.: 2016, in *AAS/Division for Planetary Sciences Meeting Abstracts*, Vol. 48 de *AAS/Division for Planetary Sciences Meeting Abstracts*, p. 112.01

Debes, J. H., Jang-Condell, H., Weinberger, A. J., Roberge, A., and Schneider, G.: 2013, ApJ **771**, 45

Donati, J. F., Moutou, C., Malo, L., Baruteau, C., Yu, L., Hébrard, E., Hussain, G., Alencar, S., Ménard, F., Bouvier, J., Petit, P., Takami, M., Doyon, R., and Cameron, A. C.: 2016, Nature **534**, 662

Downes, J., Román-Zúñiga, C., Ballesteros-Paredes, J., Mateu, C., Briceño, C., Hernández, J., Petr-Gotzens, M. G., Calvet, N., Hartmann, L., and Mauco, K.: 2015, *ArXiv e-prints*

Downes, J. J., Briceño, C., Mateu, C., Hernández, J., Vivas, A. K., Calvet, N., Hartmann, L., Petr-Gotzens, M. G., and Allen, L.: 2014, MNRAS **444**, 1793

Drake, J. J., Ercolano, B., Flaccomio, E., and Micela, G.: 2009, ApJ **699**, L35

Dullemond, C. P. and Dominik, C.: 2005, A&A **434**, 971

Dullemond, C. P., Hollenbach, D., Kamp, I., and D'Alessio, P.: 2007, *Protostars and Planets V, ISBN13: 978-0-8165-2654-3* pp 555–572

Eiroa, C., Marshall, J. P., Mora, A., Montesinos, B., Absil, O., Augereau, J. C., Bayo, A., Bryden, G., Danchi, W., del Burgo, C., Ertel, S., Fridlund, M., Heras, A. M., Krivov, A. V., Launhardt, R., Liseau, R., Löhne, T., Maldonado, J., Pilbratt, G. L., Roberge, A., Rodmann, J., Sanz-Forcada, J., Solano, E., Stapelfeldt, K., Thébault, P., Wolf, S., Ardila, D., Arévalo, M., Beichmann, C., Faramaz, V., González-García, B. M., Gutiérrez, R., Lebreton, J., Martínez-Arnáiz, R., Meeus, G., Montes, D., Olofsson, G., Su, K. Y. L., White, G. J., Barrado, D., Fukagawa, M., Grün, E., Kamp, I., Lorente, R., Morbidelli, A., Müller, S., Mutschke, H., Nakagawa, T., Ribas, I., and Walker, H.: 2013, A&A **555**, A11

Emerson, J. P., Sutherland, W. J., McPherson, A. M., Craig, S. C., Dalton, G. B., and Ward, A. K.: 2004, *The Messenger* **117**, 27

Ercolano, B., Mayr, D., Owen, J. E., Rosotti, G., and Manara, C. F.: 2014, MNRAS **439**, 256

Erickson, K. L., Wilking, B. A., Meyer, M. R., Robinson, J. G., and Stephenson, L. N.: 2011, AJ **142**, 140

Espaillat, C., Calvet, N., D'Alessio, P., Hernández, J., Qi, C., Hartmann, L., Furlan, E., and Watson, D. M.: 2007, ApJ **670**, L135

Espaillat, C., D'Alessio, P., Hernández, J., Nagel, E., Luhman, K. L., Watson, D. M., Calvet, N., Muzerolle, J., and McClure, M.: 2010, ApJ **717**, 441

Espaillat, C., Ingleby, L., Hernández, J., Furlan, E., D'Alessio, P., Calvet, N., Andrews, S., Muzerolle, J., Qi, C., and Wilner, D.: 2012, ApJ **747**, 103

Espaillat, C., Muzerolle, J., Najita, J., Andrews, S., Zhu, Z., Calvet, N., Kraus, S., Hashimoto, J., Kraus, A., and D'Alessio, P.: 2014, *Protostars and Planets VI, ISBN:9780816598762 0816598762*

Evans, N. J., Dunham, M. M., Jorgensen, J. K., Enoch, M. L., Merin, B., van Dishoeck, E. F., Alcala, J. M., Myers, P. C., Stapelfeldt, K. R., Huard, T. L., Allen, L. E., Harvey, P. M., van Kempen, T., Blake, G. A., Koerner, D. W., Mundy, L. G., Padgett, D. L., and Sargent, A. I.: 2009, *VizieR Online Data Catalog* 218

Evans, T. M., Ireland, M. J., Kraus, A. L., Martinache, F., Stewart, P., Tuthill, P. G., Lacour, S., Carpenter, J. M., and Hillenbrand, L. A.: 2012, ApJ **744**, 120

Fazio, G. G., Hora, J. L., Allen, L. E., Ashby, M. L. N., Barmby, P., Deutsch, L. K., Huang, J.-S., Kleiner, S., Marengo, M., Megeath, S. T., Melnick, G. J., Pahre, M. A., Patten, B. M., Polizotti, J., Smith, H. A., Taylor, R. S., Wang, Z., Willner, S. P., Hoffmann, W. F., Pipher, J. L., Forrest, W. J., McMurty, C. W., McCreight, C. R., McKelvey, M. E., McMurray, R. E., Koch, D. G., Moseley, S. H., Arendt, R. G., Mentzell, J. E., Marx, C. T., Losch, P., Mayman, P., Eichhorn, W., Krebs, D., Jhabvala, M., Gezari, D. Y., Fixsen, D. J., Flores, J., Shakoorzadeh, K., Jungo, R., Hakun, C., Workman, L., Karpati, G., Kichak, R., Whitley, R., Mann, S., Tollestrup, E. V., Eisenhardt, P., Stern, D., Gorjian, V., Bhattacharya, B., Carey, S., Nelson, B. O., Glaccum, W. J., Lacy, M., Lowrance, P. J., Laine, S., Reach, W. T., Stauffer, J. A., Surace, J. A., Wilson, G., Wright, E. L., Hoffman, A., Domingo, G., and Cohen, M.: 2004, ApJS **154**, 10

Feigelson, E. D. and Montmerle, T.: 1999, ARA&A **37**, 363

Flaccomio, E., Damiani, F., Micela, G., Sciortino, S., Harnden, Jr., F. R., Murray, S. S., and Wolk, S. J.: 2003, ApJ **582**, 398

Flaccomio, E., Micela, G., and Sciortino, S.: 2012, A&A **548**, A85

Franciosini, E., Sacco, G. G., and Randich, S.: 2011, in J.-U. Ness and M. Ehle (eds.), *The X-ray Universe 2011, XMM-Newton Science Operations Centre,*, p. 207

Gahm, G. F.: 1990, in L. V. Mirzoian, B. R. Pettersen, and M. K. Tsvetkov (eds.), *Flare Stars in Star Clusters, Associations and the Solar Vicinity*, Vol. 137 de *IAU Symposium*, pp 193–206

Gáspár, A. and Rieke, G. H.: 2014, ApJ **784**, 33

Getman, K. V., Feigelson, E. D., Broos, P. S., Micela, G., and Garmire, G. P.: 2008a, ApJ **688**, 418

Getman, K. V., Feigelson, E. D., Grosso, N., McCaughrean, M. J., Micela, G., Broos, P., Garmire, G., and Townsley, L.: 2005a, ApJS **160**, 353

Getman, K. V., Feigelson, E. D., Micela, G., Jardine, M. M., Gregory, S. G., and Garmire, G. P.: 2008b, ApJ **688**, 437

Getman, K. V., Flaccomio, E., Broos, P. S., Grosso, N., Tsujimoto, M., Townsley, L., Garmire, G. P., Kastner, J., Li, J., Harnden, Jr., F. R., Wolk, S., Murray, S. S., Lada, C. J., Muench, A. A., McCaughrean, M. J., Meeus, G., Dami-

ani, F., Micela, G., Sciortino, S., Bally, J., Hillenbrand, L. A., Herbst, W., Preibisch, T., and Feigelson, E. D.: 2005b, ApJS **160**, 319

Ghez, A. M., White, R. J., and Simon, M.: 1997, ApJ **490**, 353

Giuricin, G., Mardirossian, F., and Mezzetti, M.: 1983, ApJS **52**, 35

Gomez, M., Hartmann, L., Kenyon, S. J., and Hewett, R.: 1993, AJ **105**, 1927

Gorti, U. and Hollenbach, D.: 2009, ApJ **690**, 1539

Gray, R. O. and Corbally, J., C.: 2009, *Stellar Spectral Classification*, Princeton series in astrophysics, ISBN: 9780691125114

Greene, T. P., Wilking, B. A., Andre, P., Young, E. T., and Lada, C. J.: 1994, ApJ **434**, 614

Griffin, M. J., Abergel, A., Abreu, A., Ade, P. A. R., André, P., Augueres, J.-L., Babbedge, T., Bae, Y., Baillie, T., Baluteau, J.-P., Barlow, M. J., Bendo, G., Benielli, D., Bock, J. J., Bonhomme, P., Brisbin, D., Brockley-Blatt, C., Caldwell, M., Cara, C., Castro-Rodriguez, N., Cerulli, R., Chanial, P., Chen, S., Clark, E., Clements, D. L., Clerc, L., Coker, J., Communal, D., Conversi, L., Cox, P., Crumb, D., Cunningham, C., Daly, F., Davis, G. R., de Antoni, P., Delderfield, J., Devin, N., di Giorgio, A., Didschuns, I., Dohlen, K., Donati, M., Dowell, A., Dowell, C. D., Duband, L., Dumaye, L., Emery, R. J., Ferlet, M., Ferrand, D., Fontignie, J., Fox, M., Franceschini, A., Frerking, M., Fulton, T., Garcia, J., Gastaud, R., Gear, W. K., Glenn, J., Goizel, A., Griffin, D. K., Grundy, T., Guest, S., Guillemet, L., Hargrave, P. C., Harwit, M., Hastings, P., Hatziminaoglou, E., Herman, M., Hinde, B., Hristov, V., Huang, M., Imhof, P., Isaak, K. J., Israelsson, U., Ivison, R. J., Jennings, D., Kiernan, B., King, K. J., Lange, A. E., Latter, W., Laurent, G., Laurent, P., Leeks, S. J., Lellouch, E., Levenson, L., Li, B., Li, J., Lilienthal, J., Lim, T., Liu, S. J., Lu, N., Madden, S., Mainetti, G., Marliani, P., McKay, D., Mercier, K., Molinari, S., Morris, H., Moseley, H., Mulder, J., Mur, M., Naylor, D. A., Nguyen, H., O'Halloran, B., Oliver, S., Olofsson, G., Olofsson, H.-G., Orfei, R., Page, M. J., Pain, I., Panuzzo, P., Papageorgiou, A., Parks, G., Parr-Burman, P., Pearce, A., Pearson, C., Pérez-Fournon, I., Pinsard, F., Pisano, G., Podosek, J., Pohlen, M., Polehampton, E. T., Pouliquen, D., Rigopoulou, D., Rizzo, D., Roseboom, I. G., Roussel, H., Rowan-Robinson, M., Rownd, B., Saraceno, P., Sauvage, M., Savage, R., Savini, G., Sawyer, E., Scharmberg, C., Schmitt, D., Schneider, N., Schulz, B., Schwartz, A., Shafer, R., Shupe, D. L.,

Sibthorpe, B., Sidher, S., Smith, A., Smith, A. J., Smith, D., Spencer, L., Stobie, B., Sudiwala, R., Sukhatme, K., Surace, C., Stevens, J. A., Swinyard, B. M., Trichas, M., Tourette, T., Triou, H., Tseng, S., Tucker, C., Turner, A., Vaccari, M., Valtchanov, I., Vigroux, L., Virique, E., Voellmer, G., Walker, H., Ward, R., Waskett, T., Weilert, M., Wesson, R., White, G. J., Whitehouse, N., Wilson, C. D., Winter, B., Woodcraft, A. L., Wright, G. S., Xu, C. K., Zavagno, A., Zemcov, M., Zhang, L., and Zonca, E.: 2010, A&A **518**, L3

Güdel, M., Briggs, K. R., Arzner, K., Audard, M., Bouvier, J., Feigelson, E. D., Franciosini, E., Glauser, A., Grosso, N., Micela, G., Monin, J.-L., Montmerle, T., Padgett, D. L., Palla, F., Pillitteri, I., Rebull, L., Scelsi, L., Silva, B., Skinner, S. L., Stelzer, B., and Telleschi, A.: 2007a, A&A **468**, 353

Güdel, M., Telleschi, A., Audard, M., Skinner, S. L., Briggs, K. R., Palla, F., and Dougados, C.: 2007b, A&A **468**, 515

Guenther, E. and Ball, M.: 1998, in R. A. Donahue and J. A. Bookbinder (eds.), *Cool Stars, Stellar Systems, and the Sun*, Vol. 154 de *Astronomical Society of the Pacific Conference Series*, p. 1701

Guenther, E. W. and Emerson, J. P.: 1997, A&A **321**, 803

Gullbring, E., Hartmann, L., Briceño, C., and Calvet, N.: 1998, ApJ **492**, 323

Habing, H. J., Dominik, C., Jourdain de Muizon, M., Laureijs, R. J., Kessler, M. F., Leech, K., Metcalfe, L., Salama, A., Siebenmorgen, R., Trams, N., and Bouchet, P.: 2001, A&A **365**, 545

Haisch, Jr., K. E., Lada, E. A., and Lada, C. J.: 2001, ApJ **553**, L153

Hartmann, L.: 1998, *Accretion Processes in Star Formation*, Cambridge Astrophysics Series, ISBN-13: 978-0521531993

Hauschildt, P. H., Allard, F., and Baron, E.: 1999a, ApJ **512**, 377

Hauschildt, P. H., Allard, F., and Baron, E.: 1999b, ApJ **512**, 377

Hayashi, C., Nakazawa, K., and Nakagawa, Y.: 1985, in D. C. Black and M. S. Matthews (eds.), *Protostars and Planets II*, pp 1100–1153

Hebb, L., Petro, L., Ford, H. C., Ardila, D. R., Toledo, I., Minniti, D., Golimowski, D. A., and Clampin, M.: 2007, MNRAS **379**, 63

Herbig, G. H.: 1962, *Advances in Astronomy and Astrophysics* **1**, 47

Hernández, J., Briceño, C., Calvet, N., Hartmann, L., Muzerolle, J., and Quintero, A.: 2006, ApJ **652**, 472

Hernández, J., Calvet, N., Briceño, C., Hartmann, L., Vivas, A. K., Muzerolle, J., Downes, J., Allen, L., and Gutermuth, R.: 2007, ApJ **671**, 1784

Hernández, J., Calvet, N., Hartmann, L., Briceño, C., Sicilia-Aguilar, A., and Berlind, P.: 2005, AJ **129**, 856

Hernández, J., Hartmann, L., Calvet, N., Jeffries, R. D., Gutermuth, R., Muzerolle, J., and Stauffer, J.: 2008, ApJ **686**, 1195

Hillenbrand, L. A.: 1997, AJ **113**, 1733

Hillenbrand, L. A.: 2008, *Physica Scripta Volume T* **130(1)**, 014024

Hillenbrand, L. A., Hoffer, A. S., and Herczeg, G. J.: 2013, AJ **146**, 85

Hillenbrand, L. A., Strom, S. E., Calvet, N., Merrill, K. M., Gatley, I., Makidon, R. B., Meyer, M. R., and Skrutskie, M. F.: 1998, AJ **116**, 1816

Ho, P. T. P., Moran, J. M., and Lo, K. Y.: 2004, ApJ **616**, L1

Hollenbach, D. J., Yorke, H. W., and Johnstone, D.: 2000, *Protostars and Planets IV, University of Arizona press, ISBN 13: 9780816520596* p. 401

Howarth, I. D.: 2016, MNRAS **457**, 3769

Huang, S.-S.: 1963, ApJ **138**, 342

Hughes, J., Hartigan, P., Krautter, J., and Kelemen, J.: 1994, AJ **108**, 1071

Ingleby, L., Calvet, N., Bergin, E., Herczeg, G., Brown, A., Alexander, R., Edwards, S., Espaillat, C., France, K., Gregory, S. G., Hillenbrand, L., Roueff, E., Valenti, J., Walter, F., Johns-Krull, C., Brown, J., Linsky, J., McClure, M., Ardila, D., Abgrall, H., Bethell, T., Hussain, G., and Yang, H.: 2011, ApJ **743**, 105

Ivanov, P. B., Papaloizou, J. C. B., and Polnarev, A. G.: 1999, MNRAS **307**, 79

Johns-Krull, C. M., McLane, J. N., Prato, L., Crockett, C. J., Jaffe, D. T., Hartigan, P. M., Beichman, C. A., Mahmud, N. I., Chen, W., Skiff, B. A., Cauley, P. W., Jones, J. A., and Mace, G. N.: 2016a, ApJ **826**, 206

Johns-Krull, C. M., Prato, L., McLane, J. N., Ciardi, D. R., van Eyken, J. C., Chen, W., Stauffer, J. R., Beichman, C. A., Frazier, S. A., Boden, A. F., Morales-Calderón, M., and Rebull, L. M.: 2016b, ApJ **830**, 15

Jones, E., Oliphant, T., Peterson, P., et al.: 2001, *SciPy: Open source scientific tools for Python*, [Online; accessed 2015-08-06] http://www.scipy.org/

Joy, A. H.: 1945, ApJ **102**, 168

Kamiaka, S., Masuda, K., Xue, Y., Suto, Y., Nishioka, T., Murakami, R., Inayama, K., Saitoh, M., Tanaka, M., and Yonehara, A.: 2015, PASJ **67**, 94

Kenyon, S. J., Gómez, M., and Whitney, B. A.: 2008, *Low Mass Star Formation in the Taurus-Auriga Clouds*, p. 405, Handbook of Star Forming Regions, Volume I, Reipurth Bo., ISBN:978-1-58381-670-7

Kenyon, S. J. and Hartmann, L.: 1987, ApJ **323**, 714

Kenyon, S. J. and Hartmann, L.: 1995, ApJS **101**, 117

Kenyon, S. J., Hartmann, L. W., Strom, K. M., and Strom, S. E.: 1990, AJ **99**, 869

Khalafinejad, S., Maaskant, K. M., Mariñas, N., and Tielens, A. G. G. M.: 2016, A&A **587**, A62

Kim, K. H., Watson, D. M., Manoj, P., Forrest, W. J., Najita, J., Furlan, E., Sargent, B., Espaillat, C., Muzerolle, J., Megeath, S. T., Calvet, N., Green, J. D., and Arnold, L.: 2013, ApJ **769**, 149

Kim, K. H., Watson, D. M., Manoj, P., Furlan, E., Najita, J., Forrest, W. J., Sargent, B., Espaillat, C., Calvet, N., Luhman, K. L., McClure, M. K., Green, J. D., and Harrold, S. T.: 2009, ApJ **700**, 1017

Kirkpatrick, J. D., Reid, I. N., Liebert, J., Cutri, R. M., Nelson, B., Beichman, C. A., Dahn, C. C., Monet, D. G., Gizis, J. E., and Skrutskie, M. F.: 1999, ApJ **519**, 802

Koda, J., Scoville, N., Sawada, T., La Vigne, M. A., Vogel, S. N., Potts, A. E., Carpenter, J. M., Corder, S. A., Wright, M. C. H., White, S. M., Zauderer, B. A., Patience, J., Sargent, A. I., Bock, D. C. J., Hawkins, D., Hodges, M., Kemball, A., Lamb, J. W., Plambeck, R. L., Pound, M. W., Scott, S. L., Teuben, P., and Woody, D. P.: 2009, ApJ **700**, L132

Koen, C.: 2015, MNRAS **450**, 3991

Königl, A. and Salmeron, R.: 2011, *The Effects of Large-Scale Magnetic Fields on Disk Formation and Evolution*, pp 283–352, Physical Processes in Circumstellar Disks around Young Stars, Paulo Garcia, ISBN-13: 978-0226282299

Kopal, Z.: 1959, *Leaflet of the Astronomical Society of the Pacific* **8**, 81

Kraus, A. L. and Ireland, M. J.: 2012, ApJ **745**, 5

Kraus, A. L., Ireland, M. J., Martinache, F., and Hillenbrand, L. A.: 2011, ApJ **731**, 8

Kraus, A. L., Ireland, M. J., Martinache, F., and Lloyd, J. P.: 2008, ApJ **679**, 762

Krautter, J., Wichmann, R., Schmitt, J. H. M. M., Alcala, J. M., Neuhauser, R., and Terranegra, L.: 1997, A&AS **123**, 329

Krivov, A. V., Eiroa, C., Löhne, T., Marshall, J. P., Montesinos, B., del Burgo, C., Absil, O., Ardila, D., Augereau, J.-C., Bayo, A., Bryden, G., Danchi, W., Ertel, S., Lebreton, J., Liseau, R., Mora, A., Mustill, A. J., Mutschke, H., Neuhäuser, R., Pilbratt, G. L., Roberge, A., Schmidt, T. O. B., Stapelfeldt, K. R., Thébault, P., Vitense, C., White, G. J., and Wolf, S.: 2013, ApJ **772**, 32

Krumholz, M. R.: 2011, in E. Telles, R. Dupke, and D. Lazzaro (eds.), *American Institute of Physics Conference Series*, Vol. 1386 de *American Institute of Physics Conference Series*, pp 9–57

Lada, C. J.: 1987, in M. Peimbert and J. Jugaku (eds.), *Star Forming Regions*, Vol. 115 de *IAU Symposium*, pp 1–17

Lada, C. J., Muench, A. A., Luhman, K. L., Allen, L., Hartmann, L., Megeath, T., Myers, P., Fazio, G., Wood, K., Muzerolle, J., Rieke, G., Siegler, N., and Young, E.: 2006, AJ **131**, 1574

Lada, C. J. and Wilking, B. A.: 1984, ApJ **287**, 610

Law, N. M., Dekany, R. G., Rahmer, G., Hale, D., Smith, R., Quimby, R., Ofek, E. O., Kasliwal, M., Zolkower, J., Velur, V., Henning, J., Bui, K., McKenna, D., Nugent, P., Jacobsen, J., Walters, R., Bloom, J., Surace, J., Grillmair, C., Laher, R., Mattingly, S., and Kulkarni, S.: 2010, in *Ground-based and Airborne Instrumentation for Astronomy III*, Vol. 7735 de Proc. SPIE, p. 77353M

Lestrade, J.-F., Matthews, B. C., Sibthorpe, B., Kennedy, G. M., Wyatt, M. C., Bryden, G., Greaves, J. S., Thilliez, E., Moro-Martín, A., Booth, M., Dent, W. R. F., Duchêne, G., Harvey, P. M., Horner, J., Kalas, P., Kavelaars, J. J., Phillips, N. M., Rodriguez, D. R., Su, K. Y. L., and Wilner, D. J.: 2012, A&A **548**, A86

Lin, D. N. C. and Papaloizou, J.: 1986, ApJ **309**, 846

Lin, D. N. C. and Papaloizou, J. C. B.: 1993, in E. H. Levy and J. I. Lunine (eds.), *Protostars and Planets III*, pp 749–835

Lin, M.-K. and Papaloizou, J. C. B.: 2010, MNRAS **405**, 1473

Lissauer, J. J.: 1993, ARA&A **31**, 129

Liu, F., Cutri, R., Greanias, G., Duval, V., Eisenhardt, P., Elwell, J., Heinrichsen, I., Howard, J., Irace, W., Mainzer, A., Razzaghi, A., Royer, D., and Wright, E. L.: 2008, in *Modeling, Systems Engineering, and Project Management for Astronomy III*, Vol. 7017 de Proc. SPIE, p. 70170M

Loinard, L., Mioduszewski, A. J., Rodríguez, L. F., González, R. A., Rodríguez, M. I., and Torres, R. M.: 2005, ApJ **619**, L179

Lommen, D. J. P., van Dishoeck, E. F., Wright, C. M., Maddison, S. T., Min, M., Wilner, D. J., Salter, D. M., van Langevelde, H. J., Bourke, T. L., van der Burg, R. F. J., and Blake, G. A.: 2010, A&A **515**, A77

Lucas, P. W., Roche, P. F., Allard, F., and Hauschildt, P. H.: 2001, MNRAS **326**, 695

Luhman, K. L., Rieke, G. H., Young, E. T., Cotera, A. S., Chen, H., Rieke, M. J., Schneider, G., and Thompson, R. I.: 2000, ApJ **540**, 1016

Mamajek, E. E.: 2009, in T. Usuda, M. Tamura, and M. Ishii (eds.), *American Institute of Physics Conference Series*, Vol. 1158 de *American Institute of Physics Conference Series*, pp 3–10

Mamajek, E. E., Meyer, M. R., Hinz, P. M., Hoffmann, W. F., Cohen, M., and Hora, J. L.: 2004, ApJ **612**, 496

Manara, C. F., Beccari, G., Da Rio, N., De Marchi, G., Natta, A., Ricci, L., Robberto, M., and Testi, L.: 2013a, A&A **558**, A114

Manara, C. F., Robberto, M., Da Rio, N., Lodato, G., Hillenbrand, L. A., Stassun, K. G., and Soderblom, D. R.: 2012, ApJ **755**, 154

Manara, C. F., Testi, L., Rigliaco, E., Alcalá, J. M., Natta, A., Stelzer, B., Biazzo, K., Covino, E., Covino, S., Cupani, G., D'Elia, V., and Randich, S.: 2013b, A&A **551**, A107

Mann, A. W., Newton, E. R., Rizzuto, A. C., Irwin, J., Feiden, G. A., Gaidos, E., Mace, G. N., Kraus, A. L., James, D. J., Ansdell, M., Charbonneau, D., Covey, K. R., Ireland, M. J., Jaffe, D. T., Johnson, M. C., Kidder, B., and Vanderburg, A.: 2016, AJ **152**, 61

Mannings, V. and Barlow, M. J.: 1998, ApJ **497**, 330

Marsh, K. A. and Mahoney, M. J.: 1992, ApJ **395**, L115

Masset, F. S.: 2008, in M.-J. Goupil and J.-P. Zahn (eds.), *EAS Publications Series*, Vol. 29 de *EAS Publications Series*, pp 165–244

Masset, F. S. and Papaloizou, J. C. B.: 2003, ApJ **588**, 494

Matrà, L., Merín, B., Alves de Oliveira, C., Huélamo, N., Kóspál, A., Cox, N. L. J., Ribas, Á., Puga, E., Vavrek, R., Royer, P., Prusti, T., Pilbratt, G. L., and André, P.: 2012, A&A **548**, A111

McGehee, P. M.: 2006, AJ **131**, 2959

Menten, K. M., Reid, M. J., Forbrich, J., and Brunthaler, A.: 2007, A&A **474**, 515

Merín, B., Brown, J. M., Oliveira, I., Herczeg, G. J., van Dishoeck, E. F., Bottinelli, S., Evans, II, N. J., Cieza, L., Spezzi, L., Alcalá, J. M., Harvey, P. M., Blake, G. A., Bayo, A., Geers, V. G., Lahuis, F., Prusti, T., Augereau, J.-C., Olofsson, J., Walter, F. M., and Chiu, K.: 2010, ApJ **718**, 1200

Merín, B., Jørgensen, J., Spezzi, L., Alcalá, J. M., Evans, II, N. J., Harvey, P. M., Prusti, T., Chapman, N., Huard, T., van Dishoeck, E. F., and Comerón, F.: 2008, ApJS **177**, 551

Mohanty, S., Basri, G., and Jayawardhana, R.: 2005, *Astronomische Nachrichten* **326**, 891

Monin, J.-L., Clarke, C. J., Prato, L., and McCabe, C.: 2007, *Protostars and Planets V* pp 395–409

Montes, D., López-Santiago, J., Crespo-Chacón, I., and Fernández-Figueroa, M. J.: 2005, in F. Favata, G. A. J. Hussain, and B. Battrick (eds.), *13th Cambridge Workshop on Cool Stars, Stellar Systems and the Sun*, Vol. 560 de *ESA Special Publication*, p. 825

Moreno-Corral, M. A., Chavarria-K., C., and de Lara, E.: 1995, in M. Pena and S. Kurtz (eds.), *Revista Mexicana de Astronomia y Astrofisica Conference Series*, Vol. 3 de *Revista Mexicana de Astronomia y Astrofisica Conference Series*, p. 121

Moro-Martín, A., Wyatt, M. C., Malhotra, R., and Trilling, D. E.: 2008, *Extrasolar Kuiper Belt Dust Disks*, pp 465–480, Unversity of Arizona press, ISBN-13:9780816527557

Mortier, A., Oliveira, I., and van Dishoeck, E. F.: 2011, MNRAS **418**, 1194

Muzerolle, J., Allen, L. E., Megeath, S. T., Hernández, J., and Gutermuth, R. A.: 2010, ApJ **708**, 1107

Muzerolle, J., Hillenbrand, L., Calvet, N., Briceño, C., and Hartmann, L.: 2003, ApJ **592**, 266

Muzerolle, J., Luhman, K. L., Briceño, C., Hartmann, L., and Calvet, N.: 2005, ApJ **625**, 906

Najita, J. R., Strom, S. E., and Muzerolle, J.: 2007, MNRAS **378**, 369

Natta, A., Testi, L., Comerón, F., Oliva, E., D'Antona, F., Baffa, C., Comoretto, G., and Gennari, S.: 2002, A&A **393**, 597

Natta, A., Testi, L., and Randich, S.: 2006, A&A **452**, 245

Nelson, R. P., Papaloizou, J. C. B., Masset, F., and Kley, W.: 2000, MNRAS **318**, 18

Neugebauer, G., Habing, H. J., van Duinen, R., Aumann, H. H., Baud, B., Beichman, C. A., Beintema, D. A., Boggess, N., Clegg, P. E., de Jong, T., Emerson, J. P., Gautier, T. N., Gillett, F. C., Harris, S., Hauser, M. G., Houck, J. R., Jennings, R. E., Low, F. J., Marsden, P. L., Miley, G., Olnon, F. M., Pottasch, S. R., Raimond, E., Rowan-Robinson, M., Soifer, B. T., Walker, R. G., Wesselius, P. R., and Young, E.: 1984, ApJ **278**, L1

Ofek, E. O., Laher, R., Law, N., Surace, J., Levitan, D., Sesar, B., Horesh, A., Poznanski, D., van Eyken, J. C., Kulkarni, S. R., Nugent, P., Zolkower, J., Walters, R., Sullivan, M., Agüeros, M., Bildsten, L., Bloom, J., Cenko, S. B., Gal-Yam, A., Grillmair, C., Helou, G., Kasliwal, M. M., and Quimby, R.: 2012, PASP **124**, 62

Onitsuka, M., Fukui, A., Narita, N., Hirano, T., Kusakabe, N., Ryu, T., and Tamura, M.: 2017, *ArXiv e-prints*

Ott, S.: 2010, in Y. Mizumoto, K.-I. Morita, and M. Ohishi (eds.), *Astronomical Data Analysis Software and Systems XIX*, Vol. 434 de *Astronomical Society of the Pacific Conference Series*, p. 139

Oudmaijer, R. D., van der Veen, W. E. C. J., Waters, L. B. F. M., Trams, N. R., Waelkens, C., and Engelsman, E.: 1992, A&AS **96**, 625

Owen, J. E., Ercolano, B., and Clarke, C. J.: 2011, MNRAS **412**, 13

Owen, J. E., Ercolano, B., Clarke, C. J., and Alexander, R. D.: 2010, MNRAS **401**, 1415

Papaloizou, J. C. B.: 2003, *Celestial Mechanics and Dynamical Astronomy* **87**, 53

Papaloizou, J. C. B. and Nelson, R. P.: 2005, A&A **433**, 247

Pascucci, I., Apai, D., Hardegree-Ullman, E. E., Kim, J. S., Meyer, M. R., and Bouwman, J.: 2008, ApJ **673**, 477

Pecaut, M. J., Mamajek, E. E., and Bubar, E. J.: 2012, ApJ **746**, 154

Pepliński, A., Artymowicz, P., and Mellema, G.: 2008, MNRAS **387**, 1063

Percy, J. R.: 2011, *Understanding Variable Stars*, Cambridge University press, ISBN-13: 978-1107403703

Petigura, E., Marcy, G. W., and Howard, A.: 2013, in *American Astronomical Society Meeting Abstracts #221*, Vol. 221 de *American Astronomical Society Meeting Abstracts*, p. 216.05

Pilbratt, G. L., Riedinger, J. R., Passvogel, T., Crone, G., Doyle, D., Gageur, U., Heras, A. M., Jewell, C., Metcalfe, L., Ott, S., and Schmidt, M.: 2010, A&A **518**, L1

Pizzolato, N., Maggio, A., Micela, G., Sciortino, S., and Ventura, P.: 2003, A&A **397**, 147

Plavchan, P., Jura, M., Kirkpatrick, J. D., Cutri, R. M., and Gallagher, S. C.: 2008, ApJS **175**, 191

Poglitsch, A., Waelkens, C., Geis, N., Feuchtgruber, H., Vandenbussche, B., Rodriguez, L., Krause, O., Renotte, E., van Hoof, C., Saraceno, P., Cepa, J., Kerschbaum, F., Agnèse, P., Ali, B., Altieri, B., Andreani, P., Augueres, J.-L., Balog, Z., Barl, L., Bauer, O. H., Belbachir, N., Benedettini, M., Billot, N., Boulade, O., Bischof, H., Blommaert, J., Callut, E., Cara, C., Cerulli, R., Cesarsky, D., Contursi, A., Creten, Y., De Meester, W., Doublier, V., Doumayrou, E., Duband, L., Exter, K., Genzel, R., Gillis, J.-M., Grözinger, U., Henning, T., Herreros, J., Huygen, R., Inguscio, M., Jakob, G., Jamar, C., Jean, C., de Jong, J., Katterloher, R., Kiss, C., Klaas, U., Lemke, D., Lutz, D., Madden, S., Marquet, B., Martignac, J., Mazy, A., Merken, P., Montfort, F., Morbidelli, L., Müller, T., Nielbock, M., Okumura, K., Orfei, R., Ottensamer, R., Pezzuto, S., Popesso, P., Putzeys, J., Regibo, S., Reveret, V.,

Royer, P., Sauvage, M., Schreiber, J., Stegmaier, J., Schmitt, D., Schubert, J., Sturm, E., Thiel, M., Tofani, G., Vavrek, R., Wetzstein, M., Wieprecht, E., and Wiezorrek, E.: 2010, A&A **518**, L2

Pojmanski, G.: 2003, *Icarus* **53**, 341

Preibisch, T.: 2007, Mem. Soc. Astron. Italiana **78**, 332

Preibisch, T., Kim, Y.-C., Favata, F., Feigelson, E. D., Flaccomio, E., Getman, K., Micela, G., Sciortino, S., Stassun, K., Stelzer, B., and Zinnecker, H.: 2005, ApJS **160**, 401

Preibisch, T., Zinnecker, H., and Schmitt, J. H. M. M.: 1993, A&A **279**, L33

Qian, S.-B., Wang, J.-J., Zhu, L.-Y., Snoonthornthum, B., Wang, L.-Z., Zhao, E. G., Zhou, X., Liao, W.-P., and Liu, N.-P.: 2014, ApJS **212**, 4

Raetz, S., Schmidt, T. O. B., Czesla, S., Klocová, T., Holmes, L., Errmann, R., Kitze, M., Fernández, M., Sota, A., Briceño, C., Hernández, J., Downes, J. J., Dimitrov, D. P., Kjurkchieva, D., Radeva, V., Wu, Z.-Y., Zhou, X., Takahashi, H., Henych, T., Seeliger, M., Mugrauer, M., Adam, C., Marka, C., Schmidt, J. G., Hohle, M. M., Ginski, C., Pribulla, T., Trepl, L., Moualla, M., Pawellek, N., Gelszinnis, J., Buder, S., Masda, S., Maciejewski, G., and Neuhäuser, R.: 2016, MNRAS **460**, 2834

Reggiani, M., Robberto, M., Da Rio, N., Meyer, M. R., Soderblom, D. R., and Ricci, L.: 2011, A&A **534**, A83

Ribas, Á., Bouy, H., and Merín, B.: 2015, A&A **576**, A52

Ribas, Á., Merín, B., Bouy, H., Alves de Oliveira, C., Ardila, D. R., Puga, E., Kóspál, Á., Spezzi, L., Cox, N. L. J., Prusti, T., Pilbratt, G. L., André, P., Matrà, L., and Vavrek, R.: 2013, A&A **552**, A115

Ribas, Á., Merín, B., Bouy, H., and Maud, L. T.: 2014, A&A **561**, A54

Ricci, L., Robberto, M., and Soderblom, D. R.: 2008, AJ **136**, 2136

Rieke, G. and Su, K.: 2004, *Debris Disk Evolution in A stars*, Spitzer Proposal

Rizzuto, A. C., Ireland, M. J., Dupuy, T. J., and Kraus, A. L.: 2016, ApJ **817**, 164

Robberto, M., Soderblom, D. R., Bergeron, E., Kozhurina-Platais, V., Makidon, R. B., McCullough, P. R., McMaster, M., Panagia, N., Reid, I. N., Levay, Z., Frattare, L., Da Rio, N., Andersen, M., O'Dell, C. R., Stassun, K. G.,

Simon, M., Feigelson, E. D., Stauffer, J. R., Meyer, M., Reggiani, M., Krist, J., Manara, C. F., Romaniello, M., Hillenbrand, L. A., Ricci, L., Palla, F., Najita, J. R., Ananna, T. T., Scandariato, G., and Smith, K.: 2013, ApJS **207**, 10

Robitaille, T. P.: 2011, A&A **536**, A79

Robitaille, T. P., Whitney, B. A., Indebetouw, R., Wood, K., and Denzmore, P.: 2006, ApJS **167**, 256

Roman-Duval, J., Israel, F. P., Bolatto, A., Hughes, A., Leroy, A., Meixner, M., Gordon, K., Madden, S. C., Paradis, D., Kawamura, A., Li, A., Sauvage, M., Wong, T., Bernard, J.-P., Engelbracht, C., Hony, S., Kim, S., Misselt, K., Okumura, K., Ott, J., Panuzzo, P., Pineda, J. L., Reach, W. T., and Rubio, M.: 2010, A&A **518**, L74

Roussel, H.: 2012, *Scanamorphos: Maps from scan observations made with bolometer arrays*, Astrophysics Source Code Library

Rygl, K. L. J., Benedettini, M., Schisano, E., Elia, D., Molinari, S., Pezzuto, S., André, P., Bernard, J. P., White, G. J., Polychroni, D., Bontemps, S., Cox, N. L. J., Di Francesco, J., Facchini, A., Fallscheer, C., di Giorgio, A. M., Hennemann, M., Hill, T., Könyves, V., Minier, V., Motte, F., Nguyen-Luong, Q., Peretto, N., Pestalozzi, M., Sadavoy, S., Schneider, N., Spinoglio, L., Testi, L., and Ward-Thompson, D.: 2013, A&A **549**, L1

Safronov, V. S. and Zvjagina, E. V.: 1969, **10**, 109

Samus, N. N., Kazarovets, E. V., Kireeva, N. N., Pastukhova, E. N., and Durlevich, O. V.: 2010, *Odessa Astronomical Publications* **23**, 102

Savitzky, A. and Golay, M. J. E.: 1964, *Analytical Chemistry* **36**, 1627

Sicilia-Aguilar, A., Henning, T., and Hartmann, L. W.: 2010, ApJ **710**, 597

Siess, L., Dufour, E., and Forestini, M.: 2000, A&A **358**, 593

Skrutskie, M. F., Cutri, R. M., Stiening, R., Weinberg, M. D., Schneider, S., Carpenter, J. M., Beichman, C., Capps, R., Chester, T., Elias, J., Huchra, J., Liebert, J., Lonsdale, C., Monet, D. G., Price, S., Seitzer, P., Jarrett, T., Kirkpatrick, J. D., Gizis, J. E., Howard, E., Evans, T., Fowler, J., Fullmer, L., Hurt, R., Light, R., Kopan, E. L., Marsh, K. A., McCallon, H. L., Tam, R., Van Dyk, S., and Wheelock, S.: 2006, AJ **131**, 1163

Skrutskie, M. F., Dutkevitch, D., Strom, S. E., Edwards, S., Strom, K. M., and Shure, M. A.: 1990, AJ **99**, 1187

Stelzer, B., Frasca, A., Alcalá, J. M., Manara, C. F., Biazzo, K., Covino, E., Rigliaco, E., Testi, L., Covino, S., and D'Elia, V.: 2013, A&A **558**, A141

Stetson, P. B.: 1996, PASP **108**, 851

Strom, K. M., Strom, S. E., Edwards, S., Cabrit, S., and Skrutskie, M. F.: 1989a, AJ **97**, 1451

Strom, S. E., Edwards, S., and Strom, K. M.: 1989b, in H. A. Weaver and L. Danly (eds.), *The Formation and Evolution of Planetary Systems, Cambridge University Press, ISBN-13: 9780521366335*, pp 91–106

Syer, D. and Clarke, C. J.: 1995, MNRAS **277**, 758

Tanaka, H., Takeuchi, T., and Ward, W. R.: 2002, ApJ **565**, 1257

Telleschi, A., Güdel, M., Briggs, K. R., Audard, M., and Palla, F.: 2007, A&A **468**, 425

Terquem, C. E. J. M. L. J.: 2003, MNRAS **341**, 1157

Traficante, A., Fuller, G. A., Pineda, J. E., and Pezzuto, S.: 2015, A&A **574**, A119

Trilling, D. E., Bryden, G., Beichman, C. A., Rieke, G. H., Su, K. Y. L., Stansberry, J. A., Blaylock, M., Stapelfeldt, K. R., Beeman, J. W., and Haller, E. E.: 2008, ApJ **674**, 1086

Tsukagoshi, T., Momose, M., Hashimoto, J., Kudo, T., Andrews, S., Saito, M., Kitamura, Y., Ohashi, N., Wilner, D., Kawabe, R., Abe, L., Akiyama, E., Brandner, W., Brandt, T. D., Carson, J., Currie, T., Egner, S. E., Goto, M., Grady, C., Guyon, O., Hayano, Y., Hayashi, M., Hayashi, S., Henning, T., Hodapp, K. W., Ishii, M., Iye, M., Janson, M., Kandori, R., Knapp, G. R., Kusakabe, N., Kuzuhara, M., Kwon, J., McElwain, M., Matsuo, T., Mayama, S., Miyama, S., Morino, J.-i., Moro-Martín, A., Nishimura, T., Pyo, T.-S., Serabyn, E., Suenaga, T., Suto, H., Suzuki, R., Takahashi, Y., Takami, H., Takami, M., Takato, N., Terada, H., Thalmann, C., Tomono, D., Turner, E. L., Usuda, T., Watanabe, M., Wisniewski, J. P., Yamada, T., and Tamura, M.: 2014, ApJ **783**, 90

Uzpen, B., Kobulnicky, H. A., and Kinemuchi, K.: 2009, AJ **137**, 3329

van der Marel, N., van Dishoeck, E. F., Bruderer, S., Andrews, S. M., Pontoppidan, K. M., Herczeg, G. J., van Kempen, T., and Miotello, A.: 2016, A&A **585**, A58

van der Marel, N., van Dishoeck, E. F., Bruderer, S., Birnstiel, T., Pinilla, P., Dullemond, C. P., van Kempen, T. A., Schmalzl, M., Brown, J. M., Herczeg, G. J., Mathews, G. S., and Geers, V.: 2013, *Science* **340**, 1199

van Eyken, J. C., Ciardi, D. R., Rebull, L. M., Stauffer, J. R., Akeson, R. L., Beichman, C. A., Boden, A. F., von Braun, K., Gelino, D. M., Hoard, D. W., Howell, S. B., Kane, S. R., Plavchan, P., Ramírez, S. V., Bloom, J. S., Cenko, S. B., Kasliwal, M. M., Kulkarni, S. R., Law, N. M., Nugent, P. E., Ofek, E. O., Poznanski, D., Quimby, R. M., Grillmair, C. J., Laher, R., Levitan, D., Mattingly, S., and Surace, J. A.: 2011, AJ **142**, 60

van Eyken, J. C., Ciardi, D. R., von Braun, K., Kane, S. R., Plavchan, P., Bender, C. F., Brown, T. M., Crepp, J. R., Fulton, B. J., Howard, A. W., Howell, S. B., Mahadevan, S., Marcy, G. W., Shporer, A., Szkody, P., Akeson, R. L., Beichman, C. A., Boden, A. F., Gelino, D. M., Hoard, D. W., Ramírez, S. V., Rebull, L. M., Stauffer, J. R., Bloom, J. S., Cenko, S. B., Kasliwal, M. M., Kulkarni, S. R., Law, N. M., Nugent, P. E., Ofek, E. O., Poznanski, D., Quimby, R. M., Walters, R., Grillmair, C. J., Laher, R., Levitan, D. B., Sesar, B., and Surace, J. A.: 2012, ApJ **755**, 42

Vanderplas, J., Connolly, A., Ivezić, Ž., and Gray, A.: 2012, in *Conference on Intelligent Data Understanding (CIDU), ISBN:978-1-4673-4625-2*, pp 47 –54

Venuti, L., Bouvier, J., Flaccomio, E., Alencar, S. H. P., Irwin, J., Stauffer, J. R., Cody, A. M., Teixeira, P. S., Sousa, A. P., Micela, G., Cuillandre, J.-C., and Peres, G.: 2014, A&A **570**, A82

Ward, W. R.: 1997, **126**, 261

Ward, W. R. and Hahn, J. M.: 2000, *Protostars and Planets IV, ISBN 13: 9780816520596* p. 1135

Weingartner, J. C. and Draine, B. T.: 2001, ApJ **548**, 296

Werner, M. W., Roellig, T. L., Low, F. J., Rieke, G. H., Rieke, M., Hoffmann, W. F., Young, E., Houck, J. R., Brandl, B., Fazio, G. G., Hora, J. L., Gehrz, R. D., Helou, G., Soifer, B. T., Stauffer, J., Keene, J., Eisenhardt, P., Gallagher, D., Gautier, T. N., Irace, W., Lawrence, C. R., Simmons, L., Van

Cleve, J. E., Jura, M., Wright, E. L., and Cruikshank, D. P.: 2004, ApJS **154**, 1

White, R. J. and Hillenbrand, L. A.: 2003, in *American Astronomical Society Meeting Abstracts*, Vol. 35 de *Bulletin of the American Astronomical Society*, p. 1366

Wilking, B. A., Gagné, M., and Allen, L. E.: 2008, *Star Formation in the ρ Ophiuchi Molecular Cloud*, p. 351, Reipurth, Bo; ISBN:978-1-58381-671-4

Wilking, B. A., Lada, C. J., and Young, E. T.: 1989, ApJ **340**, 823

Wilking, B. A., Meyer, M. R., Robinson, J. G., and Greene, T. P.: 2005, AJ **130**, 1733

Williams, J. P. and Cieza, L. A.: 2011, ARA&A **49**, 67

Wootten, A. and Thompson, A. R.: 2009, *IEEE Proceedings* **97**, 1463

Wright, E. L., Eisenhardt, P. R. M., Mainzer, A. K., Ressler, M. E., Cutri, R. M., Jarrett, T., Kirkpatrick, J. D., Padgett, D., McMillan, R. S., Skrutskie, M., Stanford, S. A., Cohen, M., Walker, R. G., Mather, J. C., Leisawitz, D., Gautier, III, T. N., McLean, I., Benford, D., Lonsdale, C. J., Blain, A., Mendez, B., Irace, W. R., Duval, V., Liu, F., Royer, D., Heinrichsen, I., Howard, J., Shannon, M., Kendall, M., Walsh, A. L., Larsen, M., Cardon, J. G., Schick, S., Schwalm, M., Abid, M., Fabinsky, B., Naes, L., and Tsai, C.-W.: 2010, AJ **140**, 1868

Wyatt, M. C.: 2008, ARA&A **46**, 339

Xiang-Gruess, M. and Papaloizou, J. C. B.: 2013, MNRAS **431**, 1320

Yu, L., Winn, J. N., Gillon, M., Albrecht, S., Rappaport, S., Bieryla, A., Dai, F., Delrez, L., Hillenbrand, L., Holman, M. J., Howard, A. W., Huang, C. X., Isaacson, H., Jehin, E., Lendl, M., Montet, B. T., Muirhead, P., Sanchis-Ojeda, R., and Triaud, A. H. M. J.: 2015, ApJ **812**, 48

Zuckerman, B. and Song, I.: 2004, ARA&A **42**, 685